JOURNAL OF THE ELECTROCHEMICAL SOCIETY

ELECTROCHEMICAL
CIENCE AND TECHNOLOGY

SOL STATE
SCIENCE AND TECHNOLOGY

EWS AND NEWS
for Papers
hiladelphia, Pennsylvania,
Meeting

VOL. 133, NO. 11 NOVEMBER 1986

JESOAN 133 (11) 2215-2440, 435C-472C

FUTURE MEETINGS

PHILADELPHIA, PENNSYLVANIA—MAY 10-15, 1987—HEADQUARTERS AT ADAM'S MARK HOTEL

See the detailed Call for Papers published in the July-November 1986 issues of **This Journal.** Final program to be published in the March 1987 issue of **This Journal.**

HONOLULU, HAWAII—OCTOBER 18-23, 1987—HEADQUARTERS AT HILTON HAWAIIAN VILLAGE

Cosponsored by The Electrochemical Society of Japan and with the cooperation of The Japan Society of Applied Physics.

The detailed Call for Papers will be published in the December 1986-April 1987 issues of **This Journal.** Final program to be published in the August 1987 issue of **This Journal.**

Planned symposia for the Honolulu Meeting include the following Divisions, Groups, and subjects. **Battery**—Lithium Batteries; Load Leveling; Manganese Dioxide; General Session. **Battery/High Temperature Materials/Corrosion**—High Temperature Fuel Cells. **Corrosion**—Corrosion, Electrochemistry, and Catalysis of Metallic Glasses; Statistical Aspects of Corrosion Science and Engineering; General Session. **Corrosion/High Temperature Materials**—Corrosion in High Temperature Aqueous Solutions. **Corrosion/Physical Electrochemistry**—Stress Corrosion Cracking. **Dielectrics and Insulation**—Low Temperature Electronics. **Dielectrics and Insulation/Electronics**—Dielectric Films for Compound Semiconductors; Laser Processes for Microelectronic Applications; Polymeric Materials for IC's. **Dielectrics and Insulation/Luminescence and Display Materials/Electronics**—Patterning Science and Technology. **Electrodeposition**—Electroless Plating; Surface Finishing for Electronics; General Session. **Electrodeposition/Corrosion**—Corrosion Resistance of Metallic Coatings. **Electronics**—Amorphous Semiconductors; Second International Symposium on Silicon Molecular Beam Epitaxy; Process Induced Defects in Device Degradation. **Electronics/Dielectrics and Insulation**—Automated IC Manufacturing III; State-of-the-Art Program on Compound Semiconductors VII; Joint General Session; Joint Recent News Papers Session. **Electronics/Dielectrics and Insulation/High Temperature Materials**—Symposium on Advanced Materials Technologies for the 21st Century. **Energy Technology**—Energy Storage Systems for Remote Applications. **Energy Technology/Dielectrics and Insulation/High Temperature Materials**—Materials and New Processing Technologies for Photovoltaics. **Energy Technology/Organic and Biological Electrochemistry**—Biomass Electrochemistry. **Energy Technology/Physical Electrochemistry**—Photoelectrochemistry and Electrosynthesis on Semiconducting Electrodes; Membrane Processes in Electrosynthesis. **High Temperature Materials**—High Temperature Materials Chemistry IV. **High Temperature Materials/Dielectrics and Insulation**—Electro-Ceramics and Solid-State Ionics; Properties and Processing of Magnetic Thin Films. **High Temperature Materials/Dielectrics and Insulation/Electronics**—Tenth Int'l Conference on Chemical Vapor Deposition. **Industrial Electrolytic**—Electrochemical Engineering of Chlor-Alkali and Chlorate Cells; The Future of the Chlor-Alkali Industry. **Luminescence and Display Materials**—CRT Manufacture and New CRT Technologies; Electroluminescence; Optical Imaging: IR Light Sources, Detectors, and Imaging Techniques; Physics and Chemistry of CRT Phosphors; Rare Earth Phosphors: Spectroscopy and Technology; Science and Technology of Laser Materials; General Session; Recent News Papers Session. **Luminescence and Display Materials/Dielectrics and Insulation**—Materials and Fabrication Techniques for Storage Displays. **Organic and Biological Electrochemistry**—Redox Mechanism and Interfacial Behavior of Molecules; Organic Electrosynthesis; General Session. **Organic and Biological Electrochemistry/Physical Electrochemistry**—Bioanalytical Chemistry. **Physical Electrochemistry**—Modified Electrodes; General Session. **Physical Electrochemistry/High Temperature Materials**—Sixth International Symposium on Molten Salts. **Physical Electrochemistry/Organic and Biological Electrochemistry**—Research in Electrochemical and Spectroelectrochemical Chemistry. **Joint Society Symposium**—Sensors.

ATLANTA, GEORGIA—MAY 15-20, 1988—HEADQUARTERS AT THE ATLANTA HILTON HOTEL

The detailed Call for Papers will be published in the July-November 1987 issues of **This Journal.** Final program to be published in the March 1988 issue of **This Journal.**

Planned symposia for the Atlanta Meeting include the following Divisions, Groups, and subjects. **Battery**—General Session; Solid Materials for Energy Conversion and Storage. **Corrosion**—General Session. **Dielectrics and Insulation**—Applications of Colloidal Dielectrics. **Dielectrics and Insulation/Electronics**—Deposition of Insulating Films from Metallo-Organics; Packaging of Electronics Devices; Plasma Processing; Pulse Annealing; Reliability for Microelectronics. **Electronics**—Symposium on Manufacturing Methods for III-V Compound Devices and Circuits. **Electronics/Dielectrics and Insulation**—First International Symposium on Advanced Materials; Materials and Technology for Radiation Hardened Devices; Physics and Chemistry of Thermally Oxidized Silicon; State-of-the-Art Program on Compound Semiconductors VIII; Joint General Session; Joint Recent News Papers Session. **Energy Technology**—Applications of Amorphous Materials in Energy Conversion and Storage; Electrochemical Technologies for Manufacturing in Space; General Session. **Energy Technology Battery/Physical Electrochemistry**—Energy Conversion and Storage Aspects of Conductive Polymers. **Energy Technology/High Temperature Materials**—Chemistry and Physics of Composite Media. **High Temperature Materials**—Electrochemical Phenomenon at High Temperature Interfaces; High Temperature Lamp Chemistry; Physics and Chemistry of Porous Media. **High Temperature Materials/Corrosion**—Oxidation of High Temperature Refractory Metals and Alloys. **High Temperature Materials/Physical Electrochemistry/Corrosion**—Studies of Interfacial Reactions Using Surface Analytical Techniques. **Industrial Electrolytic**—Electrochemistry in Mineral and Metal Processing II; Tutorial on the Fundamentals of Mineral and Metals Processing. **Industrial Electrolytic/High Temperature Materials**—Advanced Ceramics for Electrochemical Applications; Tutorial on Advanced Ceramics for Electrochemical Applications. **Organic and Biological Electrochemistry**—Reactivity in Organic Chemistry and Electrochemistry II; General Session. **Physical Electrochemistry**—Physical Chemistry of Electrolytes; Substrate Morphology and Single Crystal Surfaces; The Transfer Coefficient—A Critical Assessment; Ultramicroelectrodes; X-Ray Characterization in Electrochemistry; General Session. **Physical Electrochemistry/Battery** Fundamentals of Active Metal Battery Electrodes. **New Technology Subcommittee/Industrial Electrolytic**—Numerical and Analog Simulation of Heat Mass and Fluid Flows Applied to Process Technologies.

THE ELECTROCHEMICAL SOCIETY BOOKS IN PRINT

Society Proceedings Series
1982-1986

The following softbound proceedings volumes are sponsored and published by The Electrochemical Society, Inc., 10 South Main Street, Pennington, NJ 08534-2896. Orders filled at the list price given, subject to availability. Enclose payment with order.

Semiconductor Technology. D. A. Doane, D. B. Fraser, and D. W. Hess, Editors. A 1982 symposium. 264 pages, **$18.00.**

VLSI Science and Technology. C. J. Dell'Oca and W. M. Bullis, Editors. A 1982 symposium. 392 pages, **$20.00.**

Materials and New Processing Technologies for Photovoltaics. J. P. Dismukes, E. Sirtl, P. Rai-Choudhury, and L. P. Hunt, Editors. A 1982 symposium. 544 pages, **$25.00.**

Inorganic Resist Systems. D. A. Doane and A. Heller, Editors. A 1982 symposium. 320 pages, **$15.00.**

Transport Processes In Electrochemical Systems. R. S. Yeo, T. Katan, and D-T. Chin, Editors. A 1982 symposium. 288 pages, **$18.00.**

Electron and Ion Beam Science and Technology, Tenth International Conference. R. Bakish, Editor. A 1982 symposium. 474 pages, **$30.00.**

Membranes and Ionic and Electronic Conducting Polymers. E. B. Yeager, B. Schumm, Jr., K. Mauritz, K. Abbey, D. Blankenship, and J. Akridge, Editors. A 1982 symposium. 380 pages, **$22.00.**

Corrosion in Fossil Fuel Systems. I. G. Wright, Editor. A 1982 symposium. 522 pages, **$20.00.**

Electrochemical Process and Plant Design. R. C. Alkire, T. R. Beck, and R. D. Varijian, Editors. A 1982 symposium. 288 pages, **$20.00.**

Electroplating Engineering and Waste Recycle—New Developments and Trends. D. D. Snyder, U. Landau, and R. Sard, Editors. A 1982 symposium. 428 pages, **$22.00.**

Porous Electrodes: Theory and Practice. H. C. Maru, T. Katan, and M. G. Klein, Editors. A 1982 symposium. 492 pages, **$18.00.**

Molten Carbonate Fuel Cell Technology. J. R. Selman and T. D. Claar, Editors. A 1982 symposium. 533 pages, **$15.00.**

High Temperature Materials Chemistry II. Z. A. Munir and D. Cubicciotti, Editors. A 1983 symposium. 480 pages, **$30.00.**

Silicon Nitride Thin Insulating Films. V. J. Kapoor and H. J. Stein, Editors. A 1983 symposium. 522 pages, **$25.00.**

Defects in Silicon. W. M. Bullis and L. C. Kimerling, Editors. A 1983 symposium. 660 pages, **$30.00.**

Plasma Processing. G. S. Mathad, G. C. Schwartz, and G. Smolinsky, Editors. A 1983 symposium. 660 pages, **$35.00.**

Materials and New Processing Technologies for Photovoltaics. J. A. Amick, V. K. Kapur, and J. Dietl, Editors. A 1983 symposium. 512 pages, **$25.00.**

III-V Opto-Electronics Epitaxy and Device Related Processes. V. G. Keramidas and S. Mahajan, Editors. A 1983 symposium. 289 pages, **$25.00.**

Lithium Batteries. A. N. Dey, Editor. A 1983 symposium. 460 pages, **$35.00.**

Fourth International Symposium on Molten Salts. M. Blander, D. S. Newman, M-L. Saboungi, G. Mamantov, and K. Johnson, Editors. A 1983 symposium. 776 pages, **$35.00.**

Fundamental Aspects of Corrosion Protection by Surface Modification. E. McCafferty, C. R. Clayton, and J. Oudar, Editors. A 1983 symposium. 364 pages, **$25.00.**

Advances In Battery Materials and Processes. J. McBreen, R. S. Yeo, D-T. Chin, and A. C. C. Tseung, Editors. A 1983 symposium. 320 pages, **$26.00.**

The Electrochemistry of Carbon. S. Sarangapani, J. R. Akridge, and B. Schumm, Editors. A 1983 symposium. 648 pages, **$32.00.**

The Chemistry and Physics of Electrocatalysis. J. D. E. McIntyre, M. J. Weaver, and E. B. Yeager, Editors. A 1983 symposium. 684 pages, **$27.00.**

7/86

Ninth International Conference on Chemical Vapor Deposition. McD. Robinson, C. H. J. van den Brekel, G. W. Cullen, J. M. Blocher, Jr., and P. Rai-Choudhury, Editors. A 1984 symposium. 824 pages. **$36.00.**

VLSI Science and Technology/1984. K. E. Bean and G. A. Rozgonyi, Editors. A 1984 symposium. 520 pages, **$30.00.**

Equilibrium Diagrams; Localized Corrosion. R. P. Frankenthal and J. Kruger, Editors. A 1984 symposium. 611 pages, **$36.00.**

Electrochemistry in Mineral and Metal Processing. P. E. Richardson, S. Srinivasan, and R. Woods, Editors. A 1984 symposium. 677 pages, **$30.00.**

Advances in the Chlor-Alkali and Chlorate Industry. M. M. Silver and E. M. Spore, Editors. A 1984 symposium. 374 pages, **$18.00.**

Computer Aided Acquisition and Analysis of Corrosion Data. M. W. Kendig, U. Bertocci, and J. E. Strutt, Editors. A 1984 symposium. 276 pages, **$17.00.**

Manganese Dioxide Electrode Theory and Practice for Electrochemical Applications. B. Schumm, Jr., R. L. Middaugh, M. P. Grotheer, and J. C. Hunter, Editors. A 1984 symposium. 696 pages, **$40.00.**

Electromigration of Metals/Multilevel Metallization and Packaging. J. R. Lloyd, R. A. Levy, J. Pierce, and R. G. Frieser, Editors. A 1984 symposium. 201 pages, **$16.00.**

Materials and New Processing Technologies for Photovoltaics. V. K. Kapur, J. P. Dismukes, and S. Pizzini, Editors. A 1984 symposium. 432 pages, **$27.00.**

Advances in Lead-Acid Batteries. K. R. Bullock and D. Pavlov, Editors. A 1984 symposium. 548 pages, **$28.00.**

Plasma Processing. G. S. Mathad, G. C. Schwartz, and G. Smolinsky, Editors. A 1984 symposium. 636 pages, **$40.00.**

High Temperature Lamp Chemistry. E. G. Zubler, Editor. A 1985 symposium. 340 pages, **$25.00.**

VLSI Science and Technology/1985. W. M. Bullis and S. Broydo, Editors. A 1985 symposium. 572 pages, **$35.00.**

Silicon Molecular Beam Epitaxy. J. C. Bean, Editor. A 1985 symposium. 455 pages, **$36.00.**

The Chemistry and Physics of Composite Media. M. Tomkiewicz and P. N. Sen, Editors. A 1985 symposium. 373 pages, **$35.00.**

Molten Salts. M.-L. Saboungi, D. S. Newman, K. Johnson, and D. Inman, Editors. A 1985 symposium. 612 pages, **$45.00.**

High Temperature Materials Chemistry—III. Z. A. Munir and D. Cubicciotti, Editors. A 1985 symposium. 346 pages, **$37.00.**

Dielectric Films on Compound Semiconductors. V. J. Kapoor, D. J. Connolly, and Y. H. Wong, Editors. A 1985 symposium. 372 pages, **$27.00.**

Engineering of Industrial Electrolytic Processes. U. Landau, R. E. White and R. D. Varjian, Editors. A 1985 symposium. 292 pages, **$20.00.**

Reduced Temperature Processing for VLSI. R. Reif and G. R. Srinivasan, Editors. A 1985 symposium. 600 pages, **$45.00.**

Corrosion Effects of Acid Deposition and Corrosion of Electronic Materials. F. Mansfeld, V. Kucera, S. E. Haagenrud, F. H. Haynie, and J. D. Sinclair, Editors. A 1985 symposium. 400 pages, **$28.00.**

Semiconductor Silicon/1986. H. R. Huff, T. Abe, and B. Kolbesen, Editors. A 1986 symposium. 1096 pages, **$55.00.**

Fundamental Aspects of High Temperature Corrosion—II. D. A. Shores and G. J. Yurek, Editors. A 1986 symposium, **$22.00.**

Surfaces, Inhibition, and Passivation. E. McCafferty and R. J. Brodd, Editors. A 1986 symposium, **$40.00.**

EDITOR
Norman Hackerman
Jackie Bourne, Assistant to the Editor

DIVISIONAL AND GROUP EDITORS

BATTERY
R. J. Brodd
Elton J. Cairns
Eugene G. Gagnon
G. F. Nordblom
Darrel Untereker

CORROSION
J. W. Faust, Jr.
R. P. Frankenthal
H. S. Isaacs
Barry R. MacDougall
Florian Mansfeld
Ken Nobe
W. H. Smyrl

DIELECTRICS AND INSULATION
Robert S. Alwitt
Rudolf G. Frieser
Dennis Hess
Vikram J. Kapoor
S. P. Murarka
George L. Schnable
Alan W. Swanson

ELECTRODEPOSITION
Ugo Bertocci
Huk Y. Cheh
Y. Okinaka
Mordechay Schlesinger

ELECTRONICS
John M. Andrews
Ted F. Ciszek
George R. Cronin
S. J. Fonash
D. W. Greve
James S. Harris
Eugene A. Irene
Subhash Mahajan
David L. Nelson
Arnold Reisman
Bertram Schwartz
Thomas O. Sedgwick
Don W. Shaw
G. R. Srinivasan
Ben Streetman
C. C. Wang
P. Wang
J. M. Woodall

ENERGY TECHNOLOGY GROUP
Vijay K. Kapur
Kim Kinoshita
A. R. Landgrebe
Bruce Parkinson
S. Srinivasan
M. Tomkiewicz

HIGH TEMPERATURE MATERIALS
William A. Adams
E. D. Cater
J. V. Cathcart
Daniel Cubicciotti
Lee P. Hunt
Peter J. Meschter
Zuhair A. Munir
T. A. Ramanarayanan
David A. Shores
Donald R. Vissers
Gene F. Wakefield

INDUSTRIAL ELECTROLYTIC
Richard C. Alkire
Ronald L. Dotson
Scott Lynn

LUMINESCENCE AND DISPLAY MATERIALS GROUP
Harry G. Brittain
Henry F. Ivey
Simon Larach
Melvin Tecotzky

ORGANIC AND BIOLOGICAL ELECTROCHEMISTRY
Martin Blank
Glenn Dryhurst
John H. Wagenknecht
Stanley Wawzonek

PHYSICAL ELECTROCHEMISTRY
James L. Anderson
Gregory C. Farrington
David S. Ginley
Adam Heller
Paul A. Kohl
Nathan S. Lewis
Joseph T. Maloy
Gleb Mamantov
Barry Miller
William E. O'Grady
Robert A. Osteryoung
C. W. Tobias

News Editor—Jack H. Westbrook

JOURNAL OF THE
ELECTROCHEMICAL SOCIETY
(USPS 284-140)
ISSN 0013-4651

The JOURNAL OF THE ELECTROCHEMICAL SOCIETY (USPS 284-140) is published monthly by The Electrochemical Society, Inc. at 215 Canal St., Manchester, NH 03108. The address for the Executive Offices, Editorial and Advertising Office, and Circulation Department of The Electrochemical Society, Inc., is 10 South Main St., Pennington, NJ 08534-2896. Subscription to members as part of membership service; subscription to nonmembers $195.00 plus $20.00 for postage outside U.S. and Canada. Single copies $8.00 to members, $18.00 to nonmembers. © Copyright 1986 by The Electrochemical Society, Inc. Second Class Postage paid at Pennington, New Jersey and at additional mailing offices.

POSTMASTER: Send address changes to THE ELECTROCHEMICAL SOCIETY, INC., 10 South Main St., Pennington, NJ 08534-2896.

NOVEMBER 1986

ELECTROCHEMICAL SCIENCE AND TECHNOLOGY

TECHNICAL PAPERS

Physico-Chemical Properties of Calcium Zincate ..... *R. A. Sharma* 2215

Adsorption and Absorption of Chloride Ions on Passive Iron Systems ..... *V. Jovancicevic, J. O'M. Bockris, J. L. Carbajal, P. Zelenay, T. Mizuno* 2219

Electrochemistry in Liquid Crystals. Orientational Effects in Electrochemical Processes ..... *A. M. Serra, R. D. Mariani, H. D. Abruña* 2226

Palladium/Hydrogen Membrane Electrode for High Temperature/High Pressure Aqueous Solutions ..... *Z. Nagy, R. M. Yonco* 2232

Enhanced Raman Scattering of 1,2,4-Triazole and Imidazole Adsorbed on Microlithographically Prepared Copper Surfaces ..... *D. Thierry, C. Leygraf* 2236

The Dissolution Mechanism of Iron in Chloride Solutions ..... *D. R. MacFarlane, S. I. Smedley* 2240

Laser-Controlled Wet Chemical Etching for Corrective Trimming of Thin Films. Application to Aluminum ..... *J. Y. Tsao, D. J. Ehrlich* 2244

Effect of Low Temperature Thermal Aging on Rheological Properties and Moldability Performance of Molding Compounds ..... *K. K. Chakravorty, C. R. Sporck, D. Malladi* 2248

Voltammetric Studies of Porous Molybdenum Electrodes for the Alkali Metal Thermoelectric Converter ..... *R. M. Williams, C. P. Bankston, S. K. Khanna, T. Cole* 2253

New Types of Anodes for the Oxygen Evolution Reaction in Acidic Solution. $IrO_2/TiO_2/Ti$ ..... *Y. Matsumoto, T. Tazawa, N. Muroi, E.-i. Sato* 2257

A Comparison of the Properties of CF_3SO_3H and H_3PO_4 in Relation to Fuel Cells ..... *P. Zelenay, B. R. Scharifker, J. O'M. Bockris, D. Gervasio* 2262

Glow Discharge Electrolysis of Aqueous Sulfuric Acid Solution in Various Atmosphere ..... *Y. Kanzaki, M. Hirabe, O. Matsumoto* 2267

Influence of Surface Processes on Electrical, Photochemical, and Thermodynamical Properties of Zinc Oxide Films ..... *P. Bonasewicz, W. Hirschwald, G. Neumann* 2270

An Improved Method for the Electrochemical C-V Profiling of Indium Phosphide ..... *R. T. Green, D. K. Walker, C. M. Wolfe* 2278

Impedance Spectra of p-Type Porous Si-Electrolyte Interfaces ..... *N. Koshida, M. Nagasu, K. Echizenya, Y. Kiuchi* 2283

[illegible] 3530

ELECTROCHEMICAL SOCIETY

Vol. 133 • No. 11

Time-Resolved Photoelectrochemical Measurements on Surface-Modified n- and p-InP Electrodes
R. L. Cook, P. F. Dempsey, A. F. Sammells 2287

Adsorbed Species on Nickel in Electrolyte Solutions
C. J. van der Wekken 2293

Precipitation of Solids in Electrochemical Cells
K.-C. Tsaur, R. Pollard 2296

Investigations of Sputtered Thin Film TiO_2 Electrodes with Low Donor Densities
M. Nakao, R. Schumacher, R. N. Schindler 2308

SOLID-STATE SCIENCE AND TECHNOLOGY

TECHNICAL PAPERS

The Plasma Etching of Polysilicon with CF_3Cl/Argon Discharges. I. Parametric Modeling and Impedance Analysis
K. D. Allen, H. H. Sawin, M. T. Mocella, M. W. Jenkins 2315

The Plasma Etching of Polysilicon with CF_3Cl/Argon Discharges. II. Modeling of Ion Bombardment Energy Distributions
K. D. Allen, H. H. Sawin 2326

The Plasma Etching of Polysilicon with CF_3Cl/Argon Discharges. III. Modeling of Etching Rate and Directionality
K. D. Allen, H. H. Sawin, A. Yokozeki 2331

Ellipsometric and Optical Study of Amorphous Hydrogenated Carbon Films
S. A. Alterovitz, J. D. Warner, D. C. Liu, J. J. Pouch 2339

Microstructure and Magnetic Properties of Electroless Plated Co-Ni-P and Co-P Thin Films for Magnetic Recording
E. L. Nicholson, M. R. Khan 2342

Metalization of AlN Ceramics by Electroless Ni-P Plating
T. Osaka, H. Nagata, E. Nakajima, I. Koiwa, K. Utsumi 2345

Theoretical and Empirical Studies of Impurity Incorporation into β-SiC Thin Films during Epitaxial Growth
H. J. Kim, R. F. Davis 2350

Fabrication of High Voltage Polysilicon TFT's on an Insulator
R. Pennell, R. Catero, S. Lovelis 2358

Rapid Thermal Oxidation of Silicon
S. T. Ang, J. J. Wortman 2361

On the Effect of Impurities on the Photovoltaic Behavior of Solar Grade Silicon. II. Influence of Titanium, Vanadium, Chromium, Iron, and Zirconium on Photovoltaic Behavior of Polycrystalline Solar Cells
S. Pizzini, L. Bigoni, M. Beghi, C. Chemelli 2363

Growth Kinematics of a Polysilicon Trench Refill Process
V. J. Silvestri 2374

DIVISIONS AND GROUPS

Battery Division
Sidney Gross, Chairman
Eugene Gagnon, Vice-Chairman
James McBreen, Secretary-Treasurer
Brookhaven National Laboratory
DAS Building 801
Upton, NY 11973
Ronald G. Gunther, Division Advisor

Corrosion Division
Edward McCafferty, Chairman
Robert A. Rapp, Vice-Chairman
Ronald B. Diegle, Secretary-Treasurer
11515 Manitoba NE
Albuquerque, NM 87111
Rolf H. Muller, Division Advisor

Dielectrics and Insulation Division
Robert B. Comizzoli, Chairman
John L. Mauer IV, Vice-Chairman
John P. Dismukes, Treasurer
Geraldine C. Schwartz, Secretary
IBM Corporation
East Fishkill Facility
Hopewell Junction, NY 12533
Werner Kern, Division Advisor

Electrodeposition Division
Mordechay Schlesinger, Chairman
David S. Lashmore, Vice-Chairman
Uziel Landau, Secretary-Treasurer
Department of Chemical Engineering
Case Western Reserve University
Cleveland, OH 44118
Ronald G. Gunther, Division Advisor

Electronics Division
Patricia L. Castro, Chairman
W. Murray Bullis, Vice-Chairman
Howard R. Huff, Vice-Chairman
Kenneth E. Bean, Treasurer
Stella W. Pang, Secretary
Massachusetts Institute of Technology
Lincoln Laboratory
244 Wood St.
Lexington, MA 02173
Werner Kern, Division Advisor

Energy Technology Group
Hansraj C. Maru, Chairman
David S. Ginley, Vice-Chairman
Micha Tomkiewicz, Treasurer
Vinod Jalan, Secretary
158 Hill St.
Concord, MA 01742
Ronald G. Gunther, Group Advisor

High Temperature Materials Division
Wayne L. Worrell, Chairman
Zuhair A. Munir, Senior Vice-Chairman
Vishu D. Dosaj, Junior Vice-Chairman
David A. Shores, Secretary-Treasurer
Corrosion Research Center
151 Amundson Hall
421 Washington Ave. SE
Minneapolis, MN 55455
Werner Kern, Division Advisor

Industrial Electrolytic Division
W. Bruce Darlington, Chairman
Marino Y. C. Woo, Vice-Chairman
Ralph E. White, Secretary-Treasurer
Department of Chemical Engineering
Texas A&M University
College Station, TX 77843
Ronald G. Gunther, Division Advisor

Luminescence and Display Materials Group
C. W. Struck, Chairman
R. O. Petersen, Vice-Chairman
W. M. Yim, Secretary-Treasurer
RCA Laboratories
David Sarnoff Research Center
Princeton, NJ 08540
Edward Nicollian, Group Advisor

Organic and Biological Electrochemistry Division
P. Zuman, Chairman
D. Evans, Vice-Chairman
G. Dryhurst, Secretary-Treasurer
Department of Chemistry
University of Oklahoma
620 Parrington Oval
Norman, OK 73019
Rolf H. Muller, Division Advisor

Physical Electrochemistry Division
Larry R. Faulkner, Chairman
Barry Miller, Vice-Chairman
Rolf H. Muller, Secretary-Treasurer
30 High Gate Rd.
Berkeley, CA 94707
Rolf H. Muller, Division Advisor

SOCIETY OFFICERS AND STAFF

Ronald E. Enstrom, President
RCA Laboratories
Princeton, NJ 08540

Fritz G. Will, Vice-President
General Electric Company
Research and Development Center
Schenectady, NY 12301

Bruce E. Deal, Vice-President
Fairchild Camera & Instrument Corporation
Palo Alto, CA 94304

Elton J. Cairns, Vice-President
Lawrence Berkeley Laboratory
University of California
Berkeley, CA 94720

James A. Amick, Secretary
Exxon Research & Engineering Company
Clinton Township
Route 22 East
Annandale, NJ 08801

Robert P. Frankenthal, Treasurer
AT&T Bell Laboratories
Murray Hill, NJ 07974

V. H. Branneky, Executive Secretary
The Electrochemical Society, Inc.
10 South Main Street
Pennington, NJ 08534-2896

Roque J. Calvo, Assistant Executive Secretary
The Electrochemical Society, Inc.
10 South Main Street
Pennington, NJ 08534-2896

PUBLICATION STAFF

Sarah A. Kilfoyle, **Director of Publications**

PUBLICATION COMMITTEE

Lee P. Hunt, Chairman
James A. Amick
Norman Hackerman
Bertram Schwartz
Boone B. Owens
Klavs F. Jensen
Philip N. Ross Jr.
Joseph T. Maloy
Patricia P. Trzaskoma

Manuscripts submitted to the JOURNAL should be sent in triplicate to the Editorial Office at 10 South Main Street, Pennington, NJ 08534-2896, telephone: 609-737-1902. They should conform to the revised "Instructions to Authors" available from Society Headquarters. Manuscripts so submitted, as well as papers presented before a Society technical meeting, become the property of the Society and may not be published elsewhere in whole or in part without written permission of the Society. Address such requests to the Editor.

The Electrochemical Society does not maintain a supply of reprints of papers appearing in its JOURNAL. A photoprint copy of any particular paper may be obtained from University Microfilms, Inc., 300 N. Zeeb St., Ann Arbor, MI 48106.

Inquiries regarding positive microfilm copies of issues should be addressed to University Microfilms, Inc., 300 N. Zeeb St., Ann Arbor, MI 48106.

Walter J. Johnson, Inc., 355 Chestnut St., Norwood, NJ 07648, have reprint rights to out-of-print volumes of the JOURNAL, and also have available for sale back volumes and single issues with the exception of the last eight calendar years.

The JOURNAL OF THE ELECTROCHEMICAL SOCIETY combines the JOURNAL and TRANSACTIONS OF THE ELECTROCHEMICAL SOCIETY. Statements and opinions given in articles and papers in the JOURNAL OF THE ELECTROCHEMICAL SOCIETY are those of the contributors, and The Electrochemical Society, Inc. assumes no responsibility for them.

Claims for a missing issue should be reported within 60 days of normal delivery date to the Circulation Dept., The Electrochemical Society, Inc., 10 South Main Street, Pennington, NJ 08534-2896.

Notice of a change in address should be sent to the Circulation Dept., The Electrochemical Society, Inc., 10 South Main Street, Pennington, NJ 08534-2896. Include the mailing label or the number from the mailing label from your previous issue of the JOURNAL to ensure proper identification.

SOLID-STATE SCIENCE (Cont.)

Accuracy of the Four-Terminal Measurement Techniques for Determining Contact Resistance
A. A. Naem, D. A. Smith 2377

Polycrystalline Silicon Oxidation Kinetics and Si/SiO_2 Interface Width
G. Queirolo, G. Ghidini, L. Meda, C. Signorini, A. Armigliato 2381

An Environment-Insensitive Trilayer Structure for Titanium Silicide Formation
M.-Z. Lin, Y.-C. S. Yu, C.-Y. Wu 2386

Palladium Silicide Ohmic Contacts to Shallow Junctions in Silicon
R. N. Singh, D. W. Skelly, D. M. Brown 2390

Novolac Resin Planarization Layers for Multilayer Resist Imaging Systems
T. R. Pampalone, J. J. DiPiazza, D. P. Kanen 2394

The Heat of Formation of Mercury Vacancies in $Hg_{0.8}Cd_{0.2}Te$
H. Wiedemeier, S. B. Trivedi, R. C. Whiteside, W. Palosz 2399

Thermoplastic Deformation of Silicon Wafers
A. E. Widmer, W. Rehwald 2403

Stability of Molten Carbonate Fuel Cell Nickel Anodes
C. D. Iacovangelo 2410

Dopant Redistribution during Prebake and Epitaxial Deposition
H. H. Lee 2416

Applications of Redox Contacts for Metal and Semiconductor Rotating Ring-Disk Electrodes
L. F. Schneemeyer, J. M. Rosamilia, B. Miller 2423

TECHNICAL NOTES

The Characterization of Via-Filling Technology with Electroless Plating Method
Y. Harada, K. Fushimi, S. Madokoro, H. Sawai, S. Ushio 2428

Using Photoresist Photosensitivity Values to Maintain Critical Dimensions
T. R. Pampalone, A. M. Gillfillan 2430

ACCELERATED BRIEF COMMUNICATIONS

The Electron Energy Loss Imaging Microscope. A New Look at Oxide Scales
D. F. Mitchell, M. J. Graham 2433

Microelectrodes in Corrosion Studies. Electrodissolution and Corrosion of Copper in H_2O_2/0.1*N* HCl
R. T. Atanasoski, H. S. White, W. H. Smyrl 2435

A Highly Conductive Li^+-Glass System. $(1 - x)(0.4SiS_2\text{-}0.6Li_2S)\text{-}xLiI$
J. H. Kennedy, Y. Yang 2437

Electrochemical and Spectroscopic Studies of Metal Hexacyanoferrate Films. II. Cupric Hexacyanoferrate and Prussian Blue Layered Films
L. M. Siperko, T. Kuwana 2439

REVIEWS AND NEWS

NEWS 439C

Call for Papers—Philadelphia, Pennsylvania, Meeting 467C

JOURNAL OF THE ELECTROCHEMICAL SOCIETY

ELECTROCHEMICAL SCIENCE AND TECHNOLOGY

NOVEMBER 1986

Physico-Chemical Properties of Calcium Zincate

Ram A. Sharma*

General Motors Research Laboratories, Electrochemistry Department, Warren, Michigan 48090

ABSTRACT

Pure, crystalline, fine particulate calcium zincate was prepared. Its chemical composition, $Ca(OH)_2 \cdot 2Zn(OH)_2 \cdot 2H_2O$ was established by chemical analysis, weight loss in thermogravimetric analysis, and by x-ray powder diffraction pattern. Its solubility in different KOH solutions at 298 K was determined. The solubility data were used to determine the activities of ZnO and H_2O with respect to pure solid ZnO and liquid water, respectively, in calcium zincate. They were also used to determine the vapor pressure of water over calcium zincate and other thermodynamics properties of this system. The equilibrium constant of the reaction $Ca(OH)_2 \cdot 2Zn(OH)_2 \cdot 2H_2O(S) = Ca(OH)_2(S) + 2ZnO(S) + 4H_2O(l)$ was found to be 0.049 ± 0.015. The standard free energy of formation of calcium zincate was found to be −1785 ± 150 cal/mol at 298 K. The standard heat of formation was found to be −665 cal/mol, and the standard entropy of formation was found to be 3.35 cal/deg/mol.

The zinc electrode in a Zn/NiOOH cell is limited in its cycle life due to its shape change, densification, and dendrite formation (1, 2). Shape change, (*i.e.*, the shifting of active material from the edges of an electrode plate towards its central area during cycling) and the densification of this active material decrease the electrode capacity and current density while dendrite (*i.e.*, a needle-like crystal projection) formation leads to short circuiting between the negative and positive electrodes. Shape change, densification, and dendrite formation have been attributed to occur because the discharge product (zinc oxide) of the zinc electrode is too soluble in the KOH electrolyte (see Fig. 1) (3-7). The addition of $Ca(OH)_2$ to the negative electrode has improved its performance (6-11). The improvement has been ascribed to the formation of a calcium zincate compound which lowers the solubility in the electrolyte. Little thermodynamic data are available on this compound, and there are conflicting reports as to its composition (7, 9, 11, 12). This investigation has been carried out to characterize the calcium zincate compound and to obtain a basic understanding of its role in improving zinc electrode performance. This type of knowledge may help to make further improvement in zinc electrode performance.

Experimental

Preparation.—Calcium zincate was prepared as follows. 10g of ZnO of 99.8% purity was dissolved in 1000 cm^3 of 20 weight percent (w/o) KOH solution. This amount is equal to a ZnO concentration in 20 w/o KOH solution in equilibrium with calcium zincate. Calcium hydroxide of 98% purity (100g) was slowly added to the KOH solution which was being continuously stirred. Water (146g) equal to that which was expected to be present in calcium zincate containing 100g $Ca(OH)_2$ was added to the KOH solution. Then the calculated amount of ZnO (219.7g) was slowly added to the solution. The solution was stirred for the next 24h. After that, calcium zincate was allowed to settle, and the liquid above it was decanted off. The calcium zincate was washed with water until the solution pH became about 7 and then dried at 325 K overnight. The calcium zincate prepared in this manner was a very fine crystalline powder.

Chemical composition.—There is some uncertainty in the chemical composition of the calcium zincate. It has been reported as $CaZn(OH)_4 \cdot H_2O$ (8), $3Zn(OH)_2 \cdot 2Ca(OH)_2 \cdot 5H_2O$ (10), $Ca(OH)_2 \cdot 2Zn(OH)_2 \cdot 4H_2O$ (7), and $CaZn_2(OH)_6 \cdot 2H_2O$ or $Ca[Zn(OH)_3]_2 \cdot 2H_2O$ (11, 12). In the present study, the composition of calcium zincate was determined by chemical and thermogravimetric analysis (TGA).

The chemical analysis of the powdered calcium zincate gave 12.5 w/o Ca and 43.3 w/o Zn. These values are in good agreement with a composition represented by the formula $Ca(OH)_2 \cdot 2Zn(OH)_2 \cdot 2H_2O$ which would have 12.98 w/o Ca and 42.33 w/o Zn.

The TGA tracing of the calcium zincate is shown in Fig. 2. The tracing shows that the compound started decomposing at ~410 K, and lost 22.7 w/o below 600 K and 27.6 w/o below 925 K. The 22.7 and 27.6 w/o losses correspond well to 23.3 w/o water content of $Zn(OH)_2$ and H_2O constituents, and to 29.1 w/o water content of $Ca(OH)_2$, $Zn(OH)_2$, and H_2O constituents respectively of $Ca(OH)_2 \cdot 2Zn(OH)_2 \cdot 2H_2O$. Zinc hydroxide is reported to decompose into ZnO and H_2O at 398 K (13) and $Ca(OH)_2$ is reported to decompose into CaO and H_2O at 853 K(13). The x-ray diffraction pattern of the sample from TGA after it has been heated to 925 K, confirmed the CaO and ZnO products. In another test, a weighed amount of calcium zincate was kept at

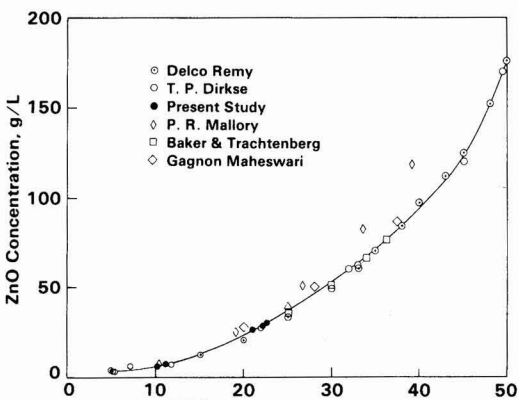

Fig. 1. Solubility of ZnO, g/l in KOH solution at 298 K vs. w/o KOH before saturation.

* Electrochemical Society Active Member.

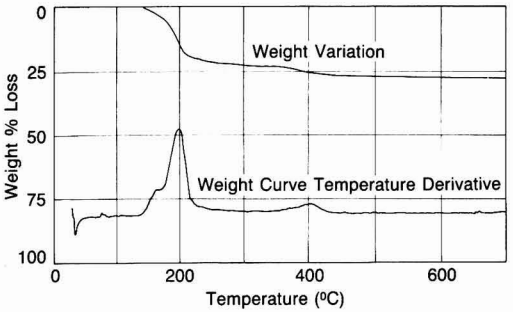

Fig. 2. TGA tracing of calcium zincate decomposition. Sample weight = 10 mg; atmosphere = N_2; flow rate = 100 ml/min; heating rate = 10°C/min.

525 K for 20h in air. It lost 20 w/o during this period. This loss compares well with the 22.7 w/o loss below 610 K during TGA.

The x-ray diffraction data for calcium zincate are given in Table I. They are in agreement with the data reported in literature for $CaZn_2(OH)_6 \cdot 2H_2O$ or $Ca[Zn(OH)_3]_2 \cdot 2H_2O$ (11, 12). The chemical analysis, TGA, weight loss on heating in air and x-ray diffraction data indicate that calcium zincate in equilibrium with 20 w/o KOH solution has a composition, best presented by $Ca(OH)_2 \cdot 2Zn(OH)_2 \cdot 2H_2O$.

Photographs of the calcium zincate powder by scanning electron microscope are given in Fig. 3 and 4. The photographs show well defined monoclinics of calcium zincate.

Density.—The density of calcium zincate powder at 296 K was determined using a pycnometer and a water medium. The weight of calcium zincate was 1.33g and that of displaced water was 0.51375g. This gave a density of 2.59 g/cm³ which compares well with 2.60 and 2.62 g/cm³ reported in literature (11, 12). It is interesting to see that the determined value of 2.59 g/cm³ is higher than 2.3 g/cm³ which was calculated from the molecular weight of the compound divided by the sum of the volumes of the $Ca(OH)_2$, $Zn(OH)_2$, and water in the compound. The compound is more compact than the mixture of its constituents.

Solubility measurements.—Zinc oxide concentrations in KOH solutions in equilibrium with calcium zincate ($Ca(OH)_2 \cdot 2Zn(OH)_2 \cdot 2H_2O$) at 298 K were determined. They were measured by equilibrating KOH solutions with calcium zincate or with $Ca(OH)_2$ and ZnO of calcium zincate composition. The zinc oxide concentrations of the equilibrated solutions were determined by chemical analysis. Potassium hydroxide concentrations were also checked by chemical analysis. In one case, a KOH solution was saturated with ZnO, and its EMF was measured against a Hg/HgO reference electrode. The zinc electrode used was a zinc strip, 30 cm long, 1 cm wide, and 0.15 cm thick which was heat sealed in a 28 cm long heat shrink plastic tubing. One centimeter at each end of the zinc strip was kept bare for contacting one end to the electrometer and the other end to the electrolyte. The ends of the plastic tubing were sealed leak-tight using a 10% polysulfone solution for preventing creeping of the KOH solution.

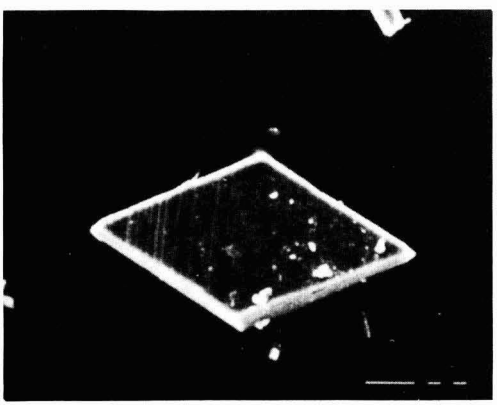

Fig. 3. SEM photograph of calcium zincate magnified ×1000

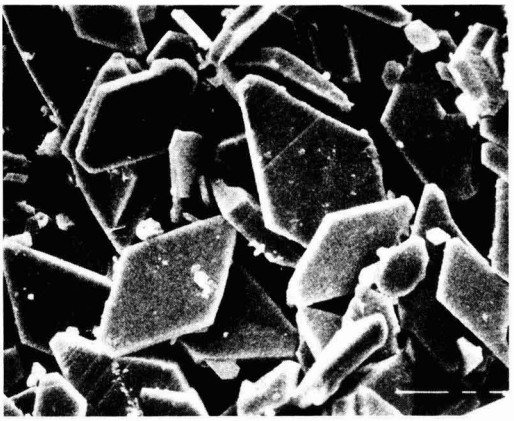

Fig. 4. SEM photograph of calcium zincate magnified ×1000

For the Hg/HgO reference electrode a 0.65 cm central hole (closed at the bottom) was drilled in a Plexiglas cylinder, 4 cm diam × 7 cm long. At the bottom of the hole, a mixture consisting of 0.5g Hg and 0.3g HgO was placed. A platinum wire as an electrical lead for the Hg/HgO mixture was sealed in a side hole of the cylinder. The KOH solution placed on the Hg and HgO mixture was connected with the electrolyte in the reaction vessel through a Teflon capillary tubing attached to another side hole of the cylinder. The electrolyte level of the reference electrode was adjusted by a syringe, the needle of which passed through the rubber stopper closing the hole. The needle dipped in the electrolyte. $Ca(OH)_2$ was added to the ZnO saturated solution in small amounts, and the corresponding EMF's were measured. After a certain amount of $Ca(OH)_2$ addition to the solution, the EMF became constant and remained unchanged for two weeks. This indicated that the solution attained a ZnO concentration in equilibrium with calcium zincate. Zinc oxide and KOH concentrations of the solution were determined by chemical analysis.

Results and Discussion

The data on zinc oxide concentrations in aqueous KOH solutions in equilibrium with calcium zincate at 298 K are given in Table II and are presented by curve B in Fig. 5. The zinc oxide concentrations obtained by equilibrating

Table I. X-ray diffraction data of calcium zincate

2 Theta	D	Norm. I	Integ. I	Max. I	Int. width
12.32	7.178	8	1117	133	0.25
12.89	6.862	7	1012	134	0.23
13.39	6.608	6	933	145	0.19
14.14	6.258	76	11196	1633	0.21
14.99	5.906	9	1322	145	0.27
15.38	5.756	9	1310	164	0.24
17.67	5.015	12	1708	208	0.25
21.48	4.134	6	926	148	0.19
28.57	3.121	100	14816	3056	0.15
30.91	2.890	9	1387	189	0.22
31.76	2.815	5	775	148	0.16
33.05	2.708	5	747	124	0.18
36.56	2.456	10	1452	277	0.16
46.64	1.946	7	1088	200	0.16
50.06	1.821	8	1200	195	0.18
58.56	1.575	7	1096	177	0.19
59.15	1.561	6	960	153	0.19

Table II. Zinc oxide solubilities and activities, and water activities in KOH solutions in equilibrium with calcium zincate; standard free energy of decomposition, ΔG°, and equilibrium constant, K, for calcium zincate, $Ca(OH)_2 \cdot 2Zn(OH)_2 2H_2O$. Temperature = 298 K

KOH concentration before ZnO soln, w/o	Mole fraction in X_{KOH} after ZnO soln	^aH_2O before ZnO soln	ZnO concentration in equilibrium with calcium zincate		ZnO concentration in equilibrium with ZnO				
			g/l	X_{ZnO}	g/l	X_{ZnO} (from curve A)	a_{ZnO}	K^a	ΔG°, cal/mol
9.75[b]	0.0335	0.920	1.23	0.000268	5.7	0.00124	0.216	0.0034	2012
19.64	0.0726	0.795	7.38	0.00159	22.6	0.00487	0.327	0.0427	1867
27.46	0.108	0.645	20.91	0.0045	45.0	0.00967	0.465	0.0374	1945
10.71[c]	0.0371	0.907	1.89	0.000411	6.7	0.00146	0.282	0.0538	1730
20.16	0.0748	0.762	10.13	0.00218	24.0	0.00517	0.423	0.0603	1663
29.0	0.116	0.610	22.4	0.00482	50.0	0.0107	0.449	0.0279	2119
29.83[e]	0.119	0.595	29.63	0.00637	53.0	0.0114	0.559	0.0392	1918
24.88[f]	0.0957	0.700	15.31	0.00329	36.8	0.00791	0.416	0.0416	1883
27.76[g]	0.109	0.640	26.64	0.00573	45.8	0.00984	0.582	0.0568	1698
29.81	0.119	0.596	36.85	0.00792	53.0	0.0114	0.695	0.0609	1656
21.25[h]	0.0795	0.768	11.35	0.00244	26.3	0.00566	0.432	0.0649	1619
28.77	0.114	0.617	30.8	0.00662	48.9	0.0105	0.631	0.0577	1689
30.89[d]	0.155	0.570	40.57	0.0109	56.4	0.0157	0.695	0.051	1762
31.46	0.159	0.555	45.18	0.0122	58.3	0.0163	0.747	0.0529	1740
32.20	0.164	0.537	51.28	0.0139	61.0	0.0172	0.809	0.0544	1724

[a] K for the reaction, $Ca(OH)_2 \cdot 2Zn(OH)_2 \cdot 2H_2O(S) = Ca(OH)_2(S) + 2ZnO(S) + 4H_2O(l)$.
[b] Equilibrated with calcium zincate for 12 days.
[c] Equilibrated with calcium zincate for 66 days.
[d] Equilibrated with calcium zincate for 16 days.
[e] Equilibrated with calcium zincate for 50 days.
[f] Added $Ca(OH)_2$ to a solution saturated with ZnO. No change in Zn electrode potential in solution with $Ca(OH)_2$ addition for 14 days.
[g] Equilibrated with $Ca(OH)_2$ and ZnO of calcium zincate composition for 21 days.
[h] Gagnon and Maheswari [Ref. (16)].

the solutions with $Ca(OH)_2$ and ZnO and reported by Gagnon and Maheswari (7) are also shown in this figure. These data are presented after correcting KOH concentrations for water consumed in forming calcium zincate by the amount of $Ca(OH)_2$ and ZnO taken in each measurement. The ZnO concentrations in KOH solutions in equilibrium with ZnO, which were obtained from Fig. 1, are also presented by curve A in Fig. 5. The zinc oxide concentrations in equilibrium with calcium zincate are much lower than these corresponding concentrations in equilibrium with ZnO in KOH solutions at lower concentrations of KOH. However, at ~34.0 w/o KOH, the ZnO concentrations are the same in both cases. The extrapolation of curve B above the experimental measurements to 34 w/o KOH concentration is based on a theoretical analysis which is detailed below.

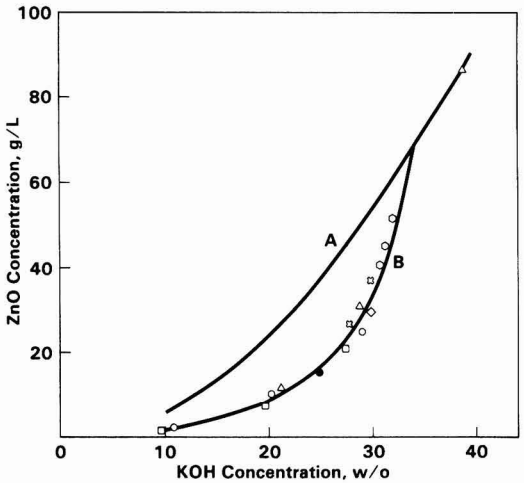

Fig. 5. ZnO concentration in KOH solutions at 298 K equilibrated with calcium zincate for 12 days □; for 66 days ○; for 16 days ⬡; for 50 days ◇; with $Ca(OH)_2$ and ZnO for 21 days ⧈; and for 14 days ●; Gagnon and Maheswari △. Curve A in equilibrium with pure ZnO; curve B in equilibrium with $Ca(OH)_2$ and calcium zincate.

Calculation of standard free energy of formation, ΔG°, of calcium zincate.—The dissolution of ZnO in KOH solutions from calcium zincate may be represented by the reaction

$$Ca(OH)_2 \cdot 2Zn(OH)_2 \cdot 2H_2O(S) \rightarrow Ca(OH)_2(S) + 2(ZnO)_{soln} + 4(H_2O)_{soln} \quad [1]$$

For this reaction, the equilibrium constant, K, is expressed in terms of the activities (a_i) of the reactants and products as follows

$$K = \frac{a_{Ca(OH)_2}\, a^2_{ZnO} a^4_{H_2O}}{a_{Ca(OH)_2 \cdot 2Zn(OH)_2 \cdot 2H_2O}} \quad [2]$$

In the presence of pure solid calcium zincate and pure solid $Ca(OH)_2$ at unit activities, the above expression becomes

$$K = a^2_{ZnO} a^4_{H_2O} \quad [3]$$

At equilibrium between KOH solutions and calcium zincate, the activities of water and ZnO in the solutions and the compound are equal. The activities of water with respect to pure liquid water were calculated from the vapor pressures of water over the KOH solutions and over pure water as reported in the literature (14, 15). It has been shown that the presence of ZnO in the KOH solutions does not change the vapor pressures of water over these solutions (16). The activities of ZnO with respect to pure solid ZnO were calculated from the ZnO concentrations in equilibrium with calcium zincate and those in equilibrium with pure solid ZnO (see Table II) by taking the ratios of respective mole fractions. The activity coefficients of ZnO have been observed to remain constant over the entire concentrations below the ZnO solubilities in KOH solutions.

The values of equilibrium constant K were calculated from the activities of ZnO and water from relation [3].

The standard free energy of decomposition of calcium zincate, ΔG°, was obtained by the relation

$$\Delta G^\circ = -RT \ln K \quad [4]$$

where R is gas constant, and T is the absolute temperature. The results of these calculations are summarized in Table II.

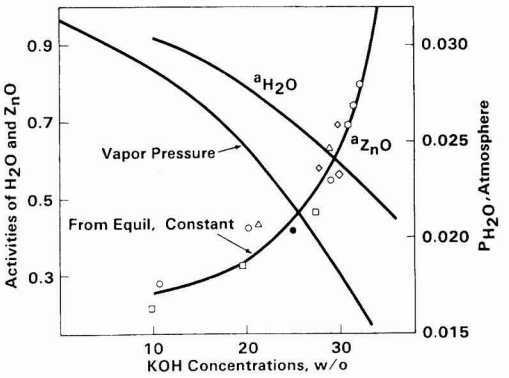

Fig. 6. Variation of vapor pressure and activities of H_2O and ZnO in calcium zincate with KOH concentration at 298 K. ZnO activities are with respect to pure solid ZnO and those of water are with respect to pure liquid water. Legend same as in Fig. 5.

The average values of K and $\Delta G°$ from the data given in Table II were found to be 0.049 ± 0.015 and 1785 ± 150 cal/mol at 298 K. The extrapolated portion of curve B in Fig. 5 to 34.0 ± 1 w/o KOH was calculated using the above value of K, and the appropriate water activity in Eq. [3]

The activities of water and ZnO, and the vapor pressure of water for solutions of different KOH concentrations in equilibrium with calcium zincate are also presented in Fig. 6. In addition to this, the activities of ZnO in calcium zincate in equilibrium with different KOH solutions were calculated using the respective values of water activities and the equilibrium constant by the relation [3]. They are presented by the curve in Fig. 6. The variation of ZnO activity from 0.255 to 1 with a corresponding variation in water activity indicates that calcium zincate is not a stoichiometric compound, but the composition variation may not be very substantial and may be within the experimental error of the techniques used.

By relation [3], the activity of ZnO will increase with a decrease in the activity of H_2O (*i.e.*, by an increase in KOH concentration at a constant temperature). This means that the effectiveness of calcium hydroxide by calcium zincate formation in lowering the ZnO concentration in KOH solutions will decrease at higher KOH concentrations. At a definite activity of water, *i.e.*, at a certain concentration of KOH, the ZnO activity will be unity. At this concentration of KOH, calcium zincate will be in equilibrium with pure solid $Ca(OH)_2$, pure solid ZnO, and water. Under these conditions, the equilibrium constant, K for reaction [1] will be

$$K = a^4_{H_2O} \qquad [5]$$

The ZnO concentration in KOH solution will be equal to the ZnO concentration in equilibrium with pure solid ZnO. This KOH concentration is shown in Fig. 5 at 34.0 ± 1 w/o KOH, where the ZnO solubility curve and the curve representing the ZnO concentration in equilibrium with calcium zincate *vs.* KOH concentration intersect. At a KOH concentration greater than ~34.0 w/o KOH, calcium zincate cannot exist in contact with KOH solution, because the water activity in these solutions will be smaller than that in equilibrium with calcium zincate, $Ca(OH)_2$ and ZnO. This indicates that $Ca(OH)_2$ will not be effective in suppressing the ZnO concentration in a KOH solution at KOH concentrations ≥34.0 w/o KOH.

In the situation where pure, solid calcium zincate is in equilibrium with pure, solid $Ca(OH)_2$, pure, solid ZnO, and a solution of a definite KOH concentration, the activity of each of the compounds, calcium zincate, $Ca(OH)_2$, and ZnO remains at unity, and only that of water changes with a change in temperature. Using this fact, the value of the equilibrium constant, K, at different temperature was calculated by relation [5] and the activity of water at the respective temperature. The activities of water at different temperatures were calculated as before (14, 15). The values of $\Delta G°$ for calcium zincate decomposition were calculated at different temperatures by relation [4]. The calculated data are summarized in Table III.

Table III. The activity of water and the standard free energy of decomposition, $\Delta G°$, for calcium zincate at different temperatures KOH solution in equilibrium with calcium zincate $Ca(OH)_2$ + ZnO = 34.0 w/o KOH

Temperature (K)	a_{H_2O}	$\Delta G°$ (cal/mol)
273	0.4854	1568
293	0.4919	1652
313	0.5011	1718
333	0.5108	1779
353	0.5200	1835

The standard heat of decomposition, $\Delta H°$, of calcium zincate was calculated by the relation

$$\Delta H° = \frac{d(\Delta G/T)}{d(1/T)} \qquad [6]$$

The value of $\Delta H°$ was found to be 665 cal/mol of calcium zincate. The standard entropy of decomposition, $\Delta S°$, of calcium zincate was calculated to be −3.35 cal/deg/mol from the intercept of the plot as well as by the relation

$$\Delta G° = \Delta H° - T\Delta S° \qquad [7]$$

For the formation of calcium zincate, the values of $\Delta G°$, $\Delta H°$, and $\Delta S°$ have opposite signs.

It is very unusual that the compound calcium zincate has its standard heat of formation greater than the standard free energy of formation and that the standard entropy of formation is positive. This is because $\Delta G°$ for this compound decreases with an increase in temperature.

Implication of $Ca(OH)_2$ addition to ZnO electrode of the Zn/NiOOH cell.—The addition of $Ca(OH)_2$ to ZnO in the negative electrode simply decreases the ZnO activity in the KOH electrolyte by forming calcium zincate. That means it decreases the ZnO concentration in the electrolyte, decreases the ZnO activity in the electrode, and increases the reversible potential of Zn/NiOOH cell. An improvement in the cell performance due to a $Ca(OH)_2$ addition to ZnO is due to a decrease in the resultant ZnO concentration in the electrolyte. The improvement should be more pronounced at the lower concentrations of KOH, *i.e.*, up to ~22 w/o KOH, because the rate of increase of ZnO concentration with increase in KOH concentration is smaller below 22 w/o KOH than that above this KOH concentration (Fig. 5). At KOH concentrations ≥34.0 w/o KOH, the addition of $Ca(OH)_2$ to ZnO should not impart any improvement to cell performance. Relation [3] indicates that $Ca(OH)_2$ must always be at unit activity to impart maximum improvement.

Calcium zincate is stable in KOH electrolyte during the cell operation, even if the temperature increases (Table III). The concentration of ZnO in KOH electrolyte in equilibrium with calcium zincate is also expected to remain constant with an increase in temperature. The standard heat of formation, −665 cal/mol, of calcium zincate is too small to influence significantly the temperature of the Zn/NiOOH cells in terms of practical operation.

Acknowledgments

The author wishes to thank Dr. Jack Johnson and Mr. Dean Walton of the Analytical Chemistry Department for x-ray analysis and chemical analysis, Mr. S. P. Maheswari for experimental work, Dr. Richard A. Murie for photographs by the Scanning Electron Microscope, and Drs. Eugene G. Gagnon and John S. Dunning for helpful suggestions.

Manuscript submitted on Jan. 4, 1986; revised manuscript received June 2, 1986.

General Motors Research Laboratories assisted in meeting the publication costs of this article.

REFERENCES

1. J. McBreen, *This Journal*, **119**, 1620 (1972).
2. J. McBreen and E. J. Cairns, in "Advances in Electrochemistry and Electrochemical Engineering," Vol. **XI**, p. 273, John Wiley and Sons, Inc., New York (1978).
3. T. P. Dirkse, *This Journal*, **106**, 154 (1959).
4. C. T. Baker and I. Trachtenberge, *ibid.*, **114**, 1045 (1967).
5. P. R. Mallory Co., in "Alkaline Storage Batteries," S. U. Falk and A. J. Salkind, Editors, John Wiley and Sons, Inc., New York (1969).
6. Delco-Remy, Private communication.
7. E. G. Gagnon and S. P. Maheswari, Private communication.
8. W. J. Van der Grinten, U.S. Pat. 3,516,862 (1970).
9. Y. Maki, M. Fujita, H. Takahaski, and T. Ino, U.S. Pat. 3,816,178 (1974).
10. Y. Maki, M. Fujita, M. Kikuchi, and T. Kamimura, in "Battery Research and New Batteries in Japan," Vol. 2, March 1972.
11. F. Lieban and A. Amel-Zadeh, *Krist. Tech.*, **7**, 221 (1972).
12. Joint Committee on Powder Diffraction Standards, 24-222-24-221 (1974).
13. "Handbook of Chemistry and Physics, College Edition," 47th ed., pp. B-163, B-240 (1966-1967).
14. G. R. Paranjpe, *J. Ind. Inst. Scien.*, **2**, 59 (1918).
15. "International Critical Tables of Numerical Data, Physics, Chemistry and Technology," Vol III, pp. 210-212, 298, 373, McGraw Hill Book Co., Inc., New York (1928).
16. W. H. Dyson, L. A. Schreier, W. P. Sholette, and A. J. Salkind, *This Journal*, **115**, 566 (1968).

Adsorption and Absorption of Chloride Ions on Passive Iron Systems

V. Jovancicevic,* J. O'M. Bockris,* J. L. Carbajal, P. Zelenay, and T. Mizuno[1]**

Department of Chemistry, Texas A&M University, College Station, Texas 77843

ABSTRACT

The adsorption and absorption of chloride on iron in borate buffer solution have been studied using a radiotracer technique. The two processes are clearly distinguishable by their different time constants, ~ 1 min for adsorption and ~ 1h for absorption. The adsorpton of chloride on bare iron and passive layer surfaces follows the Tempkin type of isotherm. The free energy of adsorption of chloride on passive layer is significantly higher than that on bare iron. Partial charge transfer between adsorbed chloride ion and Fe^{2+} and/or Fe^{3+} on the passive surface has been proposed to account for this difference. The "saturation" coverage of chloride on passive layer varies with concentration and attains a value of 0.8 at higher concentrations. The absorption of chloride into the passive layer starts at about −0.1 V/NHE, followed by a linear increase with the potential. The steady-state value of absorption of chloride at the breakdown potential varies with concentration of chloride in the solution and breakdown potential. The maximum value of absorption before breakdown occurs is $\theta = 2.5$.

Corrosion mechanisms of iron in the neutral *p*H range have been investigated (1-3). However, most of the detailed work has been on the dissolution of iron (4-8). Investigations of the mechanism of the cathodic reactions (9-16) and passivation (17-20) have been done in regions of *p*H that are acid or alkaline. Conversely, most corrosion occurs when the ambient solution is in the neutral *p*H range, particularly in sea water, where the *p*H is around 8. Therefore, it is of interest to know the behavior of chloride in respect to iron in a *p*H region nearer to that which occurs in practice (21, 22).

Further, apart from the consideration of absorption in discussion of the Cl^--stimulated breakdown of passive layers, no account has been given of the preliminary adsorption of chloride on the surface of the passive layer (23). Lastly, no account exists of the adsorption of chloride on iron itself in the *p*H range corresponding to that in which corrosion occurs, although such knowledge is vital for mechanistic views of, *e.g.*, pitting (24-29).

Consequently, in the present work, the adsorption and the absorption of chloride on iron and on passive layers has been examined from solutions in which the ambient *p*H has been held around 8.

Experimental

Preparation of the electrodes.—The iron used was from Alpha Ventron, and was 99.998% pure. In the radiotracer work, it was evaporated onto a glass scintillator disk, 3 cm diameter and 3 mm thick. The thickness of the iron layer was 3000Å.

The procedure followed in the evaporation was, first, to degrease the glass scintillator with acetone. Then, the scintillator samples were introduced in the vacuum chamber of the deposition unit. A vacuum of 2×10^{-6} mm of Hg was attained, and the glass scintillator disks were heated to about 100°C to improve adherence. A current of 25A (at 5V) was passed through the tungsten boat, resulting in evaporation of the iron onto the glass scintillator situated 15 cm above the crucible.

Following the preparation of the evaporated layer, the glass scintillator containing the film was removed from the vacuum chamber and introduced into a desiccator already filled with nitrogen. The electrodes were thus stored at room temperature and transported to the cell, whereupon they were introduced into the nitrogen-filled working electrode compartment.

The cell body was made out of Teflon with a glass top and is shown in Fig. 1.

The counterelectrode was protected from the rest of the cell by a fritted glass disk. The reference electrode was of mercury-mercurous sulfate. The scintillator, coated with an evaporated film, formed the bottom of the cell, and was connected to a light pipe, which conducted the scintillations to a photomultiplier.

When the cell was to be used, it was washed overnight with a chromic-sulfuric acid mixture. The cell was then rinsed with several changes of distilled water, being left in distilled water until use. It was then rewashed several times with triply distilled water.

The electrolytic solution was introduced and expelled from the cell by the use of nitrogen pressure without contact from the atmosphere.

Removal of the air-formed film from the electrode.—After introduction of the electrode into the cell, the preelectrolyzed solution (see below) was introduced, and the electrode placed at a potential of −0.740 V/NHE. The choice of this potential arises from the work of Bockris *et al.* (30, 31), where it was shown that this potential corresponds to that at which, under these condtions, iron is

*Electrochemical Society Active Member.
**Electrochemical Society Student Member.
[1]On leave from the Department of Engineering, Hokkaido University, Hokkaido, Japan.

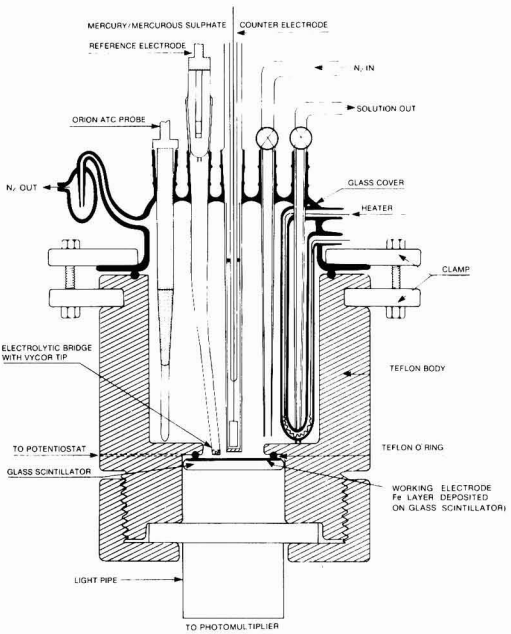

Fig. 1. Electrochemical cell for radiotracer experiment

free from oxide. The electrode was maintained at this potential for about 1h.

Preparation of the solution.—The solution was prepared from triply distilled water. The water conductivity was less than 10^{-6} mho cm^{-1}. The solution consisted of 0.0375*M* sodium tetraborate (AR), together with 0.15*M* H_3BO_3. This mixture made a buffer solution of *p*H 8.4. The *p*H was measured for each new preparation. The solution was prepared in a separate vessel (washed as the above cell) and was then subjected to a pre-electrolysis carried out on two large platinum gauze electrodes, the area of which was *ca.* 1000 cm^2. The current density used here was of the order of 10 $\mu A\ cm^{-2}$, and the pre-electrolysis was carried out for 2-3 days.

After the pre-electrolytic purification was finished, the solution—which during this time was kept in contact with a nitrogen atmosphere—was pressed over into a nitrogen-filled cell by means of nitrogen pressure.

Formation of the working electrode surface.—After the electrode had been prepared and the evaporated layer held at −0.74V as described above, the solution in which this preparation had been made was removed from the cell, though a thin layer of 1-2 mm of solution was kept in contact with the electrode during this process to decrease the possibility of reoxidation of the electrode surface. A nitrogen atmosphere was maintained throughout. The new (or working) solution was then introduced, saturated in nitrogen, and the electrode placed at that potential required by the subsequent experiment. In a typical case, the potentiostat would be adjusted from the potential of −0.74 V/NHE to the rest potential of −0.55 V/NHE. Here, there was no hydrogen evolution and the electrode was maintained for about 30 min. However, purified nitrogen was copiously bubbled through the solution with the aim of removing any hydrogen introduced into it during its first few moments of contact with the electrode, when it was at a potential of −0.74 V/NHE.

Thereafter, the potentiostat was readjusted from −0.55 V/NHE to the working potential desired for the experiment. The current was observed to decrease continuously during the time of passivation, and the final current was of the order of 1 $\mu A\ cm^{-2}$.

After the potential of choice for the experiment concerned had been introduced, and the surface was either in a state of low current density hydrogen evolution, or continuing to form a passive film, chloride ions were injected into the solution by means of a syringe emptying into the solution drainage tube, until the concentration of Cl^- ion reached the desired value.

Immediately after the chloride ion concentration was introduced, radioactive counting commenced (see below).

Radiotracer measurements.—The labeled Cl^{36} was from ICN Radiochemicals. Its specific activity was 300 mCi/mmol. The life of Cl^{36} is 3.10^5 yr. The isotope was made available in solutions of 0.1*M* sodium chloride. This solution was transferred without further purification to the syringe, which had been carefully washed, and the proper isotopic dilution in chloride concentration was then introduced into the cell. The addition took 1-2s. Counting was made at each potential and solution condition. A typical count rate was 50,000 counts/min.

The block diagram of the electronic setup for radiotracer measurement is shown in Fig. 2. The light pulse generated in a scintillator was converted into current impulse in the photomultiplier connected to a multichannel analyzer via a preamplifier or, alternatively, a preamplified signal was directed to the ORTEC NIM system. In the latter case, the number of counts was displayed digitally by the computer and printed out on a printer or plotted against time on *y-t* recorder.

During the radioactive measurements, the current on the electrode was correspondingly monitored, a technique of importance in respect to judging the moment of passive layer breakdown and connecting it with the amount of chloride that had been adsorbed or absorbed into the electrode.

The surface concentration, $\Gamma(mol/cm^2)$, of adsorbed and/or absorbed species was calculated from the equation (32)

$$\Gamma = \frac{N_{ads}}{N_{backg}} \cdot \frac{C}{R\mu} \qquad [1]$$

where N_{ads} and N_{backg} are the count rates (cpm) in the adsorption situation and that in its absence, respectively, *C* is solution concentration (mol/cm^3) of the labeled species, *R* is roughness factor, and μ is a linear absorption coefficient (30 cm^{-1}) of the radiation emitted by the radioactive nuclide.

The surface coverage, θ, is given by

$$\theta = \frac{\Gamma}{\Gamma_{max}} \qquad [2]$$

where Γ_{max} is the maximum surface concentration of adsorbed species and is derived from geometrical considerations of the adsorbent surface and adsorbate molecule (33). Assuming an equal proportion of low index crystal planes on the iron surface (bcc) and taking Fe-Fe interatomic distance as 2.5Å (34), Γ_{max} is equal to 3.10^{-9} mol/cm^2.

Reproducibility.—The reproducibility of the radioactive counting was of the order of ± 1% but in concentrated solution fell to *ca.* ± 10%, because of the difficulty provided by the high background counts.

Accuracy measurements.—In the equation for the calculation of $\Gamma(mol/cm^2)$, the various errors will add (35). Thus, the errors are as follows: counts = ± 0.4%, *R* = ± 25%, μ = ± 10%. Hence, the accuracy of the measurements is thus ±35%. This can be compared with the reproducibility, which is 1-10%.

Evaluation of the roughness factor of bare iron.—The calculation of the roughness factor on a surface such as that used in the present work is difficult. It is not possible to use a coulometric hydrogen desorption method (36) in the case of iron because the latter will dissolve at the same time to an indeterminate degree (37, 38).

For this reason, three separate methods were used for calculating the roughness factor. The first method involves the number of atoms per square centimeter of

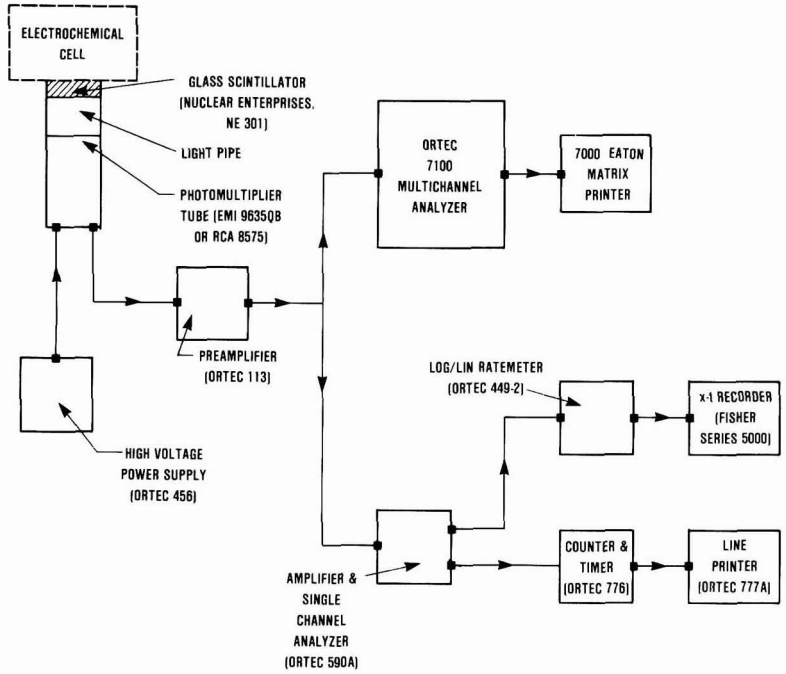

Fig. 2. Block diagram of the electronic setup for radiotracer experiment.

iron surface taken by Wieckowski *et al.* (33) to be 1.75×10^{15} (charge per atom of iron is 2). A trivial calculation shows that the number of coulombs is 5.8×10^{-4} C/cm^2. One way to calculate the number of coulombs needed to form a monolayer of the passive film on a metal surface per square centimeter of the apparent surface is to take the number of coulombs used in forming the hump for the passivation curve, as shown at Fig. 3a. Thus, for the sweep rate of 2 mV/s, the number of coulombs is 3.8×10^{-3} and the resulting roughness factor is 6.5.

Alternatively, it is possible to consider the steady-state currents that are finally developed on the iron evaporated on the glass and also the current measured when the passive film (0.3 V/NHE) is observed on a polished iron surface (Fig. 3b). The ratio between these two is 8.7. An ideal polished surface taken as a series of undulations equivalent to triangles has a base angle of 30°, giving a true to apparent surface area of 1.15. The value of the true area by this approach would, therefore, be 8.7/1.15 = 7.6.

Finally, one may take results obtained by potentiostating the iron and observing the decay of the potentiostatic transient (Fig. 3c). If one compares the coulombs taken in this operation with the ones observed on the smooth iron electrode, taking the roughness factor of this to be 1.15, the result is 10.7.[2]

Taking the mean of these values true to apparent area ratio is 8.5 ± 2.5. This value of 8.5 will be used throughout the calculations.

Results

Adsorption.—Time dependence of adsorption.— Looking at Fig. 3a, which contains the i-V curve for the dissolution of iron, in a solution of pH = 8.4, and with a borate buffer, it can be seen that the metal is not covered by an oxide layer at potentials more negative than about −0.55V on the normal hydrogen scale (NHS).

Thus, the adsorption of chloride on bare iron could be examined in the range between −0.8 V/NHE (when hydrogen evolution disturbed the measurements) and −0.55/NHE. At more anodic potentials, up to −0.2 V/NHE, adsorption occurs on the passive layer without any significant absorption as indicated by the saturation values of surface concentration (see Fig. 4).

The time dependence of adsorption of chloride on bare iron and on the passive layer was in a range too small to

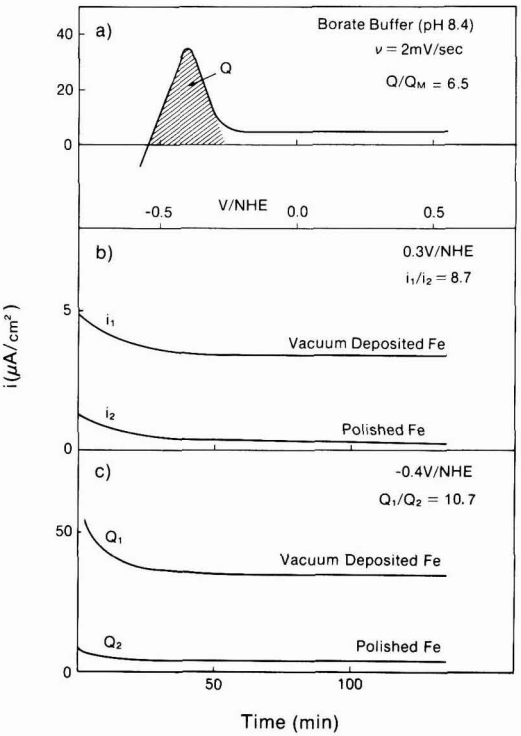

Fig. 3. Evaluation of the roughness factor of vacuum-deposited iron electrode on glass scintillator.

[2]In calculating this value, it has been assumed that the two charges per Fe atom, which corresponds to dissolution, are still used in the formation of the layer. However, at higher potentials, the film is certainly best represented by O/Fe = 1.5 and, hence, Fe^{3+} is involved.

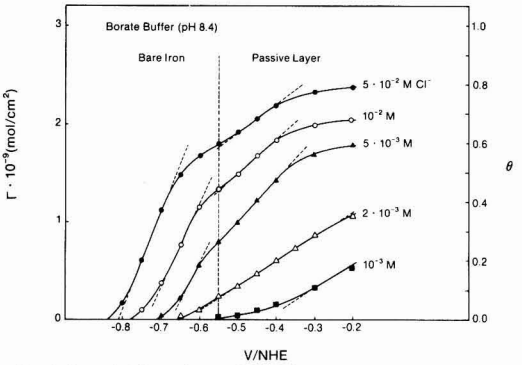

Fig. 4. Potential dependence of chloride adsorption on bare iron and passive layer as a function of concentration of chloride in the solution.

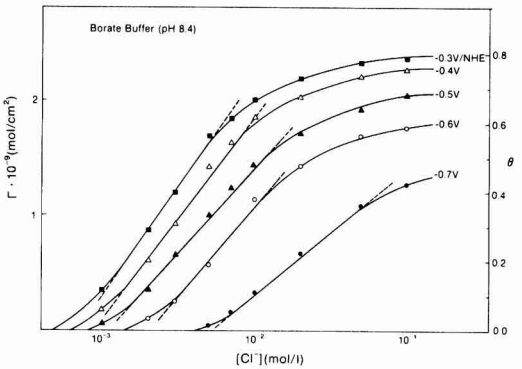

Fig. 6. Steady-state values of adsorption of chloride as a function of concentration at different potentials.

be observed by the radiotracer technique, where first measurement could be obtained only at times greater than 1 min because of the need for substantial count rates. Thus, the adsorption measurements were time independent.

Potential dependence of chloride adsorption at constant concentration.—The potential dependence of the surface concentration of chloride, Γ, on bare iron and passive layer, at different concentrations of chloride in the solution, is shown in Fig. 4. The adsorption increases linearly with potential both on bare iron and on the passive layer before saturation is reached. The saturation values for bare iron are masked by the increase of adsorption on the passive film. The slopes of the linear part of the curves are greater for bare iron than for the passive layer.

The saturation surface concentrations for bare iron (−0.5 V/NHE) and passive layer (−0.25 V/NHE) as a function of chloride concentration are shown in Fig. 5. The logarithmic relationships are obtained with the respective slopes of 0.3 and 0.7 per decade.

Concentration dependence of chloride adsorption at constant potential.—The concentration dependence of the steady-state values of Γ at different potentials is given in Fig. 6. The linear Γ-$\log(C)_{Cl^-}$ relationships indicates Temkinian behavior. The slope $d\Gamma/d \log (C)_{Cl^-}$ varies with the potential. At higher concentrations, the Temkinian behavior is replaced by that of Langmuir. Thus, the saturation value of the surface concentration depends on the potential: the more positive the potential, the higher the saturation surface concentration.

Absorption.—Absorption as a function of time at constant concentration and potential.—Absorption was examined in the situation in which the passive film was first formed in the absence of chloride and chloride added at a time zero. After it was added, the total surface concentration of chloride (adsorbed + absorbed) upon the surface of the electrode was observed as a function of time. From the time dependence of surface concentration at different potentials (Fig. 7), a large risetime can be seen. This value contrasts with the risetime obtained in the case of adsorption of chloride on the passive layer (< 1 min). The first phenomenon can be described as an absorption process controlled by the diffusion of chloride through the film. Thus, the two phenomena can be separated due to their different time constants.

Figure 7 shows the increase of Γ_{Cl^-} at $C = 10^{-3}M$ for a series of potentials from 0.0 to 1.0V. Because the variation of Γ_{Cl^-} occurs over relatively long times before saturation is reached, the variation with time is taken to represent absorption. The values at low times (< 1 min) are taken as representing adsorption. In the region of potential concerned, the ionic adsorption has reached saturation and, hence, adsorption at various concentrations are independent of potential (*cf.* Fig. 4).

The absorption of chloride in the passive layer is both potential and concentration dependent. Figure 8 shows the total "surface" concentration of chloride for $5.10^{-3}M$ Cl^- in the solution for different anodic potentials as a function of time. The saturation absorption increases with potential up to the breakdown potential (0.8V), after which no steady-state value is observed. This is associated with a sharp increase of current through the film (see Fig. 8, insert).

Absorption of chloride as a function of concentration at constant potential.—As in the case of adsorption, the concentration dependence of absorption shows a so-called "Temkinian" behavior (Fig. 9). The logarithmic in-

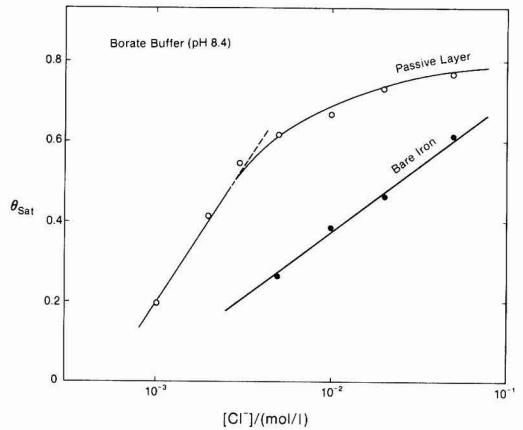

Fig. 5. Saturation surface concentration for bare iron and passive layer as a function of chloride concentration in the solution.

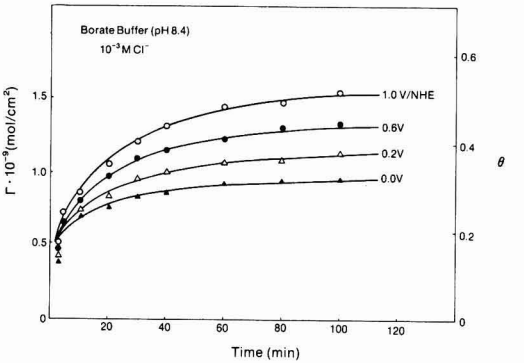

Fig. 7. Time dependence of "surface" concentration of chloride for $10^{-3}M$ Cl^- in the solution at different potentials.

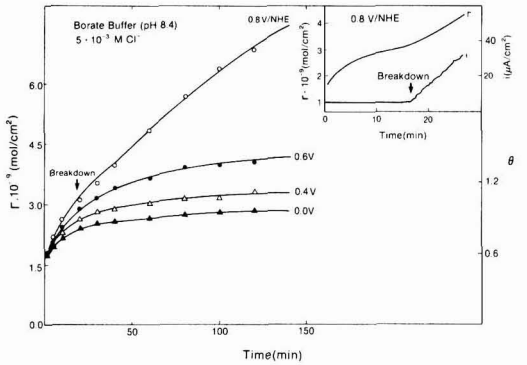

Fig. 8. Total "surface" concentration of chloride for $5 \cdot 10^{-3}$M Cl^- in the solution and different potentials as a function of time. Γ-t and i-t curves for 0.80/NHE (insert).

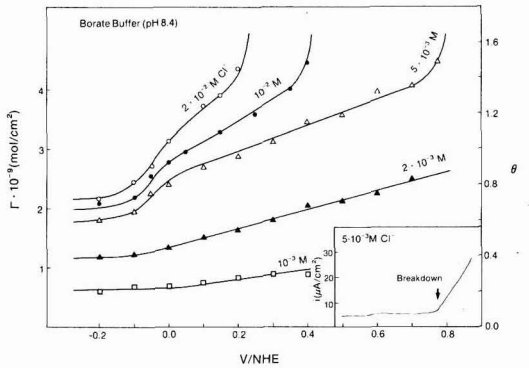

Fig. 10. Total "surface" concentration of chloride as a function of potential for different concentration of chloride in the solution. i-V curve for $5 \cdot 10^{-3}$M Cl^- (insert).

crease of absorption precedes the establishment of the saturation value at a concentration of chloride greater than $10^{-2}M$. At a potential more anodic than 0.1 V/NHE, breakdown of the passive layer (indicated by a sharp increase of current) occurs. The higher the concentration of chloride, the less anodic is the breakdown potential. For example, for Cl^- of about $10^{-2}M$, breakdown of the film occurs at 0.4 V/NHE, while at $10^{-1}M$, breakdown occurs at 0.1 V/NHE (see Fig. 10).

Absorption of chloride as a function of potential at constant concentration.—The total "surface" concentration as a function of potential for different concentrations of chloride is shown in Fig. 10. Three potential domains can be distinguished: the region below −0.15 V/NHE is characterized by constant adsorption, the intermediate region by linear increase of absorption, and the region at more anodic potentials by stepwise increase of absorption associated with the breakdown of the film.

The variation of absorption with potential is concentration dependent, as shown (Fig. 10) by the slope, which increases as the concentration of chloride increases.

Absorption as a function of breakdown potential at constant concentration.—One can see from Fig. 10 that breakdown occurs at potentials corresponding to particular concentrations and "surface" concentrations of chloride equivalent to $\theta \sim 1.3$. This is the minimal amount of chloride that causes breakdown. Figure 11 shows the "surface" concentration of chloride at breakdown potentials for different concentrations of chloride in the solution. The absorption at breakdown potential increases linearly with this potential. The slope of the straight lines increases from lower to higher concentration of chloride. Thus, at concentration of $10^{-1}M$ of chloride, absorption is twice as large as compared with that at $5.10^{-3}M$ concentration. The maximum concentration of chloride at breakdown corresponds to $\theta \sim 2.5$.

Discussion

Mechanism of breakdown—A number of models have been proposed to account for the breakdown of the passive film. Most of these can be grouped under three general models: (*i*) adsorption-displacement, (*ii*) chemico-mechanical, and (*iii*) migration-penetration models (39).

Adsorption-displacement models.—In the approach suggested by Uhlig (40) and Kolotyrkin (41), events leading to breakdown involve the adsorption of Cl^- and simultaneous displacement of O^{2-} from the monolayer, said to constitute the passive layer. As soon as the chloride ion is adsorbed, breakdown commences. The model explains the concentration dependence of film breakdown kinetics but cannot account for the influence of the thickness of the film on that kinetics.

In another view, that of Hoar and Jacob (42), the adsorption of a small number of chloride ions around an iron cation on the surface of the passive film is considered, giving rise to the formation of a "high energy complex." Once formed, this complex is readily dissolved into the solution. It results in a local thinning and the associated stronger local anodic field at the site of removal will cause further cations to diffuse to the surface where they will complex with chloride ions and dissolve. This process leads to breakdown. The model was developed to explain the dependence of the rate of breakdown on Cl^- concentration, temperature, and potential. However, a reaction order of unity with respect to chloride ion for

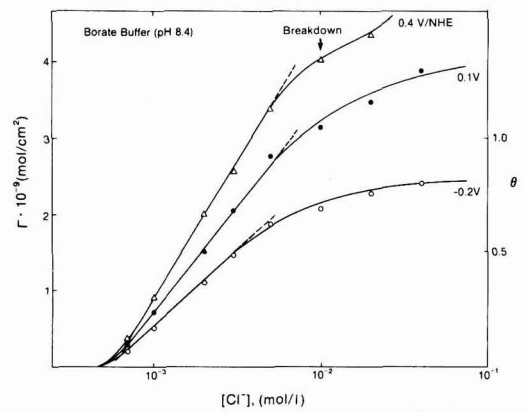

Fig. 9. Concentration dependence of absorption of chloride for different potentials.

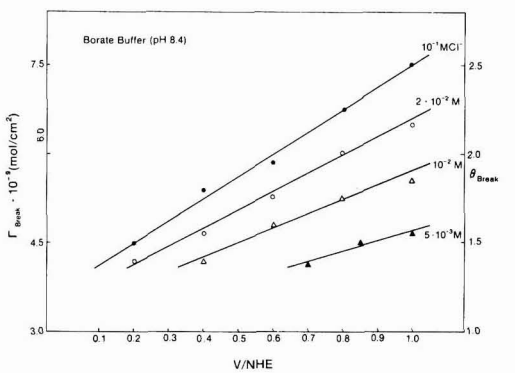

Fig. 11. Total "surface" concentration of chloride at breakdown potentials for different concentration of chloride in the solution.

breakdown, generally observed (22, 40), appears to contradict this view, which demands an order equal to the number of Cl^- ions in the complex.

Chemico-mechanical models.—Hoar (43) postulated that the adsorption of ions, *e.g.*, Cl^- on passive film surfaces, lowers the interfacial surface tension resulting in the formation of cracks or flaws when the repulsive forces between the adsorbed ions are sufficiently large.

This view has been further developed by Sato (44, 45) providing a more detailed picture of the model. The reduced interfacial tension as a result of Cl^- adsorption on the surface of a passive film was thought to increase the electrostriction pressure above a critical value to bring about breakdown. This seems difficult to accept because the lateral repulsion vector would be at right angles to the electrostrictional force. The model is not consistent with the linearity of the breakdown rate with chloride concentration: the chloride adsorption and corresponding reduction of interfacial tension would depend upon the form of the isotherm.

Migration-penetration models.—Various models have been proposed to account for the penetration of aggressive ions through passive films and upon reaching metal-film interface, resulting in breakdown. The ion migration scheme involves the exchange process via cation vacancies (46) and O^{2-} or OH^- (39).

According to the point-defect model (47), the cation diffusion rate in the film is enhanced by complexing Fe^{2+} with Cl^-, the latter arriving at the metal-oxide interface via vacancies formerly occupied by O^{2-} ions. The decrease of oxygen vacancies at the film/solution interface caused by the presence of Cl^- results in the formation of voids at the metal/film interface, due to faster Fe dissolution here than in other locations. This leads to pit growth. The model has the same limitations as the penetration one.

In a model proposed by Heusler and Fischer (23), the chemisorption of chloride ions occurs via replacement of oxygen ions or hydroxyl ions at the oxide-solution surface with long-lived chloride islands. During the lifetime of a two-dimensional chloride island, a new nucleus of Cl appears inside the second layer from the surface, leading to penetration of the oxide layer via a three-dimensional growth of the Cl (the Cl^- presumably having undergone partial charge transfer).

Pou *et al.* (22) suggested that absorbed Cl^- ions displace water molecules (or hydroxyl ions), which, according to the model of O'Grady and Bockris (48), are the essential cementing elements of the passive layer, to form soluble iron complexes containing chloride. The essence of the model relates the removal of H_2O by Cl^-, and hence the conversion of the amorphous passive layer to a crystalline layer, the precursor of breakdown.

Though these models differ in detail, due primarily to the differences inherent in models of the passive film assumed, they contain common features. The adsorption of Cl^- on the passive layer is a first step in the breakdown process. However, they differ as to the mode of penetration of the passive film by Cl^- and the associated rate-determining step.

Adsorption of chloride ions.—Concentration dependence of adsorption.—Adsorption data obtained (Fig. 6) at constant potential (bare iron and passive layer) can be discussed in terms of the Temkin formalism. A treatment in terms of more advanced isotherms will be given in a subsequent publication (49). A fitting procedure for a least squares calculations was used for the equation

$$\theta = -\frac{\Delta G^\circ_{ads}}{r} + \frac{RT}{r} \ln C \qquad [3]$$

where ΔG°_{ads} is free energy of adsorption and r interaction parameter. The results are shown in Fig. 12.

The sharp change of ΔG°_{ads} around the transition region is observed (Fig. 12). The bare iron region is at potentials more negative than −0.6 V/NHE and passive film at the potentials more positive than −0.5 V/NHE. In the transition region, ΔG°_{ads} changes abruptly from −3.2 kcal/mol (bare iron) to −4.4 kcal/mol (passive layer). A gradual increase is observed in the beginning of the passive region.

The results indicate the relatively stronger adsorption of chloride on the passive layer compared to that on bare iron. This finding is consistent with the presence of an inflection point in the θ-V curves at about −0.55 V/NHE (Fig. 4).

The pzc of bare iron is about −0.65 V/NHE (50), and the region in which the chloride adsorption is measured on this surface is −0.8-0.6 V/NHE, *i.e.*, the region is negative to the pzc and thus the free energy of adsorption of chloride on the bare iron will be relatively low.

The stronger adsorption of chloride on the passive surface can be explained by a possible charge transfer between chloride ion and Fe^{2+} and/or Fe^{3+}, the constituent of the passive layer (51, 52). In the coordination chemistry, the iron-water complexes can be described in terms of partially discharged iron ion by water molecules (53). As the passive layer contains H_2O and/or OH^- (48), it is reasonable to assume that adsorbed chloride displaces water molecule giving rise to further charge transfer.

Potential dependence of adsorption.—The coverage-potential profile (Fig. 4) both for bare iron and passive film can be described by a linear relationship as is expected in a Tempkin isotherm. The apparent slopes of the straight portion of the curves is constant for bare iron and varies slightly with concentration of Cl^- in solution for passive layer due to the difference between the saturation coverage on two surfaces.

Absorption of chloride ions.—Time dependence of absorption.—It has been observed earlier that the time constant for adsorption is ~ 1 min, and Fig. 7 shows that the corresponding quantity for absorption is around 1h.

It seems reasonable to assume [cf. Murphy *et al.* (21)] that this long time constant is a result of diffusion of Cl^- into the film.

One can apply Fick's second law with boundary conditions for the diffusion through the thin film given by (54)

$$\begin{aligned} C(x, o) &= 0,\ 0 < x < L \\ C(o, t) &= C_o,\ t > o \\ C(L, t) &= 0,\ t > o \end{aligned} \qquad [4]$$

where L is the thickness of the passive layer and C_o is the surface concentration of chloride. The Laplace transform solution for the concentration of chloride into the film at distance x from the surface and time t can be expressed as

$$C(x, t) = C_o \left[\frac{2\,(Dt)^{1/2}}{\pi^{1/2}\, x} \exp\left(-\frac{x^2}{4Dt}\right) - \frac{2(Dt)^{1/2}}{(2L\text{-}x)\,\pi^{1/2}} \exp\left(-\frac{2L\text{-}x)^2}{4Dt}\right)\right] \qquad [5]$$

where D is the diffusion coefficient of chloride in the passive layer. The integral of Eq. [5] over the thickness of the passive layer, L, obtained by numerical computation, gives the total concentration of chloride (mol/cm²) into the film as a function of time, t. The theoretical curves are compared with the experimental ones and diffusion coefficient determined using the least squares methods. The comparison for the chloride concentration of $10^{-3}M$ and at the potential of 1.0 V/NHE is shown in Fig. 13.

The diffusion coefficient obtained from the fitting was independent of concentraton of chloride and electrode potential with the value of about $1.5.10^{-17}$ cm²/s. This value is in a relatively good agreement with the value obtained by Murphy *et al.*(21) using an approximate treatment of SIMS data.

Dependence of absorption on potential and concentration.—Interesting relationships are given in Fig. 10 and 11 in respect to the potential dependence of absorption and Γ_{break} at constant concentration, respectively.

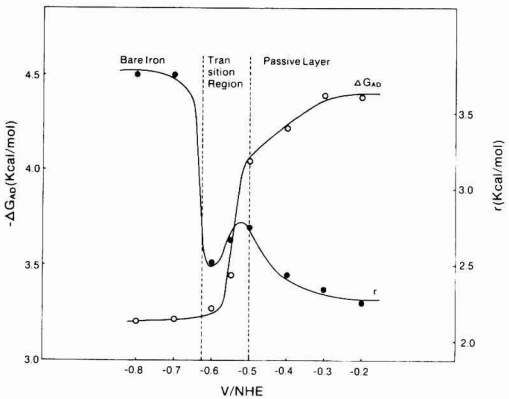

Fig. 12. Free energy of adsorption of chloride, ΔGad, and interaction parameter, r, as a function of potential.

In respect to the interpretation of the variation of Γ with potential (Fig. 10), three variations should be considered. The inflection in Γ at about −0.05 V/NHE may be interpreted in terms of an increase of hydration of the passive layer which can be observed by XPS (55). It reflects the ingress of chloride into the film accompanied with the reduction of amount of water in the film as indicated by XPS data (21, 22).

The linear variation of Γ with potential may be explained in terms of the linear variation of the thickness of the film with potential. This suggests no significant increase in concentration of chloride in the film before breakdown.

Finally, the sharp increase in Γ, which occurs at increasingly positive potentials with decreasing concentration, corresponds to the breakdown of the film and ease of chloride penetration into the oxide layer.

The linear dependence of absorption on concentration (Fig. 9) is analogous to the corresponding behavior of adsorption (Temkin isotherm). Such a relation can be attributed to causes similar to those in adsorption, *i.e.*, mutual repulsion of the anions within the film, with an increase of the saturation value as the potential grows more positive, corresponding to the increasing film thickness.

Conclusions

It has been demonstrated that the adsorption and absorption of chloride on passive layer are two distinct processes; time constants for adsorption is ~ 1 min and for absorption ~ 1h. The adsorption of chloride on both bare iron and passive layer surfaces could be described by the Temkin type of isotherm. The free energy of adsorption of chloride on passive layer is higher than that on bare iron. The partial charge transfer between adsorbed chloride ion and Fe^{2+} and/or Fe^{3+} on the passive surface has been proposed. The absorption of chloride into the passive film increases linearly with potential. The process is controlled by diffusion of chloride ions through the film ($D_{Cl^-} \simeq 1.5 \cdot 10^{-17}$ cm²/s).

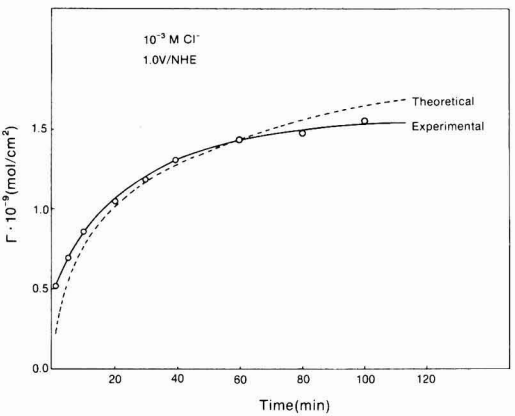

Fig. 13. Comparison between experimental and theoretical data for total "surface" concentration of chloride for 10^{-3}M Cl^- in the solution and 1.0 V/NHE.

Acknowledgments

The authors acknowledge the support of the Office of Naval Research under the Contract no. N0001480Co113 and of Dr. F. Herr for discussion of objectives of the work. They are thankful to Drs. A. Gochev, B. Scharifker, and M. Hall for discussion. Thanks are also due to F. Diniz for data processing.

Manuscript submitted Nov. 25, 1985; revised manuscript received April 28, 1986.

Texas A&M University assisted in meeting the publication costs of this article.

REFERENCES

1. J. O'M. Bockris, D. Drazic, and A. R. Despic, *Electrochim. Acta*, **4,** 325 (1961).
2. F. Hilberg, Y. Miyoshi, G. Fichkorn, and W. J. Lorenz, *This Journal*, **118,** 1919, 1927 (1971).
3. K. A. Christiansen, H. Hoeg, K. Michelson, G. Bech-Nielsen, and H. Nord, *Acta Chem., Scand.*, **15,** 300 (1961).
4. E. J. Kelly, *This Journal*, **112,** 124 (1962).
5. G. J. Bignold and M. Fleischmann, *Electrochim. Acta*, **19,** 363 (1974).
6. A. A. Elmiligy, F. Hilbert, and W. J. Lorenz, *This Journal*, **120,** 247 (1973).
7. A. C. Makrides, N. M. Komodromos, and N. Hackerman, *ibid.*, **102,** 363 (1955).
8. N. Sato, *Denki Kagaku*, **46,** 584 (1978).
9. Z. A. Foroulis, *Corrosion*, **35,** 340 (1979).
10. E. McCafferty and N. Hackerman, *This Journal*, **119,** 999 (1972); P. Delahay, *ibid.*, **97,** 198 (1980).
11. R. J. Chin and K. Nobe, *ibid.*, **119,** 1457 (1972).
12. R. J. Chin and K. Nobe, *Corrosion*, **33,** 364 (1977).
13. I. L. Rosenfeld, in "Localized Corrosion," R. W. Staehle, Editor, p. 12, NACE, Houston (1974).
14. A. Tumbull, *Br. Corr. J.*, **15,** 162 (1980).
15. M. R. Tarasevich and V. S. Bagotskii, *Elektrokhim.*, **14,** 1340 (1978).
16. V. M. Sheblovinskii, A. G. Kichev, and B. N. Yanchuk, *ibid.*, **15,** 1279 (1979).
17. J. Epelboin, C. Gabrielli, M. Keddam, and H. Takenouti, in "Comprehensive Treatise of Electrochemistry," Vol. 4, J. O'M. Bockris, B. E. Conway, E. Yeager, and R. E. White, Editors, p. 151, Plenum Press, New York (1981).
18. R. P. Frankenthal, in "Passivity and Its Breakdown on Iron and Iron Based Alloys," R. W. Staehle and H. Okada, Editors, p. 10, NACE, Houston (1976).
19. K. J. Vetter and F. Gorn, *Electrochim. Acta*, **18,** 321 (1973).
20. A. H. Sukhotin and K. M. Kartashova, *Corros. Sci.*, **5,** 393 (1965).
21. O. J. Murphy, T. E. Pou, J. O'M. Bockris, and L. L. Tongson, *This Journal*, **131,** 2785 (1984).
22. T. E. Pou, O. J. Murphy, V. Young, J. O'M. Bockris, and L. L. Tongson, *ibid.*, **131,** 1243 (1984).
23. K. E. Heusler and L. Fischer, *Werkst. Korros.*, **27,** 551, 697, 781 (1976).
24. Passivity and Its Breakdown on Iron and Iron Base Alloys, Japan-USA Seminar, Honolulu, Hawaii, 1975.
25. J. A. Smith, M. H. Peterson, and B. F. Brown, *Corrosion (Houston)*, **26,** 539 (1970).
26. M. Pourbaix, *ibid.*, **26,** 431 (1970).
27. K. J. Vetter and H. H. Strehblow, in "Localized Corrosion," R. W. Staehle, Editor, NACE, Houston (1974).
28. H. W. Pickering and P. R. Frankenthal, *This Journal*, **119,** 1297 (1972).
29. J. R. Galvele, *ibid.*, **123,** 464 (1976).
30. J. O'M. Bockris, M. A. Genshaw, and V. Brusic, *Symp. Faraday Soc.*, **4,** 177 (1970).
31. J. O'M. Bockris, M. A. Genshaw, V. Brusic, and H. Wroblowa, *Electrochim. Acta*, **16,** 1859 (1971).
32. H. Wroblowa and M. Green, *ibid.*, **15,** 1685 (1970).

33. A Wieckowski, E. Ghali, M. Szklarczyk, and J. Sobkowski, *ibid.*, **28,** 1619, 1627 (1983).
34. "International Tables for X-ray Crystallography," Kynoch Press, Birmingham, England (1962).
35. B. J. Woodruff, "Terms, Tables and Skills," p. 60, Silver Burdelt Co. (1960).
36. H. Angerstein-Kozlowska, in "Comprehensive Treatise of Electrochemistry," Vol. 9, E. Yeager, J. O'M. Bockris, B. E. Conway, and S. Sarangapani, Editors, p. 22, Plenum Press, New York (1984).
37. H. J. Flitt and J. O'M. Bockris, *Int. J. Hydrogen Energ.*, **7,** 411 (1982).
38. H. J. Flitt and J. O'M. Bockris, *ibid.*, **6,** 119 (1981).
39. J. Kruger, in "Passivity and Its Breakdown on Iron and Iron-Base Alloys," R. W. Staehle and H. Okada, Editors, p. 91, NACE, Houston (1976).
40. H. P. Leckie and H. H. Uhlig, *This Journal*, **113,** 1262 (1966); *ibid.*, **116,** 906 (1969).
41. Y. M. Kolotyrkin, *ibid.*, **108,** 209 (1961).
42. T. P. Hoar and W. R. Jakob, *Nature*, **216,** 1299 (1967).
43. T. P. Hoar, *Corros. Sci.*, **7,** 355 (1967).
44. N. Sato, *Electrochim. Acta*, **16,** 1683 (1971).
45. N. Sato, *This Journal*, **129,** 255 (1982).
46. M. A. Heine, D. S. Keir, and H. S. Pryor, *ibid.*, **112,** 29 (1965).
47. C. Y. Chao, L. F. Lin, and D. D. MacDonald, *ibid.*, **128,** 1194 (1981).
48. W. E. O'Grady and J. O'M. Bockris, *Surf. Sci.*, **10,** 245 (1973).
49. V. Jovancicevic, J. L. Carbajal, and J. O'M. Bockris, In preparation.
50. K. I. Noninski and E. M. Lazarova, *Electrochim.*, **9,** 673 (1974); *ibid.*, **11,** 1103 (1975).
51. M. Froelicher, A. Hugot-Le Goff, and V. Jovancicevic, in "Passivity of Metals and Semiconductors," M. Fromet, Editor, p. 471, Elsevier Science Publishers, Amsterdam (1983).
52. V. Jovancicevic and J. O'M. Bockris, Submitted to *This Journal.*
53. F. A. Cotton and G. Wilkinson, "Advanced Inorganic Chemistry," p. 754, Interscience Publishers, New York (1980).
54. J. McBreen, L. Nanis, and W. Beck, *This Journal*, **113,** 1218 (1966).
55. V. Jovancicevic, R. Kainthla, Z. Tang, B. Yang, and J. O'M. Bockris, Submitted to *This Journal.*

Electrochemistry in Liquid Crystals

Orientational Effects in Electrochemical Processes

Angela M. Serra, Robert D. Mariani, and Hector D. Abruña*

Department of Chemistry, Cornell University, Ithaca, New York 14853

ABSTRACT

The electrochemical characterization of the room temperature nematic phases of MBBA (p-methoxybenzilidene p-butyl aniline), MBAB (methoxy-butyl azoxybenzene), and K-15 (4-pentyl-4′ cyano-biphenyl) has been performed in acetonitrile, as well as in the neat phases, and it is found that they all possess a wide range of potentials over which electrochemical experiments can be carried out. MBBA and MBAB exhibit large ohmic drops making experimentation difficult. K-15, on the other hand, proved to be very well behaved. A number of model redox couples were investigated in K-15, and it is found that the electrochemical response can be significantly different from that observed in conventional solvents such as acetonitrile. These differences can be ascribed to the formation of ion aggregates as well as to differences in diffusion coefficients. We also present some preliminary findings on the effect of orientation on the observed electrochemical response of TCNQ (tetracyanoquinodimethane), ferrocene, and TCNE (tetracyanoethylene).

One of the central goals of electrochemical research is to control the reactivity of substrate molecules at the surface of an electrode. In the present context, we are trying to control electrochemical reactivity through solute/solvent interactions. Specifically, we are interested in ascertaining how the electrochemical behavior and transport properties of redox systems are altered when electrochemical experiments are carried out in highly ordered solvent systems. In such an environment, a redox species can be oriented in a particular fashion relative to the electrode surface, and this allows for the study of the effects of orientation on redox potentials, rates of electron transfer, as well as transport rates. We are approaching this by making use of liquid crystals as solvents in which to perform electrochemical experiments.

Liquid crystals (LC) encompass a variety of chemical species whose most prominent feature is that they exhibit more than a single transition in going from solid to isotropic liquid (1-3). It is these intermediate phases that are known as mesophases or liquid crystals. Liquid crystals are generally catalogued as being either thermotropic or lyotropic. Thermotropic liquid crystals are those in which transitions are effected by changes in temperature. These materials are further subdivided into nematic, cholesteric, and smectic. The nematic phase is characterized by having long range orientational order with a principal axis in a fixed direction. For these phases, the temperature at which the nematic phase is converted into an isotropic liquid is known as the nematic/isotropic (n/i) transition temperature. There are significant changes in physicochemical properties that accompany such a transition. For example, nematic phases scatter light very strongly, whereas the isotropic phases are clear. In addition, there are significant changes in viscosity. The cholesteric phase is similar to the nematic, but, in this case, the principal axis follows a helical course so that cholesteric phases exhibit optical activity. The smectic phases are characterized by having one degree of translational ordering resulting in layered structures which are much more viscous than either the nematic or cholesteric phases.

Another salient feature of liquid crystals is that they can be oriented in parallel or perpendicular manner relative to a surface and that this orientation can be accomplished in a variety of ways including electric (4) or magnetic (5) fields, addition of surfactants (6), evaporation of inorganic films onto a surface (7), and others. Furthermore, it is known that interacting solutes dissolved in oriented liquid crystals will themselves be oriented by the liquid crystalline phase (8-12).

As far as electrochemical studies of liquid crystals are concerned, most have been related to the use of liquid crystals for display devices. Of special interest in this respect is a phenomenon known as dynamic scattering. This is a conduction-induced fluid flow which takes place when a nematic phase is subjected to an applied voltage. In investigating dynamic scattering, some mesophases have been electrochemically characterized in order to obtain accessible potential limits (13-17). There have also been studies where the conductance of liquid-crystal electrolyte systems has been investigated (18, 19). In recent studies, Margerum and Barret (20, 21) used electroactive dopants in nematic phases and found that these reduce the potential required for the onset of dynamic scattering. Herino and

* Electrochemical Society Active Member.

co-workers have also reported some voltammetric studies in mesophases (22-25).

We describe a series of studies on the electrochemical characterization of three room temperature nematic phases: MBBA (p-methoxybenzilidene p-butyl aniline), MBAB (methoxy butyl azoxybenzene), and K-15 (4-pentyl-4′ cyano-biphenyl) (see structures below). MBBA was investigated because it is one of the best

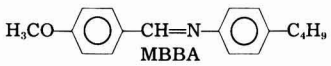

MBBA

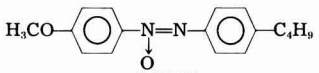

MBAB

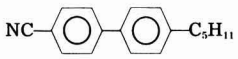

K-15

characterized liquid crystals, MBAB for its very broad nematic temperature range (up to 75°C), and K-15 because of its stability, relatively high dielectric constant, and because preliminary studies by Gosse (14) on the heptyl analog indicated a broad range of accessible potentials.

In addition, we present electrochemical studies on a number of redox species in these liquid crystalline matrices including some preliminary results on the effects of orientation on the electrochemical behavior.

Experimental

Reagents.—MBBA (Frinton Laboratories) and MBAB (E.M. Chemicals) were vacuum distilled. K-15 was obtained from Atomergic Chemetals and E.M. Chemicals. We also prepared this material by a modified version of the procedures given by Gray and co-workers (26) and Oh (27). Acetonitrile (Burdick and Jackson Distilled in Glass) was dried over 4A molecular sieves.

Tetra n-butyl ammonium perchlorate (TBAP, G. F. Smith) and tetra n-butyl ammonium tetrafluoroborate (TBAF, Southwestern Analytical) were recrystallized three times from ethyl acetate and dried *in vacuo* at 70°C for 72h. Tetrahexyl ammonium perchlorate was prepared by mixing aqueous solutions of tetrahexyl ammonium bromide and perchloric acid. The precipitated salt was washed with water, dried, and recrystallized three times from ethyl acetate. Tetrabutyl ammonium tetraphenyl borate was prepared by mixing aqueous solutions of tetra n-butyl ammonium bromide and sodium tetraphenyl borate. The precipitate was washed with water, dried, and recrystallized from acetone/ether. Dicyclohexyl 18-crown-6/KBF_4 (18C-6/KBF_4), 15-crown-5/sodium tetraphenyl borate (15C-5/NaO_4B), and cryptofix-2-2-2/KBF_4 (K*/BF_4) were prepared by mixing stoichometric methanol solutions of the salt and the ligand. The solutions were stirred for 1h, and the methanol was removed under vacuum. The resulting white solids were washed with water and then with ether and dried in vacuum.

All of the redox active components investigated were purified either by recrystallization or by sublimation.

Instrumentation.—Electrochemical experiments were performed with PAR Models 173 Potentiostat, 179 Digital Coulometer, and 175 Universal Programmer, or with a locally built potentiostat and signal generator. Data were recorded on either Soltec or Hewlett Packard X-Y recorders. For experiments in acetonitrile, conventional three-compartment cells separated by medium porosity frits were employed.

For experiments with the neat liquid crystalline phases, a single compartment cell was constructed from a $29/42 joint. The male part was provided with four $10/30 joints through which the three electrodes were connected, and the fourth connection was used to evacuate the cell. The bottom part of the joint was cut and ground flat, and a Pyrex flat was attached (to make the cell bottom) using paraffin and epoxy. The thickness of the LC layer was typically 3 mm. Alternatively, cells were constructed from 3 dram Pyrex vials whose bottoms were cut and polished flat. The cell bottoms consisted of microscope slides that were attached as described above for the Pyrex flats. In all cases, a platinum working electrode (shrouded in glass) and a platinum counterelectrode were used.

Potentials in acetonitrile are referenced to an aqueous sodium saturated calomel electrode (SSCE). In the liquid crystals, either a silver quasi-reference electrode or an Ag/Ag^+ reference electrode (10 m*M* $AgBF_4$ dissolved in the liquid crystal in contact with a silver wire) were used.

Orienting materials.—The Pyrex flats and glass slides used as cell bottoms were treated with either ACM-72 or Surfine 150 (both from Atomergic Chemetals) according to the manufacturer's procedure. These materials produce surfaces that will orient the liquid crystals parallel and perpendicular to the surface, respectively. Orientation of the liquid crystalline layers was confirmed by the use of an optical microscope with crossed polarizers. To prevent contamination, the Pyrex flats and glass slides were used only once.

Results

Electrochemical characterization of liquid crystalline phases.—In order to assess the potential limits within which the LC phases could be used in electrochemical studies, they were characterized in acetonitrile/TBAP.

MBBA was investigated first, since there were already some studies on its electrochemical characterization. Similar to the results reported by Bard and co-workers (17), we find that MBBA has two irreversible oxidation processes at E_p values of +1.43 and +2.05V *vs.* SSCE, respectively. (The latter, however, appears to be a composite of at least two waves, since there is a shoulder present.) We also observe an irreversible reduction with an E_p value of −2.10V *vs.* SSCE, again in good agreement with previous reports.

The electrochemical response of MBAB in acetonitrile/TBAP exhibits two well-defined irreversible oxidation waves at E_p values of +1.59V and 1.75V *vs.* SSCE, respectively, as well as two additional waves at +1.95V and +2.18V. MBAB has a single reduction wave with an E_p value of −1.58V. In this case, there is a current peak on the reverse sweep, indicating some stability of the product. At sweep rates above 20 V/s the wave appeared to be chemically reversible and an $E^{o'}$ value of −1.53V was obtained. A sweep rate study of this wave coupled with controlled potential electrolysis seems to indicate an ECE type mechanism; however, no further studies were performed.

K-15 had two irreversible oxidations (Fig. 1a) at E_p values of +2.01V and +2.41V *vs.* SSCE, as well as one reversible reduction wave with a formal potential of −2.09V *vs.* SSCE. This latter process is likely due to the generation of the radical anion (*e.g.*, analogous to benzonitrile and related materials). Comparison of the peak currents for the reductive and oxidative processes seems to indicate that the latter involve multielectronic transfers.

Using these measured potentials as a guide, the operating range of potentials for the different materials was operationally defined to be about 150 mV positive and negative of the first reductive and oxidative processes, respectively. This represents a lower limit, since in the neat phases the ion radicals generated are expected to be much more poorly solvated, and, as such, the range of accessible potentials will likely be extended over the values mentioned.

Supporting electrolyte studies.—In order to be able to employ these LC phases as electrochemical solvents, the appropriate supporting electrolytes had to be identified. This presented some difficulties, since these materials typically have small dielectric constants; therefore, even if dissolved, the degree of dissociation of an electrolyte would be expected to be small. In addition, we did not know in what way(s) the presence of a supporting electrolyte would affect the other properties of the LC phases. A

number of supporting electrolytes were screened, including traditional ones such as TBAP and TBAF, as well as more esoteric systems such as KBF_4/Kriptofix-2,2,2 (K^*BF_4) and others (see Experimental section). The studies were performed by adding an excess of the supporting electrolyte and warming the LC past its nematic/isotropic (n/i) temperature in order to enhance dissolution, and stirring for 1h. The LC was allowed to cool, and the undissolved electrolyte was filtered off. A cyclic voltammogram at low sweep rate (typically 20 mV/s) was then performed on the LC with the dissolved electrolyte. From the properties of the voltammogram obtained, a qualitative judgement could be made as to the utility of the given supporting electrolyte. (The criterion employed was the presence of flat voltammetric charging currents such as those shown in Fig. 2.) From these studies, it was determined that for both MBBA and MBAB the best system was K^*BF_4, whereas for K-15, TBAF was not only soluble, but, in addition, seemed to dissociate to a significant extent. This is consistent with the larger dielectric constant of K-15 (*ca.* 16). In addition, it was found that, for K-15, when the concentration of the supporting electrolyte was above 80 m*M*, there seemed to be a significant disruption of the LC phase as evidenced by the fact that the LC turned clear (indicating the transition from the nematic to the isotropic phase). Due to this, electrolyte concentrations were kept below these values—typically at 35 m*M*.

Figures 2A, B, and C show cyclic voltammograms for the different LC phases with the appropriate supporting electrolytes. From the voltammograms it was determined that the range of accessible potentials was somewhat broader than we had originally estimated. This is consistent with the arguments presented previously concerning the solvating ability of these phases. A decrease in the solution resistance was noticed as the temperature was raised (especially at temperatures above the n/i transition), consistent with a higher degree of dissociation of the supporting electrolyte.

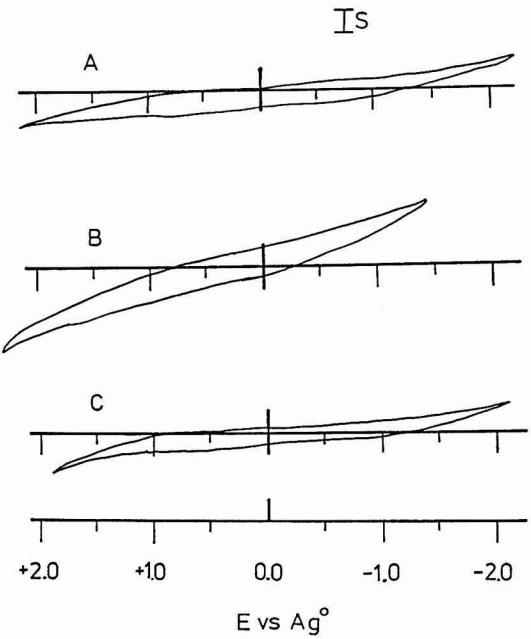

Fig. 2. Cyclic voltammograms for the liquid crystals as solvents containing the appropriate supporting electrolyte. (A) MBBA/K^*BF_4; 20 mV/s; S = 0.2 μA. (B) MBAB/K^*BF_4; 20 mV/s; S = 0.2 μA. (C) K-15/TBAF; 20 mV/s; S = 0.2 μA.

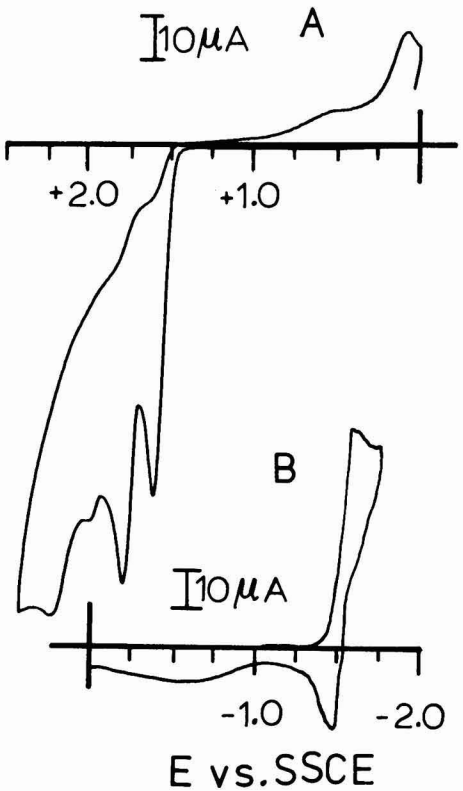

Fig. 1. Cyclic voltammogram at 200 mV/s for a 1 mM solution of K-15 in acetonitrile/TBAP. (A) Sweep between 0.0 and +2.5 V. (B) Sweep between 0.0 and −2.5V.

Electrochemical studies in liquid crystals.—Having identified suitable supporting electrolytes for the various LC phases, we attempted the electrochemical characterization of a number of electrochemically well-behaved redox systems. In general we found that the very high ohmic resistance of both MBBA and MBAB made electrochemical studies difficult. The observed voltammetric responses were typically very broad, and in many instances a response was obtained only when the solvents were present in the isotropic phase.

Electrochemical studies in pentylcyano biphenyl (K-15).—In contrast to both MBBA and MBAB, K-15 was a well-behaved solvent for electrochemical studies both in the liquid crystalline and isotropic forms. This allowed the investigation of a wide-range of electroactive materials. In addition, we were able to perform some studies on the effect of orientation on the observed electrochemical response. We begin by considering the redox characterization of the different systems. Afterwards we will focus on orientational effects.

Although K-15 was a well-behaved solvent for electrochemical studies, the fact that we had to keep the concentration of supporting electrolyte low (*vide supra*) meant that large ohmic drops were encountered. Nevertheless, a number of materials gave well-defined responses including decylviologen, dodecylviologen, ferrocene, $Ru(bpy)_3^{+2}$, $Fe(bpy)_3^{+2}$, TCNQ, TCNE, tetramethylbenzidine (TMB), and chloranil.

In the viologen group both the decyl and dodecyl derivatives gave well-behaved responses, whereas methyl viologen did not give a measurable response (Fig. 3A, B). This might point towards a more favorable solute/solvent interaction with increasing length of the hydrocarbon chain as well as enhanced solubility. There was also a very dramatic supporting electrolyte concentration effect. Specifically, when the concentration of supporting electrolyte was about 0.1*M* a very well-defined electrochemical response was obtained, although the ΔE_p value was still over

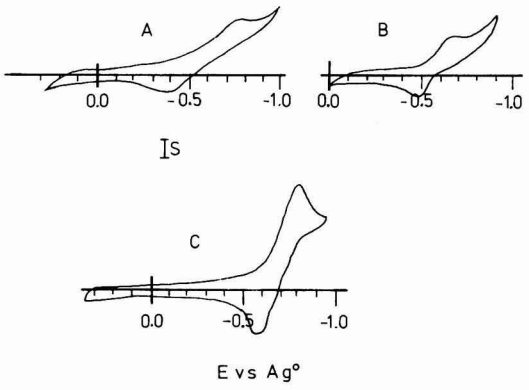

Fig. 3. Cyclic voltammograms at 10 mV/s for long chain viologens in K-15 with 35 mM TBAF. (A) 3.5 mM decyl viologen; S = 50 nA. (B) 2.2 mM dodecyl viologen; S = 20 nA. (C) 3.25 mM dodecyl viologen with 0.1M TBAF; S = 50 nA.

150 mV (Fig. 3C). In addition, the LC crystal turned clear, even though the temperature was well below the n/i transition temperature, an indication that an isotropic, and not a liquid crystalline, phase was present. The peak current was also enhanced as compared to values obtained for example at 35 m*M* supporting electrolyte concentration, reflecting the significant change in viscosity that accompanies the transition. Peak currents similar to those observed at 0.1*M* concentration of supporting electrolyte could be obtained at a concentration of 0.04*M*, if the temperature of the medium was adjusted to be above the n/i transition (47°C); again, this is consistent with the previous results. A sweep rate dependence study (for the dodecyl derivative) showed that the formal potential for reduction remained invariant, and a plot of peak current *vs.* square root of the sweep rate was linear ($r = 0.998$) indicating a diffusion-controlled process. Analogous results were obtained for the decylviologen, $Ru(bpy)_3^{+2}$ and $Fe(bpy)_3^{+2}$.

Ferrocene, TCNE, TCNQ, and TMB were among the best-behaved redox systems investigated in these studies. Very well-developed voltammograms could be obtained when the K-15 was present in either liquid crystalline or isotropic form. As with the other systems, the peak current increased, and the ΔE_p values decreased at temperatures above the n/i transition temperature. The formal potentials were independent of sweep rate, and the dependence of the peak current on the square root of the sweep rate indicated that the processes were diffusion controlled. These systems were investigated in regard to possible specific solvent and orientational effects and will be discussed in more detail below.

Specific solvent effects.—The fact that liquid crystals are highly ordered systems, and oriented layers can in turn orient substrate molecules dissolved in them, raised the interesting question of whether the electrochemical response of a given reactant could be altered by orienting it relative to an electrode surface. The highly anisotropic properties of liquid crystals (*e.g.*, viscosity and dielectric constants) could also affect transport rates and kinetics of electron transfer.

To determine if there are orientational or specific solvent effects, many variables need to be considered. Of particular importance are the mode of alignment used for the liquid crystalline matrix, the propagation distance of such alignment, and the types of molecules used to determine if such an effect is, indeed, present.

In addition, there could be (and more than likely there are) solvent/solute interactions that are not related to orientational effects, and allowance must be made for these.

Finally, since the experimental observables are potential and current, one must be certain that these will be sufficiently stable during the course of the experiment.

In order to minimize the large ohmic drops that were typical of these systems, we used small area platinum electrodes (350 μm diam) which gave well-behaved responses and easily measured currents with tolerable ohmic drops.

Since the accurate and reproducible measurement of potentials was considered critical, close attention was given to the design of an appropriate reference electrode. After examining a wide range of materials, we concluded that the most reliable measurements were obtained by using the Ag^+/Ag couple. We found that a silver wire in contact with a solution of the liquid crystal with 10 m*M* $AgBF_4$ gave very reproducible results, and this reference electrode was used in subsequent studies. In order to test the stability of this reference electrode, we examined the electrochemical response of ferrocene in an unoriented layer of K-15/TBAF. We found that the formal potential (taken as $[Ep_c + Ep_a]/2$) varied by no more than 8 mV during the course of 24h. We also used the measured values of the formal potentials of ferrocene in the liquid crystal ($E^{o\prime} = +0.09V$ *vs.* Ag^+/Ag) and in acetonitrile ($E^{o\prime} = +0.438V$ *vs.* SSCE) to provide a means of relating the measured potentials in the liquid crystal to those measured in acetonitrile. This analysis places the Ag^+/Ag potential in K-15 at $-0.348V$ *vs.* SSCE. Although this approach is widely used, its validity could be argued. Nonetheless, it provides a means for comparing redox potentials in both solvents. Variations in the measured peak currents were about 10% during the same time interval, if the solutions were kept under nitrogen and away from direct light. These results indicated that reproducible potential and current values could be obtained under these conditions.

TCNQ.—The electrochemical response of TCNQ in K-15/TBAF was characterized by two well-developed voltammetric waves (Fig. 4) at $E^{o\prime}$ values of $-0.195V$ and $-0.950V$ *vs.* Ag^+/Ag, respectively. Although on a cathodic going sweep, the waves appeared diffusional (and, in fact, a plot of i_p *vs.* $(v)^{1/2}$ was linear), the anodic counterpart of the wave centered at $-0.950V$ was much sharper which is typical of processes involving adsorption. Upon warming past the n/i temperature (to 42°C) the shape of this wave changed to that typical of a diffusion controlled process (Fig. 4) and upon cooling back to a liquid crystalline state, it reverted to the shape characteristic of adsorptive process. We ascribe this to adsorption or precipitation of the dianion of TCNQ on the electrode surface. However, holding the potential of the electrode past the second reduction wave for a period of 5 min did not cause a significant enhancement of the peak current of this wave, indicating that the material does not accumulate on the electrode surface.

More dramatic were the effects on the formal potentials for the processes as well as the $\Delta E^{o\prime}$ values. In acetonitrile/TBAP, TCNQ exhibits two reversible one-electron reductions at $E^{o\prime}$ values of $+0.240$ and $-0.302V$ *vs.* SSCE. If we apply the correction factor derived from the measurements on ferrocene we obtained values of $+0.153V$ and $-0.602V$ *vs.* SSCE for TCNQ in K-15. Not only are these values significantly shifted from the values observed in acetonitrile, but the $\Delta E^{o\prime}$ value increases from 542 mV in acetonitrile to 755 mV in K-15, indicative of a very strong solvent effect in these processes, especially for the second reduction. Such shifts could imply that the liquid crystal has very different affinities for TCNQ, its radical anion, or dianion. However, the direction of the shifts would indicate that the liquid crystal interacts more strongly with TCNQ than with the ion radical or dianion. Although we have no evidence to discount this, we believe that the opposite (that is, the liquid crystal interacting more strongly with the dianion and ion radical than with TCNQ) would be more probable. It should also be mentioned that the voltammetric response of TCNQ in benzonitrile/TBAF was essentially identical to that in acetonitrile. This indicates that the benzonitrile-like part of K-15 is not responsible for the observed effect. An alternative explanation could be formulated in terms of large differences in the diffusion coefficients for the different species (28). In this framework, the dianion would have a smaller diffusion coefficient than the ion radical which would, in turn, have a

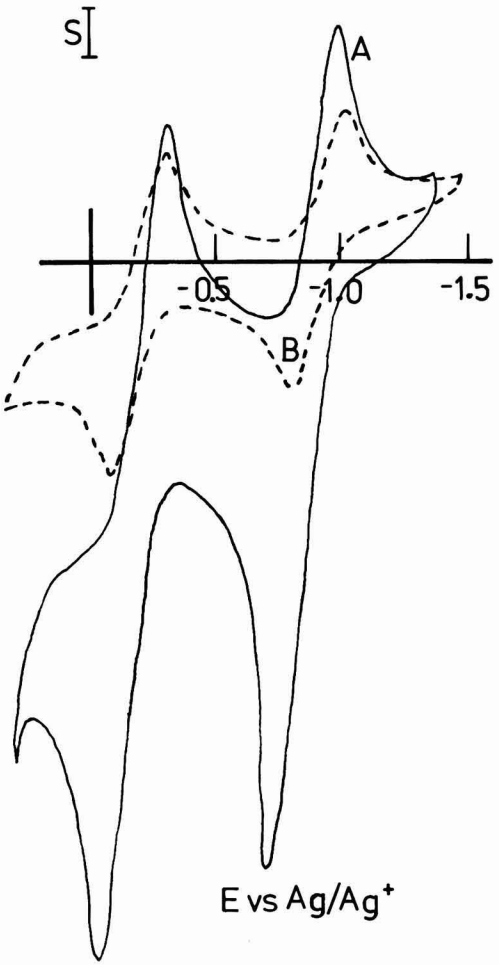

Fig. 4. Cyclic voltammograms for 2.54 mM TCNQ in K-15 with 35 mM TBAF. (A) At 22°C, sweep rate is 10 mV/s; S = 10 nA. (B) At 42°C (isotropic) at 20 mV/s; S = 50 nA.

smaller diffusion coefficient than the parent TCNQ. This is quite plausible, if we consider that the ion radical and dianions are likely to be strongly ion-paired and, as such, would exhibit much smaller diffusion coefficients. This would be in accordance with studies of Herino and coworkers (24) who reported large differences in the diffusion coefficients (in liquid crystalline phases) of tetramethyl p-phenylenediamine (TMPD) and its ion radical. These differences were ascribed to strong ion pairing, and this was confirmed via conductometric experiments.

In order to test for the effect of ion-association (ion pairs or higher aggregates) voltammetric studies of TCNQ in THF with 35 m*M* TBAF as electrolyte were performed. Given the low dielectric constant of THF, the presence of ion association should be quite apparent, and, in fact, the voltammetric response for TCNQ under these conditions shows that the $\Delta E^{0\prime}$ value (650 mV) is close to that observed in K-15. However, the fact that in K-15 the $\Delta E^{0\prime}$ value is still significantly higher, points to the presence of an additional effect that we have not yet identified.

We have also performed analogous studies on chloranil in K-15/TBAF. Although the electrochemical response observed is not as well defined as for TCNQ, the $\Delta E^{0\prime}$ values in acetonitrile and K-15 remain essentially the same. (There is, however, a small shift (*ca.* 100 mV) in the $E^{0\prime}$ values to somewhat more negative potentials.) Since these redox processes also involve the generation of an ion radical and a dianion, we had anticipated that ion pairing would also play a prominent role and thus lead to large variations in the diffusion coefficients. This in turn would give rise to the shifts observed for TCNQ. The fact that smaller shifts were observed seems to indicate that there are other effects involved in the case of TCNQ, perhaps the formation of a charge transfer complex. In fact, TCNQ in K-15 has an orange color whereas in acetonitrile it is yellow. This points to the presence of either a charge transfer complex or a very strong solvatochromatic shift; and we are currently undertaking a spectral study of this effect.

TMB.—A cyclic voltammogram of TMB in K-15/TBAF (Fig. 5) exhibits two well-developed oxidation waves at E_p values of +0.30 and +0.575V *vs.* Ag^+/Ag, whereas a reductive sweep shows only a single reduction wave at an E_p value of −0.245V. This latter wave has an adsorptive shape, and the area under it is much larger than either of the anodic waves but comparable to the sum of the areas of the two anodic processes. If a cathodic sweep is initiated after the first oxidation wave, no reduction current is observed. The shape of the voltammetric response remained unchanged upon warming the solution to 42°C (past the n/i transition), although the waves were shifted on the potential scale, probably reflecting a decrease in the ohmic drop of the solution. This response is to be contrasted with that of TMB in acetonitrile/TBAF where two reversible one electron redox process are observed at $E^{0\prime}$ values of +0.470 and +0.650V *vs.* SSCE.

The electrochemical response of TMB in K-15 proved to be very sensitive to the addition of very small amounts of acetonitrile/TBAF. Such addition caused the K-15 layer to become transparent, indicating that the liquid crystallinity had been lost. The resulting voltammetric response was very similar to that observed in acetonitrile/TBAF.

We had suspected that the high viscosity of the K-15 might be responsible (at least in part) for the observed behavior. To investigate this, we performed cyclic voltammetric experiments of TMB in dimethylsulfoxide (DMSO) whose viscosity was adjusted by the addition of sucrose according to the procedure of Bard and coworkers (29). The shape of the electrochemical response of TMB remained essentially unchanged in solutions whose viscosities ranged from 5 to 50 cP. The viscosity of K-15 at 22°C can be as high as 39 cP (measured perpendicular to the director) (30, 31), and, since in the previous experiments we did not see any dramatic change in the wave shape in a solvent of comparable viscosity, we do not believe that the viscosity of K-15 is responsible for the observed response. This is further confirmed by the fact that warming the K-15 solution past the n/i temperature did not

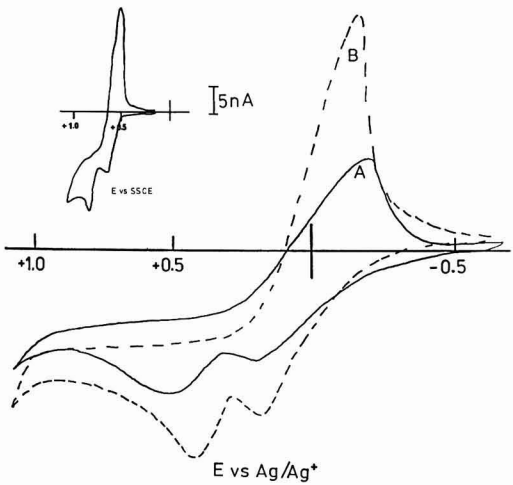

Fig. 5. Cyclic voltammograms at 10 mV/s for 2.1 mM TMB in K-15 with 35 mM TBAF. (A) At 22°C. (B) At 42°C (isotropic). Inset: cyclic voltammogram at 50 mV/s for 1 mM TMB in THF with 35 mM TBAF.

significantly alter the wave shape, although the viscosity at this temperature is of the order of 18 cP. We believe that the anodic processes correspond to the oxidation of TMB to the cation radical and dication and that the cathodic wave represents the reduction of the dication to the neutral TMB in a two-electron process. The fact that the reduction waves for TMB merge into a single wave whose potential is shifted negative of the corresponding processes for TMB suggests the presence of a significant barrier to electron transfer. This could be due to the formation of a tight ion triplet with a high overpotential for reduction. In addition, the direction of the shift is consistent with a stabilization of the dication of TMB by the K-15.

To test for the formation of ion aggregates, we performed voltammetric measurements in THF/TBAF (35 m*M*). Under these conditions the wave shape of TMB is essentially identical to that obtained in K-15 (Fig. 5 inset). Given the low dielectric constant of THF and the fact that no significant interaction of the radical cation and dication with THF would be expected, we ascribe the observed behavior to the formation of very tight ion aggregates (pairs and triplets). Furthermore, the addition of acetonitrile/TBAF (35 m*M*) changed the voltammetric response to that observed in acetonitrile/TBAF. Thus, it is clear that the response of TMB in K-15 is dominated by ion aggregation effects.

Orientational effects.—As mentioned previously, LC can be oriented by the use of electric and magnetic fields as well as by the modification of surfaces with surfactants or other materials. Since the use of electric or magnetic fields could severely interfere with electrochemical measurements, we decided to employ surfactants for orienting the LC phases. Thus we chose Surfine 150 and ACM-72 (see Experimental section) as materials to obtain a homogeneous (parallel to the surface) and a homeotropic (perpendicular to the surface) alignment, respectively. In terms of propagation of the alignment, this can vary widely depending on specific systems, but distances as large as 1 cm have been reported (32, 33). We tried to minimize the distance between the orienting layer (the cell bottom) and the working electrode by having the electrode rest on it. Such an arrangement is estimated to give an effective distance of about 20-50 μm between the electrode and the cell bottom.

When considering orientational effects in the present context, one must distinguish between the effects due to the anisotropy in properties of the liquid crystal (for example, dielectric constant and viscosity) from other specific solute/solvent interactions. We initially focused on viscosity effects since the temperature dependence of the viscosity of K-15 had been determined previously (31), and we could estimate an effective viscosity from an electrochemically determined diffusion coefficient and the Stokes-Einstein relation. The initial measurements were on ferrocene and TCNQ in K-15. The K-15 was oriented parallel to the surface by either the use of ACM-72 or simply by using a clean polished glass slide, since this is also known to give rise to this orientation for K-15. Because the viscosities in the parallel and perpendicular directions are quite different from each other and from that of the isotropic phase, the measurement of diffusion coefficients appeared to be a very attractive way of determining the orientation of the liquid crystalline layer and the interaction of the solute with it. Specifically this could be ascertained from the voltammetric peak currents for the different orientations as well as for the isotropic phase. Since the viscosity of the isotropic phase was known, we could derive a value for the viscosity of the liquid crystalline phase and, from this, infer the orientation.

For example, for ferrocene in K-15 oriented parallel to the surface (at 25°C) or present as an isotropic phase (at 42°C), we find that the diffusion coefficients are 2.7 and 5.8 $\times 10^{-8}$ cm²/s, respectively. Taking the value of the viscosity of K-15 at 42°C as 18 cP (31) and comparing the ratio of the diffusion coefficients under both conditions, we obtain an effective viscosity of 36.6 cP for the K-15 in the liquid crystalline form. This is in good agreement with the reported value of 39 cP (31) for the viscosity of K-15 perpendicular to the director (at 25°C). (The fact that the K-15 is oriented parallel to the electrode surface implies that the appropriate viscosity will be that which is perpendicular to the director as found.) If the liquid crystal had been oriented perpendicular to the surface, the viscosity would have been expected to be close to 28 cP which is the value measured parallel to the director.

In the case of TCNQ, we find similar results with the diffusion coefficients at 4.0 and 8.6 $\times 10^{-8}$ cm²/s for the liquid crystal (at 25°C) oriented parallel to the electrode surface and as an isotropic phase (at 42°C), respectively. We can estimate that the effect of temperature alone will account for no more than a 10% difference in the diffusion coefficients. (This would be the difference in diffusion coefficients, if the experiments could be performed at two temperatures in solvents of identical viscosity.)

It should be mentioned that there was some scatter in the values of the diffusion coefficients; however, the relative magnitudes were reasonably reproducible. (The scatter is due in part to uncertainties in the weighing of the electroactive material [typically a few micrograms], because of the cost of the liquid crystal, we typically prepared 1 ml portions for study.) In addition, we believe that the presence of an electrolyte in the liquid crystal will affect the viscosity of the medium; however, as a first approximation we have chosen to neglect this effect. Finally, we would also like to make some remarks (based on some preliminary results) concerning the formal potential for the reduction of TCNE under different orientations. Although there was some scatter in the data, there appears to be a trend where the formal potential for reduction in the homogeneous orientation is positive to that in the perpendicular orientation. The use of ferrocene as an internal standard, however, allowed the reliable measurement of differences in $E^{o\prime}$. This effect (about 20 mV beyond experimental error) could be rationalized in terms of stabilization of reactant, or product, or in terms of orbital overlap between the reactant and the electrode. These are only tentative interpretations, and at this time we cannot unambiguously identify the phenomena associated with these observed shifts.

We are presently involved in a very systematic study of the variations of peak currents and formal potentials for various redox couples under different orientations. From these studies, we hope to be able to establish firmly the nature of these observed effects. We are also currently addressing the effect of the electric field at the working electrode on the propagation distance of the nematic, which may elucidate the proposed orientation effects for the TCNE/K-15 system.

Acknowledgments

We thank the Office of Naval Research and the Donors of the Petroleum Research Fund, administered by the American Chemical Society for the support of this work.

Manuscript submitted Dec. 23, 1985; revised manuscript received April 2, 1986.

The Department of Chemistry, Cornell University, assisted in meeting the publication costs of this article.

REFERENCES

1. G. H. Brown, J. W. Doane, and V. D. Neff, "A Review of the Structure and Properties of Liquid Crystals," CRC Press, Cleveland (1976).
2. E. B. Priestly, P. J. Wojtowicz, and P. Sheng, "Introduction to Liquid Crystals," Plenum Press, New York (1975).
3. "Liquid Crystals: The Fourth State of Matter," F. D. Saeva, Editor, Marcel Dekker, New York (1979).
4. E. F. Carr, *Mol. Cryst. Liq. Cryst.*, **7**, 253 (1969).
5. R. S. Porter and J. F. Johnson, *J. Phys. Chem.*, **66**, 1826 (1962).
6. I. Haller and H. A. Huggins, U.S. Pat. 3,656,834 (1972).
7. J. L. Janning, *Appl. Phys. Lett.*, **21**, 173 (1972).
8. W. E. Balon and G. H. Brown, *Mol. Cryst. Liq. Cryst.*, **6**, 155 (1969).
9. F. D. Saeva, P. E. Sharpe, and G. R. Olin, *J. Am. Chem. Soc.*, **97**, 204 (1975).
10. L. Verbit, T. R. Halbert, and R. B. Patterson, *J. Org.*

Chem., **40**, 1649 (1975).
11. L. C. Snyder and S. Meibom, *Mol. Cryst. Liq. Cryst.*, **7**, 181 (1969).
12. S. Meibom and L. C. Snyder, *Science*, **162**, 1337 (1968).
13. A. Denat, B. Gosse, and J. P. Gosse, *Chem. Phys. Lett.*, **18**, 235 (1973).
14. B. Gosse and J. P. Gosse, *J. Appl. Electrochem.*, **6**, 515 (1976).
15. A. Denat and B. Gosse, *Chem. Phys. Lett.*, **22**, 91 (1973).
16. M. Voinov and J. S. Dunnet, *This Journal*, **120**, 922 (1973).
17. A. Lomax, R. Hirasawa, and A. J. Bard, *ibid.*, **119**, 1679 (1972).
18. A. Sussman, *Mol. Cryst. Liq. Cryst.*, **14**, 183 (1971).
19. Y. Ohnishi and M. Ozutsumi, *Appl. Phys. Lett.*, **24**, 213 (1974).
20. H. Lim, J. D. Margerum, and A. Graube, *This Journal*, **124**, 1389 (1977).
21. H. Lim and J. D. Margerum, *ibid.*, **123**, 837 (1976).
22. S. Barret, F. Gaspard, R. Herino, and F. J. Mondon, *J. Appl. Phys.*, **47**, 2375 (1976).
23. S. Barret, F. Gaspard, R. Herino, and F. J. Mondon, *ibid.*, **47**, 2378 (1976).
24. F. Gaspard and R. Herino, *J. Phys.*, **40**, C3-285 (1979).
25. R. Cocco, F. Gaspard, and R. Herino, *J. Chim. Phys.*, **76**, 383 (1979).
26. G. W. Gray, K. J. Harrison, and J. A. Nash, in "Liquid Crystals and Ordered Fluids," Vol. II, J. F. Johnson and R. S. Porter, Editors, p. 617, Plenum Press, New York (1974).
27. C. S. Oh, in "Liquid Crystals and Ordered Fluids," Vol. III, J. F. Johnson and R. S. Porter, Editors, p. 53, Plenum Press, New York (1978).
28. G. J. Kruger, *Phys. Rev. Lett.*, **82**, 229 (1982).
29. X. Zhang, J. Leddy, and A. J. Bard, *J. Am. Chem. Soc.*, **107**, 3719 (1985).
30. R. Herino, *J. Chem. Phys.*, **74**, 3016 (1981).
31. F. Kiry and P. Martinoty, *J. Phys.*, **38**, 153 (1977).
32. W. L. Kuhn and B. R. Finlayson, *Mol. Cryst. Liq. Cryst.*, **36**, 307 (1976).
33. J. Cognard, *Mol. Cryst. Liq. Cryst. Suppl. Sect.*, **1**, 1 (1982).

Palladium/Hydrogen Membrane Electrode for High Temperature/High Pressure Aqueous Solutions

Z. Nagy* and R. M. Yonco

Argonne National Laboratory, Materials Science and Technology Division and Chemical Technology Division, Argonne, Illinois 60439-4837

ABSTRACT

Several reference electrodes have been reported for high temperature/high pressure aqueous solutions, but none of them are fully satisfactory for fast relaxation measurements of electrode kinetics. The charged palladium electrode seems to fulfill all requirements at lower temperatures, but above 200°C the diffusional loss of hydrogen, into a solution not saturated with hydrogen, is very fast and the electrode must be recharged frequently. This problem can be overcome by use of a palladium-silver alloy membrane as an electrode with suitable hydrogen partial pressure on the dry side. Several electrodes of this type were built and tested over the temperature range from 100° to 300°C at a constant system pressure of 10,000 kPa and a hydrogen pressure range of 300-7000 kPa, in boric acid/lithium hydroxide solutions with a pH range of 5-11. The palladium membrane electrode was found to operate as a classical hydrogen electrode and is usable either as a pH electrode (combined with a pH-independent reference electrode) or as a reference electrode (in a constant pH solution).

Several reference electrodes have been reported for high temperature/high pressure aqueous solutions, extending to temperature and pressure limits of approximately 300°C and 10,000 kPa (1-3), but none of them are fully satisfactory for fast relaxation measurements of electrode kinetics under such extreme conditions. A common problem is the use of a junction (*e.g.*, porous plug) with high ohmic resistance to separate the internal solution from the test solution; this resistance can cause a considerable and unwanted increase in signal risetime (4). Reference electrodes of the "second kind" invariably have this disadvantage (1-2), and, by the nature of its construction, the recently proposed stabilized zirconia pH-sensitive electrode also has a high impedance (3, 5-9). Metal/metal oxide electrodes may have lower impedance but do not have the required stability (10-12). Low impedance electrodes, suitable for transient measurements, can be achieved by the use of metal electrodes directly immersed in the test solution, for example, a redox electrode could be used as a reference electrode if there was a well-defined redox couple in the solution. In a constant pH solution, the classical platinum/hydrogen electrode would be suitable, in principle, but the introduction of hydrogen into the test solution is experimentally difficult and the saturation of the solution with hydrogen may be undesirable.

A palladium electrode, cathodically charged with hydrogen to the two-phase ($\alpha + \beta$) hydride region, seems to be a suitable reference electrode up to a temperature of about 200°C (13-15). It is easy to construct and use, it has a stable potential directly relatable to the standard hydrogen potential, and it has the low impedance characteristics needed for fast pulse measurements. Unfortunately, at higher temperatures the composition range of the stable two-phase region becomes small, the diffusional loss of hydrogen into a solution not saturated with hydrogen becomes too fast, and the electrode needs very frequent recharging resulting in complex electrode and electronics design (16-17). It has been suggested (18) that this problem might be overcome by use of a palladium membrane as an electrode with suitable hydrogen partial pressure on the dry side to maintain the Pd/H ratio at the working surface in the ($\alpha + \beta$)-phase region. While such an electrode may work initially, it will fail mechanically after temperature cycling because of the repeated $\alpha - \beta$ transitions which are accompanied by a volume change of approximately 10% (19). This problem can be avoided by the alloying of palladium with silver, which depresses the $\alpha - \beta$ miscibility gap below room temperature (19-21). The hydrogen permeability of this alloy is even greater than that of pure palladium (21-24), and the alloy has been shown to be a suitable catalytic substrate for the hydrogen electrode reaction (25). The characteristics of an electrode based on these ideas have never been reported, though it may have been used in practice (26). This paper reports the results of an investigation on the feasibility of the palladium membrane pH/reference electrode concept.

Experimental

Several palladium membrane electrodes were built with the general construction design shown in Fig. 1. The sensing element was a 75% palladium-25% silver al-

*Electrochemical Society Active Member.

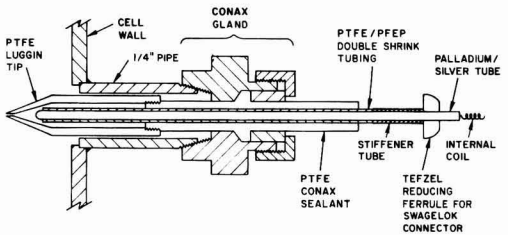

Fig. 1. Cross-sectional schematic view of a palladium membrane electrode.

loy tube of 0.16 cm diameter and 7.6×10^{-3} cm wall thickness, supplied with a steel internal coil for mechanical strength.[1] The tube was closed at one end by arc welding in helium atmosphere. The palladium tube was covered with Teflon heat-shrinkable tubing over most of its length with only a few millimeters of sensing end exposed to the test solution. A Conax high pressure electrode sealing gland[2] with Teflon sealant was used to connect the electrode to the cell. The open end of the tube was connected with a Swagelok tee connector to the hydrogen supply and a vacuum line. The Conax gland and the Swagelok tee were mechanically braced together (not shown in the figure) to avoid extrusion of the Teflon-coated tubing through the Teflon sealant. The full length of the palladium tube, between the two connectors, was covered with a snugly fitting metal stiffener tube to avoid bending under the extruding force. Most of the tests were carried out without the Teflon Luggin-tip. For some tests, an additional electrode was added in the form of a platinum wire coil surrounding the sensing tip of the palladium tube and separated from the tube by a perforated layer of Teflon. The connecting platinum wire was isolated from the tube and the solution by a third layer of heat-shrinkable Teflon. For some tests, the exposed end of the palladium tube was cathodically palladized at 0.1 A cm^{-2} for 2 min using 2% $PdCl_2$ in 2*M* HCl solution, after a cathodic cleaning in 0.1*M* H_2SO_4 at 0.5 A cm^{-2} for 5 min.

The reference electrode was an external, pressure-balanced 0.1*M* KCl Ag/AgCl electrode (2, 27) of modified design (28). A cross-sectional view of the electrode is shown in Fig. 2. The silver rod and wire were anodically chloride coated in 0.1*M* HCl at a current density of about 2 mA cm^{-2} for several hours. The junction end was attached to the test cell through a Swagelok connector, while the other end was kept at room temperature. The measured EMF was corrected for the thermal junction potential and was converted to the standard hydrogen scale at cell temperature using published correction factors (2). Liquid junction potentials were estimated to be less than ±25 mV for these conditions (16) and were ignored. Some irreproducibility of the reference electrode potential was noted, and most of our measurements were carried out with two external reference electrodes. Data were accepted only if the difference between the two readings was less than ±10 mV.

[1]Consolidated Technologies, Incorporated, Westchester, Pennsylvania.
[2]Conax Corporation, Buffalo, New York.

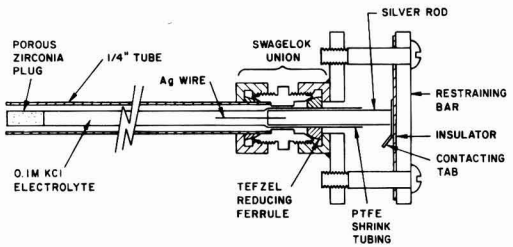

Fig. 2. Cross-sectional schematic view of an external reference electrode.

The high temperature/high pressure test cell was a tubular, flow-through cell with external band heaters. The test solution was continuously pumped through the cell with a stainless steel diaphragm pump[3] and the system pressure was controlled by a pneumatic back-pressure regulator[4] at the outlet end. The cell and the high temperature flow system were constructed completely of titanium. Drawings of the cell and flow system have been published previously (29).

Twelve palladium membrane electrodes were built and tested. The first six of these were used to prove feasibility and to refine design details; the second six electrodes were built as shown in Fig. 1 and were tested under widely ranging conditions. Usually, three electrodes were tested simultaneously in an experiment. A typical test procedure consisted of measuring the EMF as a function of internal hydrogen pressure of the electrodes at two to five pressures during a single day. The temperature or the pH of the solution would then be changed and the system equilibrated overnight. The cell was opened and the electrodes inspected after approximately two weeks of operation. The temperature, pressure, and flow conditions were continuously monitored. The EMF of the electrodes was measured through a 14 MΩ input impedance voltage follower. The electrodes were tested over the temperature range from 100° to 300°C, at a constant system pressure of 10,000 kPa and hydrogen pressure range of 300-7000 kPa, in boric acid/lithium hydroxide solutions, deaerated with nitrogen sparging, with the pH ranging from 5 through 11 (16).

Results and Discussion

A membrane electrode based on a 75% palladium-25% silver alloy does not have a two-phase hydride region (β-phase precipitation) above room temperature and, therefore, does not have a constant EMF plateau. The EMF of the electrode is controlled by the activity of the hydrogen ions and of the dissolved hydrogen in the vicinity of the electrode surface.[5] The dissolved hydrogen activity, in turn, is a function of the hydrogen activity in the gas phase on the other side of the membrane and the diffusion rate of the hydrogen through the membrane and in the solution. For ideal operation of the electrode, it is required that the diffusion rate through the membrane be much faster than that in the solution. In this case, one can assume that the dissolved hydrogen at the electrode surface is in pseudoequilibrium with the hydrogen gas in the tube, and, therefore, the EMF of the electrode is the same as a classical hydrogen electrode in the same solution and at a hydrogen pressure equal to that of the hydrogen pressure in the palladium tube.

In principle, the dissolved hydrogen concentration can be calculated from a steady-state flux equation, but the required physical constants are generally not available. However, at a temperature of 300°C there are reasonably reliable data available to make the following estimation. The hydrogen flux through the membrane can be expressed by the following empirical relation (22)

$$\Phi_m = 6.11 \times 10^{-9} \frac{\sqrt{P_{H_2}} - \sqrt{P_s}}{\delta_m} \quad [1]$$

where Φ_m is the flux in mol cm^{-2} s^{-1}; P_{H_2} (kPa) is the hydrogen pressure in the tube; P_s is the hydrogen partial pressure that would be in equilibrium with the hydrogen dissolved in the solution at the membrane solution interface; and δ_m (cm) is the thickness of the membrane.

The hydrogen flux in the solution (into a solution containing zero dissolved hydrogen) can be estimated as

$$\Phi_s = D_{H_2} \times \frac{C_{H_2}}{\delta_s} \quad [2]$$

where D_{H_2} is the diffusion coefficient of hydrogen, for which a value of 5×10^{-4} cm^2 s^{-1} is used based on a 5 ×

[3]Pulsafeeder, Interpace Corporation, Rochester, New York.
[4]Grove Valve and Regulator Company, Oakland, California.
[5]Gas bubbles will not form in the solution as long as the overall system pressure is larger than the hydrogen pressure in the palladium tube.

10^{-5} value at room temperature (30) and an estimated one order of magnitude general increase of diffusion coefficients from room temperature to 300°C (31); C_{H_2} (mol cm^{-3}) is the concentration of the dissolved hydrogen at the membrane solution interface, which is equal to the solubility of hydrogen at a partial pressure of P_s and can be calculated from: $P_s/25 \times 1.1 \times 10^6$, where 25 cm^3 mol^{-1} is the molar volume of water at 300°C and 10,000 kPa (32), and 1.1×10^6 (kPa per mole fraction) is the Henry law constant of hydrogen in water at 300°C (33); and δ_s is the thickness of the nernstian diffusion layer which in the stagnant solution is taken as 0.1 cm. In steady state, the two fluxes will be equal and the equation can be solved for P_s.

Calculations for hydrogen pressures of 300 and 7000 kPa indicated that the solution side partial pressure is only 0.8 and 3.6% lower than the gas pressure, resulting in 0.2 and 0.9 mV deviation, respectively, of the EMF from that of the classical hydrogen electrode. Based on these estimates, it is reasonable to expect that the membrane electrode will behave as a classical hydrogen electrode, within the error of our measurements. Therefore, the EMF of the electrode is expected to follow the equation

$$\mathrm{EMF}(V) = A - B \times p\mathrm{H} - C \times \log \frac{P_{H_2}(\mathrm{kPa})}{101.325} \qquad [3]$$

and, if the EMF is expressed against the standard hydrogen electrode at the same temperature, the theoretical values of the coefficients are: $A = 0.0$, $B = 2.3RT/\mathbf{F}$, and $C = 1.15RT/\mathbf{F}$, where R is the universal gas constant; T is the absolute temperature; and $\mathbf{F}$ is the Faraday constant.

As examples of some of the experimental data, the combined results for six electrodes at 200° and 300°C are shown in Fig. 3-4. Similar results were obtained at all temperatures. The experimental data were converted to the standard hydrogen scale, and a multidimensional nonlinear least squares fitting of all data was carried out to determine the experimental coefficients of Eq. [3]. The results are summarized and compared to the theoretical coefficients in Table I. The measured coefficients are close to but not exactly equal to the theoretically expected values. With the exception of the value of 100°C, coefficient A is always more negative than zero; this is partly due to the lower than theoretical pH-slope values (see discussion of coefficient B below), and partly to the long extrapolation since no data were taken below a pH of 5. The pH sensitivity of the electrodes (coefficient B)

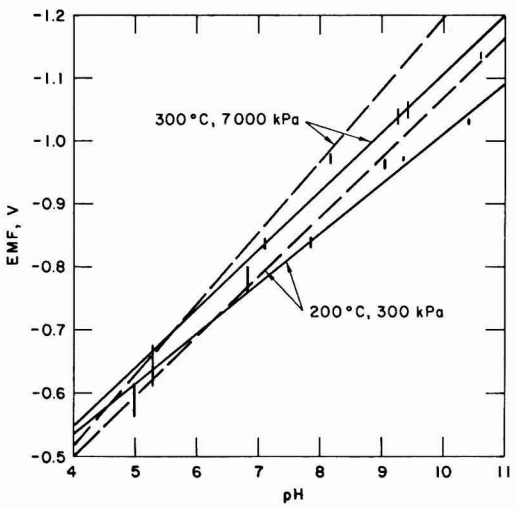

Fig. 3. Examples of the pH response of palladium membrane electrode, measured against external, pressure-balanced 0.1M KCl Ag/AgCl reference. Dashed line: theoretical equation; solid line: curve-fitted results of six electrodes; bars: range of experimental data.

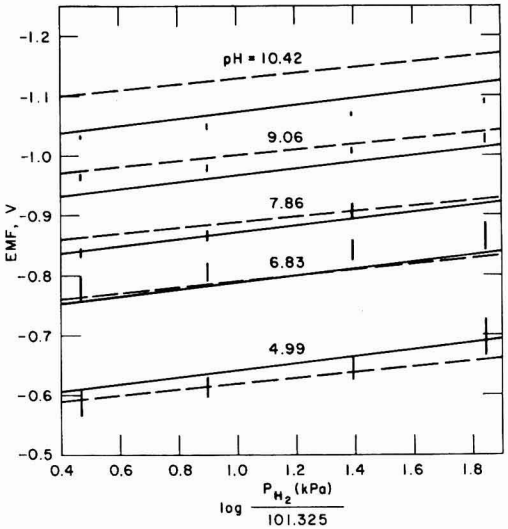

Fig. 4. Internal hydrogen pressure response of palladium membrane electrode at 200°C, measured against external, pressure-balanced 0.1M KCl Ag/AgCl reference. Dashed lines: theoretical equation; solid lines: curve-fitted results of six electrodes; bars: range of experimental data.

was invariably less than theoretical, though it increased with temperature, as expected. The largest deviation from theoretically calculated EMF values was always observed at the highest pH values, as exemplified by the 200°C data shown in Fig. 3-4. This deviation is at least partly due to the uncertainty in the calculated pH values of the solutions (16, 34). Previous work with charged palladium electrodes (16), using the same calculated pH values, has also resulted in negative deviations of the slope of the EMF *vs.* pH plot. The pressure sensitivity of the EMF (coefficient C) exhibits only normal experimental errors and does not seem to have any biased deviation from theoretical values. The spread of the data taken under identical experimental conditions is also shown on Fig. 3-4. This spread was largely due to irreproducibility of the external reference electrodes. At higher pH's, the curve-fitted line and the experimental data do not quite coincide in Fig. 4; this happens because the curve-fitted equation was obtained by a three-parameter least squares fitting using all the experimental data at a given temperature, rather than individual curve fitting at each pH value.

An ideal evaluation of the palladium membrane electrode would be a comparison to a classical hydrogen

Table I. Measured and theoretical coefficients of Eq. [3]

Temperature °C	Coefficients		
	A(V)	B(V)	C(V)
100	+0.002 (0.000)	0.068 (0.074)	0.040 (0.037)
150	−0.115 (0.000)	0.068 (0.084)	0.045 (0.042)
200	−0.088 (0.000)	0.079 (0.094)	0.057 (0.047)
250	−0.109 (0.000)	0.084 (0.104)	0.058 (0.052)
275	−0.131 (0.000)	0.088 (0.109)	0.050 (0.054)
300	−0.132 (0.000)	0.093 (0.114)	0.052 (0.057)

Theoretical values of coefficients are shown in parentheses.

electrode in the same solution. This was approximated in our tests with an additional platinum wire incorporated in the electrode, as described above. In these cases, the platinum wire electrode was always many tens of millivolts less negative than the palladium when the Luggin-tip was not used on the electrode; with the use of the Luggin-tip, however, this difference was only between 5 and 10 mV. The EMF of the palladium electrodes was independent of the Luggin-tip. Within the protected and stagnant volume of the Luggin-tip, the whole solution is probably nearly saturated with hydrogen since the only loss of hydrogen is by slow diffusion through the capillary opening. The close agreement between the palladium and platinum potentials under these conditions indicates that the palladium membrane electrode behaves, indeed, as a classical hydrogen electrode and that deviations from the theoretically calculated EMF must be ascribed to uncertainties in the calculated solution pH and the irreproducibility of the external reference electrode. Without the protective Luggin-tip, one expects the hydrogen concentration around the platinum wire to be much smaller and more irreproducible, being dependent on slight variations of the solution flow rate, than the concentration at the palladium membrane. This is in agreement with the experimental data, including the results of flow rate sensitivity measurements as described below.

The linear flow velocity of the solution was normally 1 cm min^{-1}, but, in some tests, the velocity was varied between 0.5 and 10 cm min^{-1}. Within these limits, the palladium membrane electrode was not sensitive to the flow rate, with or without the Luggin-tip. On the other hand, the additional platinum wire electrode was very sensitive to flow rate when used without the Luggin-tip, but insensitive with the tip. The results indicate that the diffusion layer is practically independent of the solution flow, while the conditions at the platinum wire, which is outside the stagnant diffusion layer, are flow rate dependent. The maximum velocity of our tests was very low, and at higher velocities one would expect the palladium membrane electrode to be flow sensitive. This may not be a practical problem. As a reference electrode, it will be used mostly with the Luggin-tip, which will protect it from flow effects, and as a pH electrode it could be surrounded with a porous structure to retain a stagnant layer at the price of increased pH response time.

The response time of the palladium membrane electrode to a step change of the internal hydrogen pressure was rather long, typically in the 15-45 min range, except at 100°C, where it took sometimes several hours to reach an equilibrium potential, reflecting the considerably reduced hydrogen permeability of the membrane material at the lower temperature. The palladized and unpalladized membrane electrodes behaved similarly in every respect, except at 100°C, where the unpalladized electrode was unstable and very slow to reach equilibrium. Apparently, at the higher temperatures, the smooth palladium-silver alloy is an adequate electrocatalyst for the hydrogen reaction. The response time of the electrodes to pH or temperature change was not tested.

It can be concluded that the palladium/hydrogen membrane electrode is a suitable high temperature/high pressure reference electrode, at least in the temperature range of 150°-300°C, with a potential equal to the classical hydrogen electrode in the same solution and at a hydrogen pressure equal to that on the dry side of the membrane. The impedance of the electrode is low and is largely controlled by the solution resistance in the Luggin-tip. Therefore, with appropriate design of the Luggin-tip, it can be made suitable for fast transient measurements. The palladium membrane electrode can also be used as a pH sensing electrode when combined with a stable reference electrode.

Acknowledgments

This work was performed under the auspices of the Division of Materials Science, Office of Basic Energy Sciences, U. S. Department of Energy, under Contract W-31-109-Eng-38. We are grateful to T. F. Kassner and W. E. Ruther for their help and advice in the design of the test apparatus and for providing facilities for the initial testing, and to V. A. Maroni for critical reading of the manuscript.

Manuscript submitted Feb. 3, 1986; revised manuscript received April 28, 1986. This was Paper 13 presented at the Boston, MA, Meeting of the Society, May 4-9, 1986.

Argonne National Laboratory assisted in meeting the publication costs of this article.

REFERENCES

1. D. D. Macdonald, *Corrosion*, **34,** 75 (1978).
2. D. D. Macdonald, A. C. Scott, and P. Wentrcek, *This Journal*, **126,** 908 (1979).
3. L. W. Niedrach and W. H. Stoddard, *Corrosion*, **41,** 45 (1985).
4. B. D. Cahan, Z. Nagy, and M. A. Genshaw, *This Journal*, **119,** 64 (1972).
5. L. W. Niedrach, *ibid.*, **127,** 2122 (1980).
6. L. W. Niedrach, *ibid.*, **129,** 1445 (1982).
7. T. Tsuruta and D. D. Macdonald, *ibid.*, **129,** 1221 (1982).
8. M. J. Danielson, O. H. Koski, and J. Myers, *ibid.*, **132,** 296 (1985).
9. S. Hettiarachchi, P. Kedzierzawski, and D. D. Macdonald, *ibid.*, **132,** 1866 (1985).
10. K. Kinoshita and M. J. Madou, *ibid.*, **131,** 1089 (1984).
11. M. J. Madou and K. Kinoshita, *Electrochim. Acta*, **29,** 411 (1984).
12. M. J. Madou, K. Kinoshita, and M. C. H. McKubre, *ibid.*, **29,** 419 (1984).
13. J. V. Dobson, *J. Electroanal. Chem. Interfacial Electrochem.*, **35,** 129 (1972).
14. J. V. Dobson, M. N. Dagless, and H. R. Thirsk, *J. Chem. Soc. Faraday Trans. I*, **68,** 749 (1972).
15. J. V. Dobson, M. N. Dagless, and H. R. Thirsk, *ibid.*, **68,** 764 (1972).
16. D. D. Macdonald, P. R. Wentrcek, and A. C. Scott, *This Journal*, **127,** 1745 (1980).
17. T. Tsuruta and D. D. Macdonald, *ibid.*, **128,** 1199 (1981).
18. D. D. Macdonald, in "Modern Aspects of Electrochemistry," Vol. 11, B. E. Conway and J. O'M. Bockris, Editors, p. 141, Plenum Press, New York (1975).
19. A. G. Knapton, *Platinum Met. Rev.*, **21,** 44 (1977).
20. J. B. Hunter, U. S. Pat. 2,773,561 (1956).
21. J. B. Hunter, *Platinum Met. Rev.*, **4,** 130 (1960).
22. F. J. Ackerman and G. J. Koskinas, *J. Chem. Eng. Data*, **17,** 51 (1972).
23. D. Fort and I. R. Harris, *J. Less-Common Met.*, **41,** 313 (1975).
24. D. T. Hughes and I. R. Harris, *ibid.*, **61,** P9 (1978).
25. A. M. Polcaro, P. F. Ricci, and A. Viola, *Ann. Chim.*, **66,** 711 (1976).
26. J. V. Monter, J. P. Sorenson, and G. J. Theus, U. S. Pat. 4,290,872 (1981).
27. M. J. Danielson, *Corrosion*, **35,** 200 (1979).
28. P. L. Andresen and W. E. Ruther, Private communication.
29. Z. Nagy and R. M. Yonco, Abstract 13, p. 20, The Electrochemical Society Extended Abstracts, Vol. 86-1, Boston, MA, May 4-9, 1986.
30. A. J. Appleby, H. Kita, M. Chemla, and G. Bronoel, in "Encyclopedia of Electrochemistry of the Elements," Vol. 9A, A. J. Bard, Editor, p. 383, Marcel Dekker, New York (1982).
31. W. T. Lindsay, EPRI Report, NP-1963 (1981).
32. J. H. Keenan, F. G. Keyes, P. G. Hill, and J. G. Moore, "Steam Tables," Wiley-Interscience, New York (1978).
33. D. M. Himmelblau, *J. Chem. Eng. Data*, **5,** 10 (1960).
34. S. Hettiarachchi and D. D. Macdonald, *This Journal*, **131,** 2206 (1984).

Enhanced Raman Scattering of 1,2,4-Triazole and Imidazole Adsorbed on Microlithographically Prepared Copper Surfaces

D. Thierry and C. Leygraf*

Swedish Corrosion Institute, S-114 86 Stockholm, Sweden

ABSTRACT

Surface-enhanced Raman scattering from molecules adsorbed on Cu electrodes may be significantly increased when using Cu surfaces with well-controlled periodicities. This is demonstrated for 1,2,4-triazole and imidazole adsorbed on periodic Cu produced by microlithographical technique. Interpretations of Raman results suggest that the molecules are nondissociatively adsorbed on Cu and show, furthermore, that oxidation-reduction cycling of Cu under present conditions has no influence on the orientation of the molecules upon adsorption.

In recent years, surface-enhanced Raman spectroscopy (SERS) has become a powerful *in-situ* tool for characterization of electrode surfaces during electrochemical reactions (1-3). Surface-enhanced Raman spectra have been observed for molecules adsorbed on rough Ag, Cu, Au, and other metal surfaces (4). These observations were possible because of a discovered 10^4-10^6 fold enhancement of the effective Raman cross section for adsorbed molecules compared to nonadsorbed species at the same concentrations. Such enhancements were only obtained after an electrode preparation consisting of an oxidation-reduction cycling (ORC), the purpose of which is to increase surface roughness at the metal electrode (5). Recently, numerous SERS experiments have been performed with corrosion inhibiting molecules adsorbed on Cu and Ag (6-9). These studies were based on electrodes which were treated by means of ORC. However, the strong polarization during ORC of the corroding electrode may result in irreversible changes at the electrode surface. Hence, a comparison between information obtained by SERS and classical electrochemical techniques, such as polarization-resistance measurements, may be difficult. Furthermore, SERS spectra exhibit a great potential dependence of Raman line intensities with a maximum close to the potential of zero charge [between −600 and −700 mV/SCE for Cu under present conditions (2)]. From this may follow difficulties in the recording of SERS spectra at potentials close to the corrosion potentials (between −100 and −200 mV/SCE for Cu under present conditions).

A recent study of SERS from molecules adsorbed on periodic Ag surfaces produced by microlithographical technique and with no ORC seems to open new ways for application of surface Raman spectroscopy, for instance in corrosion science (10). From this follows a need to compare vibrational data obtained with such surfaces and those found by ORC of the same metal electrodes.

The primary aim of this work is to examine further the possibility of using Cu surfaces produced by microlithographical technique. This is done by means of SERS studies of 1,2,4-triazole and imidazole adsorbed either on Cu surfaces subjected to an ORC or on microlithographically produced Cu surfaces. The vibrational information found with these two surface preparations will be presented and discussed, as will also the orientation on Cu of 1,2,4-triazole and imidazole upon adsorption. Although derivatives of benzotriazole such as 1,2,4-triazole and imidazole have been used as corrosion inhibiting molecules on Cu for over 20 years, the mechanisms leading to their excellent inhibition still remain uncertain (11-14).

Experimental

Microlithography.—A glass substrate 10 × 10 mm was coated with 5000Å of photoresistant material and then patterned by exposure to a periodic interference formed by two argon lasers. A second exposure, in which the sample was rotated 90°, was necessary in order to form a cross-grating pattern. This resulted in islands of unexposed material in two directions on which 1000Å of Cu was deposited. The spacing between the peaks is 5500Å. Such surfaces exhibit a very well-controlled surface roughness that can be used to obtain large surface enhanced Raman signals (10).

Scanning electron microscopy.—Scanning electron micrographs were obtained in the secondary electron image mode at an accelerating voltage of 25 keV. The incoming electron beam was perpendicular to the Cu sample, and the detector was located at an exit angle of 30°.

Raman experiments and electrochemical treatments.—The laser-Raman spectrometer with a Dilor RTI 30 triple monochromator and the electrochemical cell with three-electrode configuration have been described in detail elsewhere (6). Electrolytes were prepared by mixing solutions of inhibitors in 0.1*M* NaCl. In all cases, distilled water and pure reagents were used as ingredients. In what follows, all values of polarizing potential will be given with respect to the saturated calomel electrode (SCE).

Cu samples treated by means of ORC were cut from a 99.99% pure polycrystalline rod. The surface area of 0.25 cm^2 was diamond polished down to 1 μm, rinsed with distilled water, and degreased with acetone. ORC treatment consisted of one triangular sweep from −700 mV/SCE to +100 mV/SCE in 0.1*M* NaCl resulting in a total charge in either direction of 25 mC/cm^2. The ORC was performed in the absence of both laser illumination of the Cu surface and inhibitor molecules in the electrolyte.

SERS measurements on ORC-treated Cu surface were performed with 0.1*M* NaCl solutions containing 5 m*M* or 5 μ*M* of inhibitors, whereas SERS measurements on microlithographically prepared Cu surfaces were prepared in solutions containing 5 μ*M* of inhibitors.

All surface Raman data were obtained with a krypton laser (6471Å) at approximately 50 mW focused on a circular spot on the Cu surface of diameter 2 mm, a spectral bandpass of 5.82 cm^{-1}, and a scan rate of 64 cm^{-1}/min resulting in sweep times of approximately 10 min for SERS spectra shown throughout this study. All normal Raman data were obtained with an argon laser (5145Å) at approximately 300 mW, a spectral bandpass of 1.78 cm^{-1}, and a scan rate of 64 cm^{-1}.

Results and Discussion

SERS with oxidation-reduction cycling.—Figure 1 illustrates the Raman lines of a normal Raman spectrum (lower part) of 1,2,4-triazole in ethanol (used as solvent) and SERS spectra obtained at different potentials or concentrations in 0.1*M* NaCl. The SERS spectra were recorded after an ORC, after which the Cu electrode was potentiostatically controlled at −700 mV/SCE (Fig. 1a and c) and −150 mV/SCE (Fig. 1b). The latter potential is close to the actual corrosion potential. In agreement with results shown in Ref. (2), the most intense SERS signals were found at −700 mV/SCE. As is seen from Fig. 1,

*Electrochemical Society Active Member.

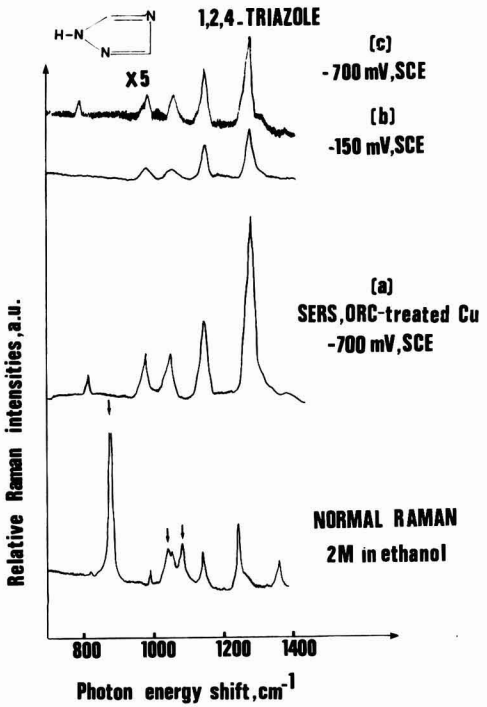

Fig. 1. Raman spectrum of 1,2,4-triazole in ethanol (bottom) and SERS spectra of the same molecule in 0.1M NaCl. Arrows indicate normal Raman peaks of ethanol used as solvent. (a) SERS from 1,2,4-triazole on Cu at −700 mV/SCE with 5 mM concentration of 1,2,4-triazole. (b) same as (a) but at −150 mV/SCE. (c) same as (a) with 5 μM concentration of 1,2,4-triazole.

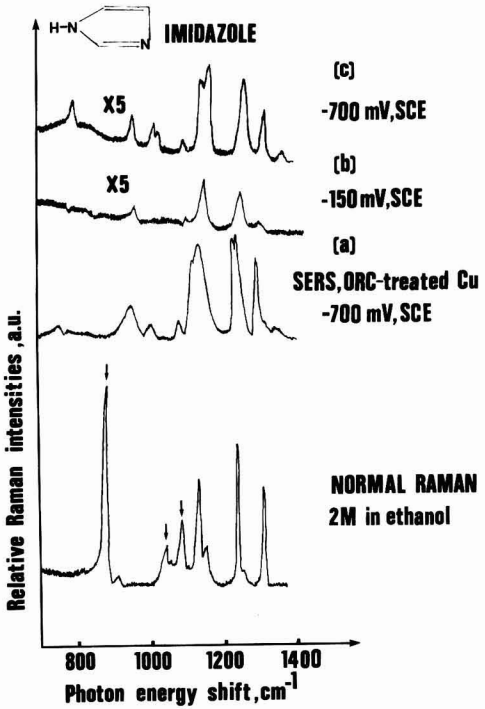

Fig. 2. Normal Raman and SERS spectra of imidazole. See text of Fig. 1 for further explanation.

SERS spectra from micromolar concentrations (Fig. 1c) of 1,2,4-triazole show very small differences, aside from intensity, from those with millimolar concentrations (Fig. 1a and b). However, the intense SERS signals from micromolar concentrations of 1,2,4-triazole (Fig. 1c) found at −700 mV/SCE practically disappear when going to −150 mV/SCE. Furthermore, normal Raman spectra of concentrated 1,2,4-triazole and SERS spectra exhibit similar features, with Raman modes at approximately the same frequency shifts. This suggests that 1,2,4-triazole is nondissociatively adsorbed on Cu.

Figure 2 illustrates the same studies for imidazole. Again, normal Raman and SERS spectra show similarities with Raman modes at approximately the same positions, suggesting no dissociation of imidazole upon adsorption on Cu.

The normal Raman spectra of concentrated 1,2,4-triazole and imidazole solutions have been reported and discussed elsewhere (15, 16). Hence, Tables I and II summarize the data in the literature concerning frequency shifts and notations of the more intense Raman lines in the ring breathing mode region for 1,2,4-triazole and imidazole, respectively.

SERS without oxidation-reduction cycling.—The inhibiting properties of organic corrosion inhibitors are, generally, discussed at the corrosion potential of the investigated system. Hence, it is of primary importance to study 1,2,4-triazole and imidazole at their actual corrosion potentials and without an anodic or cathodic polarization that may produce irreversible changes of the corroding electrodes.

Figures 3 and 4 illustrate the Raman lines of SERS spectra of 1,2,4-triazole and of imidazole, respectively, adsorbed on Cu after two different surface preparations, namely, diamond polishing and microlithographic preparation. This time, Raman spectra were recorded without ORC but with the Cu electrode after each surface preparation immersed in a micromolar solution and spontaneously held at its corrosion potential. As seen in Fig. 3 and 4, intense Raman lines are found with microlithographically prepared Cu surfaces, whereas no Raman lines are found on mechanically polished Cu surfaces. This may be explained by the nature of surface enhancement of Raman scattering. It is now well established that the total enhancement of Raman scattering is a contribution of short-range and long-range enhancement (17). The long-

Table I. Frequency shifts and tentative assignments of Raman lines of bulk 1,2,4-triazole

Raman frequency (cm^{-1})	Notation [Ref. (15, 22)]
840	Out-of-plane C-H deformation
980	In-plane ring bending
1065	In-plane C-H bending
1150	Ring breathing
1260	Ring stretching
1270	In-plane C-H bending
1380	Ring stretching
1485	Ring stretching

Table II. Frequency shifts and tentative assignments of Raman lines of bulk imidazole

Raman frequency (cm^{-1})	Notation [Ref. (16, 22)]
755	Out-of-plane C-H deformation
840	Out-of-plane C-H deformation
1065	In-plane C-H deformation
1095	In-plane C-H deformation
1135	Ring stretching
1160	In-plane N-H deformation
1260	In-plane C-H deformation
1330	Ring stretching
1430	Ring stretching
1485	Ring stretching

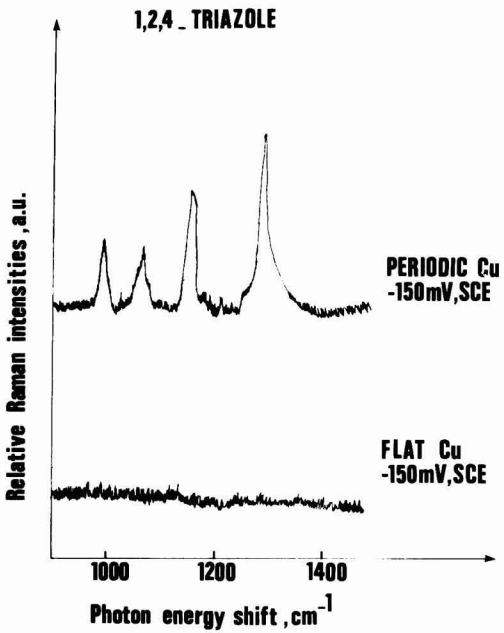

Fig. 3. SERS spectra with 5 μM solution of 1,2,4-triazole in 0.1M NaCl obtained by using two different surface preparations without oxidation-reduction cycling.

range contribution is caused by the enhancement of electromagnetic fields near the surface, which may arise, for instance, from excitations of surface plasmon polaritons. The strong enhancement of Raman lines found on Cu electrodes with controlled surface periodicities and the absence of Raman lines from flat, diamond-polished Cu surfaces indicate that electromagnetically induced long-range contribution seems to be essential in order to record SERS spectra from 1,2,4-triazole and imidazole adsorbed on Cu.

In the same way as was observed on Cu electrodes with ORC, normal Raman and SERS spectra on periodic Cu surfaces without ORC exhibit similar features, with Raman modes at approximately the same frequency

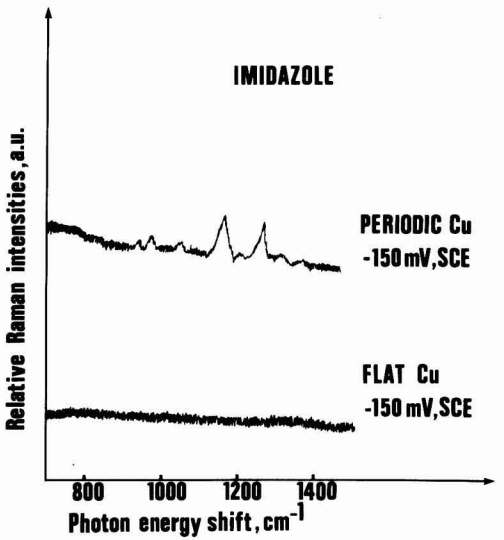

Fig. 4. SERS spectra of imidazole. See text of Fig. 3 for further explanation.

Table III. Frequency shifts and relative Raman intensities of 1,2,4-triazole adsorbed on ORC-treated Cu (at −150 mV/SCE) and on microlithographically prepared copper surfaces (at the corrosion potential, −150 mV/SCE)

SERS from ORC-treated Cu		SERS from periodic Cu	
Raman frequency (cm^{-1})	Intensity[a]	Raman frequency (cm^{-1})	Intensity[a]
992	25	992.5	25
1065	20	1067.5	20
1154	76	1155	75
1287.5	100	1288	100

[a] Intensity relative to the strongest band, given arbitrary value 100.

shifts. Again, this suggests that 1,2,4-triazole and imidazole are nondissociatively adsorbed on Cu at present conditions.

Table III exhibits frequency shifts and relative Raman intensities of the more intense Raman lines in the ring-breathing region mode of 1,2,4-triazole when adsorbed on Cu. These spectra were recorded at −150 mV/SCE on Cu with ORC and on microlithographically prepared Cu without ORC. The similarities in frequency shifts and relative Raman intensities of adsorbed 1,2,4-triazole suggest that the ORC has no influence on the orientation or possible dissociation of 1,2,4-triazole on Cu at this potential.

Figure 5 illustrates a scanning micrograph of a representative part of the Cu substrate produced by microlithography and used for SERS studies. The copper particles are uniform in size and are of similar appearance to the silver particles produced by the same technique and shown in Ref. (10). The size of each copper particle is 2000-3000Å, and the periodicity is 5500Å. The maximum in SERS has been attributed to surface roughness with particle size in the range of 100-1000Å (18, 19). From this follows that the high SERS signals found are very encouraging when considering that the present particle size or periodicity is far from optimized. Controlled surface roughness in the range of 100-1000Å may result in further surface enhancement from inhibitor complexes adsorbed on Cu at the corrosion potentials or may facilitate SERS studies of molecules adsorbed on different transition metals which are not strong surface-enhanced Raman scatterers.

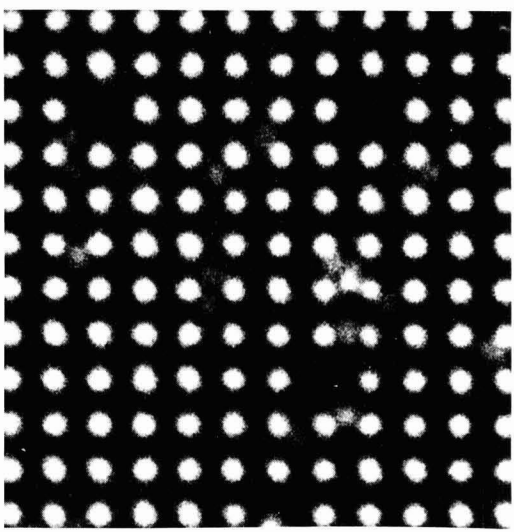

Fig. 5. Scanning electron micrograph of a copper electrode produced by microlithographic technique. The spacing between each copper particle is 5500Å.

To investigate the possibility that laser-induced roughening of the microlithographically prepared Cu surface served as an alternate source of surface-enhanced Raman scattering, a series of scanning electron microscopy studies was undertaken. The studies were based on a 1000Å thick Cu film which was evaporated on a glass substrate coated with 5000Å of photoresist. Figure 6 shows a representative scanning electron micrograph after exposure of evaporated Cu for 15 min in 0.1*M* NaCl during simultaneous krypton laser illumination at 50 mW. As inferred from Fig. 6, no signs of roughening can be detected suggesting that no features with the dimensions of 200Å or larger have been produced upon exposure and simultaneous laser illumination. However, the present study cannot exclude the formation of features in the range of 100-200Å or smaller.

Interpretation of SERS spectra.—As shown in previous sections (Table III) SERS spectra recorded at −150 mV/SCE after ORC and SERS spectra obtained from microlithographically produced Cu surfaces exhibit similarities, with Raman lines at very similar positions. This suggests that 1,2,4-triazole and imidazole are nondissociatively adsorbed on Cu in the range of applied potentials examined in this work.

Furthermore, most SERS peaks of imidazole and 1,2,4-triazole at −700 mV/SCE exhibit comparatively small shifts compared to normal Raman peaks in bulk solutions. For instance, the triazole ring breathing mode at 1150 cm^{-1} exhibits a shift of only 6-7 cm^{-1} when going from normal to surface Raman spectra. As a comparison, the corresponding peaks of the triazole ring breathing mode in benzotriazole exhibits a shift of almost 30 cm^{-1} when going from normal to surface Raman spectra (6, 7). In the case of benzotriazole, the results were interpreted as the molecule being adsorbed in an end-on configuration on Cu. The present results, on the other hand, may be interpreted as the investigated molecules being adsorbed towards more flat configurations characterized by more limited electronic interactions with the Cu substrate. This may be supported by independent electrochemical measurements showing that imidazole and 1,2,4-triazole under present conditions exhibit poor corrosion efficiency on Cu (23). Imidazole and 1,2,4-triazole exhibits strong intermolecular N- - - H-N hydrogen bonds with vibrational modes in the region of 2500-3100 cm^{-1} (15, 22). In a recent SERS study of imidazole and some derivatives adsorbed on Cu and Ag, Loo *et al.* examined this spectral region and interpreted the results as imidazole being adsorbed end-on on both Cu and Ag at −700 mV/SCE and −600 mV/SCE, respectively (22). However, in contrast to the present study, these authors did not consider any changes in frequency shift between bulk and SERS spectra.

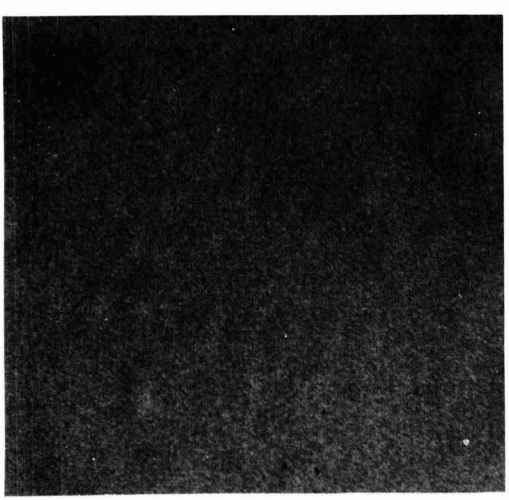

Fig. 6. Scanning electron micrograph of evaporated 1000Å Cu film on glass substrate exposure for 15 min in 0.1M NaCl during simultaneous krypton laser illumination at 50 mW.

Conclusions

Surface-enhanced Raman scattering (SERS) may be significantly increased by periodicity-controlled Cu surfaces obtained by microlithographic techniques as compared with pretreated surfaces obtained by oxidation-reduction cycling.

The results show that 1,2,4-triazole and imidazole under present conditions are nondissociatively adsorbed on Cu and, tentatively, in flat configuration. The results seem to be independent of surface pretreatment used.

The results presented are encouraging with regard to new applications of SERS in corrosion science, for instance when considering its possible use in nonaqueous, low conducting media, where, in general, no anodic polarization is possible, or when studying transition metals from which so far no SERS has been observed.

Acknowledgments

The financial support of the Swedish Board for Technical Development (STU) is gratefully acknowledged. We thank Mr. B. Wennergren, Swedish Telecommunications Administration, for help with scanning electron microscopy studies.

Manuscript submitted June 20, 1985; revised manuscript received July 10, 1986.

The Swedish Corrosion Institute assisted in meeting the publication costs of this article.

REFERENCES

1. M. Fleischmann, P. J. Hendra, and A. S. McQuellan, *Chem. Phys. Lett.*, **26,** 163 (1974).
2. C. L. Jeanmaire and R. P. Van Duyne, *J. Electroanal. Chem.*, **84,** 1 (1977).
3. "Surface Enhanced Raman Scattering," T. E. Furtak and R. K. Chang, Editors, Plenum Press, New York (1982).
4. H. Seki, *J. Electron. Spectrosc. Relat. Phenom.*, **30,** 287 (1983).
5. S. G. Schultz, M. Janik-Czachor, and R. P. Van Duyne, *Surf. Sci.*, **104,** 419 (1981).
6. D. Thierry and C. Leygraf, *ibid.*, **149,** 592 (1985); *This Journal*, **132,** 1009 (1985).
7. J. J. Kester, T. E. Furtak, and A. J. Bevolo, *ibid.*, **129,** 1716 (1982).
8. B. H. Loo, Annual Report, INCRA project no. 341 (1982).
9. J. Rabim, G. R. Gutz, O. Sala, and W. J. Orville-Thomas, *J. Mol. Struct.*, **100,** 571 (1983).
10. P. F. Liao, in "Surface Enhanced Raman Scattering," T. E. Furtak and R. K. Chang, Editors, p. 379, Plenum Press, New York (1982).
11. P. G. Fox and P. A. Bradley, *Corros. Sci.*, **20,** 643 (1980).
12. R. Walker, *Corrosion (Houston)*, **31,** 97 (1975).
13. G. W. Poling, *Corros. Sci.*, **10,** 359 (1970).
14. D. Chadwick, and T. Hashemi, *ibid.*, **18,** 39 (1978).
15. D. Bougeard, N. Le Calvé, B. Saint Roch, and A. Novak, *J. Chem. Phys.*, **64,** 5152 (1976).
16. "Characteristic Raman Frequencies of Organic Compounds," F. R. Dollish, W. G. Fateley, and F. F. Bentley, Wiley Interscience, New York (1974).
17. S. S. Jha, J. R. Kirtley, and J. C. Tsang, *Phys. Rev. B*, **22,** 3973 (1980).
18. Y. Mo, I. Mörke, and P. Wachter, *Surf. Sci.*, **133,** 452 (1983).
19. S. K. Miller, A. Barker, M. Meier, and A. Wokaun, *J. Chem. Soc., Faraday Trans. 1*, 1305 (1984).
20. F. W. King, R. P. Van Duyne, and G. C. Schatz, *J. Chem. Phys.*, **69,** 4472 (1978).
21. G. C. Schatz, in "Surface Enhanced Raman Scattering," T. E. Furtak and R. K. Chang, Editors, p. 35, Plenum Press, New York (1982).
22. B. H. Loo, Y. G. Lee, and A. El Hage, in Proceedings of the 9th International Conference on Raman Spectroscopy, p. 538 (1984).
23. D. Thierry and C. Leygraf, Unpublished results.

The Dissolution Mechanism of Iron in Chloride Solutions

Douglas R. MacFarlane

Department of Chemistry, Monash University, Clayton, Victoria, Australia

Stuart I. Smedley

Department of Chemistry, Victoria University of Wellington, Wellington, New Zealand

ABSTRACT

We have measured the polarization curve and the electrochemical impedance for the dissolution of iron in sodium chloride solutions of varying pH of [xNaCl + yHCl, $x + y = 4.5M$] pH = 0, 1, 2, 3, 4. The polarization curves are comparable with those of previous workers and exhibit two distinct Tafel slopes: 75 mV/s at low polarization, and 40 mV/decade at high polarization for pH = 0, 1, 2, 3. The impedance diagrams exhibit a high frequency capacitive loop, followed by one inductive loop at low overpotentials, and a further inductive loop at high overpotentials. We have interpreted these phenomena in terms of two parallel dissolution paths.

The mechanism of the corrosion of iron has for some time been the subject of much study and controversy. This controversy has been heightened by the recent application of the technique of impedance electrochemistry to the study of the dissolution mechanism (1, 2). Earlier mechanisms, based principally on polarization measurements, have been shown to be in error and somewhat too simple. Impedance measurements of the dissolution of iron in sulfate solutions have indicated that there are at least three rate controlling steps involving three different intermediate species.

The dissolution mechanism of iron in chloride ion solution seems to be even more complicated since the chloride ion participates in the dissolution process. Kuo and Nobe (3) have reviewed previous work on the dissolution of iron in chloride solutions up to 1978. Their experiments in [xNaCl + yHCl, $x + y = 4.5M$] solutions contradict some of the findings of earlier work (4), but in agreement with the work of Chin (5) show that the polarization curve has two quite distinct Tafel slopes. At low polarization potentials, the rate is accelerated by chloride ions and hydroxide ions with a Tafel slope of 0.075 V/decade where the proposed mechanism is

$$\mathrm{Fe \cdot H_2O + Cl^- \underset{k_{-1}}{\overset{k_1}{\rightleftarrows}} [FeClOH]_{ad}^- + H^+ + e} \quad \theta_1 = [\mathrm{FeClOH^-}] \qquad [1]$$

$$\mathrm{[FeClOH]_{ad}^- \xrightarrow[\text{rds}]{k_2} FeClOH + e} \qquad [2]$$

$$\mathrm{FeClOH + H^+ \rightarrow Fe^{2+} + Cl^- + H_2O} \qquad [3]$$

At high polarization potentials the rate is accelerated by hydroxide ions with a Tafel slope of 0.04 V/decade and the predominant process is the mechanism

$$\mathrm{Fe \cdot H_2O \underset{k_{-3}}{\overset{k_3}{\rightleftarrows}} [FeOH]_{ad} + H^+ + e} \quad \theta_2 = [\mathrm{FeOH}] \qquad [4]$$

$$\mathrm{[FeOH]_{ad} \xrightarrow[\text{rds}]{k_4} [FeOH]^+ + e} \qquad [5]$$

$$\mathrm{FeOH^+ + H^+ \rightarrow Fe^{2+} + H_2O} \qquad [6]$$

The purpose of our work is to add to the experiments of Kuo and Nobe by measuring the electrochemical impedance iron corroding in chloride solutions of constant ionic strength over a range of frequencies, pH's, and potentials. An analysis of the data of the type made by Keddam *et al.* (1) for the dissolution of iron in sulfate solutions should provide support, or otherwise, for the dissolution mechanism proposed above.

Experimental

Steady-state polarization and impedance measurements were made for the dissolution of a rotating disk of iron in [xNaCl + yHCl, $x + y = 4.5M$] solutions of pH = 0, 1, 2, 3, 4. The rotation speed was 1000 rpm^{-1} and the electrode material constructed from a disk of Johnson Matthey Chemicals "Puratonic" iron. The electrode was polished with "jewellers' rouge," washed with acetone, and then dipped in 0.5M sulfuric acid for 10 min. Prior to each experiment the electrode was polarized anodically in the experimental cell to current density of 70 mA cm^{-2} for 5 min in order to provide a reproducible initial state of the electrode.

Solutions were prepared from doubly distilled water, oven dried analytical grade BDH sodium chloride, and oxygen was removed from the solutions by bubbling nitrogen into the cell.

All experiments were performed in the potentiostatic mode using a three-electrode cell. The reference electrode was a saturated calomel electrode and, in the manner of Scheickert, Lorenz, and Friedburg (2), this electrode was connected by means of a capacitor in parallel with a platinum electrode. This technique reduces the impedance of the reference electrode and minimizes phase shifts at higher frequencies.

Polarization measurements were carried out with a PAR Model 173 potentiostat incorporating a PAR Model 179 plug-in coulombmeter. Current measurements were made when, at a set potential, the current had reached a steady state. Impedance measurements were performed by applying the sine wave output of a Solartron frequency response analyzer, Model 1174, to the input of the potentiostat, the X and Y inputs of the FRA being taken from the output of the PAR Model 178 electrometer and the current from the coulombmeter output. Data from the FRA were then transferred to a HP 85A microcomputer and displayed as a complex impedance plane diagram. The high frequency intercept of the impedance curve with the real axis was taken as a measure of the uncompensated resistance between the working and reference electrodes and was used to amend the polarization curves for the potential drop caused by this uncompensated resistance.

The apparatus was tested for instrumentally induced phase shifts, and these experiments indicated that the system was free from such effects up to 10^5 Hz (6).

The corroding system was also tested for reproducibility by reversing the direction of the scan at the completion of an experiment. At a given frequency, the impedances measured under different scanning directions did not differ by more than 10%, and the shape of the impedance curves was unchanged. Furthermore, the dc current density before and after an impedance scan did not change by more than 10%, if at all.

Results and Discussion

The results of the polarization experiments are displayed in Fig. 1. In agreement with the work of Kuo and Nobe (3), the data for pH = 0, 1, 2, and 3 clearly exhibit two Tafel regions, one of slope 0.075 V/decade at low po-

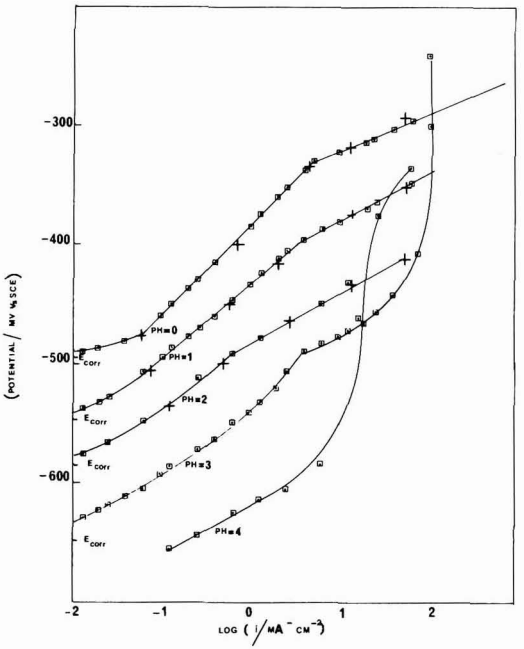

Fig. 1. Anodic steady-state polarization curves for the dissolution of iron in (xNaCl + yHCl) = 4.5M solutions of pH = 1, 2, 3, 4. Experimental data □; simulated data +.

larization and one of slope 0.04 V/decade at high polarization. The data for pH = 3 and 4, however, exhibit a transition region which is not found in previous work. Impedance diagrams for solutions of pH = 0, 1, and 4 at different overpotentials are displayed in Fig. 2, 3, and 4, respectively. Data for pH = 2 are comparable with those for pH = 0 and 1, whilst the data for pH = 3 are comparable with those for pH = 4. At the lowest overpotential, the data in Fig. 2 and 3 indicate that the impedance curve is possibly the sum of two semicircles, the equivalent of two parallel RC networks in series; however, the low frequency relaxation process becomes inductive at higher overpotentials, and, at even higher overpotentials, where the Tafel slope changes, two inductive semicircles are apparent.

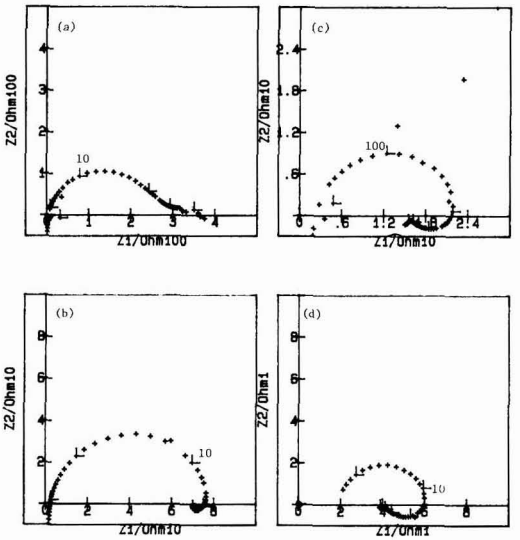

Fig. 3. Impedance diagrams for iron in NaCl/HCl solutions for pH = 1. Potential vs. SCE. (a) −504 mV, (b) −449 mV, (c) −415 mV, (d) −375 mV. Large crosses denote decade frequency intervals.

The impedance data in Fig. 4 for pH = 4 solutions show similar characteristics to those of lower pH, *i.e.*, at an overpotential corresponding to the break in the Tafel slope there are two inductive semicircles in the complex impedance plane; however, with increasing overpotential the semicircle occurring at the lowest frequency transforms into a capacitive loop, which in turn transforms back into an inductive loop at even higher overpotentials.

Very similar observations have been made by Keddam *et al.* (1) for the dissolution of iron in sulfate solutions. They observe a single but distorted capacitive loop at po-

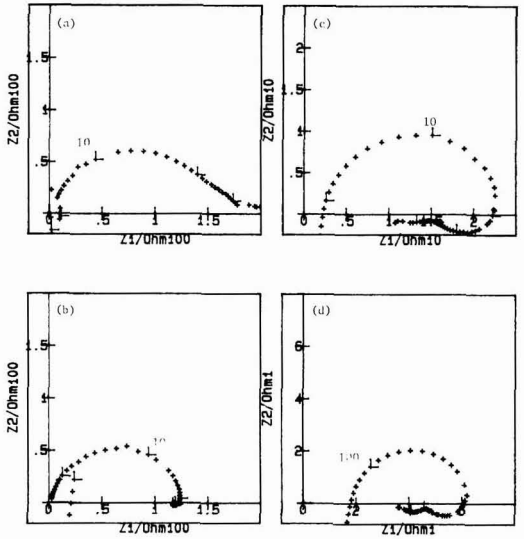

Fig. 2. Impedance diagrams for iron in NaCl/HCl solutions for pH = 0. Potential vs. SCE. (a) −475 mV, (b) −392 mV, (c) −332 mV, (d) −304 mV. Large crosses denote decade frequency intervals.

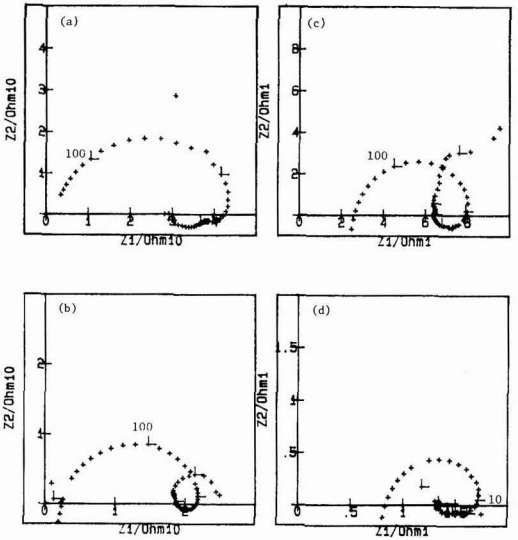

Fig. 4. Impedance diagrams for iron in NaCl/HCl solutions for pH = 4. Potential vs. SCE. (a) −598 mV, (b) −532 mV, (c) −422 mV, (d) −222 mV. Large crosses denote decade frequency intervals.

tentials cathodic to the corrosion potential, but at higher overpotentials, where hydrogen production is negligible, the impedance diagrams transform into a single high frequency capacitive loop, followed by two lower frequency inductive loops, which are attributed to separate steps in the dissolution process.

By analogy, and in agreement with the suggestion of Kuo and Nobe (3), the iron specimens in this work in chloride solutions of pH = 0, 1, 2, and 3 dissolve at low polarization by a mechanism with single rate controlling step, but at high polarizations another process becomes significant and dissolution takes place via two consecutive parallel mechanisms.

Keddam *et al.* (1) observed that for iron in sulfate solutions of pH = 2.6 and 4 (at an overpotential corresponding to a current shoulder on their polarization curve) the lower frequency inductive loop transformed into a capacitive loop as overpotential increased, the diameter of the loop being very large as the zero frequency intercept of the real axis must correspond with the slope of the polarization curve at that potential.

This same feature is apparent in our work for solutions of pH = 3 and 4 at overpotentials corresponding to the abrupt rise in the Tafel slope; but for the pH = 4 solution the low frequency loop transforms back into an inductive loop at even higher overpotentials which correspond to the decreasing Tafel slope.

The transformation from an inductive to a capacitive loop with increasing overpotential was attributed by Keddam and co-workers to an increase in surface coverage, as overpotential increases, of an intermediate species formed during the dissolution process. This species inhibits current flow as its fractional coverage approaches unity; it has a "pre-passivating" effect, thus giving rise to a capacitive loop. However, at higher overpotentials the coverage due to this species declines rapidly, the capacitive loop disappears, and the loop transforms back into an inductive loop. Since Keddam and co-workers were able to reproduce their impedance-steady state polarization data successfully with a model based on the above hypotheses, it is likely that a similar model could be developed for the system under study in this work.

The principal assumptions upon which this model is based are as follows: (*i*) the rate constants for the elementary electron transfer reactions are exponentially dependent on the overpotential, (*ii*) the transfer coefficient α can have a value between 0 and 1, although in this case the values are approximately 0.5, and (*iii*) the surface coverage due to adsorbed intermediates follows a Langmuir adsorption law, and the adsorbed species do not overlap on the surface.

The first model tested was that represented by Eq. [1]-[5] above. According to the procedures of Keddam *et al.*, this model gives the steady-state current density as

$$\frac{i}{\mathbf{F}} = k_1(1 - \theta_1 - \theta_2) - k_{-1}\theta_1 + k_2\theta_1 + (1 - \theta_1 - \theta_2)k_3 - \theta_2 k_{-3} + \theta_2 k_4 \qquad [7]$$

where k_1 and k_{-1} are pseudo-first-order rate constants. The rate of change of θ_1 and θ_2 can be written as

$$\beta_1\left(\frac{d\theta_1}{dt}\right) = (1 - \theta_1 - \theta_2)k_1 - k_{-1}\theta_1 - k_2\theta_1 \qquad [8]$$

$$\beta_2\left(\frac{d\theta_2}{dt}\right) = (1 - \theta_1 - \theta_2)k_3 - k_{-3}\theta_2 - k_4\theta_2 \qquad [9]$$

where β_1 and β_2 are constants relating the θ_1 and θ_2 to the surface concentration of adsorbed species 1 and 2. The rate constants k_i are exponentially dependent on potential where

$$k_i = k_{o,i} \exp(b_i E)\ b_i = \left\{\frac{Z\alpha_i \mathbf{F}}{RT}\right\}$$

α_i is the transfer coefficient, and z is the number of electrons involved in the stoichiometric electron transfer reaction.

By taking the Taylor expansion of Eq. [7], limited to first order, it is possible to show that the impedance z is given by

$$\frac{1}{z} = \mathbf{F}\left[\frac{1}{R_{ct}} - \frac{d\theta_1}{dE}(k_1 + k_{-1} - k_2 + k_3) + \frac{d\theta_2}{dE}(k_1 + k_3 + k_{-3} - k_4)\right] \qquad [10]$$

where

$$\frac{1}{R_{ct}} = \bar{\theta}_1[1 - 2b_{-1}k_{-1} + b_2k_2 - b_3k_3] + \bar{\theta}_2[b_1k_1 - b_{-3}k_{-3} + b_4k_4] + b_1k_1 + b_3k_3 \qquad [11]$$

$\bar{\theta}_1$ and $\bar{\theta}_2$ are the steady-state values of θ_1 and θ_2 and can be evaluated from Eq. [8] and [9] when $d\theta_1/dt = d\theta_2/dt = 0$. The expressions for $d\theta_1/dE$ and $d\theta_2/dE$ were obtained in the manner of Keddam *et al.*; these are complex quantities and contain the parameters k_i and b_i. Finally z is written as being in parallel with the double layer capacitance C_{dl}.

To simulate the steady-state and impedance curves, we first of all set $k_3 = 0$ and, therefore, $\theta_2 = 0$ and attempted to fit the parameters $k_{o,1}$, $k_{o,-1}$, $k_{o,2}$, b_1, b_{-1}, and b_2 to the low current portion of the steady-state curve for pH = 1, and the impedance diagrams pertaining to that section of the Tafel plot. This was readily achieved. Next, we attempted to simulate the high current portion of the Tafel plot where the Tafel slope is 0.04 V/decade. This was possible, if it was assumed that the forward step of reaction [4] is independent of iron activity, or that $(k_4 + k_{-3}) >>$ and $k_{-3} >> k_4$, *i.e.*, $k_{-3} >> k_3$, which is unlikely at high overpotentials. Whilst these assumptions made it possible to obtain a fit to the steady-state curve, it was impossible to obtain a fit to the appropriate impedance diagrams. It became apparent that the only other way to simulate to 0.04V Tafel slope was to include a two-electron step in the mechanism. An obvious way to achieve this was to adapt the mechanism of Keddam *et al.* by adding to their reaction scheme steps [1] and [2] of this paper, and by neglecting steps [5] and [6] in their paper.

The result is a mechanism that can be written in simplified form as

$$\mathrm{Fe} \underset{k_{-1}}{\overset{k_1}{\rightleftarrows}} \mathrm{Fe(I)_{ads}}^1 + e \qquad \theta_1 \equiv \mathrm{Fe(I)_{ads}}^1 = [\mathrm{FeClOH}]^- \qquad [12]$$

$$\mathrm{Fe(I)_{ads}}^1 \overset{k_2}{\rightarrow} \mathrm{Fe(II)_{sol}} + e \qquad [13]$$

$$\mathrm{Fe} \underset{k_{-3}}{\overset{k_3}{\rightleftarrows}} \mathrm{Fe(I)_{ads}}^2 + e \qquad \theta_2 \equiv \mathrm{Fe(I)_{ads}}^2 = (\mathrm{FeOH})_{ads} \qquad [14]$$

$$\mathrm{Fe(I)_{ads}}^2 \overset{k_4}{\rightarrow} \mathrm{Fe(II)_{sol}} + e \qquad [15]$$

$$\mathrm{Fe(I)_{ads}}^2 \underset{k_{-5}}{\overset{k_5}{\rightleftarrows}} \mathrm{Fe^*(I)_{ads}}^2 \qquad \theta_3 \equiv \mathrm{Fe^*(I)_{ads}}^2 \qquad [16]$$

$$\mathrm{Fe^*(I)_{ads}}^2 + \mathrm{Fe} \underset{k_6}{\rightarrow} \mathrm{Fe^*(I)_{ads}}^2 + \mathrm{Fe(II)_{sol}} + 2e \qquad [17]$$

Where $\mathrm{Fe^*(I)_{ads}}^2$ in a dissolution intermediate species, reaction [17] is a "self-catalytic process."

Using the same assumptions as above with regard to the model, the charge balance equation gives the current density as

$$\frac{i}{\mathbf{F}} = \Sigma_{k_1} - \theta_1 k_{-1} + \theta_1 k_2 + \Sigma k_3 - \theta_2 k_{-3} + \theta_2 k_4 + \theta_3 2k_6 \quad [18]$$

where $\Sigma = (1 - \theta_1 - \theta_2 - \theta_3)$.

The time dependence of the θ_i can be expressed through the mass balance equations

$$\beta_1 \frac{d\theta_1}{dt} = \Sigma k_1 - \theta_1 k_{-1} - \theta_1 k_2 \quad [19]$$

$$\beta_2 \frac{d\theta_2}{dt} = \Sigma k_3 - \theta_2 k_{-3} - \theta_2 k_4 - \theta_2 k_5 + \theta_2 k_{-5} \quad [20]$$

$$\beta_3 \frac{d\theta_3}{dt} = \theta_2 k_5 - \theta_3 k_{-5} \quad [21]$$

Using the same procedure as described above, the expression for the impedance becomes

$$\frac{1}{z} = \mathbf{F}\left[\frac{1}{R_{ct}} - \frac{d\theta_1}{dE}(k_1 + k_{-1} - k_2 + k_3) - \frac{d\theta_2}{dE}(k_1 + k_3 + k_{-3} - k_4) - \frac{d\theta_3}{dE}(k_1 + k_3 - 2k_6)\right]$$

where

$$\frac{1}{R_{ct}} = \Sigma b_1 k_1 - b_{-1} k_{-1}\theta_1 + b_2 k_2 \theta_1 + \Sigma b_3 k_3 - b_{-3} k_{-3}\theta_2 + k_4 k_4 \theta_2 + 2b_2 k_6 \theta_3$$

The expression for the $d\theta_i/dE$ were also derived in the manner referred to above. Finally, the impedance was written as being in parallel with the double layer capacitance.

As outlined above, if $\theta_2 = \theta_3 = 0$, it was relatively simple to obtain a reasonable fit to the low current density portion of the steady-state curve, and hence the appropriate impedance diagrams. This we duly did and then attempted to fit the complete reaction sequence to the full current-potential curve. The fit thus obtained for the steady-state current potential curves for pH = 0, 1, and 2 are illustrated by reference to Fig. 1, and the appropriate values of $k_{0,i}$ and b_i are listed in Table I. Impedance diagrams for pH = 1 only are displayed in Fig. 5, and these simulated diagrams should be compared with the experimental results displayed in Fig. 3. Except for the lowest overpotentials the simulated steady-state curves agree quite well with the experimental results. A significant portion of the deviation at low overpotentials probably arises from the shift of the corrosion potential towards more positive values than would be predicted on the basis of the standard electrode potentials. As expected, this effect becomes more significant with increasing $[H^+]$. In fact, it is so significant for pH = 0 that it was not possible to simulate the steady-state curve by using the measured open-circuit potential for this system, and the value for $E_{i=0}$ was chosen from the extrapolated log i/E curve, see Table I. The simulated impedance diagrams in Fig. 5 compare quite well with the experimentally determined ones. The quality of the fit was judged by the correspondence of the following points: (*i*) the shape of the curves, (*ii*) the value of R_{ct}, and (*iii*) the frequency distribution of the impedances.

Table I. Rate constants k_i and parameters b_i for the dissolution of iron in 4.5M KCl of pH 0, 1, 2

pH	0	1	2
$k_{0,1}$/mol cm^{-2} s^{-1}	5.6×10^{-8}	5.6×10^{-8}	5.6×10^{-8}
$k_{0,-1}$/mol cm^{-2} s^{-1}	1.9×10^{-9}	1.9×10^{-9}	1.9×10^{-9}
$k_{0,2}$/mol cm^{-2} s^{-1}	5.8×10^{-11}	8.1×10^{-11}	9.9×10^{-11}
$k_{0,3}$/mol cm^{-2} s^{-1}	1×10^{-11}	1×10^{-11}	1×10^{-11}
$k_{0,-3}$/mol cm^{-2} s^{-1}	1×10^{-10}	1×10^{-10}	1×10^{-10}
$k_{0,-4}$/mol cm^{-2} s^{-1}	5×10^{-13}	5×10^{-13}	5×10^{-13}
$k_{0,5}$/mol cm^{-2} s^{-1}	7×10^{-9}	7×10^{-10}	8.5×10^{-10}
$k_{0,-5}$/mol cm^{-2} s^{-1}	1×10^{-10}	1×10^{-10}	1×10^{-10}
$k_{0,6}$/mol cm^{-2} s^{-1}	4×10^{-14}	2.2×10^{-13}	1.5×10^{-12}
b_1/V^{-1}	14	14	14
b_{-1}/V^{-1}	−24	−24	−24
b_2/V^{-1}	31	38	38
b_3/V^{-1}	14	14	14
b_{-3}/V^{-1}	−24	−24	−24
b_4/V^{-1}	38	38	38
b_5/V^{-1}	0	0	0
b_{-5}/V^{-1}	0	0	0
b_6/V^{-1}	39	39	39
β_1/mol cm^{-2}	5×10^{-8}	5×10^{-8}	5×10^{-8}
β_2/mol cm^{-2}	5×10^{-8}	5×10^{-8}	5×10^{-8}
β_3/mol cm^{-2}	5×10^{-8}	5×10^{-8}	5×10^{-8}
C_{dl}/F cm^{-2}	5×10^{-4}	5×10^{-4}	5×10^{-4}

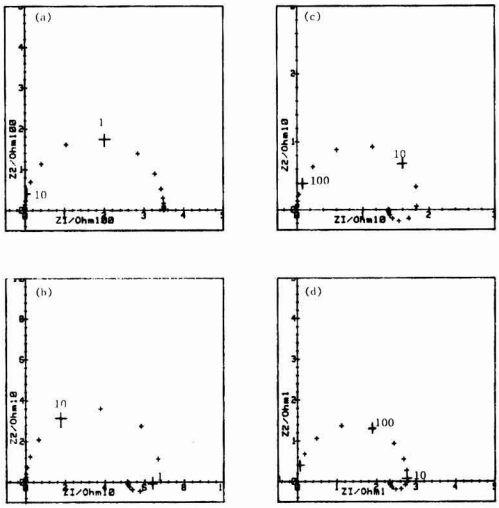

Fig. 5. Simulated impedance diagrams for iron in NaCl/HCl solutions for pH = 1. Potential vs. SCE. (a) −504 mV, (b) −449 mV, (c) −415 mV, (d) −375 mV.

For the curves at the overpotentials of 97.3, 132.3, and 172.3 mV (corresponding to −449, −415, and −375V *vs.* [SCE] respectively), all of these features correspond reasonably well with those in Fig. 3; the principal differences being that the high frequency capacitive loops are true semicircles with the center on the real axis, the "inductive" loops are also semicircles and have a smaller radius than the corresponding experimental curves, and the lowest frequency inductive loops are not sufficiently large. Also, the charge transfer resistances show some deviation from the experimental values. The simulated impedance diagram for $\eta = 43.3$ mV (or −504V *vs.* [SCE]) has similarities with the experimental curve, in that both curves have a capacitive loop at the lowest frequencies. However, the magnitude of the low frequency loop on the simulated curve is much smaller than that of the experimental one. It is possible that at this low overpotential the experimental curve is affected by the absorption of hydrogen which on iron in sulfate solutions is characterized by an inductive loop at low overpotentials. Another significant source of error arises from the fact that the impedance is very potential dependent, and therefore a 10% error in estimating the uncompensated resistance can, at high overpotentials, give rise to an error of several millivolts in the estimation of the overpotential and, for example, a 20% deviation in the value of the simulated charge transfer resistance when compared to the experimental value.

In general, it was observed that the quality of the fit to the steady-state curves or the impedance curves could be improved, but only with an accompanying degradation in the quality of one fit to the other. The set of parameters displayed in Table I represents the best overall fit to both sets of curves that could be obtained by manual adjustment of the parameters. The magnitude of the parameters indicates that at pH 0, 1, and 2, reactions [12], [14],

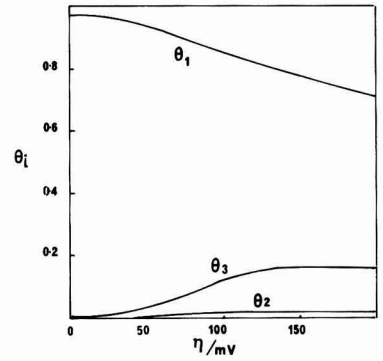

Fig. 6. Fraction surface coverage θ_i at pH = 1. θ_1 = $Fe(I)_{ads}^{1}$, θ_2 = $Fe(I)_{ads}^{2}$, θ_3 = $Fe^{*}(I)_{ads}^{2}$.

and [16] are in equilibrium but with equilibrium constants less than unity which become rapidly smaller as overpotential increases, the rate controlling steps are reactions [13], [15], and [17]. Some variation of the parameters with increasing $[H^+]$ is observed, in particular $k_{o,6}$ which decreases rapidly, in contradistinction to Keedam *et al.* who observed the opposite effect. It was not possible to determine whether $k_{o,-1}$ and $k_{o,-3}$ were $[H^+]$ dependent, since the quality of the fit showed very little change, if these parameters were altered by a factor of ten. The parameter b_2 had to be altered slightly to accommodate the small changes in the Tafel slopes of the pH = 0 steady-state plots at high overpotentials. Unlike Keddam *et al.* it was not found necessary to include a potential dependence for reaction [16]. The β_i parameters are comparable in magnitude to those used by Keddam *et al.*, *i.e.*, $\sim 10^{-8}$ mol cm^{-2} representing a monomolecular layer.

The rate constant $k_{o,1}$ and $k_{o,3}$ for the formation of the adsorbed species $(FeOCl)_{ads}$ $(FeOH)_{ads}$ are very much smaller than those of the comparable constants determined by Keddam *et al.* from their model; $k_{o,5}$, however, is of a similar magnitude. Another noticeable difference is the finite value for $k_{o,-1}$ and $k_{o,-3}$: in particular, $k_{o,-1}$ had to be greater than zero in order to reproduce the capacitive loop observed at low overpotentials for pH = 0, 1, 2, however, both constants decrease rapidly with increasing overpotential.

Figure 6 displays the variation of θ_1, θ_2, and θ_3 with potential for pH = 1. For most of the potential range, the θ_i stay above 0.8 or below 0.2, within the range of validity of the Langmuir isotherm. The corresponding data for pH = 0, 2 exhibit very similar trends.

Summary and Conclusions

We have simulated steady-state current-potential curves and impedance diagrams for pH = 0, 1, 2. The simulated steady-state curves and the impedance diagrams are very similar to the experimental ones, in particular the latter exhibit a transition from a low frequency capacitive loop at low overpotentials to a single and then two inductive loops at overpotentials corresponding to the kink in the steady-state curve. The rate constants that arise from the simulation process are, except for $k_{o,6}$, generally independent of concentration, or the fitting process is not sufficiently sensitive to detect any concentration dependence. Thus, given the simplifying assumptions made in the construction of the model, it seems to represent quite closely the dissolution of iron in chloride solutions for pH 0, 1, and 2. It also tends to confirm the postulate that the kink in the steady-state area arises from the onset of another parallel dissolution mechanism.

Manuscript submitted Nov. 15, 1985; revised manuscript received June 17, 1986.

REFERENCES

1. M. Keddam, O. R. Mattos, and H. Takenouti, *This Journal*, **128**, 257 (1981); *ibid.*, **128**, 266 (1981).
2. H. Schweickert, W. Lorenz, and H. Friedburg, *ibid.*, **127**, 1693 (1980).
3. H. C. Kuo and K. Nobe, *ibid.*, **125**, 853 (1978).
4. E. McCafferty and N. Hackerman, *ibid.*, **119**, 999 (1972); and N. A. Darwish, F. Hilbert, W. J. Lorenz, and H. Rosswag, *Electrochim. Acta*, **18**, 421 (1973).
5. R. J. Chin and K. Nobe, *This Journal*, **119**, 1457 (1972).
6. F. Mansfield, M. W. Kendig, and S. Tsai, *Corrosion*, **38**, 570 (1982).

Laser-Controlled Wet Chemical Etching for Corrective Trimming of Thin Films

Application to Aluminum

Jeff Y. Tsao

Sandia National Laboratories, Albuquerque, New Mexico 87185

Daniel J. Ehrlich

Lincoln Laboratory, Massachusetts Institute of Technology, Lexington, Massachusetts 02173

ABSTRACT

The localized enhancement of wet chemical etching by focused laser beams for corrective trimming of thin films, and its application to the selective etching of aluminum, are discussed. Since wet etching can proceed rapidly even without irradiation, it is as important to consider methods for reducing background etching as to consider those for enhancing localized etching. The process developed for aluminum etching is based upon moderate local heating to activate a reaction that is normally suppressed by a corrosion inhibitor. Another approach to the reduction of background etching is solution cooling: for the activation energies for typical wet etching, it should be possible to obtain acceptable contrast ratios between laser-enhanced and background rates over the temperature range within which many concentrated etching solutions are liquid.

Laser-controlled chemical etching for microelectronics applications has received growing attention recently (1); these applications have spawned the development of a variety of techniques optimized for various purposes (2). One important potential use for such etching is the corrective trimming of thin film lithographic

defects. Such defects can be quite expensive, especially if they arise at the end of a lengthy design and prototyping cycle. Moreover, existing corrective procedures have important shortcomings. A second photoresist-based lithography sequence, using either local exposures by a laser or electron beam or large-area exposures through a photomask, can introduce new defects, even if it corrects old ones. Direct laser ablation is difficult to control, due to potentially vastly different vaporization temperatures of thin film and substrate materials, and often causes damage to underlying devices and scatters debris over the substrate surface.

In this paper, we will discuss the use of laser-controlled chemistry as an alternative means of correcting lithographic defects. It should be pointed out that in the past few years a variety of laser-chemical etching processes have been reported (2). Laser-controlled processes based on a wide range of mechanisms (wet/dry, photochemical/thermal) have been developed and optimized for various materials. For thin film lithographic applications, however, chemical selectivity against substrate etching is critical. Therefore, despite other disadvantages, wet chemistry has an important advantage over dry chemistry because of its greater selectivity for a wider range of materials. In addition, many important thin film materials, such as metals, are not intrinsically photoactive. For these reasons, we have explored the use of thermally enhanced thin film wet etching processes. This has the additional advantage of allowing one to draw upon the vast amount of existing knowledge on selective wet chemical etching.

For the application described here, the most important figure of merit is the ratio between the laser-enhanced and the background etch rates. Even without laser enhancement, however, optimized etching solutions can have room temperature rates in excess of those required for most corrective operations. Therefore, it is as important to consider methods for reducing etching rates under ambient conditions as it is to enhance etch rates locally by laser irradiation. In this paper, we will focus on a process for laser-enhanced Al etching (3), in which the room temperature reaction is suppressed by the use of a corrosion inhibitor. At high temperatures, the inhibitor becomes ineffective and allows rapid etching to take place.

Chemistry of Al Etching

The process for selective Al etching is based on a mixture of nitric and phosphoric acids. This combination was chosen mainly because such mixtures form the basis of many commercial aluminum etching solutions. The overall electrochemistry of the system consists of simultaneous cathodic and anodic reactions (4, 5). For very low nitric acid concentrations, the cathodic reaction is mainly hydrogen evolution ($2H^+ + 2e^- \rightarrow H_2$). At higher nitric acid concentrations, the reduction of nitric acid ($3H^+ + NO_3^- + 2e^- \rightarrow HNO_2 + H_2O$) becomes the dominant cathodic reaction, and the etch rate increases. This behavior is illustrated in Fig. 1, in which are plotted constant etch-time contours on a triangle composition diagram. This is an important practical point, since the use of a nitric acid-rich solution has been observed to eliminate the formation of bubbles of H_2 gas, which can defocus the laser beam.

The dominant anodic reactions are a competition between the formation of soluble aluminum phosphates and the formation of less soluble surface oxides. The first reaction leads to dissolution; the second leads to passivation. The passivating layer, similar to bulk aluminum oxides, is inert in most solvents, and is only slowly attacked by phosphoric acid. When the reactions are biased towards passivation, the steady-state oxide layer is thicker, effectively reducing the overpotentials that drive the cathodic reaction. Therefore, at high nitric acid concentrations, the overall etching rate decreases, due to

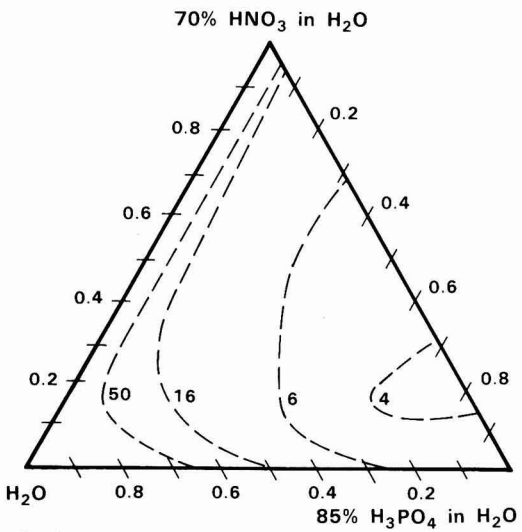

Fig. 1. Triangle diagram of unilluminated etch times for removing 200 nm of Al in etchants of various compositions at a temperature of 23°C. Constant 4, 6, 16, and 50 min etch-time contours are plotted.

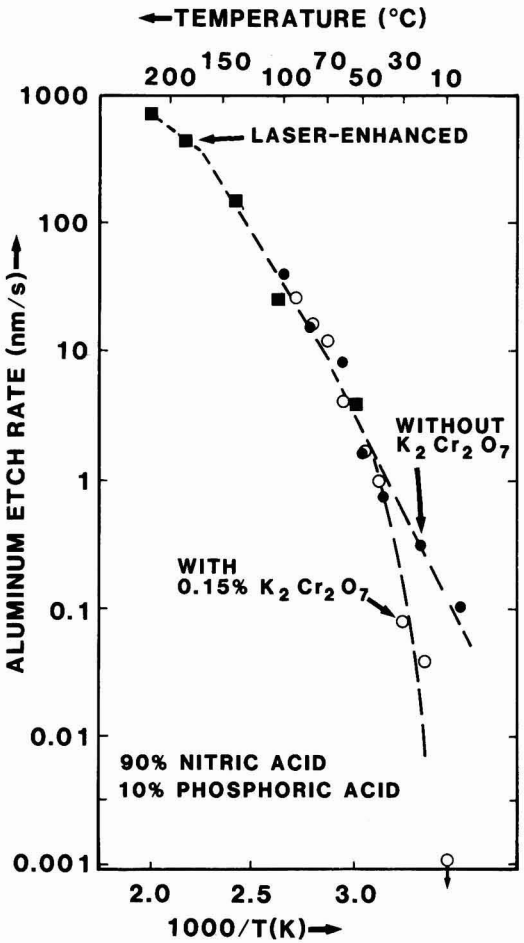

Fig. 2. Temperature dependence of Al etch rate in a 90% nitric acid/10% phosphoric acid solution, with (unfilled circles) and without (filled circles) $K_2Cr_2O_7$. High temperature measurements (filled squares) were made, as discussed in the text, using a focused laser beam heat source.

the passivation reaction $2Al^{3+} + 3NO_3^- + 3H_2O \rightarrow Al_2O_3 + 3HNO_3 + 3H^+$.

In practice, in order to eliminate H_2 gas evolution, the solution composition we have used in this work, 90% nitric acid/10% phosphoric acid, is on the nitric acid-rich side of the composition diagram. The temperature dependence of the Al etch rate in this solution is shown in Fig. 2. The moderate temperature (0°-100°C) rates were measured by immersing 200 nm thick Al films, formed by E-beam evaporation onto glass slides, in solutions heated by a hot plate or cooled by a thermoelectric cooler. In the higher temperature (60°-200°C) regime, a focused laser beam was used to heat locally Al films immersed in a room temperature solution, and rates were measured by observing the onset of self-transmission of the laser beam through the film. The effective temperature of the laser-heated spot was calibrated against the hot plate temperatures by matching the etch rates in the overlapping temperature range 60°-100°C. The temperature obtained by this procedure was consistent, to within 20%, with a separate calibration, in which the onset of bubble formation in pure H_2O was taken to occur at 100°C.

For most of the temperature range, the temperature dependence displays an Arrhenius behavior with an activation energy of 0.65 eV (15 kcal/mol). This large activation energy indicates that surface reaction rather than volume mass transport kinetics control the etch rate; this was confirmed by observing the lack of effect of solution agitation on etch rate. Only at the higher temperatures does mass transport appear to limit etch rate. For a wide range of compositions, it appears that a surface reaction involving aluminum phosphates is rate limiting, since the activation energies measured for etching in several very different solutions were found to be the same, and to be equal to that known to be characteristic of the phosphoric acid etching of sapphire (6).

Inhibition of Aluminum Etching

From Fig. 2, it can be seen that the contrast ratio between the room temperature and laser-enhanced etch rates is approximately 3.5 decades. Although high spatial resolution etching can be obtained with such a contrast ratio, for practical applications in which an Al film may be exposed to the etchant for considerable periods, a higher contrast ratio (>10^5) between illuminated and unilluminated etch rates is necessary. Therefore, it is important to consider methods for suppressing the background etch rate.

For the case of Al, the background etch rate has been suppressed by chemically biasing the reaction towards electrochemical passivity with small amounts of a strong oxidizer, $K_2Cr_2O_7$ (5, 7). As shown in Fig. 2, at moderate to high temperatures, the temperature dependence of the etch rate is the same as in the solution without $K_2Cr_2O_7$; however, at low temperatures, the etch rate decreases significantly below that in the solution without $K_2Cr_2O_7$. The mechanism for this sharp transition from dissolution to passivation is not fully understood, but can be tentatively explained by a model in which the adsorption of dichromate ions on the surface is very temperature dependent. At low temperatures, dichromate ions have largely displaced phosphate ions at the surface, and react with Al^{3+} ions diffusing through the oxide to form another layer of oxide (*e.g.*, via $Cr_2O_7^{2-} + 2Al^{3+} + 4H_2O \rightarrow Al_2O_3 + 2H_2CrO_4 + 4H^+$). At high temperatures, dichromate ions are efficiently desorbed to a low steady-state surface coverage. In practice, a 0.2 weight percent concentration of $K_2Cr_2O_7$ in a 90% nitric acid/10% phosphoric acid solution is enough to decrease the background etch rate at 10°C to less than 10^{-3} nm/s, while the laser-enhanced etch rate remains greater than 10^3 nm/s, or >6 orders of magnitude larger. Higher concentrations were found to slow the high temperature rate and are, therefore, undesirable.

Circuit Trimming and Defect Correction

To demonstrate the usefulness of these laser-enhanced wet etching processes for correcting random patterning errors in integrated circuit fabrication, or for cutting links on redundant or custom circuitry, we have made laser exposures of Al metallization patterns. In our experiment, the substrate is mounted on a water-cooled thermoelectric refrigerator which maintains a temperature below the active/passive transition point described above. For thin Al films, very little solution is required; a thin capillary layer trapped between the substrate and a cover window was found to be sufficient. The refrigera-

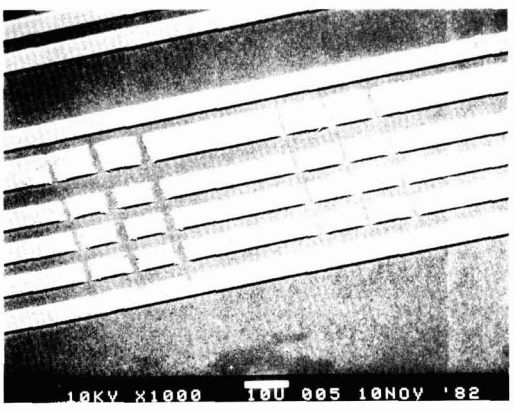

Fig. 3. Scanning electron micrograph of laser chemically etched cuts in 200 nm thick Al lines. The substrate was silicon, oxidized to a 1 μm thickness. The incident power was 0.12W and the effective dwell time was 400 ms.

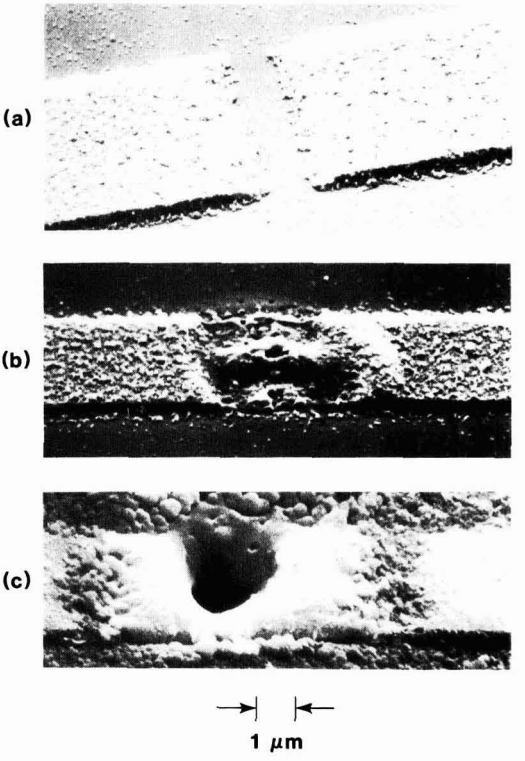

Fig. 4. Scanning electron micrographs of (a) a laser-etched cut similar to those shown in Fig. 3, and for comparison, laser exposures of the same effective duration (400 ms) made in air, at (b) ~0.35W and (c) ~0.5W of incident power.

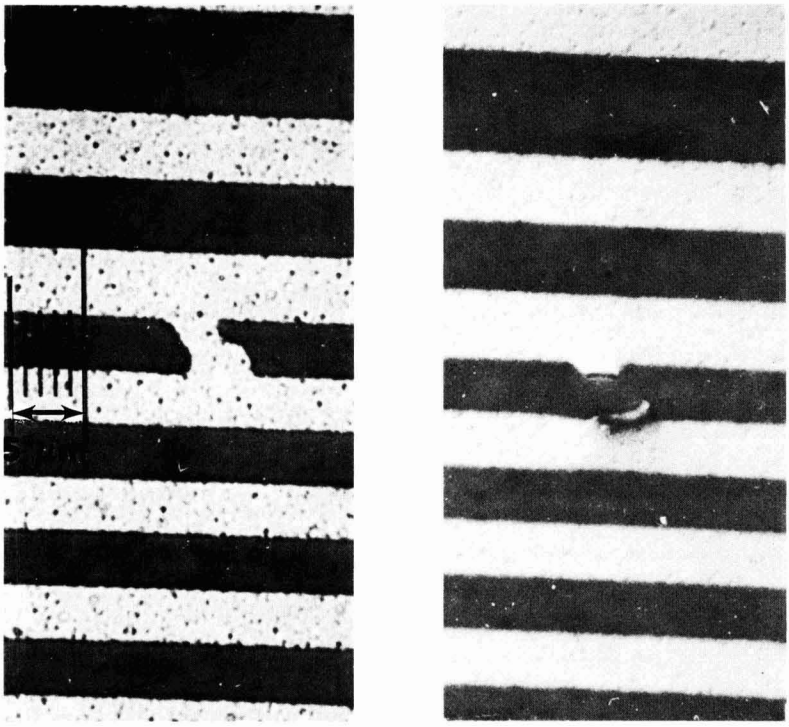

Fig. 5. Optical micrographs of a typical Al integrated circuit bridging defect (a) before, and (b) after, correction by laser-chemical etching.

tor is mounted on a 0.25 μm/step, stepping motor driven, precision X-Y translation stage. The stage can be controlled by an LSI-11/23 microcomputer for complex circuit restructuring operations, although manual control is sufficient for simple search and repair operations. The laser beam used is derived from a cw Ar^+ laser, whose excellent transverse spatial mode quality allows it to be focused to spots ~1 μm in diameter. A mechanical shutter provides accurate (~0.1 ms) control of exposure duration. The beam is steered by a coated beamsplitter into a high power microscope, which both focuses the beam onto and allows *in situ* viewing of the circuit (1).

A scanning electron micrograph of cuts laser microchemically etched into Al conductors is shown in Fig. 3. The cuts are clean and debris free, with no noticeable damage to the underlying oxide. Figure 4 shows an expanded view of a similar laser-etched cut in a 200 nm thick conductor, and, for comparison, conductors partially and fully disrupted by irradiation in air. An effective irradiation time of 400 ms was used on each case; however, the power level required for chemical etching is ~0.12W, whereas that required for complete ablation in air is ~0.4-0.5W. Based on cross calibrations, the peak temperature during etching is estimated to be ~200°C.

Optical micrographs of bridging defects in an integrated circuit, before and after correction, are shown in Fig. 5. Electrical tests of this and other circuits (8) indicate that neither the modest local temperature rise nor the photon flux of the correction procedure damaged underlying devices significantly. For some circuits, however, in which some Al conductors contacted a p^+ substrate and some contacted n^+ diffusions, it was found that marginal substrate cooling to just below the active/passive transition temperature resulted in preferential, enhanced background Al etching near the p^+ contacts. The effect is independent of overall substrate illumination and is, therefore, not related to photovoltaically driven electrochemistry. Rather, it appears to be a galvanic reaction, in which the cathodic stripping of electrons from Al occurs preferentially at the n^+ contacts, and the anodic dissolution or passivation occurs preferentially at the p^+ contacts. An apparent enhancement may occur in such a situation because the cathode is spa-

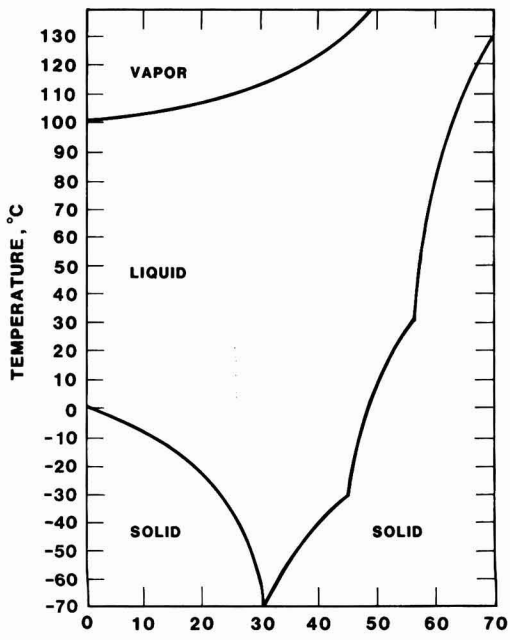

Fig. 6. Binary phase diagram of KOH and H_2O, showing the temperature-composition stability regions for vapor, liquid, and solid (9).

tially separated from the anode, and its reaction is less effectively inhibited by passivating insulating layers. For these particular circuits, therefore, it was found necessary to cool the substrate to well below the active/passive transition temperature (<0°C) in order to suppress background etching adequately.

Conclusions

Finally, it is important to emphasize that the use of corrosion inhibition to de-enhance background etching is convenient, in that it narrows the overall temperature range that must be accessed. However, for typical thermal activation energies (~0.6 eV) for wet etching, it should be possible to obtain reasonable figures of merit ($>10^5$) without corrosion inhibition, by extending the working temperature range to >130°C. In fact, as illustrated in Fig. 6 for the case of potassium hydroxide solutions (9), many concentrated etching solutions have eutectic compositions at which they are liquid over at least such a temperature range. Suppression of background etching by solution cooling may, therefore, be a more general and useful approach than corrosion inhibition to rate suppression. This also makes it possible to bring to bear on corrective trimming applications the great number of etching recipes that have been discovered and refined over the years by metallurgists and corrosion engineers. The disadvantage to this approach is the need for substrate cooling, although we have found that this can be accomplished without great difficulty with thermoelectric coolers.

Acknowledgments

The experiments in this work were performed at Lincoln Laboratory. It is a pleasure to acknowledge the technical assistance of S. Fiorillo, B. E. Duquette, D. J. Sullivan, M. N. Gilson, M. C. Finn, P. M. Nitishin, R. W. Mountain, D. J. Silversmith, and J. H. Sedlacek. Work performed at Lincoln Laboratory was sponsored by the Department of the Air Force, in part under a specific program supported by the Air Force Office of Scientific Research, by the Defense Advanced Research Projects Agency, and by the Army Research Office. Work performed at Sandia National Laboratories was supported by the U.S. Department of Energy under Contract no. DE-AC04-76DP00789.

Manuscript received Dec. 16, 1985.

Sandia National Laboratories assisted in meeting the publication costs of this article.

REFERENCES

1. D. J. Ehrlich and J. Y. Tsao, *J. Vac. Sci. Technol.*, **B1**, 969 (1983); Y. Rytz-Froidevaux, R. P. Salathe, and H. H. Gilgen, *Appl. Phys.*, **A37**, 121 (1985).
2. See, for example, C. I. H. Ashby, *Appl. Phys. Lett.*, **45**, 892 (1984); R. J. Von Gutfeld and R. T. Hodgson, *ibid.*, **40**, 352 (1982); F. W. Ostermayer, Jr., and P. A. Kohl, *ibid.*, **39**, 76 (1981); A. W. Tucker and M. Birnbaum, *IEEE Electron Device Lett.*, **edl-4**, 39 (1983); G. L. Loper and M. D. Tabat, *Appl. Phys. Lett.*, **46**, 654 (1985); P. D. Brewer, G. M. Reksten, and R. M. Osgood, Jr., *Solid State Technol.*, 273 (April 1985); and K. E. Greenberg, A. W. Johnson, J. W. Medernach, and K. Jungling, To be published.
3. J. Y. Tsao and D. J. Ehrlich, *Appl. Phys. Lett.*, **43**, 146 (1983).
4. J. O'M. Bockris and A. K. N. Reddy, in "Modern Electrochemistry," Vol 2, Sec. 11, Plenum Press, New York (1970).
5. U. R. Evans, "The Corrosion and Oxidation of Metals: Scientific Principles and Practical Applications," Chap. V, St. Martin's Press, New York (1960).
6. A. Reisman, M. Berkenblit, J. Cuomo, and S. A. Chan, *This Journal*, **118**, 1653 (1971).
7. G. G. Eldredge and R. B. Mears, *Ind. Eng. Chem.*, **37**, 736 (1945); M. G. Fontana and N. D. Greene, "Corrosion Engineering," pp. 198-203, McGraw-Hill Inc., New York (1978); C. G. Matasa and W. C. Setzer, in "Proceedings of Corrosion 78," National Association of Corrosion Engineers, Paper No. 46, Houston, Texas (1978).
8. D. J. Ehrlich, J. Y. Tsao, D. J. Silversmith, J. H. C. Sedlacek, R. W. Mountain, and W. S. Graber, *IEEE Electron Device Lett.*, **edl-5**, 32 (1984).
9. "KOH Caustic Potash," p. 25, Technical Brochure, International Minerals and Chemical Corporation, Northbrook, IL (October 1976).

Effect of Low Temperature Thermal Aging on Rheological Properties and Moldability Performance of Molding Compounds

Kishore K. Chakravorty, C. R. Sporck,* and D. Malladi

National Semiconductor Corporation, Santa Clara, California 95051

ABSTRACT

Low temperature thermal aging influences the rheological properties of epoxy based thermoset molding compounds. Moldability performance is strongly affected by changes in the rheology of the compound. Influence of thermal aging at 35°C of a typical semiconductor grade novolac epoxy molding compound on resin molecular size distribution, curing behavior, and moldability performance has been investigated. Thermal aging has been observed to result in reactive linking of the constituent epoxy and phenol novolac resin system. The extent of linking of the constituent resin system has been observed to influence the curing behavior of the molding compound as measured by differential scanning calorimetry, spiral flow length, and ram follower viscosity measurement techniques. Moldability defects parameters, such as incomplete encapsulation and resin-bleed onto the leads of the packages during transfer molding process, have been found to be intimately connected with the curing behavior of the molding compound.

Epoxy-based thermoset molding compounds are the "workhorse" material of plastic encapsulated IC's today. The quality and reliability requirements for these compounds are growing with stringent performance standards and new package assemblies (1). One key quality feature is the moldability performance, which essentially deals with the optimization and, hence, maximization of the encapsulation efficiencies (2). Improvement of the moldability performance involves homogenous filling of all mold cavities, minimum voids in the molded package, and minimal mold compound resin bleed onto the leads of the encapsulated package. Optimization of the transfer molding conditions such as transfer pressure, transfer time, and the curing cycle play an important role in the overall molding performance. But a far more important role is played by the rheological properties of the molding compound. In view of the increased emphasis on the moldability performance, there is an urgent need for understanding of the factors involved in the compositions, synthesis, and manufacturing processes that influence the overall rheological properties of the molding compound. Furthermore, the understand-

*Electrochemical Society Active Member.

ing of the microscopic features, such as resin polymer molecular size distribution (chain length) and cross-link density distribution and its dependency on curing behavior of the compound, is of paramount importance from a moldability standpoint (3). Unfortunately, little attention has been given to the dependence of the microscopic features on the moldability performance—specifically, the effect of low temperature thermal aging, almost unavoidable during the shipment of the molding compound to the assembly sites, and room temperature storage—on resin polymer size distribution, on curing behavior, and, thus, on rheological properties. Because of its relevance to engineering application, investigation of the effect of the thermal aging process on the polymer molecular size distribution, curing behavior, and moldability performance was undertaken.

Experimental

A batch of a semiconductor grade epoxy-based thermoset molding compound, used widely for IC encapsulation, was chosen. This particular batch suffered from significant moldability-related problems such as resin-bleed onto the leads of the packages during the encapsulation stage. Controlled thermal aging appeared to improve the performance. A thorough investigation of the role of thermal aging and moldability performance was carried out on this particular batch of the compound.

Thermal aging was carried out at 35°C. Aging duration varied from a few hours to several days. Degree of cross-linking of the constituent epoxy cresol novolac and phenol novolac resin units, curing behavior of the molding compounds, rheology, and moldability performance of these aged samples were investigated. The degree of reactive linking between the epoxy cresol novolac and phenol novolac resin in the molding compound was gauged in terms of the extent of extractability of the methanol soluble resin component (mainly phenol novolac resin) from the bulk of the molding compound. It was also established that this procedure of selective extraction of resin constituents of various molding compounds using methanol, also extracted the nitrogen-based catalyst used in the formulation of the molding compound. The amount of catalyst extractable was monitored in terms of measurement of the nitrogen content in the extracted sample and conversion of the nitrogen atom concentration to the weight of the catalyst extracted. Details of this selective extraction of various mold compound constituents employing methanol and other organic solvents are contained in Ref. (4).

Molecular size distribution of the constituent resin systems in the molding compounds was recorded by gel permeation chromatography (GPC) employing a Waters Associates system. This consisted of a 600A solvent delivery system, a 440 UV absorption detector, and four μ-styragel columns connected in series. The columns, with pore sizes of 5, 20, 100, and 1000Å, were connected in order of increasing pore size, and the column with the smallest pore size (5Å) was connected to the sample inlet end. The column with the largest pore size (1000Å) was connected to the sample outlet end. Tetrahydrofuran (THF) was used as the carrier solvent. Flow rate was 2 ml/min.

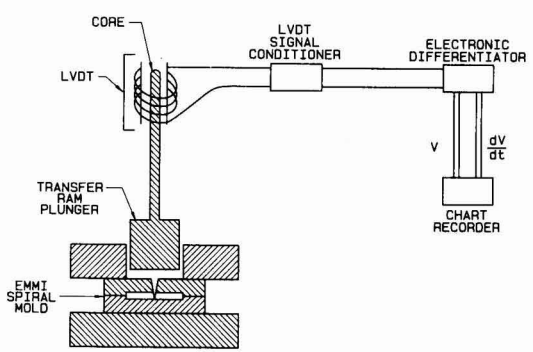

Fig. 1. Schematic of the experimental setup for the viscosity-time profile measurement of the mold compound using ram follower measurement techniques.

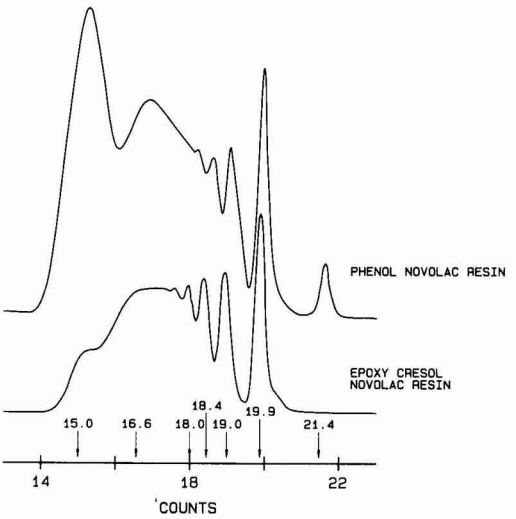

Fig. 2. GPC spectra of the constituent phenol novolac and epoxy cresol novolac resin. Abscissa counts relate to cumulative elution volume. Count values corresponding to the principal peaks are marked.

Samples were prepared by dissolving the soluble portion, *i.e.*, primarily resins, of 1g of molding compound in 10 ml of THF at room temperature. The insoluble portion, mainly silica, was separated by centrifugation followed by filtration through a 0.2 μm pore size filter. The GPC analysis was carried out at room temperature. Separated oligomeric mass peaks were detected by UV absorption at 254 nm.

A Perkin Elmer differential scanning calorimeter (DSC) Model DSC-2 system was employed for recording the curing profile of the samples. The system was operated in the isothermal mode at a temperature of 165°C (5).

Rheological characterization of the samples was carried out by recording the viscosity-time profiles of the compound during its flow in a spiral groove mold at a transfer molding pressure of 1000 psi at 175°C tempera-

Table I.

Elution counts	Oligomeric composition	Peak label
21.4	phenol (monomer)	A
19.9	dimer of phenol and epoxy cresol novolac	B
19.0	higher order oligomers	C
18.4	DO	D
18.0	DO	E
16.6	DO	F
15.0	DO	G

Table II. Percentage by weight of methanol-extractable resin and catalyst from the bulk of molding compound as a function of aging duration

Sample	Resin weight percent	Catalyst weight percent[a]
control (0h)	7.6	0.045
24h aged	5.5	0.033
48h aged	4.8	0.030
72h aged	4.3	0.025
theoretical	20.0	0.240

[a] Percentage of the total molding compound weight.

ture by employing the ram follower measurement technique. Details of this measurement technique are given in Ref. (6). Briefly, spiral flow length and velocity of the compound are recorded as a function of time. Instantaneous viscosity values are computed from the recorded instantaneous spiral flow length and velocity values. Figure 1 presents the experimental setup.

Moldability performance was gauged on a 40 lead-molded dual in-line package (MDIP) in terms of the extent of resin bleed onto the leads of the package and degree of incomplete encapsulation.

Results

Figure 2 presents the GPC spectra of the epoxy cresol novolac and phenol novolac resin present in the molding compound. Different molecular size fractions elute at different times (corresponding to different elution volumes) and are represented in terms of counts (1 count = 2 ml). Large molecular size oligomers elute first and, hence, correspond to the lower counts region of the spectra. The higher counts region of the spectra displays well-resolved sharp peaks corresponding to lower molecular weight oligomeric units. Calibration of some of these well-resolved peaks in terms of lower order oligomeric units, *e.g.*, monomer, dimer, etc., has been carried on, and the data are summarized in Table I. It is sufficient to state here that there is considerable overlap in the elution characteristics of the epoxy cresol novolac and phenol novolac, and, therefore, separation based solely on GPC elution is not possible. Instead, an approach of selective dissolution was attempted (4). Table II summarizes the percentage of extractable phenol novolac resin and phenol novolac-epoxy cresol lower order oligomer and complexes as a function of thermal aging. There is a decrease of 43% in the weight of the methanol-extractable resin fraction as the molding compound is aged to 72h. A similar trend is also observed in the amount of the methanol-extractable catalyst. It is quite apparent that the aging process involves linking of the phenol novolac resin oligomeric units with the epoxy cresol counterpart, resulting in nonextractable oligomers. The catalyst appears to be a part of this linking phenomenon.

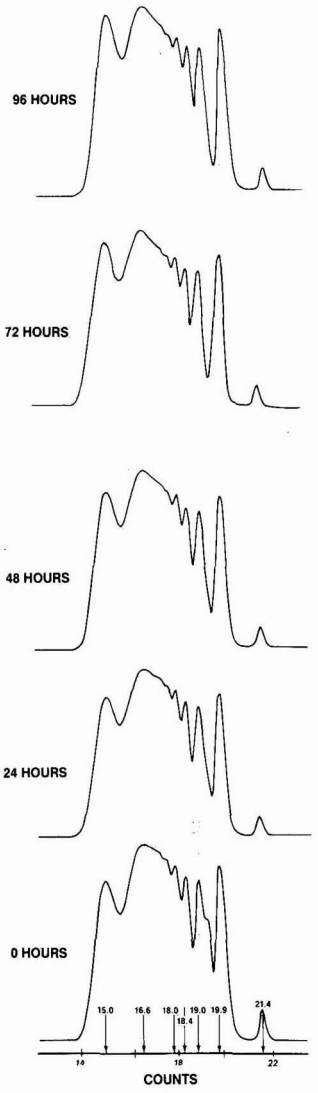

Fig. 3. GPC spectra of the combined resinous part of molding compound as a function of aging duration.

Figure 3 presents GPC spectra of the combined resinous part of the molding compound (both phenol novolac and epoxy cresol novolac resin) sample with different aging durations. Peak G shows a systematic increase with the aging duration. The buildup of larger oligomeric units at the expense of intermediate ones is quite apparent. Monomer (phenol) peaks A and B appear to remain unchanged as a function of the duration of aging. Hence, the peak G intensities were normalized to the peak B in each distribution for the purpose of comparative analysis.

Figure 4 presents normalized peak intensity of peak G as a function of the duration of aging. Also included in the same plot is the spiral flow length of the molding compound as a function of the duration of aging. In both cases, a linear dependence is observed. The increase in peak G intensity correlates with the decrease in the spiral flow length. An aging duration of 96h results in a peak intensity increase of approximately 20%, while a decrease in spiral flow length is about 35%.

A typical DSC scan is given in Fig. 5a. Figure 5b represents the DSC data as a function of the duration of aging. Time corresponding to the maximum of the recorded curing profile of the molding compound (labeled as time-to-peak) follows a gradual decline with aging duration. This decrease in "time-to-peak" correlates well with the decrease in spiral flow length.

Figure 6 displays the viscosity-time profile of the various aged samples as measured by ram-follower technique. The unaged sample (control) exhibits a curing pattern with a long duration of low viscosity value. Aging results in a shortening of this duration and, hence,

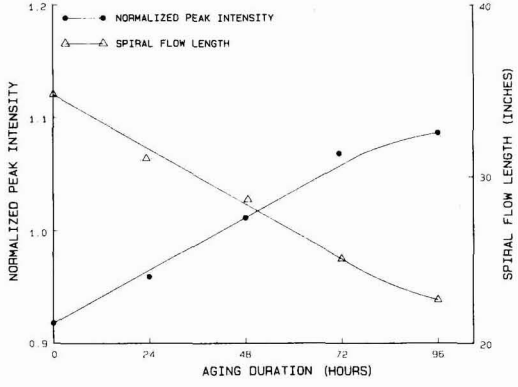

Fig. 4. Peak G intensity (normalized) and spiral flow length as a function of aging duration. Ordinate values on right relate to peak G intensities and on left relate to spiral flow length. Abscissa is aging duration.

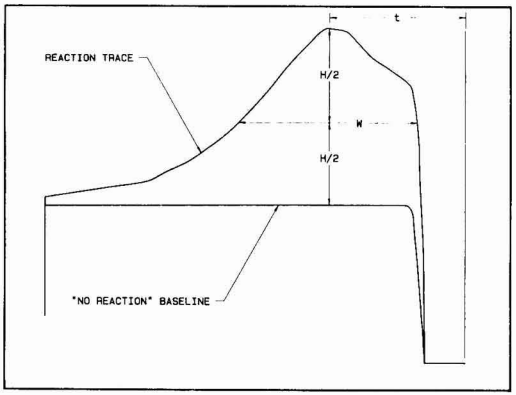

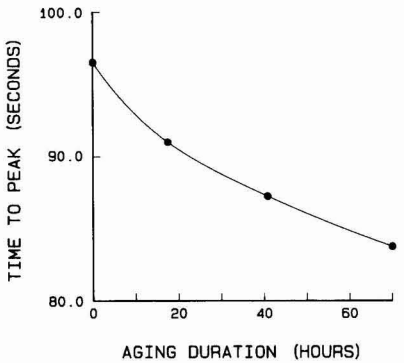

Fig. 5. (a, top) A typical DSC isothermal scan at 165°C. *t* is the time to peak, *H* is the height, and *W* is the width at half-height. (b, bottom) Time corresponding to the maximum of the curing profile of the molding compound as measured via differential scanning calorimetric (DSC) technique recorded at 165°C *vs.* aging duration.

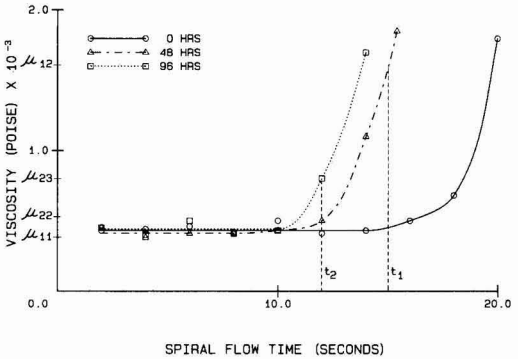

Fig. 6. Viscosity-time profiles of various samples as measured by ram follower measurement techniques.

faster gelling of the molding compound. For the first 10s of the flow, the viscosities of all the three samples appear to be very similar. However, viscosity differences show up after 10s with the 96h aged sample gelling first and the unaged sample gelling last. Once again, this viscosity-time profile appears to be in agreement with DSC and spiral flow length data. Corresponding to spiral flow length time of t_2 = 10s, samples aged to 0h, 48h, and 96h have viscosities μ_{11}, μ_{22}, and μ_{23} of respectively 200, 300, and 600 poise, while, corresponding to time t_1 = 15s, the μ_{11} and μ_{12} values are 200 and 1650 poise, respectively. Time t_1 exceeds the gel time of the 96h aged sample.

Figure 7 displays photographs of molded 40 lead MDIP packages. The package molded with the unaged sample clearly shows significant resin bleed appearing on the leads, while the one molded with 72h aged sample shows no visible resin bleed. Also, included is a shot of incomplete encapsulation obtained with 96h aged samples molded under identical conditions.

Discussion

Frequent problems associated with moldability performance, *e.g.*, resin bleed, incomplete encapsulation, voids, *etc.*, depend primarily on the rheological properties of the molding compound. In order to ensure the best results, a judicious selection of molding conditions and correct rheological properties of the compound is required. A slow cure rate (hence larger duration of low viscosity) often results in increased bleed, whereas a fast curing molding compound often results in incomplete encapsulation. The molding conditions have to be optimized with the rheology of the compound to avoid either of the frequent defects. Ideal compound rheology in terms of mold filling can be described as (*i*) instantaneous filling of mold runner, (*ii*) simultaneous filling of all mold cavities, and (*iii*) mold cavity filling accompanied by a significant instantaneous increase in the compound viscosity, which should ensure minimal bleed of the resin out of the cavity onto the leads of the package. Spiral flow length is a useful index but fails to provide adequate information. Viscosity-time profiles as recorded by ram follower measurements offer deeper insight into the rheological aspect of the compound.

Various rheological features, such as viscosity and curing behavior, can ultimately be reduced to depend on the microscopic features such as resin molecular size distribution, catalyst content, and cross-link density of the polymeric units. Thermal aging induces initiation of the polymerization process between phenol novolac and epoxy cresol novolac constituent resins, and, thus, the extent of thermal aging directly translates into shortening of the cure time. Thermal aging induced reactive linking of the resins appears to have higher probability for large oligomers. Reactive linking is a thermodynamically and kinetically controlled process. The probability of linking is higher for oligomeric units with a larger number of reactive functional groups. Di- and monomeric units have significantly lower probability of polymerization, and the concentration of these low order oligomeric units remains almost independent of the aging process. Resin bleed appears to have no direct dependence on the concentration of smaller oligomeric units, but, instead, depends on the relative depletion of the large oligomeric units with respect to the intermediate ones in the overall resin molecular size distribution.

The overall picture that emerges suggests that a critical resin molecular size distribution is required in order to ensure minimum resin bleed and complete encapsulation. A resin distribution rich in smaller oligomers will often result in low viscosity and large gell time resulting in resin bleed, while a resin distribution too rich in larger oligomers will often result in a short cure time, high viscosity, and incomplete encapsulation. Thermal aging can alter the molecular size distribution and, thus, is capable of optimization of the rheological properties of the mold compound.

Conclusion

Low temperature thermal aging induces a reaction between the constituent phenol novolac and epoxy cresol novolac resin molecules present in the molding compound. This reactive linking results in significant variations in the rheological properties of the compound and, thus, affects the moldability performance.

A critical molecular size (oligomer size) distribution is required in order to ensure optimum rheological properties, thus giving good moldability performance. The ratio of the relative population of the large and intermediate size oligomers has to be kept in a given narrow range in the overall resin polymer size distribution in order to achieve the desired curing behavior.

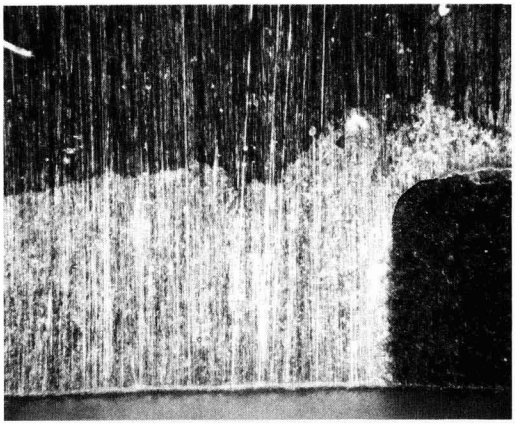

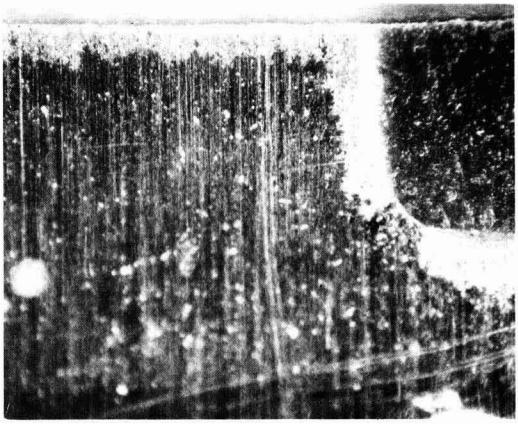

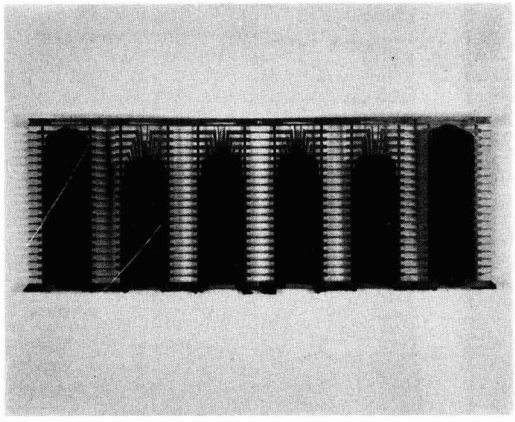

Fig. 7. Photographs of 40 lead MDIP packages: (a, top left) resin bleed (appearing as whitish region) onto leads of the package corresponding to the 0h aged molding compound sample; (b, above) absence of resin bleed achieved via aging the molding compound sample in Fig. 7a to 72h; (c, left) incomplete encapsulation as obtained with molding compound sample aged to 96h.

Acknowledgments

The authors acknowledge the contributions of Mr. Ah San Kyu in all the related experiments of this investigation. The assistance of Dr. Elizabeth Cathers in GPC characterization of the sample and Mr. Jagdish Belani for valuable discussions is also deeply appreciated.

Manuscript submitted Nov. 25, 1985; revised manuscript received June 21, 1986.

REFERENCES

1. P. Burggroff, *Semicond. Int.*, 60 (December 1984).
2. M. Ryan and M. Kamal, in "Proceedings of the 7th International Congress of Rheology," Gothenburg, Sweden, August 23-27, 1976.
3. S. C. Misra, J. A. Manson, and L. H. Sperling, in "Epoxy Resin Chemistry," R. S. Bauer, Editor p. 137, ACS Symposium Series, 114, American Chemical Society, Washington, DC (1979).
4. K. K. Chakravorty, A. S. Kyu, and J. Belani, Manuscript in preparation.
5. J. Belani and C. R. Sporck, in "Calorimetric Characterization of Catalyst Concentration in Semiconductor Molding Compound," p. 577, *SPE Antec*, Washington, DC (1978).
6. P. Heinle, *J. SPE, Ann. Tech. Conf.*, **25,** 426 (1979); *ibid.*, **26,** 447 (1980); *ibid.*, **27,** 331 (1981).

Voltammetric Studies of Porous Molybdenum Electrodes for the Alkali Metal Thermoelectric Converter

R. M. Williams,* C. P. Bankston, S. K. Khanna,* and T. Cole

Jet Propulsion Laboratory, California Institute of Technology, Pasadena, California 91109

ABSTRACT

Voltammetry of partially oxidized porous molybdenum alkali metal thermoelectric converter (AMTEC) electrodes from ~600 to ~1000 K revealed a series of redox processes within the operational voltage range of the AMTEC device. The most important of these processes involve reactions that add sodium to MoO_2, $Na_2Mo_3O_6$, and Na_2MoO_4. The redox processes can be used as an *in situ* analytical probe of oxide species in porous molybdenum electrodes. These constituents are important in establishing the electronic and ionic conductivities of AMTEC electrodes. The estimated equilibrium potentials of these reactions provide improved estimates of the free energies of formation of $Na_2Mo_3O_6$, $NaMoO_2$, and Na_3MoO_4. In the AMTEC operating regime, there is evidence for the comparatively slow corrosive attack by Na_2MoO_4 on molybdenum. The ionic conductivity of Na_2MoO_4 measured from 600 to over 1000 K shows sharp increases in conductivity at ~750, 865, and 960 K. The conductivity is sufficiently large at $T > 700$ K to explain the observed electrochemical phenomena, as well as enhanced sodium transport in AMTEC electrodes below the freezing point (960 K) of Na_2MoO_4. The results of this study are relevant to AMTEC device performance and also provide more detailed information about the ternary Na-Mo-O phase diagram in the range of conditions relevant to the AMTEC device.

The alkali metal thermoelectric converter (AMTEC) is a direct energy conversion device, utilizing a high alkali metal activity gradient across a β″-alumina solid electrolyte (BASE). It has been operated at an energy conversion efficiency of 19% and at power densities near 1.0 W/cm². Detailed descriptions of the principles of the device and its operating cycle have been given elsewhere (1-5).

At present, thin, porous molybdenum electrodes give the best power densities for AMTEC cell operation. However, the performance of these electrodes eventually degrades, apparently due to evaporation of sodium molybdate, Na_2MoO_4, which is formed within the electrodes by several mechanisms, and enhances sodium transport through the electrodes via ionic conduction. We previously reported the beneficial effect of oxygen exposure on degraded porous molybdenum AMTEC electrodes, the identification of Na_2MoO_4 and $Na_2Mo_3O_6$ in some electrodes, and a comprehensive model of chemistry and transport in these electrodes based on available data (5, 6). The model accounted for the observed enhanced sodium transport in conditioned and regenerated electrodes, above ~960 K, due to the high sodium ion conductivity of liquid Na_2MoO_4 (7-9). The reactions predicted by this model included several redox reactions which should occur within the sodium activity regime determined by the voltage and current density of the AMTEC cell. Furthermore, the role of ionic conductivity in AMTEC cell performance below 960 K was not known from our previous studies and available data. Accordingly, investigations of electrochemical reactions in molybdenum electrodes and Na^+ transport in Na_2MoO_4 have been carried out using AMTEC cells, as well as other high temperature electrochemical cells.

Experimental

Details of the AMTEC experimental cell and electrode preparation have been given previously (4-6). AMTEC cell measurements at currents greater than ~0.1A were made using a potentiometer-controlled power FET in series with a current supply, in the four-probe configuration. Measurements at less than ~0.1A were carried out with a PAR Model 175 universal programmer, Model 173 potentiostat, and Model 176 current follower. The conductivity of Na_2MoO_4 was determined in an argon-filled glove box using the potentiostat in conjunction with a Model 276 interface, 5206 lock-in amplifier, and Apple 2e computer. AC impedance spectra over the frequency range 0.01 Hz to 20 kHz were taken at lower temperatures, $T \leq 750$ K, and semicircles on the complex impedance plane plots were extrapolated, when necessary, to determine cell conductivity. At higher temperatures, $T \geq 750$ K, cell conductivity could be taken directly from the real part of the complex impedance, Z', since the phase angle $|\theta| < 5°$. The conductivity was measured with Mo electrodes on polycrystalline, previously melted samples and the known conductivity of the molten salt was used for calibration of the cell.

Molybdenum electrodes were exposed to low pressure air (5-10 mtorr) in the AMTEC chamber during warm-up to ~650 K. Composition of the AMTEC cell atmosphere was monitored with an Anavac residual gas analyzer. After initial pump-down and warm-up, the chamber atmosphere consisted of ~5 mtorr argon with smaller amounts of nitrogen and hydrogen.

X-ray diffraction analysis of electrodes following electrochemical investigations were performed, with minimal exposure (2-3 min) of samples to air, using an evacuated Guinier camera with CuKα radiation.

Results and Discussion

Figure 1 shows the conductivity of polycrystalline Na_2MoO_4, previously melted and refrozen, from 500 to 1100 K. The temperatures of phase transitions of solid Na_2MoO_4, as well as the melting transition are indicated (10). The activation energy for conduction was calculated for Na_2MoO_4 IV, III, and II, assuming $\sigma = (\sigma_o/T) \exp[-E/RT]$. Table I shows values for σ_o and E derived from fits to the conductivity data. It is clear that Na_2MoO_4 is conductive enough in the solid state to play some role in sodium transport at temperatures greater than ~745 K, and can support electrochemical processes.

A cyclic voltammogram of a lightly oxidized, porous, 2 μm thick molybdenum electrode, labeled A, obtained *in situ* in the AMTEC test cell, is shown in Fig. 2a. Two cyclics of a second electrode, B, are shown in Fig. 2b and 2c. Electrode B was exposed to temperatures from 16 to 20 K higher than electrode A with system at stand at 580-630 K for several hundred hours prior to these experiments. The AMTEC cell current obscures the parasitic cathodic electrochemical reactions first at low cell potentials and then at increasingly larger potentials as temperature increases. Likewise, anodic reactions are increasingly obscured by competition from thermal dissociation of the reduction products. Several of the observed redox processes were assigned on the basis of known and estimated free energies of formation of MoO_2, $Na_2Mo_3O_6$, $NaMoO_2$, Na_2MoO_4, and Na_3MoO_4, and the electrode compositions were verified by x-ray diffraction (6, 11-18). The large reduction and oxidation peaks that dominate Fig. 2a give an estimated equilibrium potential consistent with the free energy change calculated for the reaction

$$Na^+ + e^- + Na_2MoO_4 = Na_3MoO_4 \qquad [1]$$

X-ray diffraction analysis shows that Na_2MoO_4 is the major phase other than molybdenum in electrode A, but

*Electrochemical Society Active Member.

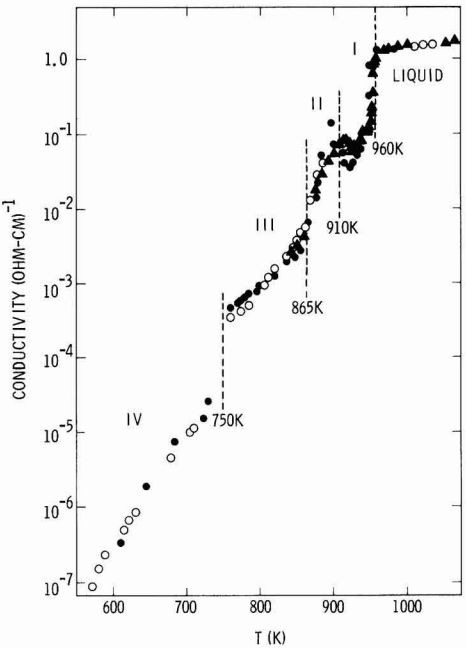

Fig. 1. Ionic conductivity of Na_2MoO_4. Solid and open circles and solid triangles represent several experiments involving both warming and cooling data. Roman numerals indicate the phase of Na_2MoO_4 (10).

that $Na_2Mo_3O_6$ is the predominant oxide phase in electrode B, with smaller amounts of Na_2MoO_4 present. Small quantities of both $Na_2Mo_3O_6$ and a previously detected, but still unidentified, phase (characterized by low angle diffraction peaks at d = 6.93, 3.307, and 3.161Å) were also found in electrode A. Electrode B was consistently kept at a 16-60 K higher temperature than electrode A throughout all experiments, due to their relative positions with respect to the heating element.

The two closely spaced reduction waves and three associated oxidation waves between 1.0 and 0.5V in Fig. 2c consistently appear with the same relative areas and show the same temperature dependence in different electrodes. The two lowest oxidation waves are associated with the lowest reduction wave, as shown by scans with successively increasing low potential cutoffs. These peaks are assigned to reaction [2]

$$Na^+ + e^- + Na_2Mo_3O_6 = 3NaMoO_2 \qquad [2]$$

Note that the compounds described are all separate crystalline phases under the experimental conditions; the double peak indicates that sodium enters two distinct sites in $Na_2Mo_3O_6$ and suggests that an intermediate phase between $Na_2Mo_3O_6$ and Na_2MoO_2 may be synthesized by potentiostatic means. Relative peak areas suggest that the intermediate phase has a composition very close to $Na_4Mo_5O_{10}$. The free energies of reactions [2a] and [2b] below have been evaluated separately, though the metastable regime for the intermediate phase is very narrow

$$Na + 5/2\ Na_2Mo_3O_6 = 3/2\ Na_4Mo_5O_{10} \qquad [2a]$$

Table I. Ionic conductivity parameters for solid Na_2MoO_4 phases

Phase	Temperature (K)	σ_0 ($\Omega^{-1}cm^{-1}$)	$E_{act.}$ (eV)
Na_2MoO_4 (II)	866-907.5	1.62×10^{23}	3.84
Na_2MoO_4 (III)	761-864	1.84×10^{8}	1.33
Na_2MoO_4 (IV)	571-709	9.44×10^{6}	1.28

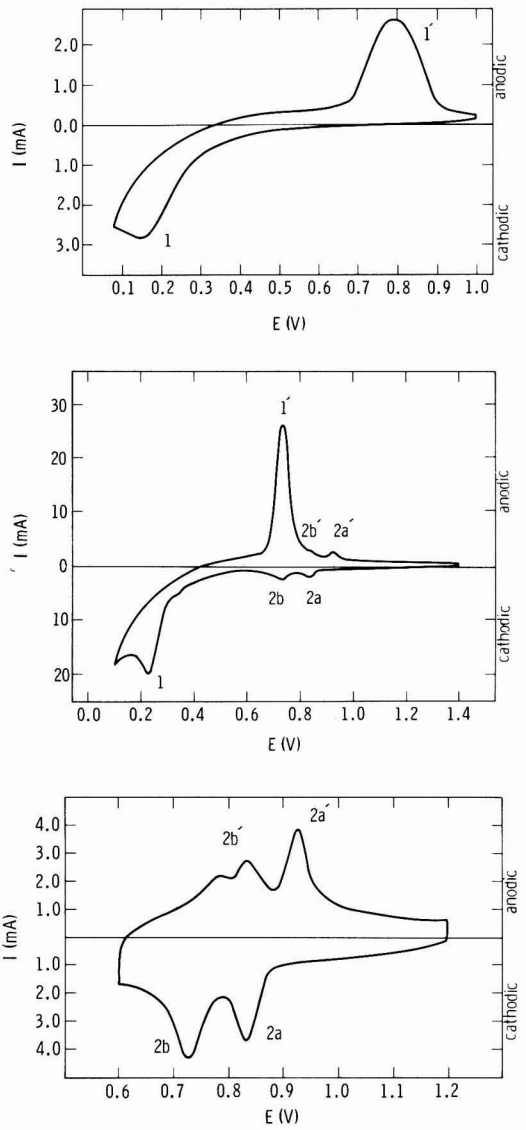

Fig. 2. Cyclic voltammograms of oxidized molybdenum electrodes. Reactions assigned to peaks indicated by number; reverse reactions are indicated by apostrophe. The reference voltage is Na^+ (β″-alumina)/Na°. (a, top) Electrode A, scan rate 10 mV/s, temperature 622 K; (b, middle) electrode B, scan rate 10 mV/s, temperature 627 K; (c, bottom) electrode B, scan rate 20 mV/s, temperature 627 K.

$$Na + Na_4Mo_5O_{10} = 5NaMoO_2 \qquad [2b]$$

The estimated standard potential for reaction [2] is a weighted average of the potentials of reactions [2a] and [2b].

A very broad, weak pair of peaks was also observed at 1.6V (not shown) and can be assigned to reaction [3]

$$2Na^+ + 2e^- + 3MoO_2 = Na_2Mo_3O_6 \qquad [3]$$

These broad peaks show little dependence of peak shape on scan rates from 1 to 50 mV/s. The scan rate independent width of the peaks may indicate a continuous range of compositions between MoO_2 and $Na_2Mo_3O_6$ or a sluggish intercalation of sodium into MoO_2. The width of these peaks suggests that the estimated standard poten-

tial for reaction [3] may not be a highly accurate approximation to the true standard potential. An additional weak, broad unassigned cathodic peak could be discerned at ~1.0V; if the scan is reversed just before the first peak of reaction [2], a weak, broad anodic peak centered just positive of 1.0V is detected. The next anodic peak is seen above 2.0V and is the first of a series of peaks that may represent successive oxidations of the paramolybdate anion, MoO_4^{-2}, in Na_2MoO_4, with eventual loss of oxygen.

Figure 3 shows the temperature dependence of the estimated standard potentials of these reactions. Table II shows the free energies of the reactions and free energies of formation of $Na_2Mo_3O_6$, $NaMoO_2$, and Na_2MoO_4 obtained from these data. The reduction and oxidation peaks of reaction [1] show a much greater separation than those of reactions [2] and [3] at lower temperatures. This separation seems to be due partly to cell resistance associated with ionic conductivity in Na_2MoO_4. The magnitude of this resistance may be estimated from the electrode porosity, total surface area, the quantity of Na_2MoO_4 present in the electrode, and the conductivity of Na_2MoO_4. Peak areas in the voltammograms indicated that the electrode contained 0.45×10^{-6} mol Na_2MoO_4 or about 3.8% by weight. Estimates of pore geometry from scanning electron microscopy indicate that typical sputtered molybdenum electrodes prepared in our laboratory are ~20% porous with a surface area 20-50 times the electrode geometrical area. Since there seems to be much smaller resistance associated with reactions [2] and [3], some information about distribution of phases within electrode pores and charge transport may be inferred from these observations. Since the density of Na_2MoO_4 is 3.28 g/cm^3, compared with 10.2 g/cm^3 for molybdenum, a considerable reduction in void volume within the electrodes is expected compared with a "pure" Mo as-deposited film after electrode oxidation and reduction by sodium. Much of the resistance associated with reaction [1] may be due to redox processes occurring throughout a significant thickness (~50 nm) of Na_2MoO_4 in the pores, since both sodium ion conduction and electron transport by exchange between MoO_4^{3-} and MoO_4^{2-} can occur at the temperature and electrochemical potential range of reaction [1]. The ionic resistance across 1 cm^2 of a 50 nm Na_2MoO_4 film will be 15Ω at 600 K.

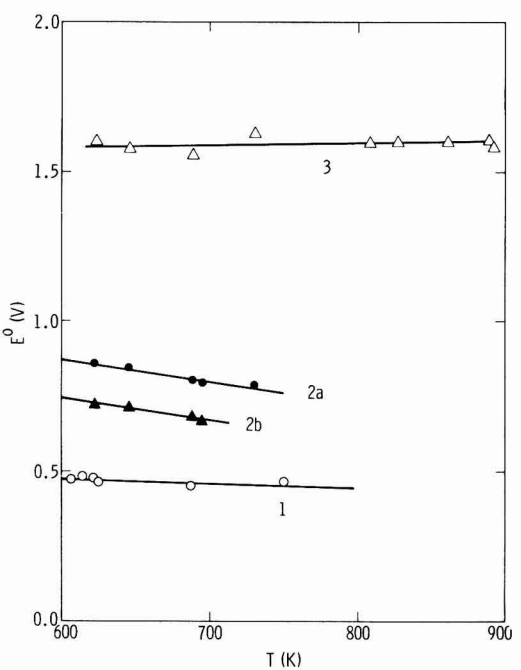

Fig. 3. Estimated standard potentials vs. temperature, with reactions indicated by number.

The narrow separation of the oxidation and reduction waves of reactions [2] and [3] suggest that the material detected may be confined near the surface of the molybdenum. Since electronic transport is generally negligible in sodium molybdate, as determined by low frequency ac impedance, then MoO_2, $Na_2Mo_3O_6$, and $NaMoO_2$ cannot undergo electrochemical reactions, if they are not in contact with the electrically conducting matrix. Conversely, since they are electronic conductors, they can facilitate electron transport within the pores at any voltage, including the potentials at which reaction [1] occurs. Therefore, the total amount of these Na_xMoO_2 phases cannot be quantitively estimated from the areas of voltammetric peaks, but the amount of Na_2MoO_4 can be estimated.

A possible mechanism for formation of $Na_2Mo_3O_6$ or $NaMoO_2$ at the surface of molybdenum involves a corrosion reaction by sodium molybdate. However, the disproportionation of $NaMoO_2$ has a negative free energy. Therefore, it is not a corrosion product

$$2NaMoO_2 \rightarrow Na_2MoO_4 + Mo \qquad [4]$$

This reaction is certainly slow, since $NaMoO_2$ can be isolated (12). The interconversion of $Na_2Mo_3O_6$ and Na_2MoO_4 is controlled by the sodium pressure

$$2Na + 2Na_2Mo_3O_6 = 3Na_2MoO_4 + 3Mo \qquad [5]$$

This reaction is presumably slow and complex, but is thermodynamically favored in each direction under appropriate conditions of sodium activity and temperature. Reactions such as these may even play an important role, along with evaporation and reduction, in determining the fate of Na_2MoO_4 in the electrode. The difference in the ratios of $Na_2MoO_4/Na_2Mo_3O_6$ in electrodes A and B suggests temperature-dependent kinetic limitations to reaction [5], but the complex temperature cycling applied to these electrodes prevents more detailed interpretation at this time.

At very low sodium pressures, Na_2MoO_4 may corrode molybdenum, yielding MoO_2 and sodium. The reverse reaction

$$2Na + 2MoO_2 = Na_2MoO_4 + Mo \qquad [6]$$

is exothermic under standard conditions, liquid Na at 1 atm, but is not likely to occur as written since formation of $Na_2Mo_3O_6$ from MoO_2 and sodium is more rapid.

The improved values of free energies of formation of $NaMoO_2$, $Na_2Mo_3O_6$, and Na_3MoO_4 calculated from electrochemical data permit a more thorough evaluation of the stability regimes of Na-Mo-O phases under AMTEC operating conditions.

Finally, the most reduced sodium addition compounds, Na_3MoO_4 and $NaMoO_2$, may be reduced to give sodium oxide and molybdenum.

$$3Na + NaMoO_2 = 2Na_2O + Mo \qquad [7]$$

$$5Na + Na_3MoO_4 = 4Na_2O + Mo \qquad [8]$$

All sodium addition compounds of MoO_2 except $Na_2Mo_3O_6$ are metastable with respect to disproportionation to Na_2MoO_4, or Na_3MoO_4, and molybdenum. However, these reactions are apparently slow. A (meta)stability regime diagram for the MoO_2 sodium addition products is shown in Fig. 4a. If disproportionation reactions are included, a true stability diagram is the result (Fig. 4b). Since Mo is produced by reaction [5], the average oxidation state of Mo decreases across all phase boundaries toward higher Na activity. The reactions determining phase boundaries are reactions [3], [5], [1], and [8] in order of increasing sodium activity. The sodium activity can be directly related to AMTEC electrode operating current density, j (in A/cm^2)

$$j = 1.17 \times 10^3 [Na] P^{\circ}_{(Na,T)} T^{-1/2}$$

Table II. Free energies of formation derived from electrochemical data and free energies of several reactions (kJ/mol). Extrapolated values indicated by parentheses

	600 K	700 K	800 K	900 K	1000 K
ΔG_f° ($NaMoO_2$)	−604.7	−584.9	(−565.3)	(−545.9)	(−526.7)
ΔG_f° ($Na_2Mo_3O_6$)	−1734.8	−1682.4	−1630.5	−1579.3	(−1528.5)
ΔG_f° (Na_2MoO_4)	−1280.8	−1241.0	(−1204.0)	(−1168.0)	(−1134.2)
ΔG° (reaction [1])	−45.7	−44.5	(−43.3)	(−42.1)	(−41.0)
ΔG° (reaction [2])	−79.2	−72.3	(−65.4)	(−58.5)	(−51.6)
ΔG° (reaction [2a])	−71.8	−64.8	(−57.9)	(−50.9)	(−43.9)
ΔG° (reaction [2b])	−84.3	−77.4	(−70.5)	(−63.6)	(−56.7)
ΔG° (reaction [3])	−305.6	−307.2	−308.8	−310.4	(−311.9)
ΔG° (reaction [4])	−25.8	−26.6	(−30.0)	(−34.1)	(−39.9)
ΔG° (reaction [5])	−235.8	−224.6	−220.9	−219.2	(−222.9)
ΔG° (reaction [6])	−282.3	−279.7	−279.5	−280.0	(−282.3)
ΔG° (reaction [7])	−68.2	−59.4	(−50.9)	(−42.6)	(−34.5)
ΔG° (reaction [8])	−64.9	−47.7	−28.5	−9.00	(+11.9)

where [Na] is the fractional sodium activity at T, and $P^\circ_{(Na,T)}$ is the vapor pressure of sodium in torr, as shown previously (2). This relation and the phase diagram allow prediction of the phases present at the electrode surface after prolonged operation at constant conditions of current and temperature. Volatility of Na_2MoO_4 must also be taken into account, and the sodium activity will be greater below the surface of the electrode. The free energies and phase boundaries have been extrapolated throughout the AMTEC operating temperature regime, to higher temperatures than those at which electrochemical data were obtained. Extrapolated data are shown with dashed lines. However, the electrochemical data agree fairly well with estimates of free energies based on thermochemical data up to temperatures of 1100-1200 K, suggesting that smooth extrapolation is reasonable.

Conclusions

Voltammetric evidence has been presented for the formation and interconversion of MoO_2, $Na_2Mo_3O_6$, $NaMoO_2$, Na_2MoO_4, and Na_3MoO_4 in porous molybdenum AMTEC electrodes close to operating temperatures. The voltammetric results give more accurate thermochemical data than can be estimated from reported synthesis and decomposition conditions for the compounds. The sodium ionic conductivity of solid Na_2MoO_4 was measured and found to be large enough to explain the existence of the observed voltammetric phenomena, as well as enhanced sodium transport in porous molybdenum AMTEC electrodes at temperatures below the melting point of Na_2MoO_4, T = 958 K. The corrosive attack of Na_2MoO_4 on molybdenum (reactions [5] and [6]) and the reverse reactions at higher sodium activity may account for the loss of Na_2MoO_4 in electrodes at low sodium activity and indicate a regenerative mode at high sodium activity. That is, at expected operating conditions for the AMTEC device, current densities from 1 to 4 A/cm² at 1000 K will be equivalent to sodium activities of 0.89×10^{-3} - 3.56×10^{-3} (*or 0.135-0.541 torr*) and the stable phase in contact with molybdenum will be Na_2MoO_4. Voltammetry provides the most convenient *in situ* technique for studying the chemical processes within molybdenum electrodes in the AMTEC cell environment.

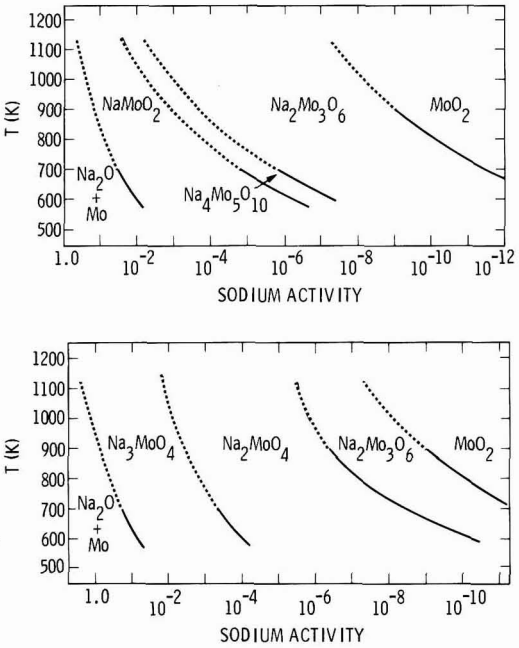

Fig. 4. Stability regimes of Na-Mo-O phases, with phase boundaries *extrapolated to higher temperatures indicated by dashed lines.* Mo at unit activity. (a, top) MoO_2 sodium addition compounds neglecting slow disproportionation reactions; (b, bottom) thermodynamic stability regime for Na-Mo-O phases.

Acknowledgments

The research described in this paper was performed by the Jet Propulsion Laboratory, California Institute of Technology, and was supported by the Air Force Office of Scientific Research and the Army Tank Automotive Command through interagency agreements with the National Aeronautics and Space Administration. The authors wish to acknowledge useful discussions with Dr. A. Thakoor, J. Lamb, who also carried out the magnetron sputter deposition of molybdenum, B. Nakamura, and Dr. B. Wheeler. Professor S. Samson at Caltech provided use of the Guinier camera, and its calibration.

Manuscript submitted Dec. 9, 1985; revised manuscript received June 19, 1986.

The Jet Propulsion Laboratory, California Institute of Technology, assisted in meeting the publication costs of this article.

REFERENCES

1. N. Weber, *Energ. Conver.*, **14,** 1 (1974).
2. T. Cole, *Science*, **221,** 915 (1983).
3. T. K. Hunt, N. Weber, and T. Cole, in "Fast Ionic Transport in Solids," J. B. Bates and G. C. Farrington, Editors, p. 263, North Holland Publishing Co., Amsterdam (1981).
4. C. P. Bankston, T. Cole, R. Jones, and R. Ewell, *J. Energ.*, **7,** 442 (1983).
5. C. P. Bankston, T. Cole, S. K. Khanna, and A. P. Thakoor, in "Space Nuclear Power Systems, 1984." Vol. II, M. S. El-Genk and M. D.Hoover, Editors, p. 393, Orbit Book Co., Malabar, FL (1985).
6. R. M. Williams, G. Nagasubramanian, S. K. Khanna, C. P. Bankston, A. P. Thakoor, and T. Cole, *This Journal*, **133,** 1587 (1986).
7. G. J. Janz, in "Molten Salts Handbook," pp. 289, 296, Academic Press, New York (1967).
8. F. M. Jaeger and B. Kapma, *Z. Anorg. Chem.*, **113,** 27 (1920).

9. K. B. Morris, M. I. Cook, C. Z. Zykers, and M. C. Templeman, *J. Am. Chem. Soc.*, **77**, 851 (1955).
10. C. Pistorius, *J. Chem. Phys.*, **44**, 4532 (1966).
11. JANAF Thermochemical Data, Dow Chemical Company, Thermal Research, Midland, MI (1967-1978).
12. I. Barin and O. Knacke, in "Thermochemical Properties of Inorganic Substances," pp. 415, 512, 584, Springer-Verlag, Berlin (1971).
13. J. M. Reau, C. Fourassier, and P. Hagenmuller, *Bull. Soc. Chim. Fr.*, 3827 (1970).
14. C. Ringebach, H. Kessler, and A. Hatterer, *C. R. Acad. Sci. Paris*, **269**, 1394 (1969).
15. H. Kessler, C. Ringebach, L. Lavielle, and A. Hatterer, *ibid.*, **277**, 763 (1973).
16. Powder Diffraction File, Joint Committee on Powder Diffraction Standards; JCPDS International Centre for Diffraction Data, Swarthmore, PA (copyrights 1972-1983).
17. National Bureau of Standards, Mono. 25, Sec. 1 (1962).
18. I. Lindqvist, *Acta. Chem. Scand.*, **4**, 1066 (1950).

New Types of Anodes for the Oxygen Evolution Reaction in Acidic Solution

$IrO_2/TiO_2/Ti$

Yasumichi Matsumoto, Takashi Tazawa, Nobuo Muroi, and Ei-ichi Sato*

Department of Industrial Chemistry, Faculty of Engineering, Utsunomiya University, Utsunomiya 321, Japan

ABSTRACT

New type of electrodes of $IrO_2/TiO_2/Ti$, where the TiO_2 films are prepared by the anodic oxidation accompanied by sparking and are porous, were tested as the anode for the oxygen evolution reaction in acidic solution. The $IrO_2/TiO_2/Ti$ electrodes were prepared by thermal decomposition of $IrCl_4$ aqueous solution on the TiO_2 films. The resistivities of the electrodes themselves became zero by the thermal decomposition process to form IrO_2, if the TiO_2 films were prepared by the anodic oxidation accompanied by sufficient sparking. It was found that the catalytic activities of the $IrO_2/TiO_2/Ti$ electrodes are higher than that of the IrO_2/Ti electrode. The electrodes prepared at a calcination temperature lower than about 500°C dissolved in the long-term test, although their surface areas were very large. The $IrO_2/TiO_2/Ti$ electrodes prepared at 550° are very superior in their catalytic activity and their stability in the long-term test for the oxygen evolution reaction. The surface difference between the $IrO_2/TiO_2/Ti$ and the IrO_2/Ti electrodes is also discussed.

It is well known that iridium oxide (IrO_2) is a good electrocatalyst for the oxygen evolution reaction (OER) and is relatively stable in acidic solution (1-9). IrO_2 prepared by the thermal decomposition on titanium substrate, *i.e.*, IrO_2/Ti electrode, is widely investigated as the anode for OER. In practical use, a large surface area of the electrode is necessary for decrease of overvoltage. If the surface area of the Ti substrate is increased before the process of the thermal decomposition of $IrCl_4$ to prepare IrO_2, the total surface area of the prepared IrO_2/Ti electrode will be larger than that of the usual IrO_2/Ti electrode whose substrate is not pretreated. From this point of view, the pretreatment of the Ti substrate was done by anodic oxidation accompanied by sparking to form the TiO_2 film, which is porous, as described in a previous paper (10). Then, IrO_2 was prepared by thermal decomposition on this layer as reported herein. This type of electrode is, therefore, denoted as $IrO_2/TiO_2/Ti$. It was discovered that the increase in the catalytic activity rather than in the surface area was observed, and that no ohmic drop in the TiO_2 layer was observed for this electrode, compared with IrO_2/Ti electrodes. In the present paper, the property of the porous TiO_2 film, prepared by anodic oxidation accompanied by sparking, and the anodic behavior of the $IrO_2/TiO_2/Ti$ electrodes for the OER were investigated in acidic solution.

Experimental

The titanium plate (99.6%, 1.5 × 5.0 × 0.1 cm, Kobe Steel Limited) was polished with emery paper and then washed with a cleanser. The sample was cleaned by an ultrasonic technique, followed by washing with acetone. The anodic oxidation was done in various electrolytes (K_2CO_3, Na_2SO_4, Na_2CO_3, K_2SO_4 aqueous solutions, and their mixed solutions, 30 ml), using a full-wave rectifier circuit system with a platinum counterelectrode (2.0 × 3.0 cm) (10). The distance between the working Ti plate and the counterelectrode was about 3.0 cm. The conditions of the surface of the prepared TiO_2 films were observed by a SEM (Akashi Limited), and their thicknesses were determined from their sectional photographs by an optical metallograph (Olympus Limited). The composition of the film was analyzed by x-ray, and the small amount of the cations (Na, K) doped in the films was detected by SIMS (Hitachi Limited).

All of the $IrO_2/TiO_2/Ti$ electrodes were prepared by thermal decomposition of 0.1*M* $IrCl_4$ in 15% HCl aqueous solution on the TiO_2 films prepared on Ti substrate. The solution on the TiO_2 films was dried at about 100°C and then decomposed in a furnace. The concentration of Ir on the surface was 3.0×10^{-6} mol/cm², and the calcination temperature was 550°C, unless otherwise stated, because a dissolution of the Ir was observed under long-term stability testing, if the calcination temperature was lower than about 500°C. Only IrO_2 was detected as the Ir compound on the $IrO_2/TiO_2/Ti$ electrode by x-ray analysis.

The relative resistivities of the electrodes themselves were measured using a LCR meter (1 kHz, 50 mV signal level, YHP Limited) in a cell where the distance between the working electrode (0.5 cm²) and the Pt counterelectrode (8.0 cm²) was held to be 4.0 cm in 1.0*M* H_2SO_4 at 20°C. 1.0*M* H_2SO_4 and an Ag/AgCl electrode were used as the electrolyte and the reference, respectively. The electrochemical tests for the OER were done at 50°C. The current-potential curve was measured by using a potentiostat (Hokuto, Limited), and a current interruptor technique was used to correct for the IR drop in the electrolyte. The surface areas of the electrodes were crudely estimated using the cyclic voltammetric technique with a function generator (Hokuto Ltd.) (8), as described in the Results section.

Results

Table I, shows the conditions of the anodic oxidation of Ti accompanied by sparking and the various properties of the oxide films prepared on the Ti substrate. The typical photographs of the surfaces of these oxide films are shown in Fig. 1. Thus, the oxide films are porous and consist mainly of rutile TiO_2, but a very small amount of anatase TiO_2 and an unknown compound are contained in some of these films as shown in Table I. Therefore, the prepared oxide films are described as TiO_2 film in the present paper for convenience. The thicknesses of these

*Electrochemical Society Active Member.

Table I. Properties of the TiO_2 films prepared by anodic oxidation accompanied by sufficient sparking

Sample no.	Electrolyte	Voltage (V)	Structure	Thickness (μm)	Pore size (μm)
1	K_2CO_3 (s)[a]	50	Rutile[b] (s) Anatase (w)	5	0.5-1.0
2	K_2CO_3 (s)	70	Rutile (s) Unknown (w)	5	0.5-2.0
3	Na_2SO_4 (s)	80	Rutile (s) Anatase (w)	2-3	0.1-2.0
4	Na_2SO_4 (s)	90	Rutile (s) Anatase (w)	2-3	0.2-3.0
5	K_2CO_3 (0.35*M*) + Na_2SO_4 (0.25*M*)	100	Rutile	2-3	0.2-1.0
6	Na_2CO_3 (0.5*M*) + K_2SO_4 (0.25*M*)	90	Rutile (s) Anatase (w)	2-3	0.2-3.0

[a] s in parentheses denotes saturation.
[b] s and w in parentheses denote the strong and the weak peak intensities in the x-ray diffraction pattern, respectively.

TiO_2 films were 2-3 and 5 μm for no. 3-6 and no. 1-2 samples, respectively. The pore sizes in the TiO_2 films were in the range of 0.1-3 μm as shown in Fig. 1 and Table I. A similar TiO_2 film was difficult to form in acidic and alkaline solutions.

Figure 2 shows the resistivities of the TiO_2 films as a function of the voltage in the anodic oxidation. In this figure, the resistivities of the $IrO_2/TiO_2/Ti$ electrodes prepared by the thermal decomposition on the TiO_2 films are also shown. The resistivity of the solution (1*M* H_2SO_4) is compensated by using a Pt black electrode (0.5 cm^2) as a working electrode and was about 3.5Ω in a test cell, which is described in the Experimental section. The voltages at which the sparking begins are illustrated by the dotted lines in this figure. It is noteworthy that the resistivities of the electrodes significantly decreased by the thermal decomposition to form IrO_2 and that the resistivities of the $IrO_2/TiO_2/Ti$ electrodes become zero when their TiO_2 films are prepared by the anodic oxidation accompanied by sufficient sparking. Probably, Ir will dope into the TiO_2 lattice, leading to the decrease of its resisitivity. Thus, the $IrO_2/TiO_2/Ti$ electrodes can be used as the anode material for the OER, if their TiO_2 films are prepared by anodic oxidation accompanied by

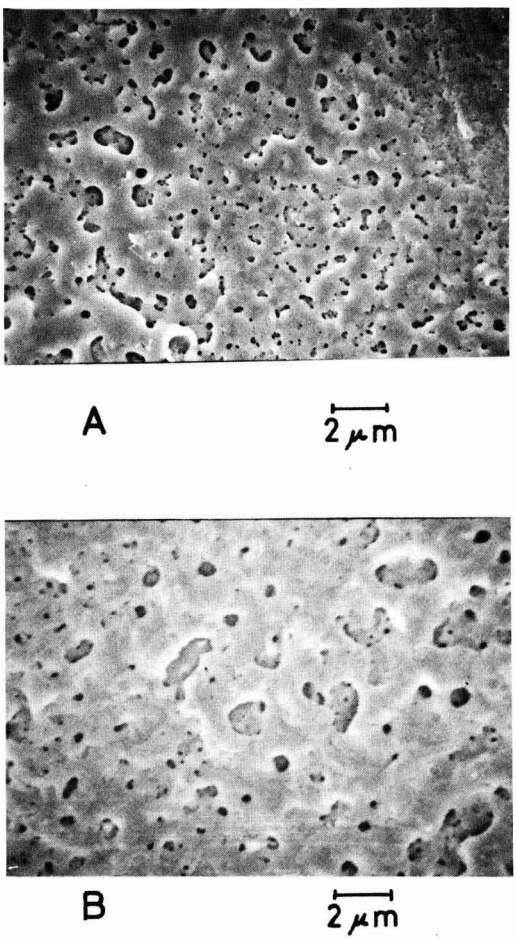

Fig. 1. Photographs of the surfaces of the TiO_2 films prepared by the anodic oxidation accompanied by sparking: (A) sample 1, (B) sample 4 (Table II).

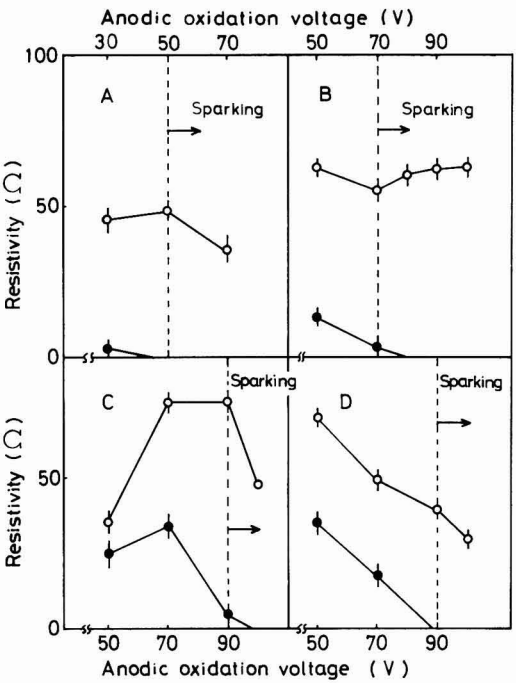

Fig. 2. Resistivities of the TiO_2/Ti and the $IrO_2/TiO_2/Ti$ electrodes whose TiO_2 films are prepared by the anodic oxidation in various electrolytes: (A) K_2CO_3 (saturated) solution, (B) Na_2SO_4 (saturated) solution, (C) K_2CO_3 (0.35M) + Na_2SO_4 (0.25M) solution, and (D) Na_2CO_3 (0.5M) + K_2SO_4 (0.25M) solution. Open and closed symbols denote the TiO_2/Ti and the $IrO_2/TiO_2/Ti$ electrodes, respectively.

sufficient sparking. The TiO_2 films in the $IrO_2/TiO_2/Ti$ electrodes, therefore, were always prepared by anodic oxidation accompanied by sufficient sparking.

The surface areas of the electrodes were estimated using cyclic voltammetry (8). The measurement was done for each electrode in the potential region between hydrogen and oxygen evolution reactions at sweep rates of 0.1-1.0 V/s. Cyclic voltammograms, limited to the potential range of 0.4-0.5V, where the anodic and cathodic currents were equal in magnitude and the capacitative current was linear with the sweep rate, were employed to obtain a crude estimate of the surface areas of each electrode. Figures 3 and 4 show the typical cyclic voltammograms and the typical linear relationships between the capacitative current and the sweep rate, respectively. The apparent capacitances and the roughness factors of each $IrO_2/TiO_2/Ti$ electrode were evaluated from these cyclic voltammograms, and the results are listed in Table II. The roughness factors were determined by assuming a double layer capacitance of 2×10^{-5} F/cm² for a smooth surface (8). The roughness factor calculated by this method does not reflect the true surface area but the relative one, since the measured capacitance is a pseudocapacitance (8). Thus, we can only compare the relative surface areas of the electrodes using this method, if the electrodes are of the same type. The sample number (denoted by superscript) in Table II corresponds to that in Table I in the preparation of the TiO_2 film. The roughness factors of samples 1 and 2, whose TiO_2 films are prepared in K_2CO_3, are about 5-6 times larger than that of the IrO_2/Ti electrode, while the other $IrO_2/TiO_2/Ti$ electrode had almost the same roughness factors as the IrO_2/Ti electrode as shown in Table II. It is judged from the above results, that the surface area of the $IrO_2/TiO_2/Ti$ electrode is large only when its TiO_2 layer is thick.

Table II. Parameters of the $IrO_2/TiO_2/Ti$ electrodes for the OER

Sample no.	Capacitance (F/cm²)	Roughness factor	Tafel slope (V/decade)	Overpotential at 100 mA/cm² (V)
1′	12.0×10^{-3}	6.0×10^{2}	0.03 (low η) 0.06 (high η)	0.33
2′	9.0×10^{-3}	4.5×10^{2}	0.04	0.35
3′	3.8×10^{-3}	1.9×10^{2}	0.08 (low η) 0.09 (high η)	0.48
4′	3.8×10^{-3}	1.9×10^{2}	0.07	0.44
5′	2.0×10^{-3}	1.0×10^{2}	0.08 (low η) 0.12 (high η)	0.42
6′	2.4×10^{-3}	1.2×10^{2}	0.07	0.44
IrO_2/Ti	2.8×10^{-3}	1.4×10^{2}	0.10 (low η) 0.16 (high η)	0.54

On the other hand, the capacitances of the TiO_2 films prepared by the anodic oxidation accompanied by sparking are very small and depend on the potential as shown in Fig. 3B. Figure 5 shows the typical Mott-Schottky plot for the no. 5 sample electrode in Table I. From the linear relationship of the $1/C^2$ *vs.* the potential, the flatband potential of this electrode was determined to be about 0.05V, which is almost the same as that of the TiO_2 semiconducting electrodes (11). It is judged from this result, that a TiO_2 layer necessarily exists in the interface between the TiO_2/Ti electrode and the electrolyte, and that the Ti substrate is never directly in contact with the electrolyte, even if the TiO_2 film is porous.

Figure 6 shows the typical Tafel plots of the $IrO_2/TiO_2/Ti$ and the IrO_2/Ti electrodes for the OER. The Tafel slopes and the overvoltages (η) at 100 mA/cm² are listed in Table II. The catalytic activities of the $IrO_2/TiO_2/Ti$

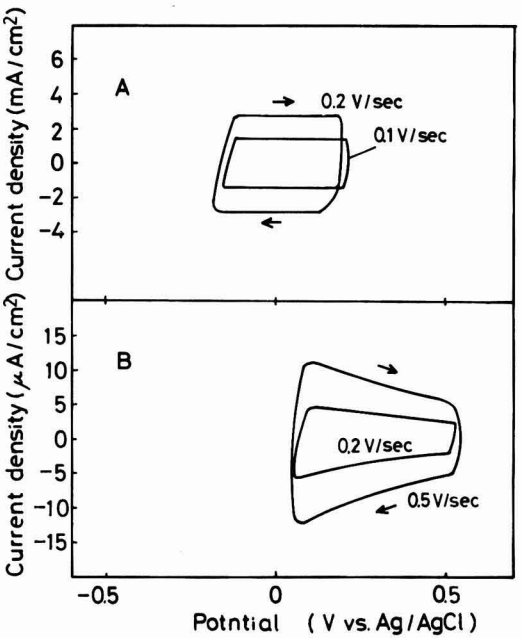

Fig. 3. Typical cyclic voltammograms of the $IrO_2/TiO_2/Ti$ and the TiO_2/Ti electrodes in 1M H_2SO_4 at 20°C: (A) sample 1′ and (B) sample 5.

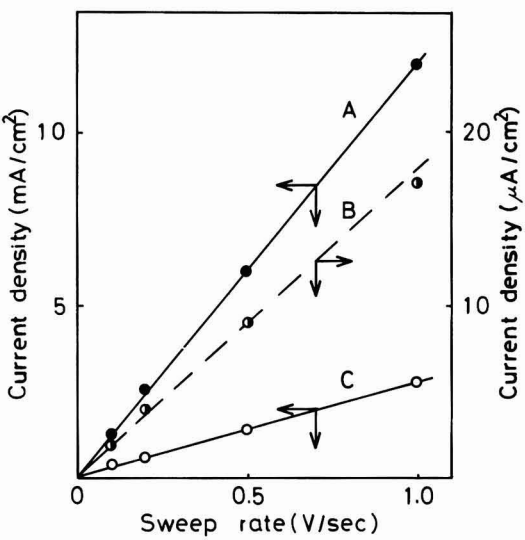

Fig. 4. Current densities as a function of sweep rate: (A) sample 1′, (B) sample 5, and (C) IrO_2/Ti electrode.

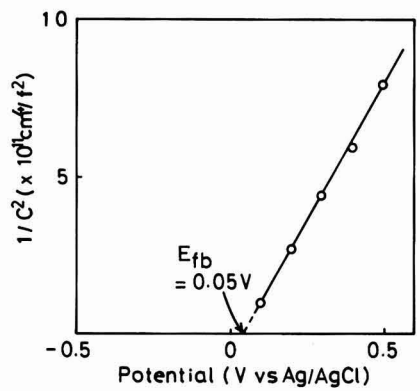

Fig. 5. Typical Mott-Schottky plot for sample 5. Flatband potential (E_{FB}) is about 0.05V *vs.* Ag/AgCl.

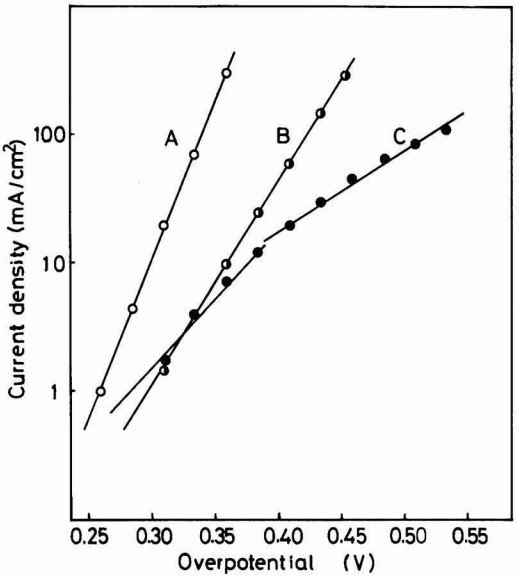

Fig. 6. Typical Tafel plots of the $IrO_2/TiO_2/Ti$ and the IrO_2/Ti electrodes: (A) sample 2′, (B) sample 6′ and (C) IrO_2/Ti electrode.

electrodes are higher than that of the IrO_2/Ti electrode in the high overvoltage region. Electrodes 1′ and 2′ have superior catalytic activity and are always higher than the IrO_2/Ti electrode in the catalytic activity in all the potential regions. The low overvoltage of the $IrO_2/TiO_2/Ti$ electrode is not only based on the electrode surface areas listed in Table II, but also on the values of their Tafel slopes which are smaller than that of the IrO_2/Ti electrode and depend on the conditions in the anodic oxidation to prepare the TiO_2 film. The Tafel slope of the IrO_2/Ti electrode prepared in the present study is larger than those already reported (2, 8). This is based mainly on the difference in the calcination temperature as described in the Discussion section. Thus, the conclusion that the $IrO_2/TiO_2/Ti$ electrode is electrocatalytically active can be made. Figure 7 shows the typical dependence of the overpotential on the electrolyzing time at 300 mA/cm² for the OER. The $IrO_2/TiO_2/Ti$ electrodes are more stable than the IrO_2/Ti electrode and always exhibit lower overpotentials. The above results demonstrate that the $IrO_2/TiO_2/Ti$ electrode, when its TiO_2 film is prepared by the anodic oxidation in K_2CO_3 solution accompanied by sufficient sparking, is the best anode for the OER in acidic solution.

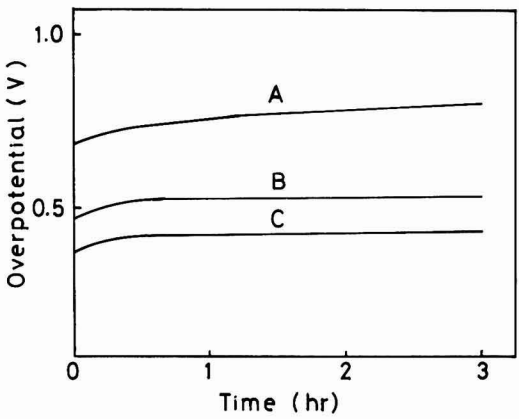

Fig. 7. Overpotentials as a function of electrolyzing time at 300 mA/cm²: (A) IrO_2/Ti electrode, (B) sample 5′, and (C) sample 2′.

Discussion

There are two interesting properties of the $IrO_2/TiO_2/Ti$ electrode. One is that the resistivity of the surface layer of this electrode is zero, if the TiO_2 film is prepared by the anodic oxidation accompanied by sufficient sparking. The other is that the catalytic activity of this electrode is higher than that of the IrO_2/Ti electrode. The former is explained by the model of the TiO_2 film in Fig. 8. Since the TiO_2 film is porous but completely covers the Ti substrate, there will be two parts in the thickness of the TiO_2 film, where one part is very thin [(b) in Fig. 8A] and the other is very thick [(a) in Fig. 8A]. When the IrO_2 is prepared by the thermal decomposition method on the TiO_2 film, a TiO_2 layer highly doped with Ir and an IrO_2 layer that is very conductive, will be formed on this surface. This is illustrated in Fig. 8B. The Ti substrate will be directly in contact with the TiO_2 layer highly doped with Ir formed in the part of the thin TiO_2 layer [(b) in Fig. 8A]. Thus, the resistivity of the surface of the $IrO_2/TiO_2/Ti$ electrode becomes zero, and the electrochemically active area of the electrode surface is large, if the porous TiO_2 film is thick (samples 1 and 2). On the other hand, the TiO_2 film prepared by the anodic oxidation without sparking is not porous, and its thickness is regular over the whole surface. In this case, the Ti substrate never is in contact with the TiO_2 layer doped with Ir formed by the thermal decomposition process, because no part of the very thin TiO_2 layer exists in the surface.

The high catalytic activity of the $IrO_2/TiO_2/Ti$ electrode is related to the change in the mechanism of the OER, because the Tafel slope of the $IrO_2/TiO_2/Ti$ is smaller than that of the IrO_2/Ti electrode. Figure 9 shows the Tafel plots of the IrO_2/Ti electrodes prepared at three calcination temperatures. The Tafel slope decreases with the decrease of the calcination temperature. This result is in agreement with that of the RuO_2/Ti electrode for the OER (12). Trasatti *et al.* proposed that the nature of the surface activities changes along with the morphology of the electrode surface, for example, defects in the lattice, as the calcination temperature is varied (9, 12, 13). According to them, a highly defective surface prepared by the low calcination temperature brings about a low value in the Tafel slope. The $IrO_2/TiO_2/Ti$ electrode corresponds to the IrO_2/Ti electrode prepared at the low calcination temperature with reference to the Tafel slope, and therefore, their surfaces may be defective. However, the surfaces of the $IrO_2/TiO_2/Ti$ and the IrO_2/Ti electrodes will be essentially different from each other as follows. Figure 10 shows the Tafel plots of the $IrO_2/TiO_2/Ti$ electrodes prepared at the various tempertures. These electrodes correspond to electrodes 2′ and 4′ in Table II, except for the calcination temperature. The Tafel slopes of

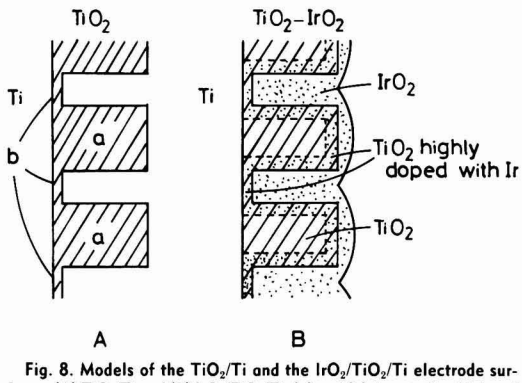

Fig. 8. Models of the TiO_2/Ti and the $IrO_2/TiO_2/Ti$ electrode surfaces: (A) TiO_2/Ti and (B) $IrO_2/TiO_2/Ti$. (a) and (b) denote the thick and the thin parts of the TiO_2 film, respectively.

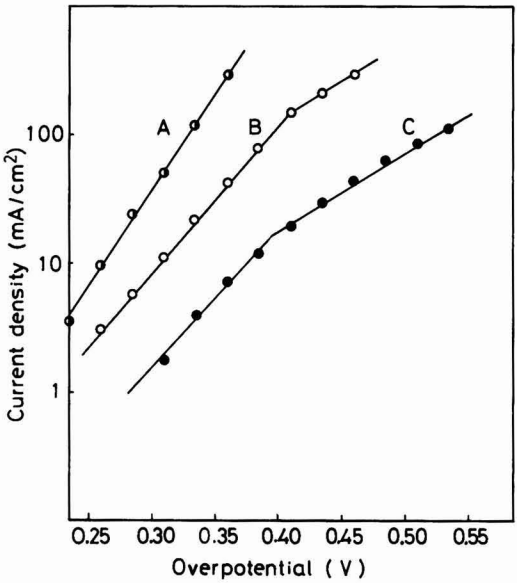

Fig. 9. Tafel plots of the IrO_2/Ti electrodes prepared at three calcination temperatures: (A) 350°C, (B) 450°C, and (C) 550°C.

these electrodes are almost independent of the calcination temperature and are about 0.04 and 0.07 V/decade for electrodes 2′ and 4′, respectively. This result is very different from that for the IrO_2/Ti electrodes in Fig. 9.

Trasatti *et al.* (12, 13) used g^*, which is the charge obtained by integration of the voltammetric curves, as a parameter to indicate the morphological change of the surface, which will reflect the change in the degree of the defect in the lattice. This parameter corresponds to the capacitance measured in this study. Figure 11 shows the

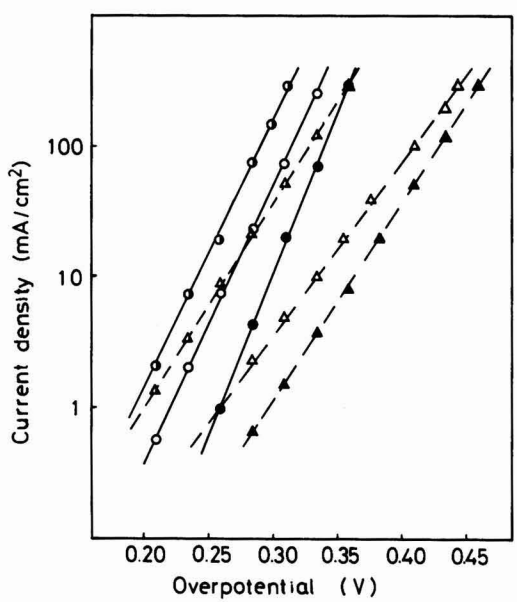

Fig. 10. Tafel plots of the $IrO_2/TiO_2/Ti$ electrodes prepared at three calcination temperatures. Circle and triangle denote samples 2′ and 4′, respectively. Closed, open, and half closed symbols denote the calcination temperatures of 550°, 450°, and 350°C, respectively.

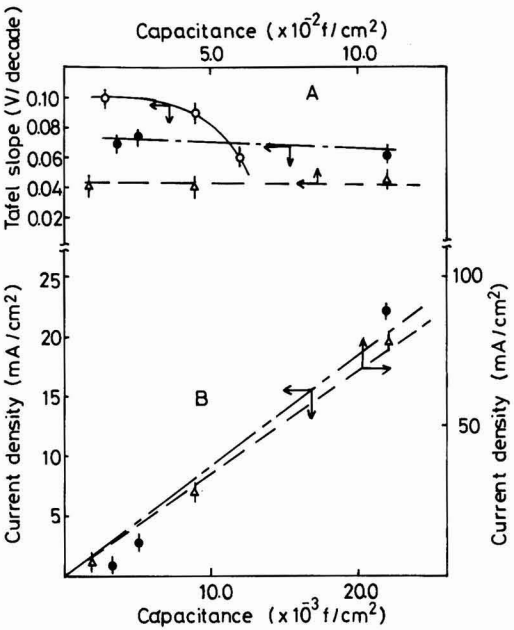

Fig. 11. Tafel slopes (A) and current densities (B) as a function of the capacitance. Open circle, closed circle, and open triangle symbols denote IrO_2/Ti, sample 2′, and sample 4′, respectively.

Tafel slopes in the low overpotential region and the current densities at $\eta = 0.30V$ as a function of the capacitance, which was varied by the change in the calcination temperature similar to the case in Fig. 9 and 10. The capacitance decreased with the increase in the calcination temperature. It is judged from the change of the Tafel slope with the capacitance for the IrO_2/Ti electrode, that its surfaces depend on surface defects. On the other hand, the $IrO_2/TiO_2/Ti$ electrodes exhibit Tafel slopes that are independent of capacitances. Therefore, the capacitance at the $IrO_2/TiO_2/Ti$ electrode will reflect only the degree of the surface area. The rough straight lines in the plots of the relationship between the current densities and the capacitances (Fig. 11B) support this explanation. Thus, the morphological difference in the $IrO_2/TiO_2/Ti$ and the IrO_2/Ti electrode surfaces is not only based on the defect in the lattice. The TiO_2 films prepared by the anodic oxidation accompnied with sparking contain K and Na cations in the lattice as described in the Experimental section. Probably, these cations in the TiO_2 films will diffuse into the IrO_2 lattice in the thermal decomposition process and will importantly affect the mechanism and the electrocatalysis of the OER for the $IrO_2/TiO_2/Ti$ electrodes.

The IrO_2/Ti and the $IrO_2/TiO_2/Ti$ electrodes prepared at calcination temperatures lower than about 500°C are better from the viewpoint of the high surface area, but dissolve in the long-term test in acidic solution. In conclusion, the $IrO_2/TiO_2/Ti$ electrodes prepared at 550°C are very superior, when compared with IrO_2/Ti electrodes as anodes for the OER in acidic solution.

Manuscript submitted Feb. 10 1986; revised manuscript received June 9, 1986.

Utsunomiya University assisted in meeting the publication costs of this article.

REFERENCES

1. E. Yeager, in "Electrocatalysis on Non-metallic Surfaces," A. D. Franklin, Editor, p. 203, NBS Special Publication no. 455, U.S. Government Printing Office, Washington (1976).

2. C. Iwakura, H. Tada, and H. Tamura, *Denki Kagaku*, **45,** 202 (1977).
3. M. H. Miles, Y. H. Huang, and S. Srinivasan, *This Journal*, **125,** 1931 (1978).
4. S. Hackwood, L. M. Shchiavone, W. C. Dautremont-Smith, and G. Beni, *ibid.*, **128,** 2569 (1981).
5. D. N. Buckley and L. D. Burke, *J. Chem. Soc., Faraday Trans. 1*, **71,** 1447 (1975).
6. D. N. Buckley, L. D. Burke, and J. K. Mulcaky, *ibid.*, **72,** 1886 (1976).
7. S. Gottesfeld and S. Srinivasan, *J. Electroanal. Chem. Interfacial Electrochem.*, **86,** 89 (1978).
8. R. S. Yeo, J. Orehotsky, W. Visscher, and S. Srinivasan, *This Journal*, **128,** 1900 (1980).
9. S. Trasatti, *Electrochim. Acta*, **29,** 1503 (1984).
10. Y. Matsumoto, T. Shimizu, A. Toyoda, and E. Sato, *J. Phys. Chem.*, **86,** 3581 (1982).
11. L. A. Harris and R. H. Wilson, *Annu. Rev. Mater. Sci.*, **8,** 99 (1978).
12. G. Lodi, E. Sivieri, A. De Battisti, and S. Trasatti, *J. App.. Electrochem.*, **8,** 135 (1978).
13. S. Trasatti and G. Lodi, in "Electrodes of Conductive Metallic Oxides Part B", S. Trasatti, Editor, p. 521, Elsevier, Amsterdam (1981).

A Comparison of the Properties of CF_3SO_3H and H_3PO_4 in Relation to Fuel Cells

P. Zelenay,[1] B. R. Scharifker,* and J. O'M. Bockris*

Department of Chemistry, Texas A&M University, College Station, Texas 77843

D. Gervasio

Case Center for Electrochemical Sciences and the Chemistry Department, Case Western Reserve University, Cleveland, Ohio 44106

ABSTRACT

The properties of CF_3SO_3H and H_3PO_4 as electrolytes in fuel cells are discussed. A comparison of their properties has been made, taking into consideration the solubility of oxygen, its diffusion coefficient, the rate of oxygen reduction, and adsorption of the electrolytes on the platinum surfaces. Under the respective operating conditions of CF_3SO_3H and H_3PO_4 fuel cells, it was found that the solubility of oxygen is more than two times higher in CF_3SO_3H, the diffusion coefficient in CF_3SO_3H is 24 times greater, and the free area available for O_2 reduction in both media are similar. The effects of the structure of electrolytes on exchange current densities for oxygen reduction are discussed.

The performance of a fuel cell is strongly affected by the electrolyte used. Certain undesirable characteristics of orthophosphoric acid used in acid fuel cells (1, 2) stimulated growing interest in the synthesis of electrolytes that combine a high dissociation constant with high affinity for oxygen (3). Fluorosubstituted organic acids, *e.g.*, trifluoroacetic acid, tetrafluoro-1,2-disulfonic acid, and trifluoromethanesulfonic acid, were chosen. So far, only trifluoromethanesulfonic acid (CF_3SO_3H, TFMSA, triflic acid) shows stability promising enough for it to be a likely substitute for H_3PO_4 in fuel cells.

The pioneering papers by Appleby (1) and Appleby and Baker (4) on the oxygen reduction velocity on a Pt electrode in H_3PO_4 and CF_3SO_3H showed that this value was as much as two orders of magnitude higher for O_2 reduction carried in dilute CF_3SO_3H solution at room temperature than that for oxygen reduction in 85% H_3PO_4 at the same temperature.

Srinivasan and Salzano (5) found that the difference between oxygen reduction velocities in CF_3SO_3H and H_3PO_4 at 80°C was much reduced, compared with that measured at lower temperatures, especially at potentials below 1V. A similar observation was made by Adams *et al.* (6) for the reduction of oxygen from air at 135°C. Nevertheless, the oxygen reduction current at 0.80V in CF_3SO_3H at 70°C is about four times higher than that in H_3PO_4 at 100°C [cf. Ross (7)]. Although results obtained for O_2 reduction on pure Pt electrodes (where i_o is easily determined) cannot be directly applied to fuel cell electrodes using Pt catalysts, it has been suggested (4) that the rate of oxygen reduction in CF_3SO_3H under fuel cell conditions at <100°C is likely to be several times higher than that in phosphoric acid at *ca.* 180°C.

There may be the following reasons for a difference in the oxygen reduction rate in different electrolytes: (*i*) lesser adsorption of CF_3SO_3H (or $CF_3SO_3^-$) than H_3PO_4 on the electrode, *i.e.*, a larger fraction of the surface available for reduction, (*ii*) larger solubility of oxygen in CF_3SO_3H than in H_3PO_4, leading to a higher limiting current, (*iii*) greater diffusion coefficient for O_2 in CF_3SO_3H than in H_3PO_4, and (*iv*) a higher rate constant for O_2 reduction in CF_3SO_3H than in H_3PO_4 due, *e.g.*, to differences in the heat of solution of protons in each solution. The present work was undertaken as an attempt to discriminate among these factors.

Experimental

Adsorption measurements.—Adsorption of trifluoromethane sulfonic acid and phosphoric acid was measured by means of Fourier transform infrared spectroscopy and the radiotracer method. A detailed experimental procedure has been recently reported elsewhere (8).

Measurements of oxygen diffusivity and solubility in CF_3SO_3H.—Solutions.—Trifluoromethanesulfonic acid (3M Company) was distilled *in vacuo* and then converted into a monohydrate. $CF_3SO_3H \cdot H_2O$ was in turn purified by a double recrystallization process followed by triple vacuum distillation of the monohydrate. The pure concentrated trifluoromethanesulfonic acid thus obtained was used for preparation of 5*M* aqueous solution of the acid in which both oxygen diffusivity and solubility were measured. In order to avoid possible contamination of the acid with organic decomposition products, the CF_3SO_3H solutions were stored in an all-Teflon cell at low temperatures, whenever they were not being used.

The distilled water used in solution preparation for diffusivity and solubility measurements was obtained from the reverse osmosis-distillation system assembled by Cahan on the basis of a design developed by Gilmont and Silvis (9).

Experimental setup.—An all-glass electrochemical cell was used for O_2 diffusivity and solubility measurements (Fig. 1). The counterelectrode was made of a bright Pt foil (99.99% Pt, Johnson-Mathey), the area of which was 2 cm^2.

* Electrochemical Society Active Member.
[1] On leave from the Department of Chemistry, Warsaw University, 02-089 Warsaw, Poland.

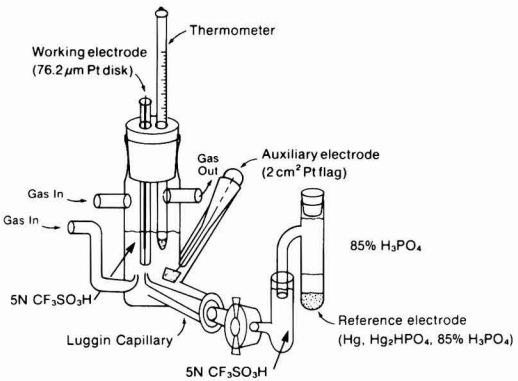

Fig. 1. Electrochemical cell for measurements of oxygen diffusivity and solubility in 5M CF_3SO_3H.

The reference electrode was a mercury-mercurous phosphate electrode containing the 85% H_3PO_4 and provided with an electrolytic bridge filled with the electrolyte in use (5*M* CF_3SO_3H). The electrode potential was measured as +0.542V *vs.* NHE. All potentials are referred to NHE.

The working electrode was made of a Pt wire, 76.2 μm diameter (>99.9% pure Pt, Johnson-Mathey) and placed between the reference electrode and the counterelectrode. The microelectrode was sealed in glass, then cut with a diamond saw and finally polished with diamond paste of different grades, down to 1 μm. After polishing, the glass seal around the electrode was carefully inspected for possible cracks, with an optical metallographic microscope at 1000 times magnification.

A PAR 173 potentiostat, a PAR 175 waveform generator, and SOLTEC EP-6432S *X-Y*$_1$, *Y*$_2$, *t* recorder were used in all O_2 diffusivity and solubility measurements.

Procedure.—Before each experiment, the Pt microelectrode was cleaned with nitric acid and rinsed with distilled water. The electrode was placed in solution and underwent further pretreatment by applying potential pulses between 0.2 and 1.6V. The performance of the microelectrode was considered satisfactory when the current response to potential pulses between 0.3 and 1.0V exhibited maxima of 0.03 μA and approached zero current within 1s. The solution purity was inspected by recording cyclic voltammograms in an inert (N_2) atmosphere with a 2 cm^2 Pt flag electrode which had been annealed in the reducing part of a methane-oxygen flame, cleaned with concentrated nitric acid, and rinsed with distilled water, followed by electrochemical pretreatment between 0.2 and 1.6V. As soon as cyclic voltammetry showed no impurities present, the solution was saturated with ultrapure O_2, and current transients for diffusion-controlled reduction of oxygen were measured and D_{O_2} and C_{O_2} determined from the slope and intercepts of *i vs.* $1/\sqrt{t}$ plots (10).

Results

Adsorption measurements.—A comparison of H_3PO_4 and $CF_3SO_3^-$ adsorption on platinum as a function of electrode potential is shown in Fig. 2. The plots presented in this figure correspond to a dilute solution of the acids (2×10^{-2} mol l^{-1}) at room temperature. The adsorption of trifluoromethanesulfonic acid and phosphoric acid was measured from the IR peaks obtained by means of an *in situ* FTIR technique and were then referred to the surface concentration of adsorbed species as determined radiometrically at 0.80V (8, 11).

In Fig. 3a and b, the amount of adsorbed species as a function of concentration at different temperatures is shown for CF_3SO_3H and H_3PO_4, respectively. The amount of adsorbed $CF_3SO_3^-$ and H_3PO_4 is given in terms of corresponding functions of θ, related to the adsorption isotherms found applicable for these two adsorption systems (8). The standard free energies of adsorption, ΔG°_{ads}, calculated from the slope of the plots in Fig. 3, are summarized in Table I.

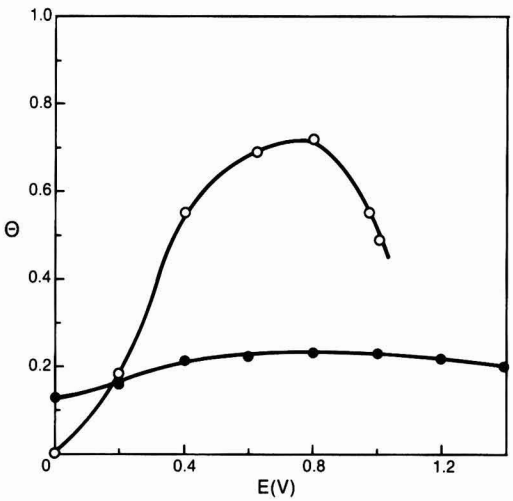

Fig. 2. A comparison of $CF_3SO_3^-$ and H_3PO_4 adsorption on platinum as a function of potential: (●) $CF_3SO_3^-$, (○) H_3PO_4. $C = 2 \times 10^{-2}$ mol l^{-1}, $T = 298$ K.

In Fig. 4a and b, $\Delta G^\circ_{ads}/T$ is plotted as a function of $1/T$ for $CF_3SO_3^-$ and H_3PO_4, respectively. The standard heat of adsorption, ΔH°_{ads}, and standard entropy of adsorption, ΔS°_{ads}, for both acids, calculated from the slope and from the intercept of the plots in Fig. 4, are given in Table I.

For the sake of comparison, the thermodynamic data presented in Table I, obtained from different adsorption isotherms having different "convenient" standard states (12), were recalculated (Table II) so that they refer to common standard-state conditions for both adsorption systems. A common standard state for coverage and concentration was chosen as 0.50 for θ at all temperatures and 1 mol l^{-1} for the solution concentration. The method of reevaluation of the thermodynamic data from the convenient standard state of the matching isotherm to the chosen comparison state is described in Ref. (13).

Measurements of oxygen solubility and diffusivity.—The current transients for oxygen reduction in 5*M* CF_3SO_3H at various temperatures are shown in Fig. 5. Each *i vs. t* plot was recorded after the electrode potential had been changed by steps from 1.0V, where the oxygen reduction rate is negligible, to 0.30V, where O_2 reduction is assumed to be entirely diffusion controlled (14). From the slope and the intercept of the corresponding *i vs.* $1/\sqrt{t}$ plots (Fig. 6), the diffusion coefficients and solubilities of O_2 in CF_3SO_3H can be calculated by using equations given by Winlove *et al.* (10) on the basis of the theory for diffusion to a microelectrode (15-18)

$$D_{O_2} = \alpha^2 A^2/\pi B^2 \quad [1]$$

$$C_{O_2} = B^2/n\mathbf{F}A\alpha^3 \quad [2]$$

where *A* and *B* are the intercept and the slope of *i vs.* $1/\sqrt{t}$ plot, and α is the radius of a planar Pt microelectrode used.

The values of D_{O_2} and C_{O_2}, as calculated from Eq. [1] and [2], are given in Table III. By using data summarized therein, the activation energy for diffusion-controlled O_2 reduction in 5*M* CF_3SO_3H is found to be 16.1 kJ mol^{-1}, and the enthalpy of dissolution of oxygen 11.6 kJ mol^{-1}.

Independent measurements carried out at 0.35 and 0.45V led to the same values of D_{O_2} and C_{O_2} as those found at 0.30V.

Discussion

The adsorption of the electrolyte species.—As was originally suggested by Appleby and Baker (14), the lower specific adsorption of the electrolyte species in CF_3SO_3H solu-

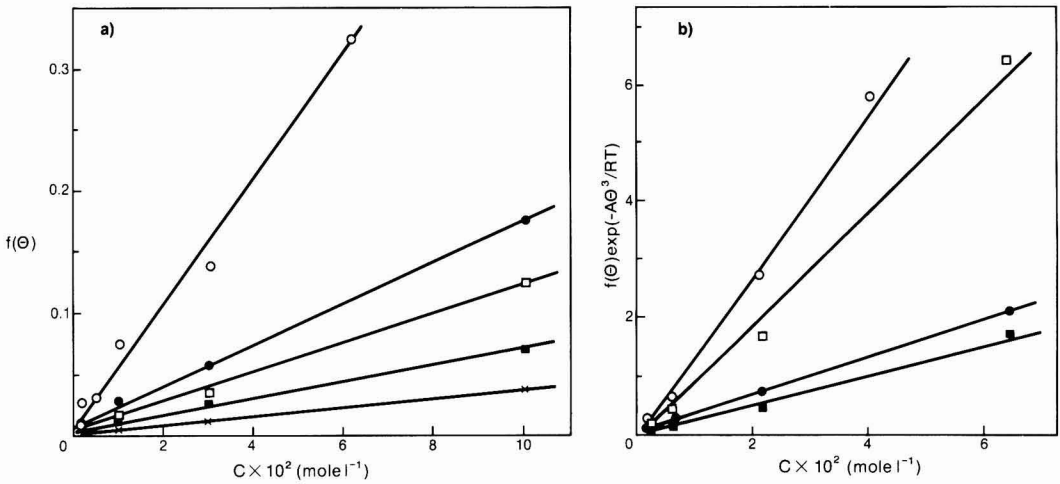

Fig. 3. Adsorption of $CF_3SO_3^-$ and H_3PO_4 at 0.80V as a function of concentration and temperature: (a) adsorption of $CF_3SO_3^-$ at 298 K (○), 323 K (●), 333 K (□), 343 K (■), and 353 K (X); (b) adsorption of H_3PO_4 at 298 K (○), 308 K (□), 318 K (●) and 328 K (■)

$$f(\theta) = \frac{\theta}{1-\theta}\,\frac{[\theta + n(1-\theta)]^{n-1}}{n^n}$$

(configurational term in the Bockris-Swinkels isotherm); where the number of water molecules displaced upon adsorption, n, is 3 for both $CF_3SO_3^-$ and H_3PO_4 (8). A = 3.9 kJ mol^{-1} (for H_3PO_4, only) (8).

tion as compared to that observed in H_3PO_4 solution may account for the better performance of trifluoromethanesulfonic acid fuel cell than that of phosphoric acid, providing a greater number of free catalytic sites per unit area in the former acid.

It is clear that, when an equal concentration of H_3PO_4 and CF_3SO_3H, a weak electrolyte and a strongly dissociated acid, respectively, is present in solution and individually competing with water for the surface of the platinum, H_3PO_4 would be expected to adsorb to the greater extent (at least within 0.3V of the pzc). Taking into account the considerable concentration (85-100%, *i.e.*, 14.5-18*M*) of phosphoric acid, the effect should be ever more marked, *i.e.*, suggest a greater blocking effect upon the access of O_2 to the electrode surface in the H_3PO_4. At first, when the only results available in our work were those taken at lower temperatures and lower concentrations, such suppositions seemed, indeed, to be borne out. Figure 2 of the present work shows that, at 25°C and comparable concentrations and potentials, the adsorption of phosphoric acid is about three times greater than that of $CF_3SO_3^-$. These suppositions, however, are subject to further consideration in the light of knowledge of adsorption behavior at higher concentrations and temperatures.

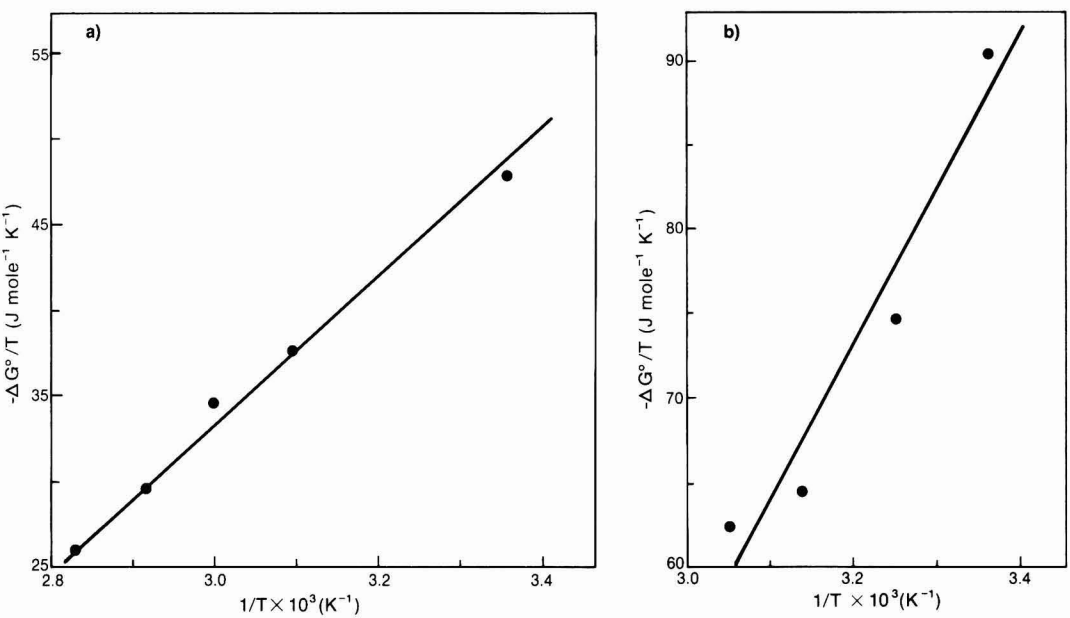

Fig. 4. Temperature dependence of the standard free energy of adsorption for (a) $CF_3SO_3^-$ and (b) H_3PO_4 (E = 0.80V)

Table I.

Thermodynamic data for $CF_3SO_3^-$ adsorption at different temperatures: $E = 0.80V$; $C^\circ = 1$ mol l^{-1}, $\theta^\circ = 0.582 \pm 0.001$

T (K)	K (l mol^{-1})	ΔG° (kJ mol^{-1})
298	322	−14.3
323	93.3	−12.2
333	66.7	−11.6
343	36.1	−10.2
353	19.3	− 8.7

Thermodynamic data for H_3PO_4 adsorption at different temperatures: $E = 0.80V$; $c^\circ = 1$ mol l^{-1}

T (K)	$K \times 10^3$ (l mol^{-1})	ΔG° (kJ mol^{-1})[a]
298	39.2	−26.2 (0.640 ± 0.001)
308	6.0	−22.3 (0.638 ± 0.001)
318	1.74	−19.7 (0.636 ± 0.001)
328	1.42	−19.8 (0.634 ± 0.001)

[a] Corresponding standard state, θ°, is given in the parenthesis.

As measurements of adsorption in the region of acid fuel cell practice bring difficulty, we have made extrapolation of the present results so that they extend to these temperatures, *i.e.*, 180°C for H_3PO_4 and 100°C for TFMSA. We have taken the two isotherms applicable to $CF_3SO_3^-$ and H_3PO_4 adsorption (the Bockris-Swinkels isotherm (19) for $CF_3SO_3^-$ and the same, but modified for dispersive interactions, in the case of H_3PO_4) and extrapolated as shown in Fig. 7. The possibility of changes in the structure of the electrolyte on going from dilute to concentrated solutions has not been considered in the extrapolations corresponding to the adsorption of H_3PO_4 on platinum.

Thus, due to the higher enthalpy of adsorption of H_3PO_4 as compared with that of $CF_3SO_3^-$ ($\Delta H^\circ = -92 \pm 20$ kJ mol^{-1} for H_3PO_4 and -44 ± 3 kJ mol^{-1} for $CF_3SO_3^-$), the relatively higher concentration of phosphoric acid on the surface at lower temperatures (*cf.* Fig. 2) will decrease as the temperature increases. At 100°C, the coverage with $CF_3SO_3^-$ would be about 0.7 while that for 98% H_3PO_4 would be close to unity.

Correspondingly, at 180°C, the plot given in Fig. 7 shows that the coverage with adsorbed H_3PO_4 is about 0.7, *i.e.*, near to that of TFMSA at 100°C. Hence, the estimated coverages for $CF_3SO_3^-$ and H_3PO_4 at 0.80V, under conditions resembling the fuel cell operation, are much closer to each other than at low temperatures and low concentrations. The calculated ratio of the free electrode area for the fuel cell operating at *ca.* 100°C in 5*M* CF_3SO_3H to the free area for the fuel cell working at 180°C in 98% H_3PO_4 is around 1:1 as compared with 3:1 at ambient temperature and dilute solutions.

Solubility and diffusion of O_2.—Now (14)

$$D_{O_2} = D^\circ_{O_2} \exp(-E/RT) \quad [3]$$

and

Table II. Comparison between thermodynamic data for $CF_3SO_3^-$ and H_3PO_4 adsorption at the standard state of $\theta^\circ = 0.5$ and $C^\circ = 1$ mol l^{-1}: $E = 0.80V$

CF_3SO_3		H_3PO_4	
T (K)	ΔG° (kJ mol^{-1})	T (K)	ΔG° (kJ mol^{-1})
298	−15.6	298	−28.0
323	−13.6	308	−24.1
333	−13.0	318	−21.6
343	−11.7	328	−21.7
353	−10.2	—	—
$\Delta H^\circ = -44 \pm$ kJ mol^{-1}		$\Delta H^\circ = -92 \pm 20$ kJ mol^{-1}	
$\Delta S^\circ = -93 \pm 10$ J mol^{-1} k^{-1}		$\Delta S^\circ = -219 \pm 63$ J mol^{-1} k^{-1}	

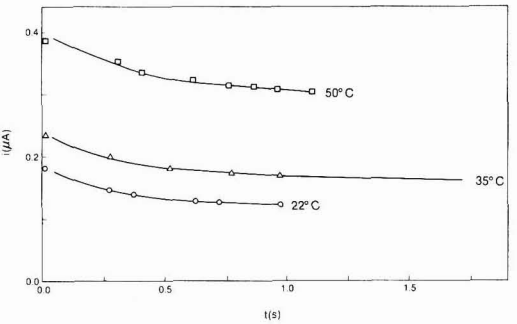

Fig. 5. The current transients for oxygen reduction in 5M CF_3SO_3H at different temperatures.

$$C_{O_2} = C^\circ_{O_2} \exp(-\Delta H/RT) \quad [4]$$

where E is the diffusion activation energy and ΔH is the enthalpy of dissolution. For oxygen diffusion in 5*M* CF_3SO_3H, (*cf.* Results), E and ΔH are, correspondingly, 16.1 kJ mol^{-1} and 11.6 kJ mol^{-1}. By using these values, the calculated diffusion coefficient for oxygen in 5*M* CF_3SO_3H at 100°C is 2.2×10^{-4} cm^2 s^{-1} and the O_2 solubility at the same temperature is found to be 9.6×10^{-4} mol^{-1}.

The oxygen diffusivity and oxygen solubility, thus obtained for 5*M* CF_3SO_3H at 100°C, can be compared with the corresponding data provided by Klinedinst *et al.* (14) and Gubbins and Walker (20) for O_2 in concentrated H_3PO_4 at 100°, 120°, and 150°C. By extrapolating the values reported there to 180°C, the corresponding data for diffusivity and solubility of oxygen in 98% H_3PO_4 at that temperature are: D_{O_2} (H_3PO_4) $= 9.1 \times 10^{-6}$ cm^2 s^{-1} and C_{O_2} (H_3PO_4) $= 3.6 \times 10^{-4}$ mol l^{-1}.

From the comparison of the values given above, the product of $D_{O_2} \times C_{O_2}$ is about 60 times greater in CF_3SO_3H at 100°C than in H_3PO_4 at 180°C. Both oxygen diffusivity and oxygen solubility are in favor of fuel cell action in CF_3SO_3H.

The rate constant.—We have considered so far the influence of diffusion coefficient, oxygen solubility, and occupancy of the electrode with adsorbed electrolyte. These factors do not, however, convey information concerning what may be the most important variable in considerations of the difference between the rates of oxygen reduction in H_3PO_4 and CF_3SO_3H, namely, the activated processes involved in the formation of the transition state complex.

At present, there is no systematic work that has allowed the precise evaluation of the rate-determining step for oxygen reduction in these two electrolytes. Therefore, we can

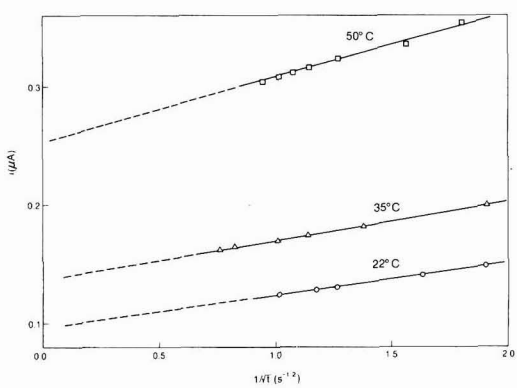

Fig. 6. The plot of i vs. $1/\sqrt{t}$ for O_2 reduction in 5M CF_3SO_3H at different temperatures.

Table III. Diffusion coefficient and solubility of oxygen in 5M CF_3SO_3H at various temperatures

T (K)	D_{O_2} (s cm^{-2})	C_{O_2} (mol l^{-1})
295	5.9×10^{-5}	3.5×10^{-4}
308	7.8×10^{-5}	3.8×10^{-4}
323	9.4×10^{-5}	5.8×10^{-4}

only assume a rate-determining step corresponding to that often put forward for O_2 reduction in acid media (23-25), namely

$$O_2 + H^+ = e^- \rightarrow HO_{2(ads)} \quad [5]$$

In order to compare the rates of O_2 reduction in these two solvents under the conditions relevant to fuel cell applications, *i.e.*, 100°C for CF_3SO_3H and 180°C for H_3PO_4, data on the activation energies for oxygen reduction in the two electrolytes are needed. Literature values reported for the energy of activation in H_3PO_4 and CF_3SO_3H solutions are given in Table IV. There is little agreement between the values of the various authors; in particular the value determined by Appleby for O_2 reduction in phosphoric acid on reduced platinum electrodes is almost two times higher than that reported by O'Grady *et al.* under similar conditions. It is clear, from a study of the values of this table, that a meaningful comparison of the rates of O_2 reduction in these two solutions under the conditions relevant to fuel cell operation, based on literature data for the energies of activation, is, at present, precluded.

Were it possible to calculate the heat of solvation of the proton in 98% H_3PO_4, and know the difference of this heat from that in CF_3SO_3H, a reasonable estimation of the heat of activation in H_3PO_4 at 180°C could be made (and, therefrom, an estimate of the i_0 value). However, when one comes to estimate this hydration heat, the difficulty is to decide upon a reasonable model. What is the concentration of free vapor? What is the bond strength of H to O in H_3PO_4? What is the dielectric constant of the very concentrated solution? In the absence of a knowledge of these factors, there is little point in making a theoretical estimation of the exchange current density for O_2 reduction in 98% H_3PO_4.

Conclusion

Table V summarizes our present knowledge with regard to the factors affecting the relative velocities of the reduction of oxygen in H_3PO_4 and CF_3SO_3H under conditions corresponding to those which would be used in fuel cells.

The solubility of oxygen is more than two times higher in CF_3SO_3H, as compared with that in H_3PO_4. Under activation-controlled conditions for oxygen reduction, C_{O_2} will influence the reaction rate according to $C_{O_2}^{1-\alpha}$, where α is the transfer coefficient. Taking α as ½, one would then expect the rate to be $\sqrt{2.7} = 1.6$ times higher due to this cause in CF_3SO_3H than in H_3PO_4.

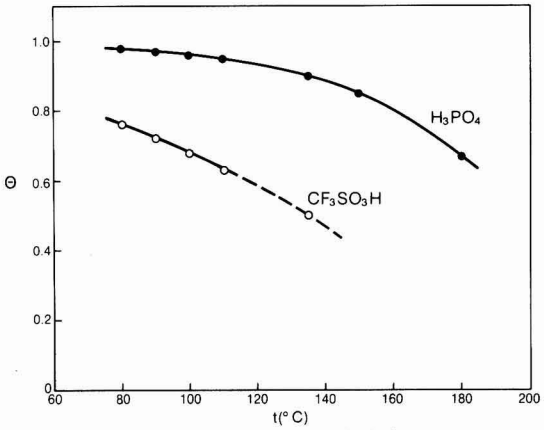

Fig. 7. Extrapolation of adsorption data to the high temperatures region: (●) 5M CF_3SO_3H, (○) 98% H_3PO_4.

Table IV. Energies of activation for oxygen reduction in H_3PO_4 and CF_3SO_3H

Solution	E_a (kJ mol^{-1}) Reduced Pt	Oxidized Pt	Reference
H_3PO_4	62		(24)
	33		(21)
	40		(22)
		55	(26)
CF_3SO_3H	53		(4)

Table V. Relevant quantities for discussion of relative reduction velocities of oxygen in CF_3SO_3H and H_3PO_4

	5M CF_3SO_3H, 100°C	98% H_3PO_4, 180°C
C_{O_2} (mol l^{-1})	9.6×10^{-4}	3.6×10^{-4}
D_{O_2} (cm^{-2} s^{-1})	2.2×10^{-4}	9.1×10^{-6}
$1 - \theta$	0.3	0.3
k	?	?

If the comparison of the reduction rates of oxygen is made at a current density less than that of the limiting current, the diffusion coefficients will have little effect. If, on the other hand, maximum power data are to be compared with that for H_3PO_4 would give a great advantage for CF_3SO_3H. The value of D_{O_2} in CF_3SO_3H at 100°C is about 24 times greater than that in H_3PO_4 at 180°C, making the availability of oxygen at the electrode surface about 60 times greater in CF_3SO_3H than in H_3PO_4.

Since the free areas available for O_2 reduction in both media are similar, adsorption of the electrolyte on the electrode surface appears to have little effect on the present comparison.

This evidence points, therefore, to a likely advantage in using TFMSA for oxygen reduction in fuel cells, with possible gains, perhaps approaching two orders of magnitude in net power.

From the considerations given above, the trends arising for acid fuel cell electrolytes are as follows.

1. In respect to the choice of acid and its effects on the oxygen reduction rate, the objective is to have low adsorption of the electrolyte and hence to maximize the available electrocatalytic area. If the rate-determining step is indeed as described in Eq. [5], then lower dielectric constant of an acid would tend to minimize the heat of solvation of the proton. Therefore, what is needed is a strong acid with low anion adsorption, *e.g.*, $HClO_4$. A polyvalent anion (increased lateral repulsion) would be helpful. A practical disadvantage of CF_3SO_3H is the need of troublesome purification. Another disadvantage is the likely orientation of the $-SO_3^-$ groups, which lay away from the electrode surface (8), leading to a diminution of the lateral repulsion and to a tendency to adsorb more than a simple acid, for which the anion would remain within the Helmholtz plane. Given that the performance of the CF_3SO_3H fuel cell is much better than that of H_3PO_4 at temperatures below 100°C, trifluoromethanesulfonic acid is recommended whenever practical requirements prevent the fuel cell from operating at higher temperatures. Otherwise, use of phosphoric anion is preferable.

2. Solubility. It is desirable to have a maximum oxygen solubility. Since O_2 solubility is enhanced by the presence of the $-CF_3$ group, a strong fluorosubstituted acid is advisable.

3. Diffusion coefficient. The netted structure of 100% H_3PO_4 is not favorable for high O_2 diffusion coefficient. A concentrated aqueous solution of a strong acid near its boiling point with a high D_{O_2} and low dielectric constant would give an optimal result.

An acid of interest may be F-SO_3H (26).

Acknowledgments

This work was carried out in the Hydrogen Research Center at Texas A&M University with the support of EPRI. Thanks are due to Dr. Ahsan Habib for extensive discussion during the writing of the paper. Thanks are also

due to Dr. Ernst Yeager for encouraging collaboration between the Texas A&M University and Case Western Reserve University work on oxygen reduction.

Manuscript submitted Oct. 10, 1985; revised manuscript received May 23, 1986.

The Department of Chemistry, Texas A&M University assisted in meeting the publication costs of this article.

REFERENCES

1. A. J. Appleby, *This Journal*, **117**, 328 (1970).
2. H. R. Kunz and G. A. Graver, *ibid.*, **122**, 1279 (1975).
3. M. S. Toy, in "Synthesize New Fuel Cell Electrolytes." Interim Report for EPRI, Contract RP-1686-3 (1982).
4. A. J. Appleby and B. S. Baker, *This Journal*, **125**, 404 (1978).
5. S. Srinivasan and F. J. Salzano, Paper presented at the ERDA-EPRI Fuel Cell Seminar, Palo Alto, California, June 29-July 1, 1976.
6. A. A. Adams, R. T. Foley, and H. J. Barger, Jr., *This Journal*, **124**, 1228 (1977).
7. P. N. Ross, Jr., *ibid.*, **130**, 882 (1983).
8. P. Zelenay, M. A. Habib, and J. O'M. Bockris, *Langmuir*, Submitted for publication.
9. P. Gilmont and S. J. Silvis, *Am. Lab.*, **6**, 46 (1974).
10. C. P. Winlove, K. H. Parker, and R. K. C. Oxenham, *J. Electroanal. Chem. Interfacial Electrochem.*, **170**, 293 (1984).
11. M. A. Habib and J. O'M. Bockris, *This Journal*, **132**, 108 (1985).
12. B. E. Conway, H. Angerstein-Kozlowska, and H. P. Dhar, *Electrochim. Acta*, **19**, 455 (1974).
13. B. R. Scharifker, P. Zelenay, M. A. Habib, and J. O'M. Bockris, *J. Phys. Chem.*, Submitted for publication.
14. K. Klinedinst, J. A. S. Bett, J. MacDonald, and P. Stonehart, *J. Electroanal. Chem. Interfacial Electrochem.*, **57**, 281 (1974).
15. K. B. Oldham, *ibid.*, **122**, 1 (1981).
16. K. Aoki and J. Osteryoung, *ibid.*, **122**, 19 (1981).
17. K. Aoki and J. Osteryoung, *ibid.*, **125**, 315 (1981).
18. B. R. Scharifker and G. J. Hills, *ibid.*, **130**, 81 (1981).
19. J. O'M. Bockris and D. A. J. Swinkels, *This Journal*, **111**, 736 (1964).
20. K. E. Gubbins and R. D. Walker, Jr., *ibid.*, **112**, 469 (1965).
21. W. E. O'Grady, E. J. Taylor, and S. Srinivasan, *J. Electroanal. Chem. Interfacial Electrochem.*, **132**, 137 (1982).
22. J. C. Huang, R. K. Sen, and E. Yeager, *This Journal*, **126**, 786 (1979).
23. A. Damjanović and V. Brusić, *Electrochim. Acta*, **12**, 615 (1967).
24. A. J. Appleby, *This Journal*, **117**, 641 (1970).
25. D. B. Sepa, M. V. Vojnović, and A. Damjanović, *Electrochim. Acta*, **26**, 781 (1981).
26. A. J. Appleby, *J. Electroanal Chem. Interfacial Electrochem.*, **24**, 97 (1970).

Glow Discharge Electrolysis of Aqueous Sulfuric Acid Solution in Various Atmosphere

Yasushi Kanzaki,*,[1] Masahiro Hirabe, and Osamu Matsumoto*

Department of Chemistry, College of Science and Engineering, Aoyama Gakuin University, Setagaya-ku, Tokyo 157, Japan

ABSTRACT

The anode glow discharge electrolysis was carried out in aqueous sulfuric acid solution, and the yields of oxidation products, H_2O_2, H_2SO_5, and $H_2S_2O_8$, were examined in various atmospheric gases, H_2, He, N_2, and Ar. When the vapor pressure of water was suppressed by means of intermittent electrolysis, the yields of the peroxides were found to depend clearly on the atmospheric gases. The plasma diagnostics, emission spectra, double-probe method, etc., revealed that the plasma state in the gas phase depended on the gases that contained significant amounts of water vapor. Comparing the oxidation yields with the results on the plasma diagnostics, it was found that (*i*) the radical formation in the gas phase does not necessarily correspond to that in the solution phase, and (*ii*) the gases that contained light-charged particles (H^+ and He^+), *i.e.* H_2 and He, gave high oxidation yields. Since the light-charged particles, which will gain high acceleration energy in the cathode, fall adjacent to the surface of the electrolyte solution, the high oxidation yields in He and H_2 were ascribed to the high yield of OH radical due to the energy transfer from such particles penetrating into the solution phase.

Glow discharge electrolysis (GDE) is a unique electrochemical technique in which either of the electrodes is set in the gas phase above the electrolyte solution and, in most cases, the electrode is an anode (anode glow discharge electrolysis [AGDE]). In this electrolysis, the anode reaction occurs at the gas-solution interface, and the charge carriers are not the electrons but the cations from the gas phase. The oxidation yields are, in the case of AGDE, governed mainly by the energy transfer from accelerated positive ions and occur greatly in excess of those expected from Faraday's law. Such phenomena in GDE have been summarized minutely in the excellent review by Hickling *et al.* (1). However, in the previous studies much attention has been payed to the oxidation yields (2, 3), and the most fundamental constituent, the glow discharge in the gas phase, has been somewhat neglected because the contribution of atmospheric gases on the oxidation yield was minor (4).

We have already reported preliminarily the gas effect on the yield of GDE from the point of view that the glow discharge in the gas phase is the most fundamental factor in GDE (5, 6). In this paper, we report more advanced results on the diagnostics of the glow discharge in the gas phase in connection with the oxidation yields of peroxides in the solution phase.

Experimental

In this study, oxygen free H_2, He, N_2, and Ar were used to avoid complications due to the chemical reactions based on oxygen (3). The solution used was 1.5 mol l^{-1} sulfuric acid in which oxidation yields of H_2O_2 and H_2SO_5 are similar and that of $H_2S_2O_8$ was expected to be rather high. In this solution, the final oxidation products were expected to be H_2O_2, H_2SO_5, and $H_2S_2O_8$, which were determined by absorptiometry reported by Denaro *et al.* (7).

The experimental apparatus was similar to those previously described (5, 6). However, a minor change was made on the electrolysis procedure: the electrolyses were carried out for every one minute intermittently for a total of 5 min in order to avoid increase in the solution temperature. The temperature of the solution by this procedure was 3°-8°C, and it was low enough to suppress the vapor pressure of water (5.7-8.0 torr in contrast with the total pressure of 50 torr: 1 torr = 133.322 Pa). The gas flow rate was 3 ml s^{-1} (space volume in the cell was about 500 cm^3). The improved procedure resulted in the significant gas effect on the oxidation yields in GDE as shown below.

*Electrochemical Society Active Member.
[1]Present address: Faculty of Science, Tokyo Institute of Technology, Meguro-ku, Tokyo 152, Japan.

In this study, the double-probe method (8) used in the plasma diagnostics was introduced in addition to the emission spectrochemical analysis. Figure 1 shows the cell design, including double probes.

Results and Discussion

In our previous papers (5, 6), we reported that the oxidation yields of some simple redox systems depended on the atmospheric gases even under such conditions that were free from the oxygen effect, the excess HO_2 being formed in the oxygenated solutions (2). Before discussing the oxidation yield, we will show the results on the diagnostics of glow discharge in the gas phase.

Discharge voltage.—Figure 2 shows the transitions of the discharge voltage in various atmospheres after the initiation of glow discharge. Although the initial voltages were dispersed from 900V (He and Ar atmospheres) to 1300V (N_2 atmosphere), the stationary discharge gave a similar voltage (about 460V at electrode solution distance of 5 mm) except for Ar atmosphere (380-400V).

Figure 3 shows the relation of the discharge voltage *vs.* the electrode-solution distance. At short distances, three gases, H_2, He, and N_2, gave a similar curve, though that of N_2 increased notably at longer distances. Although the detailed mechanism of the glow discharge in GDE has not been clarified yet, it was revealed by these simple observations that the atmospheric gases showed their own even features in the glow discharge containing significant amounts of water vapor.

Emission spectra.—We have already shown that the emissions ascribed to the atmospheric gases decreased sharply as the partial pressure of water became high (*i.e.*, as the solution temperature became higher) (5, 6). In this study, the behavior of the emissions from H and OH radicals was examined precisely. Table I shows an example of the atmospheric dependence of the emissions ascribed to H and OH radicals (656.3 and 306.4 nm, respectively) at a current density of 75 mA. In the case of OH radical, Ar showed the strongest emission. In H_2 atmosphere, the emission of H radicals was strongest, as expected, and that of OH radical was weakest. For further discussion, the ratio of the intensity of OH radical to that of H radical was calculated because the ratio would be independent of atmosphere unless anything complex occurred. (Of course, the H_2 atmosphere is exceptional.) In the present estimation, the ratio was the order of Ar > N_2 > He > (H_2).

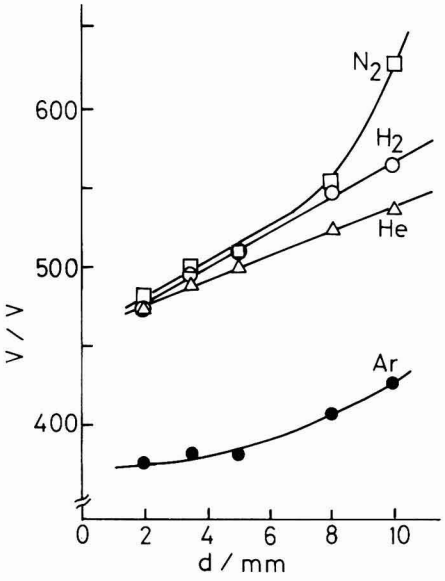

Fig. 3. Discharge voltage *vs.* electrode-solution distance curves in various atmospheres.

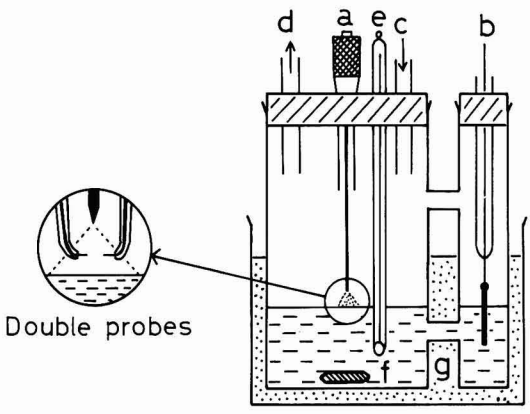

Fig. 1. Electrolytic cell for glow discharge electrolysis: (a) W anode, (b) Ni cathode, (c) gas inlet, (d) gas outlet, (e) thermometer, (f) magnetic stirrer, and (g) ice water bath. Double probes are omitted in right figure.

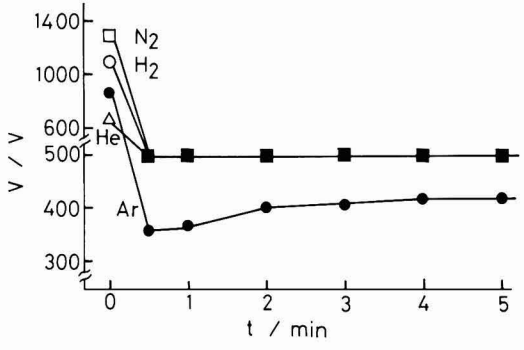

Fig. 2. Transitions of discharge voltage in various atmospheres, after the initiation of glow discharge.

These results were unexpected, for the ionization energy and the lowest metastable state are highest in He and, by intuition, the highest yield of OH radical was expected in He atmosphere. On the other hand, Ar, which has low excitation energies and the lowest stationary discharge voltage in Fig. 2, gave the most pronounced intensity of OH. These results suggest that the radical concentration in the gas phase does not necessarily correspond to those in the solution phase (*e.g.*, oxidation yields in Table IV).

Ionic concentration and electron energy.—To know the plasma state more precisely, the double-probe method was adopted. The ionic concentration and the electron energy were calculated from the current-voltage curve of the double probe. An example of the curve is shown in Fig. 4, which was observed in He atmosphere and gave a satisfactory S/N ratio. Such well-defined curves were also obtained in other gases. Table II shows the ionic

Table I. Relative intensity of emissions from OH (306.4 nm) and H (656.3 nm) radicals and their ratios. Current: 75 mA, solution temperature: 5°C, electrode-solution distance: 5 mm

Atmosphere	•OH	•H	•OH/•H
Ar	100	80	1.25
N_2	49	59	0.83
He	34	45	0.76
H_2	14	100	0.14

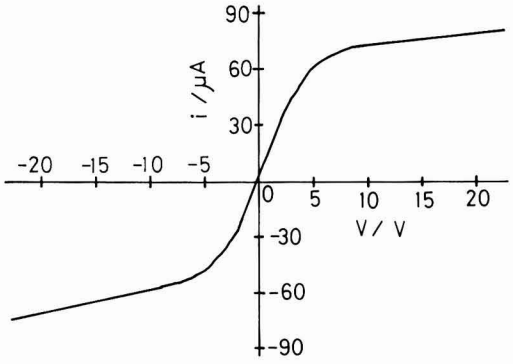

Fig. 4. Typical current-voltage curve in glow discharge measured by double probes. Atmosphere: He, solution temperature: 5°C. Small deviation from origin is due to unsymmetrical arrangement of double probe.

concentrations observed at a low solution temperature (about 5°C), in which the partial pressure of gas introduced was predominant, and at a high solution temperature (about 13°C). Table III shows the corresponding electron energies. It was found from the results that the ionic concentrations were the order of $N_2 > Ar > He > H_2$ at a low solution temperature, and $Ar \fallingdotseq N_2 > He \fallingdotseq H_2$ at a high solution temperature.

The electron energy at a low solution temperature dispersed widely, from 1.3 eV (H_2) to 5.0 eV (Ar), and they became similar, irrespective of atmospheric gases, at a high solution temperature. From the plasma diagnostics, it was suggested that high electron energy and high ionic concentration tended to decrease the oxidation yields.

Oxidation yields of peroxide.—In this experiment, the intermittent electrolysis, which kept the solution temperature low enough, was adopted, and the effect of gases on the peroxide formation was revealed more clearly than that in our previous papers. In addition, the formation of $H_2S_2O_8$ was detected with sufficient accuracy. Table IV shows the oxidation yields of peroxides in 1.5 mol l^{-1} sulfuric acid solution. The ratios $G_{H_2O_2}/G_{H_2SO_5}$, $G_{H_2O_2}/G_{H_2S_2O_8}$, and $G_{H_2SO_5}/G_{H_2S_2O_8}$ were listed in Table V.

To account for these results, it is reasonable to adopt the reaction mechanisms proposed by Denaro *et al.* (7) which were analogized from radiation chemistry. (Minor additions are made on the following equations for convenience.)

1. Gas phase, primary reaction zone (solution phase)

$$H_2O \rightsquigarrow H_2O^* \begin{cases} \rightarrow H + OH \\ \text{or} \\ \rightarrow H_2O^+ + e^- \end{cases} \quad [1], [2]$$

$$H_2O^+ + H_2O \rightarrow OH + H_3O^+ \quad [3]^2$$

$$e^- + H_3O^+ \rightarrow H + H_2O \quad [4]^3$$

$$X^* + H_2O \rightarrow X + H_2O^* \text{ (or } H_2O^+ + e^-) \quad [5]$$

$$X^+ + H_2O \rightarrow X + H_2O^+ \text{ (or } H^+ + OH) \quad [6]$$

[2]Fast > 10^{10} mol $^{-1}$dm^{3}s $^{-1}$.
[3]Slow << 10^{10} mol $^{-1}$dm^{3}s $^{-1}$.

Table II. Ionic concentrations in glow discharge measured by double-probe method in various atmospheres

Atmosphere	$n_i \times 10^{-10}$/cm^{-3} 5°C	13°C
Ar	3.5 ± 0.7	6.6 ± 2.1
N_2	4.8 ± 0.5	6.0 ± 1.6
He	2.7 ± 0.5	2.5 ± 0.4
H_2	2.1 ± 0.3	2.2 ± 0.1

Table III. Thermodynamical electron energy of glow discharge measured by double-probe method

Atmosphere	kTe/eV 5°C	13°C
Ar	5.0 ± 1.7	2.6 ± 1.1
N_2	2.3 ± 0.4	2.9 ± 0.8
He	1.5 ± 0.3	2.0 ± 0.6
H_2	1.3 ± 0.3	1.5 ± 0.4

(X: species related to atmospheric gas).

2. Solution bulk

$$OH + OH \rightarrow H_2O_2 \quad [7]^2$$

$$OH + H \rightarrow H_2O \quad [8]^2$$

$$H + H \rightarrow H_2 \quad [9]^2$$

$$OH + HSO_4^- \rightarrow HSO_4 + OH^- \quad [10]^3$$

$$OH + HSO_4 \rightarrow H_2SO_5 \quad [11]$$

$$H + HSO_4 \rightarrow H_2SO_4 \quad [12]$$

$$HSO_4 + HSO_4 \rightarrow H_2S_2O_8 \quad [13]$$

$$OH + H_2O_2 \rightarrow HO_2 + H_2O \quad [14]^3$$

These mechanisms successfully accounted for the pressure dependence and the concentration dependence of the yields of the peroxides in AGDE of sulfuric acid solution (7).

In the previous paper (6), we proposed that the high oxidation yields in He atmosphere should be ascribed to the high ionization energy or the high metastable state of He atom (19.8 eV). However, such reasoning was found to be incorrect for the net oxidation yield was also high in the hydrogen atmosphere as seen in Table IV.

To interpret the present result, we will take the reaction scheme in radiation chemistry again as a prototype in GDE. In radiation chemistry, it is known that the lighter particle gave higher G-values in Fricke dosimeter (9). Accordingly, we will first postulate in this study that the light-charged particles, like H^+ or He^+, give high oxidation yields from the results shown in Table IV. Such a phenomenon may be ascribed to the longer spur of the light particles than that of the heavy particles. In addition, the acceleration energy in GDE must be high in the light particles under a similar acceleration voltage, about 100 eV (1). The true acceleration effect would be more significant than that expected from the oxidation yields, because the observed ionic concentrations in He and H_2 (Table II) were lower in these gases than in Ar or N_2, and it would result in the low potential gradient within the cathode fall.

Table IV. Oxidation yields of peroxides in various atmospheres and sum of them [G_x = (moles of product x)/(moles of product x calculated from Faraday's law)]

Atmosphere	$G_{H_2O_2}$	$G_{H_2SO_5}$	$G_{H_2S_2O_8}$	G_{total}
Ar	0.61 ± 0.03	1.04 ± 0.01	0.31 ± 0.06	1.95 ± 0.07
N_2	0.79 ± 0.03	1.11 ± 0.03	0.34 ± 0.05	2.24 ± 0.05
He	1.34 ± 0.02	1.45 ± 0.01	0.35 ± 0.03	3.14 ± 0.04
H_2	1.23 ± 0.03	0.95 ± 0.02	0.30 ± 0.04	2.48 ± 0.06

Table V. Ratios of oxidation yields in Table IV

Atmosphere	$G_{H_2O_2}/G_{H_2SO_5}$	$G_{H_2O_2}/G_{H_2S_2O_8}$	$G_{H_2SO_5}/G_{H_2S_2O_8}$
Ar	0.59	1.97	3.34
N_2	0.71	2.32	3.27
He	0.92	3.83	4.16
H_2	1.29	4.10	3.18

Since the primary peroxide formed within the spur of penetrated particles is OH radicals, the yield of H_2O_2 (Eq. [7]) is expected to be high in cations with long spur (or penetration depth). On the other hand, the yield of H_2SO_5 will mainly depend on the bulk concentration of H_2SO_4 and be less sensitive to the length of the spur. The ratios of $G_{H_2O_2}/G_{H_2SO_5}$ in Table V, as well as the absolute values of $G_{H_2O_2}$ in Table III, support our assumption. Either value was fairly high in He and H_2 atmosphere. On the other hand, the ratio $G_{H_2SO_5}/G_{H_2S_2O_8}$ were not so different among atmospheres used. $G_{H_2S_2O_8}$, as well as $G_{H_2SO_5}$, is expected to depend on the bulk concentration of sulfuric acid (Eq. [10] and [13]). Of course, the high metastable state of He may play some role for the high oxidation yields of peroxides, though details are not known.

Conclusion

The general future of the atmospheric gas effects on the oxidation yields of GDE was clarified through the intermittent electrolysis and the diagnostics of glow discharge in the gas phase. Although the gas effect is minor in comparison with those of the pressure, the concentration, or the current density, the nature of GDE was revealed most successfully through the present study on the glow discharge in the gas phase.

Manuscript submitted Oct. 28, 1985; revised manuscript received July 22, 1986.

Aoyama Gakuin University assisted in meeting the publication costs of this article.

REFERENCES

1. A. Hickling, in "Modern Aspects of Electrochemistry," Vol. 6, J. O'M. Bockris and B. E. Conway, Editors, p. 329, Butterworth, London (1971).
2. A. Hickling and J. K. Linacre, *J. Chem. Soc.*, 711 (1954).
3. G. Mazzochin, G. Bontempelli, and F. Mango, *J. Electroanal. Chem. Interfacial Electrochem.*, **67,** 191 (1976).
4. A. R. Denaro and A. Hickling, *This Journal*, **105,** 265 (1958).
5. Y. Kanzaki, N. Nishimura, J. Toba, M. Konuma, and O. Matsumoto, *Denki Kagaku*, **52,** 126 (1984).
6. Y. Kanzaki, N. Nishimura, and O. Matsumoto, *J. Electroanal. Chem. Interfacial Electrochem.*, **167,** 297 (1984).
7. A. R. Denaro and K. Hogh, *Electrochim. Acta*, **17,** 549 (1972).
8. R. H. Huddlesstone and S. L. Leonard, "Plasma Diagnostics Techniques," Academic Press Inc., New York (1965).
9. J. W. T. Spinks and R. J. Woods, "An Introduction to Radiation Chemistry," John Wiley and Sons, Inc., New York (1964).

Influence of Surface Processes on Electrical, Photochemical, and Thermodynamical Properties of Zinc Oxide Films

P. Bonasewicz, W. Hirschwald, and G. Neumann

Institut für Physikalische Chemie, Freie Universität Berlin, D-1000 Berlin 33, Germany

ABSTRACT

Conductivity investigations have been performed at highly pure zinc oxide films under equilibrium conditions in the temperature range from 300 to 1000 K in oxygen (1 to 150 mbar). The conductivity behavior has to be divided into two temperature ranges. Above 800 K, the slope of ln σ *vs.* $1/T$ corresponds to 1.6 eV and the oxygen pressure dependence is $\sigma \propto p_{O_2}^{-1/4}$, while at low temperatures (>500 K) the respective values are 0.8 eV and $p_{O_2}^{-1/2}$. This behavior is interpreted as an incongruent decomposition at high temperatures and oxygen chemisorption of O^- (electrons from frozen-in donors) at low temperatures. This concept is further supported by the results of photoconductivity measurements. The temperature and pressure dependence of the conductivity σ in the whole measuring range can be expressed by

$$\sigma = \sigma_o/\{1 + (p_{O_2}/p_{O_2}{}^o)^{1/2}/A_1 \exp(-0.8 \text{ eV}/kT)\} + A_2 \exp(-1.6 \text{ eV}/kT)(p_{O_2}/p_{O_2}{}^o)^{-1/4}$$

A_1, A_2, and σ_o are adjusting parameters, $p_{O_2}/p_{O_2}{}^o$ is a normalized pressure. The carrier concentrations are ranging from 10^8 to 10^{15} cm^{-3} in the temperature range from 500 to 1000 K. The maximum concentration of uncompensated donor impurities is about 10^{12} cm^{-3}.

Zinc oxide is an n-type semiconductor with a bandgap energy of about 3.2 eV at room temperature.[1] The n-type conductivity arises from zinc excess in the nonstoichiometric compound $Zn_{1+\delta}O$. Hitherto, intrinsic conductivity could not be observed, much less p-conductivity. Even when doping with oxides acting as acceptors (*e.g.*, Li_2O) p-conductivity could not be generated. Obviously, it cannot be excluded that impurities with donor character prevent the occurrence of intrinsic conductivity.

As yet, there is only a small number of conductivity investigations on highly pure zinc oxide samples in which the intrinsic defect concentration is in thermodynamic equilibrium. Nonequilibrium of the defect concentration typically leads to hystereses in the temperature function of the conductivity (1). Moreover, in crystals frozen-in point defects can influence the conductivity behavior. For example, Hagemark and Chacka (4, 5) have interpreted the results of their combined conductivity Hall measurements on ZnO crystals with the presence of a deep donor and an acceptor in addition to the shallow donor. Contrarily, the conductivity behavior of thin films strongly depends on the purity of the adjacent gas phase. In order to avoid surface reactions, all condensable gases must be frozen at a cooling trap.

The defect structure.—The n-type character of the conductivity of ZnO can be deduced from the sign of the Hall effect and thermoelectric power, respectively. Zinc excess is responsible for the n-type character, which is concluded from the increase of the conductivity after hydrogen treatment or annealing in zinc vapor. In ZnO, excess zinc can exist in the form of zinc interstitials or oxygen vacancies

$$Zn_g \rightarrow Zn_i \rightarrow Zn_i{}^+ + e \qquad [1a]$$

$$Zn_g \rightarrow Zn_{Zn} + V_O{}^+ + e \qquad [1b]$$

(For nomenclature, see Table I.) As the donor level is about 0.05 eV below the conduction band, at room temperature all donors are singly ionized.

The direct observation of the defects led to controversial results. Mohanty and Azaroff (6) concluded from x-ray investigations of as-grown and zinc-saturated crystals to a maximum zinc interstitial concentration of $6 \cdot 10^{20}$ per cm^3 (14,000 at ppm). Contrarily, Appleton and Feldman (7), by use of the channeling-blocking tech-

[1]The conductivity behavior of zinc oxide is comprehensively reviewed by Heiland *et al.* (1), Brown (2), and Hirschwald *et al.* (3).

Table I. Defect nomenclature

Zn_{Zn}, O_O	zinc, oxygen on lattice site
Zn_i, O_i	zinc, oxygen in interstitial position
V_{Zn}, V_O	zinc, oxygen vacancy
O_2, Zn_g	gaseous oxygen, zinc
e, h	electron, hole
n, p	density of e, h
D, D^+, D^{++}	neutral, singly, doubly ionized donor
A, A^-, A^{--}	neutral, singly, doubly ionized acceptor
In_{Zn}^+	indium on zinc lattice site
Li_{Zn}^-	lithium on zinc lattice site
Li_i^+	lithium in interstitial position
$Zn_{Zn,s}$	surface atom of zinc
$V_{O,s}$	surface vacancy in the oxygen sublattice
$O_{2,s}^-$, O_s^-	chemisorbed oxygen molecule, atom

nique, came to the result that within the measuring accuracy of about 300 at ppm zinc interstitials could not be detected. However, the determination of excess zinc with the aid of analytic chemical methods reveals that probably at most 500 at ppm zinc ($2 \cdot 10^{19}$ cm^{-3}) can be dissolved in zinc oxide (8).

Conductivity and optical investigations do not permit conclusions with respect to the type of defect. Moreover, it is not possible to distinguish between intrinsic and extrinsic defects (impurities).

The diffusion-controlled sinter process refers to the existence of zinc interstitials. The sintering rate of hydrogen pretreated samples is distinctly larger than that of unpretreated ones and increases with increasing oxygen pressure (9). These experimental findings can be explained with the out-diffusion of zinc interstitials.

The results of the EPR investigations were distinctly interpreted. Natural zinc oxide reveals a weak EPR signal with a g-factor near 1.96. This signal was ascribed to the delocalized donor electron (10) and to the singly ionized oxygen vacancy (11), respectively. Hydrogen and zinc vapor treatment enlarges the signal intensity. According to Eq. [1], zinc excess leads to an increase of the carrier density and to an increase of the Zn_i^+ or V_O^+ concentration, respectively.

Doping with oxides of trivalent metals (*e.g.*, In) can be described by

$$In_2O_3 + Zn_i^+ \rightarrow 2In_{Zn}^+ + 3\,O_O + Zn_{Zn} + e \qquad [2a]$$

or

$$In_2O_3 + V_O^+ \rightarrow 2In_{Zn}^+ + 3\,O_O + e \qquad [2b]$$

The conductivity and the 1.96 signal intensity increase while the concentration of Zn_i^+ or V_O^+, respectively, is decreased.

Contrarily, doping with oxides of monovalent metals (*e.g.*, Li) leads to a drastic decrease of σ and to the disappearance of the 1.96 signal. Li-doping mainly occurs according to

$$Li_2O \rightarrow Li_{Zn}^- + Li_i^+ + O_O \qquad [3a]$$

Only a small fraction of the Li interstitials changes its site with a zinc lattice ion

$$Li_i^+ + Zn_{Zn} + e \rightarrow Li_{Zn}^- + Zn_i^+ \qquad [3b]$$

or generates an oxygen vacancy

$$Li_i^+ + e \rightarrow Li_{Zn}^- + V_O^+ \qquad [3c]$$

The fact that indium doping leads to an increase of σ and of the intensity of the 1.96 signal, while the concentration of Zn_i^+ or V_O^+, respectively, is reduced, and the fact that the opposite occurs in the case of Li-doping, clearly demonstrates that the EPR signal near $g = 1.96$ arises from the donor electron (12).

Electron irradiation of crystals creates Frenkel pairs in both sublattices. The threshold energies for oxygen and zinc Frenkel pairs are 310 and 900 keV (13), respectively. Electron irradiation at 600 keV results in

$$O_O \rightarrow V_O + O_i \overset{+2e}{\rightarrow} V_O + O_i^{--} \qquad [4]$$

σ decreases by orders of magnitude and the 1.96 signal vanishes. EPR signals with a g-factor close to 1.995 (14, 15) are observed. As illumination enlarges the signal intensity, this means that the paramagnetic center is V_O^+ or O_i^-.

Galland *et al.* (15, 16) have ascribed this signal to the singly ionized oxygen vacancy V_O^+. This was concluded from the undeformed tetrahedral symmetry of the hyperfine structure of the signal. Furthermore, a symmetric outward relaxation is observed (15). Schallenberger and Hausmann (17), contrarily, have assumed that the 1.99 signal arises from oxygen on the tetrahedral interstitial site. This, however, seems to be impossible because of the large anisotropy of the O_i-O_O distances (12).

In electron-irradiated crystals, Hausmann and Schallenberger (18) have observed a strongly anisotropic signal with g factors near 1.80 and 2.39 at temperatures below 13.5 K, appearing under illumination. This signal was ascribed to an oxygen interstitial on octahedral interstitial site.

Irradiation with 2-3 MeV electrons (17-19) results in further EPR signals with g factors near 2.00 and 2.02, appearing without illumination. These signals were identified to arise from a hole trapped at a zinc vacancy, V_{Zn}^-, corresponding to ($V_{Zn}^{--}O_O^+$). Further signals appearing after 2.7 eV illumination are ascribed to a neutral zinc vacancy corresponding to two trapped holes, ($O_O^+V_{Zn}^{--}O_O^+$). Signals that could be attributed to zinc interstitials are not observed.

Summarizing the results of the EPR investigations, the following statements can be made with respect to the defect structure of ZnO. (*i*) The signal near $g = 1.96$ has to be attributed to the conduction electron. (*ii*) Although zinc Frenkel pairs are created after 2-3 MeV electron irradiation, there is no signal that can be ascribed to zinc interstitials. (*iii*) The signal near $g = 1.99$, which appears only after low energy electron irradiation, has to be attributed to the oxygen vacancy. This is supported by the tetrahedral symmetry and the thermal stability of this defect. Oxygen interstitials, contrarily, annihilate at very low temperatures. The consequence of these considerations is that in thermal equilibrium zinc interstitials are the native lattice defects, while oxygen vacancies only are created after electron irradiation.

It may be mentioned that Schallenberger and Hausmann (20) recently have proposed a covalent binding model. Accordingly, besides the sp^3 hybrid bonds additional d-d bonds are formed between O_O-O_O and Zn_{Zn}-Zn_{Zn}. These d-d bonds extend far into the interstitial lattice. According to this model, $Zn_{i,tetr}^+$ and the neutral $Zn_{i,oct}$ are diamagnetic defects and, thus, are EPR-inactive, while $O_{i,oct}^-$ and $O_{i,tetr}$ are paramagnetic centers. However, although the zinc-oxygen distance is just the sum of the covalent radii, it is generally accepted that the charge of zinc and oxygen is about 1.0-1.2 (21). Furthermore, as discussed before, the existence of the paramagnetic center $O_{i,tetr}$ is highly questionable.

Surface reactions and defects.—Intrinsic conductivity.—In pure and stoichiometric ZnO, electric conduction could occur if electron-hole pairs are created thermally (or by photoexcitation with bandgap energy), *i.e.*

$$o \rightleftarrows e + h, \qquad K_i = np = K_i^o \exp\left(-\frac{E_g}{kT}\right) \qquad [5a]$$

In this case, the intrinsic conductivity σ is given by

$$\sigma = e_o\,(\mu_e n + \mu_h p) \qquad [5b]$$

μ_e and μ_h are electron and hole mobility, respectively, e_o is the elementary charge, and E_g is the gap energy. As $n = p$, this leads to

$$\sigma \propto \exp\,(-E_g/2kT), \qquad \sigma \neq f(p_{O_2}) \qquad [5c]$$

where σ is independent of oxygen pressure.

As yet, neither intrinsic conductivity, nor p-type conductivity could be detected. p-Type would need oxygen excess, *i.e.*

$$\tfrac{1}{2}\,O_2 \rightarrow O_i^- + h \qquad [6a]$$

or

$$\tfrac{1}{2}\,O_2 \rightarrow O_O + V_{Zn}^- + h \qquad [6b]$$

Even doping with Li_2O does not result in p-type conductivity, as, with rising Li_2O content, the fraction of Li_i that displaces zinc to interstitial sites (see Eq. [3b]) decreases (22). This means a hole creation according to

$$Li_i^+ + Zn_{Zn} \rightarrow Zn_i^+ + Li_{Zn}^- + h \qquad [6c]$$

cannot be expected.

Oxygen chemisorption.—At the surface of nonstoichiometric ZnO oxygen can be adsorbed (23). With rising temperature this can be described by the charge transfer model (24)

$$O_2 \rightarrow O_{2,s} \overset{+e}{\rightarrow} O_{2,s}^- \overset{+e}{\rightarrow} 2\,O_s^- \qquad [7a]$$

Physisorption is observed at temperatures ranging from about 100 to 250 K (25, 26).

Between 300 and 650 K, oxygen is chemisorbed. In the lower temperature range, O_2^- is chemisorbed with an activation energy of about 0.25 eV (27) for the charge transfer from O_2 to O_2^-. The maximum desorption rate is obtained at about 430 K (25), and the desorption energy is 1.05 eV (25, 28). Thus, the heat of chemisorption for the O_2^- species is about 0.8 eV.

Above about 500 K O_2^- is converted to O^-. This charge transfer was deduced from a number of experimental findings. The existence of O_2^- below 470 K was concluded from the lack of isotope exchange (25), from the first-order desorption kinetics (25, 28), and from the spin density of the EPR signals before and after the adsorption (25). The fact that the species O^- predominates at temperatures above 510 K was confirmed by the oxygen pressure dependence of σ (29), the appearance of atomic oxygen above 475 K (30-32), the association of two electrons per oxygen molecules deduced from combined conductivity-Hall and BET measurements (33), and the interpretation of TDS measurements combined with EPR (28) and conductivity measurements (34).

The equilibrium constants of chemisorption and the respective oxygen pressure dependence of σ are given by

$$K_{1a} = \frac{n p_{O_2}}{[O_{2,s}^-]}, \qquad \sigma \propto p_{O_2}^{-1} \qquad [7b]$$

and

$$K_{1b} = \frac{n p_{O_2}^{1/2}}{[O_s^-]}, \qquad \sigma \propto p_{O_2}^{-1/2} \qquad [7c]$$

Incongruent and congruent decomposition.—Incongruent decomposition becomes remarkable above 600 K (see, *e.g.*, Ref. [30]). *In vacuo* at lower temperatures, incongruent decomposition starts with the formation of oxygen vacancies in the surface plane

$$(Zn_{Zn}O_O)_s \rightleftarrows Zn_{Zn,s} + V_{O,s}^+ + e + \tfrac{1}{2}\,O_2 \qquad [8a]$$

If zinc atoms become mobile (zinc interstitials are much more mobile than oxygen vacancies (35)) zinc can be dissolved in ZnO according to

$$Zn_{Zn,s} + V_{O,s}^+ \rightarrow Zn_i^+ \qquad [8b]$$

that means the surface vacancy disappears. Thus, the incongruent decomposition can be written as

$$(Zn_{Zn}O_O)_s \rightarrow Zn_i^+ + e + \tfrac{1}{2}\,O_2 \qquad [8c]$$

The respective equilibrium constant and oxygen pressure dependence, respectively, are

$$K_2 = [Zn_i^+] n p_{O_2}^{1/2}, \qquad \sigma \propto p_{O_2}^{-1/4} \qquad [8d]$$

as

$$n = [Zn_i^+]$$

At temperatures larger than 1000 K the second electron dissociates from Zn_i, which leads to

$$(Zn_{Zn}O_O)_s \rightarrow Zn_i^{++} + 2e + \tfrac{1}{2}\,O_2 \qquad [9a]$$

with the respective equilibrium constant and oxygen pressure dependence

$$K_3 = [Zn_i^{++}] n^2 p_{O_2}^{1/2}, \qquad \sigma \propto p_{O_2}^{-1/6} \qquad [9b]$$

as

$$2[Zn_i^{++}] = n$$

Congruent decomposition (for a review, see Ref. (36)) becomes measurable above 1050 K (see, *e.g.*, Ref. (30)). Equilibrium vapor pressure measurements correspond to

$$ZnO \rightarrow Zn_g + \tfrac{1}{2}\,O_2 \qquad [10a]$$

with the equilibrium constant

$$K_v = p_{Zn}\, p_{O_2}^{1/2} \qquad [10b]$$

High temperature steady-state Langmuir evaporation, however, leads to atomic oxygen

$$ZnO \rightarrow Zn_g + O \qquad [10c]$$

while less than 0.01% vaporizes as ZnO molecules (37).

The evaporation rates are face specific. The evaporation rate of the $(000\bar{1})$ zinc face is a factor of three larger than that of the $(000\bar{1})$ oxygen face (38), while the rate of the prismatic $(10\bar{1}0)$ faces is not far from that of the $(000\bar{1})$ face (39, 40).

The congruent decomposition has no influence on the conductivity, as the stoichiometry deviation is in thermal equilibrium.

The consequence of these considerations is that the oxygen pressure dependence of σ is an important indicator to the conductivity determining reaction.

Photoinduced reactions.—Illumination with bandgap energy can also induce reactions [5a], [8c], and [7a] (in opposite direction). This leads to photoconductivity, photodesorption, and photolysis (36, 41) according to

$$h\nu \rightarrow e + h \qquad [11a]$$

$$O_{x,s}^- \overset{h\nu}{\rightarrow} \frac{x}{2}\,O_2 + e \qquad x = 1,2 \qquad [11b]$$

$$ZnO \overset{h\nu}{\rightarrow} Zn_i^+ + \tfrac{1}{2}\,O_2 + e \qquad [11c]$$

$$ZnO \overset{h\nu}{\rightarrow} Zn_g + \tfrac{1}{2}\,O_2 \qquad [11d]$$

The quantum yield for these reactions depends on the recombination rate

$$h + e \rightarrow o \qquad [11e]$$

or

$$h + O_{x,s}^- \rightarrow x/2\,O_2 \qquad [11f]$$

Furthermore, if oxygen is chemisorbed, part of the photon energy is consumed due to photodesorption according to Eq. [11b].

At temperatures larger than 600 K photolysis and thermolysis are additive effects occurring simultaneously. Photolysis is exclusively observed on oxygen pretreated (0001) faces (30). The UV irradiation enhances the decomposition rate up to 100%. With decreasing quantum yield, the decomposition is restricted to about 100 monolayers. Further photolysis is impeded because of the high recombination rate arising from enlarged Zn_i and, thus, electron concentration. After the end of the photolysis, thermolysis of about 300 monolayers is observed, probably until the equilibrium concentration of Zn_i is reached. On oxygen-annealed $(000\bar{1})$ faces, photolysis is not detectable.

In the temperature range of steady-state thermolysis, photolysis cannot be expected because of the Zn_i equi-

librium concentration. Experimentally, photolysis could not be detected by Hirschwald *et al.* (30, 40). Carey *et al.* (42), however, found evaporation rates under illumination for the (0001) and (000$\bar{1}$) faces slightly different from those of the unilluminated ones.

The sequence of stepwise dissociative vaporization (thermally and by photolysis) can be described in the following manner. The first step of bond breaking is the electron-hole pair generation according to Eq. [11a], which can also be written as

$$(Zn_{Zn}O_O)_s \rightarrow (Zn_{Zn}^{\cdot}\,O_O^{\cdot})_s$$

Transfer to the self-adsorption layer occurs without charge transfer, *i.e.*

$$(Zn_{Zn}\,O_O^{\cdot})_s \rightarrow Zn_s^{\cdot} + O_s^{\cdot}$$

The following steps are oxygen and zinc desorption, respectively zinc diffusion into the bulk

$$O_2^{-} \rightarrow \tfrac{1}{2}\,O_2 + e$$

$$Zn_s^{\cdot} \overset{+e}{\rightarrow} Zn_g$$

or

$$Zn_s^{\cdot} \rightarrow Zn_i^{\cdot}$$

It was argued (40) that the electron-hole pair formation is the rate limiting step in the Langmuir evaporation with an activation energy of $E_a = 3.4\ \text{eV} = E_g^{o}$ (30, 40). Although the bandgap energy decreases with temperature according to $E_g = E_g^{o}(1 - \alpha T)$, with $\alpha = 8 \cdot 10^{-4}\ \text{eVK}^{-1}$, the vaporization rate i increases with T according to

$$i = i_o \exp(-E_g/kT) = i_o \exp\left(\frac{\alpha E_g^{o}}{K}\right) \exp\left(-\frac{E_g^{o}}{kT}\right)$$

that means with the energy requirement E_g^{o}. The fact that both thermolysis and photolysis require the same activation energy of E_g^{o} indicates that bond breaking represents the rate limiting step in both cases.

Investigation of the electrical conductivity of thin zinc oxide films with high resistances.—As discussed in the preceding section, a number of reactions can influence the conductivity behavior of ZnO. Whether or not intrinsic conductivity could be realized possibly depends on the experimental conditions. Obviously, bulk impurities and surface contamination must be reduced to a minimum. Defect concentrations must be in thermodynamic equilibrium. The incongruent decomposition should be suppressed as much as possible.

Conductivity investigations have been performed with highly pure zinc oxide films up to 1000 K.

Experimental.—4-40 μm thick zinc oxide films (thickness measurement with SEM) were prepared from nominal 5*N* zinc (main impurities: < 10 ppm Pb, < 3 ppm Cd, 1.5 ppm Fe, < 0.7 ppm S, < 0.1 ppm Sn, < 0.05 ppm As; rest < 1 ppm) (Demetron, Hanau), sputtered onto a cleaned alumina support and oxidized in 150 mbar 5*N* oxygen at 625 K (43).

The oxidation process was controlled by measuring the conductivity. The oxidation process began when passing a temperature of about 550 K, that means when the zinc interstitials become mobile. The oxidation process was finished after about 20h, when the conductivity had become constant (that means when the defect equilibria had been attained). Surface contamination was avoided by the presence of a trap filled with liquid nitrogen during the oxidation and all following conductivity measurements. In the absence of liquid nitrogen, irreversible conductivity changes are observed (see Fig. 1).

Traces of alkaline and alkaline earth metals had been detected with the aid of SIMS, probably introduced from the alumina support. Aluminum, however, could not be detected. With the aid of XPS, very small concentrations of carbon, which could be further reduced by high temperature annealing in oxygen, had been detected in the as-grown films.

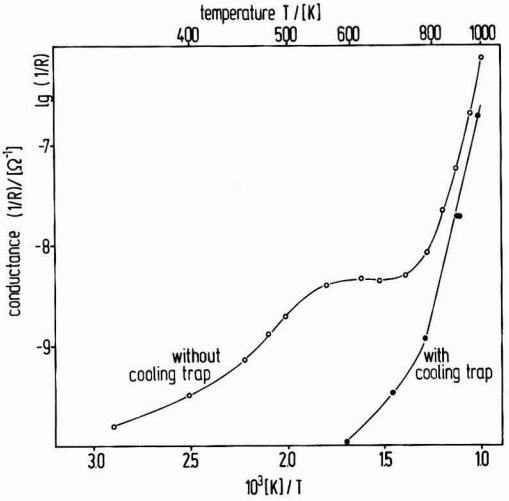

Fig. 1. The influence of the cooling trap on conductivity behavior [from Ref. (43)].

The conductivity of the ZnO films was measured in steps in the temperature range from 500 to 1000 K at constant oxygen pressure (150 mbar) and in oxygen pressures ranging from 1 to 150 mbar at constant temperatures between 620 and 1000 K. After every change in temperature or pressure, the attainment of the defect equilibrium had been waited for. Furthermore, care was taken that the trap was filled with liquid nitrogen during the whole time.

The measuring parameters, temperature and pressure, were limited by the following conditions: vaporization of ZnO at higher temperatures and lower oxygen pressures, duration for reaching the defect equilibria, measuring range of the electrometer ($\leq 10^{14}\Omega$), and the oxygen partial pressure at liquid nitrogen temperature.

The conductivity measurements were performed in dc fields between 1 and 10 V/cm, which led to current densities ranging from 10^{-5} to 1 A/cm². The films revealed ohmic behavior. Rectifier effects were not observed in the entire measuring range. This demonstrates that bulk properties are measured and that grain-boundary crossing had no influence on the conductivity.

Results.—The results of the conductivity investigations are presented in Fig. 2-4. The measured conductivities range from 10^{-10} to $10^{-3}\ \Omega^{-1}\,\text{cm}^{-1}$.

Figure 2 shows the temperature dependence of σ between 500 and 1000 K at constant oxygen pressure of 150 mbar. The temperature function has to be divided into two branches. At temperatures above 800 K the activation energy of σ is about 1.6 eV. In the low temperature range (500-600 K), the respective energy value is 0.8 eV.

The activation energy of 1.6 eV ($\cong E_g/2$, see Eq. [5c]) suggests the dominance of intrinsic conductivity in the high temperature range. Moreover, this seems to be supported by the calculated intrinsic conductivity, which is merely smaller by a factor of two than the experimentally observed σ in the upper temperature range (44). However, because of the uncertainties of the experimental data and of the data used in the calculations, this result should be considered with caution.

According to Eq. [5c], the intrinsic conductivity is independent of p_{O_2}. The evaluation of the measured oxygen pressure dependence of σ (see Fig. 3) according to $\sigma \propto p_{O_2}^{-m}$ (see Fig. 4) leads to values of m very close to ¼ at temperatures above 800 K. This clearly demonstrates that the incongruent decomposition (see Eq. [8c, d]) is responsible for the conductivity increase with temperature. The observed oxygen pressure dependence of σ reveals that the contribution of holes as well as that of

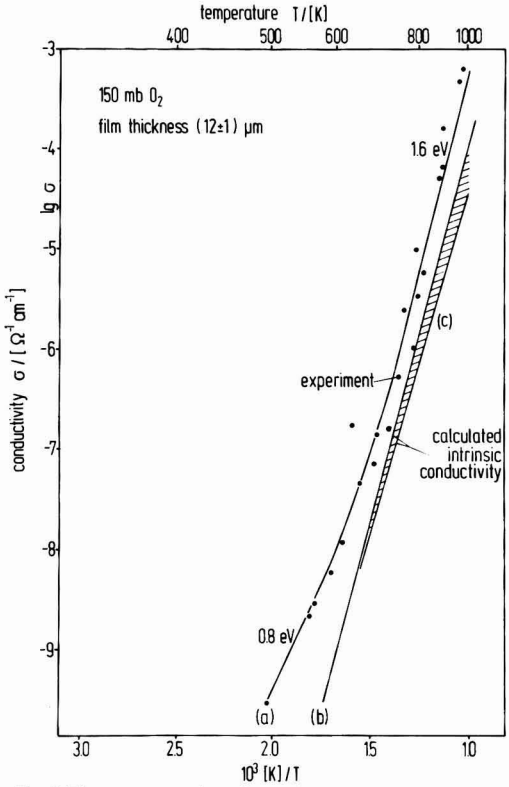

Fig. 2. The temperature dependence of σ at constant oxygen pressure in comparison with the calculated intrinsic conductivity [from Ref. (43)].

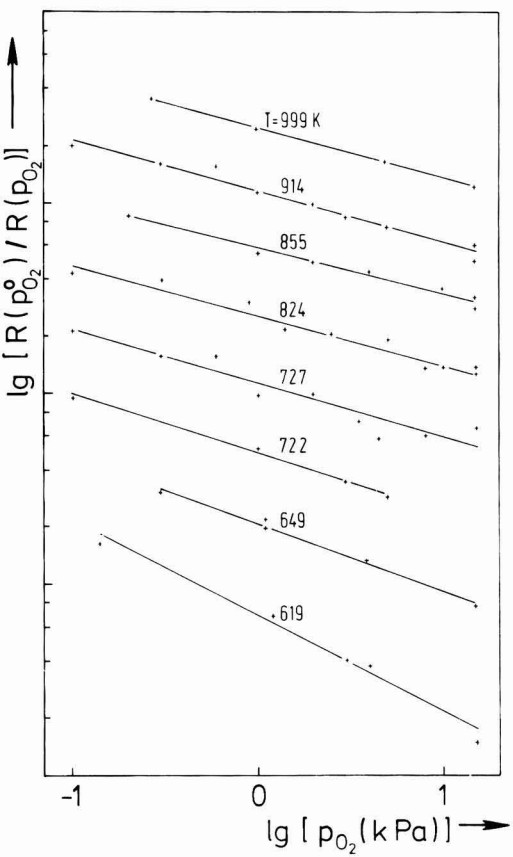

Fig. 3. The oxygen pressure dependence of σ at constant temperatures ranging from 620 to 1000 K.

twofold ionized interstitials is negligible (see Eq. [5] and [9]).

In the low temperature region, the oxygen pressure dependence of σ increases up to $m \cong ½$ (see Fig. 3 and 4). This is consistent with the assumption that the O^- chemisorption dominates the conductivity behavior (see Eq. [7c]). At temperatures lower than 500 K, the experimental value of m is expected to increase up to unity (see Eq. [7b]).

The fact that the low temperature branch of ln σ *vs.* 1/*T* is situated above the extrapolated high temperature branch reveals that the actual donor concentration is larger than that expected for the equilibrium of incongruent decomposition. The enhanced donor concentration can arise from frozen-in (*i.e.*, immobile) intrinsic donors Zn_i or from uncompensated extrinsic donors (impurities incorporated during the ZnO preparation).

The conclusion that incongruent decomposition and oxygen chemisorption are responsible for the conductivity behavior of ZnO is further supported by the temperature dependence of the quantum yield of photoconductivity measurements after illumination with bandgap energy (see Fig. 5). In the lower temperature range, photoexcitation creates electron-hole pairs or induces photodesorption (see Eq. [11a, b]), while recombination occurs according to Eq. [11e, f]. This means that the quantum yield decreases with increasing concentration of recombination centers. Figure 5 shows that the quantum yield q increases with rising temperature as the concentration of chemisorbed oxygen decreases with rising temperature. The maximum of the quantum yield is reached when the chemisorbed oxygen is completely desorbed. With further rise of the temperature, the electron concentration increases due to the incongruent decomposition leading to a drastic decrease of q. In agreement with the results of Fig. 2, the maximum of q is in the transition range of the two conductivity branches.

The electron concentrations n can be estimated with the aid of Eq. [5b] (when neglecting p) if the temperature function of the electron mobility μ_e is known. μ_e depends on the degree of lattice distortions and on the impurity content. In polycrystalline samples, grain-boundary scattering dominates. From combined conductivity-Hall measurements at thin films, μ_e (300 K) = 30 cm²/Vs was obtained (45). At highly disturbed thin layers, mobilities of 1 cm²/Vs are observed (45), while at sintered samples 10-60 cm²/Vs were found (46). Contrarily, in single crystals, room temperature mobilities as large as 150-200 cm²/Vs are observed [see, *e.g.* Ref. (4)].

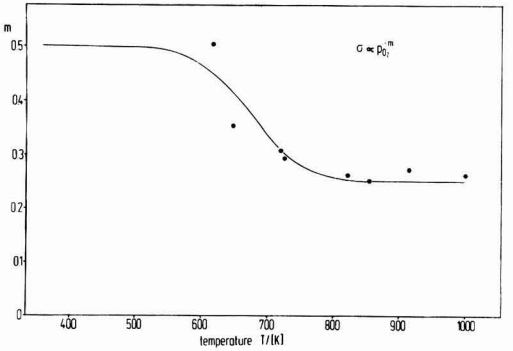

Fig. 4. The oxygen pressure dependence of σ fitted to $\sigma \propto p_{O_2}^{-m}$

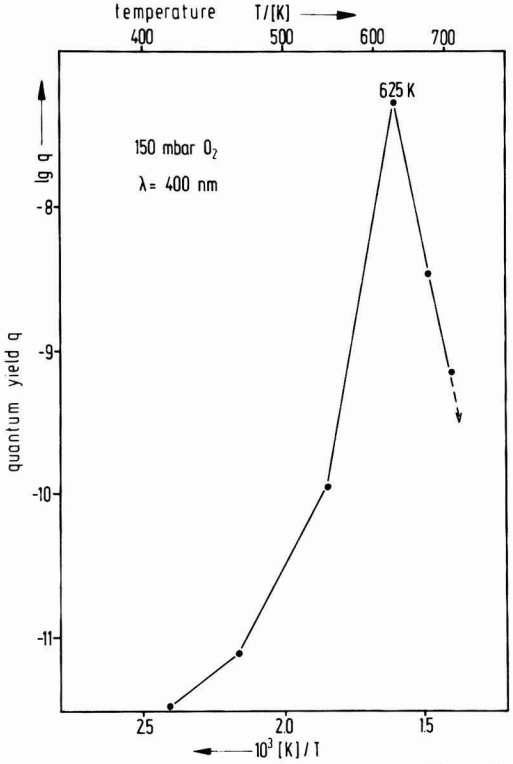

Fig. 5. The temperature dependence of the quantum yield for ZnO films illuminated with bandgap energy.

For temperatures larger than 150 K μ_e decreases according to $\mu_e \propto T^{-3/2}$ as a result of phonon scattering. This holds for crystals (4) as well as for polycrystalline materials (46). In the present calculations, $\mu_e(T)$ was extrapolated up to 1000 K from

$$\mu_e(T) = A \cdot T^{-3/2}, \qquad A = 1.56 \cdot 10^5 \text{ cm}^2\,\text{K}^{3/2}/\text{Vs} \quad [12]$$

which corresponds to μ_e (300 K) = 30 cm²/Vs.

With $\mu_e(T)$ according to Eq. [12], the carrier density in the 12 μm thick film is estimated to range from 10^{8} cm^{-3} at 500 K up to 10^{15} cm^{-3} at 1000 K.

The conductivity behavior of zinc oxide.—The quantitative description of the temperature and oxygen pressure dependence of the conductivity.—The total conductivity can be described by the sum of intrinsic and extrinsic contributions

$$\sigma = \sigma_1 + \sigma_2 \quad [13]$$

The intrinsic contributions dominating at high temperatures are composed of donor electrons arising from singly and doubly ionized zinc interstitials formed by the incongruent decomposition. Possibly, intrinsic conductivity contributes to σ_2. Charge neutrality leads to

$$n = p + [\text{Zn}_i^{\cdot}] + 2[\text{Zn}_i^{\cdot\cdot}] \quad [14a]$$

With the aid of the equilibrium constants according to Eq. [5a], [8d], and [9b], the electron concentration can be expressed by

$$n = \frac{K_i}{n} + \frac{K_2}{n}\, p_{O_2}^{-1/2} + \frac{2K_3}{n^2}\, p_{O_2}^{-1/2} \quad [14b]$$

As the oxygen pressure dependence of σ is very close to $\sigma \propto p_{O_2}^{1/4}$, corresponding to negligible contributions of holes and doubly ionized donors, Eq. [14b] is simplified to

$$n = K_2^{1/2}\, p_{O_2}^{-1/4} \quad [14c]$$

Thus, the high temperature contribution to σ takes the form

$$\sigma_2 = e_0 \mu_e K_2^{1/2}\, p_{O_2}^{-1/4} \quad [15]$$

In the low temperature range, frozen-in interstitials of zinc and/or (uncompensated) impurities with donor character corresponding to a total electron concentration n_0 can contribute to σ_1. Then, the effective carrier concentration is given by

$$n = n_0 - [O_{2,s}^{-}] - [O_s^{-}] \quad [16a]$$

That means n_0 is reduced by the number of trapped electrons. With the equilibrium constants according to Eq. [7b] and [7c], this results in

$$n = n_0/(1 + p_{O_2} K_{1a}^{-1} + p_{O_2}^{1/2} K_{1b}^{-1}) \quad [16b]$$

In the temperature range under investigation, the O_2^- species can be disregarded, which simplifies Eq. [16a] and [16b].

For taking into account the actual number of adsorption sites, the chemisorption equilibrium is written in the form

$$\text{Zn}_{\text{Zn,s}} + \tfrac{1}{2}\,O_2 + e \rightleftarrows (\text{Zn}_{\text{Zn}}\text{O}^{-})_s \quad [17a]$$

with the equilibrium constant

$$K_1 = \frac{[\text{Zn}_{\text{Zn,s}}]n}{[(\text{Zn}_{\text{Zn}}\text{O}^{-})_s]}\, p_{O_2}^{1/2} \quad [17b]$$

where $\text{Zn}_{\text{Zn,s}}$ is a potential adsorption site and $(\text{Zn}_{\text{Zn}}\text{O}^{-})_s$ is the chemisorption complex.

In Eq. [16a], $[O_s^-]$ and $[O_{2,s}^-]$ are volume concentrations, and the same holds for Eq. [17b]. Thus, the volume concentration $[\text{Zn}_{\text{Zn,s}}]$ of adsorption sites depends on the actual surface to volume ratio. Consequently, $[\text{Zn}_{\text{Zn,s}}]$ in Eq. [17b] has to be replaced by an actual concentration $[\text{Zn}_{\text{act}}]$ of adsorption sites per cm³ film

$$[\text{Zn}_{\text{act}}] = s \cdot f\,[\text{Zn}_{\text{Zn,s}}] \quad [18]$$

$f < 1$ represents the fraction of adsorption sites for those donor electrons that exist in the space charge layer (SCL), *i.e.*

$$f = \frac{[\text{Zn}_{i,\text{SCL}}]}{[\text{Zn}_{\text{Zn,s}}]_A}\, \delta_{\text{SCL}} \quad [19a]$$

δ_{SCL} is the thickness of the space charge layer, $[\text{Zn}_{\text{Zn,s}}]_A = d[\text{Zn}_{\text{Zn,s}}]$ is the concentration of potential adsorption sites per cm² (about 10^{15} for ZnO), and d is the film thickness, $s \geq 1$ is given by

$$s = \frac{A_{\text{act}}}{V} \cdot d \quad [19b]$$

A_{act}/V is the actual surface-to-volume ratio. The upper limit for $f \cdot s$ is reached when $[\text{Zn}_{\text{act}}] = [\text{Zn}_i]$, which means that all donor electrons are available for chemisorption. This has to be expected in the case of thin films. Contrarily, for a crystal $f \cdot s$ is δ/d. This means that only a small fraction of the donor electrons can be trapped due to chemisorption.

Inserting Eq. [15] and [17b] (with $[\text{Zn}_{\text{act}}]$ instead of $[\text{Zn}_{\text{Zn,s}}]$) into Eq. [13] and replacing K by

$$K = K^0 \exp(-E/kT) \quad [20]$$

leads to

$$\sigma(T, p_{O_2}) = \sigma_0/[1 + (p_{O_2}/p_{O_2}{}^0)^{1/2}/A_1 \exp(-E_1/kT)] + A_2 \exp(-E_2/2kT)(p_{O_2}/p_{O_2}{}^0)^{-1/4} \quad [21]$$

where p_{O_2} is replaced by a normalized pressure $p_{O_2}/p_{O_2}{}^0$ with $p_{O_2}{}^0 = 150$ mbar. The quantities σ_0, A_1, and A_2 are given by

$$\sigma_0 = e_0 \mu_e n_0 \quad [22a]$$

$$A_1 = K_1^{o}(p_{O_2}^{o})^{-1/2}/[Zn_{act}] \quad [22b]$$

$$A_2 = (K_2^{o})^{1/2}(p_{O_2}^{o})^{-1/4}\, e_0\mu_e \quad [22c]$$

As μ_e depends on temperature, the same holds for σ_n and A_2.

The evaluation of the adjusting parameters.—The experimental results for the 12 μm thick film are fitted to Eq. [21], assuming $E_1 = 0.8$ eV and $E_2/2 = 1.6$ eV. The obtained parameters are listed in the first line of Table II. The solid lines in Fig. 2 and Fig. 4 are calculated with the aid of these parameters. A_2 is determined from σ(1000 K), where the influence of chemisorption can be disregarded. The product $A_1\sigma_n$ is estimated from σ(500 K), where 1 in the denominator is negligible. The temperature dependence of σ_n and A_2, respectively, are taken into account by use of

$$\sigma_n(T) = \sigma_n(500\text{ K}) \cdot (T/500)^{3/2} \quad [23a]$$

and

$$A_2(T) = A_2(1000\text{ K}) \cdot (1000/T)^{3/2} \quad [23b]$$

It is not possible to separate A_1 and σ_n(500 K) from the temperature function of σ measured at constant oxygen pressure (p_{O_2} = 150 mbar), as the second term in the denominator of Eq. [21] remains distinctly larger than unity up to 700 K. A_1 and σ_n(500 K) can be separated when fitting Eq. [21] to the oxygen pressure dependence of σ, as, for small values of p_{O_2}, 1 in the denominator of σ_1 is no longer negligible against the second term. The temperature function of σ at p_{O_2} = 150 mbar was also measured for a less pure ZnO film prepared from 4*N* zinc by RF-sputtering. A shoulder appears in the Arrhenius plot of σ (see Fig. 6). In this case A_1 and σ_n(500 K) can be separated by fitting Eq. [21] to the temperature range from 600 to 700 K. The evaluated parameters are compiled in the second line of Table II.

The conductivity at 1000 K corresponds to a donor concentration of about 10^{15} cm^{-3} (0.025 at ppm). From σ_n, the total concentration of frozen-in plus uncompensated impurity donors is estimated to about 10^{12} cm^{-3} for the sample prepared from 5*N* zinc. 10 at ppm impurities in ZnO, however, correspond to $4 \cdot 10^{17}$ cm^{-3}. An almost total compensation of the impurities originally contained in zinc is highly improbable. Therefore, some possible explanations for the extremely small electronic active donor concentrations are presented. (*i*) The sputtering yield for part of the impurities is distinctly smaller than that for zinc. (*ii*) Part of the impurities is divalent in ZnO with states in the valence band. The remainder with donor as well as acceptor character partly compensates mutually. (*iii*) The impurities become inactive with respect to the conductivity as a result of surface segregation.

With respect to the impurities contained in the film prepared from 5*N* zinc, the following assumptions can be made.

1. It is possible that, for part of the impurities, the sputtering yield is drastically smaller than for zinc.

2. Cd as well as Pb and Sn should be divalent in ZnO and thus be electronically inactive. Sulfur (and carbon traces), mainly is oxidized and frozen at the cooling trap. Arsenic acts as a donor. The same holds for the alkaline traces stemming from the sample support, while the alkaline earth traces are electronically inactive. Fe^{3+} seems to be an acceptor in ZnO (47), and the intensity of the EPR signal near $g = 1.96$ is not enhanced after Fe^{3+} doping (48).

Table II. The fitting parameters of Eq. [21] for two films of different purity

Sample	Fig.	Zinc purity (*N*)	*d* (μm)	σ_n (500 K) (Ω^{-1}cm^{-1})	A_1	A_2 (1000 K) (Ω^{-1}cm^{-1})
1	2, 3, 6	5	12	$2.6 \cdot 10^{-6}$	$1.6 \cdot 10^{4}$	$5.3 \cdot 10^{4}$
2	6	4	5	$5.0 \cdot 10^{-7}$	$2.0 \cdot 10^{6}$	$6.0 \cdot 10^{4}$

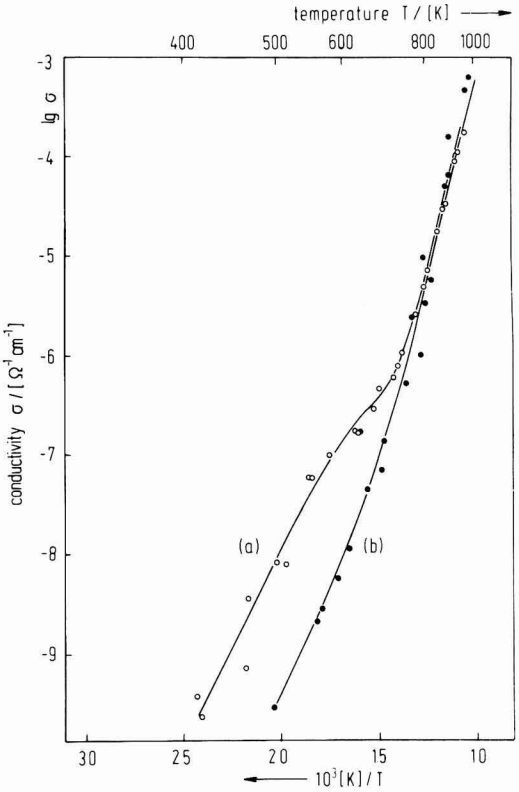

Fig. 6. The temperature dependence of σ at constant oxygen pressure. Comparison of the results obtained for films prepared from 4*N* zinc (a) and 5*N* zinc (b).

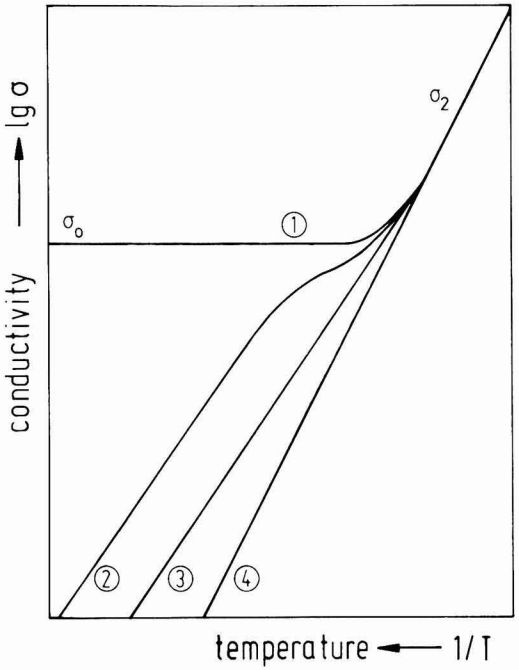

Fig. 7. Schematic Arrhenius plot of σ: 1, n_0 uncompensated donors, no chemisorption; 2, 3, n_0 donors, nearly all donor electrons are available for chemisorption; and 4, no impurities, no chemisorption.

3. The small donor impurity content can further be discussed in terms of the surface segregation. The fact that all electrons are available for chemisorption reveals that the grain diameter must be in the order of magnitude of δ_{SCL}. This leads to a number of potential adsorption sites $[Zn_{Zn,s}]$ of about $3 \cdot 10^{19}$ cm^{-3}. As the maximum impurity content is $4 \cdot 10^{17}$ and $4 \cdot 10^{18}$ cm^{-3} for the 5 and 4*N* zinc, respectively, this means that about 1 and 10% of the surface sites should be inactive with respect to the chemisorption. In reality, however, fewer than 10^{18} electrons/cm^3 compared to $n_0 \cong 10^{12}$ are not available for chemisorption. This consideration, too, refers to a much smaller impurity content in ZnO than in the starting material zinc. However, the fraction of electrons not available for chemisorption is larger by a factor of 100 for the less pure sample (see A_1 in Table II and Fig. 6).

If an uncompensated donor concentration of about 10^{15} cm^{-3} (arising from impurities) were to exist in the film, the conductivity behavior would be strongly different from the experimental findings. A plateau from 1000 to 700 K had to be expected, and a decrease with 0.8 eV at lower temperatures where oxygen adsorption becomes remarkable. This means that the observed conductivity behavior clearly demonstrates the high purity of the prepared ZnO films.

The influence of different adsorption conditions on the shape of the Arrhenius plot of the conductivity.—Varied adsorption conditions, *i.e.*, variations in p_{O_2}, σ_0, and A_1, influence the shape of the Arrhenius plot of σ. The possible curve shapes are schematically shown in Fig. 7. The high temperature conductivity σ_2 is dominated by the incongruent decomposition. If, in the low temperature range, adsorption is negligible (to be expected for crystals), the conductivity σ_1 becomes temperature-independent ($\sigma_1 = \sigma_0$, curve 1 in Fig. 7). In curves 2 and 3, different fractions of the n_0 donor electrons are trapped by chemisorption. Finally, curve 4 in Fig. 7 represents the limiting case of no frozen-in defects and no chemisorption.

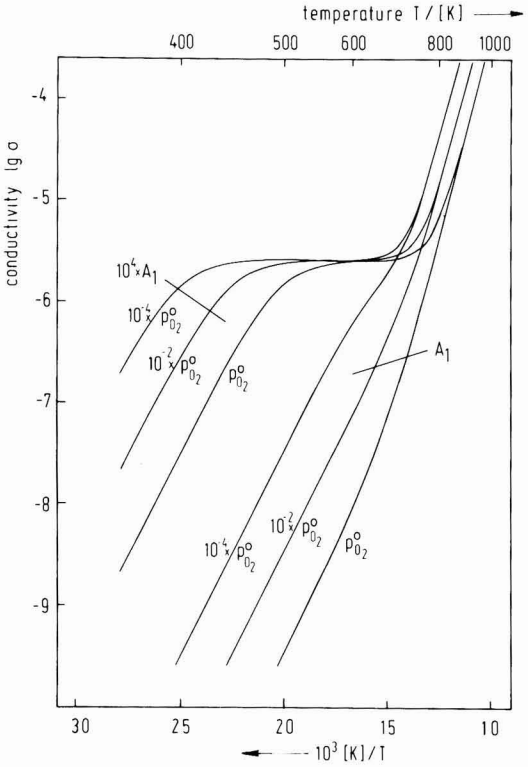

Fig. 8. The influence of oxygen on the shape of the Arrhenius plot (with A_1 according to Table II). For large values of A_1, the oxygen pressure dependence of σ vanishes in the transition range of *T*.

Increasing values of A_1 and decreasing oxygen pressures lead to the formation of a shoulder (curve 3 in Fig. 7). If $1/A_1$ and p_{O_2} decrease simultaneously, the shoulder becomes more pronounced. This can lead to a complete disappearance of the oxygen pressure dependence (see Fig. 8).

While, for a constant reference temperature, A_2 has nearly the same value for different samples (μ_e alone depends on the degree of lattice distortions), σ_0 is proportional to the total concentration of extrinsic and frozen-in intrinsic donors, and A_1 depends on the actual number of adsorption sites, primarily determined by the surface-to-volume ratio. However, surface segregation of bulk impurities as well as surface contamination due to adsorbed impurities can reduce the number of adsorption sites (see Fig. 1 and 6).

Conclusions

The conductivity behavior of highly pure, porous films strongly differs from that of crystals or dense sintered samples. The differences arise from the distinct donor concentrations and surface-to-volume ratios. In crystals and sinter materials, the zinc excess, generally, is much larger than in thin films, as the defect equilibria cannot be attained. The reason is that the large zinc excess generated during the sample preparation cannot be removed, as this is a slow bulk diffusion process. Furthermore, in less pure samples, uncompensated donor impurities enhance the conductivity. This means that, in the Arrhenius plot of σ, the branch arising from the incongruent decomposition is shifted to larger values of σ and, thus, to higher temperatures. For sintering materials, the influence of chemisorption on the shape of the Arrhenius plot depends on the grain diameter and on the x-ray density. In dense sintered samples, and, of course, also in crystals, the influence of chemisorption on σ is unimportant because of the small surface-to-volume ratio [for typical results, see Ref. (1)]. Contrarily, in porous films all donor electrons can be trapped by chemisorption, if the donor concentration is not too large.

In highly pure zinc oxide films, intrinsic conductivity could not be observed in an oxygen atmosphere of 150 mbar. In the high temperature range up to 1000 K, incongruent decomposition dominates, while, below 700 K oxygen chemisorption is responsible for the conductivity behavior.

From the experimental results, the conclusion can be drawn that the intrinsic conductivity is at least smaller by a factor of 10 than the measured one. A drastic enhancement of the oxygen pressure should lead to the decrease of σ. However, as such experimental conditions do not allow the presence of a liquid nitrogen cooling trap, surface contamination could falsify the results.

Stoichiometric ZnO had never been observed. The instability of oxygen-annealed samples (30) leads to the conclusion that zinc excess results in a higher thermal stability. This, possibly, arises from additional Coulomb attraction forces due to the zinc ions in the octahedral interstitial positions.

The excitation of an electron from the valence band into the conduction band is the first step of bond breaking and the rate limiting process in thermolysis and photolysis. Photoexcitation of samples pretreated in oxygen leads to incongruent decomposition and the formation of a stable ZnO with zinc excess. So it seems that the thermal or photoexcited creation of an electron-hole pair immediately leads to incongruent decomposition. Consequently, in ZnO with equilibrium zinc excess, the recombination rate for holes and electrons is so large that no measurable steady-state concentration of holes can exist.

Acknowledgment

The authors wish to thank the Deutsche Forschungsgemeinschaft for the financial support of this study.

Manscript submitted Oct. 15, 1985; revised manuscript received June 24, 1986. This was Paper 382 presented at the Las Vegas, NV, Meeting of the Society, Oct. 13-18, 1985.

REFERENCES

1. G. Heiland, E. Mollwo, and F. Stöckmann, *Solid State Phys.*, **8**, 191 (1959).
2. H. E. Brown, in "Zinc Oxide—Properties and Applications," International Lead and Zinc Research Organization, New York (1976).
3. W. Hirschwald, P. Bonasewicz, L. Ernst, M. Grade, D. Hofmann, S. Krebs, R. Littbarski, G. Neumann, M. Grunze, D. Kolb, and H. J. Schultz, *Curr. Top. Mater. Sci.*, **7**, 143 (1981).
4. K. J. Hagemark and L. C. Chacka, *J. Solid State Chem.*, **15**, 261 (1975).
5. K. J. Hagemark, *ibid.*, **16**, 293 (1976).
6. G. P. Mohanty and L. V. Azaroff, *J. Chem. Phys.*, **35**, 1268 (1961).
7. B. R. Appleton and L. C. Feldman, *J. Phys. Chem. Solids*, **33**, 507 (1972).
8. G. Neumann, *Curr. Top. Mater. Sci.*, **7**, 143 (subchap. 3.3) (1981).
9. V. J. Lee and G. Parravano, *J. Appl. Phys.*, **30**, 1735 (1959).
10. K. M. Sancier, *Surf. Sci.*, **21**, 1 (1970); *J. Phys. Chem.*, **76**, 2527 (1972).
11. A. Hausmann, *Z. Phys.*, **237**, 86 (1970).
12. G. Neumann, *Phys. Status Solidi B*, **105**, 605 (1981).
13. J. M. Meese and D. R. Locker, *Solid State Commun.*, **11**, 1547 (1972).
14. J. M. Smith and W. E. Vehse, *Phys. Lett.*, **A31**, 147 (1970).
15. C. Gonzales, D. Galland, and A. Herve, *Phys. Status Solidi* B, **72**, 309 (1975).
16. V. Soriano and D. Galland, *ibid.*, **77**, 739 (1976).
17. B. Schallenberger and A. Hausmann, *Z. Phys.*, **B23**, 177 (1976).
18. A. Hausmann and B. Schallenberger, *ibid.*, **B31**, 269 (1978).
19. D. Galland and A. Herve, *Phys. Lett.*, **A33**, 1 (1970); *Solid State Commun.*, **14**, 953 (1974).
20. B. Schallenberger and A. Hausmann, *Z. Phys.*, **B44**, 143 (1981).
21. G. Neumann, *Curr. Top. Mater. Sci.*, **7**, 143 (subchap. 3.1) (1981).
22. D. Zwingel, *J. Lumin.*, **5**, 385 (1972).
23. P. Bonasewicz, R. Littbarski, and M. Grunze, *Curr. Top. Mater. Sci.*, **7**, 143 (subchap. 3.13) (1981).
24. S. R. Morrison, *Adv. Catal.*, **7**, 259 (1955).
25. W. Göpel, *Ber. Bunsenges. Phys. Chem.*, **82**, 744 (1978).
26. P. Esser and W. Göpel, *Surf. Sci.*, **97**, 309 (1980).
27. D. Eger, Y. Goldstein, and A. Many, *RCA Rev.*, **36**, 508 (1975).
28. K. Tanaka and G. Blyholder, *J. Phys. Chem.*, **76**, 3184 (1972).
29. E. E. Gutman, I. A. Myasnikow, and L. M. Chipurilina, *Russ. J. Phys. Chem.*, **50**, 1074 (1976).
30. M. Grunze, W. Hirschwald, and E. Thull, *Z. Phys. Chem. N.F.*, **100**, 201 (1976); *Thin Solid Films*, **37**, 351 (1976); W. Hirschwald and E. Thull, *Farad. Disc. Chem. Soc.*, **58**, 176 (1974).
31. D. Kohl, M. Henzler, and G. Heiland, *Surf. Sci.*, **41**, 403 (1974).
32. W. Göpel, *Z. Phys. Chem. N.F.*, **106**, 211 (1977).
33. H. Chon and J. Pajares, *J. Catal.*, **14**, 257 (1969).
34. P. Bonasewicz, Doctoral Thesis, Freie Universität, Berlin (1982).
35. G. Neumann, *Curr. Top. Mater. Sci.*, **7**, 143 (subchap. 3.7) (1981).
36. M. Grade, *ibid.*, **7**, 143 (subchap. 3.11) (1981).
37. M. Grade, W. Hirschwald, and F. Stolze, *Z. Phys. Chem., N.F.*, **100**, 165 (1976).
38. J. E. McVicker, R. A. Rapp, and J. P. Hirth, *J. Chem. Phys.*, **63**, 2646 (1975).
39. R. B. Leonhard and A. W. Searcy, *J. Appl. Phys.*, **42**, 4047 (1971).
40. W. Hirschwald and F. Stolze, *Z. Phys. Chem. N.F.*, **77**, 21 (1972).
41. P. Bonasewicz and W. Hirschwald, *Curr. Top. Mater. Sci.*, **7**, 143 (subchap. 3.14) (1981).
42. D. A. Carey, R. A. Rapp, and J. P. Hirth, *J. Chem. Phys.*, **79**, 3160 (1983).
43. P. Bonasewicz, W. Hirschwald, and G. Neumann, *Thin Solid Films*, **147** (1986), In press.
44. P. Bonasewicz, W. Hirschwald, and G. Neumann, *Phys. Status Solidi A*, **97** (1986), In press.
45. R. Littbarski, Doctoral Thesis, Freie Universität, Berlin (1981).
46. S. E. Harrison, *Phys. Rev.*, **93**, 52 (1954).
47. J. Schneider and O. Schirmer, *Z. Naturforsch., Teil A*, **18**, 20 (1963).
48. A. Igelmund and A. Hausmann, *Z. Phys.*, **B21**, 65 (1975).

An Improved Method for the Electrochemical C-V Profiling of Indium Phosphide

R. T. Green,[1] D. K. Walker,[2] and C. M. Wolfe

Semiconductor Research Laboratory, School of Engineering and Applied Science, Washington University, St. Louis, Missouri 63130

ABSTRACT

C-V analysis of n-type InP using metal-semiconductor Schottky contacts is inadequate for determining free carrier concentration *vs.* depth profiles due to low barrier heights, uncontrolled oxide formation, and metal semiconductor chemical reactions. Concentration *vs.* depth profiles can be obtained over a wide range of carrier concentrations to virtually unlimited depth using electrochemical C-V (ECV) analysis. However, the 0.5*M* HCl in aqueous solution reported in the literature is not ideal for the anodic dissolution of InP. This work reports an improved anodic etchant for ECV profiling of n-type InP and the design of a constant current etch, difference method ECV profiler utilizing a new sample mounting technique.

C-V analysis is widely used as a tool to determine impurity *vs.* depth profiles in semiconductors. The most widely used implementation of this technique involves the formation of a Schottky diode by placing a small metallization of known area on the surface of the sample. The carrier concentration is determined at the edge of the resulting depletion region using (1)

$$n(w) = \frac{-C^3}{q\epsilon A^2}\left(\frac{dC}{dV}\right)^{-1} \quad [1]$$

where A = area of the rectifying contact, q = electronic charge, ϵ = permittivity of the material, C = the capacitance measured at some dc reverse bias, dc/dV = the change in capacitance with a small change in the reverse bias, w = the distance from the edge of the depletion region to the surface of the sample, and n = the calculated free carrier concentration. w is calculated using the depletion approximation from

$$w = \frac{\epsilon A}{C} \quad [2]$$

Profiling the sample to greater depths is achieved by increasing the applied reverse bias resulting in a wid-

[1]Present address: Varian Associates, Palo Alto, California 94303.
[2]Present address: Millitech Corporation, South Deerfield, Massachusetts 01373.

ening of the depletion region, w. The maximum distance from the surface of the sample that can be measured is limited by two factors: the leakage current in reverse bias and the reverse breakdown voltage. Both factors introduce error into the measurement by degrading the Q (quality factor) of the test circuit (2). Thus, for accurate profiles, a low leakage current, high reverse breakdown voltage rectifying contact is necessary. Such a Schottky contact is not reproducibly available in InP (3-6) due to low barrier heights, native oxides, and metal-semiconductor chemical reactions. Therefore, an alternative to metal-semiconductor junctions must be adopted to form the rectifying contacts necessary for C-V analysis of InP.

Rectifying contacts demonstrating the sufficiently large barrier heights and low leakage currents necessary for C-V analysis can be fabricated using electrolyte-semiconductor junctions. Such rectifying contacts can be used with increasing reverse bias for C-V profiling (7), but they are still limited in maximum depth achievable by the reverse breakdown voltage. An elegant solution to this problem, developed by Ambridge and Faktor (8), utilizes an electrolyte-semiconductor junction for the C-V measurements where the electrolyte is also an anodic etchant for the material being profiled. In this scheme, the depth profiling is accomplished by alternately etching the surface of the material to some depth, creating a crater-like etch profile, and then performing a low reverse bias C-V measurement. Using this method the sample can be profiled to virtually any depth, immune to reverse breakdown effects present at high reverse voltage. This method is also more tolerant of leakage current since the leakage current near zero bias is very small (high Q) (9). Consequently, electrochemical C-V (ECV) profiling is applicable to and attractive for use with InP.

An ECV profiler of the type developed by the Post Office Research Department (8) is shown schematically in Fig. 1. This profiler has been used successfully to profile several semiconductor materials (10-13), including InP. The profiler consists of an electrochemical cell, a C-V analysis section, and a depth analysis section. The body of the cell, through which the electrolyte flows, is fabricated from some chemically resistant material (Teflon or PVC). The sample is situated on a mounting ring that defines the area of the electrolyte-semiconductor junction. The sample is sealed to the mounting ring by means of pressure applied to the back of the sample through the ohmic contact. Because the n-type sample is to be anodically etched, the contact area must be illuminated to provide sufficient minority carriers to support the dissolution current. Illumination of the sample is accomplished by shining light through the window opposite the sample. The cell voltage is monitored using a saturated calomel electrode (SCE). A carbon cathode is provided to carry the dissolution current, and a separate Pt electrode is present in close proximity to the sample for the capacitance measurements.

The depth analysis section contains a potentiostat, which insures that the cell potential does not vary during the etch, a current meter, which measures the anodic dissolution current, and an integrator, which monitors the total charge transferred during the etch cycles. The amount of material removed during an etch cycle is given by (8)

$$w_E = \frac{M}{NF\rho A}\int i\,dt \qquad [3]$$

where M = molecular weight, N = dissolution number, F = Faraday's constant, ρ = density of the material, A = contact area, i = anodic current, and t = time. The dissolution number is the number of electrons transferred per molecule of material dissolved. For Eq. [3] to be accurate, the dissolution number must be constant; that is, there is only one dissolution reaction taking place (14).

The C-V analysis section consists of a capacitance meter operating at 3 kHz and 50 mV rms on which a low frequency (30 Hz) signal is superposed to extract the differential change in capacitance with voltage. From this information, the depletion depth and carrier concentration are obtained. The total depth at which the measurement is made with respect to the original surface of the sample is

$$x = w + w_E \qquad [4]$$

The C-V analysis depends on accurate knowledge of the contact area. Large errors result if the electrolyte seeps between the mounting ring and the sample by capillary action. This effect and its resulting equivalent circuit are shown in Fig. 2 (15). C_s represents the capacitance due to the contact area which is illuminated during the etch cycle and undergoes anodic dissolution. R is the resistance of the thin sheet of electrolyte present due to capillary action. C_m is the capacitance due to the "wetted" surface of the sample external to the mounting ring. This failure to keep the contact area well defined results in a degradation of the overall Q of the test circuit and introduces an unknown capacitance-resistance network that increases the measured capacitance. In addition to the excess capacitance, C_m which is determined by the area the electrolyte occupies external to the mounting ring and the surface carrier concentration, the capacitance becomes frequency dependent with greater error at lower frequencies. Another source of error is introduced by the small free chemical (zero anodic current

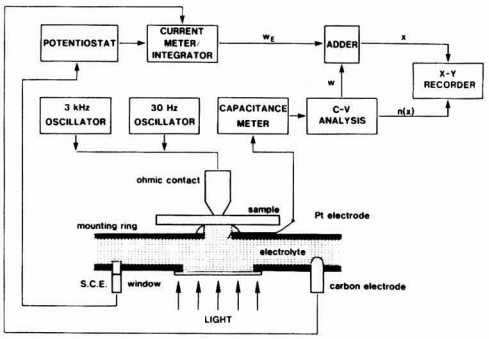

Fig. 1. The Post Office ECV profiler (after Ambridge and Faktor)

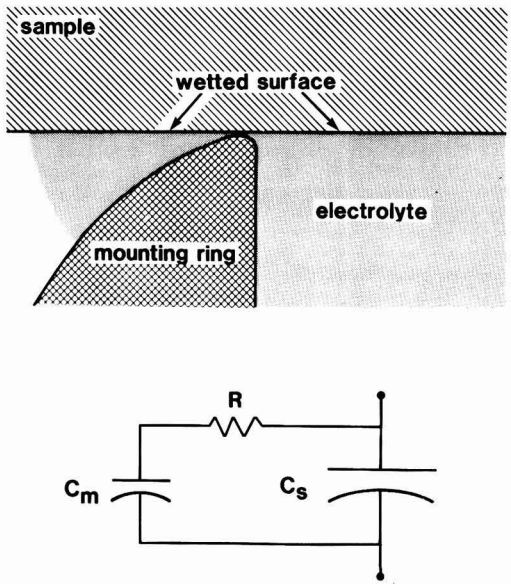

Fig. 2. Cross section of contact area formed by a mounting ring and the resulting equivalent circuit (after Ambridge *et al.*).

in the dark) etch rate. ECV profiling of thick layers requires hours of exposure of the sample to the electrolyte. This results in etching around the perimeter of the contact area and further seepage of the electrolyte around the mounting ring, as well as etching of the crater floor independent of the anodic current. Consequently, the depth resolution degrades with the time the sample is in the electrolyte.

From the preceding, an "ideal" anodic etchant for use in ECV profiling should possess the following properties: (*i*) it should have low free chemical etch rate (*ii*) it should be contained completely in the contact area, (*iii*) it should make a good rectifying contact (low leakage current), and (*iv*) it should have a constant dissolution number (only one anodic dissolution reaction takes place).

Apparatus

The profiler used in this work is schematically shown in Fig 3. The electrochemical cell is similar in design to the Post Office profiler, but includes a modified sample mounting scheme and eliminates the saturated calomel electrode. The cell consists of a Teflon body through which the electrolyte flows either by siphon feed or by using a pump. A graphite cathode is provided externally to the cell using a Teflon tee. A Pt electrode is embedded in the cell body within 1 mm of the sample for capacitance and cell voltage measurements. Because the etching method used in this study was not potentiostatic, the use of a calomel reference electrode was deemed unnecessary. Provided the dissolution number remains constant during etching, this simplification is admissible. The light input window is fabricated from a 0.2 mm thick glass cover slip and sealed to the cell body using black wax (Apiezon wax W). The light source used is a 250W tungsten-halogen lamp with a single focusing lens and a 550 nm narrow-band filter. The purpose of the filter is to eliminate the anomalous etch associated with below-bandgap illumination of the sample (8).

The sample mount (Fig. 4) consists of a 1 in.^{2} piece of printed circuit board with a ⅛ in. hole (contact area) machined into the center. Surrounding the contact area is a recessed annulus (black wax well). The glass fiber epoxy sample mount is used, because it is electrically insulating and resistant to heat and to the organic solvents used in subsequent mounting and cleaning procedures. To mount a sample, the sample mount is prepared by placing a small piece of black wax at the periphery of the contact area. The sample mount is then placed on a hot stage at 180°C until the black wax flows around the entire contact area. The sample mount preparation is completed by making the black wax level with the top of the sample mount by polishing the sample mount against a glass microscope slide onto which a few drops of trichloroethylene (TCE) are applied.

The sample is prepared for mounting by cleaning sequentially in TCE, acetone, and methanol. A 20 mil Sn sphere is then alloyed into either the front or the back surface for 1 min at 280°C in H_2. A lead wire is then attached to the Sn ohmic contact, and the sample is placed

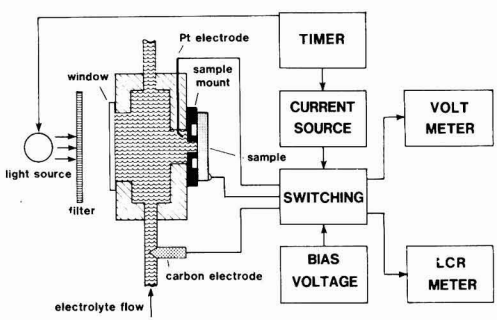

Fig. 3. The constant current, difference method ECV profiler used in this work.

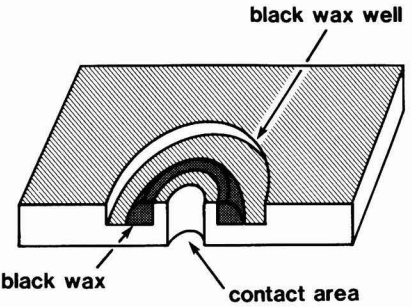

Fig. 4. Cross section of sample mount used in this work

on the hot stage where the sample mount is placed on the sample. The contact area is defined and sealed by the molten black wax, which flows onto the sample by capillary action until checked by the surface tension of the wax. This ensures a smooth, circular contact perimeter. Finally, the sample and sample mount are removed from the hot stage and allowed to cool. This sample mounting procedure, excluding the alloying of the ohmic contact, takes less than 5 min. After the sample is mounted, the diameter of the contact area is measured using an optical microscope yielding typical contact diameters around 2.4 mm. The sample mount is then attached to the cell body using black wax, and an electrolyte flow is initiated.

The black wax used in this mounting technique is electrically insulating and opaque to light. The wax film that defines the contact area is thick enough that no parasitic capacitance is introduced into the measurement. The black wax seal extends well beyond the perimeter of the contact area and adheres well to the sample so that the seepage problems (including the formation of a wetted area ouside the contact area) associated with the Post Office profiler are eliminated. Because molten wax is used, the seal can be formed over even large surface irregularities. The use of a sample mount separate from the cell body provides mechanical support for the sample and allows the sample to be removed for microscopic examination during the course of the measurements without disturbing the contact area.

The circuitry for the profiler is divided into an etch section and a measurement section. Each section is completely isolated from the other during the respective etch and measurement cycles by means of a switching network. The etch section consists of a Keithley 225 current source and an etch duration timer. During the etch cycle, the timer switches on both the light and current sources. The cell voltage, measured with respect to the platinum electrode, is monitored using the multimeter. The current levels used in this work were chosen so that the anodic etch rate did not exceed 0.1 μm/min. The voltage monitor is used to insure that the cell voltage did not rise above −0.3V during the etch. The cell voltage of −0.3V was chosen empirically to obtain a smooth, uniform etch. Higher cell voltages gave rise to anomalous etching characteristics (10). It must be noted that, because no SCE was incorporated in the apparatus used in this work, the cell voltage is not the inner potential of the cell, and that the cell voltage was used only to indicate the upper limit to the faradaic dissolution regime. The "safe" cell voltage depended upon the electrolyte used and was determined experimentally. In order to make the cell voltage independent of the condition of the electrolyte during the ECV measurement, electrolyte was constantly pumped through the cell from a 1 liter electrolyte reservoir.

For a constant current anodic etch, Eq. [3] reduces to

$$W_E = \frac{Mti}{NF\rho A} \qquad [5]$$

Following the etch cycle, the profiler is switched to the measurement mode, activating the HP4261A LCR meter

and the HP6116A dc power supply. The purpose of the dc power supply is to provide the ±0.1V bias for the difference capacitance measurement. The capacitance measurements are made using a 50 mV rms test signal at 1 kHz. Because the test signal and bias voltage are small, the Q of the test circuit is very high (as indicated by the dissipation factor monitor on the LCR meter). The depletion depth and carrier concentration are computed using

$$w = \frac{\epsilon A}{C_0} \quad [6]$$

and

$$n(x) = \frac{C_0^3}{qA^2\epsilon}\left[\frac{V_+ - V_-}{C_+ - C_-}\right] \quad [7]$$

where C_0 = zero bias capacitance minus lead capacitance, V_- = ±0.1V dc, C_+ = capacitance measured with $\pm V$ applied, and $x = w + w_E$. The capacitance readings generally require several seconds to achieve their final values. This is probably due to changes in the Gouy-Helmholtz layer or slow surface states.

To verify the accuracy of the profiler, concentration profiles were obtained for GaAs layers using the ECV profiler described in this section with Tiron used as the electrolyte and checked against profiles obtained from a commercial, mercury probe profiler. For doping concentrations ranging from 5×10^{14} to 5×10^{18} cm^{-3}, the results from the two profilers differed by less than 5%. Comparison of ECV profiles and van der Pauw analysis performed on layers grown on Cr-doped GaAs substrates yielded differences in carrier concentrations of less than 10%.

Electrolyte

The electrolyte used for the ECV profiling of InP reported in the literature is a 0.5M aqueous solution of HCl (13). The developers of this technique, Ambridge and Ashen, state that the HCl solution is not ideal for profiling of InP due to problems with maintaining adequate definition of the contact area. Attempts at profiling InP layers using the profiler described in the previous section confirm this observation. In experiments performed on n$^+$ InP substrates to determine the free chemical etch rate of the HCl electrolyte, we found that the increase in contact area was due to rounding of the crater wall under the black wax (not due simply to seepage between the black wax seal and the surface of the sample by capillary action). In these experiments, the free chemical etch rate of the 0.5M HCl solution was determined to be 0.3 μm/h, which is 100 times greater than that reported by Ambridge and Ashen.

The task in developing an ideal electrolyte for use with InP is to reduce the free chemical etch rate and the associated rounding at the crater rim (due to enhanced etching at crystal edges), while satisfying the other criteria for an ideal electrolyte discussed earlier in this paper. To achieve this, a number of electrolytes were examined: 0.5M hydrochloric acid in aqueous solution; 40% tartaric acid, 30% hydrogen peroxide (3:1); 0.1M Tiron in aqueous solution; 5 weight percent iodic acid in aqueous solution; phosphoric acid, 30% hydrogen peroxide (1:1); sulfuric acid, hydrogen-peroxide, water (10:1:1); 0.1M potassium hydroxide in aqueous solution; 37% hydrochloric acid, 70% nitric acid, ethanol in various proportions; and 37% hydrochloric acid, 70% nitric acid, isopropanol in various proportions. From this list we found that the best electrolyte for ECV profiling of InP is a solution of 37% hydrochloric acid; 70% nitric acid: isopropanol in the proportions 36:24:1000. For brevity, we refer to this solution as the "pear electrolyte," because the proportions of the chemical constituents are similar to that of a pear.

The pear electrolyte makes good rectifying contacts with InP while exhibiting a free chemical etch rate of 0.066 μm/h and little rounding of the crater edge for n$^+$ material. The dissolution number for the pear etch was confirmed to be a constant, exactly 6, from crater depth measurements performed optically and with a Sloan Dektak I surface profilometer, thus indicating the presence of only one significant dissolution reaction. When performing the anodic etch, it is necessary to maintain a minimum electrolyte flow through the cell of 100 ml/min to keep the cell voltage below the 0.3V safe level. The pear electrolyte is contained well within the contact area and yields sharp crater walls and flat crater bottoms. Figure 5 shows the contrast between crater profiles using the pear and 0.5M HCl electrolytes.

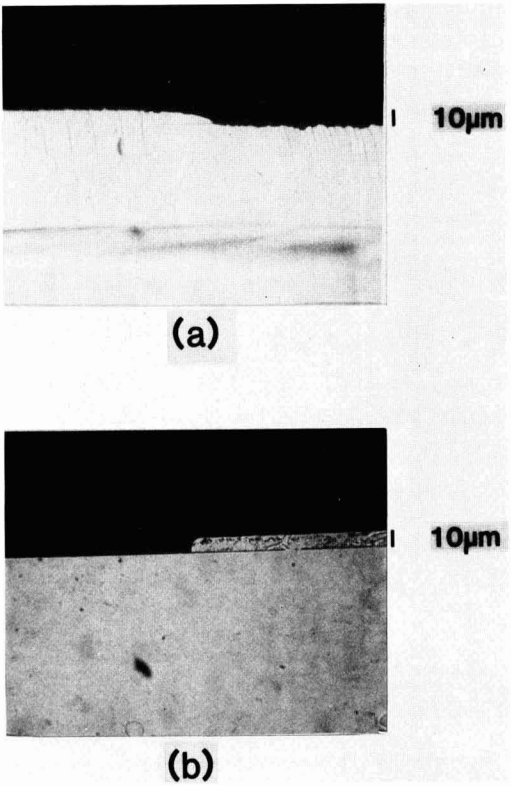

Fig. 5. Cleaved sections of ECV craters of a 10 μm undoped InP layer using (a) 0.5M HCl and (b) pear.

Figure 6 shows the results of using the pear electrolyte on an undoped, 10 μm thick InP layer grown on an n$^+$ substrate oriented 0.6° off {100} towards <100>. As with the other examples in this work, the epitaxial layers were grown in a PCl_3-In-H_2 vapor-phase epitaxial reactor. The concentration profile shows the expected constant concentration extending from the surface of the sample to near the layer-substrate interface. The "bump" in the concentration profile between 6 and 9 μm is attributed to small changes in the III-V ratio when growth is initiated (16). The width of the interfacial region observed in the concentration profile is due partially to Debye spreading and a slightly nonuniform etch profile (*e.g.*, due to nonuniform sample illumination) (15).

Figures 7 and 8 show the results of ECV profiling using the pear electrolyte on sulfur-doped, InP layers grown on both n$^+$ (0.6° off {100} towards <110>) and semi-insulating (2° off {100} towards <100>) substrates during the same growth run. The concentration profiles indicate a difference in layer thickness, but this was expected because of the difference in orientation between the n$^+$ and semi-insulating substrates (17). Microscopic measurements of cleaved and stained sections of the two samples confirmed that the layer thicknesses indicated by the concentration profiles were correct. Although the concentrations in the undoped and moderately doped re-

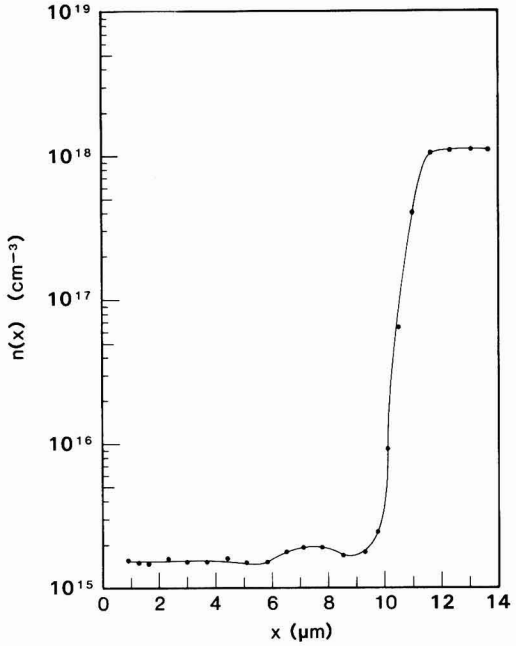

Fig. 6. ECV profile of an undoped InP epitaxial layer grown on an n^+ substrate.

gions are virtually the same for both samples, the peak carrier concentration is higher in the layer grown on the n^+ substrate. The difference in peak concentration levels for the two layers can be attributed to orientation-induced differences in growth rate (18) and impurity incorporation (19). The behavior of the concentration profiles near the layer-substrate interface has been observed by Clarke (16) and postulated as being due to changes in the III-V ratio during the initial growth and/or coulombic interactions during growth (20).

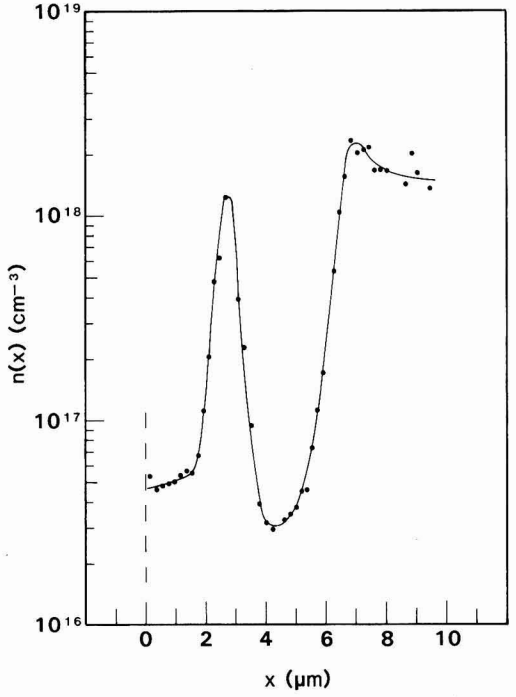

Fig. 7. ECV profile of a sulfur-doped InP epitaxial layer grown on an n^+ substrate.

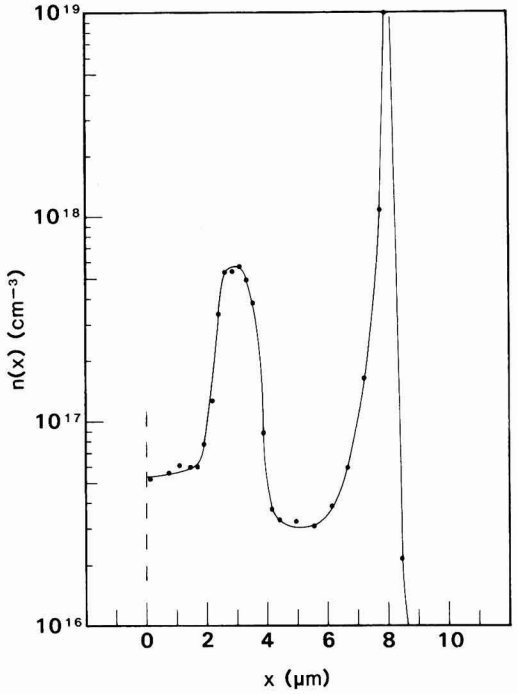

Fig. 8. ECV profile of sulfur-doped InP epitaxial layer grown on a SI substrate.

The accuracy of the ECV technique using the pear electrolyte was verified by performing ECV measurements using the pear electrolyte on homogeneously doped and undoped InP layers with carrier concentrations previously determined by the method of van der Pauw and, alternatively, mercury probe C-V analysis. Mercury probe C-V data were taken only near the wafer surface (*i.e.*, low reverse bias) due to the aforementioned problems with InP Schottky contacts. The results of the three different methods differed by less than 10%. The agreement between the van der Pauw, mercury probe C-V, and ECV data indicates that the etched surface of the InP remains relatively devoid of oxides, which would cause error in the ECV measurement.

Summary

C-V analysis of InP using Schottky contacts is severely restricted in concentration range and maximum depth by low barrier heights and nonreproducibility. Electrolyte-semiconductor junctions produce rectifying contacts of sufficient quality that C-V profiling using increasing reverse bias voltage to probe deeper into the material can be employed; however, the maximum depth achievable is limited by the carrier concentration dependent reverse breakdown voltage. The more powerful method of ECV, which allows carrier concentration profiling to unlimited depth, has been used with 0.5*M* HCl in aqueous solution as the electrolyte/anodic etchant. However, problems in maintaining a constant, well-defined, rectifying contact area introduce complications and error in the C-V measurements.

It was discovered that the difficulties in maintaining the contact area when the 0.5*M* HCl solution is used result from an increase in contact area due to excessive rounding of the crater rim. This excessive rounding was found to be caused by the relatively high etch rate at crystal edges. Consequently, the pear electrolyte (37%

hydrochloric acid: 97% nitric acid: isopropanol; 36:24:1000) was developed and used in conjunction with an ECV profiler of a different design from that of the Post Office profiler. The pear electrolyte demonstrated a low free chemical etch rate of 0.066 μm/h with little rounding of the crater rim. This resulted in complete containment of the electrolyte within the contact area. Good rectifying contacts were achieved using the pear electrolyte on material ranging from 1×10^{15} to 3×10^{18} cm^{-3} (the limits of the material available to us). The anodic etch characteristics of the pear electrolyte were excellent, yielding flat crater floors and sharp, perpendicular (to the sample surface) crater walls. Thus, the pear electrolyte represents an improvement over the 0.5*M* HCl electrolyte used previously.

Acknowledgment

This work was supported by Office of Naval Research Contracts N00014-80C-0762 and N00014-79C-0840.

Manuscript submitted Feb. 3, 1983; revised manuscript received July 2, 1986.

Washington University assisted in meeting the publication costs of this article.

REFERENCES

1. D. P. Kennedy, P. C. Murley, and W. Kleinfelder, *IBM J. Res. Dev.*, **12**, 399 (1968).
2. J. D. Wiley and G. L. Miller, *IEEE Trans. Electron Devices*, **ed-22**, 265 (1975).
3. V. L. Wrick, W. J. Choyke, and R. C. Clarke, *DARPA Report* No. 243-023-T1 (1980).
4. J. M. Bornholdt, R. E. Goldwasser, and F. J. Rosenbaum, *Off. of Naval Research Technical Report*, ONR-82-2 (1980).
5. R. H. Williams, R. R. Varma, and A. McKinley, *J. Phys. C.*, **10**, 4545 (1977).
6. R. H. Williams, V. Montogeny, and R. R. Varma, *ibid.*, **11**, L 735 (1978).
7. D. L. Lile and D. A. Collins, *Electron., Lett.*, **14**, 457 (1978).
8. T. Ambridge and M. M. Faktor, *J. Appl. Electrochem.*, **5**, 319 (1975).
9. R. T. Green and C. M. Wolfe, To be published.
10. T. Ambridge and M. M. Faktor, *J. Appl. Electrochem.*, **4**, 135 (1974).
11. C. D. Sharpe, P. Lilley, and T. Ambridge, *Electron. Lett.*, **15**, 622 (1979).
12. B. Wakefield, J. L. Stevenson, R. M. Redstall, and T. Ambridge, *Appl. Phys. Lett.*, **35**, 347 (1979).
13. T. Ambridge and D. J. Ashen, *Electron. Lett.*, **15**, 647 (1979).
14. C. R. Elliott and J. C. Regnault, *This Journal*, **128**, 113 (1981).
15. R. Ambridge, J. L. Stevenson, and R. M. Redstall, *ibid.*, **127**, 222 (1980).
16. R. C. Clarke, *DARPA Doc.* No. 80-1F7-SEMIC-P2 (1980).
17. D. W. Shaw, *Inst. Phys. Conf. Ser.*, **7**, 50 (1968).
18. J. A. Burton, R. C. Prim, and W. P. Slichter, *J. Chem. Phys.*, **21**, 1987 (1953).
19. A. E. Blakeslee, *Trans. Metall. Soc. AIME*, **245**, 577 (1969).
20. H. Rhodin, M. W. Muller, and C. M. Wolfe, *J. Electron. Mater.*, **11**, 517 (1982).

Impedance Spectra of p-Type Porous Si-Electrolyte Interfaces

N. Koshida, M. Nagasu,[1] K. Echizenya, and Y. Kiuchi

Department of Electronic Engineering, Faculty of Technology, Tokyo University of Agriculture and Technology, Koganei, Tokyo 184, Japan

ABSTRACT

Frequency dispersion of the impedance of the p-type porous Si layer (PSL)/aqueous electrolyte interface has been investigated to characterize its electrical properties. The PSL electrodes are formed on (100) p-Si substrates (3.5-4.5 Ωcm in resistivity) by anodic treatment in HF solution. Impedance measurements over a wide frequency ranging from 2 Hz to 100 kHz are carried out as a function of PSL thickness. At low frequencies and low bias voltages, the impedance shows the characteristic behavior expected from the microporous structure. The flatband potential at the rear surface of PSL, determined from Mott-Schottky plots, shifts to the negative side with increasing PSL thickness. This is presumably related to the ionic adsorption in PSL.

In previous papers (1, 2), we reported the photoelectrochemical properties of microporous Si. The porous Si layer (PSL) can be formed by an anodic dissolution technique first described 30 years ago (3, 4). According to the recent studies of structural and physical properties of PSL (5-11), it consists of a great number of micropores with high aspect ratios. Mean pore radii, density, and crystallographical parameters of PSL depend on the resistivity of the Si substrate, its conduction type, and conditions of anodic dissolution.

In aqueous electrolytes, PSL photoelectrodes under backward bias showed the current-voltage curves like normal photodiodes. The introduction of the porous structure was useful primarily in suppressing the dark current of p-Si photocathodes (1) and in extending the life of n-Si photoanodes (2). However, dissolution and oxidation under illumination are still major reactions in p- and n-PSL electrodes, respectively. In addition, the increase in PSL thickness resulted in somewhat reducing the photosensitivity because of the increase in surface recombination losses of photogenerated carriers. The electrical properties of the PSL-aqueous electrolyte interface must, therefore, be characterized in order to obtain a significant improvement in the photosensitivity and operating stability of PSL.

To provide a basis for the understanding of the interfacial charge transfer process in PSL, we have studied the impedance spectra of the PSL-electrolyte interface over a wide frequency range. In general, the measurement of frequency dispersion of the impedance makes it possible to identify interfacial variables in terms of passive elements with physical significance (12). Analysis of an equivalent circuit gives information on the depletion layer capacitance, the flatband potential, and possibly the surface-state density (13).

This paper concerns the interface between p-type PSL and aqueous electrolytes. The influence of the introduction of the porous structure is described by making comparison of the impedance behavior of PSL with that of as-etched p-Si.

Experimental

PSL cells.—Silicon wafers used in this experiment were (100) p-type single crystals (3.5-4.5 Ωcm in resistivity) with a mirror surface. The PSL electrodes were prepared by the procedure described previously (1). The PSL thickness was evaluated by scanning electron microscopic observation. Judging from the condition of anodic dissolution, the PSL presented here is assumed

[1] Present address: Tokyo Research Laboratory Engineering Center, Sharp Corporation, Kashiwa, Chiba 277, Japan.

to have a crystalline structure, and its density is about 50% of that of bulk silicon. The experimental cell was composed of a PSL electrode (1 × 1 cm in useful area), a Pt counterelectrode, and a reference electrode (SCE). The electrolyte used was 0.005*M* (pH = 7.8) or 0.1*M* (pH = 9.1) Na_2HPO_4.

Impedance spectra.—The measurement of the impedance was carried out in two ways depending on the frequency range. The experimental arrangement in the low frequency range (f = 2-100 Hz) is shown in Fig. 1. The relationship between the unknown impedance of the cell, Z, and the impedance of the reference circuit, Z_r, can be represented by the following equation

$$Z = Z_r(E_A - E_B)/E_B \quad [1]$$

where E_A and E_B are the complex voltage at terminals A and B, respectively. The real and imaginary parts of Z can be deduced from Eq. [1] by using the angular frequency, the phase angle, the absolute value of E_B/E_A, and the relaxation time, C_rR_r, of the reference circuit. The amplitude of a signal for measurements was about 10 mV_{p-p}. In the high frequency range (f = 0.1-100 kHz), the impedance was directly measured using a multifrequency LCR meter. Besides the overall impedance, the capacitive component can be obtained as a function of bias voltage as well. In this case, the amplitude of a signal for measurements was about 100 mV_{p-p}. The bias voltage, V_b, was varied from 0 V to about − 5V (*vs.* SCE). The PSL thickness, d, was controlled in the range from 0 to 40 μm. In the dark, no appreciable cathodic current was observed even at $V_b = -5V$.

Results and Discussion

As-etched p-Si.—In Fig. 2 and 3, the impedance spectra of a naked p-Si/electrolyte interface for two different electrolyte concentrations are shown as a function of V_b. This sample (d = 0 μm) was prepared by chemical etching in HF + HNO_3 solution. The observed impedance spectra are characterized by four regions, namely, I, II, III, and IV. In regions I and III, the impedance is capacitive (the slope of log $|V_b|$ *vs.* log f curves is −1) and in regions II and IV, it shows resistive properties (frequency independent). At V_b = 0 V, the impedance remains capacitive over a frequency range up to 1 kHz and becomes resistive at higher frequencies. For $|V_b| \simeq$ 0.6-0.8V, the impedance shows a transition from region I to III, passing through region II. The resistance in region II depends strongly on V_b. As $|V_b|$ is increased further, the capacitive region III extends to the lower frequency region. It should be noted that the capacitance in region III is bias voltage dependent. The only difference between the results of Fig. 2 and 3 is the resistance value in region IV. Hence, the resistance in this region is thought to be related to the electrolyte.

These results can be explained from an equivalent circuit shown in Fig. 2. The element R_{SO} is the resistance of the solution, and C_H and C_{SC} are the capacitances associated with the Helmholtz layer and the space charge layer, respectively. The bias voltage-dependent resistance R_{SC} is related to the space charge layer, including information on the surface states. According to the condition of the frequency and the bias voltage, one of these four elements becomes a predominant factor of the impedance, as illustrated in Fig. 4. Both the shunt and series resistances associated with the faradic current and semiconductor bulk can be excluded here, since they have no significant effects on the experimental results.

In regions I and IV, where the contribution of the space charge layer to the result is negligible, the impedance at low and high frequencies is predominantly determined by C_H and R_{SO}, respectively. The respective values of C_H and R_{SO} obtained from Fig. 2 were 1.8 μF/cm² and 55 Ωcm². When the bias voltage is applied, the

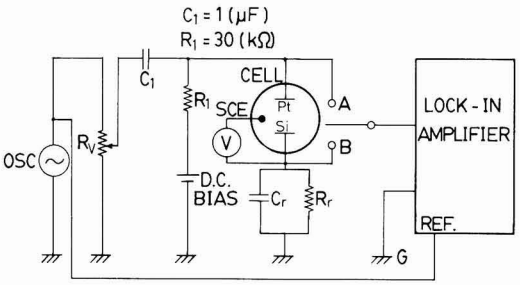

Fig. 1. Schematic diagram of the impedance measurement at low frequency range from 2 to 100 Hz.

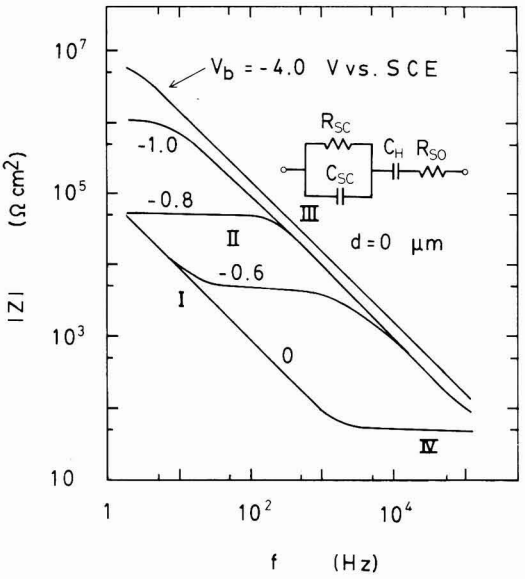

Fig. 2. Impedance spectra for as-etched p-Si in 0.1M phosphate as a function of bias voltage. Equivalent circuit expected from the response curves is also shown. C_H, R_{SC}, C_{SC}, and R_{SO} become predominant factors of the impedance in region I, II, III, and IV, respectively.

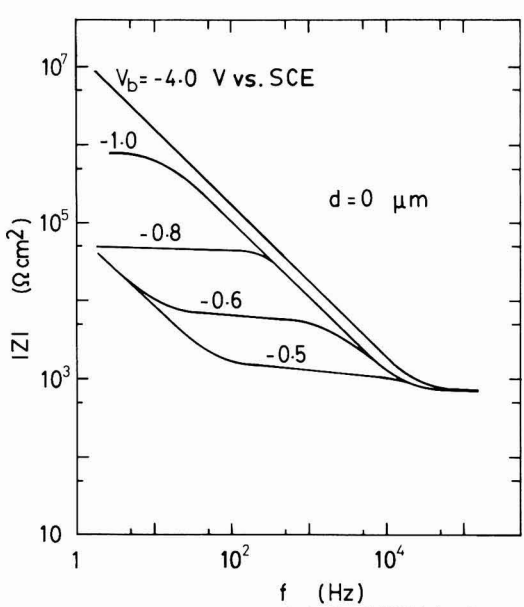

Fig. 3. Impedance spectra for as-etched p-Si in 0.005M phosphate as a function of bias voltage.

space charge layer comes to play an important role in determining the impedance behavior. In region II, however, the depletion layer width is still comparatively small, so that the impedance is to a large extent determined by the resistance part R_{SC}. If the contribution of the surface-state capacity is neglected in this frequency range, then R_{SC} effectively consists of two parallel resistances, r_{SC} and r_{SS}, associated with the space charge layer and the surface states, respectively.

At $V_b \sim 0$ V, R_{SC} is determined by r_{SC}. At that time, r_{SC} is some sort of tunneling resistance. Since it is relatively low, R_{SC} would be negligible. With increasing $|V_b|$, however, $r_{SC} >> r_{SS}$, and R_{SC} is dominated by r_{SS}. A change of charge in the surface states with potential might account for the behavior of region II by effectively shunting C_{SC}. Under this situation, information on C_{SC} and C_H can be obtained at sufficiently high and low frequencies, respectively.

At $|V_b| \geq 1$V, the impedance shows capacitive properties in the whole range of interest for frequency. There is no frequency dispersion in the C_{SC} values. The depletion layer capacitance C_{SC} can then be determined directly from the corresponding data as a function of V_b.

PSL electrodes.—The impedance spectra observed with the PSL electrodes of $d = 8$ and 40 μm are shown in Fig. 5a and b. The electrolyte and its concentration were the same as Fig. 2. It can clearly be seen from these results that there are distinct differences with Fig. 2 especially in region I, II, and IV. First, in contrast to as-etched p-Si, the region associated with C_H is modified in the PSL case. Second, as d is increased, the bias voltage dependence of the impedance for $|V_b| < 1$V becomes very small. Moreover, the region corresponding to region IV is not observed with PSL.

PSL consists of many micropores with extremely small diameters. This structure can be regarded as a typical example of the single-pore model. In accordance with the analysis by De Levie (14), the impedance of the electrode with an infinitely deep cylindrical pore is proportional to the square root of a planar electrode impedance. Thus, the Helmholtz layer capacitance behaves as the impedance proportional to $f^{-1/2}$. Such behavior becomes apparent at frequencies low enough for an ac signal to penetrate the entire pore. At sufficiently high frequencies, on the other hand, the entire porous structure is not probed, but only planar behavior should be detectable. These properties were confirmed experimentally by impedance measurements of porous metal electrodes (15, 16) and surface morphology controlled semiconductor electrodes (17, 18).

At $d = 8$ μm, the impedance for $|V_b| \lesssim 0.5$V has a slope of $-½$ as shown in Fig. 5a. This is consistent with the morphology of PSL. It appears that in this region the diffusion resistance of the electrolyte which has penetrated into PSL is a predominant factor of the impedance. The impedance for $d = 40$ μm shows a more distinct characteristic feature of PSL, as shown by regions A, B, C, and D in Fig. 5b. Both region A, showing a $-½$ slope, and subsequent region B, corresponding to region II in Fig. 2, are now restricted in a lower frequency range, a behavior consistent with the increase in PSL thickness. Instead of this, the impedance for $|V_b| \lesssim 0.5$V has region D characterized by another RC element. This is presumably related to the resistance and capacitance of PSL silicon, denoted by R_{PSL} and C_{PSL}, respectively. The R_{PSL} value estimated from the resistivity (6) and thickness of PSL is about 1 kΩcm² and C_{PSL} would be very small ($\sim 10^{-10}$ F/cm²). It is, thus, expected that region D should be followed by the capacitive (C_{PSL}) region at higher frequencies. Finally, the impedance would reach constant value

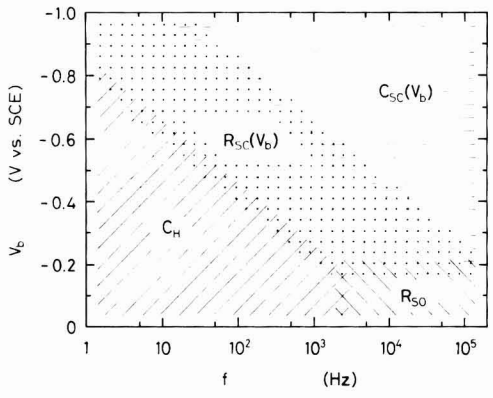

Fig. 4. Impedance map for as-etched p-Si in 0.1M phosphate. Each predominant factor represented corresponds to that shown in Fig. 2. Overlapping parts show the transitional region.

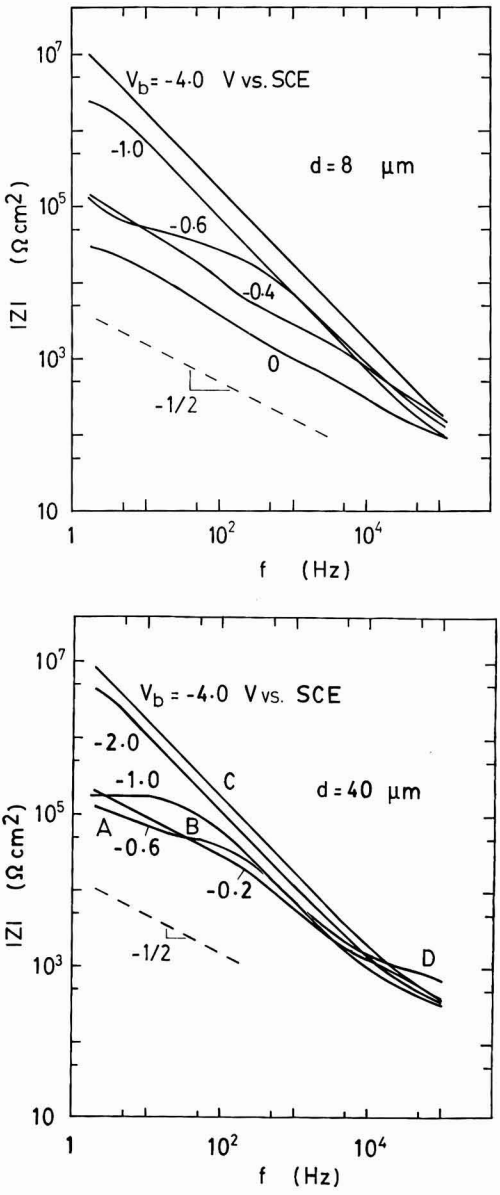

Fig. 5. Impedance spectra for PSL of (a, top) $d = 8$ μm and (b, bottom) $d = 40$ μm as a function of bias voltage in 0.1M phosphate.

R_{SO} which was observed with as-etched p-Si at $f \gtrsim 10$ kHz (region IV in Fig. 2).

As $|V_b|$ is increased, the effect of the space charge layer becomes predominant over that of the surface morphology. Therefore, information on the space charge layer capacitance of PSL can be obtained for $|V_b| \gtrsim 1$V and $f \lesssim 10$ kHz. Under these conditions, there are no differences between the impedance spectra of PSL and as-etched p-Si. In particular, at high values of $|V_b|$, both impedance spectra almost coincide with each other. This is evident from a comparison of region C in Fig. 5b with region III in Fig. 2. Only when the frequency exceeds 10 kHz can the difference between them be seen. This result shows that information obtained from region C in Fig. 5b is not associated with PSL silicon itself but with the space charge layer produced inside the substrate near the rear surface of PSL. As mentioned above, the capacitance of PSL silicon would be identified in extremely high frequencies only.

A map showing the predominant factors of the impedance for sufficiently thick PSL is drawn in Fig. 6. According to the conditions of frequency and bias voltage, the impedance is dominated by either electrolyte penetrating PSL, the PSL/electrolyte interface, or PSL silicon. Though the overall equivalent circuit of PSL is difficult to picture, information on each component can be obtained separately from the impedance data at appropriate conditions.

Mott-Schottky plots.—Further support of the above explanation is provided by Mott-Schottky plots of C_{SC} shown in Fig. 7. This result was obtained from the data in above-mentioned regions III and C where no frequency dispersion effects are observed. As in the as-etched p-Si case, the linear relationship between $1/C_{SC}^2$ and V_b is found in the PSL case as well. Although the slope is somewhat varying, the impurity concentration estimated from the slope of each linear plot was $3.8\text{-}4.4 \times 10^{15}$ cm^{-3} for $d = 0\text{-}40$ μm. These values fall within the range expected from the resistivity variation of the substrate.

As shown in Fig. 7, the effect of the introduction of PSL is to shift the flatband potential, V_{FB}, to the negative side. The change in V_{FB} is more apparent for $d \lesssim 10$ μm. For $d \gtrsim 20$ μm, V_{FB} becomes constant. The shift of V_{FB} may be caused by the OH^- adsorption in PSL. As d is increased, PSL acquires more hydroxyl ions in it. This results in a negative shift of V_{FB} at the rear surface of PSL. The increase in d would also produce an increase in the surface-state density there. The final value of V_{FB} for $d \gtrsim 20$ μm is therefore determined by the distribution of OH in PSL and, possibly, by the pinning of the surface potential by a charge in surface states. To verify this explanation, more work on the equilibrium potential between PSL and electrolyte, including the band bending at the interface, must be carried out using electrolytes with a well-defined redox potential.

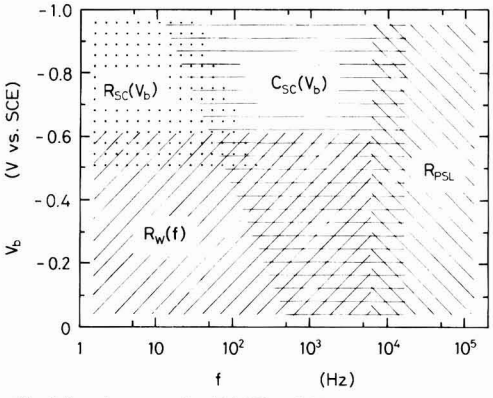

Fig. 6. Impedance map for thick PSL in 0.1M phosphate. The components $R_W(f)$, $R_{SC}(V_b)$, $C_{SC}(V_b)$, and R_{PSL} correspond to those in regions A, B, C, and D in Fig.5b.

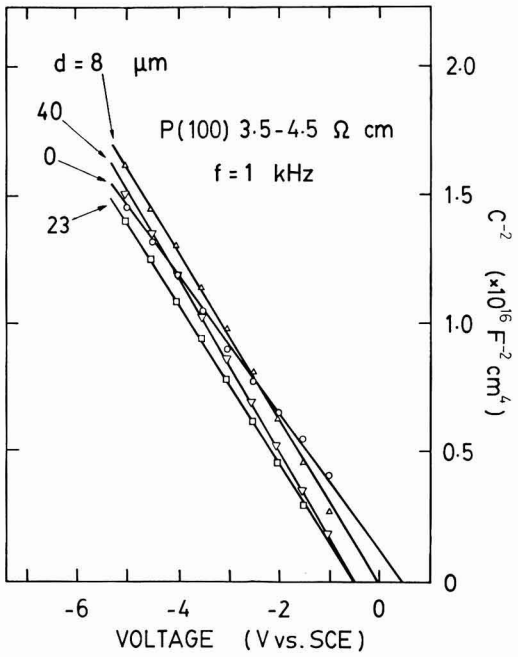

Fig. 7. Mott-Schottky plots of C_{SC} obtained from the data in 0.1M phosphate as a function of PSL thickness.

Conclusions

Dielectric properties of the p-type PSL-aqueous electrolyte interface have been investigated experimentally. From measurements of the impedance spectra over a wide frequency range, the interfacial variables can be interpreted in terms of the passive elements. Although the assignment of the circuit elements to PSL at this point is still somewhat speculative, the fundamental features of the impedance spectra for PSL can be regarded as a result of modification of those for as-etched p-Si.

Since PSL is formed on the Si substrate, PSL electrodes have properties of discrete semiconductors and as particulate systems. Separation between them was made by the impedance spectra analysis. The former property appears in the impedance spectra at high bias voltages. Mott-Schottky plots obtained at high bias voltages provide information on the space charge layer produced near the rear surface of PSL. The flatband potential of the rear surface shifted to the negative side with increasing PSL thickness. This result is correlated to the particulate property of PSL through the OH adsorption.

Distinct properties as a micropore system, which could be detected at low frequencies and low bias voltages, were to produce the diffusion resistance of the electrolyte and, possibly, the increase in the Helmholtz layer capacitance. The measurement of the impedance spectra is useful as an analytical tool for studying the PSL-electrolyte interface. The influence of the surface states as a function of PSL thickness will be reported elsewhere.

Acknowledgments

The authors would like to thank Professor S. Yoshida for his continuous guidance and encouragement.

Manuscript submitted Dec. 23, 1985; revised manuscript received June 18, 1986.

Tokyo University of Agriculture and Technology assisted in meeting the publication costs of this article.

REFERENCES

1. N. Koshida, M. Nagasu, T. Sakusabe, and Y. Kiuchi, *This Journal*, **132**, 346 (1985).

2. N. Koshida and Y. Kiuchi, *Jpn. J. Appl. Phys.*, **24**, L166 (1985).
3. A. Uhlir, *Bell Syst. Tech. J.*, **35**, 333 (1956).
4. D. R. Turner, *This Journal*, **105**, 402 (1958).
5. T. Unagami and M. Seki, *ibid.*, **125**, 1339 (1978).
6. T. Unagami, *ibid.*, **127**, 476 (1980).
7. G. Bomchil, R. Herino, K. Barla, and J. C. Pfister, *ibid.*, **130**, 1611 (1983).
8. K. Barla, G. Bomchil, R. Herino, J. C. Pfister, and J. Baruchel, *J. Cryst. Growth*, **68**, 721 (1984).
9. K. Barla, R. Herino, G. Bomchil, J. C. Pfister, and A. Freund, *ibid.*, **68**, 727 (1984).
10. M. L. J. Beale, N. G. Chew, M. J. Uren, A. G. Cullis, and J. D. Benjamin, *Appl. Phys. Lett.*, **46**, 86 (1985).
11. I. M. Young, M. I. J. Beale, and J. D. Benjamin, *ibid.*, **46**, 1133 (1985).
12. M. Tomkiewicz, *This Journal*, **126**, 2220 (1979).
13. S. R. Morrison, "Electrochemistry at Semiconductor and Oxidized Metal Electrodes," pp. 119-188, Plenum Press, New York (1980).
14. R. De Levie, in "Advances in Electrochemistry and Electrochemical Engineering," Vol. 6, P. Delahay, Editor, pp. 329-397, Interscience Publishers, Inc., New York (1967).
15. J. P. Candy, P. Fouilloux, M. Keddam, and H. Takenouti, *Electrochim. Acta*, **26**, 1029 (1981).
16. M. Kramer and M. Tomkiewicz, *This Journal*, **131**, 1283 (1984).
17. J. K. Lyden, M. H. Cohen, and M. Tomkiewicz, *Phys. Rev. Lett.*, **47**, 961 (1981).
18. M. Tomkiewicz, I. Ling, and W. S. Persons, *This Journal*, **129**, 2016 (1982).

Time-Resolved Photoelectrochemical Measurements on Surface-Modified n- and p-InP Electrodes

Ronald L. Cook,* Patrick F. Dempsey, and Anthony F. Sammells*

Eltron Research, Incorporated, Aurora, Illinois 60505

ABSTRACT

Time-resolved photoelectrochemical measurements following illumination with a pulsed laser source have been performed on surface-modified n- and p-InP photoelectrodes. The rate of the initial fast transient photopotential decay was shown to be sensitive to the nature of the surface modification used. The chemisorption of Ru ions onto the n-InP surface reduced the rapid initial decay of the transient photopotential response observed on the unmodified n-InP surface. It is proposed that Ru^{3+} chemisorption may effectively reduce surface trap density at the interface region. For p-InP either unmodified or modified by Co, Rh, Pt, Pb, Rh/Pt, or Co/Pt, the transient photopotential decay exhibited a two segment response. The fast initial decay was found dependent on the previous surface treatment of the p-InP electrode. The second slower decay, however, was found independent of previous surface treatments. Here, the average characteristic decay rate b was found to be $2.53 \times 10^7\ s^{-1}$ in agreement with the calculated value of $1.12 \times 10^7\ s^{-1}$. The similar b values obtained with metal surface modifications possessing significantly different work functions (Co and Pt) suggested that the barrier height was pinned at the interface region. The origin of this pinned barrier height was associated with the proposed formation of intrinsic surface states at 0.9 and 1.2 eV (with respect to the valence band maximum) after p-InP surface modification. Since the barrier height appears to be pinned, these results suggest that the major role of metallic surface modifications in promoting photoelectrochemical hydrogen evolution would, in part, be that of a conventional electrocatalyst.

The efficiency of solar energy conversion in liquid junction solar cells is determined by dynamic processes occurring both at the semiconductor-electrolyte interface and within the semiconductor bulk. The kinetics associated with the generation and recombination of minority carriers in the overall photoelectrochemical (PEC) process are dictated by light absorption, diffusion of the minority carrier to the semiconductor surface, recombination both within the bulk and surface, and charge transfer across the interface. These processes are fast compared to the time scale used for most current-voltage measurements. Measurement of these rapid phenomena requires the use of either transient PEC or electrochemical techniques. One of the more promising approaches, in recent years, for examination of the interfacial region on PEC electrodes has been the application of laser pulse excitation techniques for the investigation of photopotentials and photocurrents at photoelectrodes (1-6). Several theoretical calculations of the photoelectrode behavior following pulsed photogeneration of electron-hole pairs have also been performed (7, 8). In particular, Gottesfeld and Feldberg (7) have developed algorithms that can be used to relate the number of photogenerated carriers and their reaction pathways to the observed transient photopotential.

Following the laser pulse photogeneration of electron-hole pairs in which there is no net interfacial electron or hole transfer, the open-circuit transient photopotential can decay by three pathways (7). These can be summarized as: (*i*) recombination of electrons and holes in the semiconductor bulk, (*ii*) recombination via a high density of intra-bandgap surface states, and (*iii*) diffusion of minority carriers back into the semiconductor bulk. It is expected that the last mechanism is relatively slow (7). (*i.e.*, the time required for half of the holes to drift into the semiconductor bulk is 70s) and will not be a factor in the time ranges evaluated in laser pulse studies (*i.e.*, up to 100 μs). Bulk recombination occurring at defect sites can, in some circumstances, be reduced by careful consideration of dopant level and growth conditions (9). The surface recombination velocity at the semiconductor-electrolyte interface, however, can be dependent on the solvent, the presence of intrinsic or extrinsic oxides, and the history of the semiconductor surface (*e.g.*, the etchant used). For p-InP in particular, a stable ≅ 10Å layer of hydrated In_2O_3 formed at the semiconductor-electrolyte in acid electrolyte interface has been shown to reduce the surface recombination velocity, resulting in improved efficiencies for the photocathodes (10, 11). In addition, it has also been shown that the chemisorption of 1/20 to 1/5 of a metal monolayer such as silver (12) or ruthenium (13) can also effect a reduction in surface recombination velocity. Low surface recombination velocities can contribute towards efficient light to chemical conversion on photoelectrodes. Additionally, high interfacial charge transfer must also be present. For the hydrogen evolution reaction, high rates of charge transfer (reflected in higher light to chemical conversion) have been obtained with p-InP electrodes surface modified with electrodeposited platinum group metals in both acid (14) and alkaline (15) electrolytes.

Our interest has been directed toward gaining an understanding of the semiconductor-electrolyte interface, and how surface modifications in this region can enhance the efficiency of solar energy to chemical fuels

*Electrochemical Society Active Member.

production (16). Although steady-state and linear-sweep current voltage measurements can give information on the overall kinetics associated with the PEC reaction across the photoelectrode/electrolyte junction, the kinetics of photogenerated carrier recombination, both at bulk and surface photoelectrode sites, must be addressed using transient relaxation techniques. In previous work, we have observed that surface pretreatment can significantly effect the initial decay of the photopotential signal (17). Of particular interest was the effect of different etch treatments on the shape and slope of the transient photopotential decay. For p-InP etched with 12*M* HCl, two linear segments were observed in the plots of ln $[(\exp(Ep_{t=0})-1)/(\exp(Ep_t)-1)]$ *vs.* time. When the same electrode was etched with 6:1:1:1 HNO_3:HCl:CH_3COOH:$HClO_4$, only a single segment was observed. Additionally, the slope, and, thus, the rate of decay, for the 6:1:1:1 etched electrode was smaller. This suggested that the 6:1:1:1 etch might be more effective than 12*M* HCl for removing surface states acting as traps at the electrode surface. This encouraged us to further investigate the effects of surface modifications on the laser pulse induced transient photopotential decay signal. In work reported here, we discuss the application of time-resolved laser pulse PEC techniques to InP photoelectrodes surface modified by the electrochemical deposition of ≅100Å of a noble metal catalyst and, alternatively, by Ru^{3+} ions chemisorption.

Experimental

The block diagram of the experimental setup is shown in Fig. 1. The excitation source was a PAR Model 2100 tunable dye laser, which utilized a TEA nitrogen laser for excitation of a Grazing Incidence dye laser. The pertinent features of the laser pulse are a pulse width of 1 ns (FWHM) and a pulse energy of 30 μJ, giving a nominal power output by the dye laser of 25 kW throughout the tuning range. The laser dye used was rhodamine 6G which gave a maximum laser intensity when excited at 581.9 nm.

The PEC cell used in this study consisted of InP working electrodes (0.05 cm^2 area) and a large platinized platinum counterelectrode (6.25 cm^2 area) in order to minimize the capacitive contribution from the latter to the working electrode. The cell was also placed in a shielded aluminum cage to minimize noise and to reduce RF interference associated with the laser pulse. The inclusion of the 75 ns delay line was dictated by the inherent limitation of the PAR Model 162 boxcar averager. The boxcar averager has a built-in 75 ns delay after triggering, and before signal sampling begins. Thus, the delay line was needed for sampling of the entire signal. The response time of the measurement electronics was on the order of 10-20 ns after triggering of the boxcar averager via a PAR 2100/99 fast photodiode edge trigger. An initial problem encountered was the small photopotential response following initial laser photoexcitation. This problem was solved by the design and fabrication of an extremely fast differential amplifier. Figure 2 shows the circuit diagram for this device. The differential amplifier is designed around a state-of-the-art Comlinear 300A operational amplifier. This op-amp has a bandwidth of 85 MHz with a gain of 20×. Other operational parameters of this op-amp

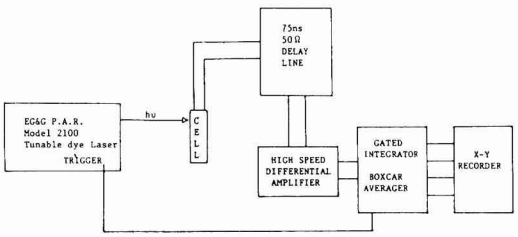

Fig. 1. Schematic of laser pulse apparatus for study of transient semiconductor photopotential response.

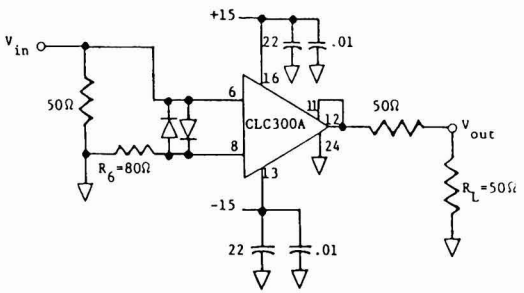

Fig. 2. Circuit diagram for differential amplifier designed around a Comlinear 300Å operational amplifier.

include a risetime of 4 ns and a slew rate of 3 V/ns. To insure undistorted amplification of the photopotential signal, inclusion of a large ground plane was also incorporated into the design. The photopotential perturbation was limited to less than kT/e (≅25 mV) by use of neutral density filters in the laser light path in order to utilize the theoretical analysis suggested by Gottesfeld and Feldberg (7).

p-InP photocathodes (100) were prepared from Zn-doped p-InP (Crystacomm, Incorporated) having bulk doping densities corresponding to $N_D = 2 \times 10^{18}$ cm^{-3}. Ohmic contacts to the crystals were made by sparking with a Zn wire utilizing a 12V dc source. Current collection was by Nichrome wire attached with silver epoxy (Epo-Tec) followed by curing at 150°C. Finally, a protective epoxy coating was applied to the back and sides of the electrode. The electrode surfaces were modified by the cathodic photoelectrodeposition of Pb, Co, Rh, and Pt from 0.01*M* solutions of the appropriate salts with the photoelectrode under 100 mW cm^{-2} illumination using a General Electric ELH 300W source. Metal deposition was performed at 0.01 mA/cm^2 until 100Å was introduced onto the p-InP surface. Microscopic examination showed that the deposited metal was dispersed in the form of islands. n-InP photoanodes were prepared from Sn-doped (100) n-InP (Atomergic Chemicals Corporation) having doping densities corresponding to 1.8×10^{18} cm^{-3}. Ohmic contacts were made by sparking Sn wire utilizing a 12V dc source. Current collection and protection of the ohmic contact area were performed similar to those used for p-InP. Transient photopotential measurements were carried out in 0.1*M* HNO_3 for n-InP and both 1.0*M* KOH and acetonitrile for p-InP. Chemisorption of Ru ions onto the n-InP surface was accomplished first by etching the n-InP surface with 12*M* HCl for 15s, rinsing with distilled water, followed by immersion in 0.01*M* $RuCl_3$/0.1*M* HNO_3 for 1h. The n-InP electrode used for a control was etched with 12*M* HCl for 15s, rinsed with distilled water for 15s, and then immersed into 0.1*M* HNO_3 (not containing $RuCl_3$) for 1h.

Forward current measurements were performed on p-InP electrodes using a three-electrode configuration consisting of a large surface area counterelectrode (platinized platinum), an SCE reference, and a p-InP working electrode. Voltage control was supplied by a Stonehart BC 1200 potentiostat and a voltage scanner.

Results and Discussion

The application of transient time resolved PEC techniques to study dynamic processes at photoelectrode/electrolyte junctions can be carried out in the presence or absence of an externally applied bias (1-6). Under open-circuit conditions, relaxation of the transient photopotential occurs by various minority carrier recombination mechanisms both within the semiconductor bulk, and at the semiconductor/electrolyte interface, since the possibility of relaxation through an external load does not exist. Comparison of previous theoretical (18) and experimental values obtained for open-circuit photopotential (19) suggests that surface recombination, not bulk recombination, is the major loss

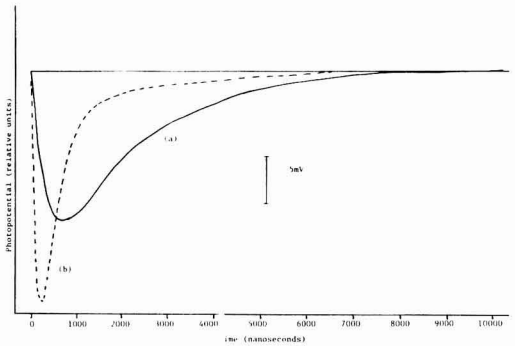

Fig. 3. Photopotential transient response for n-InP in 0.1M HNO_3: (a) with Ru ion modification; (b) unmodified.

mechanism limiting the open-circuit photopotential in liquid junction InP photoelectrochemical cells. Therefore, changes in the nature or stoichiometry of an InP surface, which result in the formation or reduction of surface-state populations, should be reflected in the transient photopotential signal. To evaluate the sensitivity of the laser pulse photopotential technique to surface modification, transient photoelectrochemical measurements were performed on n-InP photoelectrodes in the presence and absence of chemisorbed Ru ions. Surface modification of n-InP electrodes by Ru ions has been shown to diminish subbandgap response due to removal of surface states from the bandgap (13). Removal of the intra-bandgap surface states by Ru ions has also been postulated as responsible for the performance improvement observed on n-GaAs electrodes following chemisorption of Ru ions onto the GaAs surface (20). Figure 3 shows the transient photopotential response for n-InP in 0.1*M* HNO_3 both with (a) and without (b) the presence of Ru^{3+} on the n-InP surface. In both cases, the photopotential decayed back to the original equilibrium open-circuit potential. This suggested that photocorrosion was not present. As indicated in Fig. 3, the transient photopotential response was sensitive to the presence or absence of surface modification. Without Ru ions (curve b) the transient photopotential response exhibited a rapid decay following the photopotential maximum (Ep[max]). For the Ru ion modified n-InP photoelectrode, however, the decay rate was much slower. The values for $T_{50\%}$ (*i.e.*, the time necessary for the signal to decay to one-half the maximum), where 412 and 1422 ns, respectively, for the unmodified and Ru-modified n-InP electrodes. The observation of smaller photopotential for n-InP modified with Ru^{3+} ions was unexpected, since recent work has suggested that the presence of both oxygen (or oxides) and metals would pin the barrier height at essentially the same level (21). The risetimes for both the n-InP photoelectrodes discussed above and of p-InP photoelectrodes to be discussed below were ≅10-20 ns and were considered to be limited by the measurement electronics.

In order to quantify the effect of chemisorbed Ru ions on the n-InP transient photoresponse, we have applied previous theoretical analyses used by others (4, 7) for explaining the observed relaxation of transient open-circuit photopotentials following the laser-pulsed photogeneration of electron-hole pairs. Here, expressions for the open-circuit photopotential decay were developed subject to the following assumptions: (*i*) the photoelectrode has a high donor concentration, and a depletion layer is present prior to the incident laser pulse; (*ii*) only small photopotential excursions are evaluated (*i.e.*, $\Delta E < kT/e$); (*iii*) all of the photogenerated minority carriers are generated within the space charge region; and (*iv*) no net transfer of photogenerated minority carriers occurs during measurement of the transient photopotential. Under such conditions, decay of the open-circuit photopotential will be dictated by either the respective transport rates for electrons and electron holes towards each other or by their recombination. Recombination may occur within the semiconductor bulk or at its surface, where recombination velocities may be higher. As previously discussed (18, 19) surface recombination at InP photoelectrodes appears to be the major loss mechanism for photogenerated minority carriers. For decay of photopotential by a high density of surface states, the photopotential-time response can be given by (7)

$$\Delta E_t - \Delta E_{t=0} + \ln[(\exp(\Delta E_{t=0}) - 1)/(\exp(\Delta E_t) - 1)] = bt \quad [1]$$

where $\Delta Et = 0$ is the maximum photopotential and b is a characteristic rate constant for the decay process, which, for n-type semiconductors, is given by

$$b = 2e^2 d_b D_n (E_b + 1) \exp(E_b)/(kT\epsilon\epsilon_0) \quad [2]$$

where e is the electronic charge, d_b is the bulk concentrations of donors, E_b is the normalized equilibrium potential (*i.e.*, $E_b = V_b e/(kT)$), D_n is the diffusion constant for electrons and ϵ and ϵ_0 are the dielectric constant of the semiconductor and the permittivity of free space, respectively. Figure 4 shows a plot of ln $[\exp(Ep)_{t=0} - 1)/(\exp(Ep)_t - 1)]$ *vs.* t for the unmodified electrodes and Ru ion modified electrodes, respectively.

For unmodified n-InP, the photopotential decay consists of both an initial fast and subsequent slower segment. The characteristic decay constant b, for the initial fast segment obtained from the slope, is 1.28×10^8 s^{-1}. For the slower segment, b was found to be 5.49×10^6 s^{-1}. In the case of a Ru^{3+} modified n-InP surface, the observed predominant photopotential decay rate was found similar to that predicted by Eq. [1] (7). Here, the average experimentally determined decay constant (up to 1500 ns) from these n-InP electrodes was found to be 2.51×10^7 s^{-1}.

The fast initial decay observed for untreated n-InP electrodes may be a result of direct photogeneration of trapped holes. One question that arises here is the possible relationship between photopotential decay rates in the longer time segment for the untreated photoelectrode (between 900 and 2000 ns) and those found to be up to 1200 ns for Ru^{3+} modified n-InP. One might have anticipated that the rate constant b in these two cases might have been similar considering the relationship [2] above and provided the barrier height were pinned by extrinsic defect sites (21); this, however, was not found to be the case.

As discussed earlier, the electrodeposition of platinum group metals onto p-InP photocathodes has been shown

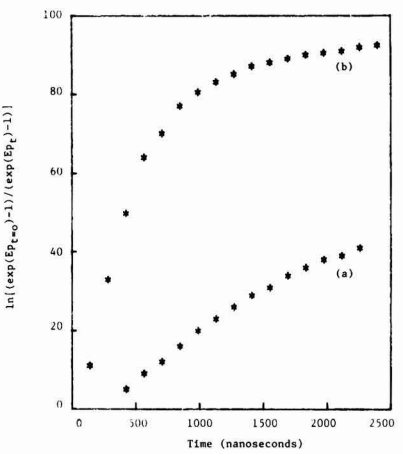

Fig. 4. Plot of ln[(exp $(Ep_{t=0})-1)/(\exp(Ep_t)-1)]$ *vs.* time for n-InP in 0.1M HNO_3: (a) with Ru ion modification; (b) unmodified.

to promote high efficiency solar to hydrogen conversions (14, 15). Such increases in efficiency are due in part to the enhanced rate of electron transfer across the semiconductor/electrolyte interface. Additionally, such surface modification could influence ultimate photoelectrolysis efficiency by either modifying the surface barrier height or suppressing recombination at the semiconductor/electrolyte interface. In order to gain insight into such questions, transient photopotential response measurements were performed using the laser-pulse techniques discussed above on p-InP electrodes in 1*M* KOH surface modified by electrodeposited Co, Rh, Pt, Co/Pt, Rh/Pt, and Pb. Figures 5a-c compare typical transient photopotential decay spectra for unmodified and surface-modified p-InP. Unlike n-InP, both unmodified and modified p-InP electrodes were not found to decay back to their original dark equilibrium potentials after their interactions with the laser pulse (over ≅10 μs time scale), but established new equilibria at somewhat more negative values. This is probably associated with the presence of some net electron transfer occurring at the interface region, leading to a reduced species. This may even involve a finite change in the presumed native oxide layer resident on the p-InP surface. To address such questions, comparative studies were performed in nonaqueous electrolyte (acetonitrile containing tetrabutylammonium hexafluorophosphate (0.1*M*) as supporting electrolyte). Figures 6a and b show these results for unmodified p-InP (etched with 12*M* HCl) and p-InP modified after electrodeposition by ≅100Å cobalt. In both these cases, the transient photopotential was found to decay completely to its initial equilibrium potential. Here, acetonitrile acts as a blocking electrolyte with no net electron transfer occurring. This suggests that net faradaic process may be occurring at the p-InP/aqueous electrolyte interface.

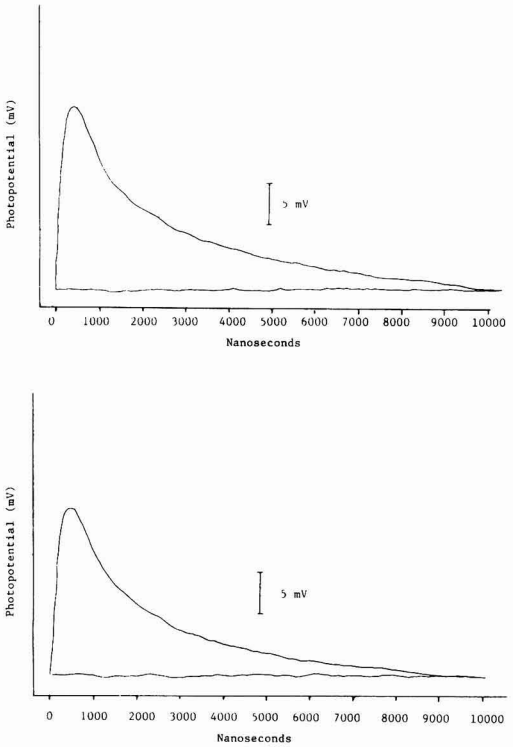

Fig. 6. (a, top) Transient photopotential for unmodified p-InP (etched with 12M HCl) in acetonitrile (0.1M $TBAPF_6$). (b, bottom) Transient photopotential for p-InP modified with 100Å of electrodeposited Co in acetonitrile (0.1M $TBAPF_6$).

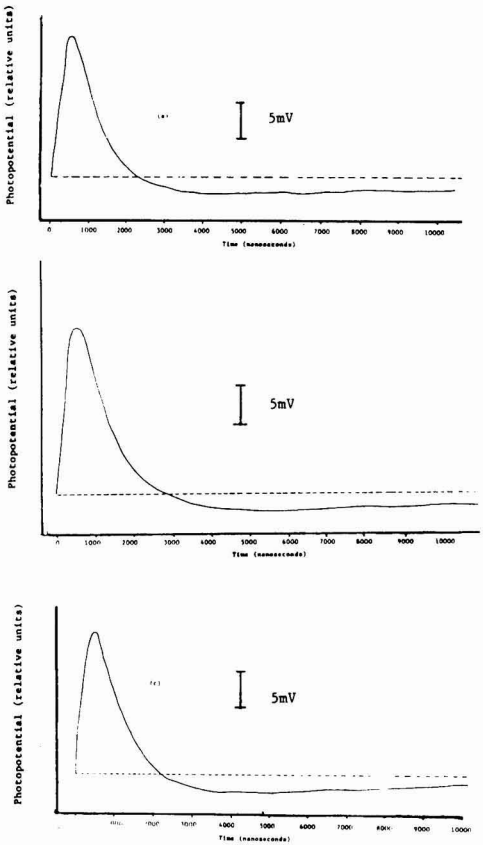

Fig. 5. Transient photopotential response for p-InP: (a) unmodified; (b) surface modified with <100Å electrodeposited Rh; (c) surface modified with <100Å electrodeposited Pb.

In order to quantify these experimental observations, Eq. [1] was used to analyze the transient photopotential response decay rates. Figures 7-9 show plots of ln [(exp ($Ep_{t=0}$)−1)/(exp (Ep_t)−1] *vs* time, for, respectively, unmodified, cobalt, and platinum-modified p-InP in 1*M* KOH. p-InP, either unmodified or surface modified with ≅ 100Å of Co, Rh/Pt, Rh, Pb, Pt, or Pb, also exhibit the

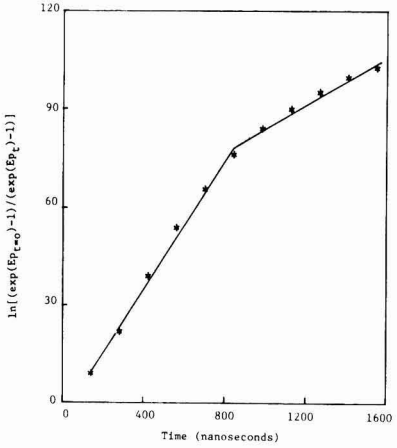

Fig. 7. Plot of ln [(exp ($Ep_{t=0}$)−1)/(exp(Ep_t) −1)] *vs.* *t* for unmodified p-InP in 1M KOH.

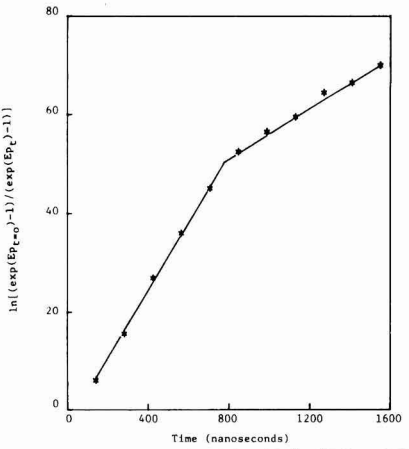

Fig. 8. Plot of ln $[(\exp(Ep_{t=0})-1)/(\exp(Ep_t)-1)]$ for p-InP surface modified by electrochemical deposition of <100Å Co.

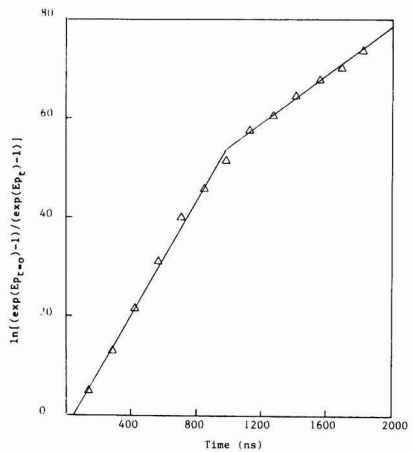

Fig. 9. Plot of ln $[(\exp(Ep_{t=0})-1)/(\exp(Ep_t)-1)]$ *vs.* time for p-InP surface modified with platinum in 1M KOH

two-segment response previously discussed for unmodified n-InP. Table I summarizes values for the characteristic rate constant b for these two segments in this reported work. Here, the slope b for the initial segment ($t < 800$ ns) varied from 4.66×10^7s to 10.31×10^7 s^{-1} for, respectively, Co/Pt and Co surface-modified p-InP. It has been suggested by others (7) that the fast segment might be explained by the decay of photogenerated carriers initially trapped at the semiconductor surface. Such an explanation would be consistent with the dependency of b on previous surface treatment. For the slower decay segment ($t = 800$ ns), b values were essentially found constant for all modified and unmodified p-InP electrodes investigated (2.53×10^7 s^{-1}).

Let us now compare the experimentally obtained b value for the slower decay segment with that calculated by use of Eq. [2]. This initially requires determination of the barrier height V_B as calculated from forward current measurements in 1M KOH. The forward current (J_F) was found to exhibit linearity in all cases when ln (J_F) was plotted *vs.* voltage. Several charge transfer mechanisms can be responsible for such an exponential voltage dependence. By analogy to solid-state Schottky barrier junctions, the relationship between forward current and voltage can be given by

$$J_F = J_S \exp(eV/nKT) \quad [3]$$

Table I. Values of b (characteristic rate constant) obtained from transient photopotential measurements at unmodified and modified p-InP/1M KOH interfaces

Modification	Initial fast decay[a] ($t < 800$ ns) s^{-1}	Subsequent slower decay segment[a] ($t > 800$ ns) s^{-1}
Co	10.31×10^7 (± 0.07)	2.60×10^7 (± 0.07)
Rh/Pt	7.29×10^7 (± 0.09)	2.73×10^7 (± 0.09)
Rh	6.94×10^7 (± 0.07)	2.49×10^7 (± 0.07)
Unmodified	6.93×10^7 (± 0.04)	2.48×10^7 (± 0.04)
Pb	6.75×10^7 (± 0.08)	2.61×10^7 (± 0.08)
Pt	5.68×10^7 (± 0.05)	2.42×10^7 (± 0.05)
Co/Pt	4.66×10^7 (± 0.08)	2.42×10^7 (± 0.08)
		Average 2.53×10^7 (± 0.09)

[a] Values are averages of four electrodes, standard deviations are in parentheses.

where J_S is the saturation current and n is the ideality factor. For p-InP/KOH junctions, it was observed that the ideality factor was ≅ 2.2 (Table II). For an ideal Schottky junction, n would be expected to be unity with recombination occurring in the bulk of the semiconductor. A value of two is indicative of a junction controlled by generation-recombination currents (22). Although the p-InP/KOH junctions here did not exhibit classical Schottky barrier behavior (*i.e.*, $n = 1$) approximate barrier heights could be calculated using the expression for the saturation current of a Schottky barrier device

$$J_S = A^* T^2 \exp(-e V_B/KT) \quad [4]$$

where A^* is the modified Richardson constant (10 A/cm^{2}K^2) for p-InP electrodes (23) and V_B is the barrier height. Table II summarizes V_B values obtained for the photoelectrodes examined here. As is evident from these results, V_B does not appear dependent upon the metal chosen for deposition on the p-InP surface, even though their work functions are significantly different [*e.g.*, Pt = 5.32 eV (24) and Co = 4.40 eV (25)]. The observations are in agreement with the constant b values obtained from the slower decay segment of transient photopotential measurements. From Eq. [2], only E_b (which contains the barrier height term V_B) would be potentially influenced by surface modifications; this was clearly not observed.

Using Eq. [2], b values were calculated using the following parameter values: $e = 1.602 \times 10^{-19}$C; b_a (the bulk acceptor concentration, equivalent to d_b in n-InP) = 2×10^{18} cm^{-3}; D_p (hole diffusion constant) = 150 cm^{2}s^{-1}; $V_B = 0.58$V; $\epsilon = 10.3$; $\epsilon_o = 8.854 \times 10^{-14}$ CV^{-1}cm^{-1}; $k = 1.3807 \times 10^{-23}$ JK^{-1}, and $T = 295$ K, giving a value of $b = 1.12 \times 10^7$ s^{-1}. For b, this value is in agreement with the experimentally obtained average b value of 2.53×10^7 s^{-1}. Both transient photopotential and forward current measurements suggest that the barrier height is pinned at a value independent of any surface modification. It has been suggested by others (21) that surface states on InP responsible for Fermi level pinning may result from the interaction of adatoms and that such interactions were similar for adsorbed oxygen as well as for deposited metals. Such surface states appear to be extrinsic, created by stoichiometric deficits at the semiconductor surface. Such deficits were proposed to induce surface states on

Table II. Forward current measurements on p-InP electrodes in 1M KOH

p-InP	V_B (eV)	J_o (A cm^{-2})	n
Unmodified[a]	0.59 (± 0.01)	1.2×10^{-4} (± 0.2)	2.22 (± 0.17)
Cobalt (100Å)[b]	0.58 (± 0.01)	1.2×10^{-4} (± 0.2)	2.90 (± 0.20)
Platinum (100Å)[b]	0.57 (± 0.01)	1.1×10^{-4} (± 0.3)	2.22 (± 0.04)

[a] Values are for eight electrodes, standard deviations are in parentheses.
[b] Values are for four electrodes, standard deviations are in parentheses.

Table III. Values of b (characteristic rate constant) obtained from transient photopotential measurements at unmodified and modified p-InP/acetonitrile interfaces

Modification	Initial fast decay[a] ($t < 800$ ns) s^{-1}	Subsequent slower decay segment[a] ($t > 800$ ns) s^{-1}
Co	6.11×10^7 (± 0.07)	1.34×10^7 (± 0.07)
Pt	4.15×10^7 (± 0.06)	1.30×10^7 (± 0.06)
Rh	3.91×10^7 (± 0.05)	1.29×10^7 (± 0.05)
Pb	3.45×10^7 (± 0.07)	1.33×10^7 (± 0.07)
Unmodified	3.26×10^7 (± 0.03)	1.36×10^7 (± 0.03)
	Average	1.32×10^7 (± 0.03)

[a] Values are averages of four electrodes, standard deviations are in parentheses.

p-InP located at 0.9 and 1.2 eV above the valence band maximum. The state at 0.9 eV is associated with P vacancy defects in the surface lattice, whereas that at 1.2 eV is related to In vacancy defects. Hence, both acid etching or metal depositions may introduce the same defects at the p-InP/electrolyte interface, resulting in barrier height pinning which is, in fact, somewhat independent of surface modification procedures. Similar results were obtained from transient photopotential measurements performed in acetonitrile (Table III). Here, an initial fast decay was observed followed by a slower subsequent decay. As was also observed for experiments performed in aqueous KOH, the initial decay was found dependent upon previous semiconductor surface treatment. Also b values obtained for the slower second segment in acetonitrile were found constant and independent of previous history. In acetonitrile, the average b value was found to be 1.32×10^7 s^{-1}, while lower than values in aqueous electrolyte were in agreement with calculated b values, thereby suggesting similar barrier heights by p-InP in both electrolytes.

Conclusions

The application of laser pulse generated transient photopotentials, together with subsequent analysis of the resulting relaxation process, appears to be a useful technique for characterizing the InP/electrolyte interface. The initial fast decay that was found dependent upon previous surface treatment may be associated with recombination of initially photogenerated trapped minority carriers. The presence of trapped, charged carriers at III-V/electrolyte interfaces has been suggested in previous work (26) as one reason that a relatively large applied bias, cathodic of the flatband potential, is needed to induce hydrogen evolution.

The slower decay segment was found to possess constant b values of $\cong 2.53 \times 10^7$ ($1M$ KOH), which was in agreement with the calculated value of 1.12×10^7 s^{-1}obtained using Eq. [2]. This result suggests that the assumptions made in relationships [1] and [2] appear valid for p-InP. One of the major assumptions was that the photopotential decay was dictated by surface recombinations via a high density of surface states. The observation that b was constant for both modified and unmodified p-InP suggests that the surface states responsible for barrier height pinning, and, hence, the decay rate, may have similar origin.

Forward current measurements also suggest that the barrier height is pinned at a value independent of the previous surface modification. These results suggest that enhanced PEC hydrogen efficiency may be related to the electrocatalytic properties of deposited metals (14, 15, 27).

Acknowledgments

Funding by the Gas Research Institute under Contract no. 5083-260-0881 is gratefully acknowledged. We would also like to thank Dr. Nate Lewis for his useful comments concerning this manuscript.

Manuscript submitted Dec. 3, 1985; revised manuscript received July 14, 1986.

Eltron Research, Incorporated, assisted in meeting the publication costs of this article.

REFERENCES

1. S. P. Perone, J. H. Richardson, S. B. Deutscher, J. Rosenthale, and J. N. Ziemer, *This Journal*, **127,** 2580 (1980).
2. J. H. Richardson, S. P. Perone, and S. B. Deutscher, *J. Phys. Chem.*, **85,** 341 (1981).
3. P. V. Kamat, and M. A. Fox, *ibid.*, **87,** 59 (1983).
4. Z. Harzion, D. Huppert, S. Gottesfeld, and N. Croitoru, *J. Electroanal. Chem.*, **150,** 571 (1983).
5. W. Jaegermann, T. Sakata, E. Janata, and H. Tributsch, *ibid.*, **189,** 65 (1985).
6. S. Prybyla, W. S. Struve, and B. A. Parkinson, *This Journal*, **131,** 1587 (1984).
7. S. Gottesfeld and S. W. Feldberg, *J. Electroanal. Chem.*, **146,** 47 (1983).
8. a) D. Laser and A. Bard, *This Journal*, **123,** 1833 (1976); b) D. Laser and A. Bard, *ibid.*, **123,** 1837 (1976).
9. N. S. Lewis, R. Dominguez, C. M. Gronet, C. M. Lieber, M. D. Rosenblum, G. W. Cogan, J. F. Gibbons, and G. R. Moddel, in "Electrocatalysis," J. F. McIntyre, Editor, pp. 460-479, The Electrochemical Society Softbound Proceedings Series, Pennington, NJ (1984).
10. A. Heller, B. Miller, and F. A. Thiel, *Appl. Phys. Lett.*, **38,** 282 (1981).
11. A. Heller, W. D. Johnston, Jr., H. J. Leamy, B. Miller, and K. E. Strege, in "Proceedings of the 15th IEEE Photovoltaic Specialists Conference," Orlando, FL, May 12-15, 1981.
12. L. J. Brillson, Y. Shapira, and A. Heller, *Appl. Phys. Lett.*, **43,** 174 (1983).
13. D. N. Bose, Y. Ramprkash, and S. Basu, *This Journal*, **131,** 850 (1984).
14. E. Aharon-Shalom and A. Heller, *ibid.*, **129,** 2865 (1982).
15. P. G. P. Ang and A. F. Sammells, *ibid.*, **131,** 1462 (1984).
16. R. L. Cook, P. F. Dempsey, and A. F. Sammells, *ibid.*, **132,** 1315 (1985).
17. R. L. Cook, P. F. Dempsey, and A. F. Sammells, *ibid.*, **133,** 1821 (1986).
18. N. W. Lewis, *This Journal*, **131,** 2496 (1985).
19. A. Heller, B. Miller, H. J. Lewerenz, and K. J. Bachmann, *J. Am. Chem. Soc.*, **102,** 6555 (1980).
20. B. A. Parkinson, A. Heller, and B. Miller, *This Journal*, **126,** 954 (1979).
21. W. E. Spicer, P. W. Chye, P. R. Skeath, C. Y. Su, and I. Lindau, *J. Vac. Sci. Technol.*, **16,** 1422 (1979).
22. S. M. Sze, "Physics of Semiconductor Devices," John Wiley and Sons, New York (1981).
23. A. Guivarc'h, H. L'Haridon, G. Pelous, G. Hollinger, and P. Pertosa, *J. Appl. Phys.*, **55,** 1139 (1984).
24. L. V. Whitney, *Phys. Rev.*, **50,** 1154 (1936).
25. H. B. Wahlin, *ibid.*, **61,** 509 (1942).
26. J. J. Kelly and R. Menning, *This Journal*, **129,** 730 (1982).
27. M. Szklarszyk and J. O'M. Bockris, *J. Phys. Chem.*, **88,** 5241 (1984).

Adsorbed Species on Nickel in Electrolyte Solutions

C. J. van der Wekken

Laboratory of Metallurgy, Delft University of Technology, 2628 AL Delft, The Netherlands

ABSTRACT

From Rehbiner effects measured during creep tests on pure nickel wires in electrolyte solutions, it is concluded that, under conditions where there is no oxide or hydroxide, there is still an adsorbed species present on the "clean" metal surface. This species, probably $(NiOH)_{ads}$, is formed by strong Ni-water interactions and can be removed by electrochemical reduction at low potentials or by lowering the solution *p*H.

From creep tests on thin gold wires in various electrolyte solutions, it has been concluded that dislocations emerging at the surface of a loaded specimen can be pinned by certain chemisorbed ions or by adsorbed oxygen containing species, including OH^- -ions and water molecules (1-3).

Reference (1) describes the characteristic features of the strain responses of stressed gold wires to cathodic potential pulses, and a definition is given of the concept of "extra strain." Strong dislocation pinning due to hydroxyl ions occurs in alkaline solutions. As a result of this pinning effect by adsorbed OH^--ions, an extra strain is observed when a gold wire specimen, loaded at a potential above the pzc in an alkaline solution, is subjected to cathodic polarization below the pzc. A confirmation of the role of OH^- ions in pinning surface dislocations is found in the fact that a change in the solution *p*H, by adding acid, causes a similar extra strain effect.

Dislocation pinning by adsorbed water molecules is demonstrated in the case of gold by the extra strain effects measured when the potential is lowered into the range where the water reduction reaction can occur at an appreciable rate, which is below −1000 mV *vs.* SCE.

Unpublished work in this laboratory has shown that for silver the effects of changes in the potential on the creep rate are very similar to those observed for gold. In contrast, attempts to find Rehbinder effects using pure iron wire specimens yielded only negative results. An experimental difficulty in the case of iron was the irregular creep behavior observed for the thin wire specimens of this metal. Frequent discontinuities in the creep rate made it difficult to distinguish any possible extra strain effects due to potential changes. Effects of cathodic polarization on the creep behavior of copper have been reported in the literature (4). In the present study, it was found that the strain effects of loaded nickel specimen wires following cathodic polarization again showed characteristic features similar to those observed in the case of gold (1). The observed similarities in the creep responses to potential pulses suggests that for the fcc metals Au, Ag, Cu, and Ni the underlying mechanisms will be essentially the same. This means that surface dislocation pinning by adsorbed species on the metal surface will significantly affect the plastic deformation behavior of the surface layers of loaded specimens. In bcc crystals the Peierls Nabarro forces opposing dislocation movement in a glide plane are known to be much larger than in the fcc structure. It is therefore possible that for bcc metals, like iron, the influence of adsorbed species on the surface on the mechanical properties will not be comparable to the effects measured on fcc metals.

Nickel being a transition metal, particularly strong metal-solvent interactions at the specimen surface are expected (5). There are, in fact, reasons for doubting if a "clean" nickel surface is ever available in aqueous solutions. The values of the parameters characterizing the anodic dissolution and the cathodic metal deposition reactions of nickel (6) suggest that both reactions occur via an intermediate reaction product $(NiOH)_{ads}$, which is adsorbed on the metal surface. The nature of the interface is also expected to depend on the type of anions in the solution.

The experimental technique (1) developed on gold specimens is used in the present work in an attempt to obtain more information on the surface of nickel in electrolyte solutions under conditions where no passive or prepassive layers are present.

Experimental

Creep tests were performed using 99.998% pure nickel wire of 0.1 mm diameter, supplied by Johnson, Matthey, and Company, London. Wire specimens were annealed in vacuum for ½h at 800°C, giving an average grain size of about 0.04 mm. These specimens were mounted in the creep test apparatus described earlier (1). The experimental procedures followed for nickel were essentially similar to those used previously for gold specimens. Some extra precautions were necessary, however. The tests were performed in oxygen-free solutions. It was not possible to have the mounted wire specimens in the test solution during the period prior to the actual creep test, since this would result in corrosion of the specimen. Cathodic protection could not be applied since this could cause hydrogen embrittlement of the nickel wires. The test solutions employed were 0.1*M* K_2SO_4 and 0.1*M* KCl, prepared using reagent grade chemicals and high purity (Milli-Q) deionized water. The solutions were deaerated in a glass vessel and admitted to the cell about 10 min before the start of the creep test. High purity nitrogen was bubbled through the solution and passed through the test cell for a 24h period before and during the creep test. The solution and the test cell were both preheated to the thermostatically controlled testing temperature of 50°C. The test solution *p*H was 5 ± 0.2 unless otherwise stated.

Taking into consideration the ϵ-*p*H diagram for Ni in aqueous solutions (7), the potential of the specimens was potentiostatically controlled at −650 mV *vs.* SCE before and during loading in order to obtain a surface free of oxide or hydroxide films. The applied stress was 160 MPa. About five minutes after loading, a series of cathodic potential pulses of increasing magnitude was applied, each pulse lasting 1 min, while, during the (1 min) interval between the pulses, the potential was maintained at −650 mV. This resulted in a sequence of applied potentials as follows: −650, −850, −650, −1050, −650, −1250, −650, −1450, −650, −1650, −650, −1850, −650 mV (see Fig. 1). In agreement with the procedures used previously (1), the extra strain responses were recorded and plotted in extra strain-potential pulse (e.s.-p.p.) diagrams.

Results and Discussion

Figure 2 shows the extra strain responses [defined as in Ref. (1)] as a function of the applied potential pulses for two 0.1*M* K_2SO_4 solutions of different *p*H. Large effects are observed in the solution of *p*H = 5. The extra strains measured in an acid solution of *p*H = 1.2 are an order of magnitude smaller.

Figure 3 gives results obtained after loading in a *p*H = 5 solution and changing the *p*H to 1.2 by adding some concentrated sulfuric acid. This change in *p*H caused a large extra strain of 56×10^{-5}. The effects measured subsequently in the *p*H = 1.2 solution as a result of potential pulsing were small and comparable to those found after loading in the acid solution as shown in Fig. 2.

There is a certain analogy between the data described above and the results obtained for gold in deaerated solutions of *p*H = 10.2, where it was concluded that dislocation

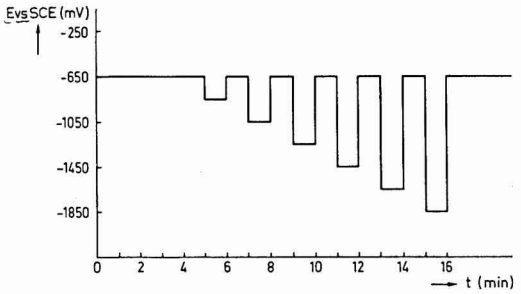

Fig. 1. The sequence of potential pulses applied to the wire specimens after loading.

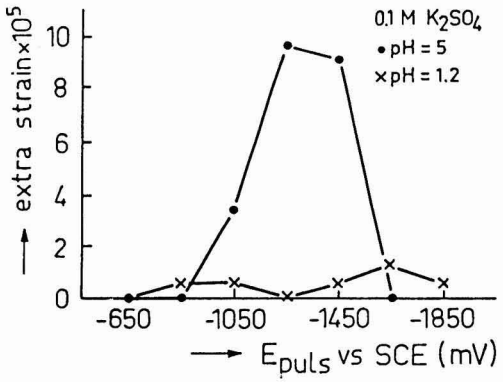

Fig. 2. The extra strains resulting from the cathodic potential pulses in 0.1*M* K_2SO_4 solutions of *p*H = 5 and *p*H = 1.2.

pinning at the gold surface by adsorbed OH^- ions was responsible. These ions have a pinning effect on dislocations emerging at the surface during loading above the pzc. Unpinning results in extra strain effects at potentials below the pzc. There are also important differences. First, in the present solution of *p*H = 5, the OH^- ion concentration is about a factor 10^5 lower. Second, the pzc values of Ni in electrolyte solutions comparable to the present one are reported (8) to be above −650 mV *vs.* SCE. For these reasons, it is very unlikely that specific adsorption of OH^- ions could play a significant role in the present tests. On the basis of the value of the pzc, specific adsorption of SO_4^{2-} or Cl^- anions can be discarded as well, since the effects measured in the present work occur at potentials up to 1000 mV below the reported pzc value.

The fact that the potential range where extra strains are observed for Ni is similar to the range associated with pinning by adsorbed water molecules in the case of gold might suggest that "water pinning" is responsible for the observed effects on Ni. It seems possible that pinning by water molecules is indeed occurring in the acid solution of *p*H = 1.2, but water pinning is not expected to show the strong dependence on the *p*H which is evident from the present data. It is, therefore, not likely to be responsible for the major effects measured in the solution of *p*H = 5.

In principle, it is conceivable that a nickel oxide or hydroxide layer on the specimen surface could account for the results given in Fig. 2 and 3. Such a layer is not stable at −650 mV *vs.* SCE in a solution of *p*H = 5 according to the ϵ-*p*H diagram for nickel (7). An oxide layer, formed during air exposure prior to the creep test, could be incompletely reduced during the period of about 10 min exposure in the test solution at −650 mV preceding the application of the load. An argument against this type of surface layer as a possible cause of the present effects is found in Fig. 4 and 5, which show the extra strains measured on wire specimens after a second test run. After having been subjected to the complete series of potential pulses up to −1850 mV,

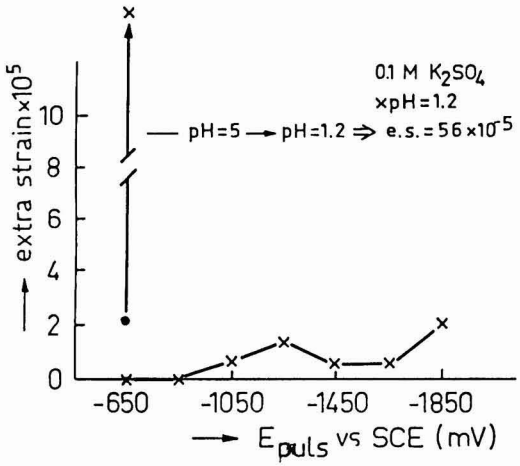

Fig. 3. The extra strain effect resulting from lowering the *p*H from 5 to 1.2 in a 0.1*M* K_2SO_4 solution, and the remaining effects observed in the solution of *p*H = 1.2 after potential pulsing.

the specimen load was increased at −650 mV and, subsequently, the extra strain-potential pulse diagram was measured again. Extra strains comparable in magnitude to those measured in the first test runs were observed. Nickel oxides and hydroxides, except those formed during strongly anodic polarization, have been found to be easily reducible electrochemically (9, 10). After a first test run involving potentials as low as −1850 mV *vs.* SCE, the specimen must therfore be considered to be free of reducible oxide or hydroxide films. Since new oxides or hydroxides are not formed at −650 mV, the second test run must be representative for a nickel surface free of oxide or hydroxide films. The similarity in the responses measured in the first and second test runs suggests that the cause of the measured effects is the same for both runs. Oxide or hydroxide films must therefore be ruled out as a likely explanation for the observed effects.

A typical difference between the extra strains measured in the 0.1*M* KCl solution (Fig. 5) and the 0.1*M* K_2SO_4 solutions is the magnitude of the extra strain response to the pulse of −850 mV, which is absent or nearly absent in the sulfate solutions, but significant in the chloride solution. This difference indicates that different species on the specimen surface are responsible for the effects observed in the two different solutions.

Having ruled out adsorbed anions, water molecules, and oxide or hydroxide films as a possible explanation, there

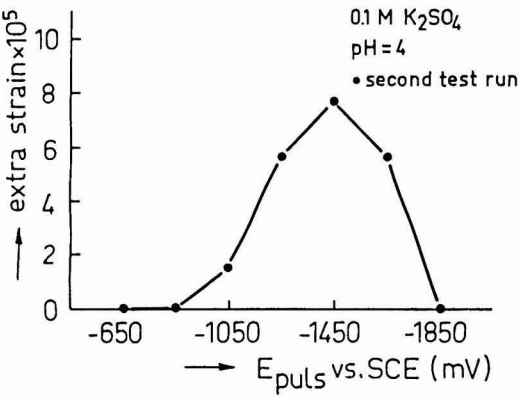

Fig. 4. The extra strain-potential pulse diagram measured in a 0.1*M* K_2SO_4 solution of *p*H = 4 during a second test run, after having increased the specimen load by 12%.

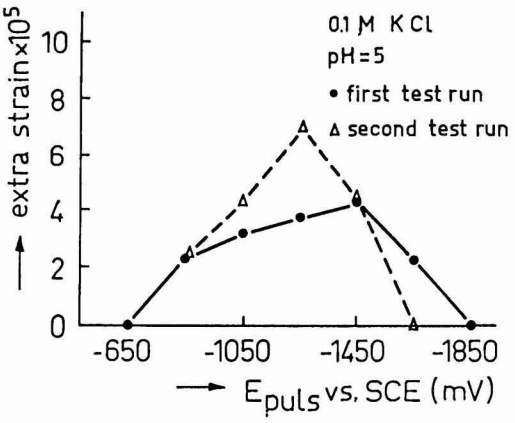

Fig. 5. The extra strain-potential pulse diagrams measured during first and second test runs in a 0.1 M KCl solution of pH = 5. For the second test run the load was increased by 25%.

remains one possibility which appears reasonable. The most likely mechanisms of anodic dissolution and cathodic deposition of nickel involve the intermediate adsorbed species $(NiOH)_{ads}$ (6). (In chloride or other complexing solutions, different mechanisms may occur.) $(NiOH)_{ads}$ is expected to form as a result of the strong interactions between nickel and water

$$Ni + H_2O \rightleftarrows (NiOH)_{ads} + H^+ + e \quad [1]$$

It may be removed from the nickel surface by cathodic polarization

$$(NiOH)_{ads} + H^+ + e \rightarrow Ni + H_2O \quad [2]$$

or

$$(NiOH)_{ads} + e \rightarrow Ni + OH^- \quad [3]$$

At constant potential $(NiOH)_{ads}$ may be removed by lowering the pH, again following reaction [2].

Our data may be compared with the findings of Bockris, Reddy, and Rao (9). These authors studied the Ni surface in a potassium sulfate solution of pH = 3.15. They observed the ellipsometric parameters to remain constant over a potential range of at least 225 mV below the potential where a prepassive oxide starts forming. This oxide was observed to form above −25 mV *vs.* NHE or −270 mV *vs.* SCE. Taking a potential dependence for the stability range of the prepassive oxide of 60 mV per pH unit, the prepassive oxide would be expected to be stable above −380 mV *vs.* SCE in a pH = 5 solution. Our tests were started after about 10 min at −650 mV *vs.* SCE. This potential is more than 250 mV below the stability range of the prepassive oxide. An oxide-free surface can be expected under these conditions. Bockris, Reddy, and Rao concluded on the basis of their ellipsometric observations, which showed that the parameters Δ and ψ remained constant between −25 and −250 mV *vs.* SHE, that the Ni surface was bare below the stability range of the oxide. Our conclusion is that an uncharged species is present on the nickel surface, which is reduced only at potentials as low as −1050 to −1650 mV *vs.* SCE in a solution of pH = 5.

Our observations may be related to a phenomenon interpreted in the literature as "hydrogen-induced" plasticity, which has been reported to occur for nickel in a hydrogen gas atmosphere (11). As a result of the introduction of H_2 gas, a large increase in the dislocation density was observed in the surface region of a thin foil mounted under a constant strain and studied by means of electron microscopy. The "hydrogen-induced" plasticity could be due to the unpinning of dislocations at the specimen surface as a result of the reduction of oxygen containing species by H atoms originating from H_2 dissociation on the nickel surface.

Conclusions

1. Extra strain effects (Rehbinder effects) have been observed to occur as a result of cathodic polarization during the creep of nickel wire specimens in sulfate and chloride solutions.

2. The most likely interpretation of the observed effects in sulfate solutions is that surface dislocation pinning occurs by $(NiOH)_{ads}$, which is present on the oxide-free nickel surface as a result of the strong interaction between Ni and H_2O.

3. In a solution of pH = 5, the adsorbed species $(NiOH)_{ads}$ can be reduced electrochemically at potentials around −1250 mV *vs.* SCE. At −650 mV, it is possible to remove the dislocation pinning caused by $(NiOH)_{ads}$ by lowering the solution pH.

4. The phenomenon known in the literature as "hydrogen-induced" plasticity, which has been reported to occur in strained nickel specimens following exposure to hydrogen gas, may be due to the reduction of adsorbed oxygen containing species by H atoms resulting from the dissociation of hydrogen on the nickel surface.

Manuscript submitted July 1, 1985; revised manuscript received March 18, 1986.

Delft University of Technology assisted in meeting the publication costs of this article.

REFERENCES

1. C. J. van der Wekken, *This Journal*, **129,** 706 (1982).
2. C. J. van der Wekken, p. 28, Extended Abstracts 33rd ISE Meeting, M. Costa, Editor, ISE Lyon (1982).
3. C. J. van der Wekken, *This Journal*, **131,** 2481 (1984).
4. R. W. Revie and H. H. Uhlig, *Acta Metall.*, **22,** 619 (1974).
5. S. Trasatti, in "Modern Aspects of Electrochemistry," Vol. 13, B. E. Conway and J. O'M. Bockris, Editors, p. 81, Plenum Press, New York (1979).
6. A. J. Arvia and D. Posadas, in "Encyclopedia of Electrochemistry of the Elements," Vol. III, A. J. Bard, Editor, p. 304, Marcel Dekker, Inc., New York (1975).
7. M. Pourbaix, "Atlas of Electrochemical Equilibria in Aqueous Solutions," Pergamon-CEBELCOR, Brussels (1966).
8. V. L. Kheifets and B. S. Krasilov, *Zh. Fiz. Khim.*, **31,** 1992 (1957).
9. J. O'M. Bockris, A. K. N. Reddy, and B. Rao, *This Journal*, **113,** 1133 (1966).
10. B. MacDougall and M. Cohen, *ibid.*, **121,** 1152 (1974).
11. J. Eastman, T. Matsumoto, N. Narita, F. Heubaum, and H. K. Birnbaum, in "Hydrogen Effects in Metals," I. M. Bernstein and A. W. Thompson, Editors, p. 397, The Metallurgical Society of AIME (1981).

Precipitation of Solids in Electrochemical Cells

Keh-Chang Tsaur* and Richard Pollard*

Department of Chemical Engineering, University of Houston, Houston, Texas 77004

ABSTRACT

A mathematical model is developed for an electrochemical cell in which a sparingly soluble product of an electrochemical reaction is precipitated. This model considers the time dependence and the position dependence of the system behavior and includes the interactions between multicomponent transport of electrolyte species in porous media and simultaneous chemical and electrochemical reaction kinetics. The model predicts that cell performance is sensitive to the magnitude of the effective rate constant for precipitation as a result of kinetic, thermodynamic, and morphological effects. In addition, the analysis indicates that local mass transport of the soluble reaction product between the electrode surface and the bulk electrolyte within a pore can influence cell behavior significantly but that redistribution of the dissolved species across a cell is usually unimportant. The calculations also suggest that a local voltage minimum can be obtained during discharge of a cell, depending on the relative rates of nucleation and growth of the solid product. Quantitative information on the precipitation of LiCl in a Li/$SOCl_2$ static cell with acidic electrolyte is presented. As part of the analysis for this system, a consistent set of transport equations is developed for a concentrated mixture of two binary electrolytes in two neutral solvents.

Many electrochemical cells have solid reaction products, and these can significantly affect system performance. In the lead-acid battery, the nucleation and growth of $PbSO_4$ crystals can influence the shape of the discharge curve (1, 2). Similarly, voltage minima in MnO_2, TiO_2, and Tl_2O_3 electrodes have been attributed to nucleation effects (2, 3). For zinc electrodes with alkali electrolytes, theoretical calculations have suggested that transport of a soluble zincate ion intermediate can influence the distribution of the ZnO precipitate (4). Also, it has been shown that dissolution-precipitation phenomena are important in Ag/AgCl and Cd/$Cd(OH)_2$ couples and that these electrodes can fail by plugging of pores with reaction products (5). Furthermore, in the lithium, thionyl chloride cell with $LiAlCl_4$, $AlCl_3$ electrolyte, the front face of the porous carbon cathode becomes plugged with LiCl crystals and this terminates the discharge (6-8).

An analysis of porous electrodes with sparingly soluble reactants has indicated that dissolution and diffusion of an active species should be fast enough to avoid significant mass transport limitations but not too fast to incur self-discharge problems (9). However, for cells with reaction products that are deposited from the electrolyte, the dependence of cell performance on nucleation and growth of a solid product has not been determined. In this paper, the influence of these factors on the quantitative behavior of the lithium, thionyl chloride primary cell is used to illustrate the effects that can be expected in general. Changes in cell voltage and lifetime are elucidated as well as the importance of operating conditions, species redistribution, crystallization rate constants, local transport phenomena, and the magnitude of the solubility product. Physical explanations are provided for the effects predicted by the model. Also, the results for the Li/$SOCl_2$ system are related to trends in behavior for other cells that involve precipitation of a sparingly soluble reaction product. In this way, general conclusions are reached concerning the influence of precipitation rate constants and associated electrolyte properties on cell discharge characteristics.

The theoretical analysis for the Li/$SOCl_2$ cell is based on a previous treatment (7, 8) which did not consider the precipitation process but, rather, assumed that the LiCl crystals were a direct product of the electrochemical reaction. The model presented here regards chloride ions as a reaction product, and includes the possibility for these ions to be transported away from the reaction site in the electrolyte. Precipitation of LiCl is treated as a separate step. Additional physical phenomena described by the model are multiple electrochemical reactions, simultaneous chemical reactions, changes in porosity and electrolyte composition, ohmic potential drop and diffusion potential in the electrolyte, ohmic potential drop in the matrix, and cell temperature variations. Variable physical properties are used in the calculations wherever experimental information is available. As part of the analysis, a consistent set of transport equations is developed for a concentrated mixture of two binary electrolytes in two neutral solvents. These equations can be used to describe the behavior of many different electrochemical cells.

*Electrochemical Society Active Member.

Model Development

A one-dimensional model is presented for a prismatic lithium, thionyl chloride cell. The cell consists of a lithium sheet negative electrode, a LiCl film adjacent to the lithium, a porous separator, a reservoir of electrolyte, and a porous carbon cathode. Current collectors are located at the back of each electrode. [A schematic diagram of the system is presented in Ref. (7)]. The kinetic relationships and transport equations used to predict the discharge behavior of the cell are described below.

Cell reactions.—The complicated processes in the positive electrode are represented by two simultaneous reactions

$$2AlCl_3 + SOCl_2 + 2e^- \rightleftarrows 2AlCl_4^- + \tfrac{1}{2}SO_2 + \tfrac{1}{2}S \quad [I]$$

$$SOCl_2 + 2e^- \rightleftarrows 2Cl^- + \tfrac{1}{2}SO_2 + \tfrac{1}{2}S \quad [II]$$

In the presence of lithium ions, Cl^- ions produced by reaction [II] can precipitate to form solid LiCl crystals

$$Li^+ + Cl^- \rightleftarrows LiCl(s) \quad [III]$$

Reactions [II] and [III] replace the reaction

$$2Li^+ + SOCl_2 + 2e^- \rightleftarrows 2LiCl(s) + \tfrac{1}{2}SO_2 + \tfrac{1}{2}S$$

considered previously (7), in which solid LiCl is regarded as a direct product of the electrochemical reaction.

In the negative electrode, the overall discharge reaction is

$$Li \rightleftarrows Li^+ + e^- \quad [IV]$$

A protective film over the lithium can be formed by reaction [III] and by a reaction between Li and the solvent according to (10)

$$2Li + SOCl_2 \rightarrow 2LiCl(s) + \tfrac{1}{2}SO_2 + \tfrac{1}{2}S \quad [V]$$

Solid lithium chloride at either electrode can be dissolved chemically by the acid

$$LiCl(s) + AlCl_3 \rightarrow Li^+ + AlCl_4^- \quad [VI]$$

Rate expressions.—For electrochemical reactions at the cathode, the Butler-Volmer equation

$$ai_{nj} = ai_{oj}[e^{\alpha_{aj}F\eta_{sj}/RT} - e^{-\alpha_{cj}F\eta_{sj}/RT}] \quad [1]$$

is used to relate the local current density i_{nj} due to reaction j to the surface overpotential, $\eta_{sj} = \eta - U_{j,w}$, where the theoretical open-circuit potential for reaction j is expressed as

$$U_{j,w} = U_j^{\theta} - U_{re}^{\theta} + \frac{RT}{n_{re}\mathbf{F}} \sum_i s_{i,re} \ln\left(\frac{c_{i,re}}{\rho_o}\right) - \frac{RT}{n_j\mathbf{F}} \sum_i s_{i,j} \ln\left(\frac{c_{i,w}}{\rho_o}\right) \quad [2]$$

The exchange current density i_{oj} in Eq. [1] is written as

$$i_{oj} = i_{oj,ref} \prod_i (c_{i,w}/c_{i,ref})^{\gamma_{ij}} \quad [3]$$

where the product sign ranges over ionic species in the electrolyte. The exponent γ_{ij} is given by $\alpha_{cj}\, s_{i,j}/n_j$ for $s_{i,j} > 0$ and by $-\alpha_{aj}\, s_{i,j}/n_j$ for $s_{i,j} < 0$, where $s_{i,j}$ is the stoichiometric coefficient for species i in an electrode reaction j described by

$$\sum_i s_{i,j} M_i^{z_i} = n_j e^- \quad [4]$$

Equations [1]-[4] are appropriate for many electrochemical systems, but they assume implicitly that the electrode reactions are reversible. If reactions [I] and [II] are irreversible, $U_{j,w}$ and i_{oj} could correspond to corrosion potentials and corrosion currents and, as a result, their composition dependences may need to be modified. The effects of changes in Eq. [2] and [3] are considered later in the paper. It is also noted that, for irreversible reactions, Tafel kinetics may be more appropriate than Eq. [1]. However, it has been established previously (7) that the exact form of the polarization relation does not influence any of the predicted trends in behavior. For this reason, the general rate expression, Eq. [1], is used in this study.

The electrode wall concentration $c_{i,w}$ in Eq. [2] and [3] is related to the corresponding concentration c_i in the bulk of a pore by

$$-\sum_j \frac{s_{i,j}}{n_j\mathbf{F}}\, a i_{nj} = a k_i (c_{i,w} - c_i) \quad [5]$$

This relation can be regarded as a local pseudosteady-state balance between material produced at the electrode surface and material transported from the wall region to the bulk electrolyte. In principle, Eq. [5] can be written for each species in the electrolyte. However, preliminary computer calculations showed that the difference between $c_{i,w}$ and c_i can only be important if c_i is small. Hence, local mass transport can be neglected for Li^+, $AlCl_4^-$, and $SOCl_2$. The effect is also negligible for $AlCl_3$ because, when c_{AlCl_3} becomes small, reaction [II] dominates and the acid that remains does not influence cell behavior significantly (8). For these reasons, it is only necessary to use Eq. [5] for Cl^- ions. The quantity a in Eq. [1] and [5] is the effective local surface area per unit volume of the electrode. An empirical expression

$$a = a^o\left[1 - \left(\frac{\epsilon_{LiCl}}{\epsilon_p{}^o}\right)^p\right] \quad [6]$$

is used to describe the reduction in the interfacial area for electrochemical reactions that occurs during discharge due to precipitation of LiCl over the cathode surface. The magnitude of the exponent p reflects the morphology of the LiCl crystals (5). This treatment assumes implicitly that carbon surfaces covered by LiCl are passivated and can no longer act as sites for reactions [I] or [II].

The precipitation rate in the positive electrode is given by

$$r_{III} = k_T[(c_{Li^+})(c_{Cl^-}) - K_{sp}] \quad [7]$$

where K_{sp} is the solubility product for LiCl in the electrolyte. The driving force term in Eq. [7] implies that the precipitation process is kinetically controlled, although this term would be similar even if another physical factor was dominant (11). The precipitation parameter k_T is evaluated using

$$k_T = k_{III,N} + (\epsilon_{LiCl})^m k_{III,G} \quad [8]$$

where $k_{III,N}$ and $k_{III,G}$ are rate constants for nucleation and growth that include the effects of mass transfer from the bulk solution in the pores to the surface of the crystals. At the beginning of discharge, the volume fraction ϵ_{LiCl} of LiCl in the cathode is zero, and it is necessary to nucleate crystals. Subsequently, growth of existing crystals and formation of new nuclei can take place simultaneously. The growth rate is expected to be directly related to the interfacial area of crystals in contact with the electrolyte. This area is assumed to be proportional to $(\epsilon_{LiCl})^m$ where m is a morphological parameter analogous to the exponent p in Eq. [6]. Values for m and p are not necessarily the same because the influence of morphology on precipitation and on electrochemical reactions may be different. Precipitation in the separator is not considered in the analysis, because LiCl crystals have not been observed in that location (12).

It is noted that, in general, Eq. [7] should use species concentrations evaluated at the crystal surface. However, elimination of surface concentrations by considering transport from the bulk to the surface tends to give expressions for r_{III} and k_T with the same form as Eq. [7] and [8]. Consequently, $k_{III,N}$ and $k_{III,G}$ account for the combined effects of local diffusion and nucleation and growth phenomena.

The rate of LiCl dissolution is assumed to be proportional to the local acid concentration and to the interfacial area of LiCl in the electrolyte, *i.e.*

$$r_{VI} = k_{VI} c_{AlCl_3} (\epsilon_{LiCl})^m \quad [9]$$

At the anode, the rate expressions are modified to reflect the planar nature of the electrode and the presence of a film of LiCl over the lithium (7, 8). The potential change across the Li/LiCl interface is determined directly from Eq. [1] because there is only one electrode reaction and, hence, i_{nIV} can be replaced with the superficial current density I. Also, i_{oIV} is assumed to be a constant. The voltage drop across the LiCl film is obtained from Ohm's law using a characteristic film conductivity and the film thickness δ_f. Changes in the thickness are dependent on the rates of chemical reactions [III], [V], and [VI], in accordance with

$$\frac{d\delta_f}{dt} = \sum_{\substack{\text{chemical} \\ \text{reactions},k}} s_{LiCl,k} r_k' \bar{V}_{LiCl} \quad [10]$$

The reaction rate r_{III}' per unit cross-sectional area of the electrode is expressed as

$$r_{III}' = k_T'[(c_{Li^+})_b (c_{Cl^-})_b - K_{sp}] \quad [11]$$

where b indicates the film-solution interface. The surface area available for growth of the film is taken to be constant.

For reaction [V], it is assumed that the reaction rate at a given time is equal to the prevailing flux of $SOCl_2$ through the film to the lithium surface. If convection of $SOCl_2$ in the film is neglected, and if film properties are constant, the rate equation can be written as

$$r_v' = N_o' = k_v'[(c_{SOCl_2})_b - (c_{SOCl_2})_a] \quad [12]$$

where k'_v is an effective mass transfer coefficient and subscript a represents the electrode/film interface. Reaction [V] is expected to be very fast and, therefore, $(c_{SOCl_2})_a$ is taken to be zero.

The rate of reaction [VI] at the anode is given by

$$r_{VI}' = k_{VI}'(c_{AlCl_3})_b \quad [13]$$

This expression is similar to Eq. [9], but the surface area at which dissolution can occur is assumed to be constant.

Transport equations.—The equations for the porous cathode and separator are based on the macroscopic theory of porous electrodes in which the solution and matrix phases are treated as superposed continua (13). With this approach, a material balance relation for species i can be expressed as

$$\frac{\partial(\epsilon c_i)}{\partial t} = a j_{in} - \nabla \cdot N_i \quad [14]$$

where the superficial transfer rate aj_{in} of species i from the solid phases to the pore solution is related to the chemical and electrochemical reaction rates by (8)

$$aj_{in} = \sum_k s_{i,k} r_k - \sum_j \frac{s_{i,j}}{n_j \mathbf{F}} a i_{nj} \quad [15]$$

The electrolyte is regarded as a concentrated mixture of Li^+ ions, $AlCl_4^-$ ions, and Cl^- ions in $AlCl_3$ and $SOCl_2$ (species 1, 2, 3, 4, and 0, respectively). Chloride ions are included in the concentrated solution analysis for the sake of generality and because c_{Cl^-} could be large if the precipitation rate is low. The reaction products S and SO_2 are not considered in the equations because their presence in the electrolyte does not change c_o significantly, even at the end of discharge, and because they usually do not interfere with the discharge process (14). Inversion of the multicomponent diffusion equations yields explicit relationships for the fluxes

$$N_2 = -\epsilon^q \nu_2^A (D_{AA} \nabla c_A + D_{AB} \nabla c_B + D_{A4} \nabla c_4) + \frac{t_2^\bullet i_2}{z_2 \mathbf{F}} + \nu_2^A c_A v^\bullet \quad [16]$$

$$N_3 = -\epsilon^q \nu_3^B (D_{BA} \nabla c_A + D_{BB} \nabla c_B + D_{B4} \nabla c_4) + \frac{t_3^\bullet i_2}{z_3 \mathbf{F}} + \nu_3^B c_B v^\bullet \quad [17]$$

$$N_4 = -\epsilon^q (D_{4A} \nabla c_A + D_{4B} \nabla c_B + D_{44} \nabla c_4) + \frac{t_4^\bullet i_2}{\mathbf{F}} + c_4 v^\bullet \quad [18]$$

$$N_o = -\epsilon^q (D_{oA} \nabla c_A + D_{oB} \nabla c_B + D_{o4} \nabla c_4) + \frac{t_o^\bullet i_2}{\mathbf{F}} + c_o v^\bullet \quad [19]$$

The derivation of these equations is presented in the Appendix together with fundamental relationships for the transport properties. The symbols A and B refer to the salts $LiAlCl_4$ and LiCl, respectively. The terms ν_i^k are stoichiometries for dissociation of the individual salts, as described by

$$M_A = \nu_1^A M_1^{z_1} + \nu_2^A M_2^{z_2}$$
$$M_B = \nu_1^B M_1^{z_1} + \nu_3^B M_3^{z_3} \quad [20]$$

where the charge number z_i is related to stoichiometry by $\sum_i z_i \nu_i^k = 0$. It is also noted that an expression for N_1 is not given above because it can be obtained directly from

$$i_2 = \mathbf{F} \sum_i z_i N_i \quad [21]$$

Substitution of Eq. [16]-[19] into Eq. [14] and rearrangement using Eq. [A-2] and [A-3] gives an overall conservation equation

$$\frac{\partial \epsilon}{\partial t} + \nabla \cdot v^\bullet = a\left[\frac{\bar{V}_A}{\nu_2^A} j_{2n} + \frac{\bar{V}_B}{\nu_3^B} j_{3n} + \bar{V}_4 j_{4n} + \bar{V}_o j_{on}\right] - \frac{\nabla \cdot i_2}{\mathbf{F}}\left[\frac{\bar{V}_A t_2^\bullet}{\nu_2^A z_2} + \frac{\bar{V}_B t_3^\bullet}{\nu_3^B z_3} + \bar{V}_4 t_4^\bullet + \bar{V}_o t_o^\bullet\right] - \frac{i_2 \cdot}{\mathbf{F}}\left[\frac{\bar{V}_A \nabla t_2^\bullet}{\nu_2^A z_2} + \frac{\bar{V}_B \nabla t_3^\bullet}{\nu_3^B z_3} + \bar{V}_4 \nabla t_4^\bullet + \bar{V}_o \nabla t_o^\bullet\right] - \epsilon^q \nabla c_A \cdot (D_{AA} \nabla \bar{V}_A + D_{BA} \nabla \bar{V}_B + D_{4A} \nabla \bar{V}_4 - D_{oA} \nabla \bar{V}_o) - \epsilon^q \nabla c_B \cdot (D_{AB} \nabla \bar{V}_A + D_{BB} \nabla \bar{V}_B + D_{4B} \nabla \bar{V}_4 - D_{oB} \nabla \bar{V}_o) - \epsilon^q \nabla c_4 \cdot (D_{A4} \nabla \bar{V}_A + D_{B4} \nabla \bar{V}_B + D_{44} \nabla \bar{V}_4 - D_{o4} \nabla \bar{V}_o) \quad [22]$$

A volume balance

$$\frac{\partial \epsilon}{\partial t} = \sum_{\substack{\text{solid} \\ \text{phases}}} \left(\sum_j \frac{s_{i,j} \tilde{V}_i}{n_j \mathbf{F}} a i_{nj} - \sum_k s_{i,k} \tilde{V}_i r_k\right) \quad [23]$$

for the solid phases is used to indicate how electrode porosity changes as a result of chemical and electrochemical reaction rates. Combination of Eq. [22] and [23], with the assumption of constant partial molar volumes and transference numbers, gives an explicit relationship for the reference velocity

$$\nabla \cdot v^\bullet = a\left[\frac{\bar{V}_A}{\nu_2^A} j_{2n} + \frac{\bar{V}_B}{\nu_3^B} j_{3n} + \bar{V}_4 j_{4n} + \bar{V}_o j_{on}\right] - \frac{\nabla \cdot i_2}{\mathbf{F}}\left[\frac{\bar{V}_A t_2^\bullet}{\nu_2^A z_2} + \frac{\bar{V}_B t_3^\bullet}{\nu_3^B z_3} + \bar{V}_4 t_4^\bullet + \bar{V}_o t_o^\bullet\right] - \sum_{\substack{\text{solid} \\ \text{phases}}} \left(\sum_j \frac{s_{i,j} \tilde{V}_i}{n_j \mathbf{F}} a i_{nj} - \sum_k s_{i,k} \tilde{V}_i r_k\right) \quad [24]$$

The current density i_2 in the solution phase that appears in Eq. [24] is given by

$$\nabla \cdot i_2 = \sum_j a i_{nj} \quad [25]$$

This equation states that the transfer current per unit electrode volume is equivalent to the sum of the electrochemical reaction rates.

The movement of electrons in the matrix phase is governed by Ohm's law

$$i_1 = -\sigma \nabla \Phi_1 \quad [26]$$

where σ is the effective matrix conductivity given by $\sigma_\infty (1 - \epsilon)^q$. The relationship between the solution potential Φ_2 and the current density in the solution phase is derived by inversion of the multicomponent diffusion equation (15). For the $LiAlCl_4$, LiCl, $AlCl_3$, $SOCl_2$ electrolyte, one obtains a modified form of Ohm's law

$$\frac{i_2}{\kappa_\infty \epsilon^q} = -\nabla \Phi_2 - W \quad [27]$$

where

$$W = \frac{\nu^A RT}{c_A n \mathbf{F}}\left(\frac{s_2}{\nu_2^A} + \frac{n t_2^\bullet}{z_2 \nu_2^A} - \frac{s_o}{c_o} c_A\right) \nabla c_A + \frac{\nu^B RT}{c_B n \mathbf{F}}\left(\frac{s_3}{\nu_3^B} + \frac{n t_3^\bullet}{z_3 \nu_3^B} - \frac{s_o}{c_o} c_B\right) \nabla c_B + \frac{RT}{c_4 n \mathbf{F}}\left(s_4 + n t_4^\bullet - \frac{s_o}{c_o} c_4\right) \nabla c_4 \quad [28]$$

provided that activity coefficients are taken to be constant. The potential in Eq. [27] is measured relative to a reference electrode at which n electrons are transferred and s_i is the stoichiometric coefficient for species i. Combination of Eq. [26], Eq. [27], and the condition $i_1 + i_2 = I$, yields an expression

$$\nabla \eta = \left(\frac{1}{\kappa_\infty \epsilon^q} + \frac{1}{\sigma}\right) i_2 - \frac{I}{\sigma} + W \quad [29]$$

for the variation of the potential difference, $\eta = \Phi_1 - \Phi_2$, between the matrix phase and the electrolyte.

Changes in cell temperature are determined from

$$C \frac{dT}{dt} = \left[\sum_j \left(U_{oj} - T_o \frac{\partial U_{oj}}{\partial T}\right) \int_0^{L_p} \frac{(-a i_{nj})}{I} dy - V\right] I - h_o (T - T_A) + \Delta H_{R,III}\left(r_{III}' + \int_0^{L_p} r_{III} dy\right) + \Delta H_{R,V} r_V + \Delta H_{R,VI}\left(r_{VI}' + \int_0^{L_p} r_{VI} dy\right) \quad [30]$$

This equation is based on the first law of thermodynamics and includes the heat generated by chemical reactions, as well as reversible heat effects, Joule heating, overpotentials associated with electrode reactions, and heat transfer to the environment. The total voltage in Eq. [30] is obtained by integration of matrix and electrolyte potential gradients across the cell (16).

The lithium, thionyl chloride system can be described by 10 variables and their governing equations. For an electrolyte with five species, three concentrations (say, c_2, c_3, and c_4) are independent; the other two compositions can be eliminated using the relation $\sum_i c_i \bar{V}_i = 1$ and the constraint of electroneutrality, $\sum_i z_i c_i = 0$. Consequently, the system variables are i_{nI}, i_{nII}, $c_{3,w}$, c_2, c_3, c_4, ϵ, v^*, i_2, and η and the corresponding equations are two Eq. [1], Eq. [5], three Eq. [14], Eq. [23], Eq. [24], Eq. [25], and Eq. [29]. The boundary conditions and initial conditions for these equations have been described in detail previously (7), and they are not repeated here. The set of equations are cast into finite difference form accurate to $O(h^2)$ and are solved simultaneously by a numerical technique (17). Each time-dependent equation is programmed between the old time and the present time with a ratio of old:new = 2:3 in order to attain stability.

Results and Discussion

Concentration profiles for chloride ions at several stages of a galvanostatic discharge are presented in Fig. 1. Initially, only reaction [I] occurs at the cathode and chloride ions are not produced. At 50s, reaction [II] has just begun, and the nonuniform distribution of this reaction gives a maximum in the composition profile at the front face of the electrode. Subsequent profiles, and the overall levels of chloride ions, are sensitive to the relative rates of Cl^- ion production (reaction [II]) and consumption (reaction [III]). The values of the rate constants $k_{III,N}$ and $k_{III,G}$ in Eq. [8] are particularly important. In the example shown, $k_{III,N}$ is relatively small, and, therefore, a large driving force is needed before precipitation can begin. For this reason, the supersaturation level rises substantially before the precipitation rate becomes significant. The small time period (from 50 to 52s) required for the concentration buildup emphasizes that large quantities of Cl^- ions are generated quickly by reaction [II] at the operating current density.

As the amount of LiCl deposited locally increases, the second term in the expression (Eq. [8]) for the effective precipitation rate constant becomes more important. With the large value for $k_{III,G}$ considered in Fig. 1, the magnitude of k_T rises rapidly and, hence, more LiCl is deposited and c_{Cl^-} is reduced. Approximately 25s after the initiation of reaction [II] ($t \approx 75$s), a balance is established between the local rates of production and consumption and the chloride ion concentration no longer changes significantly with time.

Figure 1 also shows that the chloride ion concentration at the negative electrode/separator interface remains at a relatively low value during the discharge. This can be attributed to moderately fast precipitation at this location. Furthermore, the diagram shows that a large driving force for crystallization can exist within the separator. Therefore, the absence of crystals in this region in practical cells (12) suggests that the characteristic nucleation rate constant for the separator is very small.

The trends in behavior with other values of $k_{III,N}$ and $k_{III,G}$ are similar to those shown in Fig. 1, but the concentration changes are not always so dramatic. With $k_{III,N}$ and $k_{III,G}$ both equal to 10^6 cm^3/mol · s, the concentrations for $t < 52$s are the same as those in Fig. 1. Subsequently, however, c_{Cl^-} increases slowly until the end of discharge. With a $k_{III,G}$ value of 10^{15} cm^3/mol · s and $k_{III,N}$ equal to 10^6 cm^3/mol · s, only a very small rise in chloride ion level at the beginning of reaction [II] is observed because k_T quickly becomes large. In this case, a low degree of supersaturation is maintained throughout the discharge.

Different levels of chloride ion concentration (caused by different values for the precipitation rate constants) can alter the shape of the discharge curve. Figure 2 shows predicted results for four different sets of rate constants. In each case, the hump at the beginning of discharge corresponds to reaction [I], which is unaffected by chloride ion concentration. It should be noted that the initial voltage delay shown in Fig. 2 is larger than delays predicted previously (8). The cause of the delay is the same in both cases but, for the cell in Fig. 2, the electrolyte concentration is smaller, leading to a greater initial increase in κ and, hence, a larger initial reduction in the cell resistance.

The triangle in Fig. 2 indicates the time at which the potential difference driving force at the front of the cathode is large enough to initiate reaction [II]. After this time, the behavior is dependent on the precipitation rate. The rapid changes in cell voltage that are predicted under some conditions (see curves b, c, and d) can be directly related to the concentration changes illustrated in Fig. 1. This is because the chloride ion concentration appears in the expression for the theoretical open-circuit potential (see Eq. [2])

$$U_{II,w} = U_{II}^{\theta} - U_{IV}^{\theta} - \frac{RT}{\mathbf{F}} \ln\left[(c_{Li^+,w})(c_{Cl^-,w})/(\rho_o{}^3 c_{SOCl_2,w})^{1/2}\right] \quad [31]$$

The voltage minimum for curve b at 52s corresponds exactly to the maximum chloride ion level (see Fig. 1). In

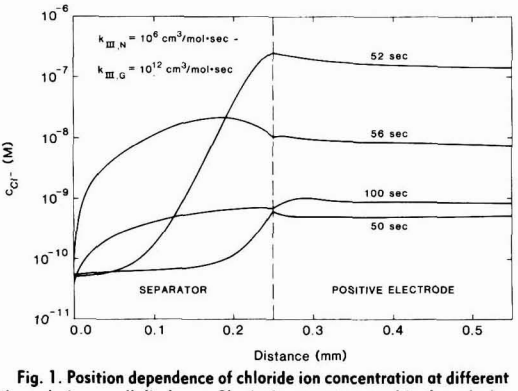

Fig. 1. Position dependence of chloride ion concentration at different times during a cell discharge. Physical parameters used in the calculations are given in Table I and cell specifications are listed in Table II. In this diagram, local mass transport of chloride ions within the pores is neglected, *i.e.*, $k_{Cl^-} = \infty$ and $c_{Cl^-,w} = c_{Cl^-}$.

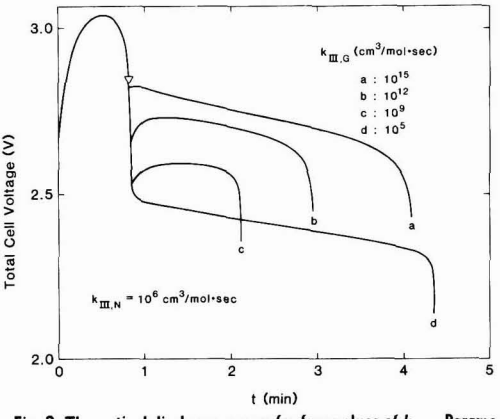

Fig. 2. Theoretical discharge curves for four values of $k_{III,G}$. Parameters are as in Fig. 1. Symbol ∇ indicates the initiation of reaction [II]. Note that, for the discharge rate considered here, a time of 4 min corresponds to a thionyl chloride utilization of 13.9%.

case d, the voltage drops substantially, but there is no voltage minimum because the concentration of chloride ions continues to rise throughout the discharge. Local voltage minima have been observed in other cells under certain operating conditions. Examples include the lead-acid system (1, 2) and electrodes of MnO_2, TiO_2, and Tl_2O_3 (2, 3). The results obtained here suggest that the minima may be due to changes in supersaturation level associated with relatively slow nucleation rates ($k_{III,N} << k_{III,G}$).

For the $Li/SOCl_2$ cell described above, changes in Cl^- ion concentration level after $t \simeq 75$s are too small to alter the cell voltage appreciably; at this stage, ohmic losses in the separator and in the LiCl film at the anode control the slopes of the discharge curves. The sharp reduction in voltage that causes cell failure is due to plugging of the pores at the front face of the positive electrode with LiCl crystals (7).

The results in Fig. 2 indicate that the cell lifetime is sensitive to the magnitude of $k_{III,G}$. Interpretation of this effect requires detailed information on the importance of the chloride ion concentration level in the system. The chloride ion is an intermediate species; its concentration influences and is influenced by the rates of reactions [II] and [III]. In general, the concentration is a function of both position across the cell and time. However, the supersaturation level is predicted to be relatively constant across the positive electrode, as illustrated in Fig. 1. Also, this level does not change appreciably shortly after reaction [II] begins (see above). Therefore, the overall effect of $k_{III,G}$ on the concentration level can be represented by c_{Cl^-} at one particular location and time (see Fig. 3). With high $k_{III,G}$ (*e.g.*, case a from Fig. 2), the level of supersaturation is very low, and an asymptote corresponding to fast precipitation is obtained. As $k_{III,G}$ is reduced, the chloride ion level in the electrolyte increases markedly. When $k_{III,G}$ is less than $k_{III,N}$ (*e.g.*, case d), the concentration is dictated by $k_{III,N}$; the larger $k_{III,N}$, the greater the quantity of LiCl precipitated by nucleation and, hence, the lower the chloride ion level.

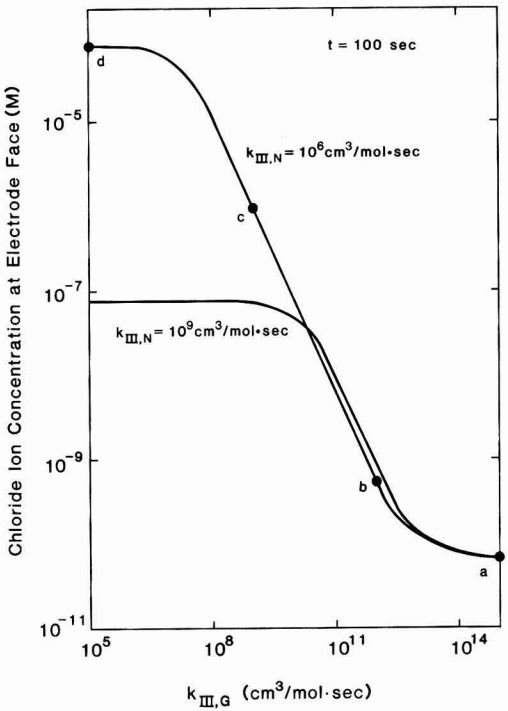

Fig. 3. Dependence of chloride ion concentration at the reservoir/positive electrode interface at t = 100s on $k_{III,N}$ and $k_{III,G}$. Parameters are as in Fig. 1. Symbols a, b, c, and d represent the cases shown in Fig. 2.

The relatively high concentrations on the left-hand side of Fig. 3 suggest that there might be significant redistribution of chloride ions across the cell. However, even with concentrations as high as $10^{-2}M$, this is not the case because: (*i*) the hold-up of chloride ions in the electrolyte is always small compared to the quantity of LiCl deposited (*e.g.*, with $c_{Cl^-} \simeq 5 \times 10^{-3}M$, 99% of the Cl^- ions produced are precipitated and with $c_{Cl^-} \simeq 3 \times 10^{-2}M$, 97% are precipitated), and (*ii*) composition gradient driving forces are too small for significant diffusion of Cl^- ions through the electrode or separator (*e.g.*, with $c_{Cl^-} \simeq 3 \times 10^{-2}M$, less than 2% of the Cl^- ions produced at any location diffuse away from the local reaction sites). Theoretical discharges were repeated with D_{BR} increased by an order of magnitude but, even at the highest Cl^- ion concentrations, redistribution was still negligible.

Redistribution is also expected to be unimportant in other cells with solid reaction products because similarities in the solubility products (*e.g.*, for $PbSO_4$, $Ni(OH)_2$, $Cd(OH)_2$, and $Fe(OH)_2$) (1, 30) indicate that concentrations, and hence concentration gradients, will be similar to those predicted for the $Li/SOCl_2$ system. In contrast, if very high concentrations ($O(10^{-1}M)$) of zincate ions are obtained in the zinc electrode, substantial redistribution may occur (4).

In the absence of redistribution, chloride ions produced locally by reaction [II] are precipitated in the same location by reaction [III]. Therefore, the distributions of the electrochemical reaction and the solid LiCl volume fraction correspond directly. It has been established previously (7) that cell lifetime for the $Li/SOCl_2$ system is directly related to the distribution of LiCl crystals; the more uniform the distribution, the longer the cell can operate before plugging of the pores occurs at the front face of the electrode. Therefore, t_{cell} is determined primarily by the distribution of electrochemical reaction [II]. This distribution is influenced by $k_{III,N}$ and $k_{III,G}$ (see Fig. 4) since these parameters alter the chloride ion concentration. The interactions between concentration and the rate of reaction [II] are described below.

1. The effective exchange current density i_{oII} depends on chloride ion concentration in accordance with Eq. [3]

$$i_{oII} = i_{oII,ref}(c_{Cl^-,w}/c_{Cl^-,ref})^{\alpha_{cII}}(c_{SOCl_2,w}/c_{SOCl_2,ref})^{\alpha_{aII}/2} \quad [32]$$

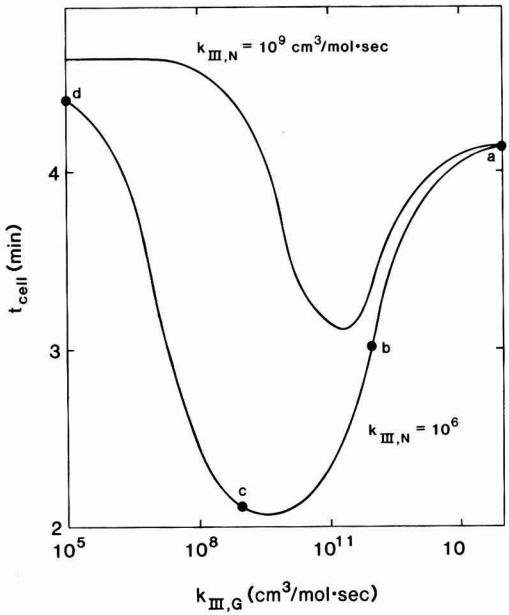

Fig. 4. Dependence of cell lifetime on $k_{III,N}$ and $k_{III,G}$. Parameters are as in Fig. 1. Symbols a, b, c, and d represent the cases shown in Fig. 2.

An increase in concentration raises i_{oII}; this tends to reduce the penetration depth for reaction [II] (7, 29) and to decrease the cell lifetime.

2. The driving force for reaction [II], $\eta_{sII} = \eta - U_{II,w}$, is influenced by the dependence of $U_{II,w}$ on the chloride ion concentration (see Eq. [31]). For the Li/$SOCl_2$ system, where the Cl^- ion is an electrochemical reaction product, the net effect of an increase in concentration is that η_{sII} becomes less negative, which tends to make the reaction distribution more uniform. However, it should be noted that a change in $U_{II,w}$ generally gives a smaller change in η_{sII} because η alters in a manner which tends to counteract the effect of $U_{II,w}$.

3. The distribution of reaction [II] at any time is a function of all previous Cl^- ion distributions and concentrations. For example, the exponent m in Eq. [8] influences the role of local volume fraction of LiCl and $k_{III,G}$ on the effective precipitation rate constant k_T, and this interacts with reaction rate through the interfacial area a, given by Eq. [6].

Factors 1-3 can oppose one another and hence give rise to a minimum t_{cell}, as shown in Fig. 4. With $k_{III,G} = 10^{15}$ $cm^3/mol \cdot s$ (*e.g.*, case a from Fig. 2), the cell lifetime is determined by the distribution of reaction [II] in the limit of negligible supersaturation of the electrolyte (*i.e.*, fast precipitation). In this asymptote, the magnitude of $k_{III,N}$ is negligible in comparison to the $k_{III,G}$ term in Eq. [8] and, hence, the results for the two values of $k_{III,N}$ are essentially the same. When $k_{III,G}$ is reduced with constant $k_{III,N}$ (*e.g.*, cases a, b, and c), the lifetime is reduced by as much as a factor of two. This can be attributed to the increase in i_{oII} (see above). If $k_{III,G}$ is reduced further (*e.g.*, see cases c and d), changes in $U_{II,w}$ become more important than changes in i_{oII} and the cell lifetime increases. On the left-hand side of Fig. 4, $k_{III,N}$ is greater than $k_{III,G}$, and the chloride ion concentration is determined primarily by the magnitude of $k_{III,N}$; with a larger $k_{III,N}$, c_{Cl^-} is lower, and the lifetime is slightly greater.

The results presented in Fig. 1-4 consider chloride ion concentration variations across the cell but do not include local mass transport of Cl^- ions from the electrode surface, where they are produced by reaction [II], to the bulk of an individual pore. With finite values for k_{Cl^-}, Eq. [5] can be included in the analysis to predict the difference between c_{Cl^-} and $c_{Cl^-,w}$. Figure 5 compares typical values of the concentrations obtained with different values of $k_{III,N}$ and $k_{III,G}$. The bulk concentrations are essentially unchanged from the results predicted in the absence of local mass transport (see Fig. 3); the supersaturation level tends to zero as $k_{III,G}$ is increased. With $k_{III,G} = 10^{15}$ $cm^3/mol \cdot s$, $c_{Cl^-,w}$ must be several orders of magnitude larger than c_{Cl^-} in order to satisfy Eq. [5]. The value of $c_{Cl^-,w}$ rises when c_{Cl^-} and $c_{Cl^-,w}$ become comparable in magnitude. This is necessary to maintain the correct concentration difference driving force for local mass transport, as defined by the right-hand side of Eq. [5]. A similar difference between c_{Cl^-} and $c_{Cl^-,w}$ still exists for $k_{III,G} < 10^8$ $cm^3/mol \cdot s$ even though it is too small to be discernible from the diagram. For $k_{III,N} = 10^9$ $cm^3/mol \cdot s$, the bulk concentration is always small by comparison with $c_{Cl^-,w}$ and, hence, the wall concentration is almost independent of $k_{III,G}$.

The magnitude of the wall concentration is influenced by the rate of reaction [II] through Eq. [5], but it also influences ai_{nII} through the dependence of i_{oII} and $U_{II,w}$ on $c_{Cl^-,w}$ as given by Eq. [31] and [32]. Consequently, the distribution of reaction [II], and, hence, the cell lifetime, is dependent on the local value of $c_{Cl^-,w}$.

In Fig. 6, lifetimes obtained with a finite value for k_{Cl^-} (*i.e.*, $c_{Cl^-} \neq c_{Cl^-,w}$) are compared with results from Fig. 4 ($k_{Cl^-} = \infty$ and $c_{Cl^-} = c_{Cl^-,w}$). With $k_{III,N} = 10^9$ $cm^3/mol \cdot s$, the lifetime is almost independent of $k_{III,G}$ because changes in the wall concentration are very small. For $k_{III,N} = 10^6$ $cm^3/mol \cdot s$ and large $k_{III,G}$, the wall concentration is the same as for $k_{III,N} = 10^9$ $cm^3/mol \cdot s$, the same lifetime is predicted. In this asymptote, the precipitation rate constants are unimportant and t_{cell} is determined by the balance of kinetic, ohmic, and mass transport limitations that set the distribution of reaction [II].

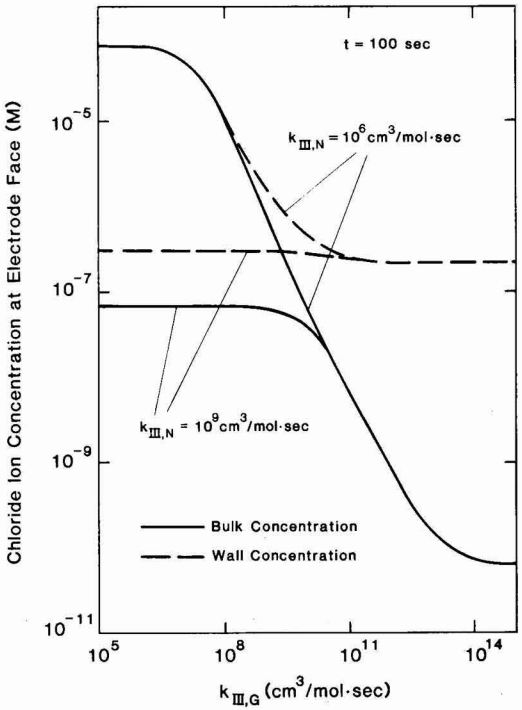

Fig. 5. Dependence of chloride ion concentration at the reservoir/positive electrode interface at $t = 100s$ on $k_{III,N}$ and $k_{III,G}$. Parameters are as in Fig. 1 except $k_{Cl^-} = 2.0$ cm/s.

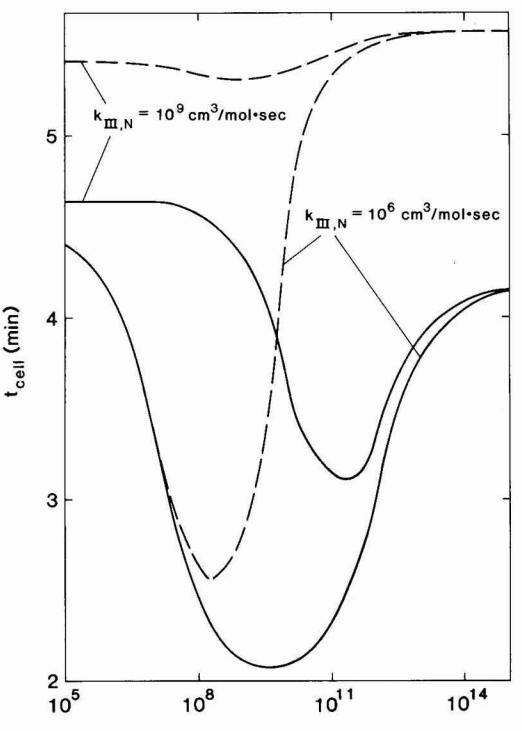

Fig. 6. Dependence of cell lifetime on $k_{III,N}$ and $k_{III,G}$. Parameters are as in Fig. 1 except $k_{Cl^-} = 2.0$ cm/s for the dashed curves. The full curves are from Fig. 4 for comparison.

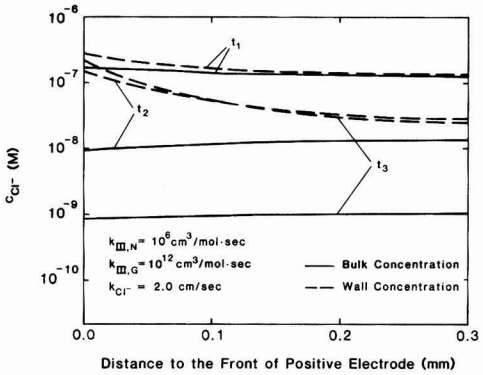

Fig. 7. Position dependence of chloride ion concentration at different times during a cell discharge. Parameters are as in Fig. 5. $t_1 \sim 52s$, $t_2 \sim 56s$, $t_3 \sim 100s$.

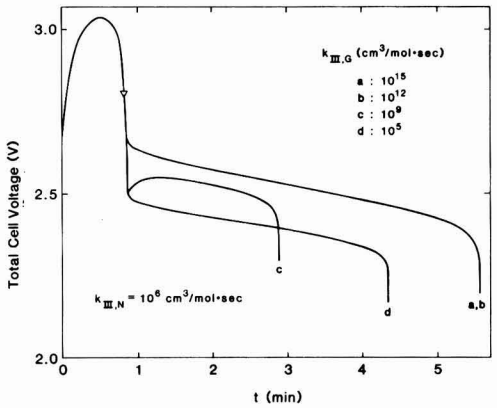

Fig. 8. Theoretical discharge curves for four values of $k_{III,G}$. Parameters are as in Fig. 5. Symbol ∇ indicates the initiation of reaction [II].

The difference in t_{cell} values for $k_{Cl^-} = \infty$ and $k_{Cl^-} = 2.0$ cm/s in the high $k_{III,G}$ asymptote can be attributed to a change in the concentration distribution. The rate of reaction [II] is fastest at the front face of the electrode and, with a finite value for k_{Cl^-}, the difference between the concentrations at the wall and in the bulk are greatest at this location (see Fig. 7). As a result, $U_{II,w}$ obtained using Eq. [31] is smaller at the front face than at the back of the electrode. The potential difference η is also smallest at the front face, and its distribution through the electrode is similar to the one for $U_{II,w}$. Hence, the driving force η_{IsII} for reaction [II] is relatively uniform, and the cell lifetime is longer. In contrast, the $U_{II,w}$ distribution with $k_{Cl^-} = \infty$ is more uniform, since $c_{Cl^-,w}$ ($= c_{Cl^-}$) is more uniform (see Fig. 1), whereas the distribution of η is similar. Consequently, the surface overpotential distribution is less uniform with $k_{Cl^-} = \infty$, and the corresponding cell lifetime is shorter.

In Fig. 6, a reduction in $k_{III,G}$ raises $c_{Cl^-,w}$ (see Fig. 5) and, hence, raises i_{oII}. This effect, in conjunction with the dependence of k_T on ϵ_{LiCl}, leads to a smaller cell lifetime. As $k_{III,G}$ is reduced, $c_{Cl^-,w}$ approaches c_{Cl^-}, and the influence of local mass transport diminishes. With $k_{III,G} < 10^7$ cm^3/mol · s and $k_{III,N} = 10^6$ cm^3/mol · s, model predictions are independent of diffusion within each pore of the electrode. For $k_{III,N} = 10^9$ cm^3/mol · s, local mass transport still influences t_{cell} when $k_{III,G}$ is small because c_{Cl^-} and $c_{Cl^-,w}$ do not become equal (see Fig. 5).

Overall, the results presented in Fig. 6 indicate that, for the $Li/SOCl_2$ system, a change in precipitation rate constant can lead to a significant change in cell lifetime. Similar results are expected for other cells where the maximum discharge time is dictated by the plugging of pores with solid reaction products. Furthermore, it is conceivable that materials added to either the electrode matrix or the electrolyte could alter the rate of nucleation and growth of the solids and, hence, have a substantial effect on cell performance.

Figure 8 shows theoretical discharge curves obtained using a finite value for the local mass transport coefficient. Curve d is identical to the corresponding result in Fig. 2 because $c_{Cl^-,w} \simeq c_{Cl^-}$ at all locations and throughout the discharge. The general shapes of curve c in Fig. 2 and 8 are the same. In particular, the local voltage minimum at the onset of reaction [II] is still predicted, because $c_{Cl^-,w}$ goes through a maximum analogous to the changes in bulk concentration shown in Fig. 1. In case b, however, changes in $c_{Cl^-,w}$ are attenuated (compare Fig. 1 and 7) and a voltage minimum is not obtained. This indicates that only certain combinations of the nucleation and growth rate constants lead to a voltage minimum; $k_{III,G} >> k_{III,N}$ is a necessary but not sufficient condition for a local minimum to occur.

For case a in Fig. 8, the chloride ion concentration is substantially higher at the wall than those with $k_{Cl^-} = \infty$. Consequently, the voltage is approximately 180 mV smaller than the result for case a in Fig. 2. The corresponding voltage reduction due to local mass transport for cases b, c, and d are 125, 40, and 0 mV, respectively.

Cell failure is caused by rapid reduction of the effective electrolyte conductivity as a result of LiCl precipitation near the front face of the cathode (7). The nonuniform nature of the LiCl distribution is illustrated in Fig. 9. The curves correspond to the cumulative reaction rate distributions for reaction [II] because redistribution of Cl^- ions is negligible. In general, the results indicate that the less uniform the reaction distribution, the shorter the cell lifetime. Also, failure occurs at the front of the electrode in all cases. Inclusion of local mass transport of Cl^- ions tends to make the reaction distribution more uniform and more LiCl is deposited toward the back of the electrode than if LiCl is assumed to be a direct product of the electrochemical reaction (*e.g.*, compare the result for the old model with solid curves a, b, and d).

The results presented in Fig. 7-9 use a specific value for the local mass transport coefficient k_{Cl^-}. This value was estimated using an average pore diameter (during discharge) of 0.5×10^{-5} cm (26), and a bulk diffusion coefficient of 10^{-5} cm^2/s. However, the estimate is approximate, and it is necessary to assess the sensitivity of the results to the magnitude of k_{Cl^-}. Figure 10 shows that similar trends in behavior are predicted for a wide range of k_{Cl^-} values. As k_{Cl^-} is increased, local mass transport

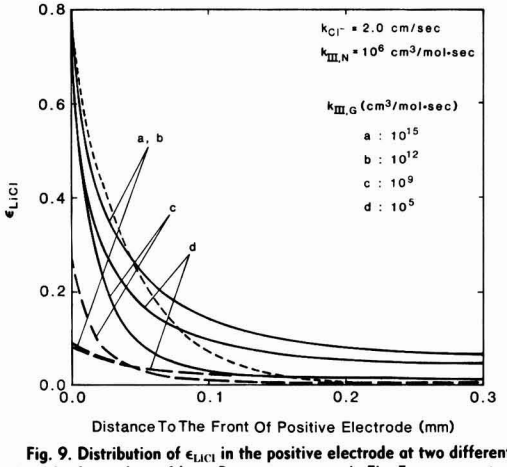

Fig. 9. Distribution of ϵ_{LiCl} in the positive electrode at two different times for four values of $k_{III,G}$. Parameters are as in Fig. 5. — — —: t = 100s. ———: end of cell discharge (*i.e.*, t_{cell} = 334s for a and b, t_{cell} = 172s for c, and t_{cell} = 264s for d). - - - -: result obtained using previous model (8) at the end of cell discharge (t_{cell} = 243s).

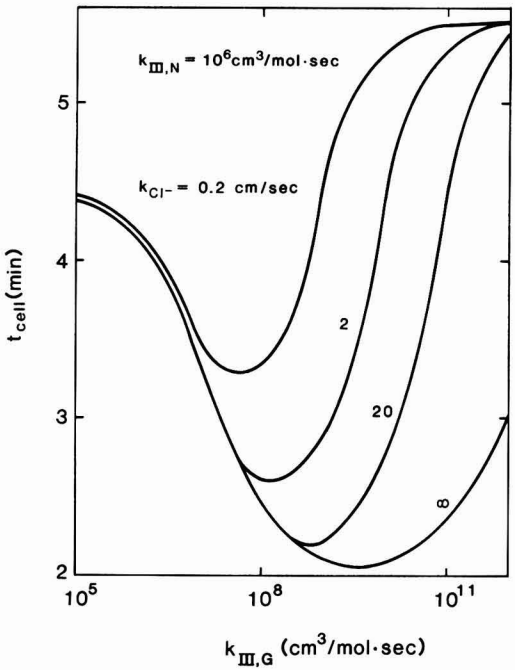

Fig. 10. Dependence of cell lifetime on $k_{III,G}$ for different local mass-transfer coefficients. Parameters are as in Fig. 5.

becomes less important, and the asymptote for $k_{Cl^-} = \infty$ is approached. In general, the smaller k_{Cl^-}, the less uniform the distributions of $c_{Cl^-,w}$ and $U_{II,w}$ and, hence, the more uniform the reaction distribution. This results in an increase in cell lifetime, but it occurs at the expense of cell voltage (see description of Fig. 8).

For conditions where local mass transport is significant, it is interesting to contrast the effects of reducing either k_{Cl^-} or $k_{III,G}$ on t_{cell}. In both cases, the wall concentration is increased, and this raises i_{oII} and lowers $U_{II,w}$. A reduction in k_{Cl^-} also makes the distribution of $U_{II,w}$ less uniform, and this effect overcomes the increase in i_{oII} and is responsible for the increase in t_{cell}. On the other hand, a reduction in $k_{III,G}$ does not alter the $U_{II,w}$ distribution noticeably, and the increase in i_{oII} dominates, leading to a shorter cell lifetime. Figure 10 indicates that the local mass transport of a sparingly soluble electrochemical reaction product can have a significant effect on the local reaction rate and, hence, on the distribution of the precipitate. In particular, slower diffusion within a pore can increase cell lifetime appreciably under some circumstances. In the Li/$SOCl_2$ cell, this change would be accompanied by a reduction in the voltage plateau for the neutral reaction, but the cell always fails by plugging of the electrode face with LiCl crystals.

There are many electrodes with soluble reaction products that have solid reactants, *e.g.*, Cd, Zn, Pb, and PbO_2. For these systems, the electrochemical reaction zone generally penetrates progressively farther into the electrode as the reactants are consumed. Consequently, the electrode volume available for reaction diminishes during cell operation, and the local transfer current required to meet the specified current density becomes larger. This tends to raise the wall concentration of the soluble reaction product and to increase the local electrode overpotential (see Eq. [31]). Under these circumstances, it is conceivable that the voltage reduction will be sufficient to cause cell failure directly, particularly if the local mass transport rate is low. This effect would be directly analogous to the behavior of cells involving sparingly soluble reactants, where a low concentration of electrochemical reactant at the electrode wall can lead to cell failure (9).

The results presented above focused attention on the effects of $k_{III,N}$, $k_{III,G}$, and k_{Cl^-} on cell behavior. However, a number of other factors can have a significant impact on the discharge characteristics. The sensitivity of model predictions to these factors is discussed below.

Morphology parameter m for precipitation.—The quantity m appears in Eq. [8], and it controls the change in the effective precipitation rate constant k_T due to an increase in the surface area of crystals at which further growth can take place. From a physical standpoint, the magnitude of the exponent m reflects the morphology of the LiCl precipitate: large values correspond to crystals with small surface/volume ratios and vice versa. In Fig. 11, cell lifetimes for $m = 0$ and 0.5 are compared with the result from Fig. 6, which used $m = 1.0$. The asymptote for fast precipitation on the right-hand side of the diagram is independent of m. Also, on the left-hand side, the $k_{III,G}$ term in Eq. [8], and hence m, is not important, because $k_{III,N}$ dominates. The sensitivity of t_{cell} to m in the intermediate region can be related to changes in k_T. The smaller the value of m, the greater the increase in k_T locally for a given amount of LiCl precipitation. This change is equivalent to having a larger $k_{III,G}$ value, but with $m = 1.0$. The effect is to lower the chloride ion concentration and, through changes in i_{oII} and $U_{II,w}$ (see Eq. [31] and [32]), to raise t_{cell}. With $m = 0$, k_T is constant throughout the discharge ($k_T = k_{III,N} + k_{III,G}$) and t_{cell} varies monotonically between the asymptotes. This suggests that the minima for t_{cell} with $m = 0.5$ and 1.0 are caused, at least in part, by the local changes in k_T that take place as precipitation proceeds. With $m = 1.0$, a local voltage minimum is predicted for $10^6 \geq k_{III,G}/k_{III,N} \geq 10^2$. A reduction in the value of the exponent m reduces the range of $k_{III,G}/k_{III,N}$ for a minimum. For $m = 0$, the Cl^- ion concentration always changes monotonically during discharge, and a local voltage minimum is never obtained.

Kinetic parameter $a^o i_{oII,ref}$ for reaction [II].—Figure 12 illustrates the sensitivity of the model calculations to the

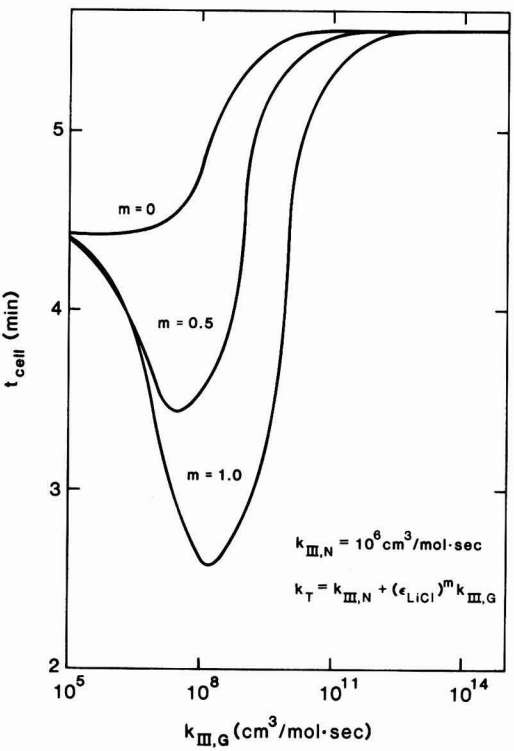

Fig. 11. Dependence of cell lifetime on $k_{III,G}$ for three values of m. Parameters are as in Fig. 5.

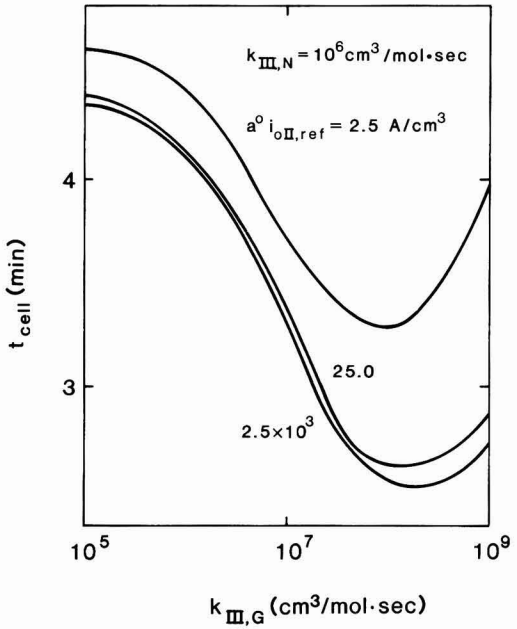

Fig. 12. Dependence of cell lifetime on $k_{III,G}$ for different values of $a^o i_{oII,ref}$. Parameters are as in Fig. 5.

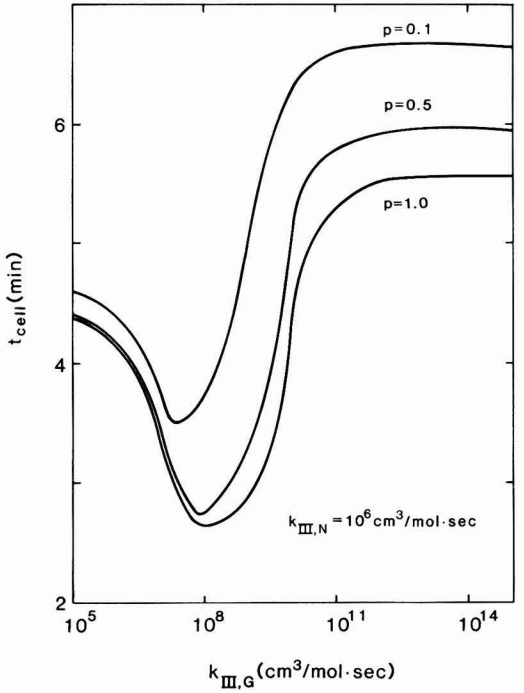

Fig. 13. Dependence of cell lifetime on $k_{III,G}$ for three values of p. Parameters are as in Fig. 5.

product of the initial specific surface area a^o and the reference exchange current density $i_{oII,ref}$ for reaction [II]. In general, a reduction in the value of the product leads to greater kinetic control and this has two main effects on cell behavior: (*i*) the reaction distribution is more uniform and, consequently, the cell lifetime is longer, and (*ii*) changes in $U_{II,w}$ are less important and, hence, there is less tendency for a minimum in t_{cell} as $k_{III,G}$ is altered. With small values of $k_{III,G}$, the rate of LiCl precipitation is more important than the rate constant for reaction [III] and, as a result, the curves are less sensitive to $a^o i_{oII,ref}$ in this region. For $k_{III,G} = 10^5$ cm³/mol · s, $k_{III,N}$ dominates in Eq. [8] and a nucleation-controlled asymptote for the cell lifetime is attained.

Coverage factor p for electrochemical reactions.—The exponent p in Eq. [6] influences the effective surface area available for the electrochemical reactions. With smaller values of p, the carbon surface in the cathode is more readily passivated by LiCl crystals. This forces the reaction deeper into the electrode and delays failure by plugging at the front face of the electrode. Figure 13 shows that longer lifetimes are predicted for smaller p values but that the influence of $k_{III,G}$ is similar in each case. With small $k_{III,G}$ values, the cell lifetime is less sensitive to p because the electrochemical reaction rate is less important than the precipitation rate (see description of Fig. 12).

With high precipitation rates (*i.e.*, large $k_{III,G}$), one might expect the dependence of t_{cell} on p to match the results obtained previously (7) when solid LiCl was regarded as an electrochemical reaction product. However, the results presented in Fig. 13 are relatively insensitive to the value of p. For example, an increase in p from 0.1 to 0.5 reduces t_{cell} by 9% in Fig. 13 but by 38% in the previous model (7). The difference can be attributed to the inclusion of local mass transport, and to the dependence of i_{oII} on the wall concentration $c_{Cl^-,w}$ rather than the bulk concentration c_{Cl^-}, in the present analysis. With large $k_{III,G}$, the ratio $c_{Cl^-,w}/c_{Cl^-}$ is much greater than unity (see Fig. 5) and, hence, the effective exchange current density is much larger with the present model. This diminishes the importance of both electrochemical kinetics and changes in the product $a^o i_{oII,ref}$ and, in turn, attenuates the dependence of t_{cell} on p. It is emphasized, however, that as k_{Cl^-} approaches infinity, local mass transport becomes unimportant, and the influence of p predicted by the two models becomes identical.

Solubility product, K_{sp}.—With slow precipitation, the supersaturation level is high, and the product $(c_{Li^+})(c_{Cl^-})$ that appears in Eq. [7] is much larger than K_{sp}. For large $k_{III,G}$, the results are also insensitive to the solubility product. With $k_{III,N} = 10^6$ cm³/mol · s and $k_{III,G} = 10^{15}$ cm³/mol · s, a hundredfold reduction in K_{sp} has no effect on t_{cell} and a hundredfold increase only lowers t_{cell} by 3.6%. The change is caused by an increase in c_{Cl^-} which raises $c_{Cl^-,w}$ slightly (to satisfy Eq. [5]) and, in turn, raises i_{oII}.

The results presented above, for a soluble reaction product, can be contrasted with those for a sparingly soluble reactant. In the latter case, the bulk concentration is much larger than the wall concentration and the magnitude of the bulk concentration can determine the mass transport rate to the reaction site and hence the limiting current density (5, 9). Therefore, the solubility of the reactant could significantly affect cell behavior.

Cell temperature.—The temperature of a Li/$SOCl_2$ cell usually rises during discharge. At higher temperatures, the electrolyte conductivity κ_∞ and the species diffusion coefficients, D_{ik}, are larger, and these factors, together with the temperature-dependent terms in Eq. [1], tend to make the reaction distribution more uniform. In general, it is also necessary to account for the temperature dependence of kinetic parameters, such as $i_{oII,ref}$, $k_{III,N}$, $k_{III,G}$, m, and p. However, information on activation energies for these parameters is not available. For the cells considered here, the heat transfer coefficient is large enough to restrict temperature rises to 10°-20°C and, therefore, the effects of temperature changes are relatively unimportant.

Corrosion potential.—In the Li/$SOCl_2$ system, it may be more appropriate to regard the open-circuit potentials and exchange current densities for the cathodic reactions as corrosion potentials and corrosion currents (23). The dependence of these quantities on chloride ion concentration can be predicted from a corrosion diagram, if

the branches of the current-overpotential relation are assumed to originate from reversible reactions. For reaction [II], if the anodic branch is taken to be oxidation of Cl^- ions to Cl_2 (23), the exponents for $c_{Cl^-,w}$ in Eq. [31] and [32] are increased from 1.0 to 1.3 and from 0.329 to 0.428, respectively. Since both $U_{II,w}$ and i_{oII} are changed in the same direction, the dependence of cell lifetime on $k_{III,G}$, as shown in Fig. 4 and 6, will be similar. Also, the criteria for the existence of a local voltage minimum in the discharge curve will be essentially unchanged. It should be noted that $SOCl_2$ reduction is a complicated process for which practically no quantitative kinetic data have been reported. As additional experimental data become available, it may be necessary to update the composition dependence of the parameters $U_{II,w}$ and i_{oII}. For example, if Cl^- ions are not involved in the rate-determining electrochemical step, the chloride ion concentration would not necessarily appear in expressions for $U_{II,w}$ and i_{oII}.

Cell design and discharge conditions.—Results obtained with the previous model showed the correct dependence of t_{cell} on the discharge rate and on the thickness and initial porosity of the positive electrode (7). For the model presented here, that includes Cl^- ions and the precipitation process, the same trends in behavior are observed. One difference that is obtained concerns the influence of initial electrolyte composition on discharge time (see Fig. 14). Previously, the dependence of the effective exchange current density i_{oII} on c_{Li^+} gave rise to a distinct maximum in the cell lifetime. In the present study, reaction [II] does not involve lithium ions, and i_{oII} is independent of c_{Li^+}. For this reason, the curves do not show a maximum and they more closely reflect the composition dependence of the electrolyte conductivity. Slight shifts in the dependence are found for slow or fast precipitation. Figure 14 suggests that detailed measurements of t_{cell} with different electrolyte compositions could be used to help distinguish between postulated reaction mechanisms.

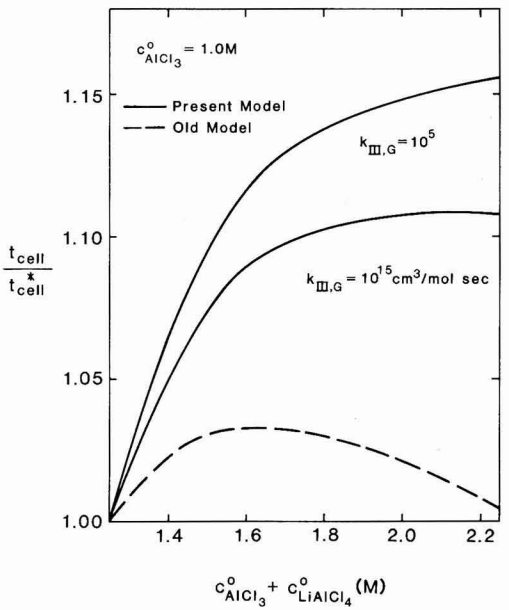

Fig. 14. Dependence of normalized cell lifetime on the sum of initial electrolyte and acid concentrations; comparison of results obtained with different models. Parameters are as in Fig. 5 and $k_{III,N} = 10^6$ cm³/mol · s. t_{cell}^* is the cell lifetime with $c_{AlCl_3}^o + c_{LiAlCl_4}^o = 1.25M$ and is equal to 236s for old model: 307s for the present model with $k_{III,G} = 10^{15}$ cm³/mol · s; 241s for the present model with $k_{III,G} = 10^5$ cm³/mol · s. It is noted that similar sets of curves are obtained with different values of $c_{AlCl_3}^o$.

Conclusions

A mathematical model has been developed that describes the precipitation of a solid in an electrochemical cell. The treatment considers the time-dependent and position-dependent behavior of the system and includes the interactions between multicomponent transport of electrolyte species in porous media and simultaneous chemical and electrochemical reactions. Quantitative results for deposition of LiCl in a $Li/SOCl_2$ static cell illustrate the trends in behavior that can be expected in general.

The rate of precipitation of a sparingly soluble reaction product in an electrochemical cell can have a significant impact on the system performance. The magnitudes of the rate constants for nucleation and growth, together with the morphology of the precipitate, dictate the local supersaturation level in the electrolyte. In many cases, a change in this level influences the wall concentration and, in turn, alters the electrochemical reaction distribution through changes in the effective exchange current density and the open-circuit potential. These changes can lead to a strong dependence of cell lifetime on precipitation rate, if discharge is terminated by local plugging of pores with the solid product. Theoretical calculations for the lithium-thionyl chloride system, indicate that cell lifetime could be altered by more than a factor of two and that the longest lifetime would occur in the fast precipitation limit.

Cell voltage and the shape of a discharge curve are also dependent on the precipitation rate. For example, a local voltage minimum can occur at the onset of precipitation, if the nucleation rate constant is several orders of magnitude smaller than the growth rate constant and if the growth rate is directly related to the crystal surface area. Local mass transport of a soluble reaction product between the electrode surface and the bulk electrolyte within a pore can influence cell behavior significantly when the precipitation rate is relatively fast. In this case, a reduction in the local mass-transfer coefficient makes the reaction distribution more uniform, lowers the cell voltage, and reduces the sensitivity of the discharge behavior to the extent of passivation of the electrode surface caused by the precipitate.

In contrast to the effects of exchange current density, open-circuit potential, and local mass-transfer coefficient, redistribution of a depositing product species through a cell is not significant unless the quantity of the species in the electrolyte is comparable to the total amount of the species that is deposited. Cell behavior is also insensitive to the magnitude of the solubility product for the precipitate.

The dependence of trends in cell performance on operating conditions and design parameters is not altered markedly by the precipitation process. For the $Li/SOCl_2$ cell, the most noticeable difference between results predicted with and without a separate step for precipitation of LiCl is a change in the influence of initial electrolyte concentration on cell lifetime.

Acknowledgment

This work was supported in part by the Office of Naval Research.

Manuscript received Sept. 18, 1985; revised manuscript received April 16, 1986.

APPENDIX

Derivation of Transport Properties for a System with Two Binary Electrolytes in Two Solvents

The multicomponent diffusion equation for an isothermal, isobaric system is expressed as (17)

$$c_i \nabla \mu_i = \sum_j K_{ij}(v_j - v_i) = RT \sum_j \frac{c_i c_j}{c_T \mathcal{D}_{ij}}(v_j - v_i) \qquad [A\text{-}1]$$

where μ_i is the electrochemical potential of species i, and j ranges over the species in the system. For a mixture of n species, there is a set of $(n - 1)$ independent force balances with the form of Eq. [A-1] and these relationships

define the binary interaction parameters $\mathfrak{D}_{ij}$, which are, in general, functions of temperature, pressure, and composition. The number of independent transport properties in Eq. [A-1] is $n(n-1)/2$ because $\mathfrak{D}_{ii}$ is not defined and, by Newton's third law of motion, $\mathfrak{D}_{ij} = \mathfrak{D}_{ji}$. Specific combinations of these properties correspond to transport parameters that can be measured directly.

For the Li^+, $AlCl_4^-$, Cl^-, $AlCl_3$, $SOCl_2$ systems (species 1, 2, 3, 4 and o, respectively), the four independent multicomponent diffusion equations may be rearranged, with the introduction of the superficial current density, $i_2 = F\Sigma_i z_i N_i$, to give explicit equations for species fluxes relative to the solvent velocity v_o (8, 15). As part of this derivation, the ten transport properties (six diffusion coefficients, three transference numbers, and the electrolyte conductivity) relative to v_o are also defined. The volume average velocity, $v^* = \sum_i \bar{V}_i N_i$, is used as the reference frame for the fluxes, because physical data for this electrolyte are correlated with concentration. The relationships for the transport properties relative to both v_o and v^* are presented below.

Diffusion coefficients.—The diffusion coefficients D_{ij} relative to v^* can be expressed in terms of the corresponding quantities D_{ij}^o relative to v_o by

$$D_{ij} = D_{ij}^o - D_{oj}(c_i/c_o); \qquad i, j = A, B, 4 \qquad [A\text{-}2]$$

$$D_{oj} = \sum_k c_o \bar{V}_k D_{oj}^o; \qquad j, k = A, B, 4 \qquad [A\text{-}3]$$

Only six of the nine diffusion coefficient relative to the solvent velocity presented in Eq. [A-2] are independent. The other three coefficients can be obtained from

$$D_{BA}^o = \frac{\nu^A c_B}{\nu^B c_A} \times \frac{(1 + d\ln f_{12}/d\ln c_A)}{(1 + d\ln f_{13}/d\ln c_B)} D_{AB}^o = P_1 D_{AB}^o \qquad [A\text{-}4]$$

$$D_{A4}^o = \frac{c_A}{\nu^A c_4} \times \frac{(1 + d\ln f_4/d\ln c_4)}{(1 + d\ln f_{12}/d\ln c_A)} D_{4A}^o = P_2 D_{4A}^o \qquad [A\text{-}5]$$

$$D_{B4}^o = P_1 P_2 D_{4B}^o \qquad [A\text{-}6]$$

where f_{12}, f_{13}, and f_4 are the molar activity coefficients for $LiAlCl_4$, LiCl, and $AlCl_3$ and are defined by

$$\mu_A = \nu^A RT \ln (c_A f_{12} \alpha_{12}^\theta) \qquad [A\text{-}7]$$

$$\mu_B = \nu^B RT \ln (c_B f_{13} \alpha_{13}^\theta) \qquad [A\text{-}8]$$

$$\mu_4 = RT \ln (c_4 f_4 \alpha_4^\theta) \qquad [A\text{-}9]$$

It should be noted that to obtain Eq. [A-4] to [A-6], f_{12}, f_{13}, and f_4 are assumed to be independent of the concentrations of the other species (*i.e.*, $\partial\mu_i/\partial c_j = 0$ if $i \neq j$).

Equations [A-2] and [A-3] indicate that only six of the twelve diffusion coefficients relative to the volume average velocity are independent. In the calculations, D_{AA}, D_{AB}, D_{4A}, D_{BB}, D_{4B}, and D_{44} are chosen as the independent coefficients. The values for D_{AA}, D_{BB}, and D_{44} are assumed to be independent of concentration and to be equal to 10^{-5} cm²/s at 298.15 K. Also, the coefficient D_{4A} is assumed to be proportional to c_4 (see Table I) and D_{AB} and D_{4B} are set equal to zero since transport of $AlCl_4^-$ and $AlCl_3$ are expected to be relatively insensitive to the presence of chloride ions. The dependent coefficients D_{oA}, D_{oB}, and D_{o4} are calculated from Eq. [A-3], and the remainder are calculated using

$$D_{BA} = \{-c_B\bar{V}_A D_{AA} - c_B\bar{V}_4 D_{4A} + P_1[(c_o\bar{V}_o + c_A\bar{V}_A)D_{AB} + c_A\bar{V}_B D_{BB} + c_A\bar{V}_4 D_{4B}]\}/(c_o\bar{V}_o + c_B\bar{V}_B) \qquad [A\text{-}10]$$

$$D_{A4} = [P_2 c_4\bar{V}_A D_{AA} + P_1 P_2 c_4\bar{V}_B D_{AB} + P_2(1 - c_A\bar{V}_A)D_{4A} - P_1 P_2 c_A\bar{V}_B D_{4B} - c_A\bar{V}_4 D_{44}]/(1 - c_4\bar{V}_4) \qquad [A\text{-}11]$$

$$D_{B4} = [-P_2 c_B c_4\bar{V}_A^2 D_{AA} + P_1 P_2 c_4\bar{V}_A(c_A\bar{V}_A + c_o\bar{V}_o)D_{AB} + P_1 P_2 c_4\bar{V}_B(1 - c_4\bar{V}_4)D_{BB} - P_2 c_B\bar{V}_A(1 - c_A\bar{V}_A)D_{4A} + P_1 P_2[c_A\bar{V}_A c_B\bar{V}_B + (c_o\bar{V}_o + c_4\bar{V}_4)(1 - c_4\bar{V}_4)]D_{4B} - c_B\bar{V}_4(c_o\bar{V}_o + c_B\bar{V}_B)D_{44}]/[(c_o\bar{V}_o + c_B\bar{V}_B)(1 - c_4\bar{V}_4)] \qquad [A\text{-}12]$$

Transference numbers.—The transference numbers presented in Eq. [16]-[19] are related to the transference numbers relative to v_o as follows

Table I. Physical parameters used in Fig. 1. Remarks: A ~ chosen to match theoretical discharge curve and experimental data (18); B ~ reference condition taken as electrolyte saturated with LiCl; C ~ corresponds to an open-circuit potential $U_{II,w}$ of 3.64V for electrolyte saturated with LiCl (19-21), see Eq. [31]; D ~ reaction (IV) chosen as the reference electrode reaction; E ~ ratio of initial active surface area at cathode per unit electrode volume to the active surface area at anode per unit cross-sectional area, estimated to be 25 cm^{-1}; F ~ no induction period needed when crystals already exist (see Ref. (1), p. 24); G ~ dissolution of LiCl in $AlCl_3$ expected to be a slow reaction; H ~ one of the ten independent transport properties, see Appendix; I ~ c_{Cl^-} not included since no information available; J ~ based on $\rho_A = (\rho_B + \rho_4)/2$; K ~ no information available

Parameter	Value	References/ remarks
$\alpha^o i_{o\text{I},ref}$ (A/cm³)	1.0	A
$\alpha^o i_{o\text{II},ref}$ (A/cm³)	25.0	A
$c_{AlCl_4^-,ref} = c_{AlCl_3,ref}$ (mol/cm³)	1.0×10^{-3}	—
$c_{Cl^-,ref}$ (mol/cm³)	0.66×10^{-13}	B
$U_I^\theta - U_{re}^\theta$(V)	3.90	(19, 20)
$U_{II}^\theta - U_{re}^\theta$(V)	2.65	C
$\partial U_I^\theta/\partial T$(V/K)	-0.228×10^{-3}	—
$\partial U_{II}^\theta/\partial T$(V/K)	-0.228×10^{-3}	(22)
$n_I = n_{II}$	2.0	—
$\alpha_{aI} = \alpha_{aII}$	0.439	(23)
$\alpha_{cI} = \alpha_{cII}$	0.329	(23)
i_{oIV} (A/cm²)	10^{-6}	(7)
$n_{re} = n_{IV}$	1.0	D
$\alpha_{aIV} = \alpha_{cIV}$	0.5	—
ρ_0 (g/cm³)	1.64	(24)
K_{sp} (mol²/cm⁶)	10^{-16}	—
p	1.0	A
m	1.0	—
k_T' (cm⁴/mol · s)	$k_{III,c}/25.0$	E, F
k_V' (cm/s)	$5.0 \times 10^{-4} \times I^{1.7}$	(7)
k_{VI} (s^{-1})	10^{-2}	G
k_{VI}' (cm/s)	$k_{VI}/25.0$	E
δ_f^o (cm)	4.0×10^{-4}	(7)
$s_{AlCl_4^-,I} = -s_{AlCl_3,I} = -2s_{SOCl_2,I}$	2.0	—
$s_{Cl^-,II} = -2s_{SOCl_2,II}$	2.0	—
$-s_{Li^+,III} = -s_{Cl^-,III} = s_{LiCl,III}$	1.0	—
$s_{Li^+,IV}$	−1.0	—
$-2s_{SOCl_2,V} = s_{LiCl,V}$	2.0	—
$s_{Li^+,VI} = s_{AlCl_4^-,VI} = -s_{AlCl_3,VI} = -s_{LiCl,VI}$	1.0	—
q	1.5	(25)
$\nu_1^A = \nu_2^A = \nu_1^B = \nu_3^B$	1.0	—
$\nu^A = \nu_1^A + \nu_2^A$	2.0	—
$\nu^B = \nu_1^B + \nu_3^B$	2.0	—
$f_{12} = f_{13} = f_4$	1.0	—
$D_{AA} = D_{BB} = D_{44}$ (cm²/s)	$3.35 \times 10^{-5} \times e^{-361/T}$	(7), H
$D_{AB} = D_{4B}$ (cm²/s)	0.0	H
D_{4A} (cm²/s)	$2.2 \times 10^{-2} \times c_{AlCl_3}$	H
t_2^*	0.45	H
$t_3^* = t_4^*$	0.0	H
κ_∞ (mho/cm)	$\kappa_{\infty,n} - 9.1 c_{AlCl_3} e^{-361/T}$	(7), I
σ_∞ (mho/cm)	45.5	(26)
σ_f (mho/cm)	5.0×10^{-4}	(7)
R_s (Ω · cm²)	4.3	A
$\bar{V}_{LiAlCl_4}$ (cm³/mol)	77.97	J
$\bar{V}_{LiCl} = \bar{V}_{LiCl}$ (cm³/mol)	20.50	(27)
$\bar{V}_{AlCl_3}$ (cm³/mol)	54.65	(27)
$\bar{V}_{SOCl_2}$ (cm³/mol)	72.63	(24)
$\Delta H_{R,III}$ (J/mol of LiCl formed)	0	K
$\Delta H_{R,V}$ (J/mol of LiCl formed)	-3.6×10^5	(28)
$\Delta H_{R,VI}$ (J/mol of LiCl dissolved)	-6.0×10^4	(8)

Table II. Cell specifications used in Fig. 1

Parameter	Value
$c_{LiAlCl_4}^o$ (mol/cm³)	0.5×10^{-3}
c_{LiCl}^o (mol/cm³)	0.66×10^{-13}
$c_{AlCl_3}^o$ (mol/cm³)	1.0×10^{-3}
L_p (cm)	3.0×10^{-2}
L_s (cm)	2.5×10^{-2}
ϵ_p^o	0.80
ϵ_s	0.92
$\bar{V}_R^o$ (cm)	1.0×10^{-2}
$T_o = T_A$ (K)	293.15
C (J/cm² · K)	0.2
h_o (W/cm² · K)	6.0×10^{-3}
I (A/cm²)	8.0×10^{-2}
Q (C/cm²)	138.5

$$t_i^{\bullet} = t_i^{o} - c_i z_i (Q' + t_4^{o}\bar{V}_4); \qquad i = 1, 2, 3$$
$$t_4^{\bullet} = t_4^{o} - c_4 (Q' + t_4^{o}\bar{V}_4) \qquad [A\text{-}13]$$
$$t_o^{\bullet} = -c_o (Q' + t_4^{o}\bar{V}_4)$$

where Q' is defined as

$$Q' = \frac{t_1^{o}\bar{V}_1}{z_1} + \frac{t_2^{o}\bar{V}_2}{z_2} + \frac{t_3^{o}\bar{V}_3}{z_3} \qquad [A\text{-}14]$$

and

$$t_1^{o} + t_2^{o} + t_3^{o} = 1 \qquad [A\text{-}15]$$

Only three of the five transference numbers defined by Eq. [A-13] are independent. Also, Q' defined by Eq. [A-14] is a quantity that cannot be measured but may be chosen arbitrarily. If both $t_4^{\bullet}$ and Q' are taken to be zero, one obtains

$$t_o^{\bullet} = 0$$
$$t_i^{\bullet} = t_i^{o}; \qquad i = 1, 2, 3 \qquad [A\text{-}16]$$

The other two independent transference numbers are chosen to be $t_2^{\bullet}$ and $t_3^{\bullet}$; $t_1^{\bullet}$ is calculated from Eq. [A-15] and [A-16]. The partial molar volume for Li^+ ions needed for calculation of the volume average velocity at the LiCl film/separator interface, is determined from Eq. [A-14] and [A-15] and is expressed as

$$\bar{V}_1 = \frac{\bar{V}_A}{\nu_1^A} t_2^{o} + \frac{\bar{V}_B}{\nu_1^B} t_3^{o} \qquad [A\text{-}17]$$

Conductivity.—The electrolyte potential in a porous medium can be measured with a suitable reference electrode with an electrode reaction defined by

$$\sum_i s_i M^{z_i} \rightarrow ne^- \qquad [A\text{-}18]$$

This potential provides the driving force for the current in the electrolyte. Combination of Eq. [A-1] and [16]-[19], together with the thermodynamic relation

$$\sum_i s_i \nabla\mu_i = -n\mathbf{F}\nabla\Phi_2 \qquad [A\text{-}19]$$

gives a modified Ohm's law expression for the superficial current density in the pore solution (see Eq. [27]). The bulk conductivity in Eq. [27] is expressed as

$$\kappa_\infty = n\mathbf{F}^2 \Big/ \left(\frac{\beta_1 t_1^{\bullet}}{z_1 c_1} + \frac{\beta_2 t_2^{\bullet}}{z_2 c_2} + \frac{\beta_3 t_3^{\bullet}}{z_3 c_3} + \frac{\beta_3 t_4^{\bullet}}{c_4} + \frac{\beta_o t_o^{\bullet}}{c_o} \right) \qquad [A\text{-}20]$$

where $\beta_i = \sum_j K_{ij}(s_j/c_j - s_i/c_i)$.

LIST OF SYMBOLS

- a interfacial area per unit electrode volume (cm^{-1})
- a_1^{θ} property expressing secondary reference state for species 1, 1 = LiCl, $LiAlCl_4$, or $AlCl_3$ (cm^3/mol)
- c_i molar concentration of species i (mol/cm^3)
- $c_{i,w}$ molar concentration of species i at the wall of electrode (mol/cm^3)
- C cell heat capacity (J/$cm^2 \cdot$ K)
- $\mathfrak{D}_{ij}$ diffusion coefficient for interaction of species i and j (cm^2/s)
- D_{ij} diffusion coefficient relative to volume average velocity, defined by Eq. [A-2] and [A-3] (cm^2/s)
- D_{ij}^{o} diffusion coefficient relative to the velocity of $SOCl_2$ (cm^2/s)
- e^- symbol for electron
- f_{12} mean molar activity coefficient of $LiAlCl_4$
- f_{13} mean molar activity coefficient of LiCl
- f_4 molar activity coefficient of $AlCl_3$
- $\mathbf{F}$ Faraday's constant (96,487 C/equiv.)
- h mesh size (cm)
- h_o heat transfer coefficient (W/$cm^2 \cdot$ K)
- $\Delta H_{R,k}$ heat of chemical reaction k (J/mol LiCl)
- i_2 superficial current density in pore phase (A/cm^2)
- i_{oj} exchange current density for reaction j (A/cm^2)
- i_{nj} local current density due to reaction j (A/cm^2)
- I superficial current density to an electrode (A/cm^2)
- j_{in} pore wall flux of species i (mol/$cm^2 \cdot$ s)
- $k_{III,G}$ rate constant for crystal growth at cathode (cm^3/mol · s)
- $k_{III,N}$ rate constant for nucleation at cathode (cm^3/mol · s)
- k_V' rate constant for reaction (V) (cm/s)
- k_{VI} rate constant for reaction (VI) at cathode (s^{-1})
- k_{VI}' rate constant for reaction (VI) at anode (cm/s)
- k_i coefficient for local mass transfer of species i from the wall of electrode to the bulk of a pore (cm/s)
- k_T precipitation parameter at cathode defined by Eq. [8] (cm^3/mol · s)
- k_T' precipitation parameter at anode defined by Eq. [11] (cm^4/mol · s)
- K_{ij} friction coefficient for interaction of species i and j (J · s/cm^5)
- K_{sp} solubility product (mol^2/cm^6)
- L electrode thickness (cm)
- m morphological parameter defined by Eq. [8]
- M_i symbol for the chemical formula of species i
- n_j number of electrons transferred in electrode reaction j ($n_j > 0$)
- N_i superficial flux of species i (mol/$cm^2 \cdot$ s)
- p coverage factor defined by Eq. [6]
- P_1 parameter defined by Eq. [A-4]
- P_2 parameter defined by Eq. [A-5]
- q coefficient for transport properties in porous media
- Q cell capacity based on moles of $SOCl_2$ (C/cm^2)
- Q' parameter defined by Eq. [A-14]
- r_{III} rate of precipitation at cathode (mol of LiCl formed/$cm^3 \cdot$ s)
- r_{III}' rate of precipitation at anode (mol of LiCl formed/$cm^2 \cdot$ s)
- r_V' rate of chemical reaction (V) (mol of LiCl formed/$cm^2 \cdot$ s)
- r_{VI} rate of chemical reaction (VI) at cathode (mol of LiCl dissolved/$cm^3 \cdot$ s)
- r_{VI}' rate of chemical reaction (VI) at anode (mol of LiCl dissolved/$cm^2 \cdot$ s)
- R universal gas constant (8.3143 J/mol · K)
- R_g grid resistance ($\Omega \cdot cm^2$)
- $s_{i,j}$ stoichiometric coefficient of species i in electrode reaction j
- $s_{i,k}$ stoichiometric coefficient of species i in chemical reaction k ($s_{i,k} < 0$ for reactants, and $s_{i,k} > 0$ for products)
- t time
- t_{cell} cell lifetime (s)
- $t_i^{\bullet}$ transference number of species i relative to volume average velocity
- t_i^{o} transference number of species i relative to the velocity of $SOCl_2$
- T absolute temperature (K)
- T_A temperature of surroundings (K)
- T_o the temperature at which U_o is measured (K)
- $U_{j,w}$ theoretical open-circuit potential for reaction j at the composition prevailing locally at the electrode surface, relative to a reference electrode of a given kind (V)
- U_j^{θ} standard electrode potential for reaction j (V)
- U_o open-circuit cell potential measured at temperature T_o (V)
- $v^{\bullet}$ volume average velocity (cm/s)
- v_i velocity of species i (cm/s)
- V total cell voltage (V)
- $\tilde{V}$ molar volume (cm^3/mol)
- $\bar{V}_i$ partial molar volume of species i (cm^3/mol)
- V_R reservoir volume per unit cross-sectional area of electrode (cm)
- z_i valence or charge number of species i

Greek Letters

- α_{aj} transfer coefficient in anodic direction for reaction j
- α_{cj} transfer coefficient in cathodic direction for reaction j
- β_i parameter in Eq. [A-20] (J · s/mol · cm^2)
- γ_{ij} exponent in Eq. [3]
- δ_f LiCl film thickness (cm)
- ϵ porosity or void fraction
- ϵ_{LiCl} volume fraction of LiCl crystals
- η $\Phi_1 - \Phi_2$
- η_{sj} surface overpotential for reaction j
- κ effective solution conductivity (mho/cm)
- $\kappa_{\infty,n}$ bulk conductivity of neutral electrolyte (mho/cm)
- μ_i electrochemical potential of species i (J/mol)
- ν_i^k number of moles of species i produced by dissociation of a mole of salt k
- ν^k total number of moles of ions produced by dissociation of a mole of salt k

ρ_o density of pure solvent (g/cm^3)
σ effective matrix conductivity (mho/cm)
Φ_1 electric potential in the matrix (V)
Φ_2 electric potential in the solution (V)

Subscripts

a LiCl electrode/LiCl film interface
A salt A, $LiAlCl_4$
b LiCl film/separator interface
B salt B, LiCl
i anion, cation, or solvent
j electrode reaction j
k chemical reaction k
o $SOCl_2$
p positive electrode
re reference electrode
ref reference condition under which the exchange current density is measured
s separator
w at the wall of electrode
1 Li^+ cation
2 $AlCl_4^-$ anion
3 Cl^- anion
4 $AlCl_3$
∞ bulk property

Superscripts

o initial value
′ negative electrode

REFERENCES

1. H. Bode, "Lead-Acid Batteries," R. J. Brodd and K. V. Kordesch, Translators, John Wiley and Sons, New York (1977).
2. H. B. Mark, Jr. and W. C. Vosburgh, *This Journal*, **108,** 615 (1961).
3. W. H. Beck, R. Lind, and W. F. K. Wynne-Jones, *Trans. Faraday Soc.*, **50,** 147 (1954).
4. W. G. Sunu and D. N. Bennion, *This Journal*, **127,** 2007 (1980).
5. J. S. Dunning, D. N. Bennion, and J. Newman, *ibid.*, **120,** 906 (1973).
6. A. N. Dey and P. Bro, in "Power Sources 6," D. H. Collins, Editor, p. 493, Academic Press, London (1977).
7. K.-C. Tsaur and R. Pollard, *This Journal*, **131,** 975 (1984).
8. K.-C. Tsaur and R. Pollard, *ibid.*, **131,** 984 (1984).
9. J. S. Dunning, D. N. Bennion, and J. Newman, *ibid.*, **118,** 1251 (1971).
10. A. N. Dey, *Electrochim. Acta*, **21,** 377 (1976).
11. A. E. Nielsen and J. M. Toft, *J. Cryst. Growth*, **67,** 278 (1984).
12. J. R. Driscoll, G. L. Holleck, and D. E. Toland, in "Proceedings of the 27th Power Sources Symposium," Atlantic City, NJ, June 21-24, 1976, p. 28.
13. J. Newman and C. W. Tobias, *This Journal*, **109,** 1183 (1962).
14. S. Szpak and J. R. Driscoll, *J. Power Sources*, **10,** 343 (1983).
15. R. Pollard and J. Newman, *This Journal*, **126,** 1713 (1979).
16. R. Pollard and J. Newman, *ibid.*, **128,** 491 (1981).
17. J. Newman, "Electrochemical Systems," Prentice-Hall, Englewood Cliffs, New Jersey (1973).
18. S. Szpak, J. R. Driscoll, R. Pollard, and J. J. Smith, Paper 859124 presented at the 20th Intersociety Energy Conversion Engineering Conference, Miami, FL, August 18-23, 1985.
19. J. J. Auborn, K. W. French, S. I. Lieberman, V. K. Shah, and A. Heller, *This Journal*, **120,** 1613 (1973).
20. K. A. Klinedinst and M. J. Domeniconi, *ibid.*, **127,** 539 (1980).
21. C. R. Schlaikjer, F. Goebel, and N. Marincic, *ibid.*, **126,** 513 (1979).
22. N. A. Godshall and J. R. Driscoll, *ibid.*, **131,** 2221 (1984).
23. M. J. Madou and S. Szpak, *ibid.*, **131,** 2471 (1984).
24. H. V. Venkatasetty, "Determination of Physico-Chemical Properties of Thionyl Chloride Based Electrolyte," Honeywell Corporate Technology Center Report No. N00123-81-C-0443, Bloomington, MN, December 1982.
25. R. E. Meredith and C. W. Tobias, *Adv. Electrochem. Electrochem. Eng.*, **2,** 15 (1962).
26. A. N. Dey, *This Journal*, **126,** 2052 (1979).
27. R. H. Perry and C. H. Chilton, "Chemical Engineers' Handbook," 5th ed., McGraw-Hill, New York (1973).
28. R. C. Weast, "CRC Handbook of Chemistry and Physics," 58th ed., CRC Press, Cleveland, Ohio (1978).
29. J. Newman and W. Tiedemann, *AIChE J.*, **21,** 25 (1975).
30. S. U. Falk and A. J. Salkind, "Alkaline Storage Batteries," John Wiley and Sons, New York (1969).

Investigations of Sputtered Thin Film TiO_2 Electrodes with Low Donor Densities

M. Nakao,[1] R. Schumacher, and R. N. Schindler

Institut für Physikalische Chemie, Universität Kiel, D-2300 Kiel, Germany

ABSTRACT

The photoelectrochemical behavior of sputtered low-doped titanium oxide electrodes was investigated and compared with low-doped TiO_2 single-crystal material. All low donor density electrodes yielded anodic and cathodic photocurrents upon illumination with bandgap light. The photoresponse spectra are characterized by two apparent current maxima centered around 380 and 300 nm. It is suggested that the low-doped sputtered oxide acts as a photoconductor with a nearly linear photocurrent/potential dependence in a limited potential range, or as a photosemiconductor depending on doping of the material and on the wavelength of illumination. The occurrence of two maxima in the photoresponse spectra is attributed to the inhomogeneous layered structure of the sputtered electrodes.

Titanium oxides are extensively used as anodes for industrial purposes, predominantly for chlorine and caustic production and various oxidation processes of dissolved species. In the last decade, TiO_2 also found wide use as a photoanode in electrochemical setups (1-3). Investigations in this latter field were concerned, in part at least, with rather practical aspects of the subject, like preparation of thin TiO_2 films for the economic fabrication of electrodes with specific properties (4-19), with metal doping to increase the absorption properties of the oxide material in the visible range (20-22) and with investigations about the catalytic behavior of this transition metal oxide upon coating with noble metal oxides (23-25).

To produce thin film titanium oxide electrodes, various techniques were employed: oxidation of titanium metal (4-8), chemical vapor deposition using volatile Ti-compounds (9-10), thermal decomposition of salts (11-13), sputtering in a RF discharge (14-16), and others (17-19). The photoresponse obtained with very thin Ti-oxide films is generally rather low and is shifted to shorter wavelengths as compared with the response of sintered oxide material. As the films grow thicker, the

[1]On leave from the Department of Synthetic Chemistry, Faculty of Engineering, the University of Tokyo, Hongo, Bunkyo-ku, Tokyo 113, Japan.

absorption spectra move to longer wavelengths, and the photocurrents gradually increase. It can be estimated that Ti-oxide material with a film thickness ≥ 2 μm should be able to develop properties similar to those of the sintered polycrystalline or even single-crystal TiO_2 with respect to its general photoelectrochemical behavior.

In a feasibility study on the use of sputtered thin film TiO_2 material in photoelectrochemical experiments, a structure in the photoresponse spectra was observed indicating at least two distinguishable contributions to the current in the illuminated electrode. The general pattern of the structure was qualitatively the same for all samples with a low defect concentration. The pattern changed, however, and finally disappeared upon extended thermal treatment of the material. Also, in the n-material having a low density of donors, an anomalous cathodic photoeffect was observed besides the normal anodic response. Again, upon thermal treatment of the sample, the cathodic photoresponse vanishes gradually and a strong anodic photocurrent develops.

Evidence for structure in the photoresponse spectra has been reported by several authors (6, 8, 15). Hope *et al.* (6) have shown that thermally grown TiO_2 samples exhibit a strong dependence of the spectral response on sample thickness, which was varied between 0.025 and 1.19 μm. In the thin samples, the response exhibits a maximum near 300 nm, while for the thick samples the peak occurs near 380 nm. Recently, similar structures and bandshifts in action spectra were reported by Lindquist *et al.* (8) upon surface polishing of TiO_2 electrodes prepared by thermal oxidation of Ti. The observed changes in action spectra were related to changes in recombination processes due to surface abrasion. More information on spectral shifts of the photoresponse can be found in the literature (7-10) and shall be treated in the discussion. Finally, attention is drawn to absorption measurements of optically transparent thin films of titanium oxides with thin Ti-metal layers (26). It is suggested in this study that thermal treatment of these samples leads to an indiffusion of Ti into the TiO_2 lattice, or vice versa, giving rise to the formation of strongly reduced Ti-oxides which absorb light of $270 < \lambda < 450$ nm to a smaller extent than stoichiometric TiO_2.

Also, cathodic photocurrents at n-TiO_2 electrodes have been observed before. Morisaki *et al.* (27) described a photoresponse at 800 nm under reverse bias. Juliao *et al.* (28) report on a light response under cathodic polarization. Sprünken *et al.* (29), investigated cathodic photoeffects as function of wavelength, light intensity, electrolyte *p*H, and the amount of reducible species present. Surface states are discussed to be involved (27, 29). Also, impurity bands near the conduction band were made responsible for large photocathodic currents of O_2 reduction (12, 30).

This paper presents results obtained with thin layer TiO_2 material sputtered on top of Ti metal. Prior to investigation, the samples were carefully pretreated thermally to adjust their conductivity. Special attention is paid to observations obtained at low donor densities.

Experimental

Polycrystalline TiO_2 thin film electrodes were used in this investigation with thicknesses in the range from 2 to 0.2 μm. All thin film electrodes were prepared on a conventional diode-type RF sputtering apparatus with vapor deposition equipment. Commercially obtained TiO_2 powder (Merck 99%) with anatase structure was pressed into an appropriate vessel to form the target. Clean quartz slides were employed as substrate. They reached a temperature of *ca.* 250°C during deposition. Sputtering was carried out in a 1:1 argon-oxygen atmosphere at pressure of 0.4 Pa. Sputtering power density was 8 W/cm² at a frequency of 13.56 MHz. Deposition rates were controlled using a quartz microbalance as thickness sensor. Some studies were performed using single-crystal TiO_2 electrodes. The single crystal was purchased from Hrand Djevahirdjian S. A. It was cut perpendicular to the c-axis in slices of *ca.* 1 mm thickness, polished with sandpaper, and finally polished with a 0.3 μm alumina slurry.

Three types of samples were studied. (i) The first type was polycrystalline TiO_2 sputtered on top of a 0.5 μm layer of Ti metal, which had been evaporated onto the quartz. In this sandwich, the total back area of the TiO_2 was in contact with Ti. These electrodes shall be labeled PC-TiO_2/Ti. (*ii*) This second type was polycrystalline TiO_2 sputtered on quartz directly. In these samples, the TiO_2 back area was in contact with quartz. These electrodes shall be labeled PC-TiO_2/Q. They were mainly used for optical characterization. (*iii*) The third type of sample was single-crystal TiO_2 electrodes with one face fully covered either with Ga/Ag-alloy or with Pt being evaporated on the crystal. These electrodes shall be labeled SC-TiO_2/M.

To increase their conductivity, the PC-TiO_2/Ti samples were thermally pretreated in a vacuum at $\sim 10^{-8}$ Pa and 400°-500°C for 0.5-24h. Thermal pretreatment in hydrogen was also performed with a number of electrodes. Since a different type of information was obtained in these experiments, the results shall be discussed elsewhere (31). Prior to use, all electrodes were dipped for 1 min into 1*N* HNO_3 solution and rinsed with distilled water.

Optical absorbances were recorded with a Philips SPB-500 spectrophotometer. For reflection measurements the Diffuse Reflectance Accessory, Type 9423, was used.

For electrochemical measurements, a standard apparatus was available with a PAR 173 potentiostat and a PAR 175 programmer. A frequency response analyzer, Solartron 1170, combined with an ITT 2020 microcomputer was used in all impedance studies for the analysis of the space-charge-capacitance of the electrodes. A saturated calomel electrode served as reference, a 1 cm² sheet of platinized platinum as a counterelectrode. All measurements were carried out in 0.5*M* Na_2SO_4 solution prepared with doubly distilled water. NaOH was added for investigations in alkaline environment (*p*H ≈ 13). Illumination of the exposed sample areas of ≈ 0.2 cm² was performed with a xenon high pressure lamp (Osram), the light of which was passed through a grating monochromator Type M 25 from Jobin Yvon. The light was chopped with a mechanical shutter at frequencies in the range 0.5-2 Hz to distinguish between dark and photocurrents

Results

Absorption measurements.—To obtain information about the optical characteristics of the sputtered Ti-oxide material, numerous absorbance and diffuse reflectance measurements were carried out on samples of type PC-TiO_2/Q as well as PC-TiO_2/Ti. Absorption coefficients were evaluated from oxide films having a thickness of 0.2, 0.7, and 2.0 μm, respectively. The results of the evaluation are compiled in Fig. 1. The data are corrected for interfacial reflections. They were experimentally determined to be about 30% of the incident photon flux (31) for $300 < \lambda < 450$ nm. The thickness of the individual oxide samples was calculated from the observation of interferences, both in absorbance as well as in reflectance. Assuming the refractive index to be $n_f = 2.5$ (32, 33) in the wavelength range investigated good agreement was obtained between these thickness determinations and the microbalance measurements (see Experimental section).

Evaluation of data obtained for 0.2 μm samples covered the wavelength range $\lambda > 300$ to ~ 350 nm, that for the 0.7 μm samples covered the range 330-380 nm, and that for the 2 μm sample covered the range > 350 nm. In Fig. 1, our results are compared with measurements reported by Lindquist *et al.* (7) (curve a), who produced thin TiO_2 films by fully oxidizing evaporated titanium films. Due to the very thin samples used by these authors, only the range $\lambda < 335$ nm was covered experimentally in their investigation. The residual part of the absorption curve was obtained by a fitting procedure.

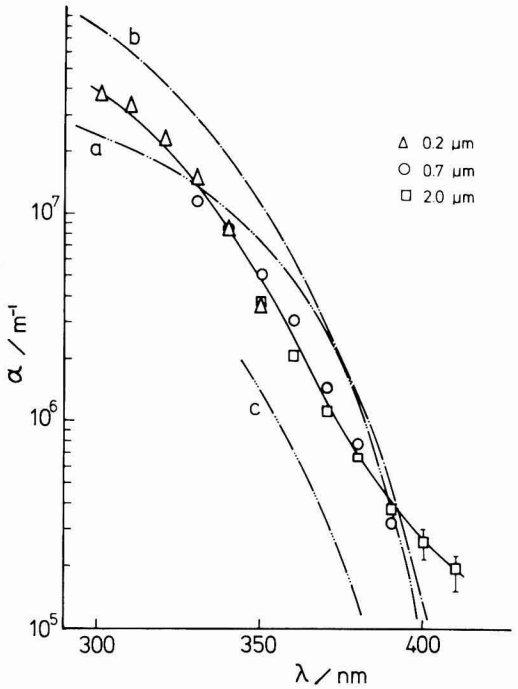

Fig. 1. Absorption coefficients of sputtered TiO_2 films as a function of wavelength. Three different film thicknesses were used for the evaluation of α from the recorded data on the optical densities. Curves (a), (b), and (c) are taken from Ref. (7, 34, 9).

Möller *et al.* (9) produced thin TiO_2 films by chemical vapor deposition. Their α-values (curve c) appear to be lower while those of Eagles (34) (curve b) are higher than ours. The evaluation of our measurements on the 2 μm sample for $\lambda > 400$ nm was hampered by the occurrence of strong interferences in this wavelength range.

From the results in Fig. 1, the penetration depth of 380 and 300 nm radiation can be estimated to be ≈ 2 and 0.01 μm, respectively.

Using the data of Fig. 1, we attempted to characterize the optical properties of the films more closely. According to Johnson (35) Eq. [1]

$$\alpha = K \cdot (\eta\nu - Eg)^{n/2} \qquad [1]$$

should be valid to describe the relation between the absorption coefficient α and the energy $\eta\nu$ of the incident light quanta. In this expression, K is a constant and Eg is the bandgap energy of the semiconductor. For direct allowed transitions, $n = 1$ is used, whereas $n = 3$ is valid for direct but forbidden transitions, and $n = 4$ for indirect allowed transitions. Equation [1] can be rewritten to yield

$$\ln(\alpha \cdot \eta\nu) = \ln K + n/2 \cdot \ln(\eta\nu - Eg) \qquad [2]$$

The α-data from the solid line in Fig. 1 were replotted using Eq. [2]. With $Eg = 3.1$ eV, a linear least squares fitting yielded a slope of 2.07 ± 0.14. This indicates that light absorption occurs via an indirect allowed transition. From the intercept $K = 1, 2 \times 10^8$ $eV^{-1}m^{-1}$ is calculated. This value is in reasonable agreement with data of $K = 8.8 \times 10^7$ (36) and 4×10^8 eV^{-1} m^{-1} (37) reported by others.

Current-potential response of PC-TiO_2/Ti and SC-TiO_2/M electrodes.—Anodic as well as cathodic photocurrents were observed in photoelectrochemical experiments with sputtered as well as with single-crystal TiO_2 working electrodes. The samples were carefully pretreated as described above and had a low capacitance in the order $< 10^{-7}$ F cm^{-2}. Although the initial properties of freshly prepared samples varied with sputter conditions, all electrodes exhibited a general behavior as outlined below.

The initially high resistive, photoinactive material started to develop a photoresponse in a narrow spectral region around 380 nm after short annealing periods in vacuo. In Fig. 2 are given two recorded examples of i-E curves for sputtered PC-TiO_2/Ti electrodes that had been thermally treated for 0.5h (a) and for 5h (b), respectively. In the drawing, the axes were omitted for clarity. Sweep range and magnitude of the light response are as indicated. The measurements were carried out at pH ~ 13 upon illumination with chopped light of wavelength $\lambda = 380$ nm. In the dark, the electrodes showed n-semiconducting properties. An anoding blocking up to several volts was observed for some samples. Under illumination, the electrodes revealed a nearly linear i_{ph}/E dependence in this potential range. Both anodic and cathodic photocurrents were registered. At the transition potential of about −0.1V for this pH, the photocurrent changed sign. Thus, upon illumination in a limited potential range, the electrodes exhibited properties as expected for a photoconductor with an ohmic resistance in the MΩ range for the light intensity applied.

Upon further thermal treatment of PC-TiO_2/Ti material *in vacuo*, a further gradual increase in photoresponse resulted. However, the rate of this increase was different for the regions around 380 and 300 nm (see below). In Fig. 3 are shown photocurrent/potential dependences i_{ph}/E at pH 7 for illumination at 380 and 300 nm. The curves (solid lines) were obtained with chopped light and were corrected for contributions from dark currents. To appreciate the degree of this correction, the dark current alone is also indicated (dotted line). For 380 nm irradiation, a nearly linear photoresponse is obtained in the investigated range, −0.75 to +1V, with a transition potential around +0.3V. Upon irradiation under otherwise identical conditions at 300 nm, a clear photocurrent onset is observed at a polarization around −0.7V. In this case, the cathodic photocurrent is superimposed by cathodic dark currents which pass through the n-semiconductor.

It is important to point out that single-crystal TiO_2 electrodes with low donor densities exhibit a similar photoelectrochemical behavior as the polycrystalline-

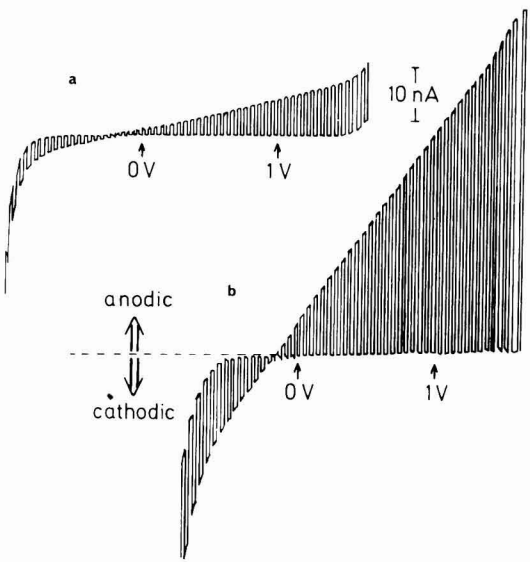

Fig. 2. Current-potential curves obtained at pH ~ 13 for sputtered PC-TiO_2/Ti electrodes, thermally pretreated *in vacuo* for 0.5h (a) and 5h (b), respectively. The monochromatic light ($\lambda = 380$ nm) was chopped with 0.5 Hz. Potentials are given *vs.* SCE (see Experimental section).

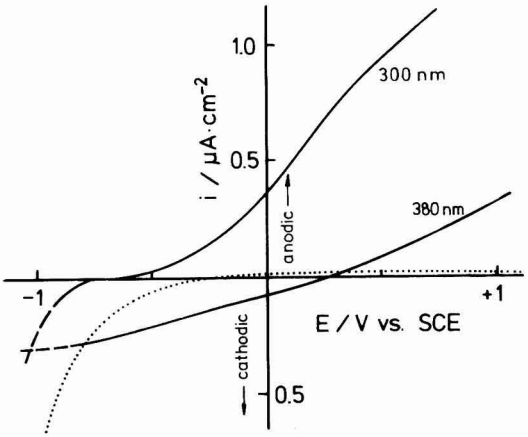

Fig. 3. Corrected photocurrent-potential characteristics obtained upon illumination with λ = 380 and 300 nm, respectively, at pH 7 for electrodes, as described in the text. The dashed line describes the current-potential behavior in the dark.

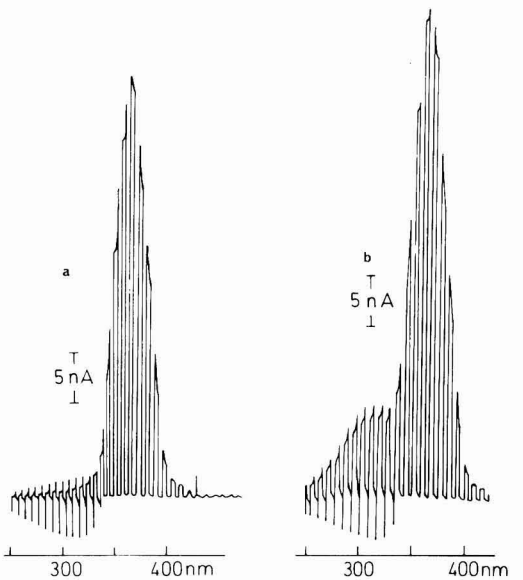

Fig. 4. Spectral response obtained at + 1V vs. SCE polarization and pH 13 for sputtered PC-TiO_2/Ti electrodes, thermally pretreated *in vacuo* for 5h (a) and 7h (b), respectively. The light was chopped with 0.5 Hz. Spectrum (a) was obtained with the identical electrode as the i-E curve in Fig. 2b.

sputtered electrodes described above. In the potential range −0.5V to +2V, the photocurrent/potential dependences of SC-TiO_2/M electrodes was found to be linear. Both anodic and cathodic photocurrents were obtained upon irradiation at around 300 nm provided the measured capacitance of the electrodes was in the range $\leq 10^{-7}$ F · cm^{-2}. Further details shall be given elsewhere (38). For action spectra of these electrodes, see below.

The properties associated with those of a photoconductor, *i.e.*, the linear photocurrent/voltage dependence and the anodic as well as cathodic photoresponse, vanish upon prolonged heat-treatment *in vacuo*. This holds for sputtered samples as well as for single-crystal materials. If the apparent doping density becomes $N_D \geq 10^{17}$ cm^{-3}, the TiO_2 photoelectrodes act as expected for a n-material.

Action spectra.—In Fig. 4 are given action spectra recorded at a polarization of +1V *vs.* SCE. Chopped light was used in the registration. Spectrum (a) was obtained with the identical electrode as the i-E curve in Fig. 2b. Spectrum (b) describes a sample that was thermally annealed *in vacuo* for about 7h. Again, the ordinates were omitted in the drawing. The wavelength range and magnitude of the photoeffect are indicated. It can be gathered from these records that the light response centered around 300 nm grows in later with annealing time indicating an induction period. It eventually develops to become a dominant contribution in the action spectrum of thin film, low-doped sputtered samples. In Fig. 5 are given action spectra of a PC-TiO_2/Ti electrode (top) and a SC-TiO_2/M electrode (bottom) as function of polarization. The spectra are corrected for dark current contributions, but they are not normalized for constant photon flux. However, all action spectra were obtained with the same optical arrangement. The spectra shown in Fig. 5 (top) were obtained with the identical electrode as the i_{ph}/E curves given in Fig. 3.

The pronounced cathodic photocurrents in Fig. 5 (top) at a polarization of −1.1V in the wavelength range $\lambda < 425$ nm diminished gradually upon changing the polarization to positive values. Of the two apparent contributions, the short wavelength response diminished faster than the contribution centered around 380 nm. In the range $-0.5V < E < \pm 0$ V, both a cathodic response at long wavelengths and an anodic response at short wavelengths were registered. Upon further increase of the applied potential, only the normal anodic photoeffect of the n-material was observed again with clearly two maxima around λ = 380 and 300 nm. Quite similar observations were made with low-doped SC-TiO_2/M electrodes (bottom) with respect to the occurrence of a cathodic/anodic photoresponse and its dependence on the potential applied. In this case, however, the long wavelength contribution was more pronounced than the response around 300 nm.

At the present time, it cannot be decided whether the minimum in the action spectra around 360 nm should be related to a reported maximum in the reflectance spectra of TiO_2, as measured by Cardona and Harbeke (32).

Again, upon extended heat-treatment *in vacuo*, the two apparent maxima in the action spectra disappear, and the action spectra reveal only one maximum, the position of which is a function of doping density (40).

Impedance measurements.—Extensive impedance measurements were carried out with sputtered low-doped PC-TiO_2/Ti electrodes in the frequency range 0.1 Hz to 10 kHz. It is deduced from the observed changes in admittance as function of frequency for electrodes as characterized by Fig. 3 and 5 (top) in the dark that the Schottky barrier that exists at positive polarizations becomes permeable at potentials close to ± 0 V SCE at pH 7 and negative thereof. Upon illumination, this effect is strongly enhanced. It was found that this photoconductive behavior of the material disappears in samples with $N_D \geq 10^{17}$ cm^{-3}. More details are given elsewhere (31).

Structure and grain size of the sputtered materials.—The TiO_2 layers produced by sputtering from TiO_2 targets in an O_2/Ar-atmosphere possess a very low conductivity. Occasional checks yielded a resistance in the range > 10 MΩ cm^{-1}. X-ray investigations (31) indicated that the material deposited was a mixture having anatase and rutile structure. The defraction pattern revealed that, with quartz as a substrate, the formation of anatase structure is preferred with some rutile contributions. Deposition of TiO_2 on a Ti layer yielded rutile material predominantly. Grain size was obtained from SEM investigations. In agreement with other reports (9, 39), it was found to be not larger than 0.1 μm. We noted that grain size increased on raising the temperature of the substrate holder. This temperature was not especially controlled. Without external heating it reached values up to 250°C during the 2-20h time needed to deposit the 0.2-1 μm films.

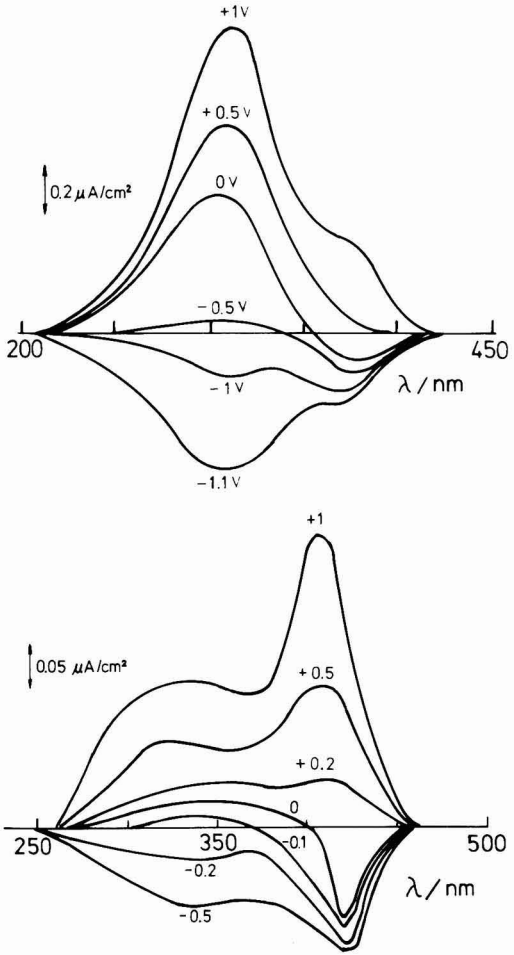

Fig. 5. Action spectra for low-doped Ti-oxide electrodes as function of polarization, given in V vs. SCE (top) PC-TiO_2/Ti-electrode of 2 μm thickness; (bottom) SC-TiO_2/Pt-electrode of 1 mm thickness (see Experimental section). Spectra (top) were obtained with the identical electrode as the i_{ph}/E-curves in Fig. 3.

There are indications from blank experiments that titanium is oxidized, in part at least, in the sputtering process. Also, reactions take place along the grain boundaries between the titanium film and the oxide cover during the sputter process resulting in a reduced oxide layer interface. Sputtering of 650Å TiO_2 on top of ~ 50Å layers of metallic titanium reacted the metal away beyond detectability. Only in the case of > 100Å Ti-layers did the metal survive—in part, at least—the reaction, as seen from measurements of transparencies at wavelength $\lambda > 450$ nm (26). Annealing the samples *in vacuo* to increase their conductivity certainly will lead to a growth of this reduced oxide interface. Thus, sputtering of TiO_2 films on top of a Ti-layer followed by the thermal treatment *in vacuo* results in the formation of a small-grain material with a metal-rich composition on its back side. The thicker the film grows, the closer is its stoichiometry to TiO_2.

Discussion

It is of interest to discuss whether the unusual properties observed with our Ti-oxide electrodes, *i.e.*, the shapes of the photoelectrochemical response spectra, and the occurrence of cathodic as well as anodic photoeffects, can be related to a gradient in the composition of the sputtered material. It is conceivable that deposition of Ti-oxide on top of a Ti-metal film using sputtering technique leads to a metal-rich composition on the back side of the electrode whereas the cover layers consist of nearly stoichiometric TiO_2 films. The development of a lightly doped film deposited on a heavily doped layer of the same material (n^+/n-layer) was suggested by Soliman and Seguin (15) to result from sputtering on a heated substrate and subsequent annealing of the sample.

The shapes observed in the photocurrent spectra with apparent maxima around 380 and 300 nm, for a wide range of electrode polarizations, might be due to several contributing factors. It is suggested that the predominant contribution comes from the strongly inhomogeneous, layered structure of the deposited oxides and thus from the inhomogeneously doped samples. A further consequence of this layered structure will be a gradient in absorptivity normal to the surface. The penetration depths for the 380 and 300 nm radiation are about 1 and 0.01 μm, respectively, for fully oxidized material. This means that the short wavelength radiation is effectively absorbed in layers close to the surface, whereas the long wavelength light also samples the deep layers of the oxide close to the back contact. The shape in the action spectrum may thus reflect changes in composition normal to the surface and, consequently, may be related to a doping profile of the layered electrode. Analytical expressions had been used to compute the spectral characteristics of thin film TiO_2/electrolyte junctions as function of, amongst others, donor density and sample thickness. The calculations indicate a strong influence on the spectra, especially for low-doped material in which the electron-hole separation in the surface electric field is small as compared to their separation by diffusion. The resulting shifts in the position of the photocurrent maxima were considered to be in qualitative agreement with experimental findings (9, 40, 41). Finally, it can be predicted that changes in composition will also lead to a more complex gradient of the electric field throughout the sample. For homogeneously doped material, a parabolic gradient is considered.

Support for the interpretation proposed can be gathered from a number of different references on the spectral distribution of photocurrents and from absorption measurements. Light absorption in TiO_2 is associated with an electronic transition from the 2p level of O^{2-} to an empty d-state of Ti^{4+}. Reduction of TiO_2 by extracting oxygen from the semiconductor with Ti metal will certainly diminish its optical absorption and, thus, shift the absorption maximum to shorter wavelength. A higher transparency will result for the reduced oxide at wavelength $\lambda > 300$ nm as compared to stoichiometric TiO_2. This effect appears to be the reason for the more pronounced shifts shown in the photoresponse spectra of 0.1-1.0 μm TiO_2 films deposited on Ti metal as compared to TiO_2 deposited on SnO_2 (9). The same arguments hold for thin samples prepared by electrochemical oxidation of Ti in molten $NaNO_3/Ca(NO_3)_2$ having a thickness of about 0.05 μm. The maximum in the photoresponse for these materials is found near 300 nm whereas for the thermally grown ≃ 2 μm samples maxima are reported in the range 350-380 nm, depending on donor density (40). Hope *et al.* (6) were the first to suggest that changes in the spectral dependence of the photoresponse might be related to compounds other than TiO_2 being produced near the metal oxide interface in the oxidation procedure. The results on the photoresponse of polycrystalline TiO_2 electrodes as reported recently by Lindquist *et al.* (8) appear to lend further support to the assumption of a depth profile in the sputtered TiO_2/Ti samples as described in this paper. In particular, the bandshifts obtained upon surface polishing give evidence for a gradient in sample composition normal to the electrode surface (8). The concept of a recombination layer at the electrode surface was introduced to explain the observations. This concept appears similar to the assumption of an "inert layer," which absorbs photons like a filter without contributing to a

photocurrent (42). A recent study of self-color anodizing titanium proves again the existence of such a profile (43). Structure in the spectral dependence was also reported in Ref. (10b).

Finally, absorption measurements carried out with optically transparent thin TiO_2/Ti films demonstrate quite clearly that there is interaction between TiO_2 and Ti at temperatures that are used for thermal treatment to the effect that the absorption of the Ti-oxide films is diminished (26). This effect is particularly important at wavelengths $\lambda > 300$ nm.

Shapes in the photocurrent spectra of single-crystal TiO_2 electrodes slightly reduced by a thermal treatment *in vacuo* may equally well result from inhomogeneous doping. The mechanism of vacuum reduction of TiO_2 single crystals at temperatures around 500°C is by no means understood. It has been suggested (44) that traces of organic material are to be made responsible for the process. Since in this case surface reactions dominate, the SC-TiO_2 surface will become roughened and covered by a reduced layer whereas the deeper layers in the bulk remain nearly unchanged. This is in contrast to sputtered PC-TiO_2/Ti electrodes in which the cover layers are less reduced than the deeper layers close to the Ti back contact. It is suggested that this difference is the predominant reason for the apparent distinction in the shapes of action spectra for PC-TiO_2/Ti and our SC-TiO_2/Pt electrodes as shown in Fig. 5. The spectral response of the slightly vacuum reduced SC-TiO_2/Pt electrodes thus resembles that of polycrystalline electrodes prepared by thermal oxidation of Ti (8, 40).

We shall now turn to the cathodic photoeffect. The pronounced cathodic photoeffect of TiO_2 (*cf.* Fig. 2 and 3) observed with the sputtered, as well as with the single-crystal electrodes, occurs upon illumination with bandgap light. Its quantum yield in low-doped material is of the same magnitude as for the anodic photoeffect at positive polarizations of the electrode. In this respect, it is distinguished from observations of cathodic photocurrents in the subbandgap regime, which were assigned to transitions involving "impurity bands" of dopants (30). As evident from Fig. 5, the action spectra obtained under anodic and cathodic polarization show very close resemblance in the whole spectral region of $250 < \lambda < 450$ nm indicating that both photocurrents follow the same excitation pathway.

It is proposed that this unusual behavior for the n-material TiO_2, with respect to cathodic photocurrents, is a consequence of the low doping density of the oxide. This is to say that the photoelectrochemical behavior of our low-doped electrodes is to be interpreted as that of a photoconductor rather than that of an irradiated semiconductor.

Reliable information on doping densities cannot be given for this inhomogeneous material. If it is assumed that the electrode can be described as a stack of differently doped layers being connected together in series, measurements of the overall inverse capacitance, $1/C$, will be composed of the sum for the inverse capacitances for each individual layer. For an electrode being covered by nearly stoichiometric TiO_2, this layer will dominate in the calculated capacitance values. Thus, the data given in the Results section only indicate the order of magnitude in the apparent capacitance. This value is more than an order of magnitude smaller than values obtained with electrodes exhibiting semiconducting properties. If, despite all these complications, an evaluation of the Mott-Schottky approach is attempted curved plots for $1/C^2$ *vs.* E are obtained. From the potential independent part at positive polarization, the depletion layer thickness of the thin films can be estimated (31). The plots became linear upon extended heat-treatment.

The low-doped material exhibits a significant conductivity only under illumination. A nearly linear photocurrent/voltage characteristics is observed. The field distribution inside the electrode is expected to be nearly linear in a similar way to that proposed for passive films on metal (45) or for amorphous hydrogenated silicon thin film electrodes (46). Thus, the unusual photophenomena would occur quite generally in systems with low defect densities: the working electrode will act as photoanode or as photocathode, depending on external polarization.

In agreement with this interpretation, the anomalous properties of the electrodes vanish upon prolonged heat-treatment of the material *in vacuo* (40) or upon extensive cathodic polarization giving way to the normal properties of an n-semiconductor. These treatments strongly increase the N_D level in the oxide electrode as experimentally observed in changes of Mott-Schottky slopes, which eventually became linear. Also the spectral response is changed. The two maxima in the action spectra obtained for low-doped material converge to yield one common maximum around 340 nm depending on the defect density (40).

Photocathodic effects at n-type TiO_2 electrodes have been reported before. Sprünken *et al.* (29) discussed surface states to mediate the electron transfer through the barrier in an attempt to evaluate the flatband potentials for TiO_2 from determinations of transition potentials and to account for large cathodic quantum yields in the presence of suitable acceptors in solution. Matsumoto *et al.* (30) preferred a d-band model to account for their observations. Laser *et al.* (33) invoked the occurrence of tunneling to describe electron transfer through TiO_2 films in a study on the electrochemical and optical properties of thin titanium oxide layers. Tunneling under reverse bias, however, can be excluded to account for cathodic photoeffects because under these conditions recombination at the surface will dominate and prevent a net photocurrent.

Also, with other materials anomalous photoeffects were obtained. At n-CdS electrodes under forward bias, the cathodic photocurrent was strongly enhanced by polishing the surface mechanically. The effect was removed when the damaged surface was etched away (47). The authors discuss the formation of a high resistance compensated surface layer which is photoconductive (48) and the participation of intrabandgap states as the preferred model to describe the photocathodic effect. Cathodic photocurrents recently (49) observed at single-crystal as well as at polycrystalline CdS electrodes were attributed to unreduced or partly reduced sulfur at the surface. Nakao *et al.* (50) have considered contributions from the back-side contact between semiconductor and metal to account for unusual behavior of illuminated n-CdS electrodes. A cathodic photoresponse was also obtained in measurements of transient photopotentials upon flash illumination at $\lambda > 520$ nm using silver as back-side contact. With indium, no cathodic photoeffect appeared. A system with two barriers was suggested to explain the results. Computer simulation supports this explanation (50). Anomalous photoeffects were observed also with the p-semiconductor selenium. Gissler (51) suggested thinning of the space charge layer upon illumination to be the reason for this behavior. For lamellar n- and p-type InSe electrodes unexpectedly cathodic and anodic photoeffects are reported together with the normal photoelectrochemical behavior (52). The authors interpret their results, which were obtained with material having a doping density in the order 10^{15} carriers cm^{-3}, as being due to the presence of photoconductive effects together with the normal photoelectrochemical behavior. Our samples also possess layers with very low donor densities. Thus, the arguments as presented above may be applied equally well to the results presented here, especially to the photoeffect at the semiconductor/electrolyte interface by illumination with short wavelength light.

Following this argument, the contribution to photocurrent from the back side of the electrode is expected to increase in low-doped material relative to the contributions from the bulk of the semiconductor on reducing sample thickness. Preliminary experiments with a set of low-doped PC-TiO_2/Ti electrodes in which the oxide layer was close to 0.2 μm revealed a strong increase of the contribution with a maximum around 380 nm.

It is interesting to point out that the observed pattern of the action spectra for the electrode SC-TiO_2/Pt (*cf.* Fig. 5b) at polarizations around ± 0 V *vs.* SCE is similar to the spectra reported by Nakao *et al.* (50) for CdS electrodes with a cathodic contribution at long wavelengths and an anodic photoresponse at short wavelength irradiation. The construction of better defined thin film electrodes would be required to discuss this point more closely.

Conclusion

The photoelectrochemical behavior of low-doped titanium oxide electrodes sputtered on top of metallic Ti was studied. It was compared with low-doped single-crystal TiO_2 material. The action spectra of all sputtered electrodes obtained under a variety of polarization potentials revealed two distinct photoresponse maxima around 380 and 300 nm. This shape was tentatively attributed to an inhomogeneous, quasi-layered structure of the material with a metal-rich oxide phase on the back side. Anodic as well as cathodic photoresponses were obtained. It is argued that, at low doping densities, the oxide acts upon illumination as a photoconductor rather than as a semiconductor giving rise to an anodic or a cathodic photocurrent, depending on electrode polarization.

Acknowledgments

One of the authors (M. M.) thanks the Konrad-Adenauer-Stiftung for a scholarship to study in West Germany from 1980 to 1983. The authors acknowledge technical help of J. Deyhle and H. Alberti. This work is supported in part by the BMFT Bonn within Project ET 4274 A.

Manuscript submitted March 4, 1985; revised manuscript received July 25, 1986.

The Institut für Physikalische Chemie, Universität Kiel assisted in meeting the publication costs of this article.

REFERENCES

1. H. Gerischer, in "Topics in Applied Physics," Vol. 31, B. O. Seraphin, Editor, Springer-Verlag, Berlin (1979).
2. R. Morrison, in "Electrochemistry at Semiconductor and Oxidized Metal Electrodes," Plenum Press, New York (1980).
3. A. J. Nozik, *Ann. Rev. Phys. Chem.*, **29,** 189 (1978).
4. D. Laser and S. Gottesfeld, *This Journal*, **126,** 475 (1979); R. D. Quinn and N. K. Armstrong, *ibid.*, **125,** 1790 (1978).
5. J. Lichtscheidl, K. J. Hartig, N. Getoff, Ch. Tauschnitz, and G. Nauer, *Z. Naturforsch.* **36a,** 727 (1981).
6. G. A. Hope, G. G. Morgan, and A. R. McKenzie, *Aust. J. Chem.*, **34,** 713 (1981).
7. S.-E. Lindquist, B. Finnström, and L. Tegner, *This Journal*, **130,** 351 (1983).
8. S. E. Lindquist, A. Lindgren, and Z. Yan-Ning, *ibid.*, **132,** 623 (1985).
9. F. Möllers, H. J. Tolle, and R. Memming, *ibid.*, **121,** 1160 (1974).
10. (a) S. N. Frank and A. J. Bard, *J. Am. Chem. Soc.*, **99,** 4667 (1977); (b) Y. Takahashi, A. Ogiso, R. Tomoda, K. Sugiyama, H. Minoura, and M. Tsuiki, *J. Chem. Soc. Faraday Trans. 1*, **78,** 2563 (1982).
11. C. Stalder and J. Augustynski, *This Journal*, **126,** 2007 (1979).
12. Y. Matsumoto, J. Kurimoto, T. Shimizu, and E. Sato, *ibid.*, **128,** 1040 (1981).
13. H. Yoneyama, H. Sasaki, and H. Tamura, *Denki Kagaku*, **49,** 222 (1981).
14. M. Takeuchi, *Phys. Status Solidi* A, **55,** 653 (1979).
15. A. A. Soliman and H. J. J. Seguin, *Solar Energ. Mater.*, **5,** 95 (1981).
16. M. F.Weber, L. C. Schumacher, and M. J. Dignam, *This Journal*, **129,** 2022 (1982).
17. F. Huber, *ibid.*, **115,** 203 (1968).
18. R. Wang and C. H. Henager, Jr., *ibid.*, **126,** 83 (1979).
19. Y. Matsumoto, J. Kurimoto, Y. Amagasaki, and E. Sato, *This Journal*, **127,** 2148 (1980); and Y. Matsumoto, T. Shimizu, A. Toyoda, and E. Sato, *J. Phys. Chem.*, **86,** 3581 (1982).
20. A. K. Ghosh and H. P. Maruska, *This Journal*, **124,** 1516 (1977).
21. J. Augustynski, J. Hinden, and C. Stalder, *ibid.*, **124,** 1063 (1977).
22. A. Monnier and J. Augustynski, *ibid.*, **127,** 1576 (1980).
23. V. Guruswany, O. J. Murphy, V. Young, G. Hildreth, and J. O'M. Bockris, *Solar Energ. Mater.*, **6,** 59 (1981).
24. E. Borgarello, J. Kiwi, M. Grätzel, E. Pelizzetti, and M. Visca, *J. Am. Chem. Soc.*, **104,** 2996 (1982).
25. M. D. Ward and A. J. Bard, *J. Phys. Chem.*, **86,** 3599 (1982).
26. D. M. Teschner, R. Schumacher, and B. Stritzker, *Ber. Bunsenges. Phys. Chem.*, **90** (1986).
27. M. Morisaki, M. Hariya, and K. Yazawa, *Appl. Phys. Lett.*, **30,** 7 (1977).
28. J. F. Juliao, F. Decker, R. Brenzikofer, and M. Abramovich, *This Journal*, **127,** 2067 (1980).
29. H.-R. Sprünken, R. Schumacher, and R. N. Schindler, *Faraday Discuss. Chem., Soc.*, **70,** 55 (1980); *Ber. Bunsenges. Phys. Chem.*, **84,** 1040 (1980).
30. Y. Matsumoto, T. Shimizu, and E. Sotoh, *Electrochim. Acta*, **27,** 419 (1982).
31. M. Nakao, Ph.D. Thesis, University of Tokyo, Tokyo, Japan (1984).
32. M. Cardona and G. Harbeke, *Phys. Rev. A.*, **137,** 1467 (1965).
33. D. Laser, M. Yamiv, and S. Gottesfeld, *This Journal*, **125,** 358 (1978).
34. D. M. Eagles, Jr., *Phys. Chem. Solids*, **25,** 1243 (1964).
35. E. J. Johnson, in "Semiconductors and Semimetals," Vol. 3, R. K. Willardson and A. C. Beers, Editors, Academic Press, New York (1967).
36. P. Salvador, *Solid State Commun.*, **34,** 1 (1980).
37. P. Salvador, *Mater. Res. Bull.*, **15,** 1287 (1980).
38. D. Teschner, Ph.D Thesis, University of Kiel, In preparation.
39. P. D. Fleischauer and J. K. Allen, *J. Phys. Chem.*, **82,** 432 (1978).
40. H.-R. Sprünken, Ph.D Thesis, University of Kiel (1982); in "Proceedings of the 2nd International Conference on Photochemical Conversion and Storage of Solar Energy," p. 84, Cambridge (1978).
41. D. Popkirov and R. N. Schindler, *Solar Energ. Mater.*, **13,** 161 (1986).
42. L. A. Harris and R. H. Wilson, This Journal, **123,** 1010 (1976).
43. J. L. Delplancke and R. Winand, Private communication.
44. W. D. Ohlsen and O. W. Johnson, *J. Appl. Phys.*, **44,** 1927 (1973).
45. N. Sato, This Journal, **129,** 255 (1982).
46. G. S. Calabrese, M-S. Lin, J. Dresner, and M. S. Wrighton, *J. Am. Chem. Soc.*, **104,** 2412 (1982).
47. B. Vainas, G. Hodes, and J. Dubow, *J. Electroanal. Chem.*, **130,** 391 (1981).
48. N. Müller, G. Hodes, and B. Vainas, *ibid.*, **172,** 155 (1984).
49. J. H. Reeves and M. Cocivera, *This Journal*, **131,** 2042 (1984).
50. M. Nakao, K. Itoh, and K. Honda, Submitted.
51. W. Gissler, *This Journal*, **127,** 1713 (1980).
52. C. Levy-Clement, N. LeNagard, O. Gorochow, and A. Chevy, *ibid.*, **131,** 790 (1984).

JOURNAL OF THE ELECTROCHEMICAL SOCIETY

SOLID-STATE SCIENCE AND TECHNOLOGY

NOVEMBER 1986

The Plasma Etching of Polysilicon with CF_3Cl/Argon Discharges

I. Parametric Modeling and Impedance Analysis

Kenneth D. Allen*,[1] and Herbert H. Sawin*

Department of Chemical Engineering, Massachusetts Institute of Technology, Cambridge, Massachusetts 02139

Michael T. Mocella*,[2]

E.I. du Pont de Nemours and Company, Incorporated, Freon® Products Laboratory, Wilmington, Delaware 19898

Mary W. Jenkins

E.I. du Pont de Nemours and Company, Incorporated, Engineering Department, Wilmington, Delaware 19898

ABSTRACT

A parallel plate plasma etching apparatus with extensive diagnostic capabilities has been constructed to study the plasma etching of heavily P-doped polysilicon in Freon® 13 (CF_3Cl)/argon mixtures. A simple ac impedance model was used to estimate time-averaged plasma properties; this model gave electron densities and sheath voltages in reasonable agreement with experimental evidence. Response surface methodology, an experimental design and statistical analysis tool, was used to efficiently obtain high quality empirical representations of the etching rate and total ion flux as functions of external parameters: power input, pressure, and composition.

In this paper, we examine the plasma etching of heavily phosphorus-doped polysilicon (an important gate and interconnect material for MOS devices) with the chlorofluorocarbon gas, CF_3Cl. The interest in and use of plasma processes is increasing, particularly in thin film etching for VLSI applications. Plasma processing allows profile control, a vital requirement as minimum feature sizes steadily decrease. Etching rates, selectivities, uniformities, and directionalities of plasma processes can be optimized for a particular application through appropriate selection of chemical system and operating conditions.

Few studies of polysilicon etching in CF_3Cl have been published, however, interesting and encouraging results have been reported. The etching rate exhibits a maximum with pressure at approximately 0.5 torr (1). Selectivities of 30:1 for Si etching over SiO_2 etching have been reported (2), more than adequate for MOS fabrication. In addition, nearly vertical profiles are obtained for CF_3Cl/C_2F_6 mixtures (2, 3). Few data are available regarding the directionality of doped polysilicon plasma etching with pure CF_3Cl.

We present a method by which polysilicon etching in a CF_3Cl plasma has been described successfully by a statistical model, and interpret the observed characteristics in terms of physical plasma properties inferred from an electrical impedance model. Although we have chosen a specific etching gas, the reader should note that many of the techniques described here are applicable to other chemical systems. Increasing demands on etching processes for improved throughput, uniformity, profiles, and selectivity require better control of these etching characteristics. Presently, etching processes are developed largely by trial and error methods or by single-variable experimentation; process development is, therefore, both difficult and expensive. To place etching process design and control on a more rational basis, models for the etching process must be formulated.

To our knowledge, CF_3Cl plasma etching processes have not been modeled previously. However, predictive kinetic models have been formulated for polysilicon etching in CF_4 discharges (4, 5). In such models, a set of chemical reactions is proposed to simulate radical and ion formation and loss, transport, and surface reaction, and the steady-state solution of the resulting ordinary differential equation set is obtained. However, rate constants for most of the reactions in the model are not known and must be estimated. Consequently, these models necessarily contain at least 10 fitted or estimated parameters. The present inability of kinetic models to predict trends in plasma properties or etching characteristics is not surprising, given the present lack of knowledge of fundamental chemical and physical processes involved in plasma etching.

We have divided the plasma process modeling problem into a series of more manageable tasks. First, each etching process "response" (*e.g.*, etching rate or total ion flux) is characterized experimentally in terms of externally controlled variables, or "factors" (*e.g.*, pressure or power input). Response surface methodology (RSM), an experimental design and data analysis strategy, is used to examine efficiently the etching response over wide factor ranges. The resulting data set is used with statistical analysis techniques to generate polynomial representations of etching process responses. These polynomial response models are valuable for process design in cases where predictive kinetic models are unavailable.

*Electrochemical Society Active Member.

[1]Present address: Honeywell, Solid State Electronics Division, Plymouth, MN 55441.

[2]Present address: E.I. du Pont de Nemours, Freon® Office and Laboratory, Chambers Works, Deepwater, NJ 08023.

Through an electrical impedance model for the plasma, the external variables are related to physically significant plasma properties, *e.g.*, electron density. The etching responses are then examined in light of the physical properties predicted by the impedance model. RSM is helpful in this endeavor, as polynomial response models are easily converted into contour plots of etching responses. The insight gained may provide an explanation for the observed trends in the etch responses and may also be used to guide the ultimate modeling step, the construction of a physically realistic kinetic model with predictive capabilities.

In the second paper of this series, energetic ion bombardment in $CF_3/Cl/Ar$ RF discharges is examined. Etching rate and directionality are successfully described in terms of the plasma impedance and ion bombardment models in the third paper.

Experimental

The parallel plate etcher used in this work is presented in Fig. 1. The stainless steel cylindrical etching chamber is 27 cm in diameter by 19 cm high. The 12.7 cm diameter lower electrode is grounded to the chamber base plate and can be removed through the load-lock for sample mounting. The 15 cm upper electrode is powered by an ENI 2100L broad-band (10 kHZ to 12 MHz) amplifier through a π-network matching system. Voltage and current waveforms at the powered electrode are acquired by a Tektronix P6009 100× high frequency (120 MHz bandwidth) voltage probe and an Ion Physics CM-100-M current sensor (30 MHz bandwidth), respectively, in conjunction with a Tektronix 7603-7D20 programmable digitizing oscilloscope (70 MHz bandwidth). The electrodes are isolated from the chamber walls by Teflon rings which shield the high electric fields, confining the plasma between the electrodes. Physically confining the discharge with a 13 cm diameter Teflon ring at the electrode periphery does not significantly alter the plasma properties.

The etchant gases are mixed using mass flowmeters, enter the reactor through a shower head arrangement in the center of the upper electrode, and flow radially outward between the electrodes. System pressure is measured with a MKS 222 capacitance manometer, and maintained independent of flow rate by a MKS Baratron Model 252A exhaust valve controller. The effluent gases are passed through a liquid nitrogen cold trap and pumped by an 80 m^3/h mechanical roughing pump. A 5 mW 632.8 nm He-Ne laser is used as an interferometer for *in situ* measurement of the polysilicon etching rate. Visible and near-UV optical emission from the plasma are monitored by a Jarrell-Ash Monospec 27 monochromator with a photomultiplier tube or a Tracor-Northern TN-6100 multielement-array detector. Diagnostic equipment control and data acquisition are performed by an 8088-based microcomputer.

A 50 μm diam pinhole in the lower electrode connects the main chamber to the lower chamber, in which a Leybold-Heraeus Quadruvac Q200 quadrupole mass spectrometer is housed. The pinhole diameter is less than the mean free path of the plasma gas so the pressure of the pinhole does not perturb the plasma; the effusive flux of species into the lower chamber is, therefore, representative of the flux upon the electrode surface. The lower chamber is differentially pumped to $\leq 10^{-6}$ torr by a 150 liter/s turbomolecular pump, and contains a LN_2 baffle to further reduce the background pressure of condensible gases. A series of three 97% transmission grids, which can be electrically biased, is used to collect and filter the ions or neutrals into the mass spectrometer. Total ion current is measured by moving a flag between the grid system and the mass spectrometer with a stepping motor. By biasing the grids above the plate to repel electrons passing through the pinhole, as well as to collect secondary electrons emitted from the flag upon ion bombardment, a Faraday cup is formed. The total positive ion current is measured with a Keithley Model 602 electrometer. Further details of the ion sampling apparatus can be found elsewhere (6).

The experimental procedure is as follows. The gas flow rates and system pressure are set. At the desired power input setting, the plasma impedance is matched with the π-network using a blank electrode (no wafer present). After shutting off the flow and evacuating the main chamber, the lower electrode is removed from the chamber, the sample is clamped to it, and the electrode and sample are degassed (evacuated to 10 mtorr) in the load-lock before being inserted into the chamber. Gas flow is resumed, and the etching process is initiated shortly after system pressure stabilizes. The laser photodiode detector output is used for end-point detection. Power input is set with a Bird Electronics Model 43 power meter; actual power input is later calculated as the product of the voltage and current waveforms.

The samples used were one-quarter sections of 4 in. wafers. The 0.4 μm heavily phosphorus-doped ($\approx 18\ \Omega/\square$ polysilicon layer was deposited by CVD on a 0.7 μm thermal oxide layer and patterned with 1.2 μm thick Kodak 820 photoresist. Polysilicon lines 2.25 μm in width were etched in this study.

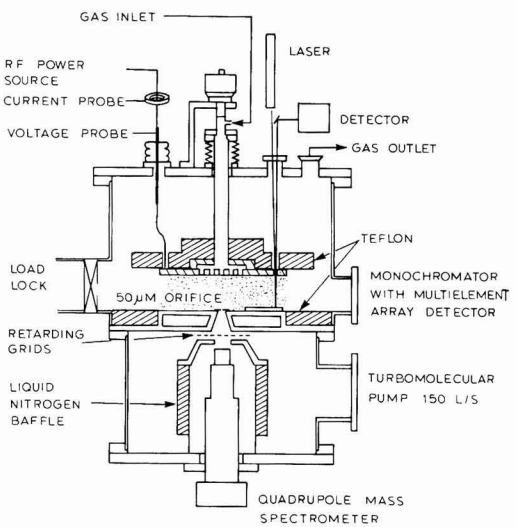

Fig. 1. Schematic of parallel plate etcher

Impedance Analysis

Circuit analogies of radio frequency glow discharges have been investigated previously (7). The measured discharge impedance determines the values of the components in the electrical analog. In turn, the circuit model can be used to estimate plasma properties (8). In this section, we derive expressions for bulk plasma resistance, sheath capacitance, potential drop across the sheaths, bulk electric field, and electron density, using a simple electrical model of an RF discharge. Each of these quantities varies with temporal position in the RF cycle, but we are concerned only with time-averaged plasma properties in this study.

The ac electrical analog model consists of a resistor and two capacitors in series, see Fig. 2. In this model, the resistive component of the impedance is attributed solely to the bulk plasma, while the reactive component arises from the sheaths; consequently, the bulk of the plasma is modeled as a resistance R_b, and each sheath is represented by a capacitance C_s. In reality, a small portion of the total capacitance (~5 pF) can be attributed to the capacitance between the electrodes, which is inversely proportional to the electrode spacing. This correction is important for highly electronegative gases (*e.g.*, $CFCl_3$ or SF_6) where bulk-resistive impedance is comparable to capacitive impedance; *i.e.*, at very high or very low pressures. Current is carried primarily by elec-

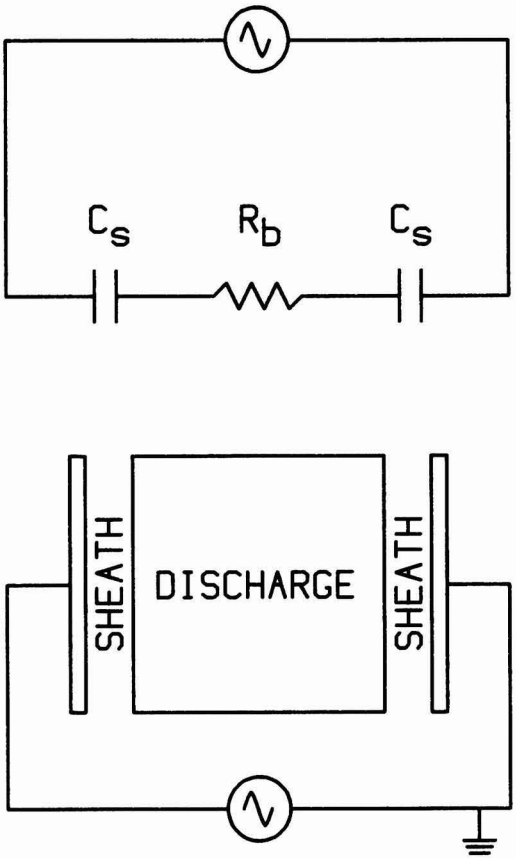

Fig. 2. AC electrical analog of plasma

trons since the excitation frequency (13.56 MHz in this study) is greater than the ion plasma frequency (~3 MHz), so ions do not respond to the ac field. No inductive component is included in the model since the electron-neutral collision frequency is much greater than the excitation frequency; therefore, electrons do not store directed energy over a RF power cycle. Higher harmonics (second and above) of the current waveform are only 0.1% of the fundamental, indicating that the electrical impedance of the discharge is nearly linear.

Physically, R_b represents the resistance to the passage of electron current through the plasma, *i.e.*, we assume that electron transport is mobility limited. More specifically, we assume that both the electron and ion concentrations are spatially uniform in the bulk plasma, and that the electrons move in response to the time averaged applied RF electric fields. The current through the sheath is primarily displacement current because the high sheath electric fields repel electrons, causing a low electron density in the sheath. Therefore, the sheaths are modeled as capacitors.

The assumption of a purely capacitive sheath is not valid if significant power is dissipated in the sheath; in this case some resistive component must be added to the model (9). Sheath power dissipation (the product of measured total ion current and measured mean ion bombardment energy) accounts for less than 20% of the total power dissipation over most of the experimental range investigated here and is lumped into the bulk resistance. The accuracy of the impedance model depends on the validity of this assumption; however, errors caused by small sheath power losses should not affect the qualitative prediction of trends. Sheath power dissipation becomes important only in the high power high pressure regime where the total positive ion current is significant compared to the discharge current. Further refinements of the impedance model must allow for sheath resistance as well as the effects of excitation frequency on ion transport and sheath thickness.

The voltage and current waveforms, measured at the upper electrode feed through and corrected for the stray capacitance between the measurement probes and the electrode (19 pF) and the power line inductance (0.3 μH), are used with standard impedance analysis techniques to determine the time-averaged values of both R_b and C_s

$$R_b = \frac{|V|}{|I|}\cos\theta \text{ and } C_s = \frac{2|I|}{\omega|V|\sin\theta} \quad [1]$$

Here, $|V|$ is the RF voltage amplitude at the powered electrode, $|I|$ is the RF current amplitude, ω is the angular excitation frequency, and θ is the phase angle between the waveforms. Phase angles varied between 25 and 65 deg; consequently, the phase angle experimental sampling error of about 2.5 deg is unimportant.

In reality, the magnitude of C_s oscillates with time during the RF cycle. The sheath width, and hence the capacitance, varies as electrons are sequentially displaced toward and away from either electrode by the RF electric fields. The periodic displacement induces a net space charge in the sheath that alters the effective sheath capacitance. The increase of the effective capacitance at one electrode should be approximately balanced by a decrease in the sheath capacitance at the opposing electrode. Therefore, the use of a fixed C_s in the impedance model gives an analogous circuit response, and the derived values of C_s are the time-averaged values.

Plasma voltage distributions for high ($\phi = 0$) and low ($\phi = \pi$) sheath voltages at the powered electrode are shown in Fig. 3. We note here that the sheath voltage is not in phase with the applied voltage, because of the complex impedance of the plasma. Bruce presented a similar diagram (10), but did not allow for the finite potential difference across the bulk plasma observed in the CF_3Cl discharge. Note that although most of the voltage is dropped in the sheaths, 20-40% of the voltage drop occurs across the bulk. The temporal variations in sheath thickness discussed above and pointed out by Bruce are not included in Fig. 3 since the impedance model predicts only time-averaged properties. Although the model only represents time-averaged plasma conditions, the requirement that the plasma potential always be positive with respect to either electrode allows evaluation of both the minimum and time-averaged sheath potentials.

First, we examine time-averaged sheath potentials for the simpler case of a dc discharge. In a dc discharge, the potential difference between the plasma and a floating electrode is given by the Bohm sheath criterion (11)

$$V_p - V_f = (kT_e/2q)\ln(m_i/2.3m_e) \quad [2]$$

where V_p is the plasma potential, V_f is the surface floating potential, T_e is the electron temperature, m_e and m_i are the electron and ion masses, q is the electronic charge, and k is Boltzmann's constant. The magnitude of the potential difference, assuming an average electron energy of 3-5 eV and an ion mass of 70 amu, is about 15-25V.

In a RF discharge, the minimum dc potential difference between plasma and electrode is considerably smaller than in a dc discharge. Charge conservation requires that the time-averaged ion and electron fluxes be equal. Positive ion current flows throughout the RF cycle, since the electrode potential is on average more negative than the plasma, and because the ions respond slowly with respect to the RF electric field for frequencies above 3 MHz. However, an appreciable electron current flows only when the sheath potential approaches a few kT_e/q, allowing the higher energy electrons to penetrate the sheath and strike the electrode. Since the fraction of the RF cycle during which the electron flux occurs is very small, the minimum sheath potential barrier must be smaller than that of the dc plasma floating potential barrier to allow a large periodic electron flux,

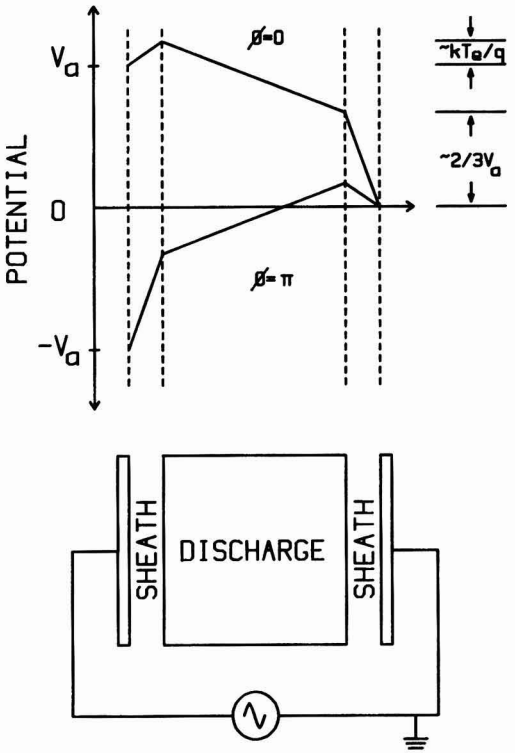

Fig. 3. Potential distributions in a CF_3Cl/argon plasma, given at high ($\phi = 0$) and low ($\phi = \pi$) extremes of the sheath potential.

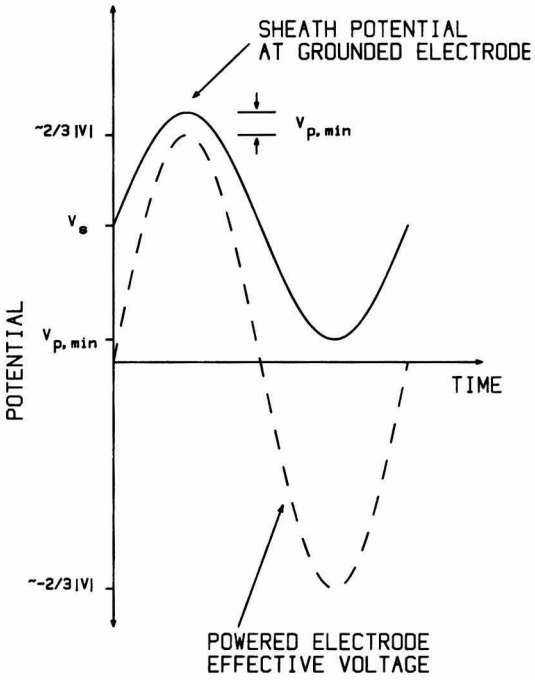

Fig. 4. Sheath potential during RF cycle at 13.56 MHz. Solid line represents the potential drop across the sheath at the grounded electrode. The dashed line represents the effective applied potential $|V|_{eff}$.

and, therefore, a net neutral flux to the surface. Assuming a Maxwellian electron energy distribution, the electron flux depends exponentially on the ratio of the regarding sheath potential to the electron energy. Therefore, an electron current sufficient to balance the ion current can be obtained only if the minimum sheath potential barrier, symbolized here by $V_{p,min}$, is on the order of kT_e/q (about 3-5V).

The limits of the sheath voltage oscillation are most clearly seen in Fig. 3 as the potentials at the grounded electrode sheath for $\phi = 0$ and $\phi = \pi$, respectively. Effective applied ac potential refers to the portion of the RF voltage not dissipated in the bulk plasma, *i.e.*, the amplitude of the effective applied potential $|V|_{eff}$ is the voltage dropped across one of the capacitors in the impedance model. Figure 4 shows the plasma potential at the sheath of the grounded electrode, assuming that a third of the applied voltage is dropped across the bulk plasma. For simplicity, the applied and sheath potentials are shown in phase in Fig. 4. In reality, there is a phase difference between the two potentials, which depends on the values of the bulk resistance and the sheath capacitance in the electrical analog (*i.e.*, the plasma process conditions). Plasma potentials of low pressure plasmas, which have a much more capacitive impedance, have been treated similarly and are discussed in detail elsewhere (9).

The plasma sheath can also be modeled as a system of diode, resistor, and capacitor in parallel (9); therefore, the sheath potential is obtained by rectifying the effective applied potential. If the frequency response of the rectifying circuit is much faster than the RF, half-wave rectification will occur (10), and the time-averaged sheath potential V_s will be

$$V_s \approx 2|V|_{eff}/\pi + V_{p,min} \quad [3]$$

Equation [3] applies for low excitation frequencies (*e.g.*, 100 kHz) where the electrons respond so rapidly to the electric field that the rectifying resistance is due solely to the ions; *i.e.*, the electron concentration in the sheath is in a pseudo-steady state with respect to the applied field.

At high excitation frequencies the ions cannot respond to the RF field, so any rectification must be due to the motion of the electrons. A correct description of this situation requires a complex dynamical model of the charged particles in the plasma, and is beyond the scope of the present work, although preliminary results indicate that the electron response time is slightly less than the half-cycle time at 13.56 MHz (12). Later in this section, we show that the electrons require about one-quarter of the RF cycle time to move a distance comparable to the sheath thickness. Therefore, the pseudo-steady-state approximation fails at 13.56 MHz. Because the pseudo-steady-state assumption is no longer valid, the sheath potential does not behave as in the 100 kHz case; in fact, the slower electron response damps the rectification response. This causes the sheath potential to approach a sinusoid in time; therefore, at 13.56 MHz we assume that the plasma potential oscillates sinusoidally. For a sinusoidal sheath potential the time-averaged potential is the midpoint between the maximum effective applied ac potential and $V_{p,min}$, *i.e.*

$$V_s \approx |V|_{eff} + V_{p,min} \quad [4]$$

In terms of the impedance model

$$V_s = \frac{|I|}{\omega C_s} + V_{p,min} \quad [5]$$

The sheath voltage predictions of the impedance model are supported by ion energy experiments, the details of which are presented elsewhere (6). If the sheath transit time is much less than the RF cycle time, the most energetic ions striking the electrode should have energies near the maximum sheath potential. However, at high frequencies (*e.g.*, 13.56 MHz) the maximum ion energy should approach the time-averaged sheath potential since sheath transit encompasses several RF cycles. In Fig. 5, the maximum observed ion energy is plotted against the predicted sheath voltage for a wide range of

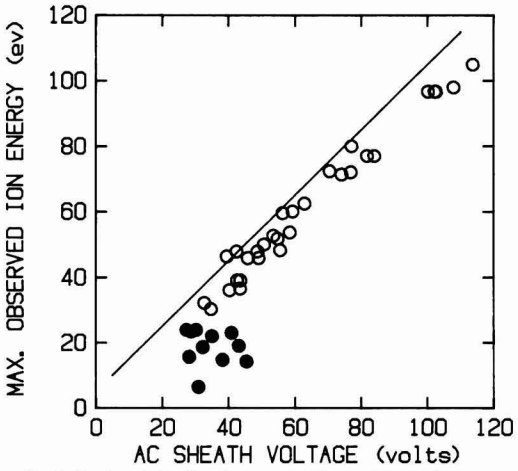

Fig. 5. Predicted sheath voltage vs. maximum observed ion energy. Filled circles represent data at 0.7-0.8 torr total pressure.

process conditions. A line with unity slope and with $V_{p,min}$ = 5V, representing the prediction of Eq. [5], is shown for comparison of the model and the data. The shaded data points in the lower left corner of Fig. 5 were taken at high pressures (0.7-0.8 torr), where virtually no ions pass through the sheath without suffering collisions. In these cases, the maximum observed ion energy may be considerably less than the actual sheath voltage.

Note that a lower dc offset would better represent the data of Fig. 5. In the previous discussion of $V_{p,min}$, it was implicitly assumed that the electrons respond instantaneously to the applied electric field. In reality, the transit time for electrons to cross the sheath is of the same order as the cycle time (74 ns at 13.56 MHz), as discussed in detail below. This time lag is due to the mobility-limited motion of electrons across the sheath, and results in a lowering of the $V_{p,min}$ at which the necessary flux of electrons is achieved. The lower $V_{p,min}$ results in better agreement between theory and experiment.

If the sheath thickness is much less than the electrode spacing d, the root mean square (rms) electric field to pressure ratio in the bulk plasma, ϵ_b/P, is

$$\epsilon_b/P = \frac{R_b|I|}{\sqrt{2}\,Pd} \qquad [6]$$

We are interested in estimating ϵ_b/P, because it is the plasma property which controls the electron energy distribution. The rms electric field incorporates our assumption that the electron concentration is uniform throughout the plasma bulk, *i.e.*, space-charge effects within the bulk plasma are neglected. Typical rms electric fields predicted by the model were between 20 and 50 V/cm.

To predict the electron density correctly from the measured plasma impedance, one must account for the variation in electron concentration with time and position. This calculation would include field-induced electron motion, electron diffusion due to concentration gradients, space-charge effects caused by electron displacement with respect to positive ions, creation of electrons by ionization, and electron losses by attachment with plasma neutrals and by collision with electrode surfaces. Using such a model, the electron concentration could be determined given the measured RF current and voltage waveforms. Since the kinetic data necessary for such a model are not available for CF_3Cl, we resort to a simplified electron transport model. This simplified model should allow us to identify the major trends in electron density with varying process conditions.

To estimate the electron density from the resistance of the circuit analog, we assume that the electron density is spatially uniform, and that the electrons oscillate with the applied RF field. Power is dissipated by inelastic electron-neutral collisions as the electrons move back and forth in the plasma bulk at a velocity determined by their mobility and the electric field strength. The ions are assumed to be uniformly distributed throughout the bulk plasma, their positions fixed with time. Since the 13.56 MHz excitation frequency is greater than the ion plasma frequency (~3 MHz), the assumption that the ions do not move in response to the RF field is quite good. To estimate the electron density, we consider the current flow through the bulk plasma by electron mobility. Since electrons are the primary charge carrier, the rms electron flux j_e is related to the discharge current by

$$j_e = |I|/\sqrt{2}\,qA \qquad [7]$$

where A is the electrode area. For mobility-limited electron motion, the electron density $[e^-]$ is related to the flux by

$$j_e = [e^-]\mu_e\epsilon_b \qquad [8]$$

where μ_e is the electron mobility. The electric field is the rms voltage across the bulk plasma divided by the interelectrode distance, leaving

$$[e^-] = d/qAR_b\mu_e \qquad [9]$$

Electron mobility in CF_3Cl was estimated from drift velocity data for CF_4 (13) and CF_2Cl_2 (14). In light of these previous data, the product of electron mobility and pressure is assumed constant at 20 m²-torr/V-s over the entire pressure range.

As mentioned previously, the uniform electron density model does not explicitly consider certain significant effects such as space charge. In response to the RF electric field, the highly mobile electrons are displaced relative to the fixed positive ions. Electric fields are induced at both sheaths by the resulting net separation of charge. These electric fields oppose the flux of electrons to the electrodes, thereby lowering the velocity of the electrons, and in turn the discharge current for a given electron density.

We now consider the importance of these space-charge effects by examining the motion of electrons in the RF electric field. Neglecting electron diffusion and assuming a uniform spatial density of electrons, the space charge is dependent only on the distance traveled by the electrons as they move during a half-cycle (recall that the positive ions are too massive to respond to the RF field). The maximum distance the electrons can be displaced during a half-cycle is equal to the sheath thickness; otherwise, they would be captured by collision with the electrodes. The validity of the electron density model is determined by both the magnitude of this space-charge-induced electric field and the amplitude of the electrons' spatial displacement in response to the applied RF potential.

The displacement of the electrons is estimated as follows. The electron velocity is determined by the mobility and the electric field

$$dx/dt = -\mu_e\epsilon_0 \sin(\omega t) \qquad [8]$$

where x and t are distance and time, respectively. The electric field is assumed to be sinusoidal in time, with amplitude ϵ_0 and angular frequency ω. The maximum displacement, L, from the average position is the distance traveled in first quadrant of the RF cycle

$$L = \int_0^{\pi/2\omega} \mu_e\epsilon_0 \sin(\omega t)\,dt = \sqrt{2}\,\mu_e\epsilon_b/2\pi f \qquad [9]$$

At 13.56 MHz and 0.5 torr, a typical field of 30 V/cm gives a maximum displacement of approximately 2 mm; therefore, the time-averaged sheath thickness must be 2 mm or greater. As discussed later, sheath thicknesses obtained from the impedance model are approximately 1 mm, indicating that electron motion is restricted by the space charge and/or other sheath fields.

The electric field caused by the uniform displacement of the electrons with respect to the ions can be calculated by integrating Poisson's equation over the displacement distance. Assuming a positive ion and electron concentration of 2×10^9 cm^{-3}, the potential difference induced by a 2 mm displacement is 70V. The existence of a 70V potential opposing the flux of electrons to the electrode would reduce the maximum displacement to less than 2 mm. If the electron and positive ion concentrations are not spatially uniform across the electrode gap (*e.g.*, a cosine distribution), the space-charge field caused by the displacement is distributed across a wider region of the plasma. The potential barrier opposing electron flow to the electrodes, which is confined to the sheath-bulk interface in the uniform electron density model, will be less abrupt in the case of a spatially-variant electron concentration, or if electron diffusion is considered.

Because space-charge effects within the bulk plasma are neglected in the uniform density model, the estimated electron concentrations may be somewhat low. The velocity of the electrons is less than predicted from mobility considerations, due to the opposing space-charge electric field. Therefore, to carry the measured current a greater number of electrons must traverse a shorter distance.

The space-charge effects are reactive, and, therefore, are incorporated into the circuit analog's sheath capacitance. As discussed before, the major fraction of the RF power is dissipated in the bulk plasma via inelastic electron-neutral collisions. Therefore, the plasma resistance should still be related to the electron density, and it is expected that the model will predict the general trends of the electron density with process conditions. Simple electrical analog model estimates for electron density compare favorably with recent continuum model results (15).

The impedance model as described here is only applicable when the plasma is well confined between the electrodes, *i.e.*, the plasma has a known constant volume. Upon loss of containment, two factors preclude use of this model: (*i*) the area of the grounded electrode is no longer known, because the plasma contacts the chamber walls, and (*ii*) the motion of electrons in the electric fields is no longer limited to one spatial dimension. In this apparatus, CF_3Cl plasmas are well confined for pressures greater than about 0.25 torr; no change in plasma volume was observed by optical emission in the range 0.25-1 torr. In addition, measured dc bias voltages on the powered electrode were small and positive (~5V), indicating that the effective electrodes are of approximately equal area. At pressures lower than 0.2 torr, the plasma fills the etching chamber and contacts the chamber walls. In this case, the dc bias is negative and relatively large (less than −50V) compared to the peak applied voltage (~150V), as would be expected for the case of unequal electrode areas (16). The sharp transition between well-contained and poorly-contained plasma behavior is observed visually as well as through the sign and magnitude of the dc bias voltage. The impedance results presented here were obtained under constant plasma volume conditions. Insertion of a Teflon ring at the perimeter of the electrodes to confine the discharge resulted in no significant changes in plasma properties for pressures greater than 0.25 torr, where the plasma was well-confined in the absence of the ring. For example, ion energies are not affected by the presence of this confining ring (6).

The desired simplicity of the electrical analog model necessitates the use of many assumptions; however, the results obtained can be quite useful in understanding the physics responsible for observed trends in etching. The assumptions made in the impedance model are fairly good for the processing conditions examined in this paper, as discussed above. Detailed balance equations for charged particles could be written; however, the complexity of this problem makes it difficult to pose as well as to solve, although work is proceeding in this area (17, 18). The utility of a simple algebraic plasma model in describing the etching process must be acknowledged, given the present status of more sophisticated modeling efforts.

Response Surface Methodology

RSM is an efficient and effective tool for empirical modeling of complex processes, and has found widespread application in the chemical process industries. Although the applicability of RSM to plasma processing has been demonstrated (19, 20), it is not commonly used in the microelectronics industry. RSM combines efficient experimental design with statistical analysis techniques to generate a mathematical representation of a data set in terms of specified process variables. Given the difficulties associated with the kinetic modeling of plasma processes, RSM is appropriate for use in plasma process modeling, development, and optimization.

The strategy involved in selecting of an optimum experimental design has been detailed elsewhere (21, 22) and is described briefly here. The three-factor design used in this study (see Fig. 6) can be visualized as a set of experimental points in factor (independent process variable) space. The design is symmetric so that each factor is given equal weight in the data analysis. A wide factor range is examined, since RSM models are not predictive and give nonsensical results upon extrapolation beyond the region explored experimentally. The number of levels selected is a trade-off between improved response representation and increased experimental work, but must be sufficient to support the proposed polynomial model; for example, at least three levels are required to allow evaluation of the curvature imposed by a quadratic model. The design must also include replicate points for experimental error estimation, and enough degrees of freedom (number of points minus number of coefficients in the model) for accurate evaluation of the lack-of-fit error, a measure of the model's ability to represent the data.

A seven-level, 37-run design is sufficient for cubic model representation of etching characteristics in terms of three independent variables. This design was developed because previous studies indicated that the etching rate behavior is complex (1) and would require a greater than quadratic polynomial fit for adequate data representation. A cubic model, including cross-product terms which account for interactions among the independent variables, is written

$$Y = C_o + \sum_{i=1}^{N} (C_i X_i) + \sum_{i=1}^{N} \sum_{j=1}^{i} (C_{ij} X_i X_j) + \sum_{i=1}^{N} \sum_{j=1}^{i} \sum_{k=1}^{j} (C_{ijk} X_i X_j X_k) \quad [10]$$

Here, Y is a particular process response (*e.g.*, etching rate), N is the number of independent variables, the X_i's are the factors (*e.g.*, power density), and the C's are the model coefficients. A three-factor cubic model, therefore, contains 20 parameters and requires at least 20 data points for coefficient determination by least squares linear regression. Statistically insignificant terms are identified by analysis of variance techniques and are removed.

Model fit qualities obtained were excellent. A standard measure of the quality of fit is the adjusted R^2 ratio, defined as the fractional variation in the data accounted for by the model on a per degree of freedom basis; the adjusted R^2 ratio is not artificially high due to the large number of model parameters. Adjusted R^2 ratios for the fits presented here were greater than 0.9, and as high as 0.97 in the case of the etching rate model, meaning that the RSM model accounts for all but 3-10% of the variation in the data. We suspected that a cubic model would better represent the complex responses of plasma processes than would a quadratic model. For example, the adjusted R^2 for the quadratic etching rate model was 0.8, adequate for representation of all major response surface trends but not sufficient for inspection of details.

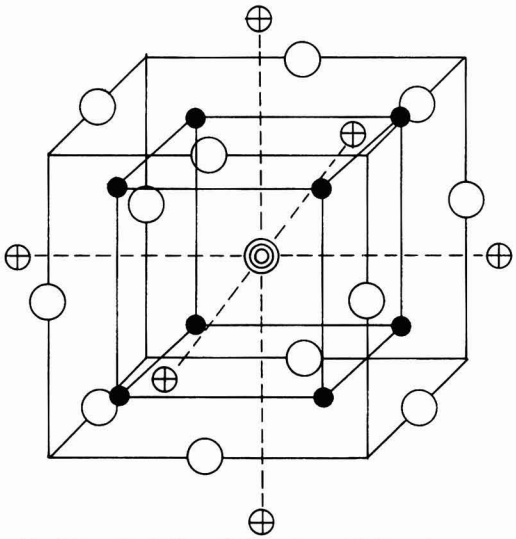

Fig. 6. Seven level, 37-run RSM experimental design in three parameters: power input, pressure, and composition.

The RSM models obtained in this study exhibit low correlation between model terms, *i.e.*, they are orthogonal for first-order interactions. Therefore, the model coefficients can have some limited physical significance; the magnitude of the coefficient directly indicates the dependence of the response on that term. The significance of the interaction terms observed serves to emphasize the importance of RSM in plasma process modeling, since conventional one-variable-at-a-time methods cannot account for interactions between variables without extensive experimental work.

Results and Discussion

The independent variables in this study were power density, pressure, and gas composition. Power density $\dot{W}$, based on the area of the grounded electrode, was varied from 0.2 to 0.6 W/cm². The experimental design levels were spaced with the square root of power, since we initially believed that several important plasma properties would scale with $\dot{W}^{0.5}$. Total pressure was varied from 0.2 to 0.8 torr. The CF_3Cl fraction of the reactor feed, γ, ranged from 0.7 to 0.95, the balance being argon. Both pressure and composition were scaled linearly in the experimental design. The following variables were fixed: electrode area (125 cm²), electrode material (stainless steel), electrode spacing (2 cm), excitation frequency (13.56 MHz), total gas flow rate (6 sccm), and wafer loading (¼ of a 4-in. wafer). Etching rate and total ion flux were measured at each design point. Plasma resistance, sheath capacitance, bulk plasma electric field, electron density, and sheath voltage were estimated using the impedance model.

The bulk plasma resistance R_b, as determined from Eq. [1], varied from 80 to 600Ω over these plasma conditions. Plasma resistance increases with increasing pressure, apparently because of the lowered electron mobility in the denser gas. Increasing power input results in a lower resistance, as does increasing the argon fraction; these effects are both attributable to increased electron density and mobility. Contour plots of R_b with power density and pressure are shown in Fig. 7a and b for $\gamma = 0.9$ and 0.8, respectively. The lines of constant R_b were generated from the RSM fit of the experimental design data set, augmented by additional points at the design edges to ensure accurate representation of the plasma behavior over the entire range of conditions displayed. The adjusted R^2 of this fit was 0.95. The dependence of R_b on power density and gas composition for $P = 0.5$ torr, is shown in Fig. 7c.

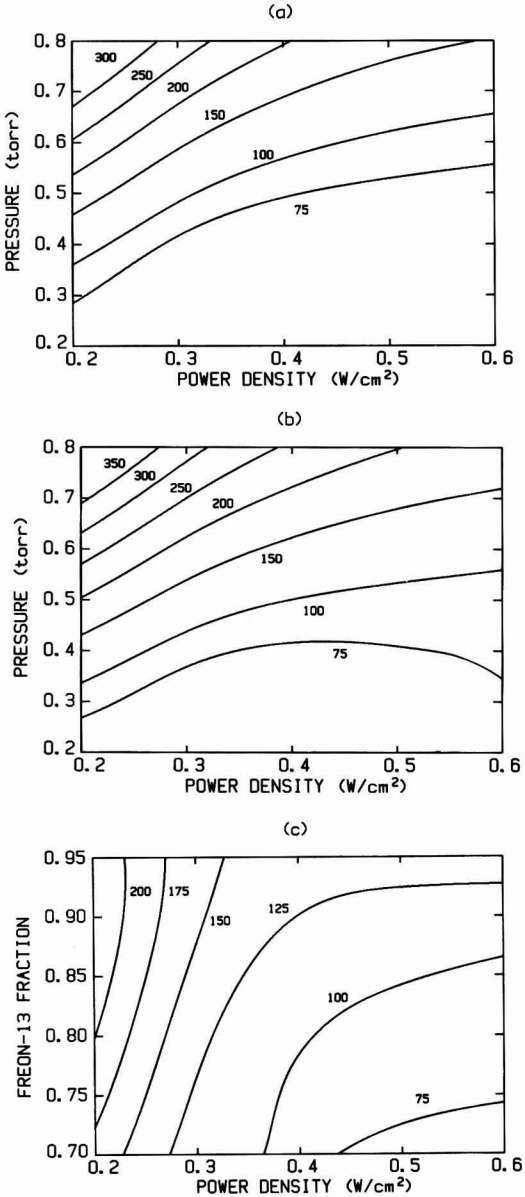

Fig. 7. Contour plots of plasma bulk resistance R_b (Ω) with: (a) power density and pressure for $\gamma = 0.8$, (b) power density and pressure for $\gamma = 0.9$, (c) power density and composition for $P = 0.5$ torr.

The sheath capacitance displays a maximum with pressure at about 0.6 torr, and increases with power density. The range of calculated capacitances is 100-250 pF, corresponding to sheath thicknesses between 1 and 0.4 mm, in qualitative agreement with visual observation of the discharge. Therefore, at high pressure and low power the plasma impedance is primarily resistive, while at low pressure and high power the reactive impedance dominates. Contour plots of C_s are shown in Fig. 8a-c. Again, a very high adjusted R^2 of 0.93 was obtained for this fit.

The measured etching rate results are presented as Fig. 9a-c. The quality of the cubic model fit was excellent, the adjusted R^2 being 0.97. Figure 9a shows the etching rate, measured *in situ* by laser interferometry, as a function of power input and pressure for a mixture of 10% argon in

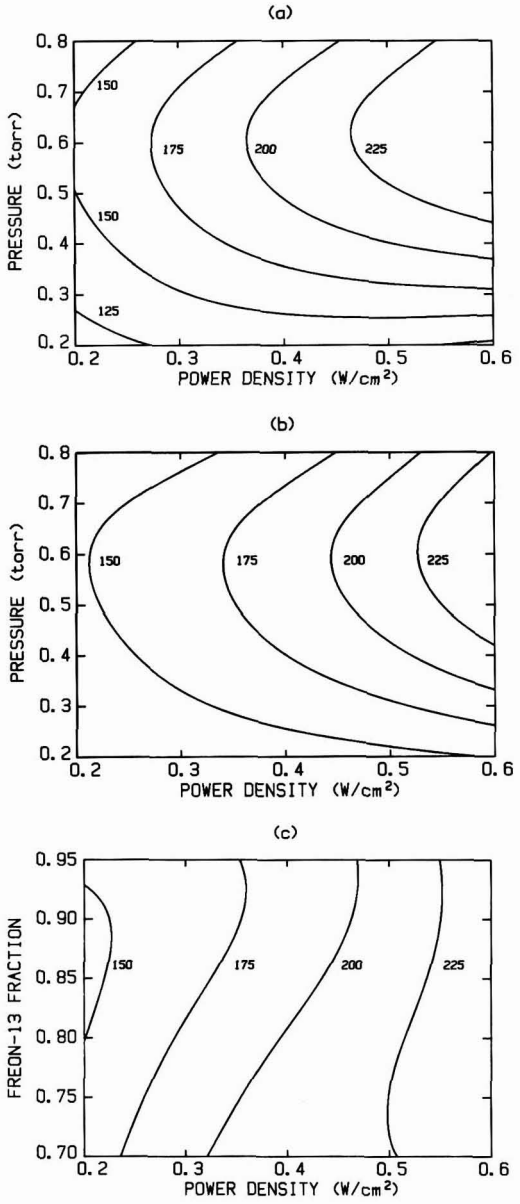

Fig. 8. Contour plots of sheath capacitance C_s (pF) with: (a) power density and pressure for $\gamma = 0.8$, (b) power density and pressure for $\gamma = 0.9$, (c) power density and composition for $P = 0.5$ torr.

CF_3Cl ($\gamma = 0.9$); Fig. 9b is a similar plot for 20% argon in CF_3Cl ($\gamma = 0.8$). Etching rates as low as 200 Å/min and as high as 3000 Å/min were obtained in this range of process conditions. The importance of the interaction between power and pressure is obvious; note that the etching rate increases with power input, rapidly at high pressures but more slowly at low pressures. At constant power, etching rate exhibits a maximum with pressure; for power densities of 0.4 W/cm² the maximum occurs at about 0.5 torr. As the power is increased, the pressure at which the peak etching rate occurs also increases. At high power densities and pressures the effect of pressure on etching rate is small. Increasing the CF_3Cl mole fraction γ, increases the etching rate at low pressures but decreases it at higher pressures. Figure 9c is a contour plot of etching rate as a function of power input and composition at 0.5 torr total pressure.

Figure 10a-c show the measured total ion flux Γ_+ for the same range of conditions. Again, a few data points were added at the corners of the experimental design. The total ion flux Γ_+ is not constant with time during etching; the flux varies by up to 50% during a run. The temporal variation of $\Gamma_+(t)$ at a given plasma condition is reproducible from run to run; however, the form of $\Gamma_+(t)$ is strongly dependent on the plasma conditions. At some process conditions, Γ_+ increases rapidly in the first 10-20s of the etch, levels off until the etch is about 90% complete, and then drops as the wafer begins to clear. At

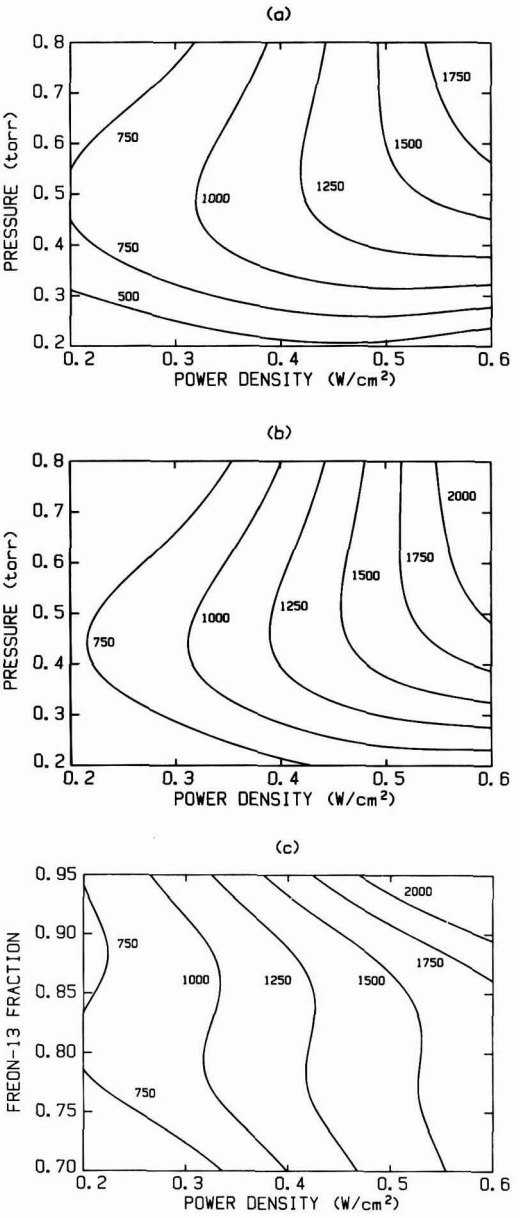

Fig. 9. Contour plots of etching rate (Å/min) of heavily P-doped polysilicon with: (a) power density and pressure for $\gamma = 0.8$, (b) power density and pressure for $\gamma = 0.9$, (c) power density and composition for $P = 0.5$ torr.

other conditions, Γ_+ reaches a pronounced maximum after about 20% of the film thickness has been etched, then decays rapidly to a steady value for the remainder of the etch. However, for a blank stainless steel electrode (no wafer) Γ_+ is constant with time; in addition, the ion flux to the blank electrode correlates very well with the time-averaged Γ_+ over an etching run (generally, Γ_+ is 20% greater during etching). Due to the simplified data interpretation, we present the blank electrode ion fluxes here.

Total ion fluxes of up to 2.5 mA/cm² (corresponding to a number flux of 1.5×10^{16} cm^{-2}s^{-1}) are obtained in the high power, high pressure region, while Γ_+ is an order of magnitude less at low powers and pressures. Despite the large range of ion currents observed, the RSM fit quality was excellent (adjusted $R^2 = 0.96$). The ion flux behavior is similar to the etching rate; Γ_+ increases sharply with power at high pressure, but changes much more slowly at low pressures. In fact, Γ_+ saturates with power at low pressures; *i.e.*, increasing the power has little effect on the ion flux. The apparent decrease of Γ_+ with increasing power in the lower right corner of Fig. 10a and b is a result of small errors in the RSM fit in this region. The ion flux typically decreases with argon dilution but increases slightly under low ϵ_h/P conditions (low power, high pressure). However, the general trends with power and pressure are not affected by argon dilution.

A cautionary note regarding ion fluxes is in order. Γ_+ is often estimated using the Bohm sheath criterion (BSC) (23)

$$\Gamma_+ = 0.6\,[e^-]\,\sqrt{(kT_e/m_i)} \qquad [11]$$

Unfortunately, several of the assumptions inherent in the derivation of the BSC are violated in plasma etching discharges. Most importantly, the potential distributions in RF plasmas are time-dependent; both the sheath thickness and potential vary during a cycle. Also, the BSC assumes collisionless transport of ions through the sheaths, whereas many collisions often occur in an RF sheath (6, 24).

For the case of constant electron energy, Eq. [11] predicts that Γ_+ is proportional to $[e^-]$. As discussed in the following paragraph, T_e is relatively constant in CF_3Cl discharges over the parameter space studied here. Assuming an insignificant negative ion concentration, contour plots of Γ_+ and $[e^-]$ should, therefore, have similar functional dependence on power, pressure, and composition. Comparison of Fig. 10 (ion flux) and 11 (electron density) suggests that the BSC is not valid for RF discharges. In addition, ion fluxes predicted by the BSC are far lower than those measured experimentally. For example, at $\dot{W} = 0.4$ W/cm², $P = 0.5$ torr, and $\gamma = 0.8$, the measured ion flux is about 0.9 mA/cm². Using an electron energy of 4 eV and an ion mass of 70 amu (CF_3^+), Eq. [11] yields an ion flux of only 0.02 mA/cm².

Electron density contours, as estimated from Eq. [9], are shown in Fig. 11a and b for $\gamma = 0.8$ and $\gamma = 0.9$. Figure 11c depicts the effects of γ and $\dot{W}$ on the electron density. Calculated electron densities are 10^9-10^{10} cm^{-3}, in good agreement with recent Langmuir probe results (25). The adjusted R^2 value was 0.87, less than in the previous cases but still adequate for representation of the electron density behavior with power, pressure, and composition. Electron density increases approximately linearly with power input, suggesting that the mean electron energy remains relatively constant with power — the product of electron density and energy should scale with power input, if electron-impact processes are primarily responsible for power dissipation in the plasma. Langmuir probe experiments confirmed the very weak dependence of mean electron energy on process conditions — the measured electron temperature varied from 4.0 to 4.3 eV over the experimental range.

There is a maximum in electron density with pressure at about 0.5 torr. An explanation for this behavior may be the competition between attachment and mobility/diffusion processes as the dominant electron loss mechanism in the discharge. At higher pressures, formation of negative ions via electron attachment is likely to be important, while electron loss by collision with the electrodes and by radial diffusion out of the plasma may be more important at lower pressures. Electron density increases slightly with decreasing γ, presumably because most of the low energy inelastic processes available to CF_3Cl cannot occur in argon. Consequently, less energy (per electron) is dissipated by electron-argon processes than by electron-CF_3Cl processes. To maintain constant power input to the plasma, the electron density must then increase with argon dilution.

Based on the Langmuir probe results, we suspect that the values of $[e^-]$ presented here may be slightly low. Because $[e^-]$ is calculated assuming that all resistive losses occur in the bulk plasma, resistive losses in the sheaths also cause a low prediction of electron density; this ef-

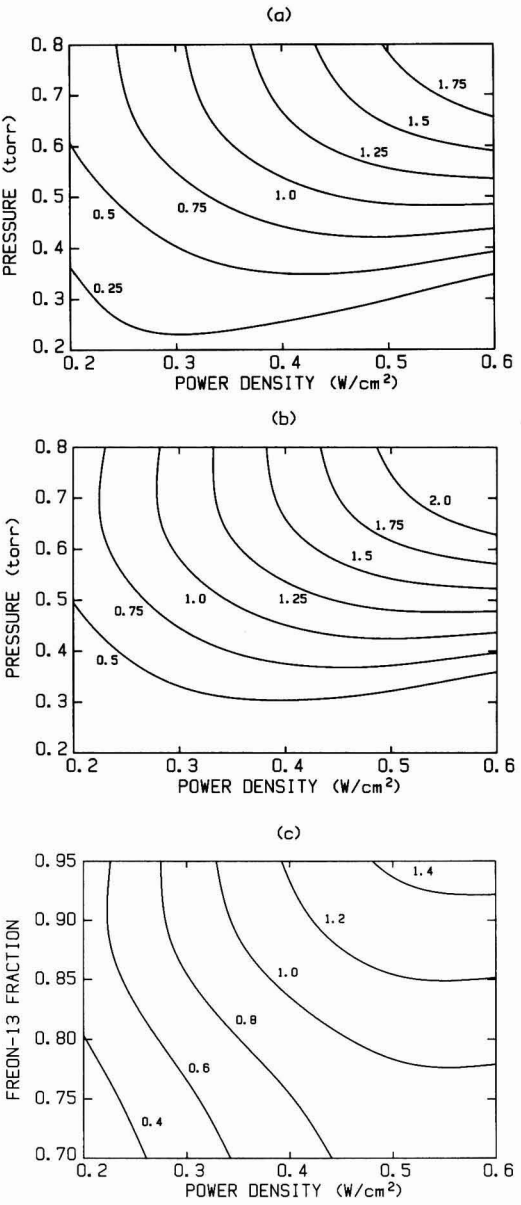

Fig. 10. Contour plots of total positive ion flux (mA/cm²) with: (a) power density and pressure for $\gamma = 0.8$, (b) power density and pressure for $\gamma = 0.9$, (c) power density and composition for $P = 0.5$ torr.

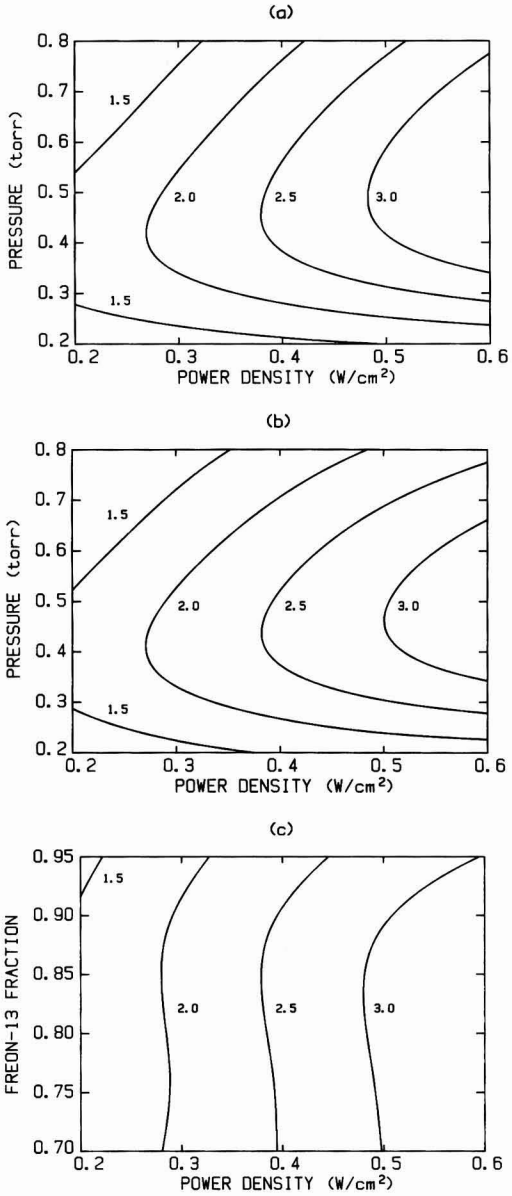

Fig. 11. Contour plots of electron density as predicted by the impedance model (10^9 cm^{-3}) with: (a) power density and pressure for γ = 0.8, (b) power density and pressure for γ = 0.9, (c) power density and composition for P = 0.5 torr.

fect will be most pronounced at the higher pressures where high ion fluxes are observed. If a parallel capacitor/resistor sheath analogy is used, R_h is generally 10-25% lower than the prediction of Eq. [1]; the estimated electron density is increased accordingly. The resistive sheath model is not discussed further in this paper, because the physical justification for the electrical analogy is unclear.

Sheath voltage contours, as determined from Eq. [5], are shown in Fig. 12a-c. The adjusted R^2 of this fit is 0.82. Sheath voltage of 20-100V are estimated for the range of conditions studied. Since sheath voltage is coupled with the sheath capacitance, the trends in V_s follow those in C_s. The sheath voltage increases with power, decreases with pressure, and slightly increases with argon dilution. Peak voltage across the discharge varies only from 100 to 250V, so V_s does not scale with $|V|$, as is often assumed in lower pressure discharges. The lack of correlation between $|V|$ and mean ion bombardment energy should also be pointed out, as ion energies are important in determining etching characteristics. The dependence of ion bombardment energies on process conditions will be treated in the subsequent paper of this series, and has also been demonstrated in SF_6 discharges (6).

Summary

A detailed experimental examination of the CF_3Cl/Ar plasma etching of polysilicon has been performed, in

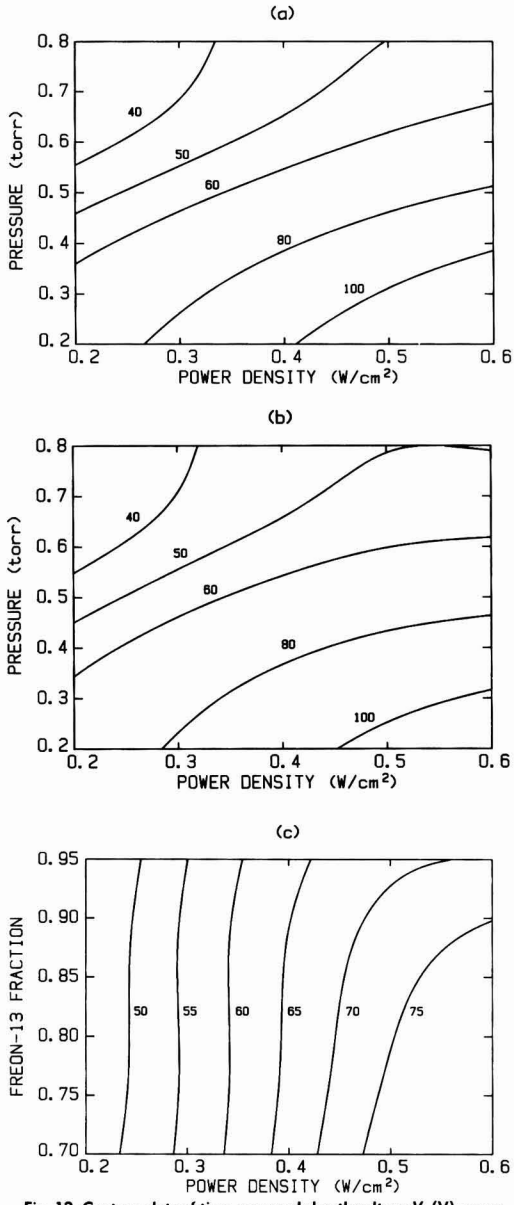

Fig. 12. Contour plots of time-averaged sheath voltage V_s (V) as predicted by the impedance model with: (a) power density and pressure for γ = 0.8, (b) power density and pressure for γ = 0.9, (c) power density and composition for P = 0.5 torr.

which etching rates, directionality, ion bombardment flux and energy, and plasma impedance were measured simultaneously and *in situ*. In addition, mass spectrometric and optical emission data were also obtained, although not presented here. The studied ranges of input power density, pressure, and gas composition were 0.2-0.6 W/cm^2, 0.2-0.8 torr, and 5-30% argon in CF_3Cl, respectively.

We have demonstrated the utility of response surface methodology by obtaining excellent representation of the etching rate and other etching responses over a wide range of conditions, with relatively few experimental trials. Although only a few etching responses are discussed here, plasma etching processes can be optimized for a variety of etching characteristics using this efficient statistical method.

The electrical analog model yields considerable insight into the physical behavior of radio-frequency plasmas, and the impedance model estimates of time-averaged plasma properties agree with independent experimental evidence. The assumptions of uniform spatial electron concentration and mobility-limited electron current flow in response to a time-averaged electric field were invoked. The reliability of these and other assumptions were discussed in light of space-charge effects caused by the fast motion of the electrons relative to the heavier ions.

Plasma resistance and reactance measurements are presented; we note that an important fraction of the applied voltage is dropped across the bulk plasma. The sheath potential, and consequently the maximum ion bombardment energy, is not well correlated with the applied voltage; this observation goes against assumptions commonly made in RIE systems. Etching rate and total ion flux measurements indicate a strong and complex power, pressure, and composition dependence; etching profiles are, therefore, expected to be sensitive to operating conditions.

In the following paper, plasma properties estimated from the impedance model are used with ion transport considerations to describe energetic ion bombardment of the etching film. Simple kinetic models, which predict the etching rate and etching directionality using the impedance and ion energy results, are presented in the third paper of this series.

Acknowledgments

This work was funded by du Pont through its Freon® Products Division. Funds for the construction of the apparatus and additional support were provided by the Semiconductor Research Corporation (Contract no. 83-01-033) and by the Digital Equipment Corporation. We thank Mike Coffey of Digital Equipment Corporation for supplying the wafer samples used in this work. Albert Richards and Brian Thompson at MIT are especially acknowledged for their efforts in constructing the apparatus and for many helpful discussions.

Manuscript submitted Sept. 10, 1985; revised manuscript received July 17, 1986.

The Freon® Products Division of E.I. duPont de Nemours and Company, Incorporated, assisted in meeting the publication costs of this article.

LIST OF SYMBOLS

A	electrode area (cm^2)
C_s	time-averaged sheath capacitance (pF)
d	electrode spacing (cm)
$[e^-]$	time-averaged bulk plasma electron density (cm^{-3})
$\|I\|$	discharge current amplitude (A)
j_e	time-averaged electron current density (A/cm^2)
k	Boltzmann constant
L	maximum electron displacement distance (cm)
m_e	electron mass (kg)
m_i	ion mass (kg)
P	pressure (torr)
q	electron charge (C)
R_b	time-averaged bulk plasma resistance (Ω)
R_s	time-averaged sheath resistance (Ω)
t	time (s)
T_e	electron temperature (K)
V_f	surface floating potential (V)
V_p	plasma potential (V)
$V_{p,min}$	minimum plasma potential (V)
V_s	time-averaged sheath voltage (V)
$\|V\|$	discharge voltage amplitude (V)
$\|V\|_{eff}$	effective applied voltage amplitude (V)
W	power input (W)
$\dot{W}$	power density based on grounded electrode area (W/cm^2)
x	distance (cm)
γ	mole fraction CF_3Cl
Γ_+	total ion flux (mA/cm^2)
θ	phase angle between voltage and current waveforms (deg)
μ_e	electron mobility (m^2/V-s)
ω	angular frequency of plasma excitation (s^{-1})
ϵ_b	rms bulk plasma electric field (V/cm)
ϵ_0	amplitude of bulk plasma electric field (V/cm)

REFERENCES

1. M. F. Leahy, in "Plasma Processing," J. Dielman, R. G. Frieser, and G. S. Mathad, Editors, p. 176, The Electrochemical Society Softbound Proceedings Series, PV82-6, Pennington, NJ (1982).
2. C. J. Mogab and H. J. Levinstein, *J. Vac. Sci. Technol.*, **17,** 721 (1980).
3. A. C. Adams and C. D. Capio, *This Journal*, **128,** 366 (1981).
4. D. Edelson and D. L. Flamm, *J. Appl. Phys.*, **56,** 1522 (1984).
5. M. J. Kushner, *ibid.*, **53,** 2923 (1982).
6. B. E. Thompson, K. D. Allen, A. D. Richards, and H. H. Sawin, *ibid.*, **59,** 1890 (1986).
7. J. H. Keller and W. B. Pennebaker, *IBM J. Res. Develop.*, **23,** 3 (1979).
8. A. J. van Roosmalen, *Appl. Phys. Lett.*, **42,** 416 (1983).
9. K. Köhler, J. W. Coburn, D. E. Horne, E. Kay, and J. H. Keller, *J. Appl. Phys.*, **57,** 59 (1985).
10. R. H. Bruce, *ibid.*, **52,** 7064 (1981).
11. B. N. Chapman, "Glow Discharge Processes," p. 70, John Wiley and Sons, Inc., New York (1980).
12. B. E. Thompson, A. D. Richards, H. H. Sawin, and A. J. Owens, Unpublished results.
13. M. S. Naidu and A. N. Prasad, *J. Phys. D.*, **5,** 983 (1972).
14. M. S. Naidu and A. N. Prasad, *Br. J. Appl. Phys.*, **2,** 1431 (1969).
15. D. B. Graves and K. F. Jensen, Paper C5.1 presented at the Materials Research Society Spring Meeting, Palo Alto, CA 1986.
16. H. R. Koenig and L. I. Maissel, *IBM J. Res. Dev.*, **14,** 168 (1970).
17. D. B. Graves and K. F. Jensen, *IEEE Trans. Plasma Sci.*, **PS-14** (2), 78 (1986).
18. M. J. Kushner, *J. Appl. Phys.*, **54,** 4958 (1983).
19. S. F. Bergeron and B. F. Duncan, *Solid State Technol.*, **25,** 98 (1982).
20. M. W. Jenkins, M. T. Mocella, K. D. Allen, and H. H. Sawin, *ibid.*, **29,** 175 (1986).
21. E.I. du Pont de Nemours and Co., "Strategy of Experimentation," course materials, F & FP, Applied Technology, Wilmington, DE.
22. G. E. Box, W. G. Hunter, and J. S. Hunter, "Statistics for Experimenters," John Wiley and Sons, Inc., New York (1978).
23. D. Bohm, in "The Characteristics of Electrical Discharges in Magnetic Fields," A. Guthrie and R. K. Wakerling, Editors, McGraw-Hill, Inc., New York (1949).
24. K. D. Allen and H. H. Sawin, *This Journal*, **133,** 2326 (1986).
25. M. Surendra, S. B. thesis, Massachusetts Institute of Technology, 1985; M. Surendra and H. H. Sawin, in preparation.

The Plasma Etching of Polysilicon with CF_3Cl/Argon Discharges

II. Modeling of Ion Bombardment Energy Distributions

Kenneth D. Allen*,[1] and Herbert H. Sawin*

Department of Chemical Engineering, Massachusetts Institute of Technology, Cambridge, Massachusetts 02139

ABSTRACT

An experimental technique for measuring total positive-ion-bombardment fluxes and energy distribution is presented. It is shown that mean ion energies in CF_3Cl (Freon® 13) plasmas can be well described by discharge electrical impedance analysis in conjunction with a simple sheath transport model. Based on the measurement of only the rms discharge current, mean ion energies are predicted. An empirical description using the mean ion energy provides a good representation of the ion energy distribution over a wide range of conditions. These results should allow estimation of ion energy distributions in other parallel plate reactors.

The etching of heavily phosphorus-doped polysilicon in CF_3Cl/Ar discharges was examined experimentally in the preceding paper of this series (1). An electrical impedance model was used to predict physical properties of the plasma, including time-averaged sheath voltage. In this paper, we examine the ion bombardment of the surface during etching—ion energy is predicted using the plasma impedance results and a simple elastic collision model for ion transport through the plasma sheath. The results obtained are crucial to the formulation of kinetic models of etching rate and directionality, to be discussed in the following paper of the series.

To obtain the essential characteristics of thin film plasma etching in VLSI fabrication, the effects of ion bombardment must be controlled. Ion bombardment influences directionality, selectivity over increasingly thin gate oxides, uniformity across the wafer (or set of wafers), surface damage, etc. Each of these etching characteristics is dependent on both the total ion flux and ion energy distribution, as well as the neutral chemistry. Etching directionality results from ion-assisted etching or the sputtering of etch-inhibiting species from the film surface. However, selectivity generally decreases with increased ion bombardment flux and energy. In the limit of high ion energies, selectivity becomes unacceptably low as physical sputtering becomes dominant. In addition, energetic ion bombardment can induce crystallographic defects and other damage in a thin layer at the device surface (2, 3). For ion-driven processes the importance of chemical reactant transport and depletion is reduced, and uniformities may therefore be improved in some chemical systems.

In a RF discharge, positive ions are accelerated toward the electrodes by plasma sheaths formed at both electrodes. The sheaths result from the larger electron flux (to the electrodes) relative to the ion flux, which induces the depletion of electrons from the bulk plasma. This electron loss creates an electric field in the sheath, which retards the time-averaged electron flux until it equals the positive ion flux. Ions formed in the bulk plasma by electron-impact processes drift to the sheath region by diffusion and with the aid of weak dc electric fields in the bulk. The large (~1000 V/cm) sheath field accelerates the ions toward the electrode, causing energetic ion bombardment at the surface. In the sheath, the ions lose energy and directionality by collisions with neutral gas particles. The balance between the sheath potential drop, and the energy lost by collisions in the sheath determines the energy of the ions striking the surface.

Experimental Apparatus and Results

The parallel-plate etcher used in this study was described in detail elsewhere (1). However, in this study the powered upper electrode was 12.7 cm in diameter, as opposed to 15 cm in the previous work—the reactor is therefore symmetric. No major changes in the plasma properties or etching trends resulted from this design change, although the etching rates increased by 30-50%.

* Electrochemical Society Active Member.

[1] Honeywell, Solid State Electronics Division, Plymouth, MN 55441

The experimental apparatus and procedure for measuring ion bombardment energy distributions are described elsewhere (4). Briefly, ions impinging on a 50 μm pinhole aperture in the grounded electrode are focused through a retarding grid (at potential V_r) and collected on a plate. By measuring the variation in collected ion current with grid bias, $\Gamma_+(V_r)$, the ion energy distribution is obtained. Since positive ions with energy E_+ less than qV_r (q is the electronic charge) are repelled by the grid and are not collected on the plate, $\Gamma_+(V_r)$ decreases as V_r is made more positive. The total positive ion flux Γ_+ is obtained when $V_r < 0$, *i.e.*, all ions are collected.

The ion energy distribution, $f(E_+)$, is defined as the derivative of the measured ion flux with respect to the ion energy

$$f(E_+) = -(1/\Gamma_+)\, d[\Gamma_+(qV_r)]/d[qV_r] \quad [1]$$

where $f(E_+)$ has been converted to a probability density function by normalizing with the total ion flux. Note that the ion energy E_+ corresponds to the retarding potential qV_r. Experimentally, the exact differentials are approximated by finite differences using ion flux data at discrete values (0.5V spacing) of V_r.

At any given process condition, the maximum observed ion energy, $E_{+,max}$, compares favorably with the sheath potential, V_s, predicted by a plasma impedance model (1). The median ion energy is defined as the retarding potential at which the measured ion flux is half the total ion flux, and allows quantitative comparison of ion energies for varying plasma conditions without obtaining the entire ion energy distribution (IED).

The mean ion energy, $\overline{E}_+$, is defined by

$$\overline{E}_+ = \int_0^\infty E_+ f(E_+) dE_+ \quad [2]$$

The experimentally measured fraction of ions with energy greater than or equal to a given energy E^* is given the symbol $\delta(E^*)$, and defined by

$$\delta(E^*) = \int_{E^*}^\infty f(E_+) dE_+ \quad [3]$$

$$= \Gamma_+(qV_r = E^*)/\dot{\Gamma}_+ \quad [4]$$

The effect of pressure on ion bombardment energy is clearly demonstrated in Fig. 1a-c, in which $f(E_+)$ is shown for constant power input (0.4 W/cm² at 13.56 MHz excitation frequency and 2 cm electrode spacing) and composition (10% argon in CF_3Cl) at 0.7, 0.5, and 0.3 torr, respectively. Note that the energy distribution shift to higher energies as pressure is decreased; $\overline{E}_+$, $E_{+,max}$, and V_s all increase with decreasing pressure. The modes of the distributions (the peaks) occur at relatively low energies (around 10 eV), even at low pressure where the maximum ion energy is about 100 eV. The mean and median energies are within a few eV, so either may be used as a figure of merit. Ion energy distributions were insensitive to flow rate.

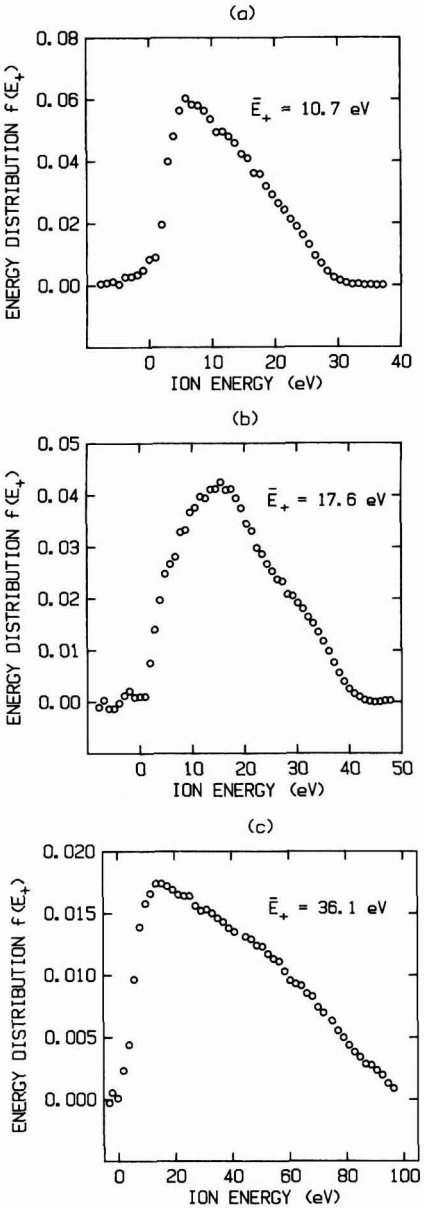

Fig. 1. Effect of pressure on ion energy distribution with power density of W/cm², 10% Ar in CF_3Cl: (a) 0.7 torr, (b) 0.5 torr, (c) 0.3 torr.

The mean ion energy was determined using blank electrodes (no wafer present) for a wide range of plasma conditions (0.1-0.8 W/cm² input power density, 0.2-0.9 torr pressure, 0-30% argon in CF_3Cl), and the data was analyzed using response surface methodology (RSM) (5). Mean ion energies varied from 2 to 40 eV, with typical values of approximately 10 eV for much of the experimental range. Figure 2 is a contour plot of $\bar{E}_+$ with power density $\dot{W}$ and pressure P for a CF_3Cl mole fraction γ of 0.85. The quality of the RSM quadratic model fit was excellent, the adjusted R^2 being 0.94 [see Ref. (1)], so the experimental data is well-represented by the contours shown in Fig. 2. Mean ion energies decrease rapidly with increasing pressure and increase slightly with increasing argon fraction. $\bar{E}_+$ also increases with power input.

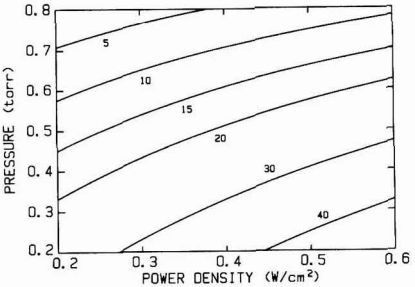

Fig. 2. Contour plot of mean ion energy (in eV) with power density and pressure for $\gamma = 0.85$.

Sheath Transport Model

In this section a simple sheath transport model is derived, which is used in conjunction with the plasma impedance model to predict mean ion energies. The mean energy is shown to be proportional to the sheath electric field to pressure ratio, ϵ_s/P, where ϵ_s is expressed as the quotient of the time-averaged sheath potential and sheath thickness. In addition, the proportionality constant obtained by fitting the model to the data gives a physically reasonable estimate of the ion-neutral scattering cross section.

Previous workers have presented more elegant treatments of ion motion at both low and high (>2 V/cm-torr) ϵ/P, but were concerned only with the fully-developed energy distribution in dc fields. Wannier (6, 7) utilized a recursive method to obtain analytical solutions of the Boltzmann equation for certain special cases, such as equal ion and neutral masses. More recently, Skullerud (8) employed a Monte Carlo technique to investigate the effects of ion-neutral mass ratio and scattering behavior on ion transport. It was found that the ion drift velocity is proportional to the ratio of the electric field to the collision frequency in the low field limit, and the ion drift energy is proportional to (electric field)/(collision frequency) in the high field limit. In each of these treatments, the time between ion-neutral collisions was assumed to be constant.

In the sheath of a glow discharge, several complications make such rigorous approaches less tenable. First, the electric field is not time-invariant; the sheath field oscillates at the plasma excitation frequency. Excitation frequency effects on maximum ion energy have been investigated for a low pressure Cl_2 discharge (9). At low frequencies (<1 MHz) and low pressures, ion transport across the sheath occurs in a fraction of a power cycle (in the absence of scattering collisions), and the maximum ion energy is approximately equal to the peak applied voltage. Maximum ion energies are considerably lower at high (>3 MHz) frequency, where the sheath transit encompasses several RF power cycles. Another complication is the effect of space charge on the sheath electric fields. The ion and electron densities are not constant with distance from the electrode, causing the electric field to vary with position.

In the following derivation of the mean ion bombardment energy, we neglect charge exchange or ion-molecule reactions in the sheath, as well as the aforementioned effects of ac excitation and space-charge perturbation of the electric field. Symmetric charge-exchange cross sections are about the same size as elastic scattering cross sections for simple ions (10), but asymmetric charge-exchange cross sections are much smaller. Also, symmetric collisions will be rare in these plasmas, as discussed later. In addition, no allowance for ion composition changes with plasma conditions is made. The major ions in a CF_3Cl/Ar discharge are generally CF_3^+ and CF_2Cl^+, as observed by mass spectrometry in this and other studies (11), although many other ions are present. We also assume that ions diffuse to the sheath/bulk plasma interface with kinetic energy thermalized to the temperature of the neutrals. In 13.56 MHz plasma etching discharges, the excitation frequency is higher than the ionic plasma frequency (~3 MHz), so ions do not respond to the ac fields. Since dc elec-

tric fields in the plasma bulk are small, ions gain little energy between collisions with neutrals, and the assumption of thermalization is reasonable. Finally, only elastic ion-neutral collisions are accounted for, between which we assume a constant mean free path.

Based on these assumptions, we now model ion transport through the sheath. Ions entering the sheath are accelerated toward the electrode by the high electric field. At high excitation frequency (13.56 MHz in this case) where sheath transit occurs over several RF cycles, ions which traverse the sheath without suffering collisions have energy $E_+ \approx qV_s$. Those undergoing collisions have energies lower than qV_s, the energy determined by the number and nature of the collision events. In an elastic collision, the maximum energy transferred from an incident ion of mass m_+ to a target neutral of mass m_0 (which is essentially motionless relative to the fast ion) is (12)

$$\Delta E/E_+ = \frac{4m_+m_0}{(m_+ + m_0)^2} \cos^2 \beta_i \qquad [5]$$

where ΔE is the energy transferred, E_+ is the energy of the incident ion prior to collision, and β_i is the angle between the line of centers at collision and the incident ion velocity vector. Hard-sphere collision scattering is isotropic with respect to the center of mass. However, the ion, and, therefore, the center of mass, is directed toward the electrode by the electric field, so the angular distribution of the scattering is directed along the field. The average angle between the electric field and the ion velocity vector after collision is given the symbol β_f. For m_+/m_0 between 0.5 and 1.0, β_f varies between $\pi/4$ and $\pi/6$ (7). Consequently, the velocity component of the ion normal to the field is about half of the field-directed velocity, meaning that a considerable fraction of the ion's kinetic energy is randomized in direction. In subsequent calculations, β_f is assumed to be $\pi/6$.

We argue that collisions involving either argon neutrals or argon ions may be neglected in this system. Collisions with argon neutrals are unimportant because the argon mole fractions are low, and argon is smaller in cross section than CF_3Cl, causing scattering events of ions with argon neutrals to be less frequent than collisions with CF_3Cl. Argon ions are ignored because few Ar^+ ions bombard the surface; since the ionization potential of argon is much higher than that of CF_3Cl, argon is not appreciably ionized in the sheath by asymmetric charge exchange with energetic ions. Also, little Ar^+ is created in the discharge by electron-impact processes; experimentally, very little Ar^+ is seen by mass spectrometry. To correctly account for all ion-molecule collisions, one must establish appropriately weighted averages for ion mass, neutral mass, and scattering cross section. The simple weighting process which we used includes only the CF_3Cl mole fraction γ in the neutral gas number density expression (*i.e.*, any argon present is assumed not to participate in ion-neutral collisions). Because argon concentrations were low (30% or less), this had no effect on the model's ability to represent the data. Therefore, argon dilution effects are not considered in the following derivation. However, for higher Ar concentrations we expect that composition would become important.

Since CF_3^+ and CF_2Cl^+ are the primary ions, we assume that the masses of the incident ion and the target neutral (CF_3Cl) are approximately equal. Consequently, the average energy loss during an elastic collision is $\Delta E/E_+ = 0.5$; *i.e.*, the post-collision ion has, on average, about one-half of its pre-collision energy. Although the mass ratio m_+/m_0 does influence the energy transfer, the effect is not large for ratios and order unity. For example, if $m_+/m_0 = \frac{1}{3}$ (corresponding to, for example, a CF^+/CF_3Cl collision), the average fractional ion energy loss is 0.375, assuming elastic hard-sphere scattering.

Consider the flight of an ion through a sheath of thickness d_s, in which the sheath electric field is $\epsilon_s = V_s/d_s$. Assume that the ion travels exactly one mean free path λ_+ between collisions, of which $\lambda_+ \cos \beta_f$ is directed along the electric-field line—this correction factor allows for the two-dimensional nature of the ion motion. We define λ_E as this field-directed component of the mean free path. After traveling a distance λ_E along the field, the ion suffers an elastic collision and transfers half its energy to a neutral. This sequence is repeated as the ion is accelerated by the field and loses energy upon collision, until the ion strikes the electrode. The mean ion energy following j such collisions is

$$\overline{E}_+ = (1\text{-}0.5^j)\, q\lambda_+ V_s/d_s \cos \beta_f \qquad [6]$$

which converges rapidly to the steady-state result, where the energy loss per collision balances the energy gained from the field between scattering events

$$\overline{E}_+ = q\lambda_+ V_s/d_s \cos \beta_f \qquad [7]$$

$$= q\lambda_E V_s/d_s = qV_s/\eta \qquad [8]$$

The number of collisions in the sheath, η, is defined by the ratio of sheath thickness d_s to the field-directed mean free path λ_E, and varied from about 2 to 25 over the range of conditions examined. The rapid convergence is demonstrated in that Eq. [6] and [7] compare within 12% for $j \geq 3$. The rate of convergence is relatively insensitive to the energy loss per collision; using as an example the mass ratio $m_+/m_0 = \frac{1}{3}$, only 5 collisions are required to converge within 6%. Note that the entire range of possible elastic collision events (*e.g.*, varying collision angle) has not been considered in this argument. The average ion energies calculated should not be significantly affected by this. However, the model cannot account for the distribution of ion energies due to the heterogeneity of the series of scattering events.

The sheath thickness is determined from the impedance model (through the sheath capacitance) by assuming that the sheath is a parallel-plate capacitor bounded by the electrode and the bulk plasma

$$d_s = \epsilon A/C_s \qquad [9]$$

where A is the electrode area, C_s is the sheath capacitance, and ϵ is the permittivity of free space. The mean free path is expressed as

$$\lambda_+ = 1/N\sigma_+ = P_0/N_0 P\sigma_+ \qquad [10]$$

where N is the neutral gas number density, σ_+ is the ion-neutral collision cross section, and N_0 is the gas number density at pressure P_0 (arbitrarily chosen as 1 torr) and temperature 350 K (typical of glow discharges). Combining Eq. [7] through [10] yields

$$\overline{E}_+ = \left[\frac{qP_0 \cos \beta_f}{\epsilon A N_0 \sigma_+}\right] \frac{V_s C_s}{P} \qquad [11]$$

Equation [11] can be expressed solely in terms of externally measurable plasma variables, since the product V_sC_s is simply related to the discharge current $|I|$ and the angular excitation frequency ω (1)

$$\overline{E}_+ = K_E\, |I|/\omega P \qquad [12]$$

The predictive power of this simple model is illustrated in Fig. 3, in which experimentally determined $\overline{E}_+$ are plotted against the quantity $|I|/\omega P$. The Fig. 3 data span wide ranges of pressure (0.2-0.8 torr), power density (0.1-0.8 W/cm²), composition (5-30% Ar in CF_3Cl), and electrode spacing (1.5-3.0 cm). The data are well described (correlation coefficient of 0.96) by the line of slope 8.8×10^8 torr-volt and intercept zero, corresponding to a collision cross section of about 3×10^{-15} cm². The standard error between the model and the data is only 2 eV. Assuming hard-sphere ion-neutral interactions, and using an estimated Lennard-Jones diameter of 4.7Å as an approximation of the diameters of both CF_3Cl and the ions (13), a collision cross section σ_+ of 7×10^{-15} cm² is obtained, corresponding to a K_E of about 4×10^8 torr-volt. Since the CF_3^+ ion is smaller than CF_3Cl and the effective cross section of high energy ion-molecule collisions is less than the Lennard-Jones potential would predict, the actual collision cross section should be smaller. For example, typical σ_+ are on the order of 5×10^{-15} cm² (14), in good agreement with the experimental result.

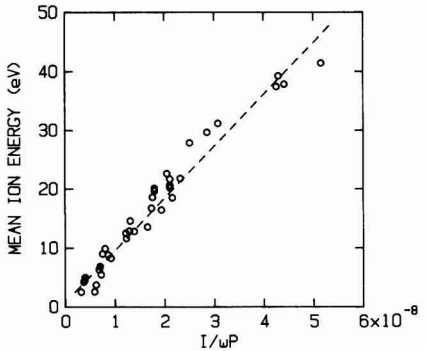

Fig. 3. Measured mean ion energy vs. sheath transport/plasma impedance model prediction.

Of course, a higher plasma temperature would result in a lower neutral density, and consequently increase the elastic-scattering cross section required for the same observed K_E. In fact, the neutral temperature estimated by Doppler linewidth broadening of N_2 in a CF_3Cl plasma is about 500 K (15). The σ_+ derived from Eq. [11] using this temperature is about 4.5×10^{-15} cm².

At pressures less than 0.2 torr, the model predictions are about 20% higher than the experimental result. One plausible explanation is that the sheath voltage predicted by the impedance model is too high. The plasma potential will decrease at lower pressures due to the expansion, and observed loss of containment, of the discharge with the increased electron mobility. The entire chamber serves as the effective ground electrode, and most of the applied voltage is dropped across the sheath of the smaller powered electrode (16). Also, the expected number of collisions in these low pressure sheaths is on the order of 1-2; the assumptions leading to Eq. [12] are not valid in this case. Another possible explanation is that both CF^+ and CF_2^+ are more important ions (relative to CF_3^+) at high ϵ/P; therefore, more energy is lost by the lighter ions upon collision with neutrals.

A similar approach to modeling ion energies was examined previously (17). The improvements offered by the present model are threefold. First, the sheath electric field is determined from the sheath voltage and capacitance, both of which are obtained by impedance analysis. In the previous work, the sheath electric field was assumed proportional to the square root of the power input, implying both that the bulk plasma is field-free and also that the discharge current and voltage each vary as the square root of power. Neither assumption is borne out by observation (the voltage remains relatively constant as the power input is increased in a CF_3Cl plasma, and the impedance model predicts a significant voltage drop across the bulk). Another practical concern is that the actual power input to the plasma may be significantly (20%) less than the power measured with the power meter, since some power may be dissipated in the matching network. The present model also predicts the effect of frequency on ion energy, at least for high frequencies (4). Also, gas composition effects are accounted for by the discharge current, and this model can be used to describe ion energies in many gases. An electronegative gas presents a higher resistance, and, therefore, a lower current flows in CF_3Cl (for a given applied voltage) than, for example, in argon. In addition, the present model offers a reasonable prediction of the proportionality constant between the ion energy and the sheath electric field to pressure ratio.

Ion Energy Distribution Model

Although the mean ion energy provides a qualitative prediction of the effects of energetic ion bombardment on the etching process, quantitative analysis requires knowledge of the ion bombardment energy distribution. The contribution of ion bombardment to the ion-assisted etching rate is likely a function of ion energy, although the form of this dependence is not generally known. The empirical expression given below adequately represents the energy distribution of a CF_3Cl/Ar plasma in terms of the mean ion energy, which was modeled in the previous section.

Examination of Fig. 1 reveals that the ion energy distribution is reproduced quite well by two intersecting lines, one for the low energy region and one for the higher energy tail. This "triangular" approximation of $f(E_+)$ is especially good at the lower pressures, where a significant fraction of the ions have energies of 20 eV or above. Unfortunately, at higher pressures ($\geq$0.7 torr), $f(E_+)$ tails off exponentially rather than linearly. However, since the fraction of ions with high energies is small at high pressures, the contribution of ion-assisted etching is relatively unimportant, and the errors in the ion energy distribution are acceptable.

The triangular approximation of the ion energy distribution is derived as follows. The model vertices are written in $\{E_+, f(E_+)\}$ coordinates as $\{0, 0\}$, $\{E_1, F_1\}$, and $\{E_2, 0\}$, see Fig. 4. E_1 and E_2 are constants representing the energy at the peak of the distribution and the maximum ion energy, respectively. The constant F_1 is chosen such that the area of the triangle is unity, making the model a probability distribution

$$F_1 = 2/E_2 \qquad [13]$$

The model distribution function, $F(E_+)$, is then expressed

$$F(E_+) = 2E_+/E_1E_2 \qquad 0 \leq E_+ \leq E_1$$
$$2(1 - E_+/E_2)/(E_2 - E_1) \qquad E_1 \leq E_+ \leq E_2 \qquad [14]$$

Upon determining the best fit of $F(E_+)$ to the data for a range of plasma conditions (some 50 data points), we find that the following rules of thumb provide good estimates of E_1 and E_2

$$E_1 \sim (P/P_0)\overline{E_+}$$
$$E_2 \sim (8/3)\overline{E_+} \qquad [15]$$

In general, these estimates for E_1 and E_2 predict the peak of the distribution within about 3 eV and the maximum ion energy within about 5 eV. The triangle model is then explicit in the mean ion energy

$$F(E_+) = 3E_+P_0/4\overline{E_+}^2P \qquad 0 \leq E_+ \leq (P/P_0)\overline{E_+}$$
$$\frac{(1 - 3E_+/4\overline{E_+})}{(8/3 - P/P_0)\overline{E_+}} \qquad (P/P_0)\overline{E_+} \leq E_+ \leq 8\overline{E_+}/3 \qquad [16]$$

The model prediction for fractional ion flux above a threshold energy E^*, $\Delta(E^*)$, is simply the area under the triangle between $E_+ = E^*$ and $E_+ = E_2$.

We define the dimensionless variables $\rho = P/P_0$ and $\xi = E^*/\overline{E}_+$ and write

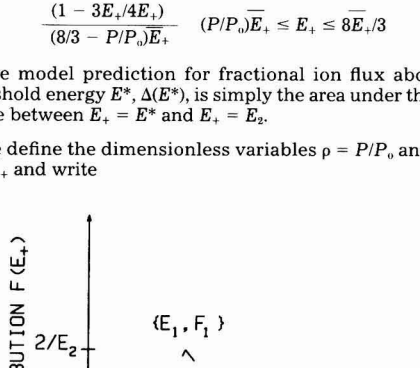

Fig. 4. Triangle model for ion energy distributions

$$\Delta(E^*) = \frac{(1 - 3\xi/8)^2}{(1 - 3\rho/8)} \qquad \rho < \xi < 8/3$$

$$= 1 - 3\xi^2/8\rho \qquad 0 \le \xi / \rho \qquad [17]$$

Equation [12] may be used with Eq. [16] and [17] to express the ion energy distribution solely in terms of impedance properties. The ion energy distribution model using the impedance result is given the symbol $\bar{F}(|I|/\omega P)$, and allows evaluation of the ion energies using only the measured discharge current. The fractional ion flux using the impedance result rather than the experimental data is given the symbol $\bar{\Delta}(E^*)$. $\bar{\Delta}(E^*)$ is obtained by using $\xi = E^*\omega P/K_E|I|$, the threshold energy divided by the impedance model prediction of $\bar{E}_+$, in place of ξ in Eq. [17]. We observed that $\Delta(E^*)$ was within 5-10% of the measured $\delta(E^*)$, and that $\bar{\Delta}(E^*)$ was in general within 10-15% of $\delta(E^*)$. $\bar{F}(|I|/\omega P)$ is compared with experiment in Fig. 5a and 5b for the same plasma conditions specified in Fig. 1b and 1c, respectively. The impedance/sheath transport model's ability to represent the ion energy distribution is good in that Fig. 5a is the poorest fit of the model to the data for the conditions examined. Figure 5b is more typical of the results obtained.

Conclusions

We conclude that, given only the measured discharge current, the impedance/sheath transport model provides a reliable estimate of both mean ion energy and ion energy distribution in CF_3Cl discharge. This method is also successful in modeling ion bombardment energies in SF_6 and CF_3Br discharges (4). Extension of the technique to other symmetric plasma reactors is expected to yield good results. It is possible that asymmetric systems may also be treated, although the impedance model must be modified to account for the voltage distribution dependence on electrode area ratio. We have not examined the asymmetric case here, because the voltage distribution between electrodes of unequal area has not been established; the dependence of sheath potential on electrode area has been reported as first order (18) as well as fourth order (16). In addition, the uniform electron density assumption must be removed in the asymmetric case because the plasma potential will be a strong function of position in the asymmetric system.

The model is not valid at low excitation frequencies (<5 MHz), where the impedance model fails because of the significant coupling of the positive ions with the RF field. Also, the large sheath potentials observed at low frequencies, combined with the relatively long RF cycle times, allow ions to traverse the sheath in a fraction of a cycle. The resulting ion bombardment energies may be quite different than those observed in the high frequency case described here. In addition, the sheath transport model cannot be applied to reactive ion etching (RIE) systems, in which ions suffer few collisions in the sheath due to the very low pressures used.

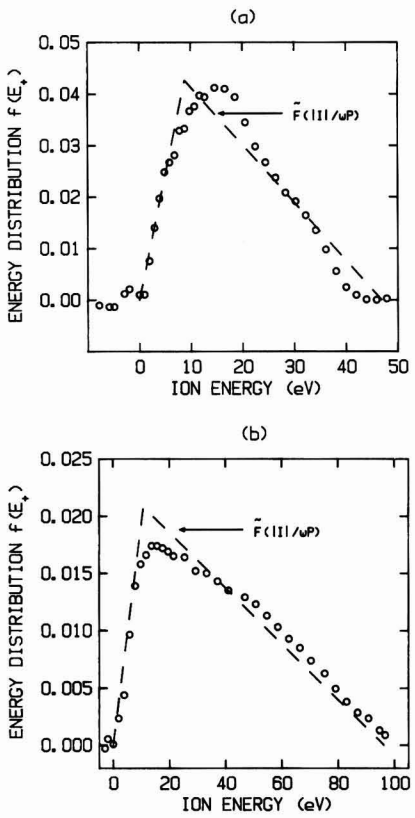

Fig. 5. (a) Poorest triangle model prediction of ion energy distribution for the 50 conditions examined. Same conditions as in Fig. 1b. (b) Typical triangle model prediction of ion energy distribution. Same conditions as in Fig. 1c.

Acknowledgment

Funding for this work was provided by du Pont through its Freon® Products Division. Additional funding was provided by the Semiconductor Research Corporation under Contract no. 83-01-033. We are grateful to Akimichi Yokozeki and Michael Mocella of du Pont for critical reading of this manuscript.

Manuscript submitted on Sept. 10, 1985; revised manuscript received July 17, 1986.

Freon® Products Division, E.I. du Pont de Nemours and Company, Incorporated assisted in meeting the publication costs of this article.

LIST OF SYMBOLS

d_s	sheath thickness
E_1	energy of peak in $F(E_+)$ (eV)
E_2	energy of maximum energy in $F(E_+)$ (eV)
E_+	ion energy (eV)
$E_{+,\max}$	maximum ion energy (eV)
$\bar{E}_+$	mean ion energy (eV)
E^*	threshold energy for ion-enhanced etching (eV)
$f(E_+)$	ion energy distribution, experimental
F_1	normalization constant in Eq. [13]
$F(E_+)$	ion energy distribution, triangle model
$\bar{F}(\|I\|/\omega P)$	ion energy distribution model using plasma impedance
j	index in Eq. [6], number of collisions
K_E	constant relating $\bar{E}_+$ to $\|I\|/\omega P$ in Eq. [13]
m_0	mass of target neutral (kg)
m_+	mass of incident ion (kg)
N	gas density (cm^{-3})
N_0	gas density at pressure P_0 and 350 K (cm^{-3})
P_0	reference pressure of 1 torr
V_r	flag bias voltage, or retarding potential (V)
β_f	average post-collision angle between ion velocity and field
β_i	pre-collision angle between line-of-centers and ion velocity
$\Gamma_+(V_r)$	positive ion flux at retarding potential V_r (mA/cm^2)
Γ_+	total positive ion flux (mA/cm^2)
$\delta(E^*)$	fraction of ions with energy $E_+ > E^*$, experimental
ΔE	energy loss of ion upon collision (eV)
$\Delta(E^*)$	fraction of ions with energy $E_+ > E^*$, triangle model
$\bar{\Delta}(E^*)$	fraction of ions with energy $E_+ > E^*$, using impedance results
ϵ	permittivity of free space (F/m)
η	average number of ion-neutral collisions in sheath
λ_E	component of ion mean free path along electric field (cm)
λ_+	mean free path of ion (cm)
ξ	energy scaling parameter based on measured mean ion energy

ξ energy scaling parameter based on predicted mean ion energy
ρ scaling parameter, P/P_o
σ_+ ion-neutral scattering cross section (cm^2)
ϵ_s time-averaged sheath electric field (V/cm)

[Additional symbols listed in Ref. (1)]

REFERENCES

1. K. D. Allen, H. H. Sawin, M. T. Mocella, and M. W. Jenkins, *This Journal*, **133**, 2315 (1986).
2. S. W. Pang, *Solid State Technol.*, **27**, 249 (1984).
3. J. M. E. Harper, J. J. Cuomo, and H. R. Kaufman, *J. Vac. Sci. Technol.*, **21**, 737 (1982).
4. B. E. Thompson, K. D. Allen, A. D. Richards, and H. H. Sawin, *J. Appl. Phys.*, **59**, 1890 (1986).
5. M. W. Jenkins, M. T. Mocella, K. D. Allen, and H. H. Sawin, *Solid State Technol.*, **29**, 175 (1986).
6. G. H. Wannier, *Phys. Rev.*, **83**, 281 (1951).
7. G. H. Wannier, *Bell System Tech. J.*, **49**, 170 (1953).
8. H. R. Skullerud, *J. Phys. B*, **6**, 728 (1973).
9. R. H. Bruce, *J. Appl. Phys.*, **52**, 7064 (1981).
10. W. H. Cramer, *J. Chem. Phys.*, **30**, 1641 (1959).
11. R. d'Agostino, F. Cramarossa, and S. De Benedictis, *Plasma Chem. Plasma Process.*, **2**, 213 (1982).
12. B. N. Chapman, "Glow Discharge Processes," p. 12, John Wiley and Sons, New York (1980).
13. R. C. Reid, J. M. Prausnitz, and T. K. Sherwood, "The Properties of Gases and Liquids," 3rd ed., McGraw-Hill, New York (1977).
14. E. W. McDaniel and E. A. Mason, "The Mobility and Diffusion of Ions in Gases," John Wiley and Sons, New York (1973).
15. A. D. Richards, H. H. Sawin, and J. Wormhoudt, Unpublished results.
16. H. R. Koenig and L. I. Maissel, *IBM J. Res. Dev.*, **14**, 168 (1970).
17. C. B. Zarowin, *J. Vac. Sci. Technol.*, **A2**, 1537 (1984).
18. J. W. Coburn and E. Kay, *J. Appl. Phys.*, **43**, 4965 (1972).

The Plasma Etching of Polysilicon with CF_3Cl/Argon Discharges

III. Modeling of Etching Rate and Directionality

Kenneth D. Allen*,[1] and Herbert H. Sawin*

Department of Chemical Engineering, Massachusetts Institute of Technology, Cambridge, Massachusetts 02139

Akimichi Yokozeki[2]

E. I. Du Pont de Nemours and Company, Incorporated, Freon® Products Laboratory, Wilmington, Delaware 19898

ABSTRACT

Three kinetic models, based on experimentally measured and theoretically estimated plasma properties, are developed to describe heavily P-doped polysilicon etching in CF_3Cl (Freon® 13) RF discharges. The models include both chemical and ion-assisted processes, and, therefore, predict etching directionality as well as etching rate. The results indicate the importance of relatively low energy (<30 eV) ion bombardment, and suggest that the dominant loss process for the chemical etchant is diffusion-limited recombination at the electrode surfaces. Agreement between measured and predicted etching rates is excellent. The major trends in etching directionality are reproduced by the model, although there is some quantitative disagreement at low pressure.

Better understanding of etching processes will allow improved control of the etching characteristics vital to present and future VLSI fabrication, *i.e.*, anisotropic profiles, selectivity over thin gate oxides, uniformity, and high etching rates for acceptable throughput in single wafer tools as wafer sizes increase. Specifically, we are interested here in identifying and investigating the important physical processes responsible for polysilicon etching in CF_3Cl/Ar discharges.

In the first paper of this series, we presented extensive experimental data for etching rates and total ion fluxes in CF_3Cl/Ar plasma etching. Important plasma properties were estimated using an electrical impedance model (1). Ion bombardment energy distributions in CF_3Cl/Ar discharges were treated in the subsequent paper, using a sheath transport model (2). In this paper, the results of the previous papers are used in the formulation of kinetic etching models.

The present understanding of plasma chemistry, and in particular, the surface processes involved in etching, is limited. It is known that energetic ion bombardment can have profound effects on thin film etching, but the details of the physical processes responsible for ion production and transport are not clear. Consequently, formulating a complex kinetic model for the etching process may not be fruitful at present. A simple model, incorporating variables of known physical importance, allows evaluation of the etching process at a level commensurate with the basic data available.

The plasma etching of heavily P-doped polysilicon with CF_3Cl and CF_3Cl-containing mixtures has been discussed previously (3-5). Halocarbon decomposition mechanisms in glow discharges have been proposed (6), and the free radical chemistry of a CF_3Cl plasma has been explained (7). To our knowledge, no previous effort has been made to model etching in CF_3Cl plasmas, although several studies have focused on CF_4. Using a mass balance model, Winters *et al.* were able to rationalize the loading effect and the selectivity of Si to SiO_2 films in a CF_4 plasma (8). Kushner (9) employed a complex reaction scheme to model CF_4 discharge chemistry with some success—however, many of the model predictions do not agree with experimental evidence. Most recently, Edelson and Flamm (10) presented a similar model of CF_4 polysilicon plasma etching—once again, there was considerable disagreement between model and experiment.

Etching of thin films can occur by several processes: chemical, ion sputtering, and ion-assisted chemical etching. For example, aluminum etching in Cl_2 discharges proceeds primarily by a chemical mechanism, and results in isotropic profiles (11). Films such as copper and gold, which at room temperature form no volatile species by chemical reaction, may be sputtered by energetic ion bombardment—the resulting profiles are anisotropic. Reactive sputter etching, in which ion bombardment enhances the chemical etching, can also achieve aniso-

* Electrochemical Society Active Member.
[1] Present address: Honeywell, Solid State Electronics Division, Plymouth, MN 55441.
[2] E. I. du Pont de Nemours and Company Incorporated, Jackson Laboratory, Chambers Works, Deepwater, NJ 08023.

tropic profiles (12). For example, the reaction rate of silicon with XeF_2 and other neutral species is increased by ion bombardment (13, 14). This synergism between neutral and ion chemistry is most clearly demonstrated in Cl_2 etching of undoped silicon, in which no etching occurs in the absence of ion bombardment (15). The importance of ion bombardment has been examined in UHV experiments, and the results modeled by a surface mass balance (16).

We model etching as the sum of chemical and ion-assisted processes. Measurements of plasma impedance, ion bombardment flux and energy, etching rate, and etching directionality are combined to generate simple descriptions of the process. Three models are presented here, differing in their assumptions about the influence of ion energy and the dominant mechanism for chemical etchant loss. The models provide physical insight into the observed trends in etching characteristics with operating conditions.

Experimental

The parallel plate etching apparatus and associated diagnostics were described previously (1). The diameter of the powered upper electrode was changed from 15 to 12.7 cm for this study. The etching rates presented here are 30-50% higher than those observed with the larger electrode, although the plasma electrical properties were not significantly different (possible explanations for the increase in etching rate are given later). Due to the change in etching rate with reactor geometry, we performed an additional 22 run experimental design for this study. To avoid variations in gas loading, the gas flow rate was set at 6 sccm for all experiments. The etching rate, time-averaged total ion flux, and impedance properties were obtained *in situ* during the etch.

The samples were one-quarter sections of 4 in. wafers; the 0.4 μm thick film was n^+-type (18 Ω/□) CVD polysilicon over an oxide substrate. The 1.25 μm thick Kodak 820 photoresist pattern consisted of 2.25 μm wide lines on a 3-5 μm pitch. Etching rate was measured *in situ* via laser interferometry, and each sample was overetched 20% as determined by laser end point. Based on repeated experiments, the standard relative error (*i.e.*, the standard deviation) of the measured etching rates is about 5%.

Directionality results were obtained with a scanning electron microscope (SEM). Samples were prepared by cutting a small area where the laser spot on the wafer was used to measure etching rate. A SEM photograph of the sample was taken at an angle slightly off parallel with the substrate surface and normal to the cut edge of the sample, *i.e.*, the poly/resist lines appeared end on. No mask erosion occurred at most plasma conditions, since the interference lines from photoresist exposure were still evident in the SEM micrographs after etching. Mask undercut at the poly/resist interface was determined by measuring the poly linewidth and substracting from the resist linewidth. For most process conditions examined in this study, poly linewidth loss at the poly/oxide interface was small.

Ion Bombardment and Etching Directionality

The importance of ion bombardment contributions to the etching process is reflected in the etching profiles. Ion-dominated etching will yield anisotropic profiles, while purely chemical etching will result in isotropic profiles. In this section, we discuss the relationship between etching mechanism and directionality. A quantitative measure of directionality is required for evaluation of external process variable effects on the resulting profiles. The anisotropy coefficient α is defined as the ratio of the etched lateral distance (mask undercut) U to the etched vertical distance T, see Fig. 1. Thus, α varies between 0 (completely vertical etching) and 1 (isotropic etching). The anisotropy coefficient can be greater than 1, if the sample is overetched; therefore α_0, the anisotropy coefficient at zero overetch, provides a more consistent measure of directionality.

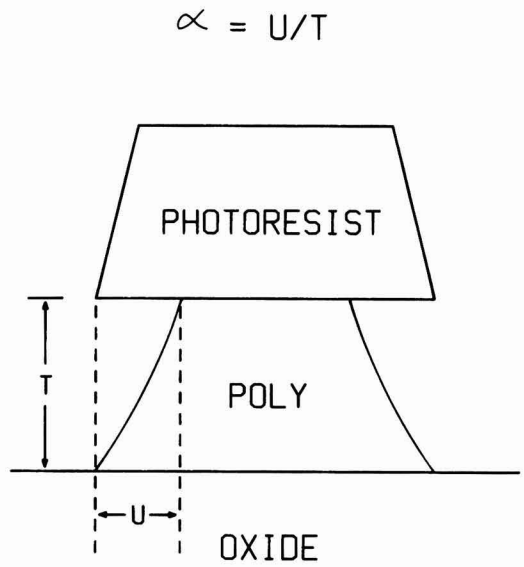

Fig. 1. Definition of anisotropy coefficient

The anisotropy coefficient is determined by the relative rates of the directional ion-assisted and isotropic chemical etching, which we assume to be independent

$$\alpha = \tau R_0/(R_0 + R_+) = \tau R_0/R \quad [1]$$

R is the total etching rate, R_0 is the etching rate attributable to purely chemical processes, R_+ is the etching rate resulting from ion-assisted etching processes, and τ is the fractional overetch, defined as the ratio of the actual etching time to the time required to etch the film to the substrate. In this study $\tau = 1.2$, *i.e.*, each sample was overetched by about 20%. The anisotropy coefficient at zero overetch is simply $\alpha_0 = \alpha/\tau$, provided that the chemical etching rate does not accelerate as the film clears, *i.e.*, loading effects are not important. We did not perform an extensive study of the acceleration of undercut upon overetch. However, several etches at 10% overetch yielded undercut rates not significantly different from the 20% overetch cases. In addition, no loading effect is seen for CF_3Cl, as discussed later. We therefore assume that R_0 is independent of τ.

We determined α_0 from SEM micrograph measurements of the undercut and the film thickness

$$\alpha_0 = U/T\tau \quad [2]$$

The standard relative error of the measured α_0 was about 15%. Figure 2 is a contour plot of α_0 with power density $\dot{W}$ and pressure P as independent variables, for CF_3Cl mole fraction $\gamma = 0.85$. The adjusted R^2 of the quadratic model Response surface methodology (RSM) fit is 0.85, which implies that the data are fairly well represented (17). The deviations between the RSM model and the data are primarily caused by random experimental errors, as discussed later. Significant anisotropy ($\alpha_0 \leq 0.5$) is only obtained at pressures less than 0.6 torr and high power densities. The directionality increases with decreasing pressure, with increasing power input, and with decreasing CF_3Cl mole fraction. These results are in general agreement with the findings of previous investigators for other chemical systems (18).

Comparison of directionality (Fig. 2) with ion bombardment energy [see Fig. 4 of Ref. (2)] reveals that directional etching ($\alpha_0 \leq 0.5$) occurs for mean ion energies above about 15 eV. If $\bar{E}_+ < 15$ eV the etching is primarily isotropic in nature and is assumed to be purely chemical. The contribution of energetic ion bombardment to etching must be included, if the model is to predict etching profiles as well as etching rates, particularly at the lower

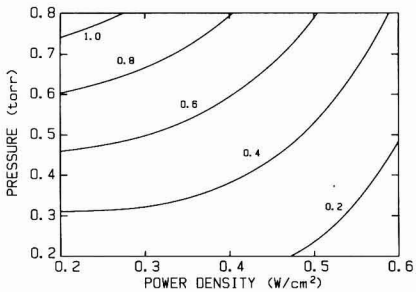

Fig. 2. Contour plot of measured anisotropy coefficient with power density and pressure for $\gamma = 0.85$.

pressures. The importance of ion bombardment is demonstrated by Fig. 3, in which the etching rate R is plotted against total ion flux Γ_+. The etching rate scales linearly with ion flux for mean ion energies greater than 10 eV, as represented by the filled circles. Directional etching was observed for these conditions. Presumably, either ion-assisted etching is the dominant mechanism here, or the rates of chemical and ion-assisted etching are well correlated. The data at lower $\bar{E}_+$ (the open squares) are scattered because of the reduced importance of ion-assisted relative to chemical processes; more isotropic etching was observed in these runs. Note also, the data at low $\bar{E}_+$ fall significantly below the data at $\bar{E}_+ \geq 10$ eV, indicating the importance of energetic ion bombardment in increasing the etching rate.

Etching Models

Three etching models are described below. In each model, the chemical and ion-assisted etching are formulated as independent processes, *i.e.*, these models neglect any interaction between chemical and ion-assisted etching. The reader is referred to the first two papers of this series for further details regarding some quantities used in the model derivations.

Model A.—Polysilicon etching is influenced by relatively low energy (<30 eV) ion bombardment. For example, recent work suggests that ion-assisted etching in CF_4 discharges is important for ion energies above 20 eV (19). Polymer film formation has been postulated to be an important effect in halocarbon discharges; anisotropy may be achieved by sidewall passivation in the absence of ion bombardment (20). Carbon-carbon, silicon-silicon, and carbon-halogen bond energies are approximately 5 eV (21). Sputter cleaning and ion-assisted etching processes may occur for ions with kinetic energy greater than the bond strength. We, therefore, postulate a threshold energy for ion-assisted etching of 10-20 eV. As seen in Fig. 3 and as observed in UHV surface science studies (22), there is evidence that ion-assisted etching rates are proportional to ion flux for large ion energies. Therefore, the ion-assisted etching rate R_{+A} is modeled as proportional to the flux of ions with energies greater than threshold energy

$$R_{+A} = k_{+A}\,\Gamma_+\,\tilde{\Delta}(E^*) \qquad [3]$$

The total ion flux Γ_+ is measured, while the fraction of ions with energy greater than threshold, $\tilde{\Delta}(E^*)$, is predicted using plasma impedance and sheath transport models (1, 2). The ion-assisted rate coefficient for model A is k_{+A}.

Because of the high free-radical fluxes at 0.1-1 torr, it is assumed that the silicon is heavily chlorinated; consequently, the etch product yield per incident ion should be relatively independent of the neutral flux to the surface. At the ion to neutral flux ratios observed in this study, surface coverage should approach unity (16) (in fact, it is likely that the surfaces are covered by several monolayers of adsorbed material).

We arbitrarily set the threshold energy to be 15 eV in light of this evidence. The kinetic model was relatively insensitive to the choice of E^* in the range 10-20 eV, although the quality of etching rate representation was slightly improved at lower E^*; conversely, the anisotropy representation was slightly better at higher E^*.

In CF_3Cl discharges, we assume that atomic chlorine (·Cl) is the primary chemical etchant, although this has not been confirmed; for example, it is known that ·F and CF_3 radicals also adsorb and/or react with silicon (23). The chemical etching rate is assumed to be a linear function of the extent of surface chlorination, which extends several atomic layers into the surface. The formation of this surface chloride is assumed to be rapid with respect to its removal by either chemical or ion-assisted etching processes. In addition, the extent of chlorination is assumed to be proportional to the concentration of gas-phase ·Cl near the surface. It follows that the chemical and ion-assisted etching should proceed independently; therefore, the observed etching rate is modeled as the superposition of these two processes.

We estimate the atomic chlorine concentration by assuming that ·Cl is formed by direct electron-impact dissociation of the CF_3Cl parent molecule, and lost by first-order processes. We also assume that the CF_3Cl is not appreciably dissociated by the plasma, that the reactor is well mixed, and that little ·Cl is lost by flow from the reactor. We support the contention that CF_3Cl is not appreciably consumed by noting that only 0.5 sccm of CF_3Cl is required to supply enough chlorine to produce $SiCl_4$ at a polysilicon etching rate of 1000 Å/min. Also, the neutral composition of the plasma as detected by mass spectrometry is indistinguishable from the CF_3Cl cracking pattern, with the exception of very small signals attributable to species formed by recombination processes (*e.g.*, Cl_2 and $C_2F_xCl_y$).

Incorporating these assumptions, we write a transient mass balance on atomic chlorine

$$d[Cl]/dt = k_F[e^-]P\gamma/RT - k_L[Cl] \qquad [4]$$

where [Cl] is the atomic chlorine concentration, $[e^-]$ is the electron concentration, k_F and k_L are total rate constants for etchant formation and loss, γ is the mole fraction of CF_3Cl in the feed gas, T is the neutral temperature, and R is the gas constant. Note that the CF_3Cl concentration is expressed in terms of input partial pressure, as we have assumed that CF_3Cl is not significantly depleted by decomposition reactions. The first and second terms on the right side of Eq. [4] are the rates of etchant production (dependent on both the electron and parent concentrations, second order overall) and loss. As k_F is assumed to be a constant, the model does not allow for electron temperature effects on the dissociation rate. Electron temperature estimation requires detailed information about the electric fields in the discharge, as well as basic data regarding electron mobility in CF_3Cl. The assumption of constant electron temperature is a good one in CF_3Cl discharges, at least over the range of process conditions investigated here (1).

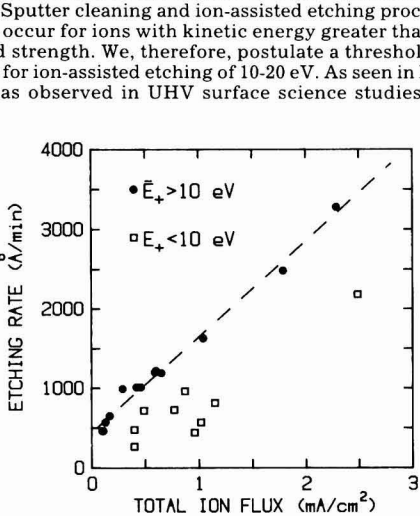

Fig. 3. Measured etching rate (Å/min) vs. total measured ion flux (mA/cm²). Filled symbols = $\bar{E}_+ > 10$ eV, squares = $\bar{E}_+ < 10$ eV.

The form of the loss expression depends on the particular discharge: temperature, reactor geometry, film being etched, electrode material, etc. In this model the loss is assumed to be first order in reactant concentration, which is consistent with consumption by polysilicon etching, by surface recombination, or by a combination of these loss processes. Solving Eq. [4] at steady state, the atomic chlorine concentration is

$$[Cl] = (k_F/k_L)\,[e^-]P\gamma \qquad [5]$$

We now relate the etching rate to [C1]. It has been suggested that the chemical etching surface reaction proceeds by a series of first-order addition steps (14, 24), one of which will be rate limiting. Consequently, for reasonably high surface coverages the chemical etching rate is linearly related to [C1] through the etching rate constant k_E (25), *i.e.*

$$\begin{aligned} R_{oA} &= k_E[Cl] \\ &= (k_E k_F/k_L)\,[e^-]P\gamma \\ &= k_{oA}\,[e^-]P\gamma \end{aligned} \qquad [6]$$

where k_{oA} is a lumped rate coefficient for model *A*. The linear dependence of R_{oA} on [Cl] is also a consequence of the pseudosteady-state assumption. If the dominant loss process for atomic chlorine is the etching process itself ($k_L \sim k_E$), Eq. [6] shows that the etching rate is proportional to the atomic chlorine production rate. If other loss processes such as surface recombination are important ($k_L > k_E$), lower etching rates will be obtained for the same atomic chlorine production rate.

The total etching rate is assumed to be the sum of the chemical and ion-assisted rates

$$R_A = k_{oA}[e^-]P\gamma + k_{+A}\dot{\Gamma}_+\bar{\Delta}(E^*) \qquad [7]$$

where we have implicitly assumed that the ion-assisted etching does not significantly affect either the extent of surface chlorination or the [Cl] of the bulk plasma. The anisotropy coefficient for model A is expressed as

$$\alpha_A = \frac{\tau}{1 + \dfrac{k_{+A}\dot{\Gamma}_+\bar{\Delta}(E^*)}{k_{oA}[e^-]P\gamma}} \qquad [8]$$

The etching rate and anisotropy models require two adjustable parameters and a specified threshold energy E^*. These parameters have physical significance to the anisotropic and chemical etching rates, and allow prediction of the etching rate and anisotropy given the measured total ion flux and discharge impedance.

Model B.—The previous model does not account for increased etching yield as a function of ion energy above the threshold. The higher energy ions contribute more energy to the surface than do lower energy ions and, therefore, should induce more surface reactions. Surface studies of the silicon chlorine system suggest that the etch yield is linearly dependent on the ion bombardment energy (26). We caution the reader that ion bombardment energies in UHV surface studies are generally much higher than those obtained in symmetric plasma reactors, and that the neutral and ion fluxes in the surface studies may not be similar to those of an etching process. Note also that the silicon surface is likely to be covered by a chlorofluorocarbon "film" when exposed to a CF_3Cl plasma. Consequently, the dependence of etch yield on ion energy may be quite different than in the the UHV studies. Nonetheless, the importance of ion energy is demonstrated by these experiments.

The energy dependence of etch yield, $g(E_+)$, can be combined with the ion energy distribution to predict the energy-dependent ion-assisted etching rate R_{+B}

$$R_{+B} = k_{+B}\dot{\Gamma}_+ \int_{E^*}^{E_{+,\max}} f(E_+)\, g(E_+)\, dE_+ \qquad [10]$$

where k_{+B} is the ion-assisted rate constant for model *B*, $E_{+,\max}$ is the maximum energy of ions striking the surface, and $f(E_+)$ is the ion energy distribution function. Assuming a linear dependence of the etch yield on the incident ion energy (above the threshold energy), and using a triangular approximation of the ion energy distribution (2), Eq. [10] yields

$$R_{+B} = \frac{k_{+B}\dot{\Gamma}_+\bar{E}_+}{(2.67 - \rho)}\,[2.37 - \bar{\xi}^2 + \bar{\xi}^3],\ \text{if } \rho < \bar{\xi} < 2.67 \qquad [11a]$$

or

$$R_{+B} = \frac{k_{+B}\dot{\Gamma}_+\bar{E}_+}{(2.67 - \rho)}\,[2.37 - \rho^2/3 + (0.25 + 0.67/\rho)\bar{\xi}^3],\ \text{if } 0 \le \bar{\xi} \le \rho \qquad [11b]$$

In Eq. [11], $\bar{E}_+$ is the mean ion energy, ρ is a dimensionless pressure, and $\bar{\xi}$ is the ratio of E^* to $\bar{E}_+$. The two forms of Eq. [11] are necessary to represent the two possible cases: (*i*) the threshold energy E^* less than the energy at the peak in the distribution ($\rho\bar{E}_+$), and (*ii*) the threshold greater than the peak.

The chemical etching rate is identical to that of model A, so the overall etching rate is

$$R_B = k_{oB}\,[e^-]P\gamma + R_{+B} \qquad [12]$$

The anisotropy coefficient α_B is obtained by combining Eq. [1], [11], and [12].

Model C.—The third kinetic model incorporates the same ion-assisted etching rate as model A, however, the expression for [Cl] differs considerably. We postulate here that the primary loss mechanism for atomic chlorine is recombination at the electrode surfaces, and that the loss rate is governed by the diffusion of atomic chlorine to the electrodes. After deriving the expression for R_C, we discuss the supporting evidence for such a mechanism.

The implications of this assumption are clear if we assume that [Cl] varies only in the axial direction *z* between the electrodes, *i.e.*, we treat the system as one-dimensional. Assume that ·Cl is created in the bulk, that the loss rate at the upper electrode is rapid with respect to transport by diffusion, and that the lower electrode covered by the wafer is essentially inert. Because the upper electrode is a sink for ·Cl, a concentration gradient exists between the bulk and the surface. The flux to the surface, and hence the ·Cl loss rate, is approximately

$$N_{Cl} \sim -D\,\Delta[Cl]/\Delta z \sim D[Cl]/d \qquad [13]$$

where N_{Cl} is the flux, *D* is the mass diffusivity of ·Cl in CF_3Cl, and *d* is the interelectrode spacing.

Note that Eq. [13] is not strictly correct. We assume in the derivation of the flux expression that atomic chlorine is generated only in one plane of the discharge, and that the concentration gradient is constant with *z*. In reality, chlorine production is a function of both position and time. In addition, we have ignored recombination on the wafer surface. However, Eq. [13] provides the proper functionality and an order of magnitude estimate of the atomic chlorine loss rate.

The transient mass balance on atomic chlorine, per unit volume, is then

$$\begin{aligned} d[Cl]/dt &\sim k_F[e^-]P\gamma/RT - D[Cl]A/Vd \\ &\sim k_F[e^-]P\gamma/RT - D[Cl]/d^2 \end{aligned} \qquad [14]$$

where the loss rate has been set equal to the diffusive flux to the upper electrode. In Eq. [14], *A* is the total electrode surface area, and *V* is the effective reactor volume (the volume contained between the electrodes). The surface area to volume ratio of the cylindrical reactor gives the square dependence of the loss term on electrode spacing.

Diffusivity in gases is inversely proportional to pressure (27), so steady-state solution of Eq. [14] yields.

$$[Cl] = k'[e^-]P^2\gamma \qquad [15]$$

where k' is a lumped constant.

Recent infrared laser absorption studies indicate that the atomic chlorine concentration in a CF_3Cl discharge is about 1 mole percent (28). Preliminary studies suggest that the measured [Cl] may vary as $P[e^-]^{0.5}$, which is consistent with diffusion-limited, second-order recombination on the electrodes as the limiting loss process. A more sophisticated model, including gas-phase as well as surface recombination processes, will be presented in a future publication.

At present, however, we use the result of Eq. [15] to express the etching rates for model C

$$R_{0C} = k_{0C}[e^-]P^2\gamma \quad [16]$$

and

$$R_C = k_{0C}[e^-]P^2\gamma + k_{+C}\Gamma_+\bar{\Delta}(E^*) \quad [17]$$

The anisotropy coefficient α_C is obtained by combining Eqs. [1], [16], and [17].

We have considerable evidence to support the assertion that recombination at the electrodes is the dominant Cl loss process. Loss by gas flow out of the effective reactor should not be important, because the residence time (~1s) is much longer than the relaxation time for both the diffusion to the electrodes (1-10 ms) and the expected characteristic times for radical recombination. Diffusive losses from the sides of the reactor will be most important at large electrode spacings, short reactor residence times, and slow recombination rates, where there is a high probability that molecules can pass out of the reactor without being consumed. We cannot discount the possibility that this loss process is important without knowing the surface recombination rates. However, the dependence of the loss rate on pressure, for a fixed flow rate, is the same as for diffusion-limited surface recombination; only the length scale is changed. Gas-phase recombination of atomic chlorine may be important at high pressures, but for atoms this is usually a three-body process, and is therefore relatively slow. It is possible that atomic chlorine may recombine with CF_2 or other radicals, but reliable rate constants for these reactions are not readily available.

Several observations indicate that Cl consumption by the etching reaction is not rapid relative to recombination at the electrodes. First, Mogab and Levinstein noted that there is no loading effect in CF_3Cl (4). If Cl were consumed rapidly by etching, the concentration would decline with increasing silicon surface area, resulting in a lower etching rate. Second, we noted in this study that the etching rate increased significantly upon decreasing the powered electrode area, despite the minimal change in discharge impedance. The decrease in electrode surface area available for recombination may account for the increased etching rate. Finally, the laser absorption studies indicate that the atomic chlorine concentration in CF_3Cl discharges is significantly higher during etching of a full 4 in. polysilicon wafer than with blank electrodes (the wafer removed). We, therefore, conclude that Cl loss on stainless steel is faster than on polysilicon.

The relative importance of diffusion and surface recombination in determining the atomic chlorine loss rate is seen by comparing the respective rates, *i.e.*, the limiting step will have a lower reaction velocity. Per unit total surface area, the recombination reaction rate is $S\bar{c}$[Cl]/4, where S is the recombination probability per surface collision and $\bar{c}$ is the mean thermal speed of a chlorine atom at the plasma temperature. The diffusion rate is D[Cl]/d. Solving for the reaction probability at which the two rates are equal, we obtain $S = 4D/d\bar{c}$. At 0.5 torr, an electrode spacing of 2 cm, and a plasma neutral temperature of 500 K, we get $S \sim 0.01$ as the critical surface recombination probability. That is, if $S >> 0.01$ the atomic chlorine loss process is diffusion-limited. Conversely, if $S >> 0.01$ the loss process is limited by the surface reaction. The reaction probability of Cl on stainless steel is not available, however, the recombination probability of atomic oxygen on quartz (a relatively inert surface) is about 0.0002 (29). We would expect the recombination of atomic chlorine on the more catalytically active metal surfaces to be faster. However, without knowledge of the recombination rate, the rate-limiting step cannot be determined.

Further experimental evidence for diffusion limitations is given by observations of wafer clearing patterns (30). At low powers and high pressures, etching is primarily chemical, as evidenced by its isotropic nature. Diffusion limitations should be most important here. The wafers clear from the sample center toward its periphery under these conditions. That is, the etching rate at the sample edges, near the electrode surface, is very slow compared to the rate in the center. Small stainless steel clips which hold the sample to the electrode also cause reduced etching rates in the neighboring area. This behavior suggests that a significant Cl concentration gradient exists between the electrode and the sample center, ostensibly caused by rapid recombination on the stainless steel. At lower pressures where diffusion limitations are less important, the clearing patterns are markedly different, and the difference in etching rate between the sample center and the edge is greatly reduced.

Results

For each model the rate constants k_0 and k_+ were determined by linear regression, for both etching rate and anisotropy data. The etching rate model contains two adjustable parameters, while the anisotropy model contains only their ratio, $K_\alpha = k_+/k_0$. Using the anisotropy data, the best value of K_α was first determined. Next, the combination of k_0 and k_+ which best fit the etching rate data was found, and the ratio $K_R = k_+/k_0$ was calculated. The parameter ratio was then fixed intermediate between K_α and K_R, and the magnitudes of the parameters were chosen to best represent the etching rate. K_α and K_R agreed well for models A and C, while there was considerable disagreement for model B. Consequently, model B cannot simultaneously describe etching rate and directionality. In all regressions, the relative error of the model (scaled by the experimental data) was minimized. The regression results are summarized in Table I; the k_+ and k_0 values listed are the "best fit" parameters determined by the procedure described above. The relative standard error, SE, of each fit to the experimental data is given in Table I. Here, SE is defined by

$$SE = \left(\frac{1}{N}\left[\sum_{i=1}^{N}(X_i^D - X_i^M)^2/(X_i^D)^2\right]\right)^{0.5} \quad [18]$$

where the X^D are the experimental data, the X^M are the model predictions, and N is the number of data points.

Using RSM, contour plots were generated from the experimental data and from the model predictions at the same conditions. In each case, the adjusted R^2 of the fit was ~0.9, so the contours represent the data well. However, there is some error caused by the relatively small number of experiments, particularly in the anisotropy fits. This error should be considered when comparing the models with the data.

Etching rates were quite reproducible; the experimental error approximated from the replicate runs is about 5%. However, measured anisotropy coefficients differed by as much as 0.3 for repeated experiments. The large relative errors in anisotropy are attributed to the nonuni-

Table I. Regression results

	Model A	Model B	Model C
K_α	3.9×10^9	1.5×10^8	3.1×10^9
K_R	3.4×10^9	6.7×10^7	2.7×10^9
k_0	5.1×10^{-7}	5.5×10^{-7}	7.9×10^{-7}
k_+	1.9×10^3	4.5×10^1	2.3×10^3
SE_R	0.19	0.30	0.13
SE_α	0.40	0.35	0.26
Units:			
k_{0A}, k_{0B}	cm³-Å/torr-min		
k_{0C}	cm³-Å/torr²-min		
k_{+A}, k_{+C}	cm²-Å/mA-min		
k_{+B}	cm²-Å/mA-eV-min		

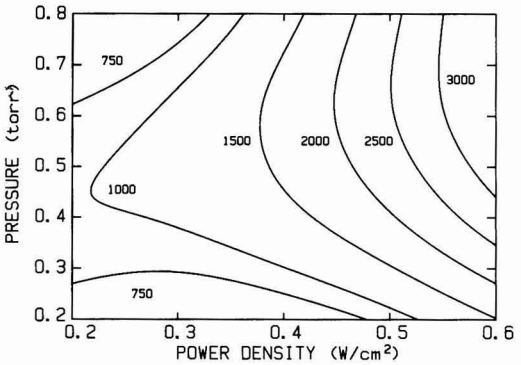

Fig. 4. Response surface methodology quadratic polynomial fit of etching rate data (Å/min) as a function of power density and pressure, γ = 0.85.

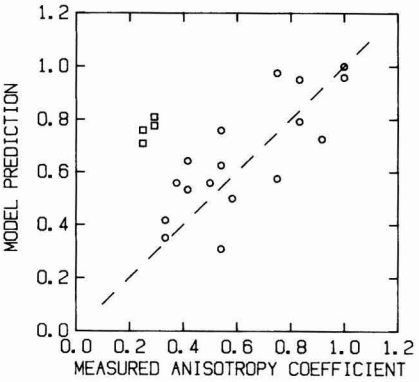

Fig. 6. Model A predictions of α_0 vs. experiment. The dashed line represents a perfect fit of the model to the data. Squares = 0.2 torr runs.

formity of the etching rate over the sample surface; distinct clearing patterns are observed for varying plasma conditions (30). Particularly in cases where chemical etching is dominant, nonuniform etching magnifies the effects of errors in overetch time (endpoint determination was done manually, by observing the laser interferometry signal) and position of the SEM sample on the etched wafer. In some cases it was also difficult to determine the undercut from the SEM micrographs.

Figure 4 is a contour plot of the etching rate experimental data for the following range of conditions: power density 0.2-0.6 W/cm², pressure 0.2-0.8 torr, and 0.85 CF_3Cl mole fraction. The etching rate varies from about 300 to 3500 Å/min over this parameter space. To facilitate comparison, contour plots for the model predictions cover the same ranges of power and pressure. The etching rate generally decreases slightly with increased argon addition, but the more significant trends with power and pressure are unchanged by the argon dilution.

The etching rate predictions of model A (energy-independent ion-assisted etching rate) are shown in Fig. 5. Note that all general trends in the data are reproduced and that the predicted etching rates are within about 500 Å/min of the data over the entire experimental range. However, the model tends to underpredict the etching rate at high pressures and overpredict at low pressures. The predicted increase in etching rate with power density at high pressure is not as rapid as observed experimentally.

The anisotropy predictions of model A are less satisfying. The model predictions of α_0 are plotted against experiment in Fig. 6. At low pressures, the predicted α_0 is about 0.8, while the experimental result is 0.3. At high pressures, the model predicts more directional etching than is observed. The errors in anisotropy and etching rate indicate that the predicted chemical etching rate is too low at high pressures and too high at low pressures. The large random errors in the predicted anisotropy resulted in a poor RSM fit, so a contour plot of the model predictions is not shown.

Etching rates predicted by model B (energy-dependent ion contribution) are shown in Fig. 7. It is obvious that agreement between model and data is poor, as reflected in the higher mean error given in Table I. The model severely underpredicts the increase of etching rate with power density, especially at moderate to high pressures. However, the qualitative shape of the model prediction with increasing pressure more closely mirrors the data than does model A. The linear dependence of etch yield on ion energy has increased the ion-assisted contribution at low pressure, but greatly reduced it for high pressures. Consequently, anisotropy representation is slightly improved over model A, see Fig. 8. Note that at the very low pressures etching is again more directional than predicted.

The model C (diffusion-limited recombination) results are excellent, as seen in Fig. 9. Model and experimental etching rates agree within 250 Å/min over the entire range; in addition, the model contours closely follow the data. Since experimental and RSM fitting errors sum to 10-15%, the model predictions and the data are indistinguishable.

Model C also predicts the etching directionality quite well, see Fig. 10. Predicted anisotropy coefficients are generally within 10% of the measured value, with the most notable exception of the 0.2 torr data. At 0.2 torr, the model predictions are α_0 = 0.4-0.5, still higher than measured experimentally, but much improved over the predictions of models A and B. The contours of Fig. 11 are somewhat poorer than the individual predictions at

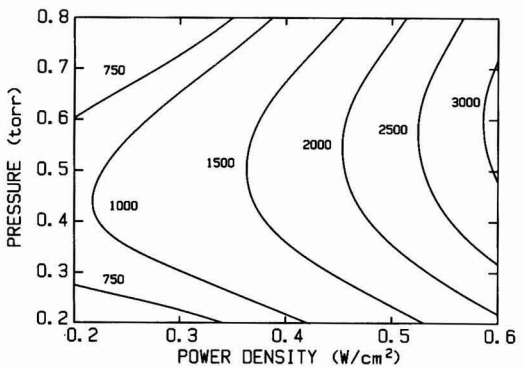

Fig. 5. Contour plot of energy-independent model (A) prediction of etching rate (Å/min) as a function of power density and pressure, γ = 0.85.

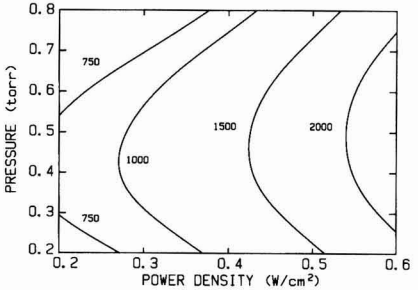

Fig. 7. Contour plot of energy-dependent model (B) prediction of etching rate (Å/min) as a function of power density and pressure, γ = 0.85.

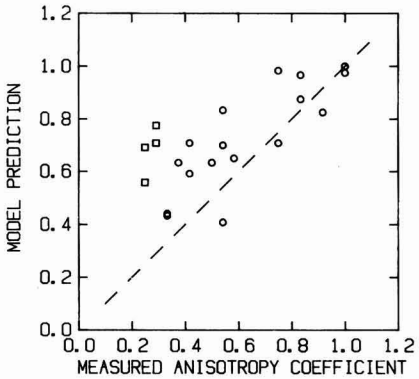

Fig. 8. Model B predictions of α_0 vs. experiment. The dashed line represents a perfect fit of the model to the data. Squares = 0.2 torr runs.

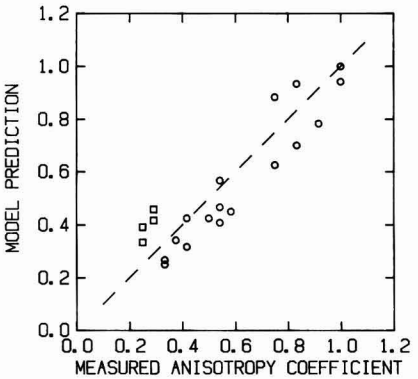

Fig. 10. Model C predictions of α_0 vs. experiment. The dashed line represents a perfect fit of the model to the data. Squares = 0.2 torr runs.

the experimental conditions, because of the influence of the low pressure points on the RSM fit.

Discussion

Some interpretation of the fitted parameter values is possible. The energy-independent ion-assisted etching rate constants k_{+A} and k_{+C} are both about 2×10^3 cm²-Å/mA-min, which corresponds to an etching yield of about one silicon atom per incident ion, assuming $SiCl_4$ to be the primary etch product. This etching yield compares favorably with literature values of 2-3 atoms/ion for 1 keV reactive ion bombardment of chlorine-dosed surfaces (31, 32). The sightly lower etching yield obtained in the present study may be due to polymer coverage of the silicon surface (which is present in chlorofluorocarbon plasmas but is absent in UHV studies), or to the lower ion energies in the plasma reactor. The ion bombardment contribution is not purely physical in nature because the yield is much larger than silicon sputtering yields for 100 eV ion bombardment, which are about 0.01 atom per ion (33-35). The chemical etching parameters are more difficult to interpret, because they contain several rate constants; also, the models do not properly account for species concentration gradients in the reactor.

The anisotropy data at 0.2 torr are poorly described by all models; the predicted profiles are more isotropic than the data. There are several possible explanations for the discrepancy. We observed a "microsensitivity" effect [see Ref. (4)] in the etching at low pressures; here, etching is slower in the immediate vicinity of the photoresist lines than on a clear polysilicon surface. This effect, the opposite of the common loading effect, may be linked with the minor resist degradation observed at 0.2 torr; resist removed from the mask by sputtering or by chemical processes may be redeposited on the polysilicon surface near the mask. Presumably, the increased resist degradation at 0.2 torr is caused by the combination of high ion

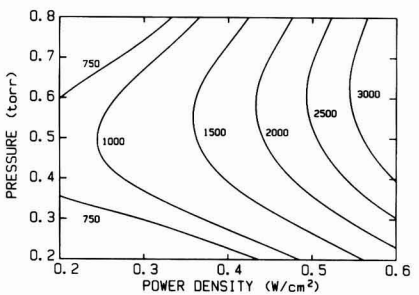

Fig. 9. Contour plot of diffusion-limited model (C) prediction of etching rate (Å/min) as a function of power density and pressure, $\gamma = 0.85$.

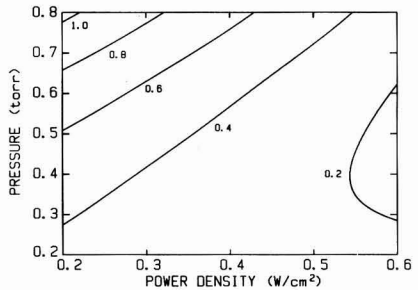

Fig. 11. Contour plot of diffusion-limited model (C) prediction of anisotropy coefficient as a function of power density and pressure, $\gamma = 0.85$.

energy and high surface temperature (50°C) reached in these experiments. Note that the etching rate at 0.2 torr is on the order of 400 Å/min so the etching time required is long (approximately 10 min). Since the low pressure decreases heat transfer from the wafer to the electrode, the sample is expected to be hotter than in the higher pressure runs. The photoresist etching rate was not measured in this work; however, there is strong evidence that chlorinated plasmas attack photoresist. The resist may act as a source for chlorocarbon species which form a thin passivating film on the sidewalls. This effect may account for the anisotropy observed in $SF_6/CFCl_3$ (Freon® 11) discharges as compared with pure SF_6 (36).

The poor prediction of anisotropy at 0.2 torr may also be attributable to inaccuracies of the impedance model. At 0.2 torr, the discharge is not well confined. Consequently, electron densities predicted by the impedance model could be artificially high due to increased plasma volume, causing a larger contribution to the chemical etching rate in the kinetic model. Lowering the electron densities of these errant points would not only improve the anisotropy prediction to within experimental error of the measured values, but would improve the etching rate predictions as well.

The simplicity of the models is not meant to imply that the chemical processes responsible for etching are well understood, but rather that such a complex system requires cautious evaluation. We have chosen the simplest model possible to describe each important phenomenon in the etching process. Obvious omissions are surface passivation of polymerization reactions, the contributions of the plasma chemistry to etchant loss, the synergy of chemical and ion-assisted surface processes (*i.e.*, the effect of surface coverage and reactant depletion on ion-assisted etching yield), and surface reaction temperature effects. In addition, the primary etchant species may not be produced solely by direct electron-impact

dissociation of the parent gas. The impedance model predictions may be in error at high pressures where significant power dissipation occurs in the sheaths, and at low pressures where loss of containment changes the plasma volume.

The most important shortcoming of these models is the lack of synergy between the neutrals and the ions. It has been shown that the surface coverage of silicon by chlorine influences the yield of etching product per incident ion (14). Surface coverage is also a weak function of ion flux, due to bombardment-induced desorption. In CF_3Cl plasma etching, the neutral to ion flux ratio, and, in turn, the surface coverage, may vary considerably with plasma conditions. The rapid increase in etching rate with power at high pressure may be due, in part, to high fractional chlorination of the surfaces, while the lesser influence of power input at low pressure may result from low fractional chlorination.

Future use of quantitative diagnostic tools such as laser-induced fluorescence (LIF) and infrared absorption may reveal the mechanism of $\cdot$Cl loss. LIF is capable of spatial resolution within the discharge and would be particularly useful for observation of diffusion-limited processes where significant concentration gradients must be present.

Summary

The importance of low energy ion bombardment on etching has been demonstrated; directionality is influenced by ions of less than 30 eV. Consequently, a 15 eV threshold for ion-assisted etching was postulated. Chemical etching effects were modeled as an independent process. Three models were formulated, each requiring two adjustable parameters to describe simultaneously the response of both etching rate and etching directionality with power, pressure, and composition. The data was not well described by two of the models—however, excellent representation of etching rate was obtained by assuming the major sink for chemical etchant to be diffusion-limited recombination at the electrodes (model C). Directionality was also adequately described by this model, except at low pressures. The lack of a loading effect in CF_3Cl plasma etching of polysilicon, as well as the observed uniformity of etching, is consistent with this assumption.

Acknowledgments

Financial support for this work was provided by du Pont through its Freon® Products Division. Funding for the construction of much of the apparatus was provided by the Semiconductor Research Corporation under Contract no. 83-01-033. The authors wish to thank Michael Mocella and Mary Jenkins of du Pont for their contributions, including some of the statistical analysis of the data. The assistance of Albert Richards and Brian Thompson of MIT is greatly appreciated.

Manuscript submitted Sept. 10, 1985; revised manuscript received July 17, 1986.

The Freon® Products Division of E. I. du Pont de Nemours and Company, Incorporated, assisted in meeting the publication costs of this article.

LIST OF SYMBOLS

A	total reactor surface area (cm^2)
$\bar{c}$	mean speed of atomic chlorine (cm/s)
[Cl]	atomic chlorine concentration (cm^{-3})
d	electrode spacing (cm)
D	mass diffusivity of atomic Cl (cm^2/s)
$f(E_+)$	ion energy distribution function
$g(E_+)$	energy dependence of ion-assisted etching
k_e	rate coefficient for consumption of $Cl\cdot$ by etching
k_F	$Cl\cdot$ total formation rate coefficient
k_L	$Cl\cdot$ total loss rate coefficient
k_{oi}	chemical etching rate constant for model i
k_{+i}	ion-assisted rate constant for model i
k'	lumped rate coefficient
K_α	ratio of k_{+i}/k_{oi} best fit to anisotropy for model i
K_R	ratio of k_{+i}/k_{oi} best fit to etching rate for model i
R_{oi}	predicted isotropic etching rate (Å/min) for model i
R_{+i}	predicted anisotropic etching rate (Å/min) for model i
S	surface recombination probability
T	etched vertical distance (μm)
U	etched lateral distance (μm)
V	effective reactor volume (cm^3)
α_i	predicted anisotropy coefficient for model i
α_o	anisotropy coefficient at zero overetch
τ	fractional overetch time

[Additional symbols are listed in Ref. (1) and (2).]

REFERENCES

1. K. D. Allen, H. H. Sawin, M. T. Mocella, and M. W. Jenkins, *This Journal*, **133**, 2315 (1986).
2. K. D. Allen and H. H. Sawin, *This Journal*, **133**, 2326 (1986).
3. M. F. Leahy, in Proceedings of the Third Symposium on "Plasma Processing," Denver, CO., Oct. 11-16, 1981. The Electrochemical Society, Inc., p. 176 (1982).
4. C. J. Mogab and H. J. Levinstein, *J. Vac. Sci. Technol.*, **17**, 721 (1980).
5. A. C. Adams and C. D. Capio, *This Journal*, **128**, 366 (1984).
6. R. d'Agostino, F. Cramarossa, and S. De Benedictis, *Plasma Chem. Plasma Process.*, **2**, 213 (1982).
7. D. L. Flamm, *J. Appl. Phys.*, **41**, 5688 (1980).
8. H. F. Winters, J. W. Coburn, and E. Kay, *ibid.*, **48**, 4973 (1977).
9. M. J. Kushner, *ibid.*, **53**, 2923 (1982).
10. D. Edelson and D. L. Flamm, *ibid.*, **56**, 1522 (1984).
11. D. W. Hess, *Solid State Technol.*, **24**, 183 (1982).
12. E. O. Degenkolb, *This Journal*, **129**, 1150 (1982).
13. J. W. Coburn, H. F. Winters, and T. J. Chuang, *J. Vac. Sci. Technol.*, **B 1**, 469 (1983).
14. J. W. Coburn, H. F. Winters, and T. J. Chuang, *J. Appl. Phys.*, **48**, 3532 (1977).
15. J. W. Coburn and H. F. Winters, *ibid.*, **50**, 3189 (1979).
16. R. A. Barker, T. M. Mayer, and W. C. Pearson, *J. Vac. Sci. Technol.*, **B 1**, 37 (1983).
17. M. W. Jenkins, M. T. Mocella, K. D. Allen, and H. H. Sawin, *Solid State Technol.*, **29**, 175 (1986).
18. C. B. Zarowin, *This Journal*, **130**, 1144 (1983).
19. N. Us, R. W. Sadowski, and J. W. Coburn, *Plasma Chem. Plasma Process.*, **6**, 1 (1986).
20. M. Millard, in "Techniques and Applications of Plasma Chemistry," J. R. Hollahan and A. T. Bell, Editors, p. 177, Wiley-Interscience, New York (1974).
21. CRC "Handbook of Chemistry and Physics," R. C. Weast, Editor, 56th Ed., Chemical Rubber Company (1975).
22. S. C. McNevin and G. E. Becker, *J. Vac. Sci. Technol.*, **B 3**, 485 (1985).
23. H. F. Winters, *J. Appl. Phys.*, **49**, 5165 (1978).
24. D. L. Flamm and V. M. Donnelly, *Plasma Chem. Plasma Process*, **1**, 317 (1981).
25. D. L. Flamm, V. M. Donnelly, and J. A. Mucha, *J. Appl. Phys.*, **52**, 3633 (1981).
26. J. W. Coburn, H. F. Winters, and T. J. Chuang, *ibid.*, **48**, 3532 (1977).
27. J. O. Hirschfelder, C. F. Curtiss, and R. B. Bird, "Molecular Theory of Gases and Liquids," John Wiley and Sons, Inc., New York (1964).
28. K. D. Allen, A. D. Richards, and H. H. Sawin, In preparation.
29. J. C. Greaves and J. W. Linnett, *Trans. Faraday Soc.*, **55**, 1355 (1959).
30. M. T. Mocella, M. W. Jenkins, H. H. Sawin, and K. D. Allen, Materials Research Society Symposium Proceedings, Vol. 38, R. P. H. Chang and B. Abeles, Editors, p. 228 (1985).
31. E. E. Krueger and A. L. Ruoff, *J. Vac. Sci. Technol.*, **B 3**, 1650 (1985).
32. U. Gerlach-Meyer, J. W. Coburn, and E. Kay, *Surf. Sci.*, **103**, 177 (1981).
33. E. B. Henschke and S. E. Derby, *J. Appl. Phys.*, **34**, 2458 (1963).
34. N. Laegreid and G. K. Wehner, *ibid.*, **32**, 365 (1961).
35. J. W. Coburn, H. F. Winters, and T. J. Chuang, *ibid.*, **48**, 3532 (1977).
36. M. Meith and A. Barker, *J. Vac. Sci. Technol.*, **A 1**, 629 (1983).

Ellipsometric and Optical Study of Amorphous Hydrogenated Carbon Films

S. A. Alterovitz, J. D. Warner, D. C. Liu, and J. J. Pouch

National Aeronautics and Space Administration, Lewis Research Center, Cleveland, Ohio 44135

ABSTRACT

A low-frequency plasma deposition system was used to prepare amorphous hydrogenated carbon (a-C;H) films. The growth energy was varied by changing the power and/or pressure of the plasma. Ellipsometry and optical absorption were used to obtain the optical energy gap, the density of states, and the refractive index. Ion sputtering was used in conjunction with ellipsometry and Auger electron spectroscopy to get absolute sputtering rates. The plasma deposited a-C:H is amorphous with optical energy gap of approximately 2.0-2.4 eV. These a-C:H films have higher density and/or hardness, higher refractive index, and lower optical energy gaps with increasing energy of the particles in the plasma, while the density of states remains unchanged. These results are in agreement and give a fine-tuned positive confirmation to an existing conjecture on the nature of a-C:H films (1).

Insulator films on semiconductors have a wide variety of applications, including passivation, insulation, capping, etc. In the case of silicon, the silicon based films SiO_2 and Si_3N_4 have been successfully used for all the required applications. However, the need for high-speed devices and integrated circuits requires the use of Group III-V semiconductor devices and substrates. SiO_2 and Si_3N_4 proved to be inadequate for some of these applications for Group III-V semiconductors. Thus, new types of insulator films for one or more of the required applications are needed. In this study we have chosen a-C:H for the insulator film. Some of the attractive properties of a-C:H are: (*i*) it is easily prepared as a homogeneous film (2): (*ii*) it is very hard mechanically and chemically: (*iii*) it has a high breakdown voltage (3) and resistivity: (*iv*) it has a relatively low interface density of states on Si (4) and InP (3): (*v*) it has a variable energy gap (1, 5); and (*vi*) it can be used in metal-insulator-metal (MIM) structures (6).

However, not all the desirable properties are achieved in a single sample, *i.e.*, the highest energy gap sample will have a rather low mechanical hardness (1). It was suggested in Ref. (1) that the growth energy environment controls the energy bandgap, the hardness, the hydrogen concentration, and bond type. Thus, it may not be possible to optimize all the desirable parameters simultaneously. This conjecture was made using samples made by different deposition methods having very large variations in growth environment energy. In the present work, we report a study of a-C:H films made by varying the growth energy in a continuous way, *i.e.*, varying the plasma power, and/or pressure, and/or the substrate temperature during deposition. We have used ellipsometry, UV-visible absorption, and Auger electron spectroscopy (AES) profiling for sample characterization. These techniques give us energy gaps, density of state parameters, indexes of refraction, and sputtering rates.

We have correlated these results with the growth environment energy in order to check the conjecture of Ref. (1).

Experimental

The sample preparation will be discussed only very briefly. The a-C:H films were prepared by 30 kHz plasma deposition using several power settings with a constant pressure or several pressures with a constant power. The substrates were positioned on the grounded (anode) electrode, while a negative dc voltage existed on the other, parallel and equal size, top electrode. In one instance, a constant power and pressure were maintained, while the temperature of the substrate was varied. Substrates used in this study were InP (for ellipsometry), fused quartz (for UV-visible absorption), and Si (for the deposition temperature dependency). More details about sample preparation are in Ref. (2 and 7).

Ellipsometry was performed using a rotating analyzer ellipsometer with a laser or a Hg arc lamp light source. The multiple angles of incidence and wavelengths method was used in the data analysis (8, 9). This method gives a unique determination of the refractive index and the extinction coefficient at each wavelength, and the thickness of the film, without an assumption on the composition of the film, or a prior knowledge of the thickness. In most cases, a three-phase model was used. However, presence of an interface or an inhomogeneous film requires a four-phase model (9, 10). At least five angles of incidence were used at each wavelength. The refractive indexes and extinction coefficients of the substrates used in the ellipsometric work, *i.e.*, InP and Si, were taken from Aspnes and Studna (11).

Absorption in the UV-visible (190 nm to 3.2 μm wavelength range) was measured using a computer controlled Perkin Elmer Lambda 9 spectrometer. The data were taken discretely using a slit width of 2 nm. 200 points or more were measured on each sample. The sample cell was continuously purged with dry nitrogen during the measurements. A blank quartz substrate was placed in the reference path for background correction. However, no correction was made for the difference in the reflectivity of the quartz reference plate and the film.

AES was used in conjunction with Ar ion sputtering for depth profiling. Absolute etch rates were determined by comparison with the ellipsometrically-determined film thickness. The sputtering was done with 2 or 3 keV Ar ions at 25 mA.

Results and Discussion

Absorption in the UV-visible range was measured on the anodic a-C:H films made on quartz substrates from methane gas (CH_4), at a power of 150W and a flow rate of 50 sccm (standard cubic cm per minute), corresponding

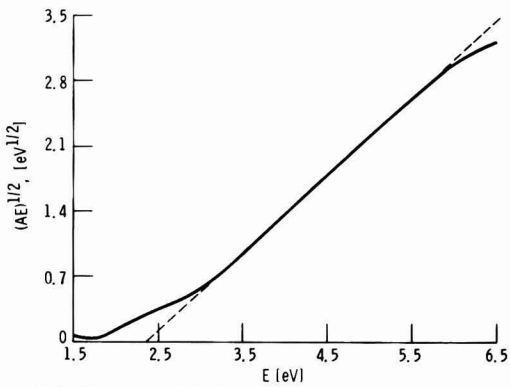

Fig. 1. Tauc plot of $(\Delta E)^{1/2}$ vs. E for a-C:H, CH_4 plasma deposited film on quartz at 150W, 245 mtorr for 20 min.

to a pressure of 245 mtorr. The directly measured parameter is the absorbance A. In Fig. 1 we show a Tauc plot, *i.e.*, $(AE)^{1/2}$ *vs.* E, where E is the photon energy. This plot is a straight line in amorphous semiconductors, according to Mott and Davis (12). The absorption coefficient α is given by

$$\alpha = \frac{4\pi}{nc} \frac{\sigma_{min}}{\Delta E} \frac{(E - E_0)^2}{E} \quad [1]$$

Here n is the refractive constant, $(\sigma_{min}/\Delta E)$ is a factor determined by the density of states in the bottom of the conduction band and/or the top of the valence band, and E_0 is the optical energy gap ($A = \alpha d$, where d is the film thickness). Usually, the factor $(4\pi\sigma_{min})/(nc\,\Delta E)$ is abbreviated by a single parameter, B[2]. A value of $E_0 = 2.4 \pm 0.1$ eV is obtained from Fig. 1. In addition, a rather significant "tail" is observed at low energies and low absorption values, similar to that found in a-C:H produced by glow discharge (13, 14). Using an estimate from our previously determined growth rates (7) for the thickness d, we calculate a value of $(\alpha E)^{1/2} \cong 100$ cm$^{-1/2}$ eV$^{1/2}$ for the "knee," in good agreement with previous data (14). This low value of the "knee" is one of the reasons why "tail" free results are prevalent in the literature (5, 15).

Ellipsometric measurements of a-C:H films on InP were done at six wavelengths for six values of the deposition power at a flow rate of 70 sccm, corresponding to a pressure of 315 mtorr. A three-phase model was used successfully in analyzing all the a-C:H ellipsometric data. Representative results of the refractive index, n as a function of deposition power, P, for several wavelengths are shown in Fig. 2. Experimental results of the extinction coefficient, K, were analyzed in a Tauc plot, as shown in Fig. 3 ($\alpha = 4\pi K/\lambda$). The straight lines were drawn through the $(\alpha E)^{1/2}$ points above the "knee" at $(\alpha E)^{1/2} \approx 100$ cm$^{-1/2}$ eV$^{1/2}$. The slopes of these lines, *i.e.*, the parameters, B, as defined previously using Eq. [1], have the same value for all powers used. Thus the density of states is not changing as a function of the deposition power in this case. The value of B is 300 cm$^{-1/2}$ eV$^{-1/2}$, *vs.* 750 cm$^{-1/2}$ eV$^{-1/2}$ for a-Si$_x$C$_{1-x}$ (16) and in good agreement with results deduced from plasma deposited a-C:H films (17, 18). The optical gap, E_0, found from Fig. 3 is depicted in Fig. 4, as function of the deposition power, P. A decrease in E_0 is clearly observed with increasing power.

We define the Ar etch rate ER as d/t_e where t_e is the Ar sputtering time through the whole thickness of the film and d is the ellipsometrically determined thickness. The experimental ER as a function of the deposition power, P, is shown in Fig. 5. A marked decrease in ER *vs.* P is apparent, denoting a harder and/or denser film with increasing deposition power. A qualitatively similar result was reported earlier for hardness *vs.* deposition power (17).

At this point, we will compare the results shown above with the conjecture forwarded in Ref. (1), where the ratio of sp^2/sp^3 bonds in a-C:H films was measured. Carbon films with a high percentage of sp^2 bonds were called "graphitic" while those with high sp^3 bond percentage

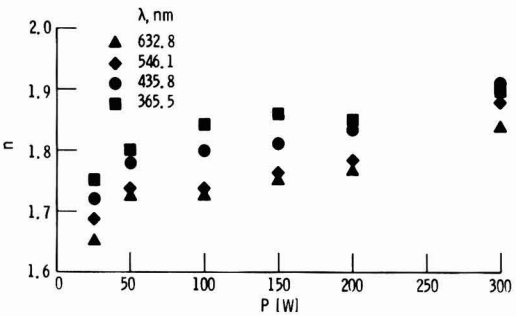

Fig. 2. Refractive index n *vs.* deposition power P for a-C:H, CH_4 plasma deposited film on InP at 315 mtorr for several wavelengths λ.

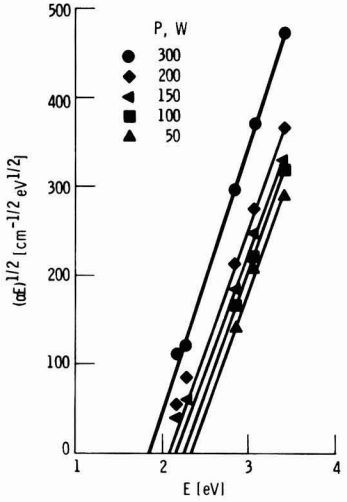

Fig. 3. Tauc plot of $(\alpha E)^{1/2}$ *vs.* E for a-C:H, CH_4 plasma deposited film on InP at 315 mtorr for several deposition powers P.

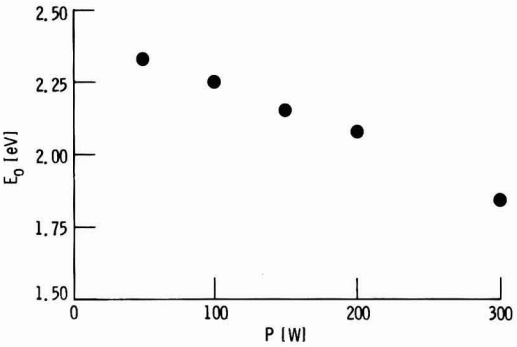

Fig. 4. Optical energy gap E_0 *vs.* deposition power P for a-C:H, CH_4 plasma deposited film on InP at 315 mtorr.

were called "diamondlike." The use of these terms is confusing and will be dropped. For example, graphite has a lower hardness *vs.* diamond. However, "graphitic" films are harder than "diamondlike", as reported in Ref. (1). We will use the term "high bandgap" instead of "diamondlike," and "low bandgap" in lieu of "graphitic." It was claimed (1) that since double bond hydro-

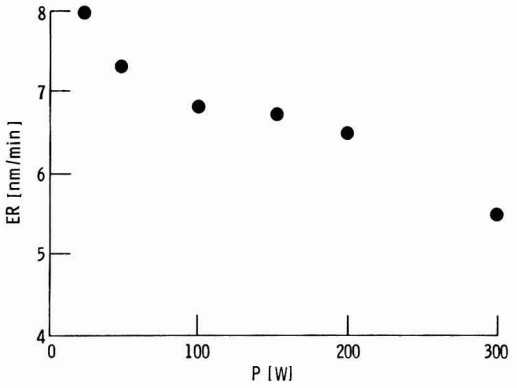

Fig. 5. Absolute argon etch rate ER *vs.* deposition power for a-C:H, CH_4 plasma deposited film on InP at 315 mtorr.

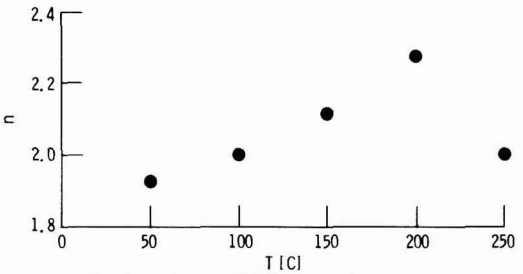

Fig. 6. Refractive index *n* at 632.8 nm vs. substrate temperature for a-C:H, CH_4 plasma deposited film on Si at 100W, 245 mtorr.

genation is an exothermic process, low bandgap behavior, associated with sp^2 bonds is favored over tetrahedral bonding (sp^3) in higher growth environment energy. Reference (1) shows evidence of this conjecture by comparing a-C:H films made by five different experimental configurations. As a-C:H properties are dependent quite strongly on the many variables encountered In different preparation conditions, it seems that a better test of this conjecture is in order.

Our results confirm this model, including the hardness test. The higher the plasma deposition power, the smaller is the bandgap (Fig. 4) and the higher is the hardness and or density (Fig. 5). At the same time, the density of states parameter, B, is unchanged. We thus conclude that the higher the plasma deposition power, the more "graphitic" or low bandgap is the a-C:H film. We further tested this model by taking more experimental data. First, we used the correlation of the refractive index, n, in the visible region with deposition power (Fig. 2), *i.e.*, higher n for lower bandgap films (grown at higher deposition powers). Figure 6 shows the results of ellipsometrically measured refractive index n of a-C:H films on Si at 632.8 nm as function of the deposition temperature. An increase in n, *i.e.*, lower bandgap behavior, is evident as the growth environment energy is increased. Similar behavior was found in the literature (14, 18). The last point in Fig. 6, at 250°C, is anomalous. We believe that the deposition process is somewhat changed above 200°C. For example, we could not deposit any a-C:H films at all (2) on III-V-semiconductors above 200°C. Changes in the deposition above 200°C were also reported elsewhere (19). In Fig. 7 we show a general decrease in the ellipsometrically measured refractive index, n, with increasing deposition pressure. The higher the pressure, the lower is the average energy per particle, *i.e.*, we expect less lower bandgap behavior.

All the experiments described above were done using a single source material, namely, methane gas, and varying three deposition parameters, namely, power, pressure, and temperature. Our tests are somewhat similar to those of Ref. (1), but much more refined and extended. The main conclusion from this work is that the physical properties of a-C:H films made from methane gas cannot

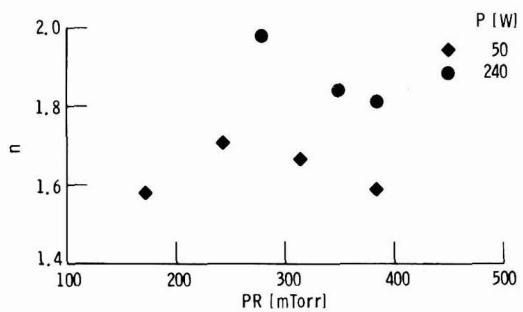

Fig. 7. Refractive index *n* at 632.8 nm vs. pressure *PR* for a-C:H,CH_4 plasma deposited film on InP at 2 deposition powers *P*.

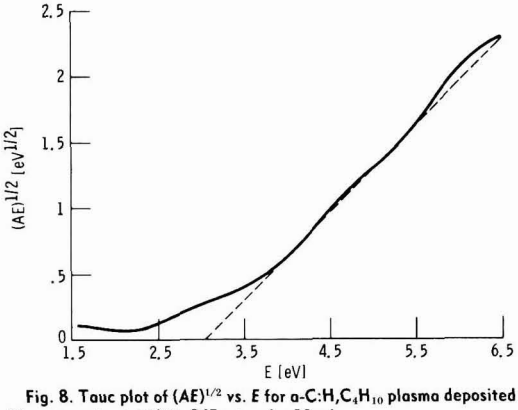

Fig. 8. Tauc plot of $(AE)^{1/2}$ vs. E for a-C:H,C_4H_{10} plasma deposited film on quartz at 150W, 245 mtorr for 20 min.

be independently optimized, as all of them are controlled by the growth environment energy. For further practical development of a-C:H films, we have to find at least one more independent experimental parameter that will control the physical properties of the films, while using the same deposition method. As proposed in Ref. (1) and (20), the more basic parameters are the hydrogen content and the percentage of sp^2 and sp^3 bonds, not the growth environment energy by itself. We tested this assumption experimentally by making samples using butane as the working gas. We show in Fig. 8 a Tauc plot obtained from absorbance results for an a-C:H film on quartz made using butane C_4H_{10}. The power (150W) and pressure (245 mtorr) are equal to those used for the film shown in Fig. 1. However, the optical energy gap is now 3.1 ± 0.2 eV *vs.* 2.4 eV. The average energy per molecule in the working gas is unchanged, but the amount of hydrogen is different between methane and butane. We should also point out that the momentum and velocity of the molecules are different. We believe the momentum difference by itself cannot explain the increase in the energy gap, as it is in the opposite direction as compared to the result of Fig. 4. It seems that more work on a-C:H films made with butane is required.

Conclusions

Our studies on a-C:H are in good agreement with the conjecture forwarded by Kaplan *et al.* (1) regarding the direct correlation between the growth environment energy during deposition and the bandgap behavior. We have tested and confirmed this assumption with measurements of the optical energy gap, the sputtering etch rate, and the refractive index. The growth environment energy was varied by changing the deposition power, pressure, and temperature. It is concluded that, using a single working gas, the properties of the a-C:H film are determined by the growth energy parameter. Thus, not all the desired physical parameters *e.g.*, energy gap, hardness, can be optimized simultaneously.

REFERENCES

1. S. Kaplan, F. Jansen, and M. Machonkin, *App. Phys. Lett.*, **47,** 750 (1985).
2. J. D. Warner, J. J. Pouch, S. A. Alterovitz, D. C. Liu, and W. A. Lanford, *J. Vac. Sci. Technol.*, **A3,** 900 (1985).
3. J. E. Oh, J. D. Lamb, P. G. Snider, and J. A. Woollam, *Solid-State Electron.* To be published.
4. A. A. Khan, J. A. Woollam, Y. Chung, and B. Banks, *IEEE Trans. Elec. Dev. Lett.*, **EDL-4,** 146 (1983).
5. F. Jansen, M. Machonkin, S. Kaplan, and S. Hark, *J. Vac. Sci. Technol.*, **A3,** 605 (1985).
6. J. D. Lamb and J. A. Woollam, *J. Appl. Phys.*, **57,** 5420 (1985).
7. J. J. Pouch, S. A. Alterovitz, J. D. Warner, D. C. Liu, and W. A. Lanford, in "Thin Films: The Relationship of Structure to Properties," C. R. Aita and K. S. SreeHarsha, Editors, pp. 201-204, Materials Research

Society, Pittsburgh (1985).
8. G. H. Bu-Abbud, S. A. Alterovitz, N. M. Bashara, and J. A. Woollam, *J. Vac. Sci. Technol.*, **A1,** 619 (1983).
9. S. A. Alterovitz, G. H. Bu-Abbud, J. A. Woollam, and D. C. Liu, *J. Appl. Phys.*, **54,** 1559 (1983).
10. S. A. Alterovitz, G. H. Bu-Abbud, J. A. Woollam, and D. C. Liu, *Phys. Status Solidi A*, **85,** 69 (1984).
11. D. E. Aspnes and A. A. Studna, *Phys. Rev. B*, **27,** 985 (1983).
12. N. F. Mott and E. A. Davis, "Electronic Processes in Non-Crystalline Materials," 2nd ed. Clarendon Press, Oxford, (1979).
13. D. A. Anderson, *Philos. Mag.*, **35,** 17 (1977).
14. F. W. Smith, *J. Appl. Phys.*, **55,** 764 (1984).
15. A. A. Khan, D. Mathine, J. A. Woollam, and Y. Chung, *Phys. Rev. B*, **28,** 7229 (1983).
16. A. Skumanich, A. Frova, and N. M. Amer, *Solid State Commun.*, **54,** 597 (1985).
17. V. Natarajan, J. D. Lamb, J. A. Woollam, D. C. Liu, and D. A. Gulino, *J. Vac. Sci. Technol.*, **A3,** 681 (1985).
18. B. Dischler, A. Bubenzer, and P. Koidl, *Appl. Phys. Lett.*, **42,** 636 (1983).
19. K. Fujii, N. Shohata, M. Mikami, and M. Yonezawa, *ibid.*, **47,** 370 (1985).
20. B. Dischler, A. Bubenzer, and P. Koidl, *Solid State Commun.*, **48,** 105 (1983).

Microstructure and Magnetic Properties of Electroless Plated Co-Ni-P and Co-P Thin Films for Magnetic Recording

Ellen L. Nicholson and Mahbub R. Khan[1]

Control Data Corporation/MPI, Minneapolis, Minnesota 55435

ABSTRACT

Co-Ni-P and Co-P thin films have been electroless deposited on Al based Ni-P plated substrates in the pH range 7.8-9.3. The effects of solution pH on nucleation, microstructure, and magnetic properties of these films were investigated by VSM, Auger, and electron microscopy techniques. The magnetic properties are dominated by the microstructure of these films. These two films, deposited at optimum pH, can be used for high density magnetic information storage media.

Electroless, or auto-catalytic, deposition process have been the subject of immense interest since the pioneering work of Brenner and Riddell (1). In recent years the magnetic thin films of Co-Ni-P and Co-P have been studied by a number of investigators for possible use in high density digital recording (2-9).

Osaka *et al.* (10-11) have reported the preparation of thin films by electroless plating method which can possibly be used for perpendicular recording. These films have a fourth or fifth component, *viz.* Co-Ni-Mn-P and Co-Ni-Mn-Re-P. The materials that have been studied here are for use in longitudinal recording.

Ternary alloys, such as Co-Ni-P provide a wide range of magnetic properties. In this study, Co-P and Co-Ni-P films produced from two different modified Brenner formulations are examined. The two systems are compared in regards to nucleation and pH dependence on microstructure and magnetic properties of films produced.

[1]Present address: Memory Products Division, Stolle Corporation, ALCOA, Sidney, Ohio 45365

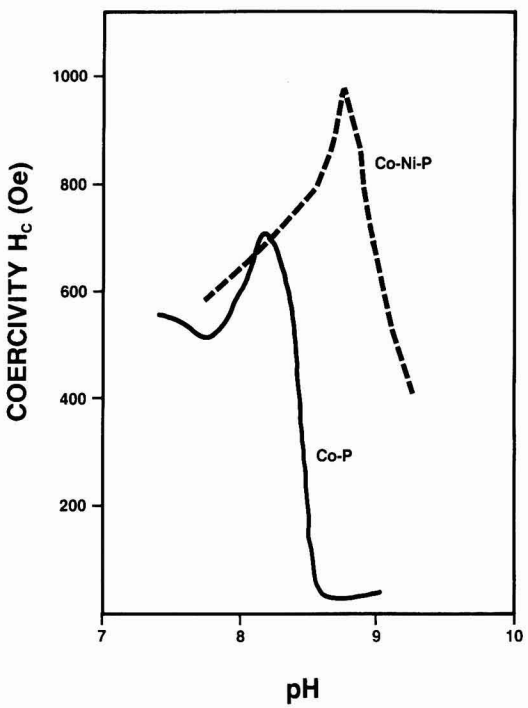

Fig. 1. Coercivity H_c vs. solution pH for Co-Ni-P (plated 80s) and Co-P (plated 90s).

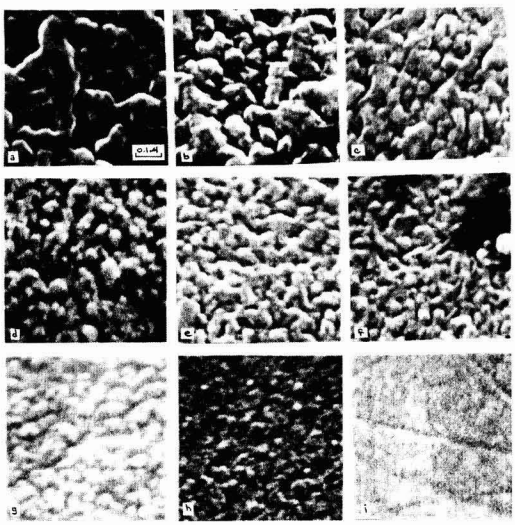

Fig. 2. Electron micrographs of Co-Ni-P films (80s) a) pH = 7.8, b) pH = 8.0, c) pH = 8.2, d) pH = 8.35, e) pH = 8.4, f) pH = 8.6, g) pH = 8.8, h) pH =9.1, i) pH = 9.3.

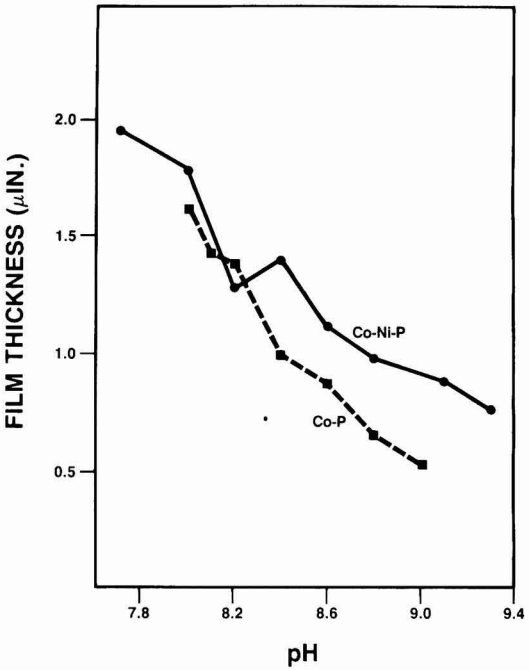

Fig. 3. Thickness vs. pH for Co-Ni-P films (80s) and Co-P films (90s)

In magnetic recording, the magnetic parameters (squareness, coercivity, remanence) and the demagnetizing field of the media and the head field gradient of the writing head determine the width of magnetization reversal in the film. For longitudinal recording, the transition parameter, l, depends on the demagnetization parameter $M_r \cdot \delta / H_c$, where M_r, δ, and H_c are the remanent moment, thickness, and coercivity, respectively (12). Additionally, from the relations (13)

$$l \cong \frac{2M_r}{dM/dx} \qquad \frac{dM}{dx} = \frac{dM}{dH}\left(\frac{dH_h}{dx} + \frac{dH_d}{dx}\right)$$

we see that the minimum transition occurs when the

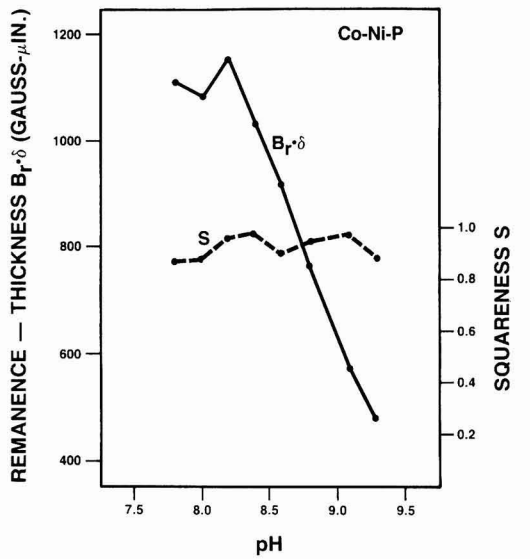

Fig. 4. $Br \cdot \delta$ and squareness vs. pH for Co-Ni-P films (plated 80s).

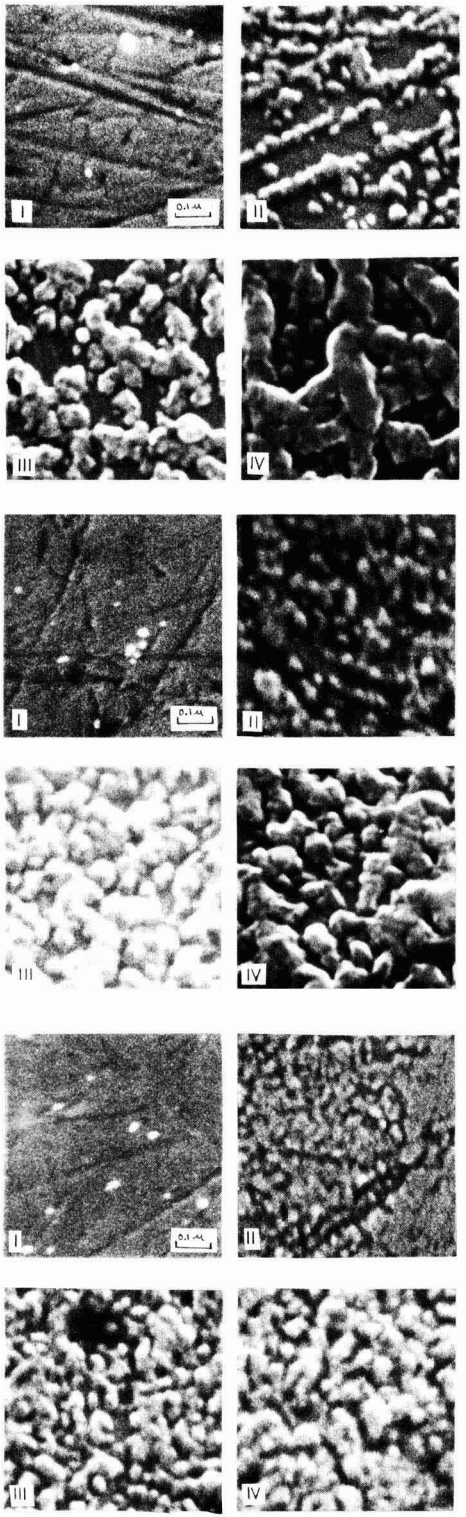

Fig 5. Electron micrographs of Co-Ni-P films
a) Nucleation at pH 7.8 IV) 80s I) 20s II) 40s III) 60s
b) Nucleation at pH 8.0 IV) 80s I) 20s II) 40s III) 60s
c) Nucleation at pH 8.35 IV) 80s I) 20s II) 40s III) 60s

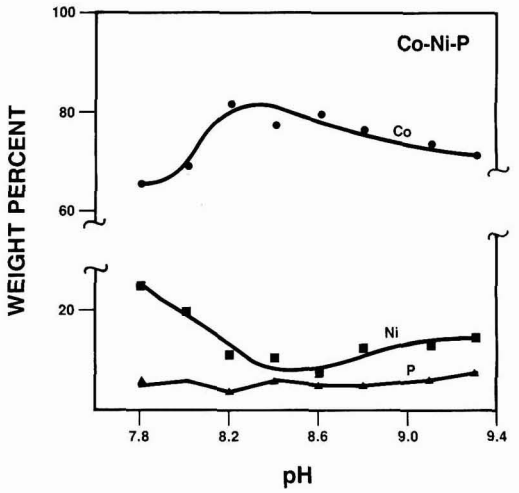

Fig. 6. Composition *vs.* *p*H for Co-Ni-P films.

magnetization gradient is maximum. Therefore, high hysteresis loop squareness and high head field gradient gives narrower transition or higher recorded density. H_h and H_d refer to head field and demagnetizing field, respectively. The head field orientation and the media anisotropy (both crystalline and shape) determine the magnetization direction in the media.

Methods for reducing l to provide higher recording densities include increasing H_c, decreasing M_r, and decreasing δ. There is a practical limit on the extent to which H_c can be increased, since a higher coercivity media requires higher head field to switch. δ cannot be reduced below 1 μin. for plated cobalt alloys, since previous studies indicate that thinner films are not continuous (9). Therefore, it is suggested that a low remanence alloy, in conjunction with high output recording head, may be useful for increased recording densities. The residual induction or remanence B_r of Co-P alloys are typically 9000-10000 Gauss, where $B_r = 4\pi M_r$. The Co-Ni-P alloy studied here has a remanence B_r of approximately 7000 Gauss (14).

Experimental Methods

The film thickness data (Fig. 3) obtained from atomic absorption measurements were in good agreement with thicknesses measured using x-ray fluorescence, profilometry, and Auger depth profiling. Electron microscopy techniques were used to study the nucleation, growth, and microstructures of the films. EDX and Auger (AES) were used for elemental analysis. A vibrating sample magnetometer was used to obtain B-H loops. Recording parameters and density response curves were obtained using a thin film head with a gap length of 30 μin.

Results and Discussion

It has been interesting to observe that the microstructures dominate the magnetic properties of these films. The nucleation and growth process in the Co-Ni-P bath at low *p*H was very different from that at high *p*H. As the *p*H of the solution is increased from 7.8, the coercivity starts to increase until the *p*H reaches 8.8, when H_c starts to drop rapidly (Fig. 1). Grain size decreases with increasing *p*H, and film continuity improves in the *p*H range 7.8-8.4, as shown in the pictures of Fig. 2. Increasing *p*H further continues to decrease grain size until, ultimately, the superparamagnetic range is approached with very small grains.

The Co-P bath showed a similar behavior; however, the peak in the H_c *vs.* *p*H curve occurs at *p*H 8.2. The H_c *vs.* *p*H curves (Fig. 1) do not take into account the effect of film thickness on H_c. Thickness decreases with increasing *p*H at constant plating time (Fig. 3). $B_r \cdot \delta$ and squareness *vs.* *p*H are shown in Fig. 4.

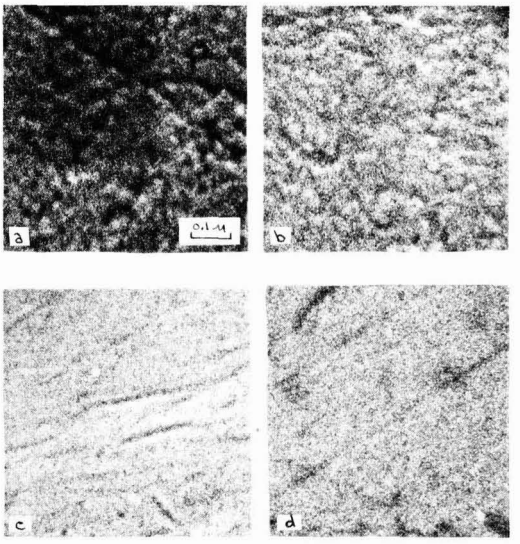

Fig. 7. Electron micrographs of Co-P films (90s)
a) *p*H = 8.15 b) *p*H = 8.2 c) *p*H = 8.4 d) *p*H = 8.6

SEM pictures of the nucleation process of Co-Ni-P films plated at low *p*H indicate that at low thickness, the nucleation sites form needle shaped crystallites (Fig. 5) which spread to cover the substrate with increased plating time. As the *p*H is increased, the needle shapes are less predominant. Crystallites begin to have a more circular appearance. Results of the Auger elemental analysis show that nickel plates preferentially at low *p*H, Ni weight percents being 22.5, 9, and 14 at *p*H values of 7.8, 8.4, and 9.3, respectively (Fig. 6). Nickel is believed to initiate plating in this formulation resulting in a nucleation and growth process that appears quite different from that in the Co-P bath. The difference is most pronounced at low *p*H, where nickel concentration in the film is the greatest. Co-P nucleation sites appear round (Fig. 7). The number of nucleation sites increases until the substrate is covered. Some microstructure studies of Co-P have been reported elsewhere (9-14).

The Co-Ni-P prepared for analysis of recording performance was plated at *p*H 8.35 resulting in a coercivity of 700 Oe, and $B_r \cdot \delta$ = 10,000 G-μin. The Co-P films was plated at *p*H 8.1 to give a coercivity of 600 Oe and $B_r \cdot \delta$ = 14,000 G-μin. The Co-Ni-P films appear to have broader distribution of grain size than the Co-P at the same thickness (1.4 μin.), which can result in broader switching

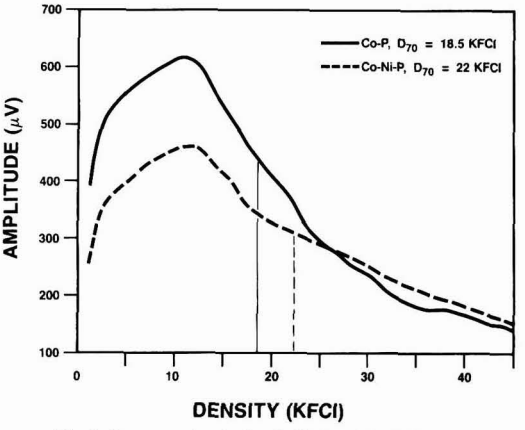

Fig. 8. Output *vs.* density for Co-Ni-P and Co-P films.

field distribution. $B_r \cdot \delta/H_c$ for the Co-Ni-P is 14.3, compared to 23.3 for the Co-P. The decrease in demagnetization parameter resulted in an increase in D_{70} from 18.5 KFCI for Co-P to 22 KFCI for Co-Ni-P (Fig. 8) when tested with a thin film head with gap length 30 μin., 15 turns, at a fly height of 8 μin. Therefore, when appropriately deposited, Co-Ni-P films can support higher recording density compared to Co-P films.

Acknowledgments

The authors wish to thank E. Henry, L. Laden, and N. Rice for their help with some sample characterization.

Manuscript submitted Feb. 25, 1986; revised manuscript received June 2, 1986.

Control Data Corporation/MPI assisted in meeting the publication costs of this article.

REFERENCES

1. A. Brenner and G. F. Riddell, *J. Res. N.B.S.*, **39,** 385 (1947).
2. J. S. Judge, J. R. Morrison, D. E. Speliotis, and G. Bate, *This Journal,* **112,** 681 (1965).
3. D. E. Speliotis, J. S. Judge, and J. R. Morrison, *J. Appl. Phys.*, **37,** 1158 (1966).
4. J. Bagrowski and M. Lauriente, *This Journal,* **109,** 987 (1962).
5. J. S. Judge, J. R. Morrison, D. E. Speliotis, and J. R. DePew, *Plating,* **54,** 533 (1967).
6. G. W. Lawless and R. D. Fisher, *Plating,* **54,** 709, (June, 1967).
7. T. Chen, D. A. Rogowski, and R. M. White, *J. Appl. Phys.*, **49,** 1816 (1978).
8. H. Tanaka, H. Goto, N. Shiota, and M. Yanagisawa, *ibid.*, **53,** 2576 (1982).
9. M. R. Khan and J. I. Lee, *ibid.*, **57,** 4028 (1985).
10. T. Osaka, N. Kasai, I. Koiwa, F. Goto, and Y. Suganuma, *This Journal,* **130,** 568 (1983).
11. I. Koiwa, M. Toda, and T. Osaka, *ibid.*, **133,** 597 (1986).
12. R. I. Potter, *J. Appl. Phys.*, **41,** 1647 (1970).
13. M. L. Williams, and R. L. Comstock, *AIP Conference Proceedings,* **5,** 738 (1971).
14. M. R. Khan and E. L. Nicholson, *J. Mag. Mag. Mat.*, **54-57,** 1654 (1986).

Metalization of AlN Ceramics by Electroless Ni-P Plating

Tetsuya Osaka,* Hiroto Nagata, Eiji Nakajima, and Ichiro Koiwa

Department of Applied Chemistry, Waseda University, Okubo, Shinjuku-ku, Tokyo 160, Japan

Kazuaki Utsumi

NEC Corporation, Fundamental Research Laboratories, Miyazaki, Miyamae-ku, Kawasaki,-shi, Kanagawa 213, Japan

ABSTRACT

Highly thermally conductive aluminum nitride ceramics were metalized by an electroless plated Ni-P film for the purpose of utilizing them in practical electronic circuit substrates. Aluminum nitride substrates were effectively etched by NaOH solution, and the adhesion strength between AlN and the Ni-P film was found to increase with an increase in surface roughness. At *Ra* value greater than 0.63 μm, adhesion strength increased to 2.0 kg mm^{-2}, and a maximum of 3.0 kg mm^{-2} was obtained at $Ra = 1.24$ μm. The NaOH-etched AlN substrates, however, had a higher adhesion strength than substrates of abraded AlN or abraded Al_2O_3 with the same roughness. SEM observation showed that the surface of AlN substrate was selectively etched in the regions between adjoining large particles, and that Ni-P projections became effective interlocking points. It was therefore concluded that substrates of new aluminum nitride of high thermal conductivity are capable of being effectively metalized by electroless plating method, and that the main factor contributing to film adhesion strength is interlocking surface structures that are formed through selective etching by NaOH.

Alumina (Al_2O_3) ceramics have been predominantly used as substrate materials for high speed, high density circuits because of their high thermal conductivity. Recently aluminum nitride (AlN) substrates have drawn attention because of their high thermal conductivity—eight to ten times that of Al_2O_3 at room temperature (1-5).

Although the thermal conductivity of AlN could theoretically be as high as 320 W $m^{-1}K^{-1}$ (3) it is greatly influenced by its density and chemical impurities (1-4). NEC Corporation has developed AlN substrates with very high thermal conductivity using hot press sintering (1) and green sheet techniques (5) obtaining values of 160 and 180 W $m^{-1}K^{-1}$, respectively. Figure 1 shows typical thermal dissipation effects of AlN and Al_2O_3 substrates, where Si transistor chips (4W) are mounted. Surface temperature measured by the thermal video system, when thermal dissipation was in a steady state, was 71.5°C for Al_2O_3 and 38.5°C for AlN. Thus, it can be seen that AlN has a thermal dissipation capability clearly superior to that of Al_2O_3, and AlN substrates seem to be promising materials for use as high speed, high density circuit boards.

Surface metalization is necessary for the application of electronic circuit to ceramic substrates. Thick films and directly bonded metals are applied to form the conductors on Al_2O_3 ceramics. With ceramic substrates, it is difficult to obtain adhesion between the metal and ceramics strong enough for circuit formation, and some sophisticated techniques such as the addition of a glass intermediate layer (4, 6) and Cu-Cu_2O eutectic melt bonding (4, 7, 8, 9) have been attempted. Direct bonding between Al_2O_3 ceramics and metal by electroless plating is especially difficult due to the etch-proof properties (10, 11). Since the wetting properties of AlN to metal are inferior to those of most oxide ceramics, direct bonding metal or the sophisticated oxide intermediate layer additional techniques have been used (4, 5). The implementation of direct metalization by electroless plating, which has advantages in terms of mass productivity and cost performance, would bring practical AlN substrate much closer.

This paper describes the metalization of AlN surfaces by electroless Ni-P plating. Heretofore, the electroless plating method has mainly been used for the metalization of plastics (12-18). Metalization of Al_2O_3 ceramic surfaces by electroless plating, with sufficient adhesion strength for circuit application, has been more difficult than for plastics due to the difficulty of etching Al_2O_3 ceramic surfaces. This paper, therefore, investigates the feasibility of metalizing new AlN substrates, with their attractive properties, by electroless Ni-P plating.

Experimental

Electroless Ni-P plating.—Table I shows bath composition and operating conditions of electroless Ni-P plating, and the catalyzing process is shown in Table II. Since AlN would be etched by a basic NaOH solution, an acidic bath was used. The phosphorus content of the Ni-P film was 12.3 weight percent (w/o) (19). Substrates of 99.5 w/o

*Electrochemical Society Active Member.

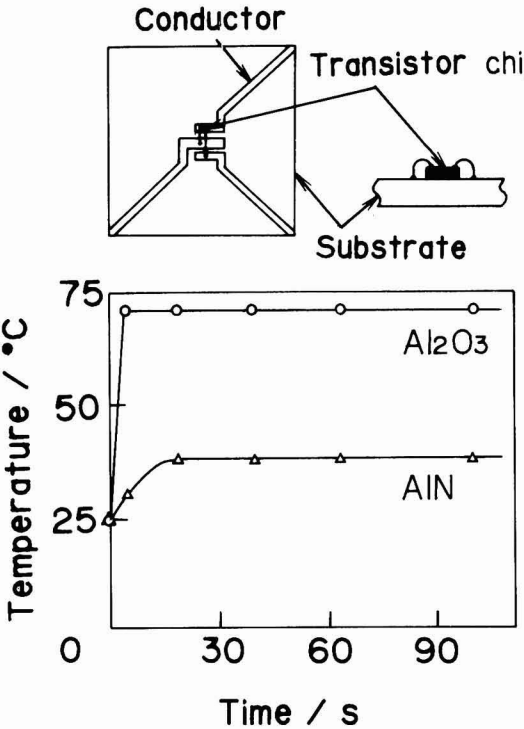

Fig. 1. Thermal dissipation effects of chip temperature on AlN and Al_2O_3 substrates where Si transistors (4W) are mounted.

AlN formed by the green sheet technique were supplied by NEC Corporation (5) and 96 w/o Al_2O_3 ceramics from Narumi China Corporation were also used. These substrates were plated to a thickness of 2.0 μm thick with electroless Ni-P film. Surface roughness was varied by using various grades of emery paper and immersion in a 1 mol dm^{-3} NaOH etchant solution. Average surface roughness, *Ra*, was measured by a stylus technique machine (Tokyo Seimitsu Company Limited).

Adhesion strength tests.— After electroless Ni-P plating on AlN ceramics, 2 mm^2 patterns were formed by photolithographic technique in accordance with the process in Table III. After 0.5 mm 0 wire soldering, the adhesion strength between substrate and metal film was measured with a direct pull tester (Model 7020 Aikoh Engineering Company Limited) pulling perpendicular to substrate.

Table I. Basic bath compositions and conditions for Ni-P plating (19)

Chemicals	Concentration/mol dm^{-3}
$NiSO_4 \cdot 7H_2O$	0.10
$C_3H_4(OH)(COONa)_3 \cdot 2H_2O$	0.20
$NaH_2PO_2 \cdot H_2O$	0.15
$(NH_4)_2SO_4$	0.50

pH = 4.0 adjusted with H_2SO_4; bath temperature: 90°C.

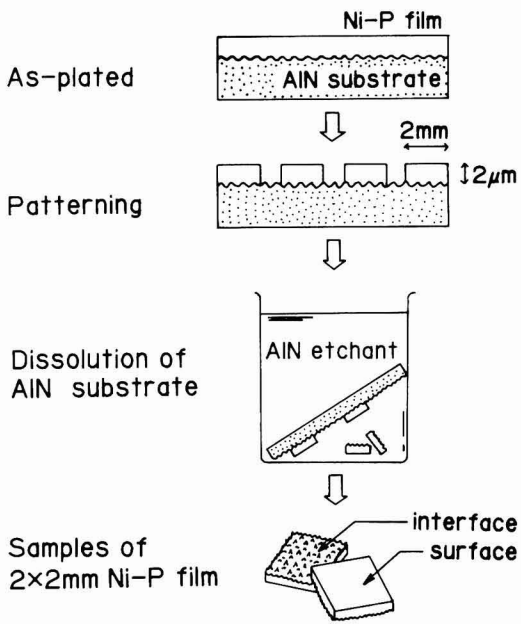

Fig. 2. Schematic of SEM sample preparation

SEM observation.—Samples of AlN surfaces etched for various periods were observed by SEM (19 kV, JEOL JSM-T20) after ion sputtering a Pt-Pd conduction film. Figure 2 illustrates the preparation of samples for the interface between the Ni-P film and substrate, showing how a 2 mm^2 pattern was formed on a 2 μm thick film by photolithography and how AlN substrate was dissolved into etchant (1 mol dm^{-3} NaOH), subjected to Pt-Pd ion-sputtering and observed by SEM.

Results and Discussion

Although Al_2O_3 ceramic surfaces are usually very difficult to etch, this new AlN ceramic is easily etched by NaOH solution. The etching process is as follows

$$AlN + NaOH + 4H_2O \longrightarrow NH_4OH + NaAl(OH)_4 \quad [1]$$

Table II. Catalyzing process for electroless plating

Process	Chemicals	Dipping time/min
1. Ultrasonic cleaning	C_2H_5OH	10
2. Etching	NaOH (1 mol dm^{-3})	0 ~ 80
3. Activating	HS-101B (Hitachi Chemical)	4
4. Accelerating	ADP-101 (Hitachi Chemical)	1
5. Electroless plating		

Table III. Patterning process for direct pull test

Process	Chemicals	Conditions
1. Ni-P plating on AlN	(See Table I)	(See Table II)
2. Photoresist coating by spinner	Photoresist OFPR 800 (Tokyo Ohka)	100 rpm, 20s
4. Drying		80°C, 20 min
3. Exposure		400W m^{-2} mercury lamp 200s
5. Development	$Na_2O\ SiO_2 \cdot nH_2O$ 21 g dm^{-3} $K_3PO_4 \cdot nH_2O$ 10 g dm^{-3}	Room temp, 120s
6. Etching	$H_3PO_4 : HNO_3 : H_2O$ = 70 : 22 : 8 volume percent	90°C, 90s

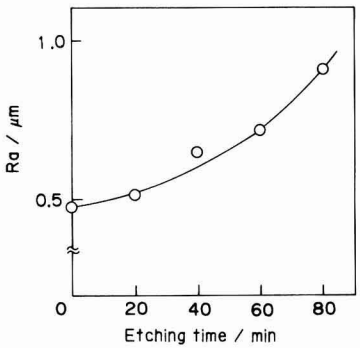

Fig. 3. Effect of etching time on average surface roughness *Ra* of AlN substrate.

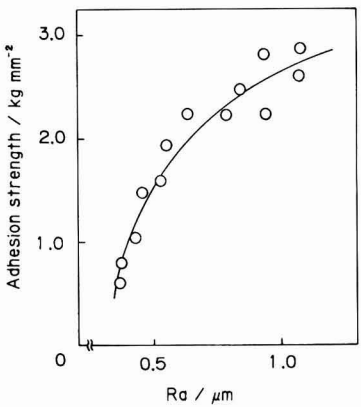

Fig. 4. Effect of average surface roughess *Ra* on adhesion strength

Figure 3 shows typical effects of etching by 1 mol dm^{-3} NaOH solution on the roughness of an AlN surface. Average surface roughness *Ra* increases with etching time, typical values being 0.66 μm after 40 min and 0.93 μm after 80 min. Etching effects varied somewhat with the preparation of the AlN substrates lots, and the most typical samples were used in these experiments.

Figure 4 shows a clear correlation between adhesion strength and *Ra*. Adhesion strength must be more than 2.0 kg mm^{-2} for the mounting of circuit devices. Very high values, 2.0 and 3.0 kg mm^{-2}, were obtained at *Ra* = 0.63 and 1.24 μm, respectively. It can be seen immediately that, as is generally considered to be the case, *Ra* is the main factor contributing to the higher adhesion strength of electroless film in respect to AlN.

Figure 5 shows typical SEM micrographs of etched AlN substrates corresponding to the results of Fig. 3. In Fig. 5a, larger AlN particles and smaller particles surrounding them are clearly observed. As NaOH etching proceeds (Fig. 5b), the intergranular small particles are selectively etched, and, finally, deep holes, which are selectively etched, appear at the AlN surface, as seen in Fig. 5c. Thus, it is seen that the etching proceeds effectively to make the holes.

Once it was confirmed that selective etching works effectively on AlN surfaces, the AlN and Al_2O_3 ceramics were worked to the same *Ra* value by different methods to allow investigation of other factors besides surface roughness. As can be seen in Table IV, for a constant *Ra* value of 0.59 μm, the adhesion strength between Ni-P film and abraded Al_2O_3 substrate is only about one-half of that between Ni-P film and emery-abraded AlN substrate. Further, the adhesion strength values obtained between Ni-P film and AlN substrates that had been adjusted differently, *i.e.*, abraded by emery paper and etched by NaOH, differ from each other. The fact that the highest value obtained was for substrate prepared by NaOH etching indicates that chemical etching of AlN surfaces provides superior conditions for adhesion. Thus, although the *Ra* value is one of the important factors in determining adhesion strength between metal and substrate, factors other than *Ra* value must also be considered.

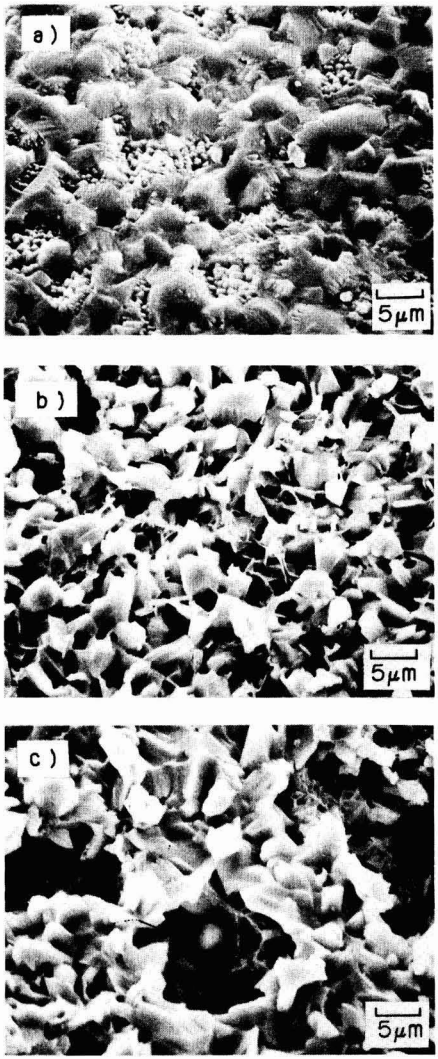

Fig. 5. SEM micrographs of AlN substrate surfaces etched for various periods: (a) no etching (*Ra* = 0.49 μm), (b) 40 min etching with NaOH (*Ra* = 0.66 μm), and (c) 80 min etching with NaOH (*Ra* = 0.93 μm).

Table IV. The effect of etching method on adhesion strength (all sample surfaces are *Ra* = 0.59 μm)

	Adhesion strength/kg mm^{-2}	
	Average	Maximum
A:	0.788	1.36
B:	1.58	2.23
C:	1.84	2.63

A: Al_2O_3 after emery paper abrasion.
B: AlN after emery paper abrasion.
C: AlN after etching in 1 mol dm^{-3} NaOH solution.

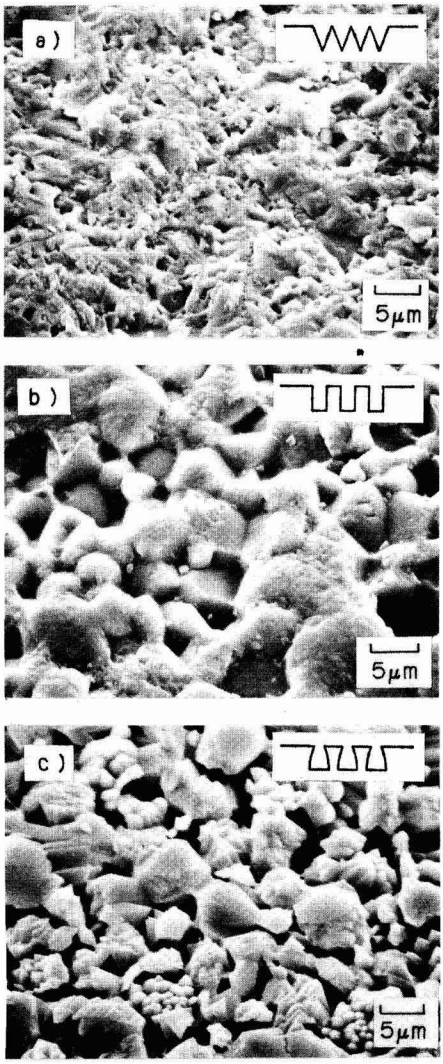

Fig. 6. SEM micrographs of Al_2O_3 and AlN substrate surfaces etched by different methods (all sample surfaces are Ra = 0.59 μm): (a) Al_2O_3 after emery paper abrasion, (b) AlN after emery paper abrasion, and (c) AlN after etching in 1 mol dm^{-3} NaOH solution.

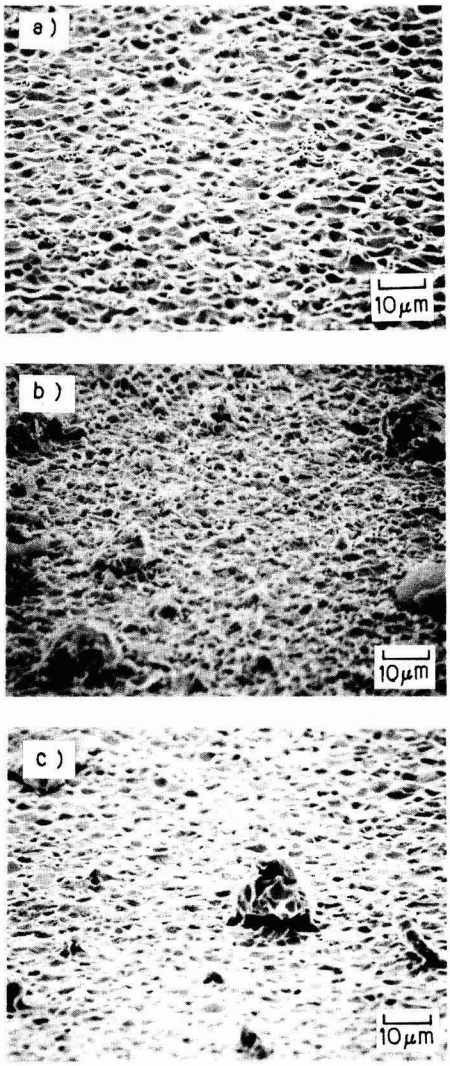

Fig. 7. SEM micrographs of Ni-P films at the substrate interface: (a) no etching (Ra = 0.49 μm), (b) 40 min etching with NaOH (Ra = 0.66 μm), and (c) 80 min etching with NaOH (Ra = 0.93 μm).

Figure 6 shows SEM observations of substrate surfaces (with schematic illustrations of surface morphology) corresponding to the results in Table IV, where all three samples have the same Ra value of 0.59 μm. Mechanically abraded surfaces of Al_2O_3 and AlN having the same Ra, 0.59 μm, display different typical surface morphologies. Moreover, AlN substrates with the same Ra value, but with surfaces that had been treated with different methods, gave different conditions; namely, NaOH etched selectively at the large particle-large particle interfaces on AlN substrates. The etched AlN surface provides superior conditions for interlocking between the substrate and the Ni-P film. Therefore, surface morphology after etching is very important, even at the same Ra.

To investigate AlN surface morphology in greater detail, we observed the substrate surface and the Ni-P film interface. Figure 7 shows SEM micrographs of Ni-P film at the substrate interface side, for samples prepared as illustrated in Fig. 2. Figure 7a shows small unevennesses of the Ni-P film surface, and Fig. 7b and c show some projections conforming to the etched substrate surface. These projections become larger as etching proceeds. The projections formed after 80 min etching with NaOH (Fig. 7c) were further investigated, as shown in Fig. 8. The typical projection, pictured in Fig. 8, has its 4 μm top side buried in the substrate. The anchor projection effectively produces an interlocking effect between substrate and Ni-P film. Figure 8c shows that there are many such anchor projections at the interface, which effectively contribute to the adhesion strength between AlN and Ni-P films.

Conclusions

An AlN substrate of high thermal conductivity with an electroless Ni-P film was first confirmed to be effectively metalized because of AlN was selectively etched by NaOH solution to produce an anchor effect. Values for the adhesion strength between AlN and Ni-P film higher than 2.0 kg mm^{-2} were obtained at Ra values of more 0.63

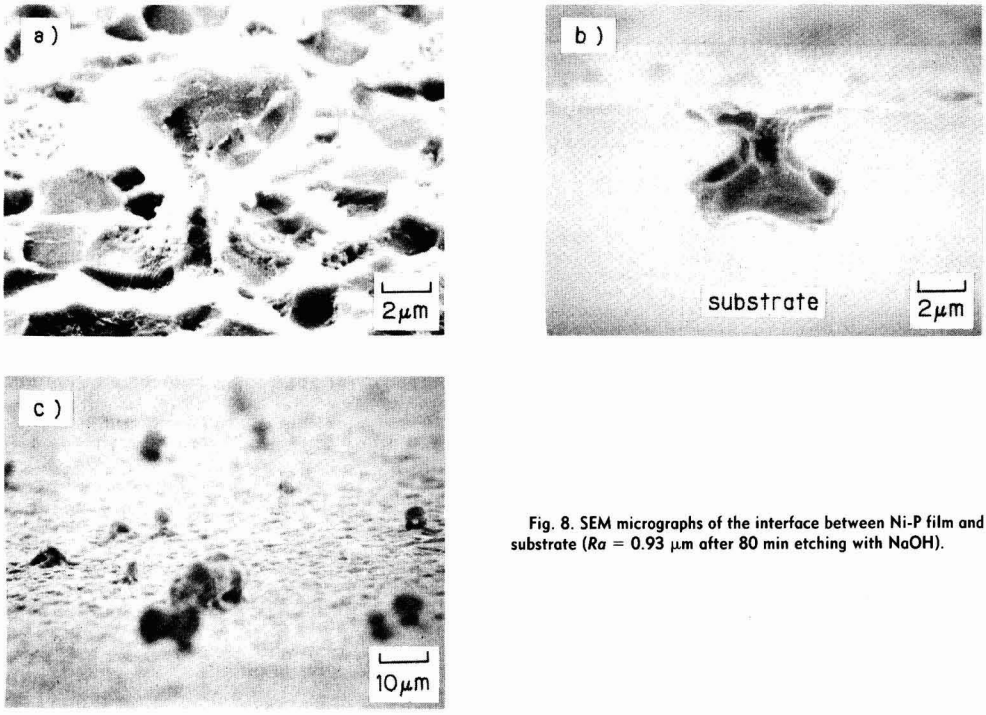

Fig. 8. SEM micrographs of the interface between Ni-P film and AlN substrate (Ra = 0.93 μm after 80 min etching with NaOH).

μm. Adhesion depended primarily on surface roughness, but the final determining factor was surface morphology, which depended on the method by which the substrate had been etched. Anchor projections played the most important role in adhesion. The AlN surface was etched in such a way as to produce anchoring holes effectively, which gave a higher adhesion strength between metal and substrate than that for Al_2O_3, even at the same surface roughness.

Manuscript submitted Feb. 5, 1986; revised manuscript received July 23, 1986.

Waseda University assisted in meeting the publication costs of this article.

REFERENCES

1. Y. Kurokawa, K. Utsumi, H. Takamizawa, T. Kamata, and S. Noguchi, *IEEE Trans. Components, Hybrids, Manuf. Technol.*, **CHMT-8,** 247 (1985).
2. K. Anzai, N. Iwase, K. Sinozaki, and H. Tuge, *Proc. 1st. IEEE CHMT Conf.*, 23 (1984).
3. G. A. Slack, *J. Phys. Chem. Solids*, **34,** 321 (1973).
4. N. Iwase, K. Anzai, K. Shinozaki, O. Hirao, T. D. Thanh, and Y. Sugiura, *IEEE Trans. Components, Hybrids, Manuf. Technol.*, **CHMT-8,** 253 (1985).
5. Y. Kurokawa, H. Hamaguchi, Y. Shimada, K. Utsumi, and H. Takamizawa, *Proc. 36th. Electro. Comp. Conf.*, Seattle, WA (May 1986).
6. C. I. Helgesson, "Ceramic To Metal Bonding," Bost. Tech. Publ., Cambridge, MA (1969).
7. J. F. Burgess, C. A. Neugebauer, and G. Flanagan, *This Journal*, **122,** 688 (1975).
8. Y. S. Sun and J. C. Driscoll, *IEEE Trans. Electron. Devices*, **ED-23,** 961 (1976).
9. M. Wittmer, C. R. Boer, P. Gudmundson, and J. Carlsson, *J. Am. Ceram. Soc.*, **65,** 149 (1982).
10. I. Ohno, Y. Ishii, and M. Mukai, *J. Met. Finish. Soc. Jpn.*, **26,** 118 (1975).
11. H. Honma and S. Mizushima, *ibid.*, **33,** 380 (1982).
12. I. Ohno, *Bull. Jpn. Inst. Met.*, **24,** 139 (1985).
13. E. B. Saubestre, L. J. Durney, J. Hajdu, and E. Bastenbeck, *Plating*, **52,** 982 (1965).
14. K. Kato, *Polymer*, **8,** 33 (1967).
15. M. Matsunaga, Y. Hagiuda, and K. Ito, *Met. Finish.*, **66,** 80 (1968).
16. G. V. Elmore and K. C. Davis, *This Journal*, **116,** 1455 (1969).
17. Y. Nakamura, K. Mori, K. Sugimoto, K. Tamura, and Y. Saito, *J. Appl. Polym. Sci.*, **16,** 2727 (1972).
18. K. Yashima, *Met. Finish. Practice Jpn.*, **27,** 567 (1980).
19. T. Osaka and I. Koiwa, *J. Met. Finish. Soc. Jpn.*, **34,** 330 (1983).

Theoretical and Empirical Studies of Impurity Incorporation into β-SiC Thin Films during Epitaxial Growth

H. J. Kim*,[1] and R. F. Davis

North Carolina State University, Department of Materials Science and Engineering, Raleigh, North Carolina 27695

ABSTRACT

The introduction into monocrystalline β-SiC thin films of the n- and p-type dopants of P and N, and B and Al, respectively, has been studied both theoretically and experimentally via thermodynamic considerations and chemical vapor deposition. The probable gas species which participate in the doping process for these elements has been theoretically investigated by initially determining the stabilities and the gas phase equilibria of the input dopant gases as a function of temperature using free energy minimization calculations. A subsequent experimental study of the amount of incorporation as a function of the partial pressure of the dopant source gas coupled with considerations of dopant incorporation based on a dilute solution model show that Al and P behave ideally while B and N apparently interact with the C or Si in the SiC or fill normally unoccupied interstitial positions. The relationships of atomic concentration or carrier concentration with partial pressure of the dopant gas follow linear and parallel paths. The ratios of ionized dopant concentration to total dopant concentration for N, P, B, and Al are 0.1, 0.2, 0.002, and 0.01, respectively. The solubility limits of N, P, and B in β-SiC at 1633 K were also determined to be approximately 2×10^{20} 10 cm^{-3}, 1×10^{18} cm^{-3}, and 8×10^{18} cm^{-3}, respectively; that of Al exceeds 2×10^{19} cm^{-3}. The more efficient n- and p-type dopants of N and Al have been used to produce what is believed to be the first p-n junction diode in a β-SiC film.

Previous efforts to use SiC in semiconductor applications were largely obstructed by the difficulty of the reproducible growth of high quality single crystals and the considerable expense and low yields of the growth processes. The principal growth techniques were the very high temperature (≥2900 K), Lely sublimation process (1), and the reaction of molten Si with the walls of a high purity graphite crucible. Alpha-SiC crystals of the hexagonal 6H polytype were the principal product of the former process; much smaller and often highly twinned crystals of the cubic 3C or β-SiC polytype were the sole product of the latter technique.

In recent years, however, SiC has received renewed attention as an electronic material because of significant advances in the growth of high quality monocrystalline β-SiC thin films on Si (100) substrates by chemical vapor deposition (CVD) (2-5). A limited number of studies have been conducted to investigate the incorporation via CVD techniques of electronically active impurities in β-SiC. Bartlett *et al.* (6), Long *et al.* (7), and Nishino *et al.* (8) produced p-type β-SiC by adding B_2H_6 or $AlCl_3$ during the growth of this normally n-type (unintentionally doped) material. In addition, von Muench and Pettenpaul (9) doped polycrystalline β-SiC p-type by flowing H_2 through trimethylaluminum (TMA) during crystal growth via the van Arkel process.

Explanations of the process of gas phase doping of Si at low concentration levels have been developed on the basis of (*i*) diffusion controlled deposition kinetics proposed by Shepherd (10) and (*ii*) the equilibrium solubility mechanism proposed by Reiss (11) and extended by Rai-Choudhury and Salkovitz (12).

The following sections present the approaches employed and the results obtained in our complementary theoretical and empirical investigations regarding (*i*) the species which most likely contribute(s) to the introduction of a particular dopant under the conditions used to grow β-SiC films, (*ii*) the gas phase equilibria for the dopant sources, and (*iii*) the determination of the atomic and carrier concentrations of dopants as a function of the partial pressure of each of the constituent source gases.

Theoretical Considerations

An investigation of the most probable specie(s) which is (are) the principal contributor(s) of the elemental species which result(s) in the *in situ* doping under equilibrium conditions of the β-SiC thin films during growth was conducted by determining (*i*) the stabilities of the various dopant sources at the deposition temperature and (*ii*) their gas phase equilibria as a function of their partial pressure. Thermodynamic calculations involving all the gases present during deposition provide important information concerning the thermal stability of the dopant gases and allow a reasonable estimate of the molecular and atomic species which are important in determining the CVD reaction.

Chemical equilibrium calculations involve the computation of the composition of a system, subjected to certain constraints, which contains the minimum free energy. The constraints in CVD systems are the preservation of the mass of each element present, constant temperature, and constant total pressure. White *et al.* (13) initially developed a computational technique which involves the minimization of the summation of the free energies of all the species present in a given system. Eriksson (14) has extended the method to include systems containing more than one condensed phase, including solid solutions, and developed a companion program (SOLGASMIX-PV) for performing the calculations. This program has been used in the present research for the calculation of gas phase equilibria for the dopant sources. The thermodynamic values for most of the species considered to possibly exist during deposition were taken from the JANAF Tables (15).

Experimental

The atomic and carrier concentrations of the p- and n-type dopants of Al and B, and N and P, respectively, were determined empirically as a function of the partial pressure of the dopant source gas. Each dopant gas was incorporated directly into the primary gas stream containing SiH_4, C_2H_4, and H_2 for the chemical vapor deposition of β-SiC. The dopant hydride gases of PH_3 and B_2H_6 contained in H_2 were employed as sources of P and B, respectively. Nitrogen or NH_3 in H_2 were employed as two different sources of N. Finally, liquid trimethylaluminum (TMA) ($Al(CH_3)_3$) was used as the source of Al rather than triethylaluminum ($Al(C_2H_5)_3$) because (*i*) the methyl radical is much more stable to decomposition and the consequent formation of unwanted C than the ethyl radical, and (*ii*) the boiling point of the former (293 K) is lower than that of latter (409 K). In this research, the concentration of the TMA in the gas stream was altered both by changing the flow rate of H_2 over the TMA and by changing the temperature of the bath (controlled within ±0.1 K) containing the bottle of this material. The vapor pressure of TMA at a specific temperature was calculated by using the equation[2]

$$\log V_p = 7.3147 - \left(\frac{1534.1}{T + 220}\right) \quad [1]$$

*Electrochemical Society Active Member.

[1]Present address: Seoul National University, College of Engineering, Department of Inorganic Materials, Seoul, Korea 151.

[2]Alpha Products, a Division of Morton Thiokol, Danvers, MA.

where V_p is the vapor pressure of TMA in mm Hg and T is the temperature in degrees Celsius. This equation is effective in the range of 17°-100°C (290-373 K). The number of moles of TMA carried into the reaction chamber by H_2 per unit time as a result of its flow through the TMA bottle was calculated by using the ideal gas equation where P in this expression is the V_p of the TMA from Eq. [1] and V is the total volume occupied by the H_2 and TMA per unit time. The value of this latter parameter was obtained from the flow rate of H_2 from the TMA, since the mole fraction of TMA is very small.

The introduction (or lack of it) of these dopants into the β-SiC films under the growth conditions of 1633 K and 1 atm total pressure has been analyzed quantitatively as a function of depth using secondary ion mass spectrometry (SIMS). A mass filtered 250 μm diam primary beam of O^+ was used for Al, B, and N; a similar beam of Cs^+ was employed for P. The atomic concentration of a particular dopant at each point in the SIMS profile was obtained by multiplying a conversion factor by the value of the dopant/Si count ratio at that point. Conversion factors were determined from the product of the dopant/Si count ratio and the theoretically calculated (LSS) atomic concentration at the peak of an implanted profile standard.

Transmission Laue x-ray procedures using Cu Kα radiation were employed to analyze the films containing the various concentrations of the dopants for the onset of polycrystallinity. A small window of ≅5 mm was etched into the center of the Si substrate supporting each film using a 2:3 mixture of HF and HNO_3. A 16h exposure at 35 kV and 20 mA was usually required to obtain a pattern. The distance between the specimen and the film was 5 cm.

The differential capacitance-voltage technique was employed to determine the carrier concentration in each of the doped films. In this method a Hg-probe is used to produce both ohmic and Schottky-barrier contacts on the surface of the epitaxial layer. The capacitance of the diode is then measured as a function of reverse voltage, and the dopant concentration of the layer calculated from the capacitance-voltage relationship.

To prepare epitaxial junctions, the n- and p-type impurities of N (from NH_3) and Al, respectively, were serially introduced into the reaction chamber of the CVD system during growth in order to fabricate in sequence a 9 μm thick n^+-layer, a 2 μm thick n-layer, and a 0.5 μm thick p-layer in the same sample, as shown in cross section in Fig. 1. The sample was removed from the CVD unit after the fabrication of each layer and was subjected to wet oxidation at 1480 K for 1.44×10^4s to remove the high concentration tail of a given dopant in each of the three near-surface regions. Each 0.6 μm thick oxide layer was subsequently removed by etching in HF acid.

An additional 0.3 μm oxide layer was subsequently grown on the surface of the final Al-containing layer, and a square window having a 400 μm edge was opened using photolithographic techniques. In the photolithographic process, a 2.0 μm thick photoresist film was applied by allowing a drop of positive photoresist liquid[3] to fall on the sample spinning at 5000 rpm. After pre-baking the photoresist at 480 K for 5400s in an oven in order to dry the film, the sample was placed in a mask aligner[4] covered with a mask containing one 400 × 400 μm solid square surrounded by transparent area, and exposed to 400 nm ultraviolet light for 30s in order to harden the photoresist film outside the solid square. The photoresist film was subsequently developed by dipping and stirring the sample in a developer[5] to remove the material inside the solid square. This was followed by baking at a temperature of 460 K for 1200s to enhance the hardness and adhesion to the oxide layer. A wet chemical process, using buffered HF, was used for 120s to etch the thermally grown SiO_2 from the β-SiC film. This was followed by the removal of the remaining photoresist film.

[3]MICROPOSIT 1400-27 Photoresist, Shipley Co., Newton, MA.
[4]Model KSM MJB 3/HP, Karl Suss, Muchen-Garching, Germany.
[5]MICROPOSIT 351 Developer, Shipley Co., Newton, MA.

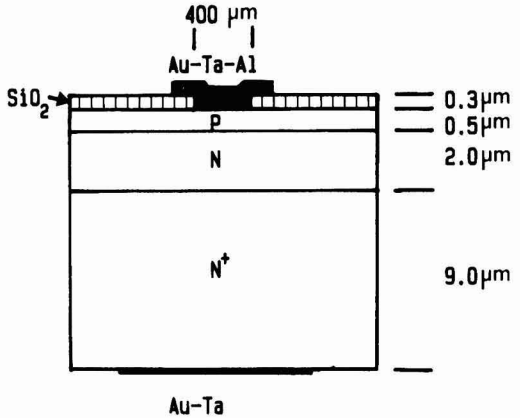

Fig. 1. Schematic diagram of a p-n junction diode produced by sequential doping during growth of a monocrystalline β-SiC thin film.

A 91 atom percent (a/o) Au-2 a/o Ta-7 a/o Al ohmic contact alloy for p-type SiC was evaporated into the window using a strip heater in a vacuum evaporator to heat the contact alloy to a temperature of 1480 K. Positive photoresist film was again applied and a 400 × 400 μm open grid employed in order to remove the evaporated Au-Ta-Al alloy film except in the area of the window. The same procedures noted above were employed. The Si substrate was subsequently removed using 50 volume percent (v/o) HF + 50 v/o HNO_3 and a 97 a/o Au-3 a/o Ta ohmic contact was evaporated onto the bottom of the n-type layer.

The resistivity of the film was determined using a standard commercial[6] four-point probe and the empirical relationship previously derived for this instrument by Combs and Albert (16) from the data of Smits (17) and given in Eq. [2]

$$\rho_s = (V/I)(t)(CF) \qquad [2]$$

In this equation, ρ_s is the sheet resistivity in Ω-cm, V is the measured voltage in mV, I is the applied current in mA, t is the film thickness in microns (measured in this research using angle lapping techniques and optical microscopy), and CF is a diameter correction factor obtained from graphs given by Sze (18). Tungsten carbide probe tips were used in these measurements. Resistivity measurements as a function of depth through the film were also conducted using an automatic spreading resistance probe.[7]

A small piece of the as-grown sample consisting of the p, n, and n^+ layers was angle lapped to provide a magnification of these regions of 50× for these latter measurements.

Current-voltage characteristics of the p-n junction were obtained using a standard probe station and a semiconductor parameter analyzer.[8]

Results and Discussion

Free energy minimization calculations and the determination of the gas species present during deposition.— The standard free energies of formation (15) of the dopant gases of B_2H_6, NH_3, and PH_3 are positive at the experimental deposition temperature of 1633 K and throughout the temperature range 1000-2000 K (data for TMA is not available). Therefore, these gases may be expected to dissociate highly at the deposition temperature. However, one must consider the effect of the other gases present during CVD on the stability of these dopant sources.

[6]Model S-301, Signatone Corp., Santa Clara, CA.
[7]Model ASR-100 c/2, Solid State Measurements, Monroeville, PA.
[8]Model 4145A, Hewlett-Packard Co., Palo Alto, CA.

The data resulting from the thermodynamic calculations using the program SOLGASMIX-PV are shown in Fig. 2. These figures show the calculated equilibrium partial pressure for the various possible dopant-containing gaseous constituents as a function of the initial reactant gas pressure for P, B and N, respectively, in the Si-C-H system. The calculations were made for the deposition temperature of 1633 K and 1 atm total pressure (the experimental conditions used for producing undoped SiC). As implied above, all the gases used in the deposition of β-SiC including SiH_4, C_2H_4, and H_2 as well as the dopant gas in the mole fractions normally em-

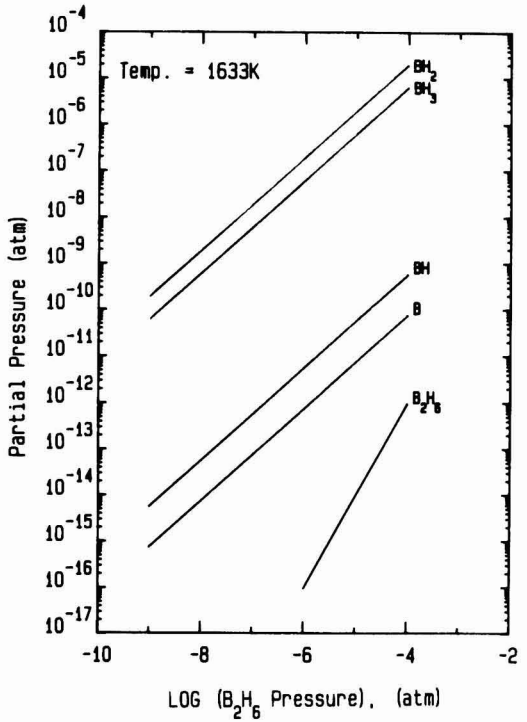

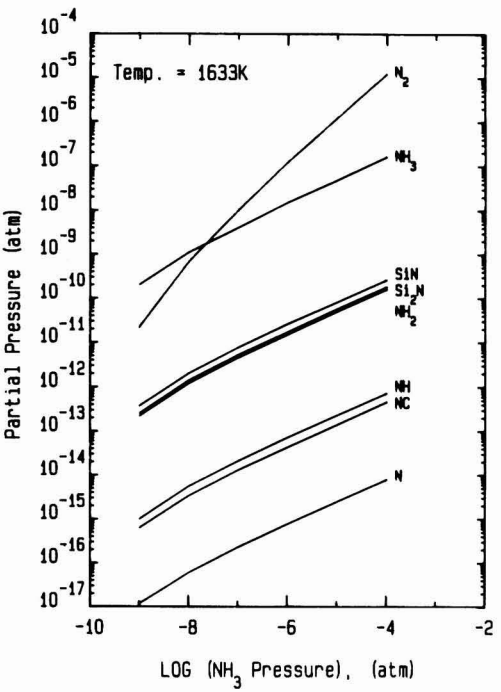

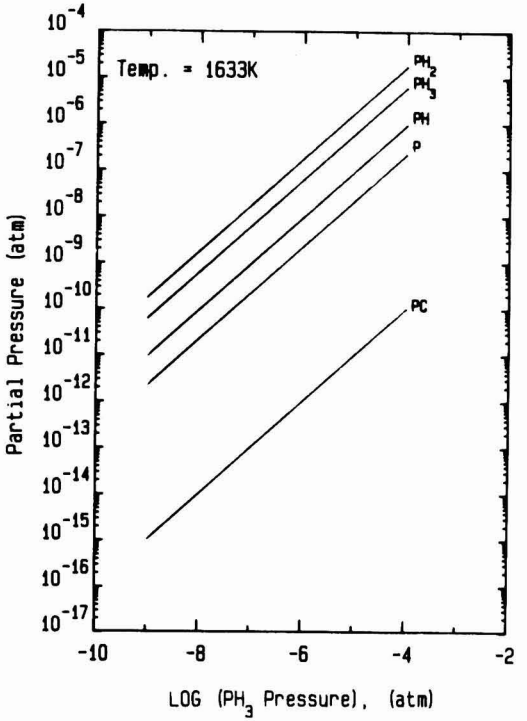

Fig. 2. Calculated partial pressures of the equilibrium gas species *vs.* the initial gas pressure for (a) B_2H_6, (b) NH_3, and (c) PH_3 for the conditions used in the CVD deposition of β-SiC: *i.e.*, the gases of C_2H_4, SiH_4, and H_2 were also considered present in the mole fractions used experimentally. The total pressure was 1.0 atm. PC and NC are the gases of phosphorous carbide and nitrogen carbide, respectively.

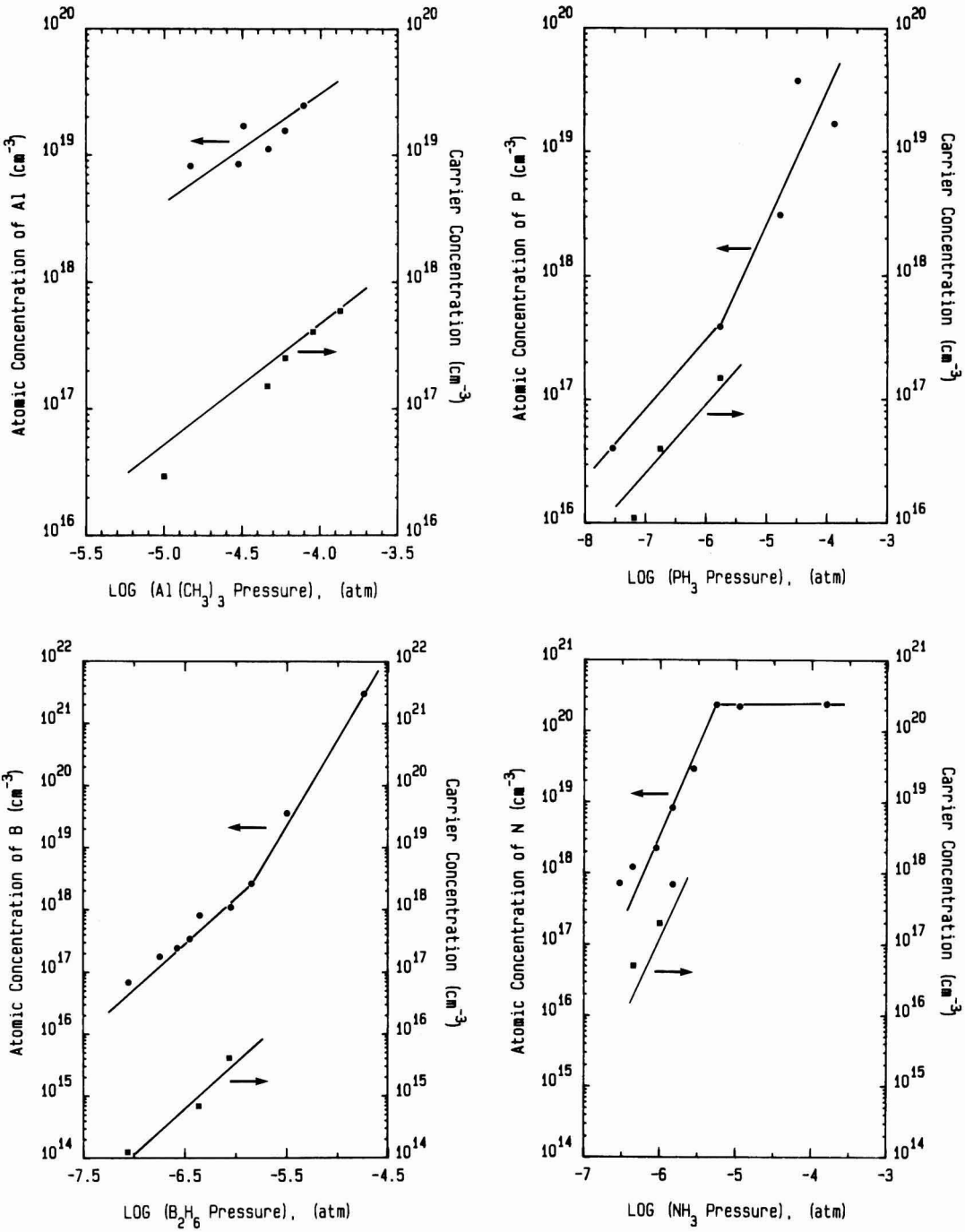

Fig. 3. Atomic and carrier concentrations of (a) Al, (b) P, (c) B, and (d) N as a function of the partial pressure in the CVD chamber of the respective dopant gases of $Al(CH_3)_3$, PH_3, B_2H_6, and NH_3. Aluminum and B are p-type dopants while P and N are n-type dopants in β-SiC.

ployed or under consideration for employment were included in the calculations. As noted above, Fig. 2 shows only dopant-containing vapor species. The reason for this is that under the conditions used in the present research, no dopant-containing condensed phases were found. An interesting result provided by these calculations is that, with the exception of N_2, the species with the highest partial pressure at the deposition temperature are hydrides. The reason for this is the large amount of H_2 carrier gas used in the deposition process which prevents the occurrence of high concentrations of the pure elemental species.

From these results alone, one cannot specify which particular dopant specie or species in the gas phase (assuming decomposition of the dopant gas) is in equilibrium with the impurity incorporated in the β-SiC, *i.e.*,

which particular elemental or compound gas species provides the dopant atoms which are actually incorporated into the β-SiC. However, it may be reasoned that those gases with the highest partial pressure contribute the majority of the dopant atoms. For the three elements of N, B, and P these species would be the various hydrides as well as N_2. Although N_2 is a very stable molecule, recent work in our laboratory has shown that the introduction of this species alone into the CVD chamber in concentrations ≅0.5 v/o provides a very effective means of controllably doping β-SiC even at growth temperature of 1633 K. Theoretical and empirical studies related to this concern are described in the next section.

Equilibrium solubility considerations.—The use of the dilute solution theory based equilibrium solubility model of Rai-Choudhury and Salkovitz (12) for dopant incorporation in Si coupled with pertinent experimental results can provide information concerning the dopant gas species which are likely to contribute to the doping of the β-SiC, as well as indications of solute-solvent interaction.

The solubility of the dopant species at the temperatures used for incorporation is often very small in semiconductor materials. As a consequence, Henry's law is usually followed (12). The solute atoms are considered to exist in monoatomic form. The overall reaction for the dopant species, entering into solution in the SiC is

$$D_y(g) = yD \text{ (in the SiC crystal)} \quad [3]$$

The equilibrium constant of Eq. [3] will be

$$K = \frac{a_D{}^y}{P_{D_y}} = \frac{\gamma_D{}^y N_D{}^y}{P_{D_y}} \quad [4]$$

where a_D is the activity of the dopant species, P_D is the partial pressure of the dopant species, $\gamma_D{}^y$ is the proportionality constant (it is the activity coefficient if N_D is the mole fraction of dopant species), and N_D is the concentration of dopant in the SiC crystal.

Since we assume that Henry's law is followed, at constant temperature

$$N_D = \frac{K^{1/y}}{\gamma_D} P_{D_y}{}^{1/y} = K' P_{D_y}{}^{1/y} \quad [5]$$

where K' is a new proportionality constant. By taking the logarithm of both sides of Eq. [5], one obtains

$$\log N_D = \log K' + (1/y) \log P_{D_y} \quad [6]$$

The ratio of the ionized dopant concentration to the total dopant concentration in the SiC crystal may be defined as follows

$$\gamma'_D = \frac{N_i}{N_D} \quad [7]$$

where N_i is the ionized dopant concentration at some actual N_D.

Combining Eq. [5] and [7], one obtains

$$N_i = K\gamma'_D P_{D_y}{}^{1/y} \quad [8]$$

By taking the logarithm of both sides of Eq. [8], it becomes

$$\log N_i = \log (K\gamma'_D) + (1/y) \log P_{D_y} \quad [9]$$

Assuming that K' and γ' are independent of the partial pressure of the given dopant species, Eq. [6] and [9] predict that plots of $\log N_D$ *vs.* $\log P_D$ and $\log N_i$ *vs.* $\log P_D$ should be linear and parallel with a slope of $1/y$ within the range of values of N_D where Henry's law is valid (for Si, $N_D = 10^{18}$ cm^{-3} for B, As, and P; analogous values for SiC are not known).

To obtain values of $1/y$ for each dopant, it is necessary to experimentally introduce a given dopant at several known partial pressures into the growth chamber during deposition and to subsequently measure its atomic and carrier concentrations in the resultant β-SiC films. The experimental aspects of this subject are discussed in the following section.

Atomic and carrier concentrations.—Figure 3 shows the results of the experimental SIMS measurements of atomic dopant concentration as a function of the partial pressure of the dopant source gas for Al, P, B, and N. The linear character of both the curve for Al and the sections of the graphs for P, B, and N at lower partial pressures is predicted by Eq. [6] and is similar to the analogous graphs reported by Rai-Choudhury and Salkovitz (12) and Bloem (19) for dopant incorporation into monocrystalline Si.

Solubility data from direct measurements such as diffusion or lattice parameter studies are not available in the literature for the various dopants for the temperature of 1633 K used for the CVD growth. However, the change in slope of the atomic concentration curves for P, B, and N as well as the changes in the surface character and the x-ray Laue patterns of the heavily doped samples relative to the undoped (or lightly doped) materials, as shown in Fig. 4 and 5, indicate the onset of polycrystallinity. These changes are believed to be triggered by the introduction of the various dopants in excess of their solubility limits. Furthermore, the grain boundaries can act as sinks for excess dopant and thus allow continued incorporation of these species at levels significantly higher than allowed by the lattice. Finally, the use of high partial pressures of TMA caused a thick coating of an Al-containing material to rapidly develop on the walls of the

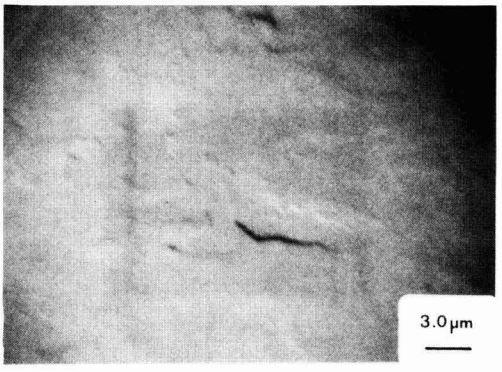

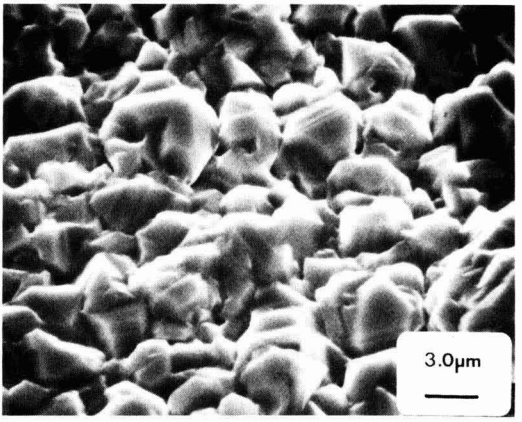

Fig. 4. SEM micrographs showing (a) the extremely smooth surface typical of the undoped (or the lightly doped) β-SiC films and (b) the very rough surface of a heavily P-doped (1.6×10^{19} cm^{-3}) quasipolycrystalline film.

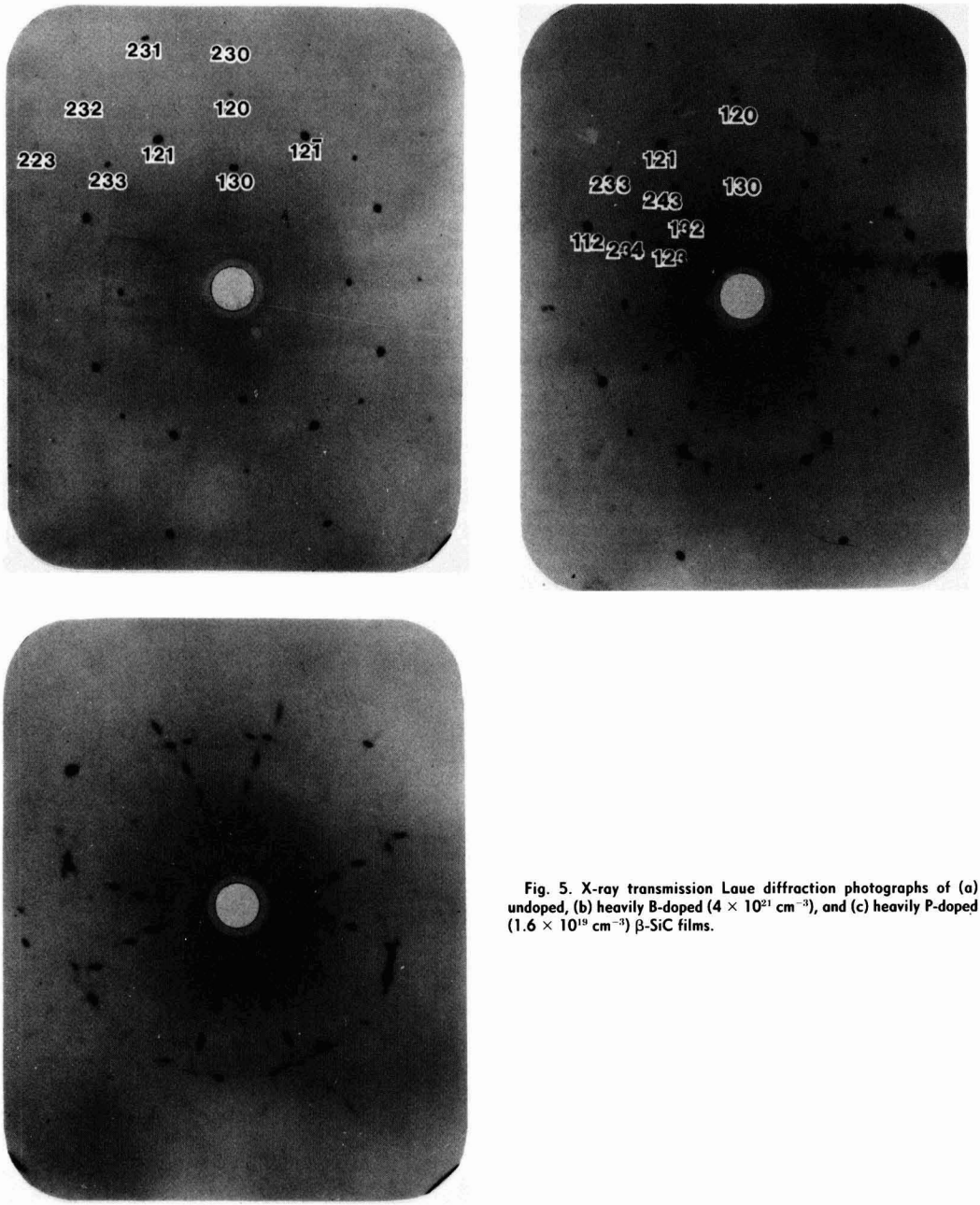

Fig. 5. X-ray transmission Laue diffraction photographs of (a) undoped, (b) heavily B-doped (4×10^{21} cm^{-3}), and (c) heavily P-doped (1.6×10^{19} cm^{-3}) β-SiC films.

CVD chamber. The formation of this coating reflected the heat of the susceptor which caused an overall increase and a redistribution of the heat in the chamber. This produced an enhancement in the gas phase nucleation and the resultant occurrence of poor films as well as the eventual melting of the Si substrates, if the input RF power was not reduced.

The carrier concentrations of each dopant were also found to be a linear function of the partial pressure of the dopant source gas when plotted on a log-log scale, as shown in Fig. 3 for Al, P, B, and N. Each figure reveals a major difference between the atomic concentration and the carrier concentration for each dopant. The reasons for this include the measured deep energy levels for the p-type dopants of Al (0.24 eV) and B (0.735 eV) as well as the possibility of compensation from unintentionally introduced n-type dopants (*e.g.*, N). Other possibilities include (*i*) line or point defects and/or trapping of impurities at dislocations and stacking faults known to be in the material, (*ii*) dopant-Si and/or dopant-C interaction, and (*iii*) location in nonelectrically active interstitial sites (especially plausible for B). Thus a portion of each of the dopants is either not ionized or located on nonelectrically active sites or forms complexes with Si or C. Combinations of these events are also probable.

In the case of the p-type dopant of Al (Fig. 3a), the slope ($1/y$) in the atomic concentration curve is 0.9. This indicates that the Al is in dilute solution in the β-SiC and

that pure Al and/or a complex containing only one Al atom are the principal species which contribute to the introduction of this dopant. The ratio of the carrier concentration to the atomic concentration is 0.01 at all partial pressures of TMA employed.

For the n-type dopant of P, the knee of the atomic concentration curve in Fig. 3b occurs at 10^{18} cm^{-3} which is believed to be very close to the solubility limit of this relatively large atom at the growth temperature of 1633 K. The value of $1/y$ of the lower section of this curve is 1.0. As in the case of Al, this indicates that ideal behavior exists, *i.e.*, there is no solute-solute or solute-solvent interaction and that gas species, containing only one P atom, are the sole contributors of this element to the β-SiC. This latter point is reinforced by the data of Fig. 2c which show that all the species present in the gas phase following the decomposition of the PH_3 contain only one P atom.

The P carrier concentration is also linearly proportional to the partial pressure of PH_3, the graph of which is also parallel to the atomic concentration. The ratio of the carrier concentration to the atomic concentration is 0.2.

The break in the atomic concentration curve is even more pronounced for B than for P, as shown in Fig. 3c. It occurs at a concentration of 2×10^{18} cm^{-3}. In this case the value of $1/y$ is 1.7. Since this value cannot exceed 1.0 under dilute solution conditions, interaction between the B and either Si or, more likely, C and/or incorporation of this species into interstitial sites or at dislocations must be occurring to produce this higher slope. The ratio of the carrier concentration to the atomic concentration for this p-type material is 0.002.

In the case of N, saturation of this constituent in β-SiC under the deposition conditions employed in this research occurs at a concentration of 2×10^{20} cm^{-3}, as revealed in Fig. 3d. The value of $1/y$ for the lower pressure portion of the atomic concentration curve is ≅2 which is twice or four times the value expected, if most of the N is derived from NH_3 or N_2, respectively. In fact, the recent use of N_2 as the input gas coupled with SIMS studies similar to those used to produce Fig. 3 resulted in a $1/y$ value of ≅1.0 — again twice the expected value. These results again imply that incorporation of the N species occurs to a greater extent than would be expected from equilibrium calculations based on dilute solution theory. In this case, it is also very likely that considerable interaction exists between the N and Si of the β-SiC; since this combination forms strong bonds and high melting point materials.

The n-type carrier concentration of the N-doped materials was measured on only three samples, as it was difficult to measure higher values with the C-V technique. The ratio of the carrier concentration to atomic concentration in the N-doped films is 0.1.

The undoped β-SiC samples grown in the same time period as the doped samples described above showed n-type character with a carrier concentration usually in the range of 5×10^{15} to 1×10^{16} cm^{-3}. Thus the p-type carrier concentration of the films doped with B or Al must exceed this native carrier concentration. This is shown for the case of B in Fig. 6. Although these measurements were made in reverse bias, the polarities were switched on the Schottky and ohmic contacts of the Hg probe to determine the n- and p-type carrier concentrations. As revealed by the separate plots of the n- and p-type concentrations, the former is dominant until a partial pressure of B_2H_6 of $\cong 10^{-6.4}$ is employed during the growth procedure. Above this B concentration of $\cong 4.5 \times 10^{17}$ cm^{-3}, the material becomes p-type in character. Note also the concentration of the n-type carrier does not decrease as increasing amounts of B are added to the material. This indicates that compensation of the n-type carriers is not extensive at any partial pressure of B_2H_6. Slight compensation does apparently occur; since the n-type carrier concentration of 9×10^{14} cm^{-3} noted in Fig. 6 has not been achieved in the undoped samples. Finally, it should be noted that the "window" of atomic concentration of B whereby p-type conductivity is achieved without exceeding the solubility limit is between $\cong 5 \times 10^{17}$ and 3×10^{18}. This means that the level of p-type carrier concentration in a B-doped β-SiC film will not exceed $\cong 10^{16}$ before the onset of increasing surface roughness and polycrystallinity. This problem is lessened considerably by the use of Al, as the films are p-type over the entire range of carrier concentrations shown in Fig. 3a. Furthermore, this p-type character is observed in Al concentrations which extend down to at least 7×10^{15} cm^{-3} (see spreading resistance measurements described below) and is very likely evident in values higher than shown in Fig. 3a. Thus, this latter element is currently the favored p-type dopant for β-SiC device applications, as illustrated in the next section.

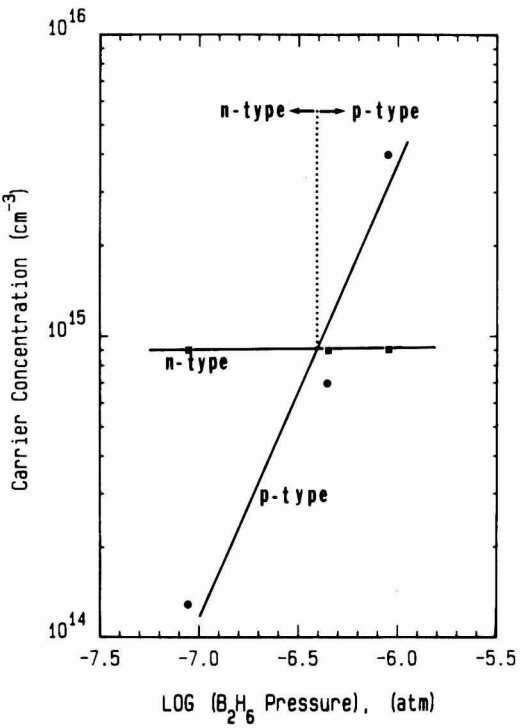

Fig. 6. The p-type and n-type carrier concentrations vs. the partial pressure of B_2H_6 in the B-doped SiC films.

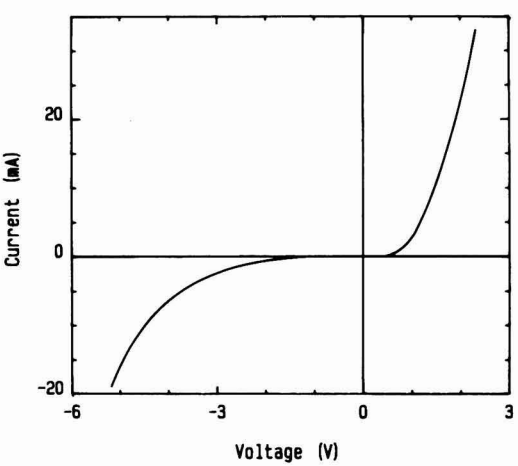

Fig. 7. The I-V characteristics of the p-n junction diode fabricated by *in situ* doping of sequentially deposited beta-SiC films with Al and N.

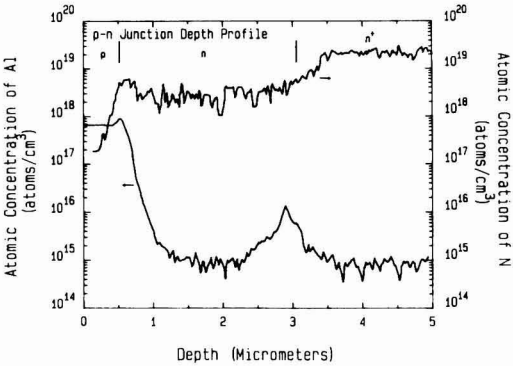

Fig. 8. SIMS depth profile of the p-n junction produced by *in situ* doping with Al and N.

P-n junction fabrication and characterization.—The aforenoted information regarding partial pressures of NH_3 and TMA and the corresponding atomic and charge carrier concentrations have permitted the successful fabrication of a square p-n junction having ≅2 mm sides. The I-V characteristics of this junction are shown in Fig. 7. Although a moderately large leakage current is evident, the junction is rectifying. The reasons for the former phenomenon are (*i*) the large contact area, (*ii*) the lack of any passivation treatment, and (*iii*) the absence of a mesa shape.

The p-n junction depth profile obtained using SIMS analysis is shown in Fig. 8. An Al concentration of 7×10^{17} cm^{-3} is revealed to a distance of 0.6 μm from the surface. The Al ion yield rises at both the p-n and n-n^+ interfaces either as a result of oxide formation (which gives a higher ion yield in SIMS than Al in SiC) on the SiC during the transfer from the HF to the CVD chamber or diffusion of Al to this interface during growth or both. This yield drops to ≅10^{15} cm^{-3} or background level outside these junctions.

At the p-n junction interface, the N concentration increases to an average of 2×10^{17} cm^{-3}; a second increase to ≅2×10^{19} cm^{-3} occurs at the n-n^+ interface. A spreading resistance profile of this junction area is shown in Fig. 9. This profile is consistent with the SIMS data. The p-layer shows a resistance of ≅4×10^7 Ω. This resistance decreases abruptly at the p-n interface to a value of 4×10^3 Ω; the n^+ layer has the resistance of 2×10^3 Ω. Using the ratios of active carrier concentration to doping concentration of 0.1 and 0.01 for N and Al, respectively, the active carrier concentrations in the p, n, and n^+ regions are calculated to be 7×10^{15}, 2×10^{17}, and 2×10^{18} cm^{-3}, respectively.

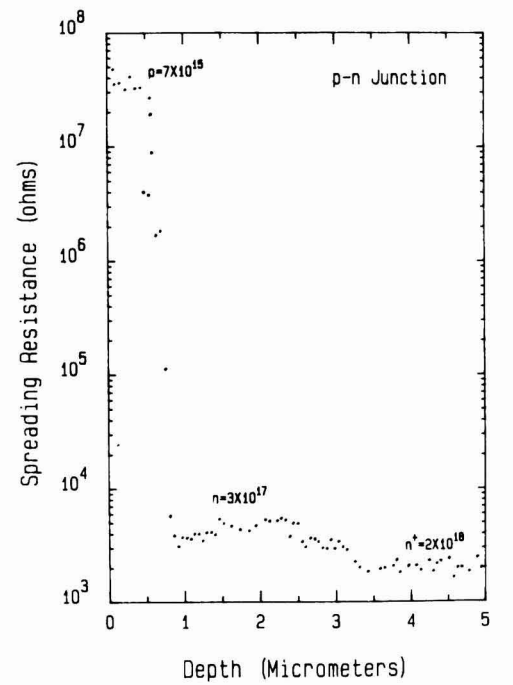

Fig. 9. Spreading resistance profile vs. depth of the p-n junction diode doped with Al and N during growth. Charge carrier concentrations are shown for the p, n, and the n^+ regions.

Summary

The vapor species present and their respective partial pressures have been theoretically determined using the SOLGASMIX-PV program for the n- and p-type dopants of N and P, and B, respectively, under the conditions used to grow monocrystalline β-SiC thin films via CVD. Experimental considerations of dopant incorporation based on a dilute solution model show that Al and P behave ideally with a $1/y$ value of ≅1.0. However, $1/y$ values of 1.7 and 2 for B and N, respectively, indicate that interaction between these dopants and C or Si and/or incorporation into interstitial sites (especially B) occurs when these dopants are introduced into β-SiC. The relationship between the carrier concentrations or the atomic concentrations and the partial pressure of the dopant source gases is linear and parallel; the ratios of the values on these two curves are 0.1, 0.2, 0.002, and 0.01 for N, P, B, and Al, respectively. Thus, N and Al are the more efficient n- and p-type dopants in β-SiC. From this knowledge the first p-n junction diode in a β-SiC film has been fabricated.

Acknowledgments

The authors express their appreciation to Dr. P. Rai-Choudhury and Mr. H. Kong for valuable discussion. The support of the Office of Naval Research under Grant no. N00014-79-C-0121 is also gratefully acknowledged.

Manuscript submitted Feb. 10, 1986; revised manuscript received May 30, 1986.

North Carolina State University assisted in meeting the publication costs of this article.

REFERENCES

1. J. A. Lely, *Ber. Deut. Keram. Ges.*, **32,** 229 (1970).
2. H. Matsunami, S. Nishino, and T. Tanaka, *Jpn. J. Appl. Phys.*, **45,** 138 (1978).
3. S. Nishino, J. A. Powell, and H. A. Will, *Appl. Phys. Lett.*, **42,** 460 (1983).
4. A. Addamiano and J. A. Sprague, *ibid.*, **44,** 525 (1984).
5. P. H. Liaw and R. F. Davis, *This Journal*, **132,** 642 (1985).
6. R. W. Bartlett and R. A. Muller, *Mater. Res. Bull.*, **4,** 5341 (1969).
7. N. N. Long, D. S. Nedzvetski, N. K. Prokofera, and M. B. Reifman, *Opt. i. Spektroskopiya*, **29,** 388 (1970).
8. S. Nishino, H. Suhara, and H. Matsunami, p. 317 in extended Abstracts of the 15th Conference on Solid State Devices and Materials, Tokyo, 1983.
9. W. von Muench and E. Pettenpaul, *This Journal*, **125,** 294 (1978).
10. W. H. Shepherd, *ibid.*, **115,** 541 (1968).
11. H. Reiss, *J. Chem. Phys.*, **21,** 1209 (1953).
12. P. Rai-Choudhury and E. I. Salkovitz, *J. Cryst. Growth*, **7,** 353 (1970).
13. W. B. White, W. M. Johnson, and G. B. Dantzig, *J. Chem. Phys.*, **28,** 751 (1958).
14. G. Eriksson, *Chem. Scr.*, **8,** 100 (1975).
15. JANAF Thermodynamic Tables, 2nd ed., D. R. Stull and H. Prophet, Editors, NSRDS-NBS 37, National Bureau of Standards, Washington, DC (1971).
16. J. F. Combs and M. P. Alberty, *Semicond. Prod. Solid State Technol.*, **6,** 26 (1963).
17. F. M. Smits, *Bell Syst. Tech. J.*, **37,** 711 (1958).
18. S. M. Sze, "Physics of Semiconductors," 2nd ed., p. 31. John Wiley & Sons, Inc., New York (1981).
19. J. Bloem, *This Journal*, **117,** 1397 (1970).

Fabrication of High Voltage Polysilicon TFT's on an Insulator

R. Pennell,* R. Catero, and S. Lovelis

Motorola Incorporated, Mesa, Arizona 85202

ABSTRACT

Using thin film transistors in active-matrixed addressed large area displays has recently become important in display development. Specifically, a PLZT ceramic dot-matrix display requires high voltage TFT pixel switching. To meet the need, a process has been developed utilizing polysilicon and temperatures less than 850°C, which yields MOSFET's capable of operating at voltages in excess of 50V with high $I_{D(on)}/I_{D(off)}$ ratios. High mobilities are obtained by fabricating n-channel, accumulation-mode devices in silicon deposited in the amorphous state and later annealed to the final polycrystalline condition.

Interest has been growing in the use of thin film transistors for addressing active dot-matrix displays. Although several materials have been investigated, polysilicon offers such advantages as the use of conventional silicon processing techniques and an easy fabrication process (1). High quality devices could also be used as driver circuitry fabricated on the display substrate.

PLZT ceramic material has been used in optical shutter applications for several years. Recently, it has been applied to display devices (2). However, for use as a substrate in dot-matrix applications, several constraints are placed on the process for fabrication of the thin film transistors. Most of the wet cleaning schemes presently used in MOS processing severely degrade the PLZT surface, reducing its electro-optic effect. Also, thermal stress due to temperature gradients produces breakage at temperatures as low as 150°C. High temperatures (over 200°C) can alter the PLZT composition with time, changing its electro-optic effect especially, whenever hydrogen is available in the processing atmosphere or in a deposited film. The lead component is easily reduced by hydrogen, rendering the substrate useless. In addition to these material effects are the requirements that the thin film transistors have low leakage currents in the off state with a high source-to-drain voltage and be able to provide sufficient charging current to charge the capacitive load of the pixel during the short time allotted. Also note that the device must be symmetric.

Adhering to the constraints of the PLZT substrate, a process has been developed, utilizing deposited oxide encapsulation, suitable for the production of acceptable thin film transistors, which can be used for pixel switching and driver circuitry. A fully populated PLZT dot-matrix display has been fabricated (3). With slight modifications, the process could be valuable in the formation of stacked transistors utilized in MOS DRAM fabrication.

TFT Process

The fabrication process for building n-channel MOSFET's in polysilicon is as follows. 2500Å of low temperature oxide (LTO) is deposited by LPCVD (on PLZT) at the temperature of 420°C. This is followed by the deposition of silicon using LPCVD at 580°C to a thickness of 5000Å. Next, the polysilicon islands for TFT fabrication are defined using normal photolithography techniques, and this step is immediately followed by defining regions for source-drain implant utilizing photoresist as an implant mask. Source-drain regions are implanted with phosphorus using a dose of 5E15 at 100 keV. Then, a maskless channel implant is done with phosphorus using a dose of 3E12 at 80 keV. The gate oxide is deposited to a thickness of 2000Å using the same conditions as the initial oxide. After the deposition, an anneal step is performed at 840°C using ambients of oxygen plus TCA, then dry nitrogen. After implant and anneal, the phosphorus in the channel region is distributed throughout the entire 5000Å thickness.

Following the pre-ohmic photostep, aluminum-1.5% silicon is evaporated at a temperature of approximately 400°C and defined. A metal anneal is then accomplished using forming gas at 450°C for 60 min.

The final step is the hydrogen passivation of the polysilicon grain boundaries. This is done by plasma annealing using ammonia as a source in a planar plasma reactor. The process conditions are 10 min at approximately 300°-350°C, using 700-800W and 2 torr of pressure.

A cross-sectional view of the final TFT structure is contained in Fig. 1.

Results and Discussion

A critical problem when trying to fabricate polysilicon transistors with uniform characteristics on large areas is the variation in grain size. Deposition results are affected by later higher temperature anneals (4). Associated with these grain size variations are the grain boundary effects. The mobility is degraded by grain boundary scattering. Trapping effects result in high thresholds and fewer free carriers than would be anticipated by classical MOS analysis.

Previous work has shown that silicon deposited in the amorphous condition will, upon higher temperature anneal, form larger grains than will silicon deposited in the polycrystalline state (4). The 400°C silicon was deposited in a planar plasma reactor. Table I lists typical data for transistors fabricated in silicon deposited at the listed temperatures. $I_{D(on)}$ is measured at 50V V_{GS} and 25V, V_{DS}, and $I_{D(off)}$ at 0 V V_{GS} and 60V V_{DS}. Threshold voltage is calculated by extrapolating the straight line fit to the plot of the square root of I_{DS} *vs.* V_{GS} to zero I_{DS}. The effective mobility is calculated using the formula

$$\text{mobility} = I_{D(on)}/C_i W/2L\,(V_g - V_{th})^2$$

For the 2000Å gate oxide, C_i is calculated to be 17.3×10^{-9} F/cm². The definition of "effective mobility" and the electrical conditions used for measuring it were chosen to best represent the TFT at high operating voltages. This allowed for better evaluation of process variations on TFT performance.

As can be noted, a significant improvement in transistor performance is achieved by using amorphous deposited silicon. Verification of the amorphous condition was done using transmission electron microscopy by the SRDL laboratory at Motorola. The reason for improved performance of 580° *vs.* 400°C deposited silicon is not known at this time.

Another method to reduce the grain boundary effects is by passivation of the defect sites with monatomic hydro-

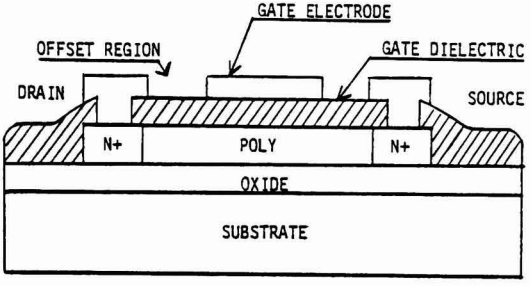

Fig. 1. TFT cross-sectional view

* Electrochemical Society Active Member.

Table I. Transistors with W/L = 6/20 μm and offset distance = 5 μm

Dep. temp. (°C)	$I_{D\ (on)}$ (μA)	$I_{D\ (off)}$ (nA)	VTN (V)	Mobility (cm^2/v-s)
400	28.0	15	9.0	6.1
580	62.0	8	4.0	10.8
630	11.0	700	13.0	2.9

gen. Various methods, including plasma annealing (5, 6), hydrogen implantation (7), and using a plasma nitride source (8), have been tried and reported with success. In our work, the most success has been achieved using ammonia plasma annealing in a planar plasma reactor. Figures 2a and b demonstrate the improved I-V characteristics obtained from a passivated device using transistors of the design in Table I. In these curves, both I_D and V_D are plotted on log scales so that both $I_{D(on)}$ and $I_{D(off)}$ can be observed. A significant improvement in effective mobility and leakage current is seen, as well as a reduction in threshold voltage.

The effectiveness of the plasma anneal hydrogenation depends on the channel doping technique. Early in the development phase of this project, it was learned that using an accumulation mode device resulted in the lowest leakage currents. By accumulation mode we mean that the channel region is doped with the same type dopant as the source-drain regions. After implant and anneal, the phosphorus in the channel region is distributed throughout the entire 5000Å thickness, as indicated by SIMS depth profile analysis. Although the opposite conclusion has been reached (9), our high voltage operation may explain the difference in results. This can be understood by examining the generation of leakage current in polysilicon. Defects present at the grain boundary sites generate localized potential barriers and act as electron-hole pair generation centers. Due to the high electric fields produced at high drain voltages, conditions exist causing excess electrons available at the source to recombine with holes fed from the source. Also, at the drain, this field causes electrons to drift to the drain producing drain current. After hydrogen

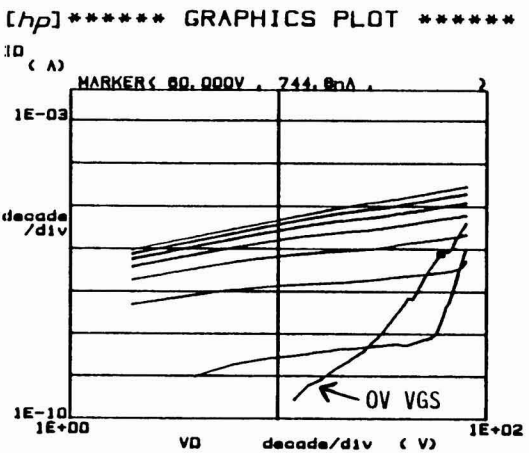

Fig. 2. (a, top; b, bottom) TFT characteristics prior to hydrogenation. Applied gate voltage starts with 0 V for eight steps in 10V increments.

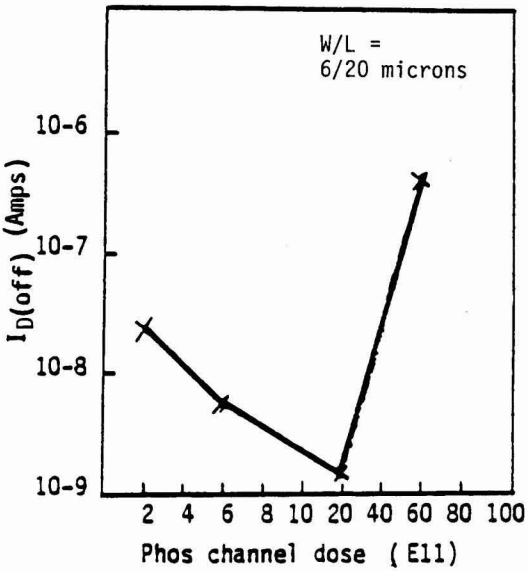

Fig. 3. $I_{D(off)}$ as a function of channel implant dose

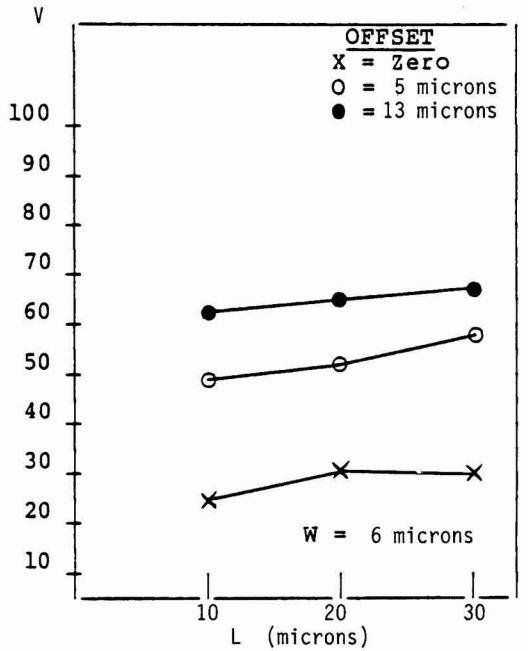

Fig. 4. Breakdown voltage as a function of total gate length ($L + 2 \times$ offset) for various offset distances.

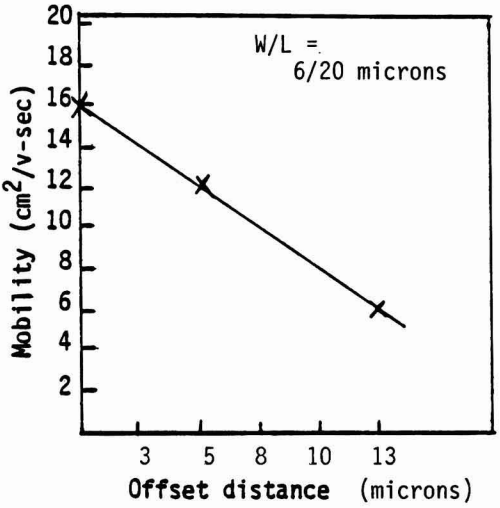

Fig. 5. Mobility as a function of offset distance

passivation, these defect sites are reduced or removed, thus reducing leakage current. Conversely, in an inversion-mode device, one in which the channel doping is the opposite type of the source-drain regions, the reduction in leakage current is not as significant. This can be explained by the fact that a p-n junction area also produces high electric fields, which generate electron-hole pairs. However, the hydrogen passivation does not affect junction characteristics.

Although hydrogen passivation is known to reduce the grain boundary defects greatly, the amount of doping in the film also has a similar effect (10). As doping levels increase, the effects of the passivation process on the polysilicon properties become less noticeable. Figure 3 shows the effect on $I_{D(off)}$ *vs.* the phosphorus channel doping level. With a standard passivation process, we see that $I_{D(off)}$ decreases until a critical doping level is reached. It is at this point that the device has changed from an enhancement to a depletion type. This is a particular problem encountered when using an accumulation mode device. Care must be taken to provide a combination of channel doping and passivation, which provides the highest mobility and lowest leakage while maintaining an enhancement mode device.

To operate a PLZT display wafer, high voltage is required. To obtain good contrast of the display, a minimum ratio for $I_{D(on)}$ to $I_{D(off)}$ of 10^4 is needed. To achieve the high voltage operation of the polysilicon TFT, the technique of using an offset region between the gate and source-drain regions was investigated (11). Figure 4 demonstrates the effect of the offset distance, between the gate and the source and drain, on the breakdown voltage with respect to L. Because of the leakage encountered in polysilicon de-

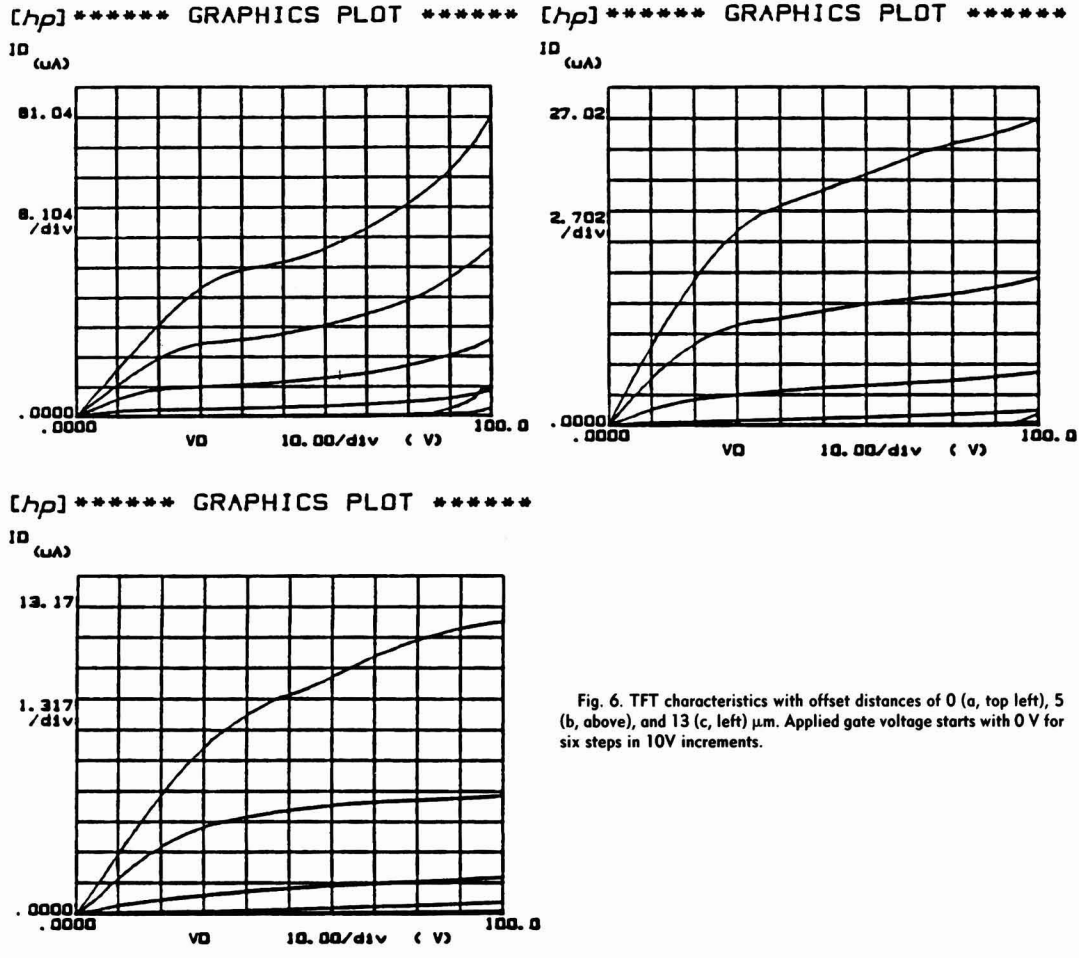

Fig. 6. TFT characteristics with offset distances of 0 (a, top left), 5 (b, above), and 13 (c, left) μm. Applied gate voltage starts with 0 V for six steps in 10V increments.

vices, breakdown voltage is defined as the point where the change in I_{DS} is greater than 10% per 2V change in V_{DS}. Offset distances greater than 13 μm could not be used to increase *BVD*, because the electric field produced under the gate metal appears insufficient to create a conductive channel to the source-drain regions. At a distance of 15 μm, $I_{D(on)}$ reduces to zero.

Although we gain the advantage of increased B_{VD} with increasing offset distance, a major disadvantage is also incurred. Figure 5 shows how effective mobility decreases with increasing offset distance. At zero offset distance, a mobility of 16 cm^2/V-s is obtained and should be sufficient to produce driver circuitry on a display wafer. Figures 6a, b, and c compare IV characteristics for transistors fabricated with 0, 5, and 13 μm offset distances, respectively. In each case, W/L is 6/20 μm and the applied gate voltage starts with 0 V for six steps in 10V increments.

Conclusions

A process flow has been described for fabricating polysilicon thin film transistors on an insulator. The process steps have been adapted to conform to PLZT substrate limitations and have resulted in characteristics suitable for display and driver circuitry applications.

Good $I_{D(on)}$ to $I_{D(off)}$ ratios have been achieved utilizing amorphous deposited silicon and ammonia plasma anneal hydrogenation. Through a design and process evaluation, it has been observed that accumulation mode devices produce the best transistor performance. Use of an offset geometry allows for high voltage operation that is limited to 50-60V.

Acknowledgments

The authors wish to thank Dr. James Rutledge and Bob McEwan for reviewing the manuscript and the Motorola MICARL area for processing assistance. Thanks also go to Henry Franklin, the project display engineer.

Manuscript submitted Jan. 13, 1986; revised manuscript received June 14, 1986.

REFERENCES

1. M. J. Powell, J. A. Chapman, and M. V. C. Stroomer, in "Proceedings of the SID," Vol. 25/4, p. 269 (1984).
2. G. H. Haertling, *Ferroelectrics*, **50**, 63 (1983).
3. H. Franklin, Presented at the IEEE 1985 International Display Research Conference, Oct. 1985.
4. T. I. Kamins, *This Journal*, **127**, 686 (1980).
5. D. R. Campbell, *Appl. Phys. Lett.*, **36**, 604 (1980).
6. T. I. Kamins, *IEEE Electron. Devices Lett.*, **EDL-1**, 159 (1980).
7. D. L. Chen, *J. Appl. Phys.*, **57**, 1408 (1985).
8. G. P. Pollack, W. F. Richardson, S. D. S. Malhi, T. Bonifield, H. Shichyo, S. Banerjee, M. Elahy, A. H. Shah, R. Womuck, and P. K. Chatterjee, *IEEE Electron. Device Lett.*, **EDL-5**, 468 (1984).
9. S. D. S. Malhi, H. Shichijo, S. K. Banerjee, R. Sundaresan, M. Elahy, G. P. Pollack, W. F. Richardson, A. H. Shah, L. R. Hite, R. H. Womack, P. K. Chatterjee, and H. W. Lum, *IEEE J. Solid State Circuits*, **SC-20**, 178 (1985).
10. T. Makino, *Appl. Phys. Lett.*, **35**, 551 (1979).
11. T. Unagami and B. Tsujiyama, *IEEE Electron. Device Lett.*, **EDL-3**, 167 (1982).

Rapid Thermal Oxidation of Silicon

S. T. Ang*

Texas Instruments Incorporated, Dallas, Texas 75265

J. J. Wortman*

North Carolina State University, Raleigh, North Carolina 27695

ABSTRACT

Incoherent light has been used to grow thermal oxides on silicon wafers with a variety of doping levels using both (100) and (111) orientations. Dry oxides have been grown at 1150° and 1200°C in the thickness range of 200-700Å and wet oxides have been grown up to 3000Å. Using MOS structures to evaluate the oxide properties, the dry oxides were found to have no negative bias-temperature instability, low interface state density, and a fixed charge in the range of 1-5 × 10^{10} cm^{-2}. Oxidation rate constants were found to be approximately the same as those reported for furnace oxidation.

Rapid thermal annealing (RTA) is receiving considerable attention for the activation of implanted dopants and the removal of ion implant damage (1). Both infrared radiation and incoherent light heatings have been used successfully in defect annealing. The purpose of RTA is to reduce the thermal budget and thereby to prevent significant diffusion of dopants. Recent work (2) has been reported on the use of tungsten-halogen lamps to grow thin device quality silicon dioxide for potential use in MOS VLSI gates. That work was limited to the growth of approximately 130Å of SiO_2 in dry oxygen at 1150°C. The present work extends the temperature range and investigates the growth of thicker oxide for both dry and wet oxidants as well as for (111) and (100) substrates with both boron and phosphorus as dopants.

The rapid thermal oxidations were carried out in commercial computer-controlled rapid thermal processors, Heatpulse 2101 and 210-T (3). Silicon substrates of 100 mm diameter with various doping concentrations of boron and phosphorus as well as (100) and (111) orientations were utilized in this study. All wafers received a H_2SO_4:H_2O_2 (4/1 by volume) clean followed by 15 min rinsing in deionized water and drying in nitrogen prior to oxidation. Dry oxidation was carried out exclusively in the Heatpulse 2101 rapid thermal processor. The quartz

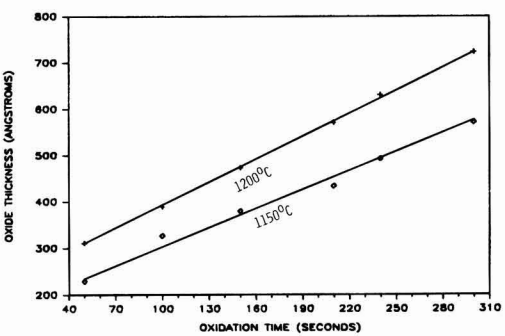

Fig. 1. Rate of oxidation in dry oxygen of (100) boron-doped (5-20 Ω-cm) silicon at 1150° and 1200°C.

*Electrochemical Society Active Member.

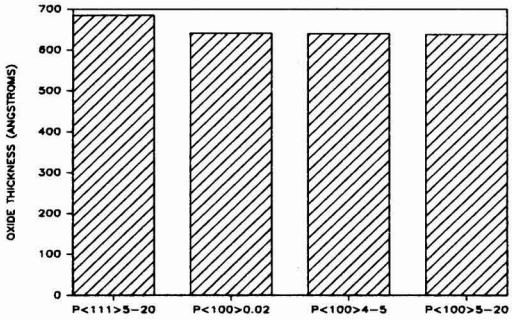

Fig. 2. Oxide thickness vs. orientations and boron doping concentrations of rapid thermal oxidation at 1200°C for 4 min in dry oxygen.

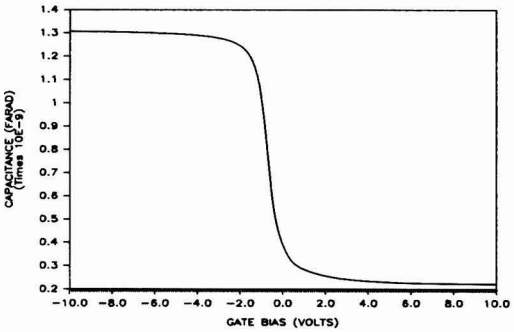

Fig. 3. 1 MHz capacitance-voltage characteristics of a dry rapid thermal oxide MOS structure on boron-doped (111) silicon.

chamber was first purged with argon for 60s and ramped to the preoxidation temperature of 1000°C in argon, stabilized for 10s, and then ramped to the oxidation temperature of 1150° or 1200°C in oxygen. After the completion of oxide growth, the oxygen flow was discontinued and the quartz chamber was again purged with argon while being held for 20-30s at the growth temperature as a postannealing cycle. Wet oxidation was performed in a modified Heatpulse 210-T fitted with a bubbler at the gas inlet to enable steam to be used as the wet oxidant. MOS capacitors were fabricated on the oxide films by evaporating approximately one micron of aluminum which was patterned and etched to produce capacitor dots of 1.5 mm in diameter. The wafers were then annealed in 100% H_2 for 30 min at 450°C followed by backgrinding and back-side gold evaporation for backside ohmic contact.

Figure 1 depicts the rate of oxidation in dry oxygen of (100) boron-doped (5-20 Ω-cm) silicon at 1150° and 1200°C, respectively. Straight lines have been drawn through the data points to show approximate linear growth rates in the oxidation duration of 50-300s. The linear rate constants are determined to be 82 and 98 Å/min for oxidation temperatures of 1150° and 1200°C, respectively. The comparable rate constants for furnace grown oxides at these temperatures are 90 (4) and 93 Å/min (5) for 1150° and 1200°C in dry oxygen, respectively. Linear growth rate similar to that reported by Deal and Grove (6) was obtained for wet oxidation in the 210-T rapid thermal annealer at 1150°C, with the resultant wet oxide thickness up to 3000Å. Light is known to enhance the growth rate of oxides (7), however, photon energies greater than 3 eV are required. The spectrum for the tungsten-halogen lamps used in this study has only a small portion in this energy range, hence the major effects are simply heating. At 1200°C, the oxidation rate for boron-doped (100) silicon was essentially independent of doping concentrations as shown in Fig. 2. Less orientation dependence of oxide growth rate was also noted. Similar trends were found to exist for phosphorus-doped silicon based on limited data. The optical refractive indexes varied from 1.44 to 1.46, with larger refractive indexes measured in the oxides grown at greater than 100s at the oxidation temperatures of 1150° and 1200°C, presumably due to the densification effects.

High frequency (1 MHz) capacitance-voltage characteristics were obtained using a HP 4192 A impedance analyzer interfaced with a HP 9920 computer for real time processing of data. Figure 3 shows typical C-V characteristics of a dry oxide MOS structure on (111) boron-doped silicon. The C-V curves were characterized by a sharp transition from accumulation to inversion regime. Oxide fixed charge densities in the range of low and middle 10^{10} cm^{-2} were measured in these (100) and (111) MOS structures, respectively. No hysteresis was observed in the accumulation, depletion, and weak inversion regimes as the gate bias swept from accumulation to inversion and vice versa, although a slight hysteresis was observed in the strong inversion regime due to the long lifetime of minority carriers. Low interface state density was found by comparing the measured 1 MHz C-V curves to the theoretical high frequency C-V characteristics. The MOS structures were subjected to a +/− 2.0 MV/cm electric field stress test at 300°C for 5 min, and the resultant C-V characteristics showed no negative bias-temperature instability. Mobile ion density lower than 10^{10} cm^{-2} was deduced from the shift of the C-V characteristics under negative and positive electric field stress. Dielectric strength of these rapid thermal oxides was centered around 8 MV/cm.

In summary, we have demonstrated that RTA systems can be used to grow device-quality silicon dioxide on silicon over a wide range of thicknesses to be compatible with most current MOS processes. Rapid thermal oxidation in wet oxidant or steam was also demonstrated. Orientation and doping concentration dependences on the grown oxide thickness were minimized in dry rapid thermal oxidation at 1150° and 1200°C. Although linear growth rate was observed over oxidation duration of 50-300s, more data are needed to better understand the growth kinetics.

Manuscript received Dec. 9, 1985.

Texas Instruments Incorporated assisted in meeting the publication costs of this article.

REFERENCES

1. J. Narayan, D. W. Holland, R. Edy, J. J. Wortman, V. Ozguz, and G. A. Rozgonyi, 41st Device Research Conference, Burlington, VT, June 20-23, 1983.
2. J. Nulman, J. R. Krusius, and A. Gat, *IEEE Electron. Device Lett.*, **EDL-6,** 205 (1985).
3. A. G. Associates, Palo Alto, CA.
4. E. A. Irene and D. W. Dong, *This Journal,* **125,** 1149 (1978).
5. B. E. Deal, Lecture Notes, CEI, Palo Alto, CA.
6. B. E. Deal and A. S. Grove, *J. Appl. Phys.,* **36,** 3770 (1965).
7. S. A. Shaffer and S. A. Lyon, *J. Vac. Sci. Technol.,* **21,** 422 (1982).

On the Effect of Impurities on the Photovoltaic Behavior of Solar Grade Silicon

II. Influence of Titanium, Vanadium, Chromium, Iron, and Zirconium on Photovoltaic Behavior of Polycrystalline Solar Cells

S. Pizzini,* L. Bigoni, and M. Beghi

Department of Physical Chemistry and Electrochemistry, University of Milano, Milano, Italy

C. Chemelli

Department of Physics, Polytechnic School of Milano, Milano, Italy

ABSTRACT

Structural, electrical, and photovoltaic properties of single impurity doped polycrystalline silicon were investigated in order to forecast the behavior of more complicated impurity matrixes, like those deriving from upgrading MG silicon. To this purpose, silicon was doped with increasing amounts of titanium, vanadium, chromium, iron, and zirconium, and the diffusion length of minority carriers was measured as a function of the impurity concentration and microstructural features like grain boundaries (GB), dislocations, twins, and stacking faults. Results are displayed in three-dimensional diagrams which permit observations on the dependence of L_D simultaneously with the impurity concentration and with the total density of electrically active structural defects.

It is already well-known that impurities, at concentration above certain critical threshold values, could severely degrade the electrical and photovoltaic characteristics of single crystal silicon (1, 2). This effect has been shown to be influenced by thermal and gettering treatments which seem to indicate that the degree of impurity deactivation is inversely proportional to the diffusion constants of the elements (3) but that interactions of less noble impurities with dissolved oxygen take place also (4-5). Very little, however, is known on the corresponding effects of the same impurities in polycrystalline silicon (6), where the situation is complicated by the additional presence of structural defects like grain boundaries, dislocations, twins, and stacking faults.

As for the influence of grain boundaries (GB), while it is known that minority carrier properties depend on the grain size up to 1 mm (7, 8), it has been also suggested that the electrical effects of GB could depend on the type of boundary and on its interaction with dislocations and impurities (7). This does not necessarily mean, as has been strongly felt in the past, that in polycrystalline materials the purity requirements are somewhat relaxed with respect to a single crystal material but that the impurities behave, in polycrystalline samples in a rather different fashion than in single crystal material. The reported evidence (1), that the threshold concentration of impurities for structural breakdown is lower by up to a factor of ten in polycrystals, supports this conclusion, as also does the reported distribution of active impurities within the grains of polycrystalline materials that depend on the individual impurities (1, 6).

There is, therefore, an urgent need of comprehensive and systematic information on the role of impurities in polycrystalline silicon, considering that a "solar grade" specification for polycrystalline silicon would permit us to define the critical threshold concentration of impurities in solar grade feedstocks.

To this purpose, we have carried out (9-12) a systematic investigation on the electrical and photovoltaic effects of those impurities, like titanium, vanadium, chromium, iron, and zirconium, which appear to be the major contaminants of solar silicon feedstocks produced via the carbothermic reduction of quartz which we still consider the most viable alternative to low cost silicon (13, 14). As independent work and interlaboratory comparison gave significant support to the reliability of diffusion length values, which are moreover a measure of the properties of the untreated material, we present here a discussion of the experimental relationships between L_D, microstructure and impurity concentration. We have reported in an earlier paper a thorough discussion of the relationships between photovoltaic properties, microstructure, and impurity concentration (9).

*Electrochemical Society Active Member.

Experimental

Crystal growth procedures.—B-doped single crystal and polycrystalline ingots were prepared from Dynamit-Nobel electronic grade silicon by Czochralski (CZ) pulling under argon gas at atmospheric pressure using an Elmat-type puller and (111) oriented single crystal seed manufactured by Dynamit-Nobel Silicon, or polycrystalline seeds cut from directionally solidified polycrystalline ingots (see below). The crystal growth rate was taken close to 7.5 cm/h, with a seed rotation of 12-14 rpm and a crucible rotation of 2-3 rpm, while keeping the growth completed when the 70% of the 1 kg charge was solidified.

The necking procedure was only performed in the case of single crystal growth. The radial temperature gradients, measured with a Pt/Pt 10% Rh thermocouple about 1 cm below the liquid interface are of the order of 12°C/50 mm at a temperature of 1450°C measured in the center of the crucible.

Doping was carried out by adding the proper amounts of boron and metals to the charge. Titanium (Carlo Erba, ACS grade), vanadium (Johnson & Matthey, Puratronic), and iron (Carlo Erba, ACS grade) were used in the form of wires, zirconium, either in form of powder (Carlo Erba, RLE grade), or sheets (Goodfellow metals, 99.8%), while chromium was used only in form of powder (Goodfellow metals, 99%). For boron doping a silicon-boron alloy (Dynamit–Nobel Silicon) having a resistivity of 0.003 ÷ 0.005 Ω/cm was used throughout. For comparison purposes, directionally solidified (DS) ingots grown in a Bridgman-Stockbarger type furnace were also considered. These ingots were prepared under reduced pressure of argon in 12 × 12 or 23 × 23 cm² square section quartz molds at an average growth rate of 1.5 cm/h and appear strictly columnar, with most of the grains oriented parallel to the vertical axis of the furnace.

The inner walls of the crucibles were coated with a few microns thick layer of silicon nitride, which was shown to avoid the sticking of silicon onto the quartz walls. In the case of DS ingots, the radial temperature gradients were not experimentally determined, but the thermal configuration of the hot and cold chamber, as well as of the heat sink, was optimized in order to ensure the propagation of a planar solidification front.

This latter condition can be easily verified by deliberately introducing a sudden freezing of the liquid when

90% of the charge is already solidified and cutting the ingot parallel to the vertical axis of the furnace in order to determine the shape of the solidification interface.

Structural characterization.—On both CZ and DS materials, microstructural characterization of slices cut normally in the growth direction was systematically carried out by measuring the average Sirtl etch pits density N_D cm^{-2} and the average length density of grain boundaries L_{GB} cm^{-1}, the former kept as a measure of the average dislocation density.

Twin patterns were neglected from the analysis of structural defects, as they were already observed to be electrically inactive or definitely less active than most of the grain boundaries (15).

For the determination of L_{GB}, the slices were first chemically polished using a modified CP4 etch ($7HNO_3$-4HF-3HAc-$4H_3PO_4$) and then Sirtl-etched at room temperature for about 10 min. Eventually, after rinsing and drying, the total length of GB on a fixed area was measured using optical microscope images at fixed magnification and a line-scanning technique.

The sampling is normally carried out on 15 or 25 positions of each sample.

This technique was shown to be remarkably sensitive and reproducible on good samples, with relatively few twin patterns or lineages and free of microcrystalline regions and meandering grain boundaries.

In this case, as can be observed in Table I, where we report an example of the reproducibility of L_{GB} values determined in two independent sets of measurements for each sample (albeit the reproducibility within the different sets of measurements is close to 30%, the standard deviation remains sensibly constant) and the L_{GB} value as determined by optical microscopy are comparable (see Table II) to the value determined by secondary electron images (SEI) and EBIC. Conversely, on heavily twinned regions or on finely microcrystalline samples, the determination of L_{GB} from optical images is difficult or even impossible, as often it occurs that strongly recombining grain boundaries can only be visualized by the EBIC technique (16).

Table I. Reproducibility of L_{GB} measurements carried out in double on different 10 × 10 cm^2 DS slices

Sample	$\bar{L}_{GB}$ (a)	S_x[a]	$\bar{L}_{GB}$ (b)	S_x	$\lvert\Delta\bar{L}_{GB}\rvert/L_{GB}$ (%)
176/41	35.33	11.40	28.71	11.15	23
236/13	16.81	11.03	9.94	8.79	69
236/31	16.31	18.07	18.33	12.00	11
236/52	24.8	13.06	22.63	13.66	10
238/14	23.19	17.32	28.19	16.80	18
238/31	23.19	13.88	14.47	12.76	60
238/73	16.40	13.05	12.87	8.64	27
240/13	29.00	13.70	17.25	9.99	68
240/31	18.33	14.79	21.50	12.13	15
				Average	33.4

[a] S_x is the standard deviation.

Table II. Comparison between L_{GB} determined via optical microscopy, SEM, and EBIC images on different positions of two as-grown samples [from Ref. (12)]

Sample	L_{GB} opt. (cm^{-1})	L_{GB} (SEM) (cm^{-1})	L_{GB} (EBIC) (cm^{-1})
220/12			
A		9.6	6.7
C		7.6	4.0
B1		17.9	10.4
B2		28.8	8.2
Average	20.4	16.0	7.3
220/31			
A		21.8	
B		6.2	
C		1.8	
Average	12.4	9.9	12.4

Table III. Comparison between impurity content in CZ and DS grown silicon ingots and in the electronic grade starting material

	E.G. silicon	W176/21	W176/61	SF21/60[a]	SF24/5[b]	Sensitivity (μg/g)
Ag	<6E-4	<3.E-4	<4E-4	3.4E-4	<3E-4	1E-3
As	1E-5	<4E-6	<4E-6	3.7E-5	4.1E-5	1E-5
Au	1.8E-5	5E-6	3.5E-6	3.2E-6	2E-6	1E-7
Ba	<7E-3	<6E-3	<6E-3	<6E-3	<8E-3	2E-2
Co	2.3E-4	2.1E-4	1.4E-4	1.8E-4	7E-5	5E-5
Cr	1.1E-4	<1E-4	<1E-4	5E-4	<2E-4	7E-5
Cu	1.6E-4	1.5E-3	8.7E-4	2.3E-3	1.8E-3	1E-3
Fe	<5E-2	<4E-2	<4E-2	<5E-2	<2E-2	7E-3
K	4E-3	<5E-3	<5E-3	<2E-3	<2E-3	
Mo	<9E-4	<5E-4	<5E-4	<4E-4	<3E-4	5E-4
Na	2.1E-4	2.3E-4	2.1E-4	8E-4	3.9E-4	1E-5
Ni	<2E-2	<1E-2	<2E-2	<9E-3	<1E-2	2E-2
Ta	<2E-4	<2E-4	<2E-4	6E-4	<1E-4	
Te	<8E-4	<6E-4	<2E-4	<8E-4	<9E-4	2E-3
Ti	<1E-1	<1E-1	<9E-2	<5E-2	<7E-2	1E-1
Zr	<2E-2	<2E-2	<2E-2	<2E-2	<3E-2	5E-2

[a] Doped with 1000 ppm of zirconium in the liquid.
[b] Doped with 1000 ppm of titanium in the liquid.

Chemical characterization.—Chemical characterization included oxygen and carbon content determination via FT-IR spectroscopy and NAA (neutron activation analysis) for metal impurities. Oxygen and carbon content was found comparable with that already reported in Ref. (9) and ranged around $1.0 \cdot 10^{17}$ atm/cm^3 for oxygen and $3.5 \cdot 10^{17}$ atm/cm^3 for carbon.

Metallic impurities content in undoped CZ and DS ingots was found significantly comparable to that of the EG silicon feedstock, as is shown in Table III, where the NAA results relative to four different DS and CZ samples and to the EG silicon feedstock are reported.

Quite generally, moreover, the concentration of the metallic impurity content in the doped solids was found below the limits of detectability of both the NAA and ICP-ES technique, as is shown in Table III and IV. Therefore, it was calculated for each slice using the effective segregation coefficients (17), and the initial melt concentration assuming normal freezing conditions (18)

$$\frac{Nx}{N^0x} = K(1 - g)^{K-1} \qquad [1]$$

where

N_x = impurity concentration present in the crystal at the freezing interface after the freezing of a fraction g of the initial melt volume
N_x^0 = impurity added to the melt before freezing
K = effective segregation coefficient

and taking into account for each particular ingot its geometrical shape in order to calculate the amount of frozen liquid at a certain length of the ingot, as well as the fraction of solid lost by cutting.

Electrical characterization.—Electrical characterization included the determination of the resistivity using the collinear four-probe method according to the ASTM specification F84-73, of the type of the majority carriers, using the hot probe method and the diffusion length of the minority carriers according to the procedure illustrated in the ASTM specification F-391-73T (1974) using for the wavelength dependence of the adsorption coefficient the expression

$$\alpha = 0.526367 - 1.14425\,\lambda^{-1} + 0.585368\,\lambda^{-2} + 0.039958\,\lambda^{-3}$$

(where λ is expressed in μm) which is characteristic of stress-relieved silicon.

A Jobin Ivon monochromator (Model H25) was used in connection with a mechanical light chopper (driven by a constant dc source), with a PIN diode and a sample holder.

The sample is arranged in a MIS configuration, using a transparent conducting glass (Baltacron 210-Balzers) as

Table IV. Results of NAA analysis of impurity doped polycrystalline silicon samples (in μg/g)

Sample	Impurity type	Impurity concentration in the melt	Impurity concentration found	Sensitivity
SF5-3	Fe	5	<1E-2	7 E-3
SF5-69	Fe	5	6E-2	
SF4A-2	Fe	50	<1E-2	
SF4A-32	Fe	50	<1E-2	
SF3B-1	Fe	500	<3E-2	
SF8A-1	Ti	2	<6E-2	1 E-1
SF8A-58	Ti	2	<8E-2	
SF7-2	Ti	20	<6E-2	
SF7-35	Ti	20	<1E-1	
SF6-2	Ti	200	<8E-2	
SF11-2	Zr	1	<4E-2	5 E-2
SF11-54	Zr	1	<3E-2	
SF10-4	Zr	10	<6E-2	
SF10-11	Zr	10	<5E-2	
SF9-1	Zr	100	<2E-2	

the metal and a 0.3 mm thick sheet of Mylar as the insulator.

The PIN diode and the sample are connected through two lock-in amplifiers (EG&G, Model 5205) to a HP-85 microcomputer, in order to considerably improve the signal-to-noise ratio obtainable using a mechanical switch to connect, alternatively, the sample and the PIN to the lock-in amplifier.

Before the measurements are taken, the silicon slices are chemically polished using standard CP4 mixtures (etching time 2-5 min, depending on the temperature of the etching solution) in order to remove the damage resulting from the slicing process.

As a standard procedure, at least 9 determinations of ρ and L_D on each sample were carried out and the average value taken as a measure of ρ and L_D. The standard deviation was found for both ρ and L_D to be close to the 20% of the average value determined, independent of the absolute value, as can be observed in Table V for individual

Table V. Distribution of the L_D values among a 10 × 10 cm² slice

Sample	L_D (μm)	Sample	L_D (μm)
W212-9	26.0	W212-71	30.3
	44.8		32.2
	31.8		25.2
	39.0		32.2
	26.6		26.8
	32.9		33.9
	39.8		22.6
	38.1		35.4
	26.8		40.2
Average	33.9		31.0
S_x	6.8		5.5

L_D determinations. An exception to this is the L_D measurements on samples presenting values in excess of 200 μm, where the standard deviations are systematically larger.

It should be remarked here that by the procedure adopted for the electrical characterization of polycrystalline samples no kind of information could be obtained on "local" properties, which actually are shown to depend on the nature of individual grains investigated and which will be discussed in another paper (16), but only good averages which can therefore be used to display the statistical dependence of a physical property like ρ or L_D on the microstructure.

Experimental Results and Discussion

Majority carriers properties.—The results of electrical and structural characterization of undoped and doped samples are reported in Tables VI and VII.

It could be remarked that for a limited number of samples an anomalous dependence of the resistivity on the fraction of the ingot solidified is observed. For this reason we submitted a selected number of specimens to short (30 min) thermal annealing cycles at 450° and 600°C, in order to activate and deactivate oxygen thermal do-

Table VI. Structural and electrical properties of reference single crystal CZ and polycrystalline DS 10 × 10 cm² silicon samples

Sample	Type of sample	Slice number	L_{GB} (cm⁻¹)	N_D (cm⁻²)	$L_{GB}N_D$ (cm⁻³)	L_D (μm)	ρ (Ω-cm)
SF1	Single crystal	2					3.5
		25		1.0E3		200:280	3.2
		49					2.9
SF2	Poly	2	20.2	1.5E4	3.0E5	120	3.8
	CZ	37	4.6	3.8E4	1.7E5	220	3.8
		81	68.8	9.6E4	6.6E6	90	3.9
SF16	Poly	5	28.8	1.1E5	3.2E6	130	4.1
	CZ	24	33.4	1.1E5	3.7E6	124	4.2
		42	35.7	1.1E5	3.9E6	61	3.1
W176	Poly	20	34.1	3.3E4	1.0E6	87	3.2
	from 10 × 10	40	27.7	1.0E4	2.9E5	220	3.0
	ingot	60	27.7	6.4E4	1.8E6	220	3.2
		80	23.8	1.2E4	2.8E5	220	
W193	Poly DS	19	20.9	1.5E4	3.1E5	174	2.7
	from 10 × 10	39	24.6	3.5E4	8.6E5	200	2.2
	ingot	61	24.7	4.1E4	1.0E6	220	
		76	30.4	6.7E4	2.0E6	66	1.5
W197	Poly DS	21	26.3	5.0E4	1.3E6	128	1.6
	from 10 × 10	40	26.4	1.1E3	2.8E4		1.4
	ingot	66	11.1	5.0E3	5.6E4	180	
		80	15.4	8.0E3	1.2E5	180	1.5
W216	Poly DS	15	19.9	8.7E4	1.7E6	68	3.5
	from 23 × 23	45	20.6	6.4E4	1.3E6	177	3.2
	ingot	65	20	6.4E4	1.3E6	142	
		85	24.5	1.7E5	4.3E6	19	1.7
W218	Poly DS	17	13.0	2.1E4	2.7E5	79	2.4
	from 23 × 23	37	10.8	8.5E3	9.1E4	143	2.6
	ingot	75	7.7	9.1E4	6.9E5	220	1.7
W220	Poly DS	13	20.4	2.2E5	4.6E6	48	2.4
	from 23 × 23	32	12.3	1.9E4	2.3E5	220	2.5
	ingot	52	11.0	8.4E4	9.3E5	220	1.6
		72	10.7	1.3E5	1.4E6	141	1.4
W221	Poly DS	13	10.5	1.5E4	1.6E5	55	4.2
	from 23 × 23	32	8.7	2.3E3	2.0E4	192	3.8
	ingot	52	9.2	2.3E4	2.1E5	220	3.2
		72	12.3	9.2E4	1.1E6	220	2.6

Table VII. Structural and electrical properties of CZ-grown, impurity doped silicon ingots

Sample	Type of impurity	C_i[a]	g[b]	Nx[c]	ρ (Ω cm)	L_{GB} (cm^{-1})	N_D (cm^{-2})	$L_{GB}N_D$ (cm^{-3})	L_D (μm) experimental	L_D (μm) theoretical	ΔL_D (%)
SF8A	Ti	2	0.02	2.1E11	3.8	27.0	9.3E4	2.5E6	120	130	− 8
			0.14	2.4E11		30.1	1.6E5	5.1E6	130	105	+19
			0.22	2.7E11	3.4	35.5	1.1E5	4.0E6	80	115	−30
			0.32	3.1E11		27.8	1.5E5	4.2E6	80	110	−27
			0.42	3.6E11	3.5	36.3	1.3E5	4.6E6	60	100	−40
SF20	Ti	10	0.02	1.1E12	3.5	25.5	6.0E4	1.5E6	90	135	−33
			0.24	1.4E12	3.0	20.9	1.0E5	2.1E6	80	124	−35
			0.43	1.8E12	3.0	29.4	1.1E5	3.2E6	60	110	−45
SF7	Ti	20	0.01	2.1E12	3.7	22.4	1.0E5	2.3E6	40	108	−63
			0.14	2.4E12		21.6	1.3E5	2.7E6	40	100	−55
			0.30	2.9E12	3.4	27.4	9.5E4	2.6E6	18	90	−80
			0.38	3.4E12		30.5	1.6E5	4.9E6	20	90	−78
			0.51	4.3E12	3.4	29.3	1.5E5	4.4E6	12	80	−85
SF19	Ti	100	0.05	1.1E13	5.0	24.4	6.7E4	1.6E6	25	81	−69
			0.14	1.2E13	4.0	25.4	7.4E4	1.9E6	25	80	−69
			0.36	1.6E13	3.3	21.1	1.2E5	2.6E6	20	70	−71
SF6	Ti	200	0.01	2.1E13	3.7	20.6	1.2E5	2.5E6	22	62	−65
			0.18	2.5E13	3.8	24.1	8.1E4	1.9E6	20	58	−66
			0.43	3.7E13	2.9	26.4	1.3E5	3.6E6	12	48	−75
SF23	Ti	500	0.03	5.5E13	4.2	27.3	9.5E4	2.6E6	14	42	−67
			0.12	6.0E13	3.2	20.8	1.0E5	2.1E6	17	40	−58
			0.35	8.1E13	3.2	20.3	1.9E5	3.8E6	13	34	−62
SF24	Ti	1000	0.03	1.1E14	3.3	25.2	6.3E4	1.6E6	18	30	−40
			0.17	1.3E14	3.8	24.1	8.9E4	2.1E6	14	27	−48
			0.39	1.7E14	4.0	18.3	8.9E4	1.6E6	9	25	−64
SF31	V	5	0.03	5.6E11	4.7	25.8	8.3E4	2.1E6	68	132	−48
			0.10	6.1E11		20.5	4.5E4	9.3E5	97	153	−37
			0.19	6.8E11		31.4	9.5E4	3.0E6	84	120	−30
			0.34	8.3E11	3.9	39.9	1.4E5	5.6E6	80	98	−19
			0.45	1.0E12		35.0	1.9E5	6.7E6	70	92	−24
			0.51	1.1E12	3.4	39.1	1.9E5	7.5E6	66	87	−24
SF32	V	50	0.09	6.0E12	3.7	26.8	1.1E5	2.9E6	40	91	−56
			0.23	7.1E12	3.4	31.8	1.0E5	3.3E6	32	85	−62
			0.36	8.5E12	3.0	35.5	1.6E5	5.9E6	27	74	−64
SF33	V	500	0.05	5.8E13	3.5	26.0	6.4E4	1.7E6	13	39	−67
			0.18	6.7E13	3.5	38.3	1.3E5	4.9E6	13	36	−64
			0.38	8.8E13	3.5	25.4	7.2E4	1.8E6	14	32	−56
SF43	V	1800	0.01	2.0E14	13.1	31.6	7.3E4	2.3E6	9	22	−59
			0.1	2.2E14	9.0	25.4	1.0E5	2.6E6	11	21	−59
			0.17	2.4E14	8.0	20.6	1.1E5	2.2E6	10	20	−50
SF44	V	3600	0.03	4.1E14	5.0	11.3	5.2E4	5.8E5	10	15	−33
			0.09	4.3E14	6.0	30.5	8.2E4	2.5E6	10	15	−33
			0.19	4.9E14	8.0	42.3	1.6E5	6.5E6	10	14	−29
SF30	Cr	100	0.16	3.5E13	3.7	17.6	5.4E4	9.5E5	39	151	−74
			0.26	4.0E13	3.5	23.5	1.0E5	2.4E6	31	126	−75
			0.38	4.7E13	3.7	24.3	1.1E5	2.7E6	31	121	−74
SF29	Cr	200	0.13	6.8E13	3.6	20.7	5.4E4	1.1E6	25	140	−82
			0.26	8.0E13	2.8	24.5	1.1E5	2.7E6	26	115	−77
			0.40	9.8E13	3.8	28.5	8.5E4	2.4E6	27	115	−77
SF28	Cr	500	0.07	1.1E14	2.8	24.5	8.8E4	2.1E6	22	117	−81
			0.22	1.9E14	2.8	17.5	1.1E5	2.0E6	18	107	−83
			0.35	2.3E14	2.6	14.1	1.5E5	2.6E6	20	99	−80
SF5B	Fe	5	0.02	8.1E11	6.6	19.6	3.7E4	7.3E5	170	170	+55
			0.07	8.6E11		36.6	1.2E5	4.4E6	164	111	+24
			0.15	9.4E11	9.5	34.0	1.4E5	4.8E6	134	108	+ 7
			0.35	1.2E12	10.3	43.0	1.7E5	7.3E6	98	92	−34
			0.43	1.4E12		32.0	1.4E5	4.6E6	73	110	
SF18	Fe	10	0.04	1.7E12	3.4	18.8	3.4E4	6.4E5	200	173	+16
			0.07	1.7E12		21.8	6.6E4	1.4E6	183	153	+20
			0.17	1.9E12	3.2	29.1	7.1E4	2.1E6	165	139	+20
			0.34	2.4E12	2.9	20.6	7.8E4	1.6E6		148	−35
			0.45	2.9E12	2.96	34.7	1.7E5	6.0E6	120	100	+20
SF17	Fe	25	0.04	4.2E12	3.4	31.1	1.1E5	3.5E6	75	120	−38
			0.07	4.3E12	3.3	40.5	1.4E5	5.7E6	109	101	+ 8
			0.11	4.5E12	3.3	33.7	9.5E4	3.2E6	121	123	− 2
			0.14	4.7E12	3.1	41.1	1.6E5	6.6E6	82	99	−17
SF4A	Fe	50	0.01	8.1E12	4.6	26.5	1.3E5	3.4E6	70	120	−42
			0.13	9.2E12	3.8	50.2	1.8E5	9.0E6	30	85	−65
			0.19	9.9E12	=	29.1	1.4E5	4.2E6	48	110	−56
			0.27	1.1E13	3.4	51.8	1.8E5	9.3E6	25	84	−70
SF13	Fe	300	0.05	5.1E13	5.3	24.5	9.5E4	2.3E6	35	130	−73
			0.24	6.3E13	5.2	26.6	1.0E5	2.7E6	32	120	−73
			0.43	8.4E13	5.9	31.0	1.3E5	3.9E6	26	110	−76
SF3B	Fe	500	0.03	8.3E13	6.6	14.5	6.0E4	8.8E5	25	150	−83
			0.22	1.0E14	9.5	26.6	1.1E5	3.1E6	30	115	−74
			0.29	1.1E14	10.0	21.7	9.5E4	2.1E4	23	126	−82

[a] C_i is the concentration of the impurity into the melt, in μg/g.
[b] g is the fraction of ingot solidified.
[c] Nx is the concentration of the impurity into the solid, in atom cm^{-3}.

Table VIII. Influence of thermal annealing on the electrical conductivity of undoped and doped silicon

Sample	Slice no.	ρ(Ω cm) as grown	Sx	ρ(Ω cm) 450°C	Sx	ρ(Ω cm) 600°C	Sx	L_{GB} (cm^{-1})	N_D (cm^{-2})	Remarks
SF16	6	4.07	1.68	4.12	1.04	4.16	0.43	28.8	1.1E5	Microcryst. regions
	22	4.25	2.33	3.72	0.37	4.55	1.58	33.4	1.1E5	Microcryst. regions
	40	3.09	0.37	3.32	0.53	3.90	1.61	35.7	1.1E5	
W176	20	3.52	1.68	3.31	0.53	3.60	1.01	34.1	3.3E4	
	40	2.87	0.27	2.96	0.40	3.32	0.29	27.7	1.0E4	
	80	2.18	1.11	2.02	0.68	3.05	0.59	23.8	1.2E4	
SF33	7	4.02	1.06	3.80	0.09	4.43	0.74	26	6.4E4	V-doped
	25	3.13	0.22	3.87	0.70	4.42	1.12	38.3	1.3E5	
	53	3.75	0.24	3.85	0.77	4.65	0.68	25.4	7.2E4	
SF44	5	5.0	0.7	6.35	0.89	6.40	0.90	11.3	5.2E4	V-doped
	15	6.0	0.92	5.92	0.35	6.97	1.23	30.5	8.2E4	
	30	8.0	2.25	6.82	2.30	6.37	1.62	42.3	1.6E5	

nors (19-20) that could be responsible of this behavior, in the absence of other effects coming from the microstructure and/or from impurities.

Both could, in fact, exercise a non-negligible influence on ρ, considering that the current paths in a resistivity measurement carried out with the collinear four-probe method do cross the GB and that the measure is affected by the height of the potential barriers existing in correspondence to GB (21-22).

The results of measurements carried out by sampling each slice on 20 positions to improve the statistics are reported in Table VIII which shows that the annealing at 600°C, in general, does increase the electrical resistivity of the sample considered and that, therefore, thermal donors are not directly responsible for the anomalous behavior of the resistivity in polycrystalline silicon samples. Considering, however, that the absolute values and the dispersion of the ρ values in the as-grown samples are definitely affected by the microstructure and by the impurity content and considering also that oxygen nucleation is supposed to occur at temperature higher than 550°C (19), we preliminarily conclude that the majority carrier properties of polycrystalline silicon are sensible functions of the microstructure and that both the absolute values and the dispersion of the resistivity are affected possibly by oxygen and impurity redistribution between the bulk of the grains and the GB.

Incidentally, the fact that the expected activation of oxygen donors does not take place appreciably at 450°C could be also an indication of carbon-oxygen interactions, which are known to occur at this temperature (19, 23).

Fig. 1. Section (×1) of a polycrystalline silicon ingot grown with the DS technique cut perpendicularly to the growth direction.

Minority carriers properties: undoped samples.—It should be remarked first from Table VI, where we report the results of diffusion length measurements of undoped silicon samples that, in spite of the remarkably different microstructures exhibited by DS grown and CZ polycrystalline ingots (the former being columnar, see Fig. 1 and the latter strongly anisotropic, see Fig. 2), both are spread in a range of dislocation density N_D cm^{-1} and GB length density L_{GB} cm^{-1} values, without any apparent relationship with the growth procedure adopted.

Moreover, the diffusion length L_D of minority carriers does not seem to be influenced too much either by the anisotropicity or by the microstructure up to N_D values not larger than 10^5 cm^{-2} and L_{GB} values not larger than 28 cm^{-1}, as is shown in Fig. 3. While, as it can be observed by the examples reported in Table IX, it is affected by a heat-treatment at 650°C, which, apparently, levels the L_D values to a flat profile, indicating a considerable influence of oxygen and/or impurity redistribution on the activity of recombination centers.

Considering, however, that outside the range of N_D and L_{GB} values defined above, L_D was already shown to be influenced both by L_{GB} and N_D (7, 24) and that the outermost electrically active boundaries as detected by EBIC (see Fig. 5 and 8) generally do not coincide with the optical or secondary electrons images of the same samples (see Fig. 4 and 7) but instead with subgrain boundaries decorated by dislocations or with lineages (see Fig. 6 and 9), it is interesting to demonstrate the usefulness of the single microstructural term approximation, proposed in a previous paper (12) by taking the product ($L_{GB}N_D$) as a measure of the effective average electrical activity of structural defects.

This might be done considering that the lifetime of a polycrystalline material could be described by the expression

$$\frac{1}{\tau} = \frac{1}{\tau_0} + \frac{1}{\tau_s} \qquad [1]$$

Fig. 2. Section (×1) of a polycrystalline silicon ingot grown with the CZ technique cut perpendicularly to the growth direction.

Table IX. Influence of the annealing at 650°C on the diffusion length of minority carriers

Sample	Slice no.	L_D (μm) as grown samples	L_D (μm) after heating at 650°C
W238	12/5	30	50.5
	29/5	101	67.5
	72/5	91	64.7
W240	12/3	22	54
	29/3	69	53
	50/3	73	48.5
	71/3	40	44.7

(where τ_0 is the recombination time of minority carriers in the bulk of a single crystalline reference material, and τ_s is the recombination time at structural defects) provided that the two recombination events are independent of each other. Furthermore, by assuming that the mobility μ or the diffusivity D_n in the equation

$$L_D = (\mu\tau kTq^{-1})^{1/2} = (D_n\tau)^{1/2} \quad [2]$$

are constants and that the recombination probability at microstructural defects

$$w_s = 1/\tau_s$$

is a function of two independent variables x, y so that

$$w_s = w_x(x = L'_{GB})w_y(y = N'_D) \quad [3]$$

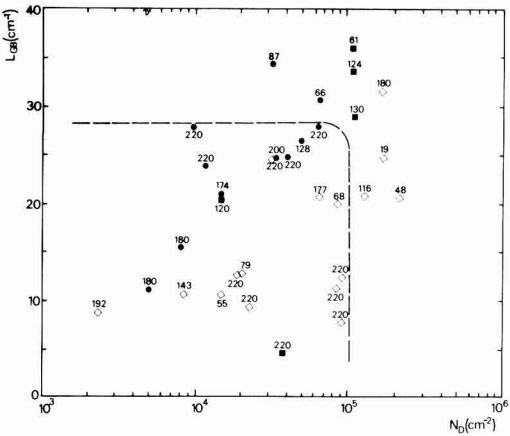

Fig. 3. Dependence of L_D on the microstructure for polycrystalline impurity free silicon samples.
▲ 20 × 20 cm² section ingots
● 10 × 10 cm² section ingots
■ CZ samples

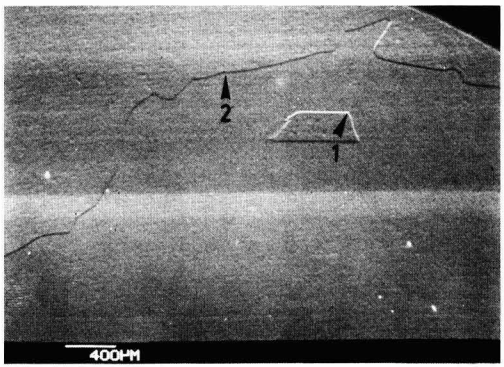

Fig. 4. S.E. image of an impurity free DS silicon sample

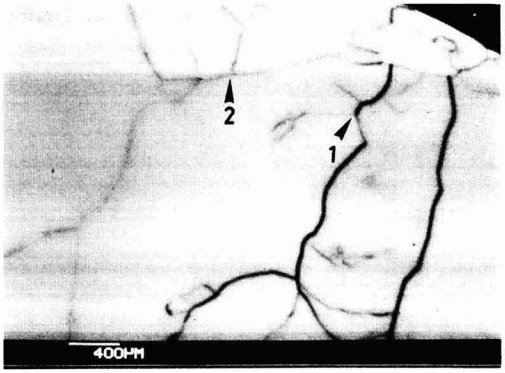

Fig. 5. EBIC image of the same sample as Fig. 4

Fig. 6. Optical image (×147), after Sirtl etch of a neighbor slice of the sample of Fig. 4 and 5.

we can write Eq. [4] by rearranging Eq. [1] using Eq. [2] and [3]

$$\frac{1}{L_D^2} = \frac{1}{L_D^{o2}} + \frac{k'k''}{C}(L_{GB} \cdot N_D) \quad [4]$$

where

L_D^o is the diffusion length in the reference single crystal

k', k'' are constants which average the different recombination cross sections of dislocations and GB in Eq. [3]

$$C = (\mu kT/q)$$

$$w_x(x = L'_{GB}) = k'L_{GB}$$

$$w_y(y = N'_D) = k''N_D$$

It appears that this model has intimate relationships with that already used by Hopkins and Davis (2) and later, within others by Maurice *et al.* (5), albeit assuming more explicitly that the only effect of structural defects is to reduce the lifetime of minority carriers while the mobility remains constant, and assuming, also, a synergistic effect of the different, individual structural defects. The fit of the experimental results with the model is shown in Fig. 10, where the model (dotted) curve has been drawn by rewriting Eq. [4] as follows

$$L_D = L_D^o\left[1 + \frac{k'k''}{C}L_D^{o2}(L_{GB}N_D)\right]^{-1/2} \quad [5]$$

and taking as the values of the constants

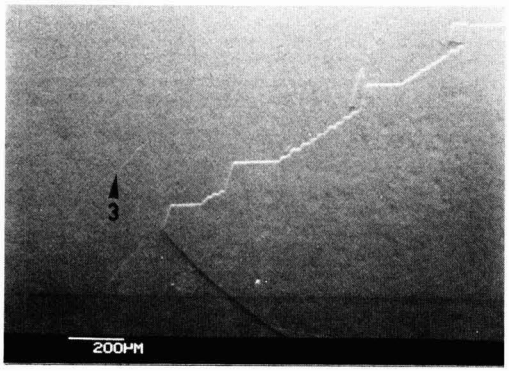

Fig. 7. S.E. image of an impurity free DS silicon sample

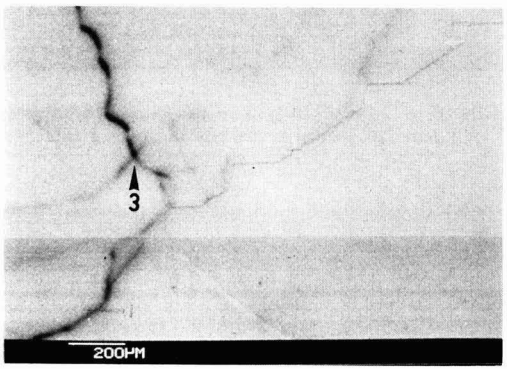

Fig. 8. EBIC image of the sample of Fig. 7

Fig. 9. Optical image (×147), after Sirtl etch of a neighboring slice of the sample of Fig. 7 and 8.

$$L_D^o = 200\ \mu m;\ \frac{k'k''}{C} L_D^o = 5 \cdot 10^{-7}\ cm^3$$

By considering that the average deviation of L_D values was shown to be close to 20% in the range of L_D where a dependence on the microstructure is particularly sensitive, one can conclude that the agreement is reasonably good.

It should be noted, however, that the assumption of constant mobility is only partially supported by experiments. As an example, a recent work of Mathian *et al.* (7) shows that the minority carrier mobility, μ_n, as deduced from independently measured L_D and τ_n values is slightly

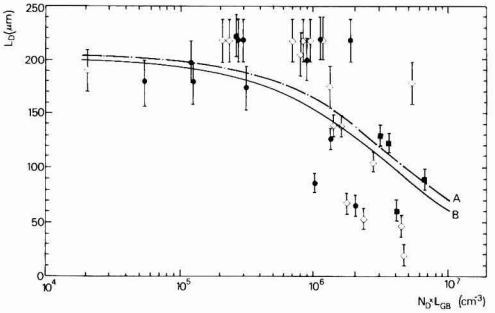

Fig. 10. Diffusion length of the minority carriers L_D in p-doped samples of impurity free polycrystalline silicon as a function of the microstructural parameter $L_{GB}N_D$ (see text).
■ CZ samples ● DS samples (10 × 10 cm² ingots)
◇ DS samples (23 × 23 cm² ingots)
dotted curve; Eq. [5] with $L_D^0 = 200\ \mu m$; $k'k''/C = 5 \cdot 10^{-7}$ cm³.

dependent on the density of all the defects which degrade the lifetime, with an empirical law which takes the form

$$\mu_n = 950\ \tau_n^{0.3} \qquad [6]$$

with μ_n in $cm^2V^{-1}s^{-1}$ and τ in μs.

As an attempt to improve the fitting, we could, therefore, rearrange Eq. [2] while using the lifetime dependent mobility term of Eq. [6]. While doing it, one obtains the equation

$$\frac{1}{L_D^{3/2}} = \frac{1}{L_D^{o3/2}} + \frac{k'k''}{C_1^{3/2}}(L_{GB}N_D) \qquad [7]$$

after having substituted μ in Eq. [2]

$$L_D = \left(9.5 \cdot 10^{-4}\tau^{1/3}\frac{kT}{q}\right)^{1/2} = C_1\tau^{2/3}$$

with τ in seconds

$$\tau = \left(\frac{L_D}{C_1}\right)^{3/2}$$

or, equivalently

$$L_D^{3/2} = L_D^{o3/2}[1 + k'k''\tau_o(L_{GB}N_D)]^{-1}$$

and

$$L_D = L_D^o\,[1 + k'k''\tau_o(L_{GB}N_D)]^{-2/3} \qquad [8]$$

where

$$\tau_o = \left(\frac{L_D^o}{C_1}\right)^{3/2}$$

We have reported, as a solid line in Fig. 10, the functional dependence of L_D according Eq. [8] using the following values for the constants

$$L_D^o = 200\ \mu m;\ k'k''\tau_o = 5 \cdot 10^{-7}\ cm^3$$

and the apparent results are that the use of a microstructure-dependent mobility term does not sensibly improve the agreement between the experimental results and the model.

Table X. Values of the model constants adopted for the calculation of L_D according to Eq. [10] for p-type materials (2)

Impurity	C_2	$N_{o,r}$
Chromium	9.2E-3	1.3E+14
Iron	1.2E-2	2.5E+14
Titanium	1.2E-2	2.6E+12
Vanadium	1.3E-2	2.5E+12
Zirconium	1.0E-2	3.6E+11

Doped samples.—The results of structural and electrical characterization of titanium, vanadium, chromium, and iron doped CZ silicon samples are reported in Table VII.

The results referring to zirconium doped samples have been omitted, because, in the $2.4 \cdot 10^{9}$-$1.9 \cdot 10^{12}$ atm/cm^3 range investigated, very large L_D fluctuations were systematically observed, that would mask any specific interaction effect. This behavior of zirconium has been accounted for already (9, 11, 12) on the basis of its large affinity with oxygen as well as its very small segregation coefficient ($K = 1.5 \cdot 10^{-8}$) that favors the setup of impurity segregation conditions (18, 20).

For the other dopants chosen, a smooth and progressive degradation of L_D is observed and in no case were constitutional breakdown conditions observed, even at the largest impurity concentrations. This is in good agreement with the expected behavior based on the known values of solubilities of the impurities added to the melt (17). Assuming, then, that in impurity doped polycrystalline materials the product $L_{GB}N_D$ also could be used to account for the influence of the microstructure on the diffusion length, the experimental values of L_D in impurity doped materials reported in Table VII can be displayed in L_D *vs.* $L_{GB}N_D$, N_x diagrams (see Fig. 11-14) where N_x is the concentration (in atom/cm^3) of the specific impurity considered.

In the same diagrams, we have also displayed the theoretical dependence of L_D on ($L_{GB}N_D$) and N_x, as $L_D = f(N_x, L_{GB}N_D)$ surfaces, which were calculated by extending the model already presented for undoped samples, by assuming:

1. That the dominant effect of both the impurities and microstructural defects is that of reducing the minority carriers diffusion length.

2. That no kind of interaction occurs between impurities and microstructure, which could be specifically responsible for the degradation of the minority carriers diffusion length. This would mean either, that no segregation of impurities takes place at GB or at the dislocations (which is contradicted by many experimental findings (1, 6, 11)) or that impurities segregated at GB or at the dislocations are electrically inactive. We assume therefore that the lifetime of the minority carriers is given by Eq. [1 bis] by adding an impurity dependent recombination time τ_i

$$\frac{1}{\tau} = \frac{1}{\tau_0} + \frac{1}{\tau_s} + \frac{1}{\tau_i} \qquad [1\text{ bis}]$$

in the case of a material containing a single impurity of the type i.

3. That the dependence of L_D on N_x in deep level doped single crystals could be deduced from the Davis and Hopkins model (2) already cited in the last section, which assumes the lifetime reduction as the dominant impurity effect. Under this assumption, the diffusion length dependence on impurity concentration is given by the equation

$$L_D = \frac{L_\lambda}{C_2}\left[1 + \frac{N_x}{N_{0,x}}\right]^{-1/2} \qquad [10]$$

where L_λ, C_2, and $N_{0,x}$ are model constants, of which C_2 and $N_{0,x}$ depend on the type of the impurity (see Table X) and $L_\lambda = 19.2$ μm. N_x is the concentration (in atom/cm^3) of the added impurity in solid solution. Considering that

$$\frac{L_\lambda}{C_2^{1/2}} = L_D^{\circ} \qquad [11]$$

we assume in our case that L_D° takes the value of 200 μm, which is the average of the measured diffusion lengths of electrons in our impurity-free single crystal or polycrystalline silicon (up to $L_{GB}N_D$ values not larger than $3 \cdot 10^{6}$

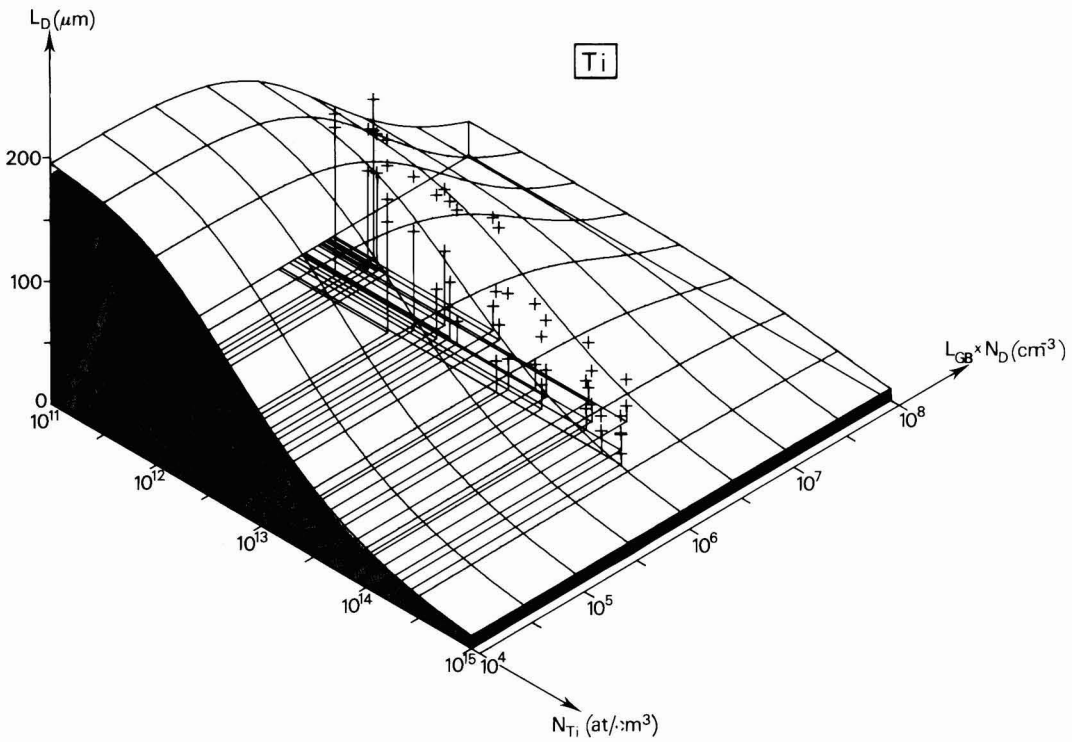

Fig. 11. Plot of the diffusion length L_D as a function of the titanium dopant concentration N_{Ti} (in the solid) and of the microstructural parameter ($L_{GB}N_D$). In the figure, the dependence of L_D on N_{Ti}, according to Ref. (2), is reported on the L_D, N_{Ti} plane and the dependence of L_D on $L_{GB}N_D$ according to Eq. [5] (using as L_D° a value of 200 μm and a $k'k'' L_D^{\circ 2} = 5 \cdot 10^{-7}$ cm^3) is displayed on the L_D, $L_{GB}N_D$ plane.

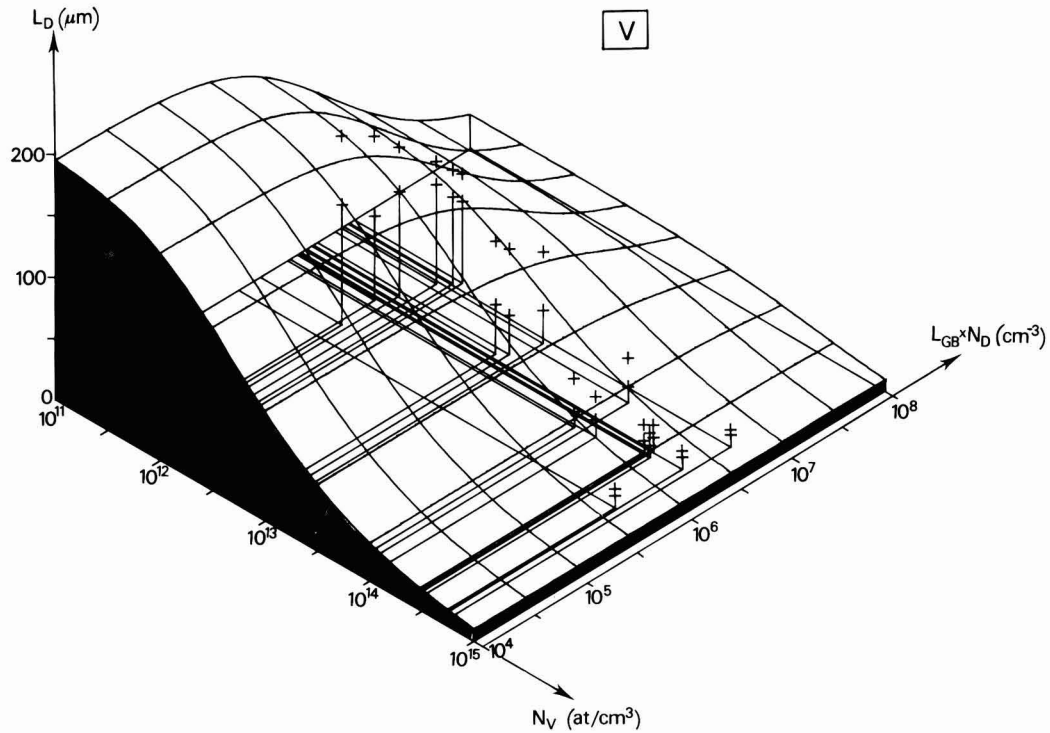

Fig. 12. Plot of the diffusion length L_D as a function of the vanadium dopant concentration N_V (in the solid) and of the microstructural parameter ($L_{GB}N_D$). In the figure the dependence of L_D on N_V, according to Ref. (2), is reported on the L_D, N_V plane and the dependence of L_D on $L_{GB}N_D$ according to Eq. [5] (using as $L_D{}^o$ a value of 200 μm and a $k'k''/C\ L_D{}^{O2} = 5 \cdot 10^{-7}$ cm^3) is displayed on the L_D, $L_{GB}N_D$ plane.

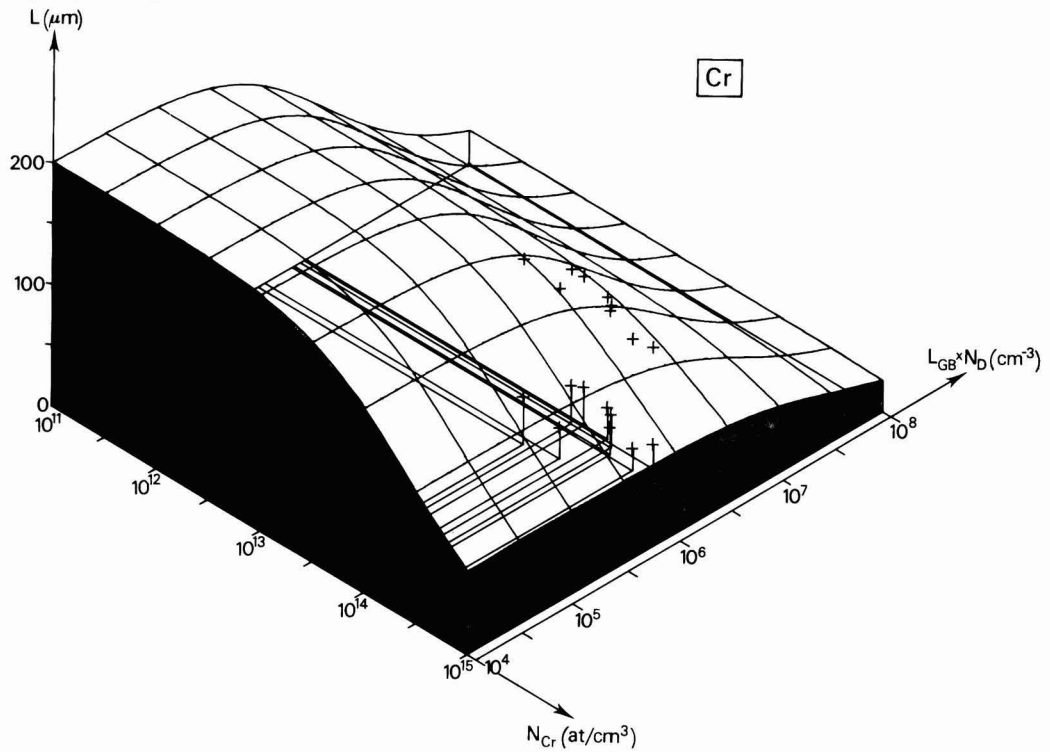

Fig. 13. Plot of the diffusion length L_D as a function of the chromium dopant concentration N_{Cr} (in the solid) and of the microstructural parameter ($L_{GB}N_D$). In the figure the dependence of L_D on N_{Cr}, according to Ref. (2), is reported on the L_D, N_{Cr} plane and the dependence of L_D on $L_{GB}N_D$ according to Eq. [5] (using as $L_D{}^o$ a value of 200 μm and a $k'k''/C = L_D{}^{O2} = 5 \cdot 10^{-7}$ cm^3) is displayed on the L_D, $L_{GB}N_D$ plane.

cm^{-3}, see last section) and which closely fit also with the Davis and Hopkins L_D^0 values, calculated from the values of C_2 reported in Table X.

4. That the dependence of L_D on microstructural defects in a polycrystalline sample is given by Eq. [5] as the effect of a microstructure-depending mobility term was shown to be small or negligible.

5. That the overall dependence of L_D on N_x and $L_{GB}N_D$ could then be calculated by the equation

$$L_D = L_D^0\left[1 + \frac{k'k''}{C} L_D^{02} (L_{GB}N_D) + \frac{N_x}{N_{0x}}\right]^{-1/2}$$

$$= L_D^0\left[1 + C_1 (L_{GB}N_D) + \frac{N_x}{N_{0x}}\right]^{-1/2} \quad [12]$$

using for the values of $C_1 = k'k''L_D^{02} = 5 \cdot 10^{-7}$ cm^3 and for the value of N_{0x} those reported in Table X.

The analysis of the diagrams of Fig. 11-14 and of Table VII where we have reported the comparison between the experimental and theoretical values, calculated for the case of negligible impurity-microstructure interactions, shows that the model predictions are satisfactorily fulfilled for iron up to N_x values close to 10^{13} cm^{-3} and for both vanadium and titanium up to 10^{12} cm^{-3}.

At higher concentrations all four impurities considered exhibit important deviations from the theoretical values.

These results would support the conclusion that at concentrations in excess of 10^{13} atom cm^{-3} interaction does occur between impurities and microstructure or/and thermal donors, or between impurities and shallow acceptors (*i.e.*, boron) giving rise to ionized impurity complexes, which, in turn, would make no longer applicable the constant mobility approximation. This last conclusion seems to be the case for iron. Iron in the presence of boron, forms boron-iron complexes which could behave like donor (E_v = 0.10 eV) or acceptor (Ec = −0.055 eV) levels (25), in good agreement with earlier findings of Davis and Hopkins (2), who showed that iron was the only impurity which does not fulfill the constant mobility approximation in p-doped silicon.

On the contrary, impurities-microstructure interactions appear to be the main cause responsible for the enhanced recombination of photogenerated carriers in the most concentrated titanium, vanadium, and chromium solutions. This is in good agreement with earlier experiments carried out by Rohatgi *et al.* (6), who showed that interaction between titanium at a $2 \cdot 10^{14}$ cm^{-3} level and GB occurs and also with the conclusions previously reported by the authors of Ref. (12), who showed that, in the range of $10^{14} \div 10^{15}$ cm^{-3}, the saturation effect in diffusion length occurs. This suggests an effective interaction between structural defects and impurities.

Conclusions

The fact that major deviations from a model based on the assumption of a substantial absence of impurity-microstructure interactions are systematically observed at concentrations in excess of $10^{12} \div 10^{13}$ atom/cm^3 for all the impurities considered, at comparable $L_{GB}N_D$ values indicates that, at least, in the case of vanadium, titanium, and chromium, interaction occurs with a sensible enhancement of recombination at GB.

In the case of iron, however, where a quite good agreement between the model predictions and the experimental results is observed in the low concentration range, complexes formation between the metal and boron would accomplish better for the observed deviations.

As has also been shown in this work, oxygen redistribution between the volume of the grains and GB does take place in the course of heat-treatments, with significant influence on both the majority and minority carrier properties. It is, however, not possible to exclude the

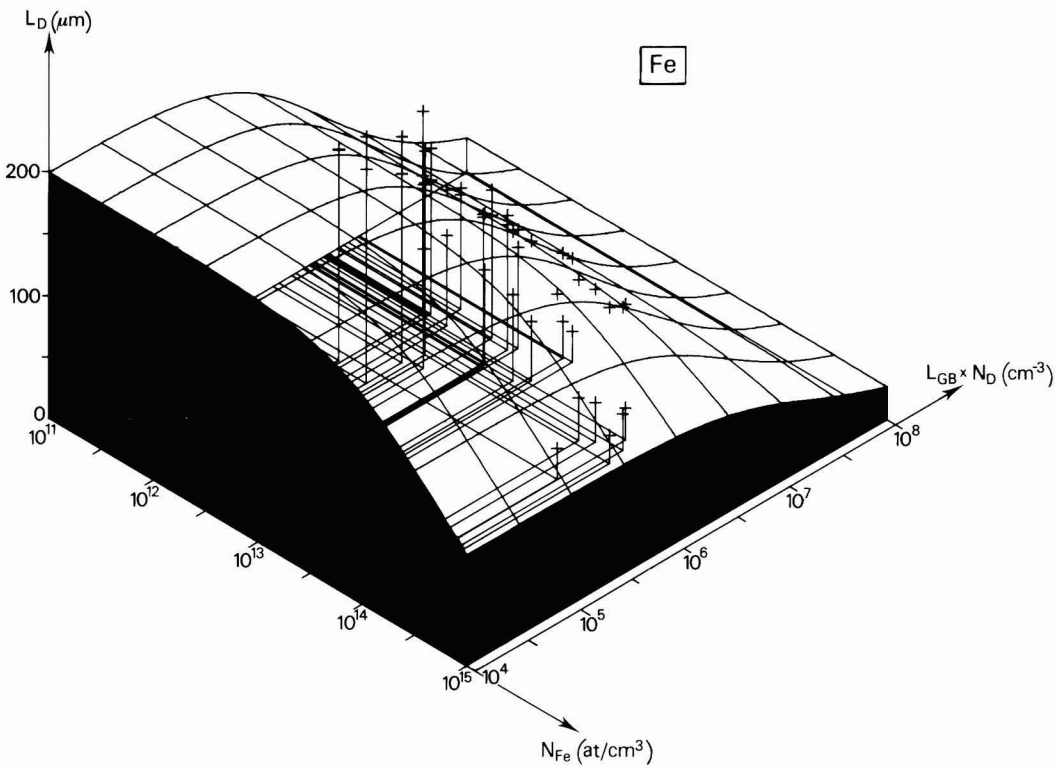

Fig. 14. Plot of the diffusion length L_D as a function of the iron dopant concentration N_{Fe} (in the solid) and of the microstructural parameter ($L_{GB}N_D$). In the figure the dependence of L_D on N_{Fe} according to Ref. (2), is reported on the L_D, N_{Fe} plane and the dependence of L_D on $L_{GB}N_D$ according to Eq. [5] (using as L_D^0 a value of 200 μm and a $k'k''/C = L_D^{02} = 5 \cdot 10^{-7}$ cm^3) is displayed on the L_D, $L_{GB}N_D$ plane.

detrimental effects of impurities on the recombination properties of GB not directly or indirectly in connection with impurity-oxygen interactions (26-28). The amount of experimental data presently available is, however, too scarce to reach a definitive conclusion on this matter, and this is the reason why we have undertaken a systematic work addressing a deeper understanding of the influence of impurity-GB interactions on the electrical activity of GB.

Acknowledgments

The authors are indebted to Dr. F. Galluzzi of ENI Ricerche S.p.A., Monterotondo (Roma) for stimulating suggestions during the initial phase of this work, to F. Rota, M. Colombo, S. Cucchi, now of Pragma S.p.A. for their continuous technical support, to Prof. G. P. Ottaviani and R. L. Fabri of the University of Modena for their scientific advice, and to A. Sandrinelli who later joined our team, for her enthusiastic support.

We acknowledge Dr. Beluet, of the CGE Laboratories at Marcussis (France) for having carried out a careful characterization work on samples of our polycrystalline material.

Manuscript submitted June 3, 1985; revised manuscript received May 1, 1986.

The University of Milano assisted in meeting the publication costs of this article.

REFERENCES

1. J. R. Davis, R. P. Hopkins, and A. Rohatgi, in "Materials and New Processing, Technologies for Photovoltaics," J. M. Dismukes, E. Sirtl, P. Rai-Choudhury, and L. P. Hunt, Editors, p. 14. The Electrochemical Softbound Proceedings Series, Pennington, NJ (1982).
2. R. H. Hopkins, J. R. Davis, A. Rohatgi, R. B. Campbell, P. O. Blais, P. Rai-Choudhury, and R. E. Stapleton, "Effects of Impurities and Processing on Silicon Solar Cells," Final Report DOE/JPL (1982).
3. A. Rohatgi, R. B. Campbell, J. R. Davis, R. H. Hopkins, P. Rai-Choudhury, H. M. Nollenkopf, and H. R. McCormick, in Proceedings of the 14th IEEE Photovoltaic Special Conference, The IEEE p. 908 (1980).
4. S. Pizzini, L. Giarda, A. Parisi, A. Solmi, G. Soncini, and C. Calligarich, *ibid.*, p. 902.
5. J. L. Maurice, J. L. Pastol, J. E. Bouree, J. Y. Laval, G. Revel, and, M. Rodot, "Poly-microcrystalline and Amorphous Semiconductors," MRS-EUROPE 1984, Les Editions de Physique, p. 323, (Les Ulis Cedex, France).
6. A. Rohatgi, R. H. Hopkins, and J. R. Davis, *IEEE Trans. Electron. Devices*, **ED-28,** 103 (1981).
7. G. Mathian, H. Amzil, M. Zehaf, J. P. Crest, S. Martinuzzi, and J. Qualid, *Solid-State Electron.*, **26,** 131 (1983).
8. A. J. Gosh, C. Fishman, and T. Feng, *Appl. Phys.*, **51,** 446 (1980).
9. S. Pizzini, C. Calligarich, C. Chemelli, M. Gasparini, P. Rava, and L. Sardi, in "Materials and New Processing Technologies for Photovoltaics," J. A. Amick, V. K. Kapur, and J. Dietl, Editors, p. 200, The Electrochemical Society Softbound Proceedings Series, Pennington, NJ (1983).
10. C. Calligarich, C. Chemelli, S. Bonfanti, S. Fossati, F. Galluzzi, D. Margadonna, and S. Pizzini, in "Proceedings of the 5th Photovoltaic Solar Energy Conference," p. 1085, D. Reidel Publishers, Doordrecht (1983).
11. S. Pizzini, in "Silicon Processing for Photovoltaics," C. P. Khattak and K. V. Ravi, Editors, p. 169, Elsevier Science Publishers, Amsterdam (1985).
12. F. Galluzzi, E. Scafè, M. Beghi, S. Fossati, M. Tincani, and S. Pizzini, in "Materials and New Processing Technologies for Photovoltaics," V. J. Kapur, J. P. Dismukes, and S. Pizzini, Editors, p. 373, The Electrochemical Society Softbound Proceedings Series, Pennington, NJ (1985).
13. S. Pizzini, *J. Power Sources*, **11,** 115 (1984).
14. S. Pizzini and M. Rustioni, in "Proceedings of 6th E.C. Photovoltaic Solar Energy Conference," p. 875, D. Reidel Publishers, Doordrecht (1985).
15. M. Beghi, C. Chemelli, S. Fossati, and S. Pizzini, "Poly-microcrystalline and Amorphous Semiconductors," MRS Europe 1984, p. 181, Les Editions de Physique (Les Ulis Cedex, France).
16. S. Pizzini, M. Beghi, D. Narducci, G. Fabri, F. Demartin, F. Morazzoni, G. P. Ottaviani, and A. Sandrinelli, Paper 309, presented at the Electrochemical Society Meeting, Boston, MA, May 5-9, 1986.
17. S. Pizzini, *Solar Energy Mater.*, **6,** 253 (1983).
18. W. Zulenhner and D. Huber, in "Crystals", **8,** 1, Springer-Verlag, Berlin (1982).
19. G. S. Oehrlein and J. W. Corbett, in "Defects in Semiconductors II," p. 107, S. Mahajan and J. W. Corbett, Editors, North Holland, New York (1983).
20. T. Abe, K. Kikuchi, S. Shirai, and S. Muraoka, in "Semiconductor Silicon, 1981," H. R. Huff, R. J. Kriegler, and Y. Takeishi, Editors, p. 54, The Electrochemical Society Softbound Proceedings Series, Pennington, NJ (1981).
21. C. H. Seager in "Defects in Semiconductors, II," p. 343, S. Mahajan and J. W. Corbett, Editors, North Holland, New York (1983).
22. C. H. Seager, G. E. Pike, and D. S. Ginley, in "Electronic and Optical Properties of Polycrystalline or Impure Semiconductors and Novel Silicon Growth Methods," K. V. Ravi and B. O'Mara, Editors, p. 19, The Electrochemical Society Softbound Proceedings Series, Pennington, NJ (1980).
23. A. R. Bean and R. C. Newman, *J. Phys. Chem. Solids*, **33,** 255 (1972).
24. H. Amzil, Ph.D. Thesis, University Aix-Marseille (July, 1985).
25. K. Graff and H. Pieper, *This Journal*, **128,** 669 (1981).
26. R. Sundaresan, D. E. Burk, and J. G. Fossum, *J. Appl. Phys.*, **55,** 1162 (1984).
27. S. Pizzini, L. Giarda, A. Parisi, A. Solomi, G. Soncini, and C. Calligarich, in Proceedings of the 14th IEEE Photovoltaic Special Conference, The IEEE, p. 902 (1980).
28. M. Zehaf, Ph.D. Thesis, University Aix-Marseille (July, 1985).

Growth Kinematics of a Polysilicon Trench Refill Process

V. J. Silvestri*

IBM General Technology Division, Hopewell Junction, New York 12533

ABSTRACT

Growth kinematics of a polysilicon refill process are described. The process employs a LPCVD polysilicon nucleating film over insulators to achieve fast and reproducible polysilicon refills. The bulk of the refill is carried out using a $SiCl_4$-H_2 reaction at 1000°C at atmospheric pressure. The kinematics of the refill growth process have been studied as a function of time and trench width and are discussed.

Polysilicon trench refill is used extensively in deep trench isolation technology. Thus far only low pressure chemical vapor deposition (LPCVD) processes have been reported for filling the trenches. LPCVD polysilicon deposition systems intrinsically produce low deposition rates (10-20 nm/min). Although such systems have advantages in depositing thin films of polysilicon, there are significant problems associated with their use for filling trenches which require long refill times. The continuous vacuum pumping of reactants leads to frequent downtime for equipment cleaning and maintenance. Other detracting features of the LPCVD fill approach include the following. The common reactants employed have associated safety concerns (100% SiH_4), and the long run times increase the potential for particulate formation. Of more importance, conformality of film coverage and deposition rate sensitivity to slight variations in parameters (doping input, pumping speed, and pressure) bring overall reproducibility of LPCVD processes into question.

Recent studies show deposition rates can be seriously reduced due to reactivity differences between dopant hydrides and the SiH_4 used for the deposition. Severe conformality differences between trench sidewall and top surface leads to severe void formation.

Examples of these effects generally associated with low temperature, homogeneous (gas phase, hot surface independent) reactions have been reported relative to void formation (1-2). Nonplanar surfaces are also possible in heavily populated trench areas. It is from the above viewpoint that a midtemperature atmospheric pressure (MT AP) process was developed (3). The MT AP process circumvents the above problems by forming a thin nucleating silicon layer on the trenches by LPCVD (approximately 30-200 nm) at 650°C. The bulk of the refill is then completed employing a midtemperature (1000°C) heterogeneous (hot surface) reaction system. Insured conformal and equal growth from all surfaces within the trench and on top surfaces results. The reactants used for the higher temperature step are $SiCl_4$ and H_2. High rates can be achieved in this system (0.22 μm/min) suitable for filling trenches within short times (approximately 15-20 min). This process has been employed for trench refill in "state of the art" epitaxial deposition reactors at atmospheric pressure. The trench refills are easily and reproducibly doped (n and p type) in these systems using conventional doping gases (AsH_3 and B_2H_6). Since growth rates on top surface, sidewalls, and bottom of the trenches are similar, void size is minimized. Voids are no longer associated with the reentrant cusp formation typical of nonconformal growth in systems as described in Ref. (1). Void size in the MT AP process is of the order of the average grain size of the polysilicon refill material (100-300 nm).

In this study, the kinematics of growth from prenucleated oxide surfaces within trenches are reported.

*Electrochemical Society Active Member.

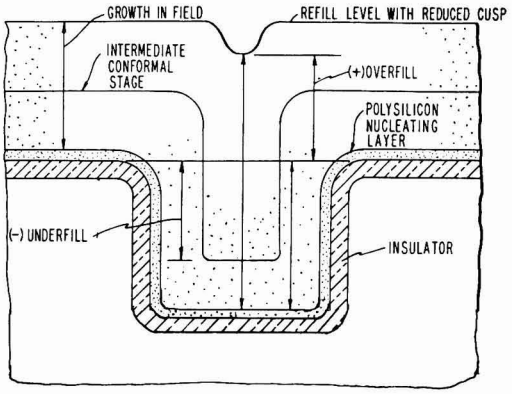

Fig. 1. Schematic diagram of trench cross section showing experimental quantities measured.

Experimental

For the experiments, line pattern masks were employed to form trenches of 3.75 μm in depth. Trench widths from 2-25 μm were produced on the silicon substrates. These trenches were thermally oxidized to form a 200 nm oxide lining. This oxide was then covered with a 200 nm LPCVD polysilicon film deposited at 650°C. Individual runs were carried out on wafers to refill the

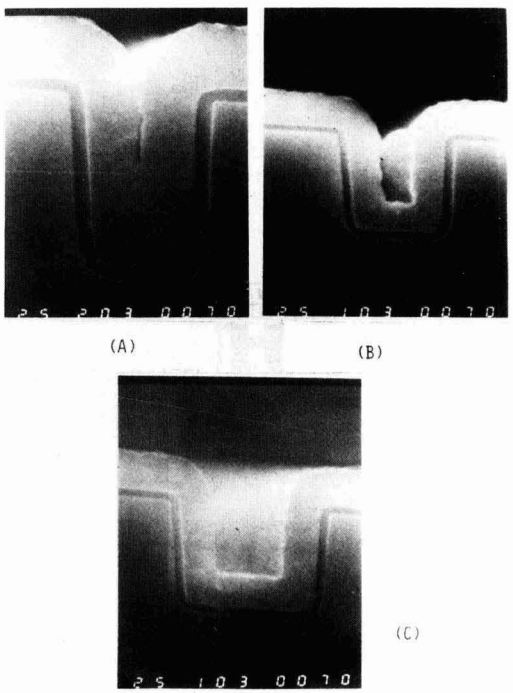

Fig. 2. SEM cross sections showing refill obtained in 2.2 μm (A), 3.6 μm (B), and 5.2 μm (C) trenches after 5 min of refill.

formed trenches using the $SiCl_4$-H_2 gas reactants. The rate of growth on silicon wafers added as monitors during the runs was 0.22 μm/min. Times of 3.3, 5, 6.6, 10, and 15 min were employed for the runs. The run times were chosen to produce polysilicon fills of differing extent (dependent on trench width) such that with SEM examination (in cross section) the kinematics of growth from the nucleated surface was thereby revealed. A series of SEM photos depicting various stages of refill were obtained for the trenches of differing width for each growth time. Measurements could also be made to extract rate data.

Results and Discussion

The growth kinematics which bring about the refill can be characterized as occurring in distinct stages. These stages are (*i*) an initial conformal stage, (*ii*) a seam formation stage, (*iii*) a seam closure stage, and (*iv*) a cusp planarization stage.

Figure 1 is a schematic diagram of a trench cross section showing the measured quantities which appear in Tables I-V. The tables contain data obtained on trench refill for different experimental times. This data is also plotted in Fig. 5 below. The SEM cross-sectional photos in Fig. 2 show three trench widths of 2.2, 3.6, and 5.2 μm following a 5 min refill. Figures 3 and 4 show SEM cross sections of trenches characteristic of the other refill stages. In Fig. 2 it is noted in the photos that, dependent on the trench width, different refill levels and stages are achieved for a chosen experimental time. Figures 2b and 2c show clearly the overall conformality that is achieved in trenches with the MT AP process. It is also an example of stage 1 as defined above. Figure 2a is an example of stage 2 where an initial cusp is formed. Figure 3 shows achievement of an exact refill level, and Fig. 4 the overfilled stage. It is important to note that at the initial cusp formation stage voids can begin to form as the two surfaces meet to close and fill the trench. Voids which form are of the order of the roughness of the two meeting sur-

Table I. Trench refill kinematics (5 min run)

Trench width (μm)	Trench depth (μm)	Underfill (−) or overfill (+) (μm)	Growth in field (μm)	Cusp depth (μm)	Cusp width (μm)	Total refill level (μm)
2.2	3.59	(+) 0.242	0.96	0.87	2.2	3.63
3.3	3.59	(−) 2.57	1.0	3.78	3.4	0.82
4.85	3.88	(−) 2.62	1.16	3.98	5.0	1.06
7.45	3.86	(−) 2.62	0.98	3.86	7.73	1.04
13.2	3.80	(−) 2.48	1.12	3.80	12.5	1.12
24.7	3.80	(−) 2.47	1.17	3.57	25.8	1.13

Table II. Trench refill kinematics (10 min run)

Trench width (μm)	Trench depth (μm)	Underfill (−) or overfill (+) (μm)	Growth in field (μm)	Cusp depth (μm)	Cusp width (μm)	Total refill level (μm)
2.44	3.66	(+) 2.0	2.3	0.49	2.0	5.46
4.0	3.6	(+) 1.38	2.2	0.9	3.4	4.78
4.9	3.7	(−) 1.59	2.13	2.7	2.8	1.90
5.4	3.5	(−) 1.43	1.8	3.5	4.2	1.87
7.46	3.98	(−) 1.49	2.28	4.2	7.4	2.29
20.0	3.97	(−) 1.49	2.12	5.6	20.8	2.28

Table III. Trench refill kinematics (15 min run)

Trench width (μm)	Trench depth (μm)	Underfill (−) or overfill (+) (μm)	Growth in field (μm)	Cusp depth (μm)	Cusp width (μm)	Total refill level (μm)
2.13	3.59	(+) 3.0	3.2	0.6		6.39
3.49	3.59	(+) 2.26	3.2	0.9	2.2	5.65
4.70	3.59	(+) 1.8	3.2	1.74	3.48	5.19
7.25	3.6	(−) 0.52	3.26		6.64	2.88
12.7	3.52		3.5			
24.0	3.13		3.52			2.9

Table IV. Trench refill kinematics (3.3 min run)

Trench width (μm)	Total refill (μm)
1.36	4.5
1.56	2.5
1.7	1.3
2.2	0.7
4.6	0.8

Table V. Trench refill kinematics (6.6 min run)

Trench width (μm)	Total refill (μm)
1.35	6.2
1.7	5.8
2.2	5.25
2.8	3.0
3.26	1.8
3.28	1.3
5.02	1.4

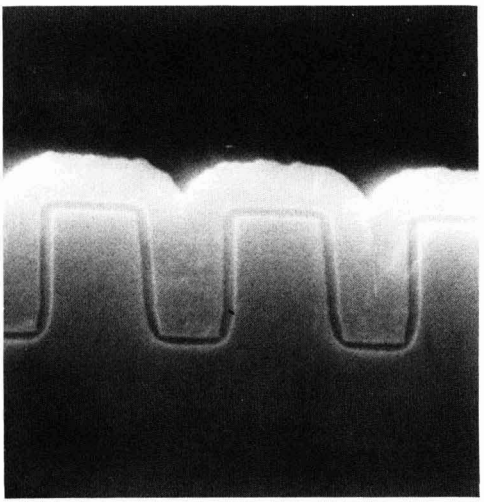

Fig. 3. Exact refill showing cusp and seam

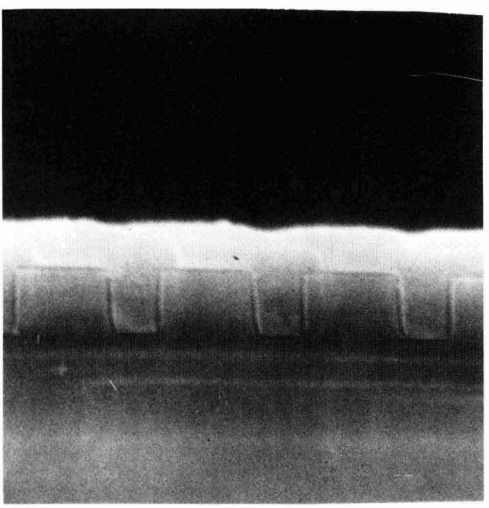

Fig. 4. Overfill stage with seam "healing"

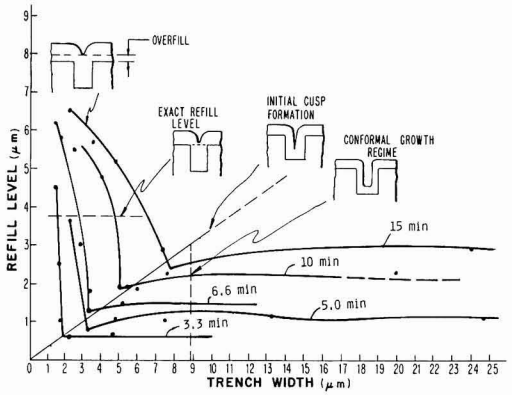

Fig. 5. Refill level *vs.* trench width plotted for experimental refill times.

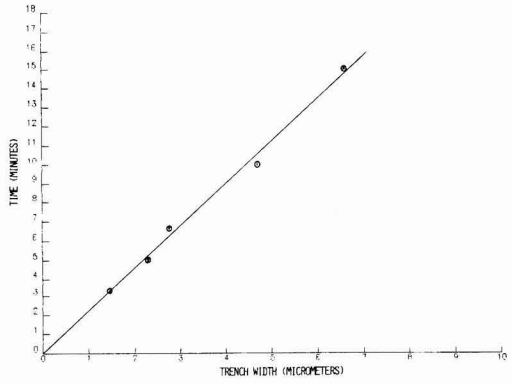

Fig. 6. Refill time required to achieve exact refill level as a function of trench width.

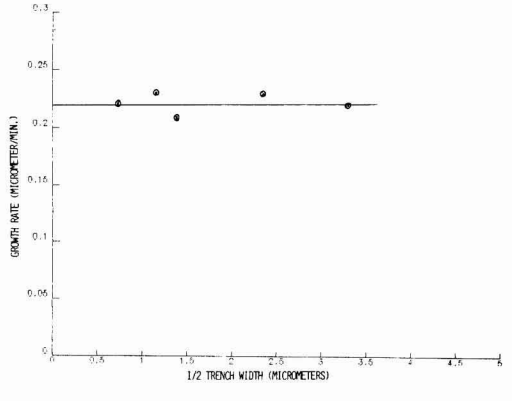

Fig. 7. Growth rate as a function of ½ the trench width

faces. It is noted in Fig. 4 that there can be "healing" or refill of these small voids with continued trench fill. There is also a self-planarization of the cusp with extended overfill as in Fig. 4. Figure 5 is a plot of the data in Tables I-V as measured according to Fig. 1. In Fig. 5, curves for refill level as a function of trench width are plotted for the experimental run times. Inset diagrams depict schematically the stages of refill observed which define regimes having common curve characteristics.

For example, conformal growth occurs for points along curve portions in the data which show relatively constant fill level. The initial cusp formation stage is found to coincide with the inflection region shown for each curve in the figure. A line has been drawn through these inflection points. A sharp rate change occurs in each curve at these points. Rapid closure of the seam then occurs to complete the refill to the final two stages. In Fig. 6, the data for trench width *vs.* time has been plotted for the "exact fill" level intersections for the curves plotted in Fig. 5. This linear plot is useful in establishing the time required for refill of trench structures in VLSI configurations where trenches of different widths exist. In Fig. 7, the data in Fig. 6 have been replotted to show rate as a function of half the trench width. It is noted that the rate is constant at 0.225 μ/min indicating the conformal nature of growth on top horizontal surfaces and within the trench.

Summary and Conclusions

The following general observations and conclusions were reached.

1. Growth propagates uniformly from the polysilicon nucleation layer provided in the trench refill process.

2. Voids when formed are the result of polysilicon grains fusing from opposite sidewalls meeting centrally in the trenches. This final closure can lock in voids of approximately the same size of the polysilicon grains formed.

3. The cusps (depressions) observed over central regions of the trench (associated with the closure seam) form and are related to the growth kinetics and corner growth at the bottom of the trenches.

4. Growth at top corners of trenches has been observed to be different than at corners within the trenches and this phenomena is being examined more closely, since these differences appear important and implicated in the reduced refill observed in overall trench patterns at intersections and 90° turns.

5. Reactant gas apparently still has access into the seams and voids, and further closure of voids can occur.

6. Slightly angled trench sidewalls will aid in filling high depth/width ratio trenches in a void free manner.

7. The process reported has a number of distinct advantages: assured conformal growth, higher deposition rates, and highly reproducible refills.

Acknowledgments

The technical assistance of G. Devine and V. T. Phan is greatly appreciated.

Manuscript submitted Jan. 27, 1986.

IBM General Technology Division assisted in meeting the publication costs of this article.

REFERENCES

1. T. Morie and J. Murota, *Jpn. J. App. Phys.*, **23**, 482 (1984).
2. R. M. Levin and K. Evans-Luttersdt, *J. Vac. Sci. Technol., B*, **54** (1983).
3. L. M. Epath, V. J. Silvestri, and D. D. Tang, U.S. Pat. 4,473,598 (1984); and K. D. Beyer and V. J. Silvestri, U.S. Pat. 4,528,047 (1985).

Accuracy of the Four-Terminal Measurement Techniques for Determining Contact Resistance

A. A. Naem and D. A. Smith

Northern Telecom Electronics Limited, Semiconductor Components Group, Ottawa, Ontario, Canada K1Y 4H7

ABSTRACT

The accuracy of five different test structures in determining the contact resistance is compared. The dependence of the measured contact resistance on the contact window size and test vehicle geometry, and the spacing tolerance between the contact window edge and semiconductor resistor edge are discussed. It is concluded that the 4-terminal measurement technique can be a valid indicator of the interfacial contact resistance, if the semiconductor sheet resistance below the contact is approximately equal to or less than the contact resistance, and, if the spacing tolerance around the contact approaches zero.

The quality of metal-semiconductor contact interfaces in integrated circuit technologies is an important factor in determining circuit performance. Particularly as the transistor and contact physical dimensions are scaled down, contact resistance is expected to play an increasingly significant role relative to other parasitic resistances and the on-resistance of the transistor. Thus, the design of efficient and accurate structures and methods for determining the contact resistance is vital to the development, characterization, and control of integrated circuit manufacturing processes. Several different techniques have been developed for the determination of contact resistance (1-5), including the use of simple contact chains, 3-contact resistor bars, and 4-terminal Kelvin structures. In general, for process research and development, it is desirable to measure the resistance associated with the metal-semiconductor interface only, and to minimize or eliminate, if possible, the parasitic contributions from the high resistivity diffusion region around the contact. From the circuit design and modelling point of view, the total resistance associated with the contact region is more meaningful for describing circuit performance.

Until recently the most widely used structure for contact resistance determination was the 3-contact resistor bar, which was first introduced by Shockley (1). This structure is customarily analyzed by a transmission line model in order to separate the contact resistance (R_c) from the semiconductor sheet resistance (2). The shortcomings and inadequacies of this method have been widely discussed (5).

In the last few years the 4-terminal Kelvin test structures have become widely used tools for the determination of contact resistance (3, 4). This method allows a direct extraction of the contact resistance without mathematical corrections or knowledge of the contact window and resistor dimensions. It has been suggested that this technique will give an accurate value for the interfacial contact resistance (7). In fact, we have found that this technique can also have some serious shortcomings, under certain circumstances as has been reported recently (8, 9), and that care must be taken in the interpretation of experimental results.

In this paper, we experimentally compare the accuracy of different 4-terminal contact resistance test structures, for contacts between Al-1%Si and diffused silicon or polysilicon layers, in both NMOS and CMOS technologies. We also show that the apparent contact resistance is strongly dependent on the contact window size, test structure geometry, semiconductor sheet resistance, and the spacing tolerance between the edges of the contact and the diffusion region edge. We shall refer to the metal-semiconductor interfacial layer resistance (*i.e.*, no parasitic resistance contribution from the high resistivity diffusion region around the contact) as R_i, the measured contact resistance as R_c, and the sheet resistance of the bulk semiconductor as R_s.

Test Structure Geometries

A convenient test structure is shown in Fig. 1 and is similar to that previously utilized by Faith *et al.* (6). This structure is a three-contact resistor bar of the type usually associated with the transmission line technique;

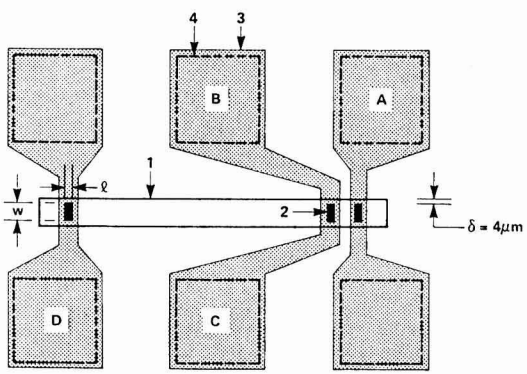

Fig. 1. The test structure (TS1) used to perform 4-terminal measurements. The upper two pads to the right (A and B) are for current probes, and the lower two pads to the left (C and D) are for voltage probes. The labels 1, 2, 3, and 4 refer to the diffused silicon (or polysilicon) regions, contacts, metal, and pyrox layers, respectively.

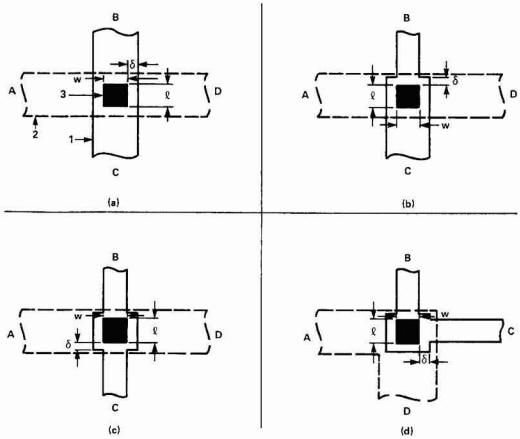

Fig. 2. The 4-terminal Kelvin structures: (a) TS2, (b) TS3, (c) TS4, and (d) TS5. The labels 1, 2, and 3 refer to the diffused regions (silicon or polysilicon), metal, and contacts layers, respectively. The sections A and B are for the current probes, and C and D are for the voltage probes.

however, each contact is accessed by dual metal sense lines and pads, allowing an isolated current force and voltage sense at each contact. The structure is used here as a 4-terminal device. In performing a 4-terminal measurement, current is forced between the two pads A and B, and the voltage is sensed, only at the contact in the middle, between the two pads C and D. In this manner, the major component of the voltage drop associated with current flow in the resistor bar and metal lines is eliminated from the voltage measurement, and the measured contact resistance is simply $R_c = V/I$, where V is the voltage sensed and I is the current forced. This test structure will be referred to as TS1.

In order to check the effect of resistor geometry and contact position on the measurement of R_c (V/I), a second set of a single-contact 4-terminal Kelvin structures was designed, in which the resistor geometry, the shape of the underlying diffusion or polysilicon layer, and the position of the voltage tap in the semiconductor with respect to the current flow directions were changed. Typical test cells are shown in Fig. 2a, 2b, 2c, and 2d and will be referred to as TS2, TS3, TS4 and TS5, respectively.

Sample Preparation

Using the test structures TS1, TS2, and TS3 described above, n⁺-diffused silicon and polysilicon resistors with various contact window geometries were fabricated on the same chip. The starting wafers were 6-10 Ω-cm, p-type <100> silicon. The n⁺-diffused resistors were fabricated by the diffusion of phosphorus into device wells resulting in a sheet resistance of 7.6 Ω/□. The polysilicon resistors, of thickness 0.37 μm, were formed on the field oxide and subjected to the same diffusion and heat-treatments as the diffused resistors, resulting in a sheet resistance of 28 Ω/□.

The test structures TS2, TS3, TS4, and TS5 (*cf.* Fig. 2) were fabricated in a 4-μm production CMOS process. Contacts were made to n⁺- or p⁺-diffused silicon and n⁺-diffused polysilicon. Starting with 4-6 Ω-cm n-type <100> silicon, the p⁺ diffusions were formed by the diffusion of boron into device wells resulting in a sheet resistance of 82 Ω/□. The n⁺ diffusions were formed by the diffusion of phosphorus into a 6 μm deep, 4.7 kΩ/□ p-well, resulting in a sheet resistance of 17 Ω/□. The polysilicon resistors, of thickness 0.35 μm, were formed on the field oxide and had a sheet resistance of 24 Ω/□.

All the data presented in this paper were obtained from contacts formed by Al-1%Si metallization sintered in hydrogen ambient for 30 min at 450°C. The R_c was calculated from the sensed voltage drop (V) and forced current (I) (3 mA). On each wafer a total of 16 dice were measured (3 wafers were used) to provide statistical information.

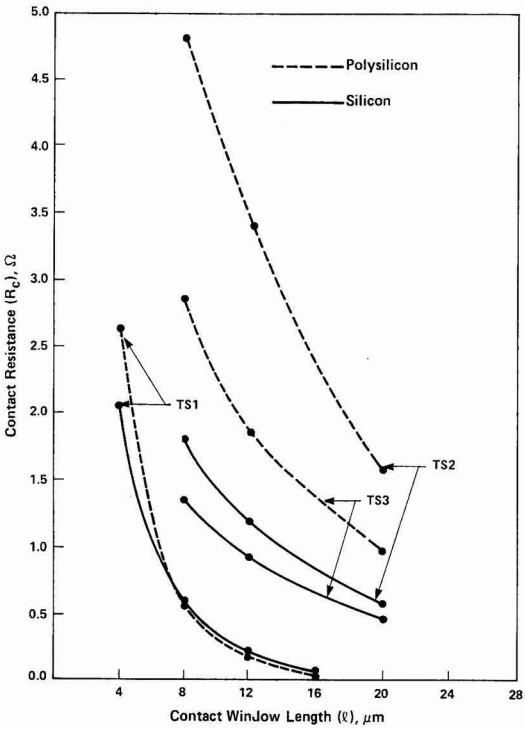

Fig. 3. The contact window length (l) influence on contact resistance (R_c) as measured using structures TS1 (δ = 4 μm), TS2 and TS3 (δ = 16 μm) of Fig. 1, 2(a), and 2(b), respectively.

Results and Analysis

Examination of the contact area in the SEM, after removing the metal film, revealed no pitting; however Si precipitates were observed, particularly in the case of contacts made to polysilicon. Uniform metal/semiconductor interfacial contacts are commonly characterized by the specific contact resistance (ρ_c). However, it is only meaningful for a uniform interfacial layer (7). In this study we prefer to use the measured R_c (V/I) to avoid errors that may be introduced from contact nonuniformity. The influence of the contact dimensions on R_c was investigated using the test structures TS1, TS2, and TS3 of Fig. 1 and 2. The effect on R_c of varying the contact window length (l), the dimension along the current flow direction, while the contact window width (w) was kept constant at 4 μm, is shown in Fig. 3. Most striking is the strong, approximately inverse, dependence of R_c on the contact length for both the diffused silicon and polysilicon samples. This variation of R_c with the contact length is consistent with the expected dependence of R_l on the contact area. But it should be recognized that the bulk of the current flows at the leading edge of the contact. The voltage sensed depends on the current which flows at the back edge of the contact, where the current density is minimum. This nonuniform flow of current through the contact area implies that the Kelvin method will not yield a direct, accurate determination of R_l.

The nonuniformity of the current flow through the contact interface depends strongly on the sheet resistance of the semiconductor and the geometry of the structure. The mathematical treatment can be adapted directly from the transmission line model, where R_c is given by (7, 10)

$$R_c = \frac{1}{w}\sqrt{R_{sm}\rho_c}\coth\left(l\sqrt{\frac{R_{sm}}{\rho_c}}\right) \quad [1]$$

if the voltage is sensed at the leading edge of the contact, or

$$R_c = \frac{1}{w}\sqrt{R_{sm}\rho_c}\,\mathrm{csch}\left(l\sqrt{\frac{R_{sm}}{\rho_c}}\right) \quad [2]$$

if the voltage is sensed at the back edge of the contact, where ρ_c is the specific contact resistance of the metal-semiconductor interface, and R_{sm} is the semiconductor sheet resistance directly under the metal. The current flows uniformly through the contact, and $R_l \simeq R_c$, if $R_{sm} << R_l$. However, if $R_{sm} >> R_l$, the measured $R_c > R_l$, the Kelvin technique can seriously overestimate the actual interfacial resistance.

As the contact length is increased, the back edge of the contact, where the actual voltage drop is sensed, is moved farther away from where most of the current is flowing. The amount of current flowing near the back edge of the contact decreases, and the semiconductor near this region is pinned closer to the metal potential. In this arrangement, the measurement can only be expected to yield a reasonable approximation to R_l, if R_c is large with respect to R_s. As R_c increases with respect to R_s, the current flow becomes more uniform through the contact area.

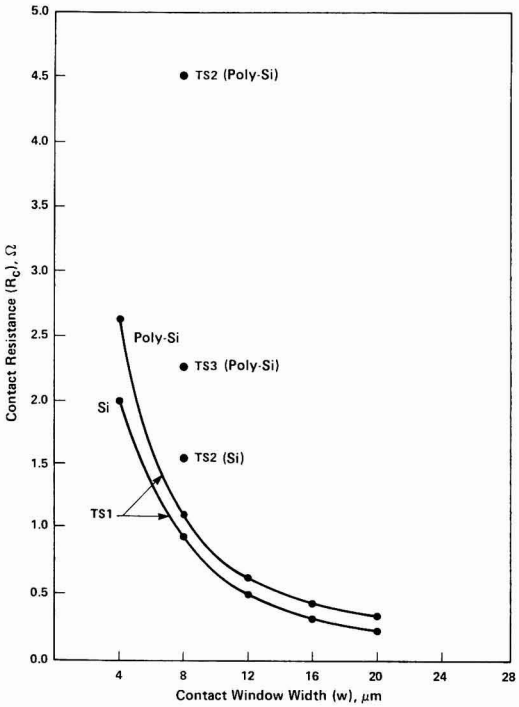

Fig. 4. The contact window width (w) effect on contact resistance (R_c), for Si and polysilicon samples, as measured using the structures TS1 (δ = 4 μm), TS2 and TS3 (δ = 16 μm), as shown in Fig. 1, 2(a), and 2(b), respectively.

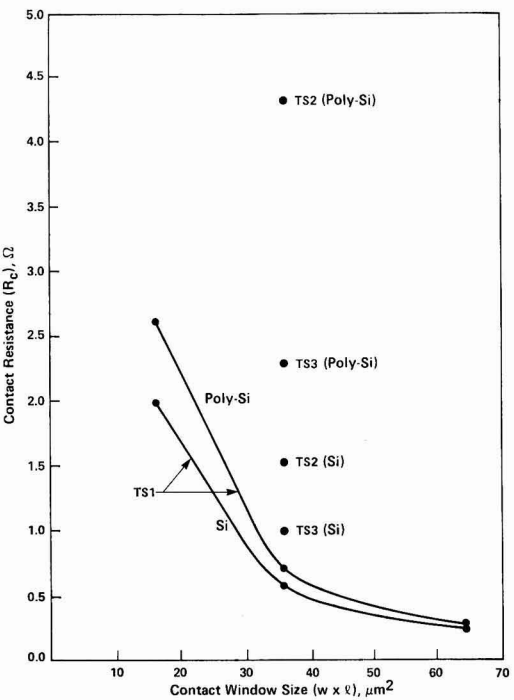

Fig. 5. The dependence of contact resistance (R_c) on the area of the contact window ($w \times l$) for square contacts, as determined using structures TS1, TS2, and TS3.

Figure 4 illustrates the dependence of R_c on the contact window width (w) while the contact length was kept constant at 4 μm. The contact window width (w) is defined as the dimension of the contact edge perpendicular to the current flow direction. As depicted from Fig. 4, R_c increases approximately in inverse proportion to the width, as expected (Eq. [2]), since the current density at the leading edge is mainly controlled by the width of the contact, provided the contact length is kept constant. The dependence of R_c on the shape of the test structure is clearly demonstrated in Fig. 3 and 4, where TS2 gives the largest values of R_c while TS1 gives the smallest for the same contact window area. The small R_c values obtained by TS1, compared to the values obtained by TS2 and TS3, can be attributed to the smaller spacing tolerance between the contact window edge and the diffused region edge. The effect of this parameter on the measured values of R_c is discussed later in more detail.

Square contacts with sizes of 4 × 4 μm², 6 × 6 μm², and 8 × 8 μm² were used to study the contact size ($w \times l$) effects on R_c by varying w and l simultaneously. As demonstrated in Fig. 5, R_c varies in approximately inverse proportion to the square of the scaling factor of w and l. Again, the shape of the test structure has a significant influence on the measured values of R_c, as can be seen in the same figure for $w \times l$ = 36 μm².

The measured value of R_c is also strongly influenced by the position of the contact edge at which the voltage is sensed with respect to the current flow direction. An additional set of 4-terminal test structures (TS2 and TS5) was fabricated to quantify this dependence. The two test structures are illustrated in Fig. 2a and 2d, where, in one case (TS2), the voltage tap is taken at the back of a minimum sized (4 μm × 4 μm) contact and, in another (TS5), the tap is taken at the side of a contact of the same size. The pads A and B were used for current forcing, and the voltage drop was sensed between pads C and D (as shown in Fig. 2). In the case of TS2, the voltage was sensed in the same direction as the current flow, while in the case of TS5 the voltage drop was sensed in a direction orthogonal to the current flow. A summary of the measured R_c values for the two structures on n⁺-polysilicon and n⁺- and p⁺-diffusions is given in Table I. The spacing tolerance (δ) between the contact edge and the diffusion region edge in all cases was 2 μm. The measured R_c of the two structures varies considerably, especially when R_s is low in comparison with R_c. Despite fringing effects due to spacing tolerances and the effect of the side tap on electric field pattern, the side tap structure yields results consistent with Eq. [1], sensing the voltage at the leading edge of the contact. Sensing the voltage at the back edge of the contact in the back tap structure is consistent with Eq. [2]. Moreover, as R_s decreases with respect to R_c, the values obtained from the two structures converge as in the case of n⁺-diffusion (Table I).

The spacing tolerance of the diffused semiconductor layer around the contact (δ) can also have a significant influence on the measurements, even though R_f itself does not change. Figure 6 shows the variation in R_c as a function of δ for a series of 8 μm² × 8 μm² contacts to n⁺-diffused silicon, in the case of a uniformly wide bar (TS2), and for a 8 μm wide bar widened only at the contact (TS4). The measured R_c varies significantly with δ; the change can be quite considerable. The change in R_c in the case of the uniformly wide bar (TS2), is as much as a factor of two from a 2 μm spacing to the self-aligned (δ

Table I. Apparent contact resistance (R_c) for different layer structure as determined by the test structures (TS2 and TS5) in Fig. 2. x_j refers to the junction depth of the diffused region or the thickness of the polysilicon film

Layer type	R_c (Ω) TS2	R_c (Ω) TS5	R_s (Ω/□)
n⁺ Polysilicon (x_j = 0.35 μm)	0.27	1.67	24
n⁺ Diffusion (x_j = 1.2 μm)	7.3	11.4	17
p⁺ Diffusion (x_j = 1.0 μm)	7.1	21.6	82

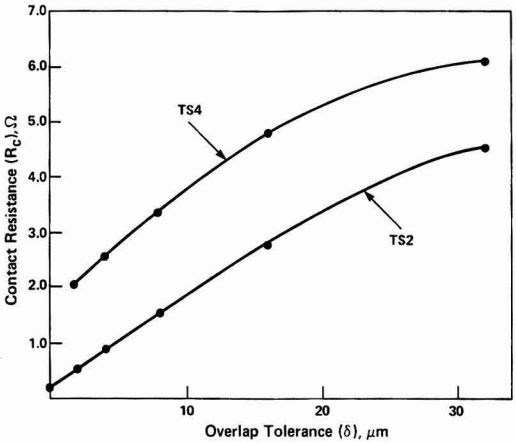

Fig. 6. Contact resistance (R_c) as a function of spacing tolerance (δ) between the edge of the semiconductor layer and the contact window edge, using 8 × 8 μm² contact.

= 0) case. For the self-aligned 8 × 8 μm contact, the calculated ρ_c from Eq. [2] is 0.75×10^{-6} Ω cm², which is consistent with values in the literature (5). The strong dependence of R_c on δ can be attributed to the current flow at the sides of the contact. This current component decreases as δ decreases, resulting in smaller values of R_c.

In the case of the side tapped structure (TS5), the side-tap itself introduces parasitic current paths around the contact which will vary with δ, alignment, and tap size. For direct measurements of an R_c useful for circuit simulation purposes, however, the side-tap structure yields the more representative value, because it senses the voltage in the diffusion at the leading edge of the contact, and the resulting resistance component can be added directly to sheet resistance components for an approximate determination of total parasitic resistance for device simulation purposes. It also has the advantage of measuring relatively larger voltages.

Conclusions

The contact resistance, as determined by the 4-terminal Kelvin technique, is strongly dependent on the physical dimensions and shape of the diffused semiconductor region. The contact window dimensions: length or width or both, have a significant effect on the contact resistance. Furthermore, the spacing between the edge of the diffused semiconductor region and the edge of the contact window, influences the current crowding outside the contact area, along the contact length, and, therefore, influences the contact resistance significantly. The accuracy of the 4-terminal technique, for certain design rules, also depends on the value of the sheet resistance of the semiconductor compared to the contact resistance; the lower the sheet resistance, the more valid is the technique in giving contact resistance values representative of the interfacial contact resistance. For the purpose of circuit simulation and modeling, the side-tap test structure is believed to be the optimum structure because it measures a resistance component more directly applicable to the total transistor parasitic resistance. However, for process monitoring, the uniformly wide bar test structure with minimum spacing tolerance is the most suitable structure, because of minimized parasitic resistance contribution to R_c.

Acknowledgments

We wish to thank H. M. Naguib, A. R. Boothroyd, J. Kolk, I. D. Calder, and A. Loro for many useful discussions, suggestions, and comments on the manuscript. We are also grateful to M. Simard-Normandin for providing us with the software.

Manuscript submitted July 1, 1985; revised manuscript received Aug. 13, 1986.

Northern Telecom Electronics, Limited, assisted in meeting the publication costs of this article.

REFERENCES

1. W. Shockley, Report No. A1-TOR-64-207, Air Force Atomic Laboratory, Wright-Patterson Air Force Base, Ohio (September 1964).
2. H. H. Berger, *ISSCC Dig. Tech. Papers*, 160 (1969).
3. S. S. Cohen, G. Gildenblat, and D. M. Brown, in "Paper 225 presented at The Electrochemical Society Meeting, Montreal, Que., Canada, May 9-14, 1982.
4. S. S. Cohen, G. Gildenblat, M. Ghezzo, and D. M. Brown, *This Journal*, **129,** 1335 (1982).
5. S. S. Cohen, *Thin Solid Films*, **104,** 361 (1983).
6. T. J. Faith, R. S. Irven, S. K. Plante, and J. J. O'Neill, *J. Vac. Sci. Technol.*, **A1,** 443 (1983).
7. S. J. Proctor, L. W. Linholm, and J. A. Mazer, *IEEE Trans. Electron. Dev.*, **ED-30,** 11, 1535 (1983).
8. M. Finetti, A. Scorzoni, and G. Soncini, *IEEE Trans. Electron. Dev. Lett.*, **EDL-5,** 12, 524 (1984).
9. W. M. Loh, K. Saraswat, and R. W. Dutton, *ibid.*, **EDL-6,** 3, 105 (1985).
10. H. H. Berger, *Solid-State Electron.*, **15,** 145 (1972).

Polycrystalline Silicon Oxidation Kinetics and Si/SiO_2 Interface Width

G. Queirolo,* G. Ghidini, L. Meda, and C. Signorini

S.G.S. Microelecttronica, S.p.A., 20041-Agrate, Milano, Italy

A. Armigliato

CNR-Istituto Lamel, 40126-Bologna, Italy

ABSTRACT

The oxidation kinetics of polycrystalline silicon in dry oxygen at 900°C is studied with Auger electron spectroscopy for undoped and for differently doped films. The SiO_2/Si interface width is measured from the Auger depth profiles and is found to depend on the film doping procedure, being more abrupt for phosphorus ion-implanted than for undoped and gas-phase doped ($POCl_3$) films. The interface width is correlated with the morphology of the film surface observed by transmission electron microscopy, with the film structure determined by x-ray diffraction, and with the electrical conductivity of the oxide.

Polycrystalline silicon films (poly-Si) are widely used in MOS devices for gate interconnections. For these applications the oxide grown on poly-Si is used only for masking and/or insulating purposes, but it has no active role, as happens, for instance, in EPROM (erasable programmable ROM) and EEPROM (electrically erasable programmable ROM) (1-4). Both type of memories rely on the very low leakage current through the oxide between the two poly-Si gates during the reading step for the permanent retention of the charge injected on the lower gate, and hence of the stored information. As a consequence, the conduction properties of the oxide film grown on poly-Si are of major concern, and the poly-Si doping and oxidation processes must be adjusted in order to obtain the lowest leak rate (5).

Experimental

Polycrystalline silicon deposition and doping.—Polycrystalline silicon films were deposited at 625°C at a thickness of about 150 nm in a low pressure chemical vapor deposition system onto (100) silicon wafer previously oxidized in dry oxygen at 1000°C to an oxide thickness of 27 nm. Chem-mechanically polished, 100 mm in diameter, boron-doped (100) silicon wafers with 30-50 $\Omega \cdot$ cm resistivity were used throughout.

Both $POCl_3$ gas phase doping and ^{31}P ion implantation were used; the first process was performed at 920°C and resulted in a sheet resistivity of ~45 Ω/□; implantation was performed at 80 keV and at a fluence of 2×10^{15} cm^{-2} (in two steps of 1×10^{15} cm^{-2} each, to avoid temperature increases) and resulted in a sheet resistivity of 200 Ω/□. Implantation at higher fluences (6×10^{15} cm^{-2}, in six different steps) was also performed, in order to compare gas-phase doped and ion-implanted films with the same sheet resistivity. For electrical measurements the fluence investigated was 4×10^{15} cm^{-2}.

Oxidation.—Oxidation of the poly-Si films was performed at 900°C. The samples were slowly introduced into the furnace held at 800°C in dry nitrogen flow. The temperature was then increased to 900°C and the oxygen introduced for the selected oxidation time.

Oxide thickness measurement.—The thickness of the oxide film grown on single crystal silicon can be easily measured down to a thickness of a few nanometers with ellipsometry or to about 10 nm with microinterferometry. These measurements cannot be easily used for the evaluation of the thickness of an oxide film grown on poly-Si. Ellipsometric measurement could be, in fact, possible (6), but it requires the precise knowledge of the poly-Si thickness, which is also changing as the oxidation proceeds. In addition, interface roughness introduces unpredictable errors, and renders this measurement not practical.

Polyoxide thickness measurement can be done with a mechanical profilometer on an etched step, from the etch time of the film in a suitable etching solution, or measuring the capacitance of a MOS with the polyoxide as a dielectric and doped poly-Si as a gate. The first method does not give reliable data for thinner oxide, especially on a rough substrate, while the second is subject to some uncertainties due to difficulties in the end point detection, variations in the etchant composition and temperature, etc. The last method, finally, requires the capacitor fabrication. In addition, not one of these methods give information on the Si/SiO_2 interface width.

Auger electron spectrometry with argon ion sputtering was used in the present study to measure both the oxide thickness and interface width. All the measurements reported here were performed with a Varian scanning Auger spectrometer equipped with a variable energy resolution cylindrical mirror analyzer and a coaxial 10 keV electron gun with a LaB_6 cathode. A differentially pumped ion gun was used for depth profiling; 1 keV ion energy was used in order to minimize the interface broadening caused by knock-on phenomena. The ion beam incidence angle is about 72° from the normal; it was defocused and scanned over an area much larger than the area scanned by the electron beam during the analysis. The electron beam energy and current density were 5 keV and 10^{-2} A cm^{-2}, respectively; the current density was low enough in order to avoid oxygen desorption or oxide reduction during the spectrum acquisition. The peak-to-peak amplitude (I_{pp}) of the O_{KLL} peak was monitored as a function of the ion etching time; the 50% point is assumed to mark the SiO_2/Si interface position (7-8). The time scale was converted into a depth scale using the etch rate obtained from the depth profiles of oxide films grown on single crystal silicon, and whose thickness is known within a nanometer from ellipsometry. In this procedure it was assumed that the etch rate for the mono and polyoxide were the same. Table I reports the thickness of these standard oxides measured with ellipsometry and microinterferometry; the mean etch rate of 5.8 nm min^{-1} and the Auger oxide thickness was obtained using these values. An error of a few percent can be estimated for the AES thickness measurements and for the reproducibility, the most important cause of error being the current instability of the ion beam. From Table I it

Table I. Thickness of oxide film grown on Si single crystal at 900°C in dry oxygen and measured with ellipsometry and microinterferometry

Oxidation time (min)	$X_{o\ (ellipsometer)}$ (nm)	$X_{o\ (nanospec)}$ (nm)
20	9.5	7.6
80	21.5	21.0
150	33.0	34.2
230	43.4	42.5
300	53.0	54.0

* Electrochemical Society Active Member.

appears that microinterferometry fails for thicknesses below 10 nm, while ellipsometry seems to slightly overestimate higher oxide thickness.

Si/SiO_2 interface width.—The width of an interface can be evaluated from AES depth profiles (7-8) measuring the depth over which the p-p amplitude of a given peak of a given element decreases from 84 to 16% of its bulk, constant value. Due to the finite depth resolution of the Auger electron spectrometry, this method will give a finite interface width even for a step distribution (ideally sharp interface). A number of measurement artifacts can increase this apparent interface width. These are for instance: interface roughness, both induced by the sputtering process or already present; preferential sputtering; recoil mixing from the primary ions; chemical effects originated by both primary ions and electrons bombardment. The effect of the induced roughness, in particular, is due to the fact that the underlying layer is exposed while the overlaying film is still present. While the contribution of the original interface roughness will be different for the different samples, all other effects are expected to be the same for all the oxidized poly-Si films. Moreover they are also expected to be not very large for amorphous layers and with the low primary energy of the ions used to obtain the depth profiles. To evaluate the contribution of these effects in our experimental conditions, a tantalum pentoxide film anodically grown on tantalum was used. This sample was prepared at NPL[1] and has a thickness of 28.4 ± 1.7 nm with an interface width of 1.41 ± 0.07 nm, when measured from the oxygen depth profile, as described above, and optimizing the experimental conditions (9). For our experimental setup, a value for the Ta_2O_5/Ta interface of about 2.7 nm was obtained. A similar increase in the measured *vs.* true SiO_2/Si interface width is also expected for SiO_2 film of comparable thickness grown on smooth samples. A value of 4 nm was obtained for the SiO_2/Si (single crystal) interface width; this value was not found to depend on the oxide thickness, at least up to 30 nm.

The contribution to the apparent interface width from the original interface roughness is somewhat different from that of the induced roughness. In fact with the high ion beam incidence angle of 70° (beam to normal) used in our setup, a shadowing effect will be experienced during the sputtering when the protrusion height is of the same order of the separation width. As a consequence, a comparison of the interface width of the different polysilicon samples with the value found for single crystal will give informations on their relative surface roughness.

Surface morphology.—Information on the surface morphology was obtained from TEM cross sections. The specimens were prepared by gluing face-to-face two rectangular slabs approximately 10 mm in length and 8 mm in width, then sawing, lapping, and polishing down to about 20 μm. The electron transparent sample is obtained by ion-beam milling. The procedure has been published elsewhere (10). An Hitachi H-800 TEM, operating at 200 kV, was employed in our experiments.

Film structure.—A Siemens D-500 x-ray diffractometer was used to obtain information on the structure of the poly-Si films, both after deposition and after doping and oxidation. Cu-Kα radiation was used, and the intensity of the different diffraction peaks was corrected in order to take into account the film thickness for the different Bragg angles and obtain meaningful information on the film preferred orientation. To this purpose the following relationship was used (11)

$$I = G_r/\{1 - \exp(-2\,\mu\, x/\sin\theta)\}$$

where G_r is the measured intensity, diffracted by a film of thickness x at a Bragg angle θ; μ is the linear absorption coefficient of silicon for the radiation used; and I is the intensity which would be diffracted by a thick specimen.

Oxide conductivity.—The oxide conductivity was measured on MOS capacitors with poly-Si gate doped either via $POCl_3$ or ^{31}P ion implantation as described above. The oxide (40-100 nm thick) was thermally grown in dry O_2 at 900°C. To reduce charge trapping due to a continuously applied stress voltage and its effects on the I-V characteristics, we applied pulsed voltage steps for each voltage amplitude. A new capacitor was used for each measurement. The injected charge *vs.* time was recorded with the voltage as parameter. We could then determine the Fowler-Nordheim characteristics after the injection of a fixed charge density ($Q \sim 10^{-10}$ C/cm^2).

[1] Certified Reference Material NPL N. S7B83, BCR N. 261, available from NPL, Teddington, Middlesex, England.

Experimental Results and Discussion

Polysilicon film structure.—The x-ray diffractogram for the as grown poly-Si is reported in Fig. 1a. The film presents a (220) preferential growth, *i.e.*, crystallites grow preferentially on the (110) planes. No texture is present, *i.e.*, the crystallites are randomly distributed in space, as is evident from the (220) rocking curve (not reported here). The x-ray diffractogram for $POCl_3$ doped films shows (Fig. 2, a-c) that the doping step causes substantial grain growth, more evident for the (111) peak. This recrystallization proceeds during the oxidation cycle and seems not to be complete even after 60 min at 900°C. On the contrary, the structure of the undoped poly-Si does not change with the oxidation, its diffractogram being practically unchanged even after 95 min at 900°C. Ion implantation with 80 keV ^{31}P ions performed at low temperature (*i.e.*, below 100°C) at a fluence of 2×10^{15} cm^{-2} causes the sample amorphization, as shown by the x-ray diffractogram of Fig. 1b in which no peak is found. After short heat-treatment at 900°C (less than 20 min), the film is completely recrystallized. The x-ray diffractogram does not further change with the oxidation time. Furthermore, the peak intensities, when corrected for the different glancing angle, are the same as those reported in the JPCDS file 26.1481.

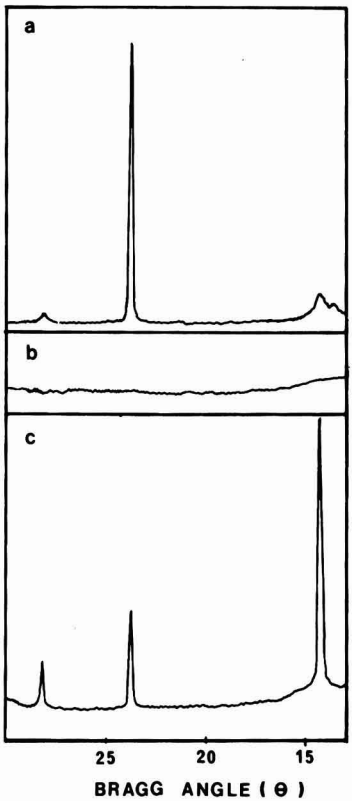

Fig. 1. X-ray diffractograms for polycrystalline silicon films. (a) as deposited; (b) ion implanted; (c) ion implanted and oxidized. See text for details on the experimental conditions.

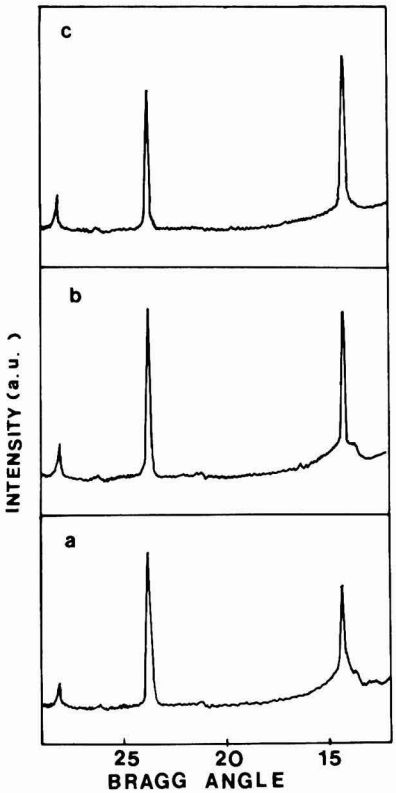

Fig. 2. X-ray diffractograms for $POCl_3$-doped polycrystalline silicon film oxidized at 900°C in dry oxygen for: (a) 10 min; (b) 30 min; (c) 60 min.

This demonstrates that the ion-implanted films do not present any preferential orientation and that their microstructure does not change during the oxidation, after the initial rapid homogeneous recrystallization.

TEM observation on cross sections.—Two cross sections of the gas-phase doped and ion-implanted samples were prepared for TEM observation. Samples with the higher interface width, as seen with AES, were chosen in order to enhance the surface morphology differences. The results obtained are shown in Fig. 3 and 4; from top to bottom one can recognize the upper oxide, the poly-Si, the lower oxide, and single crystal Si substrate. Unfortunately the quality of these TEM pictures is not very high due in part to the low thickness of the films examined. Nevertheless, the difference between the upper oxide/poly-Si interface for the two samples is evident. In addition they show a dramatic difference in the poly-Si film microstructure for the two samples. The height of the Si protrusions is about 20 nm, and less than 10 nm for the $POCl_3$ and ion implanted samples, respectively.

Oxidation kinetics.—The thickness of the oxide grown at 900°C in dry oxygen on (100) single crystal and on poly-Si films is reported in Fig. 5. Three poly-Si films were studied: undoped, doped with $POCl_3$ (ρ_s = 45 Ω/□), and ion-implanted at two different ^{31}P fluences, *viz.*, 2 and 6 × 10^{15} cm^{-2} (with a sheet resistivity of 200 and 45 Ω/□, respectively). The lightly doped (30-50 Ω · cm) single crystal silicon presents the lowest oxidation rate. For ion-implanted polysilicon films this rate increases, as expected, with the doping level (12). At the highest implantation level single crystal and poly-Si show the same oxidation kinetics. The grain structure of the poly-Si samples is stabilized within the first few minutes of oxidation resulting in large columnar structures as observed by TEM cross section (Fig. 4). The amount of dopant segregated at the grain boundaries is probably negligible, and the bulk doping is then similar for both samples since the same oxidation kinetics is observed. $POCl_3$-doped films behave quite differently: the slope of the oxidation curve is much lower than for the other poly-Si films of similar doping or for the heavily doped single crystal silicon. A possible explanation is that, in this case, a parabolic regime is already dominating the oxidation process. The main difference can be ascribed to the continuous evolution of poly-Si grains, which are changing during the oxidation of the $POCl_3$-doped samples. Even if, as stated before, the quality of our TEM plates is not very good, thickness undulations of the polyoxide shown by Irene *et al.* (13) are not found and the external surface of the polyoxide is usually the exact replica of the poly-Si surface. The same holds true for the protu-

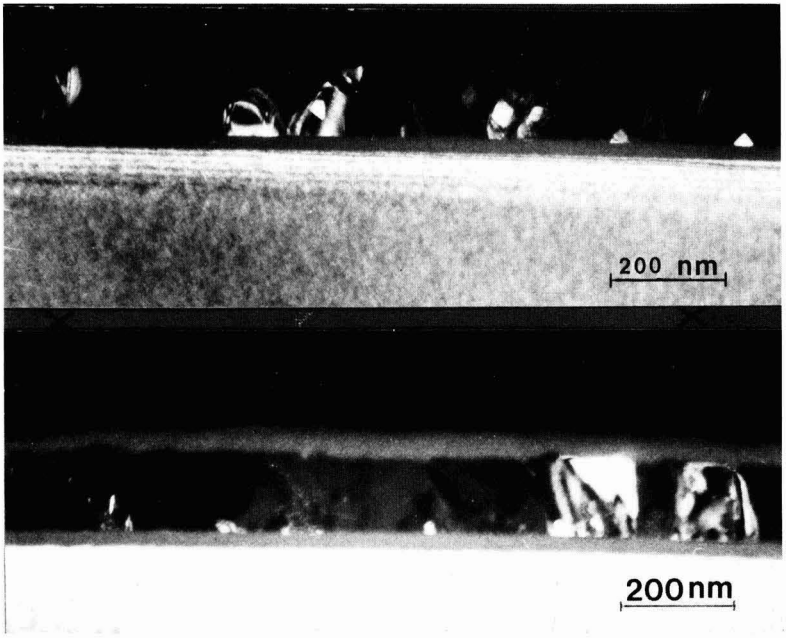

Fig. 3. Dark-field TEM micrograph taken with a portion of the (111) ring of the poly-Si in a $POCl_3$-doped film. From bottom to top: substrate Si, 1st oxide, poly-Si, polyoxide and glue.

Fig. 4. Dark field TEM micrograph taken in an ion-implanted film. Layer sequence as in Fig. 3.

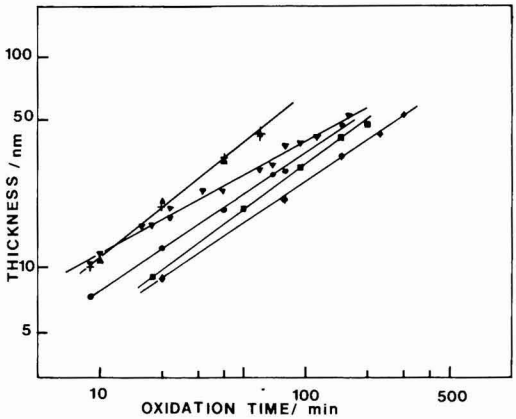

Fig. 5. Oxidation kinetics at 900°C in dry oxygen for silicon single crystal and for different polycrystalline silicon films. (◆): Single crystal, (100) p-type 30-50 Ω · cm and (+) ion implanted, 6 * 10^{15} cm^{-2}, ρ_s = 10 Ω/□. Polycrystalline film: (■), undoped; (●) ion implanted, 2 * 10^{15} cm^{-2}, ρ_s = 200 Ω/□; (▲) ion implanted, 6 * 10^{15} cm^{-2}, ρ_s = Ω/□; (▼) $POCl_3$-doped, ρ_s = 45 Ω/□.

berances of silicon into the oxide reported by Marcus *et al.* (14). They can produce a compressive stress into the oxide, and influence the oxidation process, reducing, for example, the oxidant diffusion (15), which then becomes the limiting factor. In our sample, nevertheless, the oxide thickness is much lower than in experiments of Marcus. According to the reported x-ray diffractogram and evident in the TEM cross section these protuberances are due to grain growth during the oxidation.

The linear and parabolic rate constants K_l and K_p can be calculated from the slope and intercept of the inverse of the growth velocity *vs.* the oxide thickness (Fig. 6). A lower parabolic rate constant for the $POCl_3$ doped samples is indeed found. Furthermore, it is observed that $POCl_3$-doped samples show a deviation from the straight line of the data in the small thickness range, which has already been proposed to be due to the stress effect on the oxidant diffusion in the SiO_2 (15). The experimental values determined for P-implanted and $POCl_3$-doped samples are, respectively, K_p = 1.58E3 A^2 min^{-1}, K_l = 15 A min^{-1} and K_p = 8E2 A^2 min^{-1}, K_l = 5 A min^{-1}.

Interface width.—The SiO_2/Si interface width, measured as described above, and without taking into account the spectrometer resolution function, is reported as a function of the oxide thickness in Fig. 7. The four curves refer to the

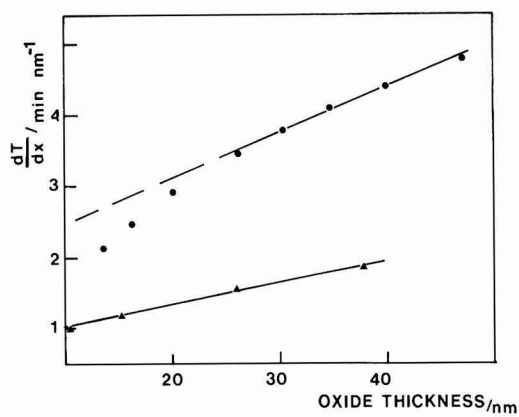

Fig. 6. Inverse of the growth velocity *vs.* the oxide thickness for P-implanted (▲) and $POCl_3$-doped (●) samples.

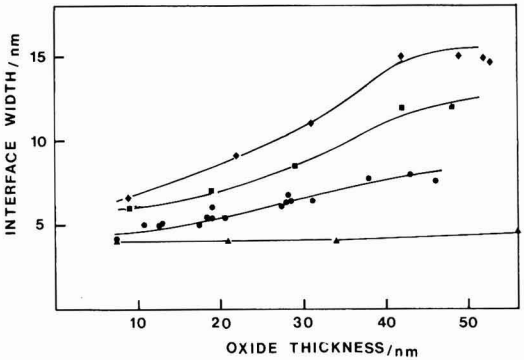

Fig. 7. Interface width, measured from the AES depth profiles as a function of the oxide thickness for: (▲) single crystal; (■) undoped, (●) ion-implanted, and (◆) $POCl_3$-doped polycrystalline silicon films.

(100) single crystal silicon and to the three poly-Si films studied. It is clear that the SiO_2/Si interface is more abrupt for silicon single crystal than for poly-Si. For (100) Si, the interface width is nearly constant; it is ~4 nm for oxide thickness smaller than ~30 nm, and increases to ~4.5 nm for 56 nm thick oxide. This small interface width increase is probably a measurement artifact, caused, for instance, by the ion beam induced roughening. The behavior of the width of the SiO_2 interface for oxide growth on poly-Si is quite interesting. In fact, the interface width for undoped poly-Si is, as expected, higher than for (100) single crystal silicon, but at a given oxide thickness it can be both increased or decreased by the doping process. In addition, the width increases with the oxide thickness in a very dif-

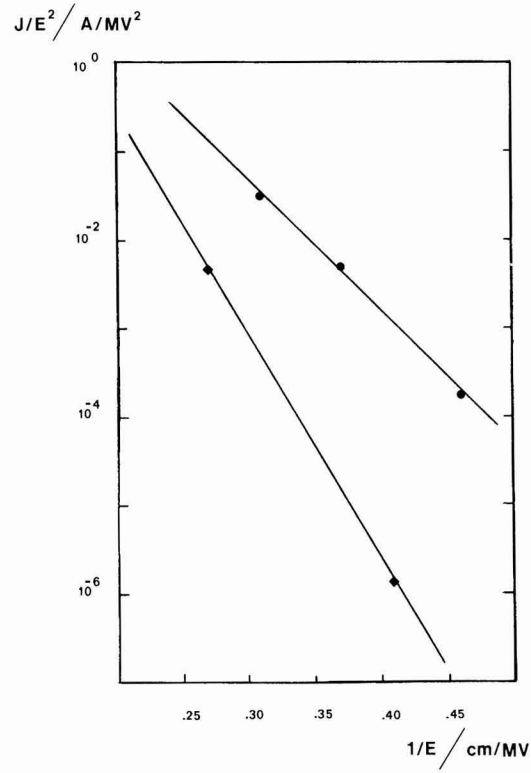

Fig. 8. Fowler-Nordheim characteristics for oxides grown on (◆) ion-implanted and (●) $POCl_3$-doped polycrystalline silicon films.

ferent way for the undoped films and for those doped with $POCl_3$ or by ion implantation. A value of ~15 nm is obtained for 40 nm thick oxide grown on $POCl_3$-doped film, as compared with a width of ~8 nm for ion-implanted poly-Si.

These results suggest that the different variation of the interface width with the oxide thickness is caused by the different structure of the poly-Si, and by its variation during the oxidation. It is, in fact, well known that oxidation induces a roughness increase in poly-Si (1-5). In particular, a sample characterized by a uniform growth of crystallites of random orientation (as for the implanted case), would be expected to give a sharper interface; on the contrary, samples with strong preferential orientation, which, in addition, is continuously changing during the oxidation cycle, will present broader interfaces. Furthermore, the dopant segregation at the grain boundaries can enhance this phenomenon.

Oxide conductivity.—The F-N characteristics (Fig. 8) are obtained according to the experimental procedure described above. In this figure the dependence of the oxide conductivity on the doping type (via $POCl_3$ or P ion implantation) is shown. Samples with the gate doped via $POCl_3$ present the largest conductivity: the F-N characteristic is shifted to higher current densities, indicating a degradation of the insulating properties of the oxide with respect to doping via ion implantation. This effect cannot be related only to oxide thickness reduction. The several orders of magnitude difference in the I-V characteristic can be ascribed to an enhanced, localized injection at the rougher poly-Si surface. TEM cross sections confirm the existence of protrusions at the oxide-polysilicon interface, which are larger for the $POCl_3$ doped than for implanted samples (Fig. 3 and 4).

A correlation between the I-V characteristics and the surface asperities has already been observed (4), with the oxidation temperature as the most important parameter affecting the polyoxide surface, but no differences with poly-Si doping level or type were reported.

Conclusions

In conclusion, we have confirmed that the leakage current through a thin oxide grown on polycrystalline silicon films can be correlated with the SiO_2/Si interface width, probably via high localized fields due to interface roughness. In addition this is strongly influenced by the poly-Si film doping, *i.e.*, whether it is performed by $POCl_3$ gas phase doping or by P ion implantation. More abrupt interfaces, and lower leakage currents are obtained via an ion implantation process, which results in film amorphization. The utilization of Auger electron spectrometry as a measurement technique for comparing interface roughnesses has been proposed as a useful tool even for SiO_2 films on polycrystalline silicon.

Acknowledgments

Thanks are due to G. Valdré for making the TEM cross sections. TEM observations were made at the Electron Microscopy Center of the University of Ferrara.

Manuscript submitted Dec. 16, 1985; revised manuscript received July 1, 1986.

S.G.S. Microelettronica S.p.A. assisted in meeting the publication costs of this article.

REFERENCES

1. L. Faraone, R. D. Vibronek, and J. T. McGinn, *IEEE Trans. Electron Devices*, **ED-32,** 577 (1985).
2. L. Faraone, Paper presented at Insulating Film on Semiconductors (INFOS), Tolosa (1985).
3. D. J. DiMaria and D. R. Kerr, *Appl. Phys. Lett.*, **27,** 505 (1975).
4. M. Anderson and D. R. Kerr, *J. Appl. Phys.*, **48,** 4834 (1977).
5. K. Shinada, S. Mori, and Y. Mikada, *This Journal*, **132,** 2185 (1985).
6. E. A. Irene and D. W. Dong, *ibid.*, **129,** 1347 (1982).
7. S. Hofmann, in "Practical Surface Analysis," D. Briggs and M. P. Seah, Editors, pp. 141-179, John Wiley & Sons, New York (1983).
8. S. Hofmann and J. M. Sanz, in "Thin Film and Depth Profile Analysis," H. Oechsner, Editor, pp. 141-158, Springer-Verlag, Berlin (1984).
9. C. P. Hunt and M. P. Seah, *Surf. Interface Anal.*, **5,** 199 (1983).
10. A. Garulli, A. Armigliato, and M. Vanzi, *J. Microsc. Spectrosc. Electron.*, **10,** 135 (1985).
11. B. D. Cullity, "Elements of X-ray Diffraction," p. 269, Addison-Wesley (1967).
12. E. A. Irene and D. W. Dong, *This Journal*, **125,** 1146 (1978).
13. E. A. Irene, E. Tierney, and D. W. Dong, *ibid.*, **127,** 705 (1980).
14. R. B. Marcus and T. T. Sheng, *ibid.*, **129,** 1278 (1982).
15. A. Fargeix and G. Ghibaudo, *J. Appl. Phys.*, **54,** 7153 (1983).

An Environment-Insensitive Trilayer Structure for Titanium Silicide Formation

Ming-Zen Lin

Institute of Electronics, National Chiao-Tung University, Hsin-Chu, Taiwan, Republic of China

Yeou-Chong Simon Yu

Tektronix Laboratories, Tektronix Incorporated, Beaverton, Oregon 97005

Chung-Yu Wu

Department of Electrical Engineering, Portland State University, Portland, Oregon 97207

ABSTRACT

A Si/Mo/Ti trilayer structure which consists of a top, insulating Si film, a middle buffering Mo film, and a bottom Ti film is proposed for $TiSi_2$ formation on n^+ polysilicon. Since residual oxidants and impurity gases are effectively blocked by the Si layer, an N_2-flowing open tube with stringent environmental control is enough for the formation process above 750°C. The resultant sheet resistance of the silicided polysilicon is as low as 2% with good uniformity. Moreover, the resultant SiO_2 thickness loss is reduced, and no metallic luster is shown on the oxide surface, even after the anneal at 800°C. The lateral formation of $TiSi_2$ is found to be greatly suppressed in the anneal at 750°C for 15 min. Low resistivity, high environmental insensitivity, small oxide loss, and less lateral growth make the $TiSi_2$ formation using the trilayer structure an attractive and promising method in many IC applications using silicides.

It is known that titanium silicide ($TiSi_2$) is one of the promising gate and interconnect materials for future integrated circuits. Generally $TiSi_2$ can be thermally formed by reacting thin titanium films with polycrystalline silicon (1) or by sintering codeposited films on polysilicon or SiO_2 (2). However, due to high oxidation rate of Ti to some oxidants, the quality of the resultant $TiSi_2$ is very sensitive to oxidizing gases in the annealing or sintering ambient. Therefore, a very stringent control on the ambient, especially the control of the residual oxygen, is required. This often increases process cost and causes difficulties in yield improvement. Recently, a Mo/Ti bilayer structure has been proposed (3) to solve this problem. However, because oxidants may penetrate the top Mo layer and react with the bottom Ti layer, it still requires some degree of ambient control.

In this study, a Si/Mo/Ti trilayer structure is proposed for $TiSi_2$ formation. Experimental results have shown that a good-quality $TiSi_2$ layer can be formed on n^+ polysilicon in a conventional N_2-flowing ambient. Thus, no stringently controlled ambient is required in the annealing or sintering process. Moreover, the undesired reaction between Ti and SiO_2 (4) can be weakened which results in a smaller SiO_2 thickness loss. As to the lateral formation problem, the trilayer structure annealed at 750°C for a shorter time (15 min) has much less lateral formation of $TiSi_2$. It is possible, therefore, to find an optimal annealing condition in which the oxide loss, the lateral formation, and the resistivity of $TiSi_2$ reach a satisfactory compromise for IC applications.

Experimental

The (100) p-type starting wafers with resistivity of 20-55 Ω/□ were first oxidized to form a 500 nm SiO_2 layer. A polysilicon layer of 500 nm was then deposited by using LPCVD and doped by using $POCl_3$ diffusion. The measured sheet resistance of the resulting n^+ polysilicon film was 50-55 Ω/□. The polysilicon layer was then patterned into long strip lines which can be employed to measure the sheet resistance after silicidation.

The wafers were then put into the vacuum chamber of a dual-E-gun multiple-crucible evaporator. A trilayer structure which consists of 50 nm Ti, 100 nm Mo, and 100 nm Si films successively deposited by using different crucibles in the same vacuum, was formed. The film thickness was controlled by a thickness monitor in the chamber. The cross-sectional view of the trilayer structure is shown in Fig. 1. Then the conventional two-step silicide formation process (3) was applied. In the first step called the sintering or the first annealing step, the wafers were sintered at five different temperatures (600°, 650°, 700°, 750°, and 800°C) for 30 or 60 min in an N_2-flowing open tube. After the first anneal, the top Si layer was removed by plasma etching, whereas the Mo layer and the unreacted Ti layer were etched in a solution of $NH_4OH:H_2O_2:H_2O$ = 1:1:2 for 10-20 min. Then the sheet resistance of the polysilicon strip line was measured. Following was the second annealing process at 800°C in an N_2-flowing open tube for 30 min. After the second anneal, the sheet resistance was measured again. Besides the resistivity measurement, the AES analyses were performed on both the as-deposited and the annealed samples to investigate their physical properties.

In the $TiSi_2$ formation process, the interaction between Ti and SiO_2 is a major concern (4), especially in self-aligned silicide technology (5). Another group of wafers was used to investigate this interaction. These wafers went through the same process cited above. The oxide thickness and the index of refraction before and after the silicide formation were measured by an ellipsometer. Selected samples were also analyzed by AES.

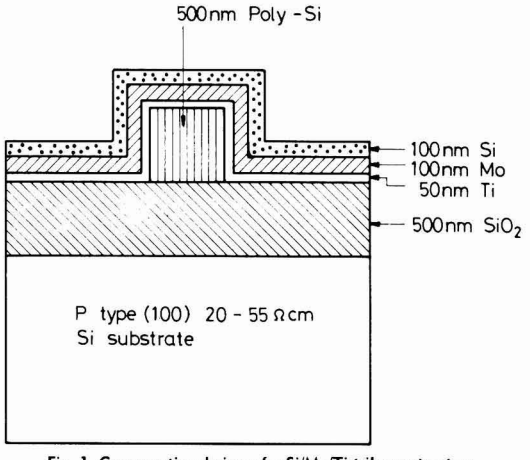

Fig. 1. Cross-sectional view of a Si/Mo/Ti trilayer structure

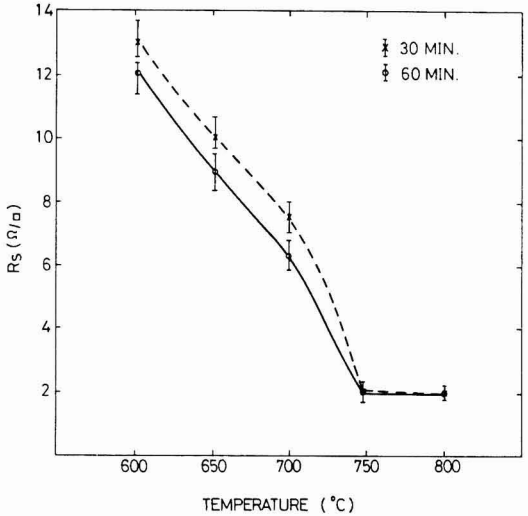

Fig. 2. Measured sheet resistance of the silicided n^+ polysilicon as a function of temperature in the first anneal for 30 min (dashed line) and 60 min (solid line).

For comparisons, the Mo/Ti bilayer structure (3) and the Ti monolayer structure were adopted in another group of wafers to form $TiSi_2$. They went through the same process in the same ambient. The AES was also applied to investigate the annealed samples.

To investigate the lateral growth (6) in the $TiSi_2$ formation using the trilayer structure, a group of p-type (100) wafers were oxidized to form a 100 nm SiO_2 layer. Then the wafers were patterned and etched to form long SiO_2 strip lines. To simulate the n^+ source/drain junction formation, the wafers were subjected to the $POCl_3$ diffusion to form n^+ single Si region with a resistance of 120 Ω/□. After the trilayer structure was formed, different annealing processes were applied to form $TiSi_2$ in the n^+ region. After stripping the Si layer, the Mo layer, and the unreacted Ti layer, SEM was applied to investigate the lateral formation. The resistivity of the resultant $TiSi_2$ was monitored from the accompanying samples of bare Si wafers and polysilicon/SiO_2/Si wafers.

Results and Discussion

The measured sheet resistance of the silicided n^+ polysilicon layer after the first annealing process is shown in Fig. 2 as a function of temperature. These data, which were taken from chips on different wafers and in different runs, have consistently shown that a low resistance of 2 Ω/□ can be obtained after annealing above 750°C for either 30 or 60 min in an N_2-flowing open tube. Below 750°C, the resistance is larger than 2 Ω/□ and is decreased with the increase of the annealing time.

The above resistance feature after the first anneal can be understood from the typical AES profiles of the silicided polysilicon as shown in Fig. 3 for the anneals performed at 600°, 650°, and 750°C for 30 min. More oxygen atoms and less titanium atoms are found in the samples annealed at a lower temperature. This means more oxide components and less $TiSi_2$ components in the polysilicon. The resultant resistivity, of course, is higher. Note that the oxygen atoms which react more easily with the samples annealed at a temperature lower than 750°C, are from contaminations both during the evaporation process and after the first anneal, but not during the first annealing process, as will be verified later.

After the second anneal at 800°C for 30 min in an N_2-flowing open tube, those samples annealed above 750°C in the first anneal show a negligible change of sheet resistance and still keep the metallic shining on the surface of the silicided n^+ polysilicon. However, the samples annealed below 750°C in the first anneal show a significant increase in resistance value even up to infinity. The surface becomes blue and no metallic shining can be observed.

Based upon the explanation of the resistance feature after the first anneal, the above results can be explained as follows. If the first annealing temperature is below 750°C, some silicide compounds besides $TiSi_2$ are formed. As compared to $TiSi_2$, these compounds may react more easily with the residual oxygen in the second annealing N_2 ambient to form SiO_2 and titanium oxides. These oxide components significantly increase the sheet resistance of the silicided polysilicon. On the other hand, if the first annealing temperature is raised above 750°C,

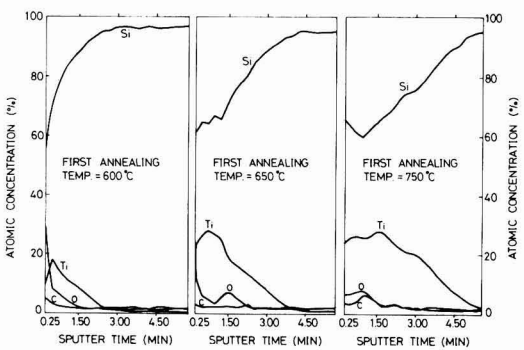

Fig. 3. AES depth profiles of the silicided n^+ polysilicon annealed for 30 min at (a) 600°C; (b) 650°C; (c) 750°C.

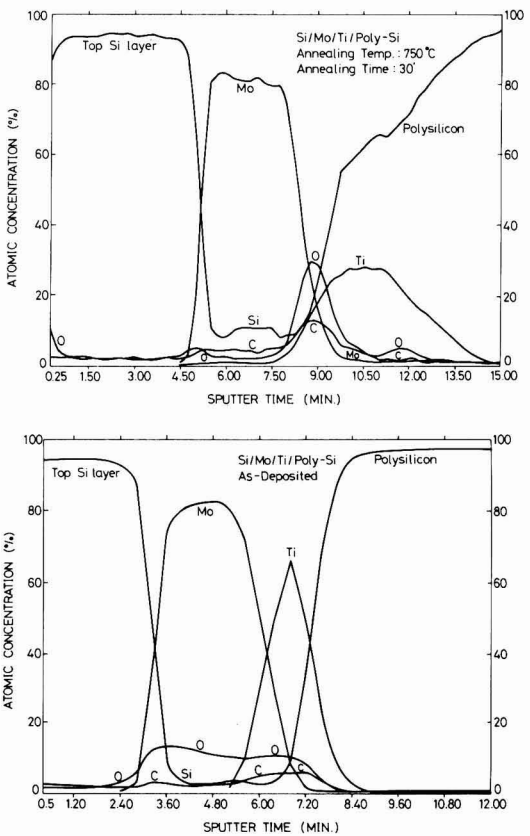

Fig. 4. AES depth profiles of the Si/Mo/Ti/poly-Si structure (a) annealed at 750°C for 30 min; (b) as-deposited.

stable $TiSi_2$ is formed, and the resistance is lowered to 2 Ω/□. In this case, the second anneal in an N_2 ambient has a negligible effect on the silicided polysilicon. Therefore, using the proposed Si/Mo/Ti trilayer, the second anneal is not necessary, if the first annealing temperature is above 750°C.

According to our observations, the top 100 nm Si layer is very effective in preventing residual oxidants and impure gases in an N_2 ambient from reaching the bottom Ti layer. Since nitrogen and oxygen still can react with the evaporated Si layer at temperatures below 800°C, a thin nitride or oxide layer may be formed on the surface of the Si layer at the beginning of the first anneal. With the aid of this nitride or oxide layer, only a very limited amount of residual oxidants and impure gases may enter the Si layer, which then are trapped within the Si layer by reacting to the Si atoms. Thus, residual oxidants and impure gases in the first annealing N_2 ambient can hardly reach the Ti layer.

The effectiveness of the top Si layer in blocking residual oxidants and impure gases can be realized by comparing the AES profile of the annealed trilayer structure in Fig. 4a to that of the as-deposited film in Fig. 4b. It is seen that the interior of the top Si layer remains unchanged after annealing, being free from any external impure elements. Note that the oxygen atoms at the Mo/$TiSi_2$ interface, as seen in Fig. 4a, are due to contamination from the Mo or Ti target, and the evaporator chamber during the evaporation process, because they are also detected in the as-deposited Mo and Ti films, as seen from Fig. 4b. Some carbon atoms are also found in the as-deposited Mo and Ti films. However, the carbon contamination source has not yet been identified.

Because of the insulating effect of the top Si layer, a stable $TiSi_2$ silicide with a low resistance of 2 Ω/□ can be formed at an annealing temperature above 750°C in an N_2 open tube instead of a stringently controlled Ar or H_2 ambient. Furthermore, the $TiSi_2$ silicide formed in a conventional N_2-flowing open tube is highly environmentally insensitive. This insensivity leads to good uniformity obtained among different wafers and different runs in our experiments.

Without the top Si layer, the Mo/Ti bilayer structure was subjected to the same annealing process in the same N_2 ambient. The resultant resistivity of the silicided n^+ polysilicon is significantly increased even up to infinity. Evidently, the residual oxidants in an N_2 ambient may easily penetrate the Mo layer and react with the bottom Ti layer to form the titanium oxides. The AES profile of the Mo/Ti/poly-Si structure annealed at 750°C for 30 min in an N_2 ambient is shown in Fig. 5a. It is seen that the residual oxygen has oxidized both Mo and Ti films and $TiSi_2$ cannot be well-formed. The oxidized Mo layer is not seen in this profile, because it was quickly etched out

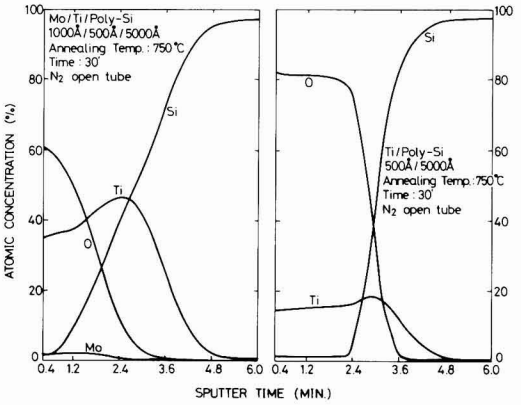

Fig. 5. AES depth profiles of (a) the Mo/Ti/poly-Si structure; (b) the Ti/poly-Si structure, both subjected to the same annealing process in an N_2-flowing open tube.

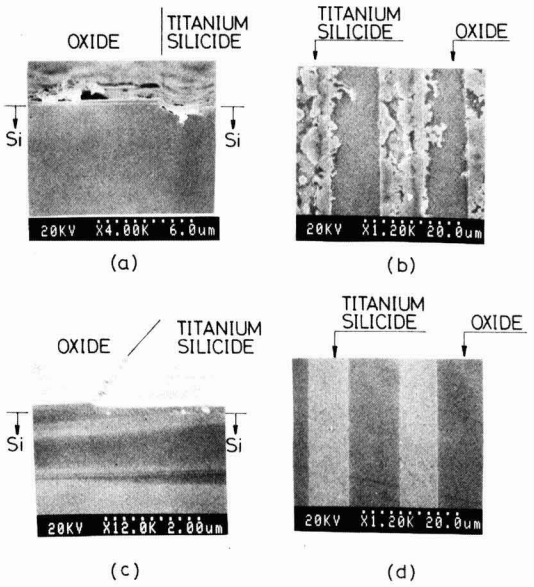

Fig. 6a. SEM cross-sectional view; b. SEM top view of the silicided single silicon subjected to 750°C 30-min annealing; c. SEM cross-sectional view; d. SEM top view of the silicided single silicon subjected to 750°C 15-min annealing.

during the preetching cycle. The depth profile of Ti/poly-Si structure subjected to the same annealing process is also shown in Fig. 5b. It can be seen that the Ti film has been more severely oxidized, and good quality $TiSi_2$ cannot be formed.

It is found that the middle 100 nm Mo layer in the trilayer structure is efficient in isolating the top Si layer from the Ti layer, because the Mo-Si reaction is not significant below 800°C, as may be seen from the depth profile in Fig. 4a. Therefore, the reaction between Si layer and Ti layer, which may interfere with the silicidation in polysilicon, can be avoided.

In this study, the ambient temperature of 750°C for stable $TiSi_2$ formation is higher by 50°C than that reported (1). This temperature increase may be attributed to the decrease of the diffusion coefficient of Si in the Ti film, which may be caused by the Mo atoms in the evaporated Ti film. Due to the substrate heating during the evaporation process, Mo atoms are very likely to enter the Ti film as may be seen from the profile in Fig. 4b. The carbon contamination in the Ti film may also lead to the decrease of the diffusion coefficient. More work will be done to find out the actual mechanism of this temperature increase.

The group of wafers used to monitor the interaction between Ti and SiO_2 were investigated after etching away the Si and Mo layer and the unreacted Ti layer. No metallic luster or any other physical changes on the oxide surface were observed, even in those samples with the first annealing temperature as high as 800°C. The index of refraction measured by an ellipsometer was 1.45, the same as that before silicidation. However, without the top Si layer, all samples with the Mo/Ti bilayer structure were found to have a metallic luster on the oxide surface after the first anneal in an N_2 ambient. Although the actual structure and the formation mechanism of the metallic luster have not yet been clear, we believe that the top Si layer is capable of preventing the generation of the metallic luster.

The SiO_2 thickness loss after the first anneal is listed in Table I for annealing temperatures from 600° to 800°C in 50° increments. As compared to the data provided by Ting *et al.* (4), the SiO_2 thickness loss is less than one-half of the loss in the $TiSi_2$ formation with a monolayer struc-

Table I. Oxide thickness loss after the first anneal at various temperatures in an N_2 ambient

Annealing temperature	Time (min)	Loss of oxide thickness (nm)
600 °C	30	4.9 ~ 8.0
	60	7.6 ~ 9.1
650 °C	30	7.2 ~ 10.2
	60	12.1 ~ 14.5
700 °C	30	17.4 ~ 22.6
	60	17.3 ~ 25.3
750 °C	30	20.5 ~ 24.3
	60	22.4 ~ 25.9
800 °C	30	27.0 ~ 29.5
	60	28.2 ~ 30.5

Table II. The measured resistance of the silicided silicon from three different anneals employed to study the lateral growth

Annealing condition	Sheet resistivity (Ω/□)	
	N^+ poly-Si	N^+ single Si
750 °C, 30min.	2.2	1.8
750 °C, 15min.	2.4	1.8
750 °C, 15min. + 600 °C, 4hr.	2.0	1.8

ture in an Ar ambient at the same ambient temperature. From the above results, it can be realized that the reaction between Ti and SiO_2 in the trilayer structure is weakened. This is possibly due to the Mo atoms and the carbon atoms in the Ti film, as mentioned before. The other possible reason for smaller oxide loss is the small thickness of the Ti film in the trilayer structure.

Three different annealing processes were performed to investigate the lateral formation of $TiSi_2$ in the trilayer structure. It is shown that the annealing at 750°C for 30 min leads to a severe lateral growth as may be seen from the SEM cross-sectional view in Fig. 6a and the top view in Fig. 6b. Reducing the annealing time to 15 min can drastically reduce the lateral formation as may be seen from the SEM photographs in Fig. 6c and d. If an extra annealing at 600°C for 4h is performed, the resistance in the silicided n^+ polysilicon can be reduced from 2.4 to 2.0 Ω/□, as listed in Table II, without affecting the lateral formation. The real cause for the reduced lateral growth in a short-time 750°C anneal has not been definitely identified yet. But we believe that it is the same cause as that which explains the higher silicidation temperature.

Conclusions

Because the top 100 nm Si layer is highly efficient in preventing residual oxidants and impure gases from reaching the bottom Ti layer, and, because the middle 100 nm Mo layer is effective in eliminating the undesired reaction between Si layer and Ti layer, the proposed Si/Mo/Ti trilayer structure has been shown to be able to thermally form high quality $TiSi_2$ silicide on n^+ polysilicon in the first anneal above 750°C in a conventional N_2-flowing open tube. No stringently controlled H_2 or Ar ambient is required. The resultant silicided n^+ polysilicon layer has shown a low sheet resistance of 2 Ω/□, as well as high environmental insensitivity and good reproducibility. These features lead to low process cost, high yield, and easy process control.

We have also found that the interactions between Ti and SiO_2 are weakened so that the SiO_2 thickness loss is reduced. Moreover, no significant lateral growth was found in samples annealed at 750°C for 15 min. From these initial observations, we believe that an optimal process can be found to obtain acceptably small oxide loss and lateral growth.

Based upon the results of this study, it is felt that the same or similar trilayer structures can also be applied to other thermally formed silicides to reduce their environmental sensitivity and to decrease their process cost.

Acknowledgment

The authors would like to thank the Semiconductor Research Center, National Chiao Tung University, Republic of China for preparing the samples and generating the SEM micrographs and the AES profiles.

Manuscript submitted May 3, 1985; revised manuscript received June 10, 1986.

Portland State University assisted in meeting the publication costs of this article.

REFERENCES

1. S. P. Murarka and D. B. Fraser, *J. Appl. Phys.*, **51,** 342 (1980).
2. S. P. Murarka and D. B. Fraser, *ibid.*, **51,** 350 (1980).
3. H. K. Park, J. Sachitano, G. Eiden, E. Lane, and T. Yamaguchi, *J. Vac. Sci. Technol.*, 1**A, 2,** 259 (1984).
4. C. Y. Ting, M. Wittmer, S. S. Tyer, and S. B. Brodsky, *This Journal*, **131,** 2934 (1984).
5. T. Shibata, K. Hieda, M. Sato, M. Konaka, R. L. M. Dang, and H. Iizuka, *IEEE J. Solid-State Circuits*, **17,** 161 (1982).
6. P. Pevesz, J. Gyimesi, L. Pogany, and G. Peto, *J. Appl. Phys.*, **54,** 2114 (1983).

Palladium Silicide Ohmic Contacts to Shallow Junctions in Silicon

R. N. Singh, D. W. Skelly, and D. M. Brown*

General Electric Corporate Research and Development, Schenectady, New York 12301

ABSTRACT

Ohmic contacts to small area and shallow pn^+- and np^+-junctions in silicon are made with palladium silicide by depositing 400Å of Pd on silicon and heating between 300° and 430°C for silicide formation. The contact resistance of Mo(5000Å)/Pd_2Si(680Å)/silicon metallization is measured by the Kelvin four-terminal method. Influence of processing steps and siliciding environment on the contact resistance is studied. The results indicate that contact resistance values are sensitive to the presence of oxygen in the siliciding environment. Vacuum siliciding leads to low contact resistance with values between 0.28 and 0.31 $\mu\Omega$ cm² for 1.3 μm diameter p^+-junctions and between 0.15-0.19 $\mu\Omega$ cm² for corresponding n^+-junctions. The thermal stability of these values is studied. Based on these results, the palladium silicide contacts appear promising for the VLSI circuit fabrication providing subsequent processing temperatures are below 475°C.

Metal silicides have attracted considerable attention for low-resistivity gates, interconnections, and ohmic contacts for very large scale integrated (VLSI) circuits because of metal-like resistivities, stability against processing chemicals, and high-temperature stability (1). Ohmic contacts with low contact resistance, low leakage current, and shallow junction characteristics are required for the emerging VLSI circuits. Palladium silicide is potentially attractive from the viewpoint of shallow junction formation because palladium forms a metal-rich silicide, Pd_2Si, after reaction with the single-crystal silicon. In contrast to platinum silicide contacts, the palladium silicide forms metal-rich silicide which remains stable up to 700°C after formation at a low temperature of ≈270°C, can be easily and selectively etched at the room temperature, and is compatible with some of the processing chemicals such as HF and HCl acids (2).

Palladium silicide contacts to a relatively large area in silicon are reported in a number of publications (3-6); however, only limited information is available for small area (≈1 × 1 μm) devices of interest to VLSI. Others have studied palladium silicide contacts covered with aluminum metallization, and they have found that the characteristics of Schottky diodes change when annealed above 300°C (7, 8). Therefore, the objectives of this investigation were to determine the contact resistance of palladium silicide to small areas in silicon and to determine their thermal stability when molybdenum was used as a substitute for aluminum for first-level metal interconnections in a multilevel metallization scheme for VLSI technology. A contact process for forming self-aligned palladium silicide ohmic contacts to shallow junctions in silicon was developed for this purpose (2). The influence of processing conditions on contact resistance is also reported in this investigation.

Experimental

The contact resistance of palladium silicide to silicon was measured on 7.6 cm diameter silicon wafers of <100> orientation. These were Czochralski-pulled boron- and phosphorus-doped p- and n-type silicon wafers of 8-10 $\mu\Omega$ cm nominal resistivity. A standard chemical cleaning procedure utilized 5 min each in Karos (50:50::H_2SO_4:H_2O_2), hot concentrated HCl at 60°C, and deionized (DI) water. The detailed processing conditions for sputter deposition, annealing for silicide formation, and selective etching of unreacted palladium are described elsewhere (2). The wafers for the contact resistance measurements were processed according to steps outlined below.

Following a standard chemical cleaning procedure, 5000Å of silicon oxide was grown in the field areas. A masking step to the active area was done followed by etching the field oxide and a standard chemical cleaning. A 200Å thick protective oxide was grown for ion implantation. The arsenic was implanted with a dosage of 8 × 10^{15}/cm² at 90 keV, and BF_2^+ was implanted with a dosage of 4 × 10^{+15}/cm² at 40 keV to form pn^+- and np^+-junctions, respectively. Following a standard chemical cleaning, the wafers were annealed at 900°C for 30 min in nitrogen to activate the dopants. The standard chemical cleaning of the wafers was repeated, and 4000Å of LPCVD silicon oxide was deposited. The second masking step was performed to open the contact vias, and dry etching of the oxide was done to the silicon surface. This was followed by a dry cleaning of the contact vias. The wafers were cleaned by standard chemical cleaning followed with a 60s etch in 1% solution of HF in an ultrasonic cleaner immediately before the palladium deposition. The palladium film of 400Å thickness was deposited in either an MRC-603 or Perkin-Elmer-2400 sputtering machine. The wafers were then annealed between 300°-430°C for 15 min in either a vacuum (1.0 × 10^{-5} Pa of sputtering system), or in a furnace using gettered argon, or an Ar-10% H_2 gas mixture ambients for the silicide formation. The unreacted palladium was selectively etched at room temperature with the 10g KI + 1g I_2 + 40 ml H_2O etching solution. The wafers were cleaned with hot HCl for 5 min and DI water rinsed for 5 min. The contacts were then cleaned with 1% HF for 60s in an ultrasonic cleaner just prior to metallization. This etching step was omitted for the first set of wafers, but incorporated in the second set of wafers. A 5000Å-thick molybdenum was sputter deposited followed by a third masking step and patterned by a reactive ion etching method. All the wafers were given a hydrogen anneal at 400°C for 60 min.

The four-terminal Kelvin-resistor test vehicle was used for contact resistance measurements. The value of contact resistance, as determined by the Kelvin technique, includes contributions from the junction underneath the contact interface along with the interface resistance. This is a situation similar to a real FET device and, therefore, Kelvin contact resistance values represent a relevant quantity (9).

Influence of processing conditions, in particular the siliciding atmosphere, on the contact resistance was studied by annealing patterned wafers in either a vacuum, gettered argon, or argon-10% hydrogen gas mixture to form the palladium silicide. The vacuum annealing was perfomed in an MRC-603 sputtering machine using quartz heating lamps. In contrast, annealing in gettered argon or argon-10% hydrogen gas mixture was done in a tube furnace. Highest purity gases were used in both cases. In the case of gettered argon, the gas was further purified by passing it over a titanium sponge at 800°C to remove small amounts of oxygen or water vapor. In all cases, the unreacted palladium was selectively etched at room temperature in a solution containing 10g KI, 1g I_2, and 40 ml H_2O (2).

The thermal stability of Mo(5000Å)/Pd_2Si(680Å)/Si metallization in contact windows and in diode structures (150 × 150 μm) was studied by isochronal annealing the

* Electrochemical Society Active Member.

wafers for 1h between 400° and 525°C. The contact resistance and the diode leakage current were measured after each isochronal annealing in a gettered hydrogen gas. The diode leakage current was measured under a reverse bias voltage of 5V.

Results and Discussion

Contact resistance includes not only the junction resistance and silicon-palladium interfacial resistance, but also any resistance produced at the interface of the thin palladium silicide layer with the conductive molybdenum layer. The silicide layer, if it is partially oxidized on the surface by even small amounts of oxygen present during the siliciding step, makes poor contact to the molybdenum subsequently deposited.

This effect was shown by a dramatically large contact resistance recorded for the first set of wafers processed by the steps shown in the experimental procedure above but omitting the 1% HF etching step prior to molybdenum deposition. The results are shown in Table I. The 1% HF etching step was to remove silicon oxide that may have formed during the annealing step at 430°C for 20 min in a gettered argon atmosphere.

The second set of wafers was processed according to steps described in the previous section, including the HF etching step. These wafers were annealed in either a vacuum, gettered argon, or argon-10% hydrogen atmosphere to study the influence of siliciding atmosphere on the contact resistance. A summary of results is given in Table II. Significantly lower contact resistance values are obtained for these wafers in comparison to data for the first set, which is shown in Table I. The lowest contact resistance values were obtained for samples annealed in the vacuum. Similarly, low contact resistance values were observed for a wafer (no. 9) that was annealed in a gettered argon atmosphere. Typical contact resistance values, for 1.3 μm-diameter contact size, are between 21 and 22.6Ω for p^+-silicon and between 11.6 and 14.1Ω for n^+-silicon. In comparison to samples annealed in a vacuum or gettered argon, the samples annealed in an ungettered argon-10% hydrogen showed higher contact resistance values between 39.3 and 44.2Ω for n^+-silicon indicating that trace amounts of oxygen and/or water is undesirable for making low resistance palladium silicide contacts to n^+- and p^+-silicon junctions. Significantly more scatter in the contact resistance values was displayed by samples annealed in an ungettered argon-10% hydrogen gas in comparison to wafers annealed in either a vacuum or gettered argon gas.

The statistical nature of contact resistance behavior is summarized in Fig. 1. These results were obtained from 26 contact resistance measurements on each wafer. All of the wafers showed 100% contact yield, which is indicative of an excellent reproducibility for the palladium silicide contact process. Relative frequency *vs.* contact resistance data for the vacuum-annealed samples is shown in Fig. 1(a) indicating a narrow distribution of contact resistance for both n^+- and p^+-Si contacts. Somewhat higher contact resistance is displayed by the p^+-Si contacts as compared to the n^+-Si contacts. This may be caused by somewhat higher dopant concentration for the n^+-silicon junction as compared to the p^+-silicon junction ($8 \times 10^{15}/cm^2$ or $2 \times 10^{20}/cm^3$ for the n^+ *vs.* $4 \times 10^{15}/cm^2$ or $1 \times 10^{20}/cm^3$ for the p^+-Si). However, surface dopant concentration, which is a better indicator of contact resistance, was not measured in this study.

The influence of siliciding environments on the statistical distribution of contact resistance value is summarized in Fig. 1(b). Lower contact resistance values and narrower distributions are shown by samples annealed in a vacuum or gettered argon atmospheres. In contrast, samples annealed in an ungettered argon-10% hydrogen atmosphere showed higher contact resistance values and a broader distribution. This finding is particularly important for small area contacts of 1.3 μm diameter for which a few contact resistance values over 100Ω are observed. Therefore, the presence of trace amounts of oxygen or water vapors in the siliciding/annealing environment should be avoided for the palladium silicide contacts to silicon. For this reason, siliciding in a vacuum is preferred because it avoids complications of higher contact resistance and etching difficulties (2) caused by the presence of a small amount of oxygen and/or water vapors in the annealing gases.

The contact resistance increases with decreasing contact dimension as shown in Table II and Fig. 2(b). However, the contact resistance does not scale with the inverse of the contact area [as shown in Fig. 2(a), where specific contact resistance (resistance × area) is plotted against contact area]. Scaling is expected for an ideal sit-

Table I. Influence of processing condition on contact resistance of palladium silicide

Processing conditions	Wafer type (no.)	Contact resistance (Ω) 1.3 (μm)	2.0 (μm)	3.0 (μm)
Annealed in gettered argon at 430°C/20 min and skipped 1% HF etching step prior to molybdenum deposition	n^+ (17)[a]	249 ± 28.4	88.3 ± 118	22.5 ± 21.4
	n^+ (18)[a]	198 ± 38.6	76.5 ± 13.6	36.9 ± 4.3
	p^+ (20)[a]	122 ± 39.1	41.4 ± 5.6	19.9 ± 2.3
	p^+ (21)[a]	84 ± 9.6	34.5 ± 2.9	16.7 ± 1.2

[a] Sputtered in Perkin-Elmer machine.

Table II. Influence of siliciding atmosphere on contact resistance of palladium silicide

Annealing conditions	Wafer type (no.)	Contact resistance (Ω) 1.3 (μm)	2.0 (μm)	3.0 (μm)
Vacuum annealed (~ 300°C/15 min)	p^+ (1)[a]	21 ± 1.39	15.0 ± 0.96	9.3 ± 0.69
	p^+ (2)[a]	22.6 ± 1.14	15.9 ± 0.88	9.8 ± 0.54
	n^+ (3)[a]	14.1 ± 2.56	9.1 ± 1.12	6.7 ± 2.03
	n^+ (4)[a]	11.6 ± 2.24	8.9 ± 2.35	5.4 ± 0.86
Gettered argon (430°C/15 min)	n^+ (9)[b]	13.9 ± 0.99	9.9 ± 0.73	6.2 ± 0.42
Ungettered argon-10% hydrogen (430°C/15min)	n^+ (11)[b]	39.3 ± 18.9	21.4 ± 6.6	15.0 ± 5.78
	n^+ (12)[b]	44.2 ± 13.9	22.5 ± 6.3	15.6 ± 6.21

[a] Sputtered in MRC-603 machine.
[b] Sputtered in Perkin-Elmer-2400 machine.

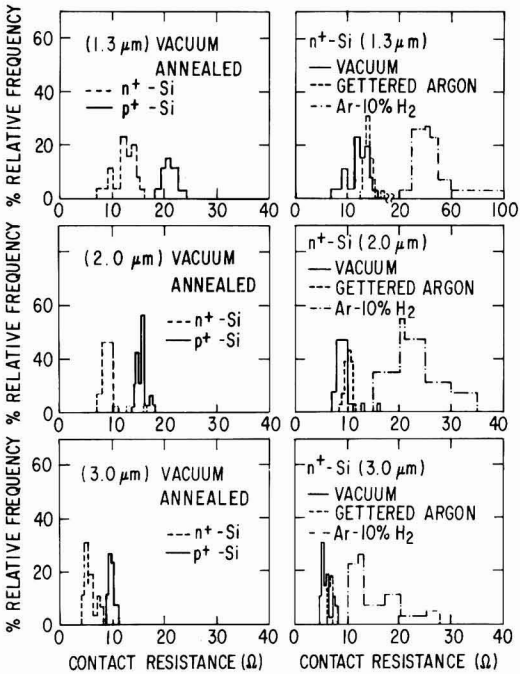

Fig. 1. Histograms of contact resistance for the Mo (5000Å)/Pd_2Si (680Å)/silicon showing influence of (a) contact size, and (b) siliciding environment on the contact resistance.

uation in which the contact resistance is entirely caused by the interface resistance (10). In reality, the contact resistance between palladium silicide and the semiconductor junction, as measured by the Kelvin four-terminal technique, includes "parasitic" contributions from the semiconductor junction in addition to the interface resistance. The parasitic contributions do not scale. Nonetheless, the actual contact resistance values are quite low [Fig. 2(b)] even for the 1.3 μm diameter contact size, which would translate into faster response times in VLSI circuits. However, extreme care is required in VLSI circuit fabrication to avoid contaminants in contact areas, which lead to unusually high values for the contact resistance.

The thermal stability of palladium silicide contacts was determined by measuring contact resistance and leakage current as a function of temperature between 400° and 525°C. The results are summarized in Fig. 3. The contact resistance values are stable up to 450°C after annealing for an hour. A small increase in the contact resistance is seen upon annealing at 475°C, but even at this temperature the contact resistance values are below 35Ω for both types of contacts. In contrast, a significant increase in the contact resistance occurs after annealing the wafers at or above 500°C [Fig. 3(a)].

The results on leakage current measurements are summarized in Fig. 3(b). Figure 3(b) shows low diode leakage currents of $\leq 10^{-11}$A for samples annealed up to 450°C. Further annealing of the p+-diode at 475°C results in an improved leakage current to 10^{-12}A whereas the n+-diode shows an increased leakage current value to 10^{-9}A. A considerable increase in the leakage current for the n+-diode is seen after annealing at the 500°C, but a similarly annealed p+-diode shows significantly lower leakage currents.

The increased contact resistance and leakage current values after annealing beyond 475°C is caused by the formation of molybdenum silicide (13, 14). Molybdenum silicide is more resistive than palladium silicide, consumes a significant amount of silicon, and may lead to junction shorting. As a consequence of thick molybdenum silicide formation, the contact resistance and junction leakage current are expected to rise. These results indicate that palladium silicide contacts with molybdenum metallization for the interconnections should show stable device characteristics up to a maximum processing temperature of 475°C. This is a considerable improvement in high-temperature capability for the palladium silicide/molybdenum metallization system in comparison to the palladium silicide/aluminum metallization system (7, 8).

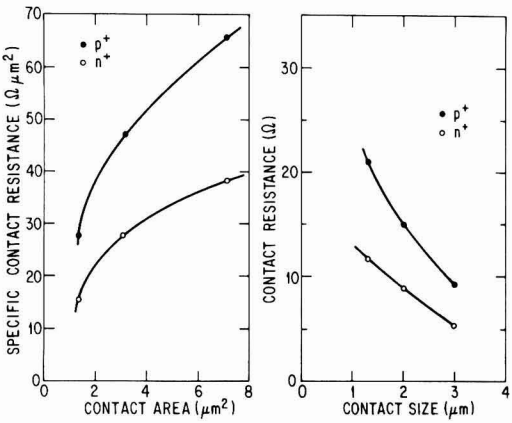

Fig. 2. Dependence of (a) specific contact resistance (V/I × contact area) on contact area, and (b) contact resistance on contact size for the Mo (5000Å)/Pd_2Si (680Å)/silicon metallization.

There are several advantages of the palladium silicide contact process for VLSI circuit fabrication. Most important is the capability of this process to produce low contact resistance values. The low contact resistance values between 20 and 23Ω for the p+-silicon and between 11 and 14Ω for the n+-silicon are comparable to CVD tungsten contacts (11), but without some of the possible problems associated with CVD tungsten such as "lateral encroachment" and the formation of "tunnel or worm-holes" (12). Furthermore, the palladium silicide contact process can produce high contact yield and narrow distribution for the contact resistance. Other advantages of the palladium silicide contact process are that it requires conventional equipment for metallization and is a low-temperature (≤400°C) process. This process is superior to platinum silicide contacts because it has the ability to form shallow junction contacts up to 700°C of postmetallization annealing and the ease of etching unreacted palladium at room temperature using the KI + I_2 etching solution. Furthermore, the palladium silicide contact process can be extended for gate metallization. In fact, gate and source-drain areas can be metallized with palladium silicide in one step using the palladium silicide process. In comparison to silicides that show Si as dominant diffuser (Ti, W, Mo) the palladium silicide forms via metal diffusion which minimizes the problem of out-diffusion.

Summary and Conclusions

The contact resistance of palladium silicide (680Å) to shallow n+- and p+-silicon junctions is measured via the Kelvin four-terminal method. The influence of processing steps and siliciding environments on the contact resistance are studied. A summary of the results is given below.

Typical contact resistance values between 21 and 22.6Ω for the p+-silicon and between 11.6 and 14.1Ω for the n+-silicon are obtained for 1.3 μm-diameter contacts using Mo (5000Å)/Pd_2Si (680Å)/Si metallization. These values are for samples silicided in a vacuum or in a gettered argon atmosphere. In contrast, wafers annealed in an ungettered argon-10% hydrogen gas mixture showed higher contact resistance values, between 39.3 and 44.2Ω for the n+-silicon. Significantly more scatter in the con-

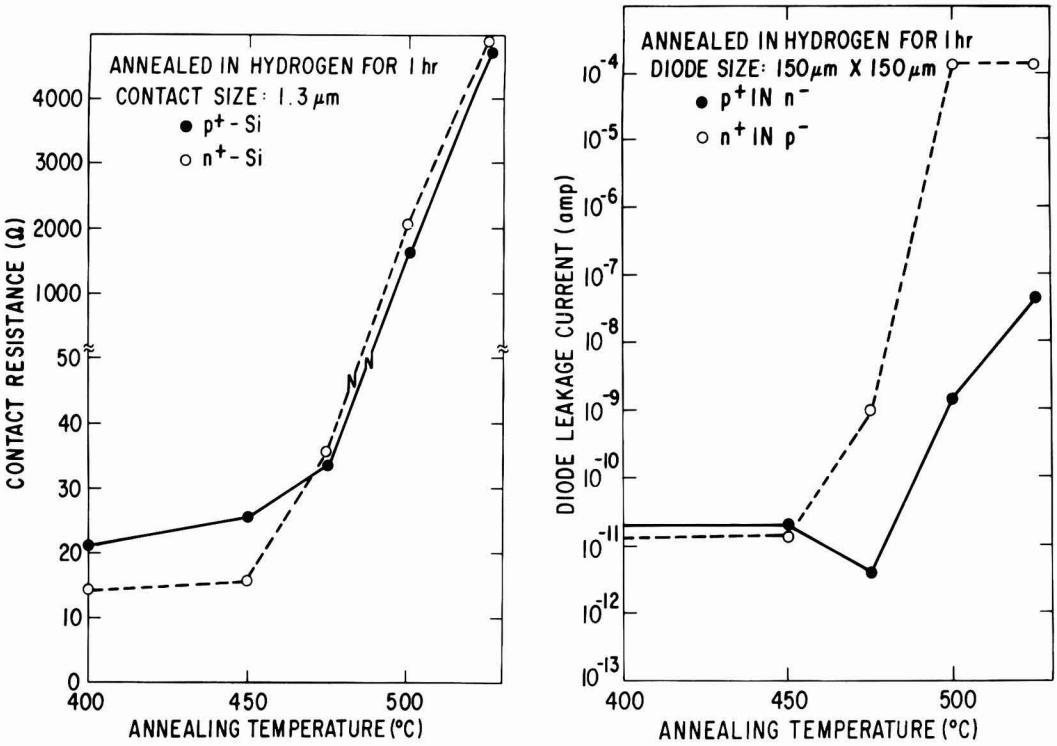

Fig. 3. Influence of annealing temperature on (a) the contact resistance, and (b) the diode leakage current for Mo (5000Å)/Pd_2Si (680Å)/silicon metallization system.

tact resistance values is also displayed by samples annealed in an ungettered argon-10% H_2 gas in comparison to wafers annealed in a vacuum or in gettered argon gas. Siliciding in a vacuum is recommended for palladium silicide contacts.

The contact resistance increases with decreasing contact size between 3.0 and 1.3 μm diameter. However, the data do not follow simple scaling relationships, probably because of several contributions to the measured contact resistance. Specific contact resistance (contact resistance × contact area) values of 28 Ω · μm² (0.28 μΩ cm²) for the p^+-silicon and 15.5 Ω · μm² (0.15 μΩ cm²) for the n^+-silicon are obtained for 1.3 μm-diameter contacts using the palladium silicide contacts.

The thermal stability of palladium silicide/molybdenum contact metallization was determined by measuring the contact resistance and leakage current as a function of temperature between 400° and 525°C. The results indicate that this metallization system should give low contact resistance and low leakage current characteristics up to a maximum processing temperature of 475°C.

Palladium silicide contacts are promising for VLSI applications because of low-temperature processing, low contact resistance, low leakage current, shallow junction characteristics, excellent contact yield, and conventional processing.

Acknowledgments

The authors wish to thank F. W. Secor, L. A. Grunke, P. A. Piacente, and L. Sprinceanu, for their help in wafer processing; M. J. Kim for lot input; K. Borst and R. E. Ostranger for sputtering; and C. A. Markowski for preparation of this paper. The encouragement and support of K. W. Browall and F. N. Mazandarany in this investigation are appreciated.

Manuscript submitted Oct. 31, 1985; revised manuscript received May 15, 1986.

The General Electric Company assisted in meeting the publication costs of this article.

REFERENCES

1. S. P. Murarka, "Silicides for VLSI Applications," Academic Press, Inc., New York (1983).
2. R. N. Singh, General Electric Report no. 85CRD080 (1985); and R. N. Singh, *Am. Soc. Test. Mater. Spec. Tech. Publ.*, 960 (1986).
3. C. J. Kircher, *Solid-State Electron.*, **4,** 507 (1971).
4. C. J. Kircher, *J. Appl. Phys.*, **47,** 5394 (1976).
5. W. D. Buckley and S. C. Moss, *Solid-State Electron.*, **15,** 1331 (1972).
6. A. Shepela, *ibid.*, **16,** 477 (1973).
7. H. Grimolds and G. Y. Robinson, *J. Vac. Sci. Technol.*, **14,** 75 (1977).
8. P. C. Parekh, R. C. Sirrine, and P. Lemieux, *Solid-State Technol.*, **19,** 493 (1976).
9. S. S. Cohen, G. Gildenblatt, and D. M. Brown, *This Journal*, **130,** 978 (1983).
10. R. H. Dennart, F. H. Gaensslen, H.-N. Yu, V. L. Rideout, E. Bassous, and A. R. LeBlanc, *IEEE J. Solid-State Circuits*, **SC-9,** 256 (1974).
11. R. H. Wilson, Private communication.
12. W. T. Stacy, E. K. Broadbent, and M. H. Norcett, *This Journal*, **132,** 444 (1985).
13. R. N. Singh, *Thin Solid Films*, **143,** 249 (1985).
14. R. N. Singh and E. F. Koch, *This Journal*, **133,** 1191 (1986).

Novolac Resin Planarization Layers for Multilayer Resist Imaging Systems

T. R. Pampalone,* J. J. DiPiazza, and D. P. Kanen

RCA, Aerospace and Defense, Microelectronics Center, Somerville, New Jersey 08876

ABSTRACT

The relationship between planarization and polymerization was examined for several phenolic resins. The best planarizing resins were those which melted and flowed before significant polymerization occurred. The edges of 100 μm^2 island features, 0.5 μm high, were planarized to 300Å using low melting novolac resins with long cure times. By comparison, commercial photoresist, typically used in multilayer imaging systems, planarized these island features to only 4250Å. Resins such as ortho-cresol novolac are suggested as planarization layer materials for submicron, trilevel electron-beam imaging systems.

Multilayer resist imaging is becoming increasingly important for patterning submicron geometries in electronic devices. In this technique, the wafer topography, consisting mainly of epitaxial silicon islands, is covered by a layer of polymer to provide a relatively flat surface. A thin layer of photo or electron-beam resist is coated over this surface and patterned. Because the imaging layer is thin and flat, pattern resolution is excellent and transferable to the substrate by anisotropic plasma etching. In the trilevel imaging scheme (Fig. 1), a thin intermediate layer of oxygen-plasma resistant material, such as silicon oxide or nitride, is applied between the planarization and resist layers.

Although much has been said about the various aspects of multilayer imaging with respect to multilayer structures (2), hardmask materials (3), etching conditions (4), etc., very little has been said about the planarization layer, especially from a materials viewpoint. This is surprising, considering the difficulty in planarizing large island features (5) common to most electronic devices and the importance of planarization in achieving uniform pattern replication (6). Planarization layers for submicron imaging must be particularly flat to maintain linewidth control. For instance, half-micrometer lines should deviate no more than $\pm 10\%$ (3σ), or ± 500Å, in order to meet manufacturing specifications.

Multilayer imaging systems described in the literature (7) typically use commercial photoresists as the planarization material. Photoresists contain novolac resins, which are made from a high percentage of meta-cresol. Such resins have been shown to polymerize readily (8). As we demonstrate in this paper, the best planarization resins are those which can flow significantly before the onset of polymerization. In this regard, photoresist is a poor choice for a planarization material. Large island features (>50 μm on a side), for instance, are planarized very slightly, if at all, and small island features (10 μm on a side) are only about 90% planarized (5). The best planarization resins, we propose, are those in which the planarization and subsequent polymerization can occur independently. This is most likely to happen when the resin melts at low temperatures and polymerizes at high temperatures. O-cresol novolac is presented as an example of such a resin used as the planarization layer in a trilevel electron-beam imaging system.

Experimental

Planarization materials.—Four novolac resin planarization materials were evaluated in this study: (*i*) Varcum® 29-801, an ortho-cresol novolac supplied by Reichold Chemicals, Incorporated, Specialty Phenolics Division; (*ii*) UCAR® CK-0036, an amyl phenol novolac supplied by Union Carbide Corporation, Specialty Chemicals Division; (*iii*) Alnovol® 429K, a photoresist resin previously supplied by Hoechst, A. G.; and (*iv*) Microposit® 1400-30, a novolac/diazoquinone photoresist supplied by Shipley Company, Incorporated. Varcum 29-801, CK-0036, and Alnovol 429K were dissolved 35, 40, and 25% by weight, respectively, in propylene glycol methyl ether acetate and filtered through an 0.2 μm PTFE membrane. Microposit 1400-30 was used as supplied.

Application of planarization materials.—The wafers used in the study were 3 in. sapphire wafers containing 100×100 μm epitaxial silicon islands 100 μm apart and 0.50 μm high. Silicon cosputtered with tantalum was deposited over the wafers. The planarization solutions described above were spin coated on the wafers and then soft baked at 90°C for 1 min on a GCA Corporation Wafertrac® hot plate to remove most of the residual solvent. The wafers were then hard baked in the Wafertrac oven purged with dry air for the time and temperatures indicated to melt and flow the resins. The Wafertrac oven consists of two moving hot copper foils, which heat the wafers from the bottom and carry them through the oven at a programmable rate.

Monitoring planarization.—The planarization after baking was monitored for each wafer using a Tencor Corporation Alpha-step® profilometer, by measuring the step heights remaining in the planarization layer across four islands (eight steps) and reporting the average step height as the average planarization value (see Fig. 2). Therefore, the lower the average planarization value, the higher the degree of planarization.

Monitoring polymerization.—The polymerization of the planarization layer was monitored by measuring the solubility and thickness of the planarization layer near the edge of the wafer after hard bake.

Measurement of solubility.—The planarization layer was immersed in acetone for 30s, then allowed to air-dry for 2 min. The thickness of the remaining coating was measured in four places 1 cm from the edge of the wafer. The four values were always within 1000Å of each other. From the average film thickness remaining and the initial thickness, the percentage of the coating that dissolved was reported as percentage of solubility (Fig. 3-6, curves C).

Measurement of thickness.—Thickness after baking was measured where the surface contained no islands (most conveniently, about 1 cm from the edge of the wafer) using a Rudolph Research Corporation FTM® film

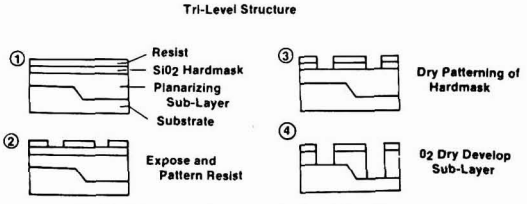

Fig. 1. Schematic diagram of trilevel imaging system

*Electrochemical Society Active Member.

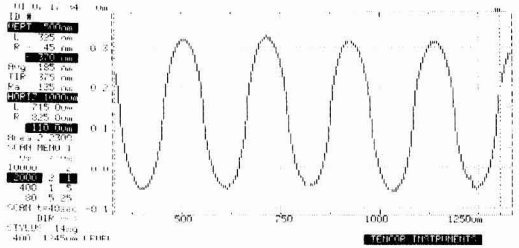

Fig. 2. Profilometer trace of planarized islands

thickness analyzer at 1.64 refractive index setting. The initial thickness after soft bake was chosen to be 10-20% above the final thickness desired after hard bake. This required a considerable amount of trial and error, since the percent solids of the four planarization solutions and, often, the polymerization temperature of the tests were different. The thicknesses of the planarization layers in a series of wafers for a particular test varied no more than ±100Å. After soft bake, each wafer was passed through the Wafertrac oven at the prescribed bake temperature. The bake time was increased 30s for each wafer until a maximum of 720s bake time was reached. The thickness of the planarization layer for each wafer at each bake time was then measured, and the thickness with bake time plotted (Fig. 3-6, curves B).

Measurements of gel permeation chromatography (GPC) molecular weights.—The planarization layer was dissolved from the wafer with a stream of 10 ml of chromatography grade THF, and the solution concentrated to 3 ml and then filtered through an 0.2 PTFE membrane. Twenty μl of the filtrate was injected into the GPC instrument fitted with Ultrastyragel® (Waters Corporation) size exclusion columns. The polymer trace was recorded and weight-average (Mw) and number-average (Mn) molecular weights calculated for the resin using polystyrene standards. GPC analysis of novolac resins has been described previously (8).

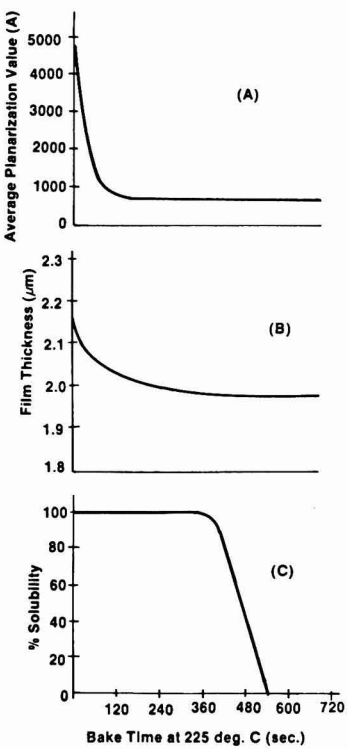

Fig. 3. Average planarization value (a), film thickness (b), and percentage of solubility (c) as a function of bake time at 225°C for Varcum 29-801.

Results and Discussion

The relationship between planarization and polymerization with increasing bake time at 225°C is shown for each of the four planarization materials in Fig. 3-6. The planarization is represented by the average planarization value (curve A) and the polymerization is represented by the film thickness (curve B) and percentage of solubility (curve C) of the planarization layer. Thickness loss of the planarization layer upon baking is expected because of solvent evaporation in the early stages of heating and because of cross-linking densification later on. At 225°C, all of the solvents are removed from the coatings within 120s. This is confirmed by coating 2 μm of the planarization layers on silicon wafers, baking for 120s, and scanning the ester carbonyl region of the infrared (1720 cm^{-1}) for residual solvent using Fourier transform infrared (FTIR) analysis (9). No ester peaks remained after 120s baking. Microposit 1400-30 photoresist contains other solvents not having an ester carbonyl, but these solvents (xylene and n-butyl acetate) do not remain in the photoresist after baking (10).

Figure 3 shows the planarization and polymerization data for Varcum 29-801 resin. The average planarization value decreased nearly to its minimum value of 700Å within 120s bake time. The film thickness decreased quickly as solvent evaporated, then decreased slowly after 120s, as the resin began to polymerize, to the final film thickness after polymerization of 1.97 μm. The percentage of solubility was 100% at 360s bake time, then decreased rapidly as the resin continued to polymerize. After 540s, the film was fully polymerized as defined by its 0% solubility in acetone.

Figure 4 shows the planarization and polymerization data for CK-0036 resin. The average planarization value decreased to 300Å within 60s bake time, then unexpectedly increased to over 2000Å with continued baking and the onset of polymerization. The polymerization was shown to cause the decrease in planarization; for instance, when the wafer planarized with CK-0036 was heated at 225°C in a convection oven purged with nitrogen so that no polymerization occurred, the average planarization value remained at 300Å even after 30 min. The reason for this unexpected decrease in planarization with polymerization is unclear. Thickness measurements made with a Nanometrics, Incorporated, Nanospec AFT® film thickness measurement system show the resin film thickness over the islands increased 300Å and the resin film thickness away from the islands decreased 1600Å after polymerization. One would expect the film to shrink uniformly across the wafer on polymerization.

The film thickness of CK-0036 decreased quickly with baking to 2.07 μm (Fig. 4), then decreased slightly after 120s to the final thickness after polymerization of 2.06 μm. The percentage of solubility was 100% at 180s bake time, and 0% after 300s. As pointed out, CK-0036 does not retain its good planarization properties upon polymerization and, for this reason, may not be a satisfactory planarization material for a multilayer imaging system. However, the example demonstrates that novolac resins, which are low melting and slow polymerizing, are best for planarizing large island features.

Figure 5 shows the planarization and polymerization data for Alnovol 429K resin. The average planarization value decreased to a minimum of only 3500Å within 120s bake time. The film thickness decreased quickly to 2.02 μm, then decreased very slightly after 120s to the final thickness after polymerization of 2.01 μm. The percentage of solubility was 100% at 120s bake time, and nearly 0% after 240s baking. As shown in Table I, and discussed later, the polymerization of this resin actually began after only 60s baking at 225°C according to GPC data, but it remained completely soluble in acetone for 120s. Al-

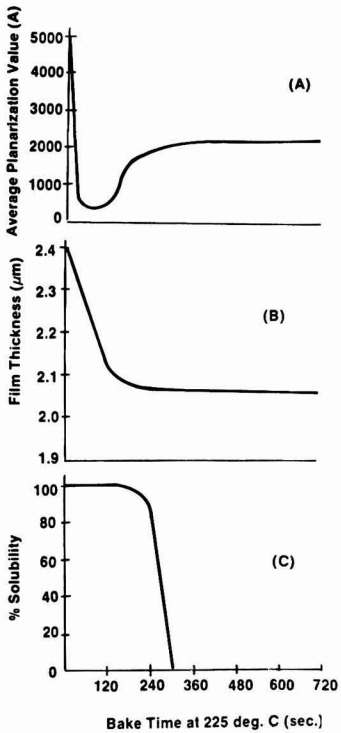

Fig. 4. Average planarization value (a), film thickness (b), and percentage of solubility (c) as a function of bake time at 225°C for CK-0036.

Table I. GPC molecular weights as a function of bake time at 225°C

Material	Bake time (s)	Mw	Mn
Varcum 29-801	0	29,943	26,759
	120	30,292	27,999
	240	45,924	40,348
CK-0036	0	26,954	26,060
	60	27,010	26,100
	90	31,507	29,420
	120	34,085	31,290
Alnovol 429K	0	29,200	23,455
	60	31,690	25,740
	120	34,924	27,954

though this photoresist resin is a slightly better planarization layer material than Microposit 1400-30, it is unsuitable for planarizing large island features. As the data shows, polymerization is taking place so rapidly that the Alnovol 429K resin does not flow and planarize as well as less reactive resins, such as CK-0036 and Varcum 29-801.

Figure 6 shows the planarization and polymerization data for Microposit 1400-30 photoresist. The average planarization value decreased to only 4250Å after 720s bake time. The film thickness decreased quickly as solvent evaporated, then decreased slowly after 120s bake time, as the resin continued to polymerize, to the final thickness of 2.00 μm. The percentage of solubility decreased dramatically to 42% after only 30s baking, indicating polymerization began almost immediately. Then, the percentage of solubility decreased slowly as polymerization continued. Even after 720s baking, the Microposit 1400-30 was not completely polymerized. In contrast, the percentage of solubility for the three resins discussed previously decreased from 100 to 0% within a baking time interval of only 180s. Photoresist film consists of about 20% photoactive component, which may explain the difference in the solubility results. Upon

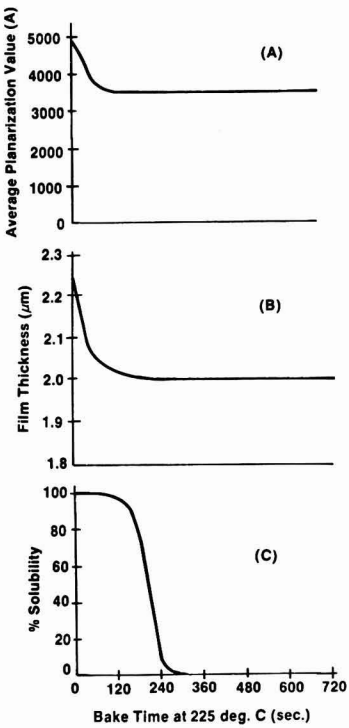

Fig. 5. Average planarization value (a), film thickness (b), and percentage of solubility (c) as a function of bake time at 225°C for Alnovol 429K.

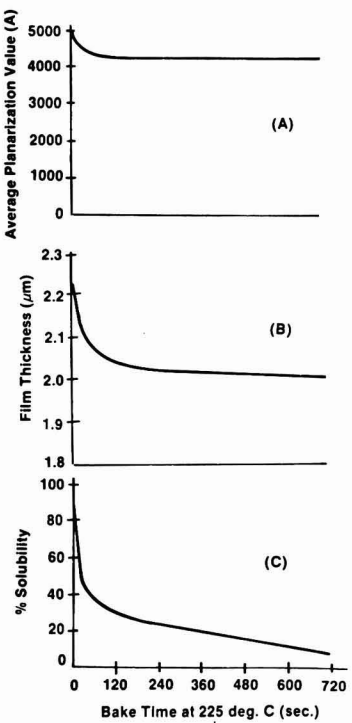

Fig. 6. Average planarization value (a), film thickness (b), and percentage of solubility (c) as a function of bake time at 225°C for Microposit 1400-30.

heating, the photoactive component may convert to acid or dimer product (11), but neither the photoactive component nor its thermolysis products are expected to polymerize. The photoresist coating remains partially soluble for a longer period of baking because of the large amount of nonpolymerized material remaining in the polymerized matrix.

Solubility measurements of baked planarization coatings indicate when significant polymerization has occurred; however, small degrees of polymerization are not detectable by this technique. Even a small amount of polymerization of the resin in the melted state can greatly increase flow viscosity so that further planarization is arrested. For instance, the Varcum 29-801, CK-0036, and Alnovol 429K resins are all totally soluble in acetone after 360, 180, and 120s, respectively, when baked at 225°C. A small amount of polymerization may have taken place in these resins at lesser bake times, but not enough to affect their solubilities in acetone. To test this likelihood, the planarization coatings listed in Table I were stripped from the wafers with THF and analyzed by GPC. The resultant data were reported as *Mw* and *Mn* referred to polystyrene standards. *Mw* values generally correspond better to polymer viscosities. As the molecular weight of a polymer increases, the elution volumes decrease (example shown in Fig. 7). For all three resins analyzed in Table I, the molecular weights increased before they became insoluble in acetone. Alnovol 429K, for instance, increased in molecular weight after only 60s baking at 225°C from 29,200 to 31,690, CK-0036 increased after 90s baking from 26,954 to 31,507, and Varcum 29-801 increased after 120s from 29,200 to 31,690. These GPC results correlate with the planarization results observed (Fig. 3-6, curves A) and reemphasize the point made earlier. The best planarization resins are those that can melt and flow substantially before polymerization takes place. In the case of Varcum 29-801, the resin can planarize for 120s before polymerization begins, and, as Fig. 3, curve A, shows, only 120s is required for planarization. CK-0036 begins to polymerize after 60s, and, as Fig. 4, curve A, shows, only 30s is required for planarization. Alnovol 429K (Fig. 5, curve A) has less than 60s to flow before significant polymerization begins. This last resin, therefore, shows correspondingly less planarization. The Microposit 1400-30 planarization coating was not completely soluble in THF after only 30s bake time and, therefore, was not analyzed by GPC.

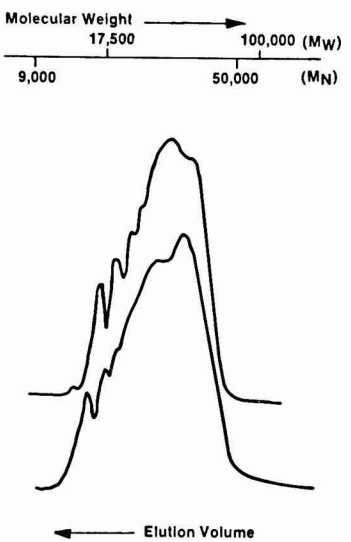

Fig. 7. Example of GPC analysis of planarization resin. Varcum 29-801 before hard bake (top) and after 240s hard bake at 225°C (bottom).

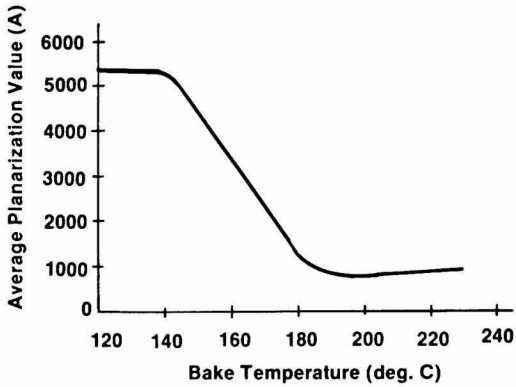

Fig. 8. Average planarization value as a function of bake temperature for Varcum 29-801 (720s bake).

The melting point of the resin also affects its ability to planarize. Lower melt temperatures would favor planarization, as seen in the case of Varcum 29-801 and CK-0036, which melt at 90°-100° and 70°-85°C, respectively. Microposit 1400-30 and Alnovol 429K melt at 120°-140°C. The solvents for these planarization materials are high boiling to provide good coating qualities. Propylene glycol methyl ether acetate boils at 146°C and ethylene glycol ethyl ether acetate (the principal solvent in Microposit 1400-30) at 156°C. If the planarization material melts below the boiling point of the residual solvents, it can flow during the first 120s of baking even though the temperature rise is restrained by the evaporating solvent. This probably occurs for Varcum 29-801 and CK-0036 but not for Alnovol 429K or Microposit 1400-30. It should be emphasized that a novolac resin must be both low melting and slow reacting to be a good planarization layer. Resins which are only low melting will not planarize well. For instance, UCAR® CK-1282 (Union Carbide Corporation), described as heat reactive resin (mp 80°-110°C), was also evaluated as a planarization material. In no instance did the average planarization value measure less than 4000Å.

For a resin, there may be a bake temperature that optimizes planarization by separating the planarization and polymerization processes. At that temperature, the viscosity of the melted resin will be low enough to allow the resin time to flow rapidly, and the polymerization rate will be low enough to allow the resin time to flow. After planarization is complete, the bake temperature can be increased to polymerize the resin more quickly. In the Wafertrac oven, the three heating zones can be programmed to accomplish this in one processing operation. This optimum planarization temperature is shown in Fig. 8 for Varcum 29-801. As the temperature increased to 200°C (for 720s), the average planarization value decreased to 700Å. Above 200°C, the average planarization value increased to 900Å. The difference in the minimum average planarization value for the CK-0036 and Varcum 29-801 resins (300 *vs.* 700Å) may be due to small differences in the surface energies of these resins in the melted state.

In most trilevel resist imaging schemes proposed in the literature, the planarization layer is 2.0 μm thick. This thickness is considered necessary for good planarization. However, for the better planarizing resins, even 1.5 μm film thickness may be adequate. In Fig. 9 are shown the average planarization values resulting for varying film thicknesses of CK-0036 baked for 12 min at 165°C. Even at planarization thicknesses of 1.5 μm, the average planarization values for large-island features were only 150Å higher than at 2.0 μm thicknesses. Only when the film thicknesses decreased below 1.5 μm did the average planarization values increase significantly.

The polymerization of the planarization layers proceeded from the bottom of the coating to the top using

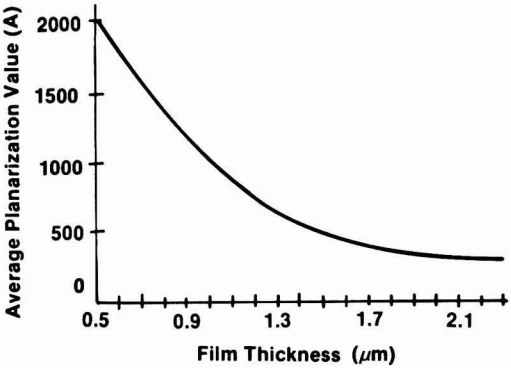

Fig. 9. Average planarization value as a function of film thickness for CK-0036 (12 min, 165°C bake).

the hot plate bake. This was demonstrated by increasing the immersion times in acetone and measuring the film thickness losses. As shown in Table II for Microposit 1400-30 (baked 30s at 225°C), additional immersion time did not significantly increase the thickness loss (percentage of solubility). If the polymerization of the layer was uniform or gradual, the film thickness loss would increase with increasing immersion time. These results demonstrate that the polymerization of the planarization coating occurred as a sharp gradient from the hot wafer substrate. The top of the planarization layer was apparently last to polymerize. If heat were applied to the top of the coating, one might expect polymerization to proceed from the top of the coating, preventing or limiting planarization. This expectation was tested by placing a wafer coated with 2.1 μm of Varcum 29-801 planarization layer horizontally in a 225°C air convection oven. The average planarization value after 720s was 1600Å, compared to 700Å when the wafer was heated from the bottom in the Wafertrac oven (Fig. 3, curve A). The technique of applying heat to the bottom of the wafer to improve planarization has been claimed in the patent literature (12).

The four planarization materials investigated in this paper work equally well with respect to deposition of hardmask materials and oxygen RIE. The planarization layer materials must be thermally cured (cross-linked) before plasma-enhanced chemical vapor deposition (PECVD) of silicon dioxide or silicon nitride to increase their mechanical strength. If this is not done, the compressive or tensile stresses of the hardmask at room temperature will cause the planarization layer to wrinkle. The oxygen RIE rates of all four materials after a 12 min hard bake were comparable, 500-700Å/min in a parallel plate reactor (power 400W, pressure 10 mtorr, flow 30 sccm, temperature 27°C). For the trilevel electron-beam imaging application, O-cresol novolac (Varcum 29-801) demonstrates the best planarization properties.

Although the novolac resins and photoresist described in this work were evaluated as planarization layers for multilayer imaging systems, the results apply as well to other processing situations where planarization is required. One important application is the planarization of dielectric material before the deposition of metal. In this technique, polymer material is spun over the dielectric and both are etched back at nearly the same rate to produce a semismooth surface (13).

Table II. Solubility as a function of immersion time in acetone for Microposit 1400-30

Immersion time (s)	Solubility (%)
15	20
30	38
45	38
60	39
120	39

Conclusions

The best novolac planarizing resins were those with low reactivity that flowed before significant polymerization occurred. GPC data was used to support these findings. Polymerization of the resins on the coated wafers was monitored by measuring film thickness and percentage of solubility. Large island features 0.5 μm high were planarized to 700Å using o-cresol novolac and 300Å using amyl phenol novolac, as compared to 4250Å using commercial photoresist. A two-step baking procedure was proposed, consisting of a low temperature bake to optimize planarization, followed by a higher temperature bake to induce polymerization.

Acknowledgment

The authors would like to thank P. Zanzucchi at David Sarnoff Research Center for providing the GPC data used in this report.

Manuscript submitted Dec. 20, 1985; revised manuscript received July 20, 1986.

RCA Laboratories assisted in meeting the publication costs of this article.

REFERENCES

1. B. J. Lin, in "Introduction to Microlithography," L. F. Thompson, C. G. Wilson, and M. J. Boden, Editors, Chap. 6, ACS Symposium Series 219, The American Chemical Society, Washington, DC (1980).
2. M. A. Listvan, M. Swanson, A. Wall, and S. A. Campbell, *SPIE*, **470,** 85 (1984); A. W. McCullough, E. Pavelchek, and H. Windischmann, *J. Vac. Sci. Technol.*, **B1,** 1241 (1983); Y. Lin, S. Jones, and G. Fuller, *ibid.*, **B1,** 1215 (1983).
3. B. R. Soller, C. R. Snider, and R. F. Shuman, *This Journal*, **131,** 868 (1984); G. W. Ray, S. Peng, D. Burriesci, M. O'Toole, and E. Liu, *ibid.*, **129,** 2152 (1982); M. Gellrich, H. Beneking, and W. Arden, *J. Vac. Sci. Technol.*, **B3,** 335 (1985); S. K. Gupta and G. C. Audain, *SPIE*, **469,** 179 (1984).
4. H. Namatsu, Y. Ozaki, and K. Hirata, *J. Vac. Sci. Technol.*, **21,** 672 (1982); N. J. Chou, C. H. Tang, J. Paraszczak, and E. Babick, *Appl. Phys. Lett.*, **48,** 31 (1985).
5. L. K. White, *This Journal*, **130,** 1543 (1983).
6. D. W. Widmer and H. Binder, *IEEE Trans. Electron Devices*, **ED-22,** 467 (1975); A. R. Neurether, P. K. Jain, and W. G. Oldham, *SPIE*, **275,** 110 (1981).
7. B. J. Lin, *Solid State Technol.*, **26,** 105 (May 1983).
8. T. R. Pampalone, *ibid.*, **27,** 115 (May 1984).
9. T. R. Pampalone, A. M. Gilfillan, and P. J. Zanzucchi, *This Journal*, **133,** 1917 (1986).
10. J. M. Shaw, M. A. Frisch, and F. H. Dill, *IBM J. Res. Develop.*, **21,** 219 (1977).
11. P. Yates and E. W. Robb, *J. Am. Chem. Soc.*, **79,** 5760 (1957).
12. RCA, U.S. Pat, 4,427,713 (1984).
13. D. Barton and C. Maze, *Semicond. Int.*, **1,** 98 (1985).

The Heat of Formation of Mercury Vacancies in $Hg_{0.8}Cd_{0.2}Te$

H. Wiedemeier, S. B. Trivedi, R. C. Whiteside, and W. Palosz

Department of Chemistry, Rensselaer Polytechnic Institute, Troy, New York 12181

ABSTRACT

A modified mass loss measurement technique has been employed, for the first time, for the direct *in situ* determination of vacancy concentrations in $Hg_{0.8}Cd_{0.2}Te$ at elevated temperatures. This technique can also be used to establish the pressure-temperature phase diagram for this type of systems. The derived mean value for the heat of formation of mercury vacancies in the above alloy is 0.43 eV. Theoretical considerations concerning the vacancy formation in HgTe and in $Hg_{0.8}Cd_{0.2}Te$ are in qualitative agreement with our experimental value.

The superior electro-optical properties of $Hg_{1-x}Cd_xTe$ for infrared detection in the 3-5 and 8-14 μm ranges are well known. The usefulness of this material is based on the availability of bulk or layer-type single crystals with a high degree of compositional and structural uniformity. Although the growth of $Hg_{1-x}Cd_xTe$ crystals has been reviewed (1-4) extensively in recent years, the defect nature of this material is not fully understood. Three types of native defects, namely, Hg and Te vacancies and Hg interstitials are believed (4) to exist in $Hg_{1-x}Cd_xTe$. These and the presence of foreign impurities (2) affect the electrical characteristics of this compound. Materials prepared at elevated temperatures invariably have a significant concentration of Hg vacancies and are of p-type character. In general, information on vacancies in compound semiconductors is obtained from electrical measurements of the type and concentration of predominant charge carriers. In the presence of compensating charge carriers, one cannot quantitatively correlate electrically measured concentrations of p-type carriers with the vacancy concentration. In addition, the vacancy concentration of $Hg_{1-x}Cd_xTe$ is usually obtained from electrical measurements at room or lower temperature of samples which have been annealed at higher temperatures under mercury or tellurium pressure and then rapidly quenched. This may not correctly describe the high temperature equilibrium defect concentration. For these reasons, the determination of the enthalpy of vacancy formation from electrical measurements is not possible for this material.

As a part of continued research, we have reported on the growth of bulk crystals (5) and of epitaxial layers (6, 7) of $Hg_{0.8}Cd_{0.2}Te$ by chemical vapor transport in closed ampuls. In both cases, good compositional and structural homogeneity of the resulting materials were observed. We have also investigated dislocations in bulk $Hg_{0.8}Cd_{0.2}Te$ crystals employing chemical etching and TEM techniques (8). The present work is concerned with the direct measurement of the vacancy concentration of $Hg_{1-x}Cd_xTe$ at elevated temperatures and with the determination of the P-T phase diagram of this system. For this purpose, the vapor pressure of Hg over mercury cadmium telluride is measured in a closed ampul employing a dynamic balance technique. This technique is based on an experimental method used for transport studies of tantalum (9), and on the knowledge that the partial pressures of Cd and of Te_2 are orders of magnitude lower than that of Hg (10, 11). The measurements are performed in specially designed ampuls using an automatic semimicrobalance system and the lever principle to determine the mass of mercury vapor in the ampul. This is the most direct technique to determine the vacancy concentration and the enthalpy of vacancy formation for mercury cadmium telluride. This technique, in conjunction with electrical measurements, may yield a better understanding of point defects and vacancies, in particular for $Hg_{1-x}Cd_xTe$. The results of this work may also contribute to a further elucidation of the p-type to n-type conversion on which considerable disagreement still prevails (12-17).

Experimental and Calculational Procedures

Materials.—Our method consists of measuring the mass of mercury in the vapor phase in equilibrium with the condensed source material, $Hg_{0.8}Cd_{0.2}Te$ and excess elemental mercury. The compound $Hg_{0.8}Cd_{0.2}Te$ was prepared by annealing stoichiometric ratios of elemental cadmium (99.999%), tellurium (99.999%), and electronic grade mercury (99.999%) according to procedures discussed earlier (5). The identity of the annealing product was confirmed using Debye-Scherrer x-ray diffraction powder techniques. When desired, excess mercury was added to the synthesized compound.

Ampuls.—The fused silica ampuls of 15 cm length and 1.5 cm inner diameter had a "bubble extrusion" near the rounded closed end of the ampul. A pair of thin, 5 mm long fused silica legs were attached to the outer wall near the center of the "bubble extrusion" and served as a fulcrum (Fig. 1). The ampuls were pretreated and outgassed (at about 1000°C and 10^{-5} torr) as described previously (5). Before outgassing, the volume of the ampul is determined by filling it with water to the constriction where it will be sealed off. The outgassed ampul is loaded with about 1g of presynthesized $Hg_{0.8}Cd_{0.2}Te$ and a known amount of excess elemental mercury. The source materials are located in the "bubble extrusion" which prevents any displacement of the condensed material during experimental runs. The loaded ampul is evacuated under continuous cooling of the source end and sealed at the constriction under a pressure of 10^{-5} torr or less. After sealing, a 3 mm diameter fused silica extension rod is attached to the sealed end of the ampul coaxially with the axis of the ampul. A hook on the other end of the extension rod is used to connect the ampul to the hang-down wire from one arm of the balance.

Apparatus.—The weight measurements as a function of temperature were performed using an automatic, vacuum, semimicrobalance in connection with a strip chart recorder. The vertical tube of the vacuum line, connecting the balance port to the mechanical pump, contains the hang-down wire attached to one balance pan. At the level of the lower end of the wire, the vertical tube has a horizontal extension serving as the vacuum envelope for the ampul. Under experimental conditions, the source end of the ampul rests on the fulcrum, and the other end is connected via the extension rod to the hang-down wire. This is schematically represented in Fig. 1. Heating of the source material in the ampul was accomplished by

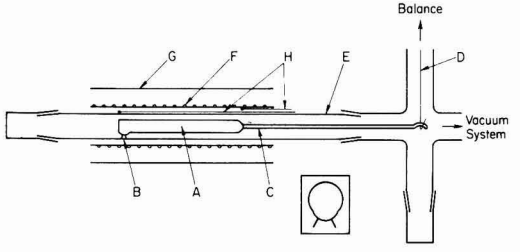

Fig. 1. Schematic representation of the experimental setup used in this work. A, Fused silica ampul; B, fused silica legs acting as fulcrum; C, extension rod of fused silica; D, tungsten hang-down wire; E, vacuum envelope; F, furnace core; G, furnace outer tube; H, thermocouples. Inset shows cross section of source region of ampul with "bubble extrusion" and fulcrum.

means of a two-zone, tubular resistance furnace surrounding the horizontal reaction tube (Fig. 1). The furnace core is a fused silica tube of about 30 cm length and 3.5 cm inner diameter with the heater wire on the outside wall. This tube is mounted with insulating end plates in a fused silica protection tube of about the same length and 8.0 cm inner diameter. To minimize heat losses and draft through the furnace, the space between the reaction tube and furnace core was also tightly closed. The temperatures of each furnace zone were controlled independently within ± 1°C using proportional temperature controllers providing an isothermal zone (± 1°C) of about 3 cm length in the source region of the ampul. The temperatures were monitored by two Chromel-Alumel thermocouples whose hot junctions were in a fixed position on the outside wall of the vacuum reaction tube in the immediate vicinity of the source material and of the sealed end of the ampul. The temperature difference between those locations and the inside of the ampul were determined by placing the hot junctions of two additional Chromel-Alumel thermocouples inside the reaction tube at the precise locations of the source material and sealed end of an empty ampul. These measurements as well as the determination of the temperature profile over the entire length of the ampul were carried out while the system was at a pressure of about 10^{-3} torr. All thermocouples employed for these measurements were calibrated using the melting point of high purity zinc and a Pt-Pt/10%Rh NBS secondary standard thermocouple.

Calculations.—In order to prevent transport and deposition of the source material in the ampul during experimental runs, a temperature difference of about 15°C was imposed over the length of the ampul with the source in the lower temperature zone. For each temperature setting, a weighted average internal temperature of the ampul, T_m, was calculated based on the actual temperature profile in the ampul for that particular setting. The average temperature, which was generally about 8°C above the source temperature, was used for subsequent pressure calculations.

After positioning the loaded ampul in the balance system (Fig. 1), the system is evacuated to about 10^{-3} torr, and the sensitivity and full scale deflection of the balance recorder are adjusted. As the ampul is heated to the desired temperature setting, the balance records a weight gain corresponding to the increase in the mass of the vapor as a result of the vaporization of Hg from the source material. After constant temperature and recorded weight have been attained, the temperature was raised again. This procedure was followed for all weight gain readings over the desired temperature range.

As mentioned above, under present experimental conditions the partial pressures of Cd and Te_2 relative to that of Hg are insignificant. Thus, any weight gain detected by the balance can be attributed to mercury evaporated from the source. The Hg atoms in the vapor phase exert their weight at the center of the mass of the bulk gas in the free volume of the ampul which is approximately one-half the distance between the ampul ends. Since the condensed source material lies on the fulcrum, any mass change of the source will not be detected by the balance other than as described above. Employing the lever principle, the actual mass of the total number of Hg atoms in the vapor phase can be determined according to the expression

$$M \times A = W \times B \qquad [1]$$

where M is the weight recorded by the balance in grams, A is the distance from the fulcrum to the hook in centimeters (*i.e.*, the lever arm for M), W is the weight of mercury atoms in the gas phase of the ampul in grams, and B is the distance (cm) from the fulcrum to the center of mass of the free volume of the ampul (*i.e.*, the lever arm for W). With the knowledge that mercury exists as a monatomic gas, and combining the ideal gas equation with the lever principle (Eq. [1]), the mercury pressure can be expressed as

$$P = \left(\frac{M \times (A/B)}{\text{At. Wt. of Hg}} \right) \times \frac{RT_m}{V_f} \text{ (atm)} \qquad [2]$$

where T_m is the average temperature as defined above, and V_f is the free volume of the ampul. When the ampul is heated, the buoyancy of the surrounding atmosphere is reduced causing an apparent weight gain of the ampul. The weight gain due to the buoyancy effect was determined as a function of temperature employing an empty ampul under otherwise identical conditions. The recorded weight M during actual runs was corrected accordingly.

In order to assess the accuracy and reproducibility of the experimental method, the system was calibrated using elemental mercury as a source material. The vapor pressure data of mercury have been reviewed by Hicks (18). Based on those and additional data (19) obtained by Sugawara *et al.*, Brebric and Strauss (20) derived an expression for the pressure-temperature relationship of mercury [$\log P_{Hg}(\text{atm}) = 4.891 - 3.08(10^3)\, T^{-1}$]. We have used the latter equation (20) to correct our experimentally determined values of the saturated vapor pressure of Hg over liquid mercury. The experimental data were found to be systematically lower than those computed. Using a linear least squares analysis for the comparison of experimental and computed (20) data, the following relation was obtained

$$\log P_{corr} = 0.90332 \times \log P_{exp} + 0.13291 \qquad [3]$$

where P_{corr} and P_{exp} are the corrected and experimental vapor pressures of Hg, respectively. The number of figures of the constants has only calculational significance. All Hg pressures reported in this work are corrected values according to Eq. [3]. The combined (added) uncertainties in measuring the quantities M, A, B, V_f, and T_m in Eq. [2] yield a maximum uncertainty in the vapor pressure of Hg of about 9%. Based on this and repeated calibration procedures, a more realistic uncertainty of the pressure measurements is less than 9%.

Results and Discussion

For all vapor pressure measurements performed in the present work, the ratio of the sample volume to the free volume of the ampul (v/V_f) was kept constant at 0.0054.

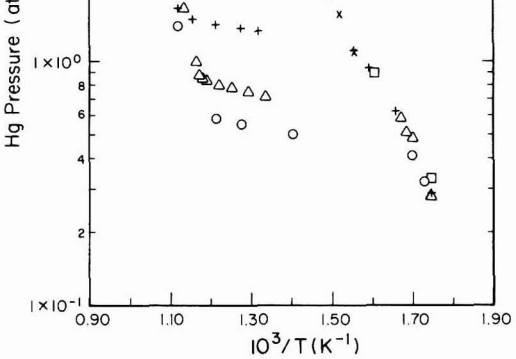

Fig. 2. Mercury pressures as a function of temperature over elemental mercury (□) (calibration data), and over $Hg_{0.8}Cd_{0.2}Te$ for different amounts of added excess Hg. (○) 0.41 atm excess Hg at 585.5 K; (△) 0.59 atm excess Hg at 602.2 K; (+) 1.10 atm Hg at 636.1 K; (×) 2.29 atm excess Hg at 681.3 K.

Table I. Equilibrium vapor pressures of Hg over $Hg_{0.8}Cd_{0.2}Te$ as a function of temperature for different amounts of excess Hg added initially

Run no. 1 $P_{Hg,exc}$ = 0.41 atm*		Run no. 2 $P_{Hg,exc}$ = 0.59*		Run no. 3 $P_{Hg,exc}$ = 1.10 atm*		Run no. 4 $P_{Hg,exc}$ = 2.29 atm*	
$10^3/T(K^{-1})$	P (atm)	$10^3/T(K^{-1})$	P (atm)	$10^3/T(K^{-1})$	P (atm)	$10^3/T(K^{-1})$	P (atm)
1.730	0.32	1.745	0.28	1.745	0.29	1.555	1.09
1.700	0.41	1.700	0.48	1.658	0.62	1.520	1.56
1.406	0.50	1.686	0.51	1.592	0.94	1.497	1.89
1.277	0.55	1.672	0.58	1.555	1.11	1.477	2.15
1.215	0.58	1.337	0.71	1.319	1.32	1.456	2.40
1.121	1.39	1.295	0.74	1.277	1.36	1.295	2.44
1.096	2.15	1.253	0.77	1.215	1.42	1.181	2.91
		1.222	0.79	1.158	1.49	1.148	3.00
		1.192	0.83	1.121	1.64	1.129	3.08
		1.181	0.84	1.096	2.21	1.116	3.09
		1.175	0.87	1.080	3.20	1.079	3.63
		1.165	0.99			1.066	4.14
		1.134	1.64			1.057	4.80
		1.109	2.31				
		1.084	3.24				
		1.050	5.16				

* $P_{Hg,exc}$ is the pressure of the initially added excess Hg at the temperature of the onset of the homogeneity region (Table II).

Practical considerations such as furnace limitations and safety precautions suggested an upper experimental temperature of about 700°C. As indicated above, the weight of the vapor and, hence, the pressure determined is solely due to mercury evaporating from the source material. When the exact amount of elemental mercury, added in excess to the source material, is vaporized completely, the composition of the solid $Hg_{0.8}Cd_{0.2}Te$ in equilibrium with the mercury vapor is close to that at the Hg-rich, three-phase boundary. The number of Hg vacancies of the solid corresponds to the equilibrium vacancy concentration at that particular pressure and temperature.

The numerical results in terms of pressure as a function of temperature for different amounts of excess elemental mercury added are summarized in Table I. A graphical representation of experimental Hg pressures *vs.* $1/T$ on semilogarithmic scales is shown in Fig. 2. As long as liquid mercury is present in the condensed source materials, the pressures lie on the three-phase boundary of the Hg-rich side of the pressure-temperature phase diagram. The pressure and temperature at which the total amount of excess mercury is just vaporized, represent the onset of the homogeneity range of $Hg_{0.8}Cd_{0.2}Te$. Upon further increasing the temperature, the pressure increases at a considerably lower rate in the two-phase region (homogeneous solid $Hg_{0.8}Cd_{0.2}Te$ and vapor) of the system relative to that along the three-phase boundary. This increase is mainly caused by the temperature change of the equilibrium gas phase. A small contribution to this pressure increase is due to the addition of Hg vapor to the gas phase resulting from the formation of Hg vacancies in the solid. At the termination of the homogeneity range, the pressure again increases steeply with temperature, and the pressures lie on the three-phase boundary of the Te-rich side of the phase diagram. This pressure increase is due to a partial decomposition of the solid to a Te-rich liquid and Hg vapor. It is apparent from Fig. 2 that the Hg-rich and Te-rich limits of the homogeneity range shift toward higher pressure and temperature with increasing amounts of excess mercury added. Based on the phase rule (with c = 2), each temperature-pressure point in the two-phase region corresponds to one composition of the condensed source material.

In order to derive pressure-temperature data for the onset and termination of the homogeneity range for the different runs, the data of the three-phase boundaries on the Hg-rich and Te-rich sides and within the homogeneity range of the phase diagram were subjected to a linear least squares treatment. The intersections of the resulting straight lines (equations) within the two-phase region with those of the three-phase boundaries yield the terminal pressure-temperature coordinates of the homogeneity range for the different runs. These data are summarized in Table II and reveal that with increasing temperature higher equilibrium mercury pressures are required in order to maintain $Hg_{0.8}Cd_{0.2}Te$ within the homogeneity range.

For a given experimental run and ignoring the formation of new vacancies, the equilibrium vapor pressure of mercury at the temperature of the termination (upper limit) of the homogeneity range can be calculated from the pressure-temperature data at the onset (lower limit) of the homogeneity range. The difference between this calculated Hg pressure and the corresponding experimental pressure at the Te-rich boundary (Table II) is due to the formation of Hg vacancies within the homogeneity range. These mercury pressures, ΔP_{vac}, and the corresponding changes in vacancy concentrations, ΔN_v, are listed for each run in Table III.

The formation of vacancies in solids is generally described by an exponential relationship according to the expression

$$N_v = N_0 \cdot e^{-\Delta H/kT} \quad [4]$$

where N_v is the vacancy concentration at temperature T, N_0 is the total number of lattice sites occupied by Hg atoms, k is Boltzmann's constant, and ΔH is the enthalpy of formation of vacancies. With Eq. [4] and the knowledge of N_0, values of ΔH can be computed from values of N_v at a given T. The value of N_0 (number of Hg atoms) for

Table II. The onset and termination of the single phase homogeneity region of $Hg_{0.8}Cd_{0.2}Te$ in terms of Hg pressure and temperature

Run no.	Onset of homogeneity region P_1(atm)	T_1(K)	Termination of homogeneity region P_2(atm)	T_2(K)
1	0.41	585.5	0.59	833.3
2	0.57	602.2	0.84	851.5
3	1.10	636.1	1.56	886.4
4	2.29	681.3	3.16	929.4

The number of figures of the temperature data has only calculational significance.

Table III. Change in Hg pressure caused by the formation of vacancies within the homogeneity range, corresponding change in vacancy concentration, enthalpy of formation of vacancies, and total vacancy concentration at the Te-rich limit of the homogeneity range

Run no.	ΔP_{vac} (atm)	ΔN_v (cm^{-3})	ΔH_v (eV)	N_v (cm^{-3})
1	0.007	1.15×10^{19}	0.49	1.2×10^{19}
2	0.034	5.49×10^{19}	0.38	6.2×10^{19}
3	0.027	4.20×10^{19}	0.42	4.8×10^{19}
4	0.037	5.47×10^{19}	0.42	6.5×10^{19}

$Hg_{0.8}Cd_{0.2}Te$ has been calculated from crystallographic data (13) to be about 1.16×10^{22} per cm^3. Using the data for ΔN_v (Table III) and the temperature limits of the homogeneity range (Table II) for each run in combination with Eq. [4] yields the following set of equations

$$N_{v,T_1} = N_o \cdot e^{-\Delta H/kT_1} \quad [5a]$$

and

$$N_{v,T_2} = N_{v,T_1} + \Delta N_v = N_o \cdot e^{-\Delta H/kT_2} \quad [5b]$$

Here T_1 and T_2 are the temperatures of the lower and upper limits of the homogeneity range, respectively. With the above equations values of ΔH_v and of the vacancy concentration can be calculated. Enthalpies of vacancy formation and total vacancy concentrations (at the upper temperature limit of the homogeneity range) are listed in Table III. The agreement between the different ΔH_v values is quite reasonable. The average enthalpy of vacancy formation based on our data is $\Delta H_v = 0.43$ eV with an estimated uncertainty of about ± 15%. The last column in Table III contains the total vacancy concentration at the upper temperature limit of the homogeneity range based on the individual ΔH_v values for the different runs. The average trend of these data is consistent with an expected increase in vacancy concentration with temperature. The data in Table III also reveal that N_v at the lower temperature limit of the homogeneity range of a given run is about one order of magnitude lower than that at the upper limit.

A comparison of these results with the literature is not possible, because no direct measurements of the enthalpy of formation and of the concentration of vacancies have been reported to date. To derive this information from conductivity or charge carrier concentration data is not possible. The exponential temperature dependence of acceptors has been described by empirical expressions (15, 17). However, these expressions cannot unambiguously give the enthalpy of vacancy formation because it is difficult to distinguish between the contribution of native acceptors, compensating donor impurities, and compensating native donors. Based on theoretical considerations (21), the heat of formation of mercury vacancies in HgTe was proposed to be 0.5 eV. More recent theoretical calculations (22, 23) suggest, that the cadmium atoms in $Hg_{1-x}Cd_xTe$ destabilize the Hg-Te bonds. Thus, the bond strength of "HgTe" in $Hg_{1-x}Cd_xTe$ should be less than that in pure HgTe. Based on our experimental value for the heat of vacancy formation of 0.43 eV, the above estimations for HgTe (21) and $Hg_{1-x}Cd_xTe$ (22, 23) seem to be of the right order.

Summary and Conclusions

The dynamic mass loss measurement technique has been modified, using the lever principle, to determine mass changes of a material in a closed container. Using an automatic semimicrobalance, this technique has been employed, for the first time, to investigate the vacancy formation in $Hg_{0.8}Cd_{0.2}Te$. The results of this work demonstrate the feasibility of this method for the direct, *in situ* measurement of vacancy concentrations at elevated temperatures and for the derivation of P-T phase diagrams for this type of system. From the experimental data, values for the heat of formation of vacancies can be derived unambiguously employing conventional thermodynamic methods. Theoretical predictions concerning the vacancy formation in HgTe (21) and the destabilizing effect of Cd on the Hg-Te bonds (22, 23) are in qualitative agreement with our experimental mean value for the heat of vacancy formation (0.43 eV). The portion of the phase diagram of this system (Fig. 2) established by this relatively simple technique is consistent with the literature (11). In order to further investigate the validity of these predictions and to compare the vacancy concentrations for different $Hg_{1-x}Cd_xTe$ alloys, analogous studies are planned for these compounds with other x-values. This method should also be useful for vacancy studies of other electronic materials.

Acknowledgments

The authors are pleased to acknowledge the support of this work by the National Aeronautics and Space Administration through the Office of Microgravity Science and Applications, Washington, D.C., and through the Experiments Development Office, George C. Marshall Space Flight Center, Huntsville, Alabama.

Manuscript submitted Feb. 10, 1986; revised manuscript received June 25, 1986.

Rensselaer Polytechnic Institute assisted in meeting the publication costs of this article.

REFERENCES

1. W. F. H. Mickelthwaite, in "Semiconductors and Semimetals," Vol. 18, R. K. Willardson and A. C. Beer, Editors, p. 48, Academic Press, New York (1981).
2. J. L. Schmit, *J. Cryst. Growth*, **65,** 249 (1983).
3. M. A. Herman and M. Pessa, *J. Appl. Phys.*, **57,** 2671 (1985).
4. H. Maier and J. Hesse, "Crystals (Growth, Properties, and Applications), 4," H. C. Freyhardt, Managing Editor, p. 145, Springer-Verlag, Berlin, Heidelberg, New York (1980).
5. H. Wiedemeier and D. Chandra, *Z. Anorg. Allg. Chem.*, **488** 137 (1982).
6. H. Wiedemeier and A. E. Uzpurvis, *This Journal*, **130,** 252 (1983).
7. H. Wiedemeier, A. E. Uzpurvis, and D. Wang, *J. Cryst. Growth*, **65,** 474 (1983).
8. E. A. Irene, E. Tierney, H. Wiedemeier, and D. Chandra, *Appl. Phys. Lett.*, **42,** 710 (1983).
9. J. H. E. Jeffes and T. N. R. Marples, *J. Cryst. Growth*, **17,** 46 (1972).
10. J. P. Schwartz, Tse Tung, and R. F. Brebrick, *This Journal*, **128,** 438 (1981).
11. T. Tung, L. Golonka, and R. F. Brebrick, *ibid.*, **128,** 451 (1981).
12. D. Long and J. L. Schmit, in "Semiconductors and Semimetals," Vol. 5, R. K. Willardson and A. C. Beer, Editors, p. 234, Academic Press, New York (1970).
13. R. Dornhaus and G. Nimtz, in "Solid State Physics," Vol. 78, p. 7, Springer-Verlag, New York (1976).
14. R. A. Farrar, G. J. Gilham, R. Bartlett, and M. Quelch, *J. Mater. Sci.*, **12,** 836 (1977).
15. J. L. Schmit and E. L. Stelzer, *J. Electron. Mater.*, **7,** 65 (1978).
16. R. F. Brebrick and J. P. Schwartz, *ibid.*, **9,** 485 (1980).
17. H. R. Vydyanath, *This Journal*, **128,** 2609 (1981).
18. W. T. Hicks, *J. Chem. Phys.*, **38,** 1873 (1963).
19. S. Sugawara, T. Sato, and T. Minamiyama, *Bull. Jpn. Soc. Mech. Eng.*, **5,** 711 (1962).
20. R. F. Brebrick and A. J. Strauss, *J. Phys. Chem. Solids*, **26,** 989 (1965).
21. R. F. Bailly, "Lattice Defects in Semiconductors," p. 21, University of Tokyo Press, Tokyo (1968).
22. A. B. Chen, A. Sher, and W. E. Spicer, *J. Vac. Sci. Technol.*, **A1(3),** 1674 (1983).
23. A. Sher, A. B. Chen, W. E. Spicer, and C. K. Shih, *ibid.*, **A3(1)** 105 (1985).

Thermoplastic Deformation of Silicon Wafers

A. E. Widmer and W. Rehwald

Laboratories RCA Limited, CH-8048 Zurich, Switzerland

ABSTRACT

In order to study the problem of warping of silicon wafers during thermal treatment, we subjected stacks of wafers to heating and cooling under various processing parameters. During these processes, the temperatures were measured as a function of time at various locations on a test wafer. These data form the basis for a calculation of the thermoplastic stresses. From a comparison with the temperature-dependent yield stress, we can decide whether thermoplastic deformation, leading to warpage and increased dislocation density, is to be expected under these specific processing conditions.

All the photolithographic processes and many handling and transporting procedures during device fabrication require a good planarity of the wafer surface. Tolerances are of the order of 10 μm or less in vertical displacement, but the trend towards smaller device structures and larger wafer diameters will certainly aggravate this problem in the future.

Warpage, *i.e.*, deviations from planarity, can have many reasons (1-3). Usually, the initial warping of the freshly cut and polished wafer is rather small, but can increase drastically after thermal treatments. There are two major categories of processes causing warpage. (*i*) When bare silicon wafers are introduced into the furnace or extracted from it, each wafer is heated or cooled nonuniformly, resulting in a temperature gradient between rim and center. This inhomogeneous temperature field generates thermal stresses (4-6). Although these stresses disappear as soon as the wafer has reached thermal equilibrium, they can cause permanent plastic deformations, if they exceed the upper yield stress of the material during their buildup period. (*ii*) Silicon wafers, covered on one side with layers of a different material, experience large stresses after a temperature change, even if the temperature is uniform. The reason for this is the difference in the thermal expansion coefficients of substrate and layer (7). Warpage is generated in the same way, if the thermal stresses rise beyond the yield point.

During plastic deformation, a large number of dislocations is introduced into the wafer. They are located in certain crystallographic planes, called slip planes. It is known that dislocations exert negative effects upon the performance of the transistor elements (3). Examples are an excessive emitter-collector leakage current in analog circuits and element failure in digital circuits. All these considerations show that warpage and all its accompanying features are highly undesirable in silicon device manufacturing and should be avoided.

In our present study of the warpage problem, we concentrate on the case of bare uniformly doped bulk silicon wafers, loaded vertically in a boat and forming a long row. Our goal is to specify the conditions under which warpage can be safely avoided by using a combination of experiments (measurements and observations) and theoretical analysis. Among the parameters studied (furnace temperature, insertion, and extraction speed), the oxygen content and its state (interstitial or precipitated) play an important role (3, 8-10). To our present knowledge, interstitial oxygen increases the yield stress and the mechanical strength within a certain concentration range. On the other hand, oxygen precipitates act as dislocation sources and drastically lower the yield stress. Precipitated oxygen is often used for internal gettering, a fact that may require conditions opposite to those for keeping thermal warping small.

In the following section, we describe a series of experiments performed on silicon wafers under conditions simulating heat-treatments of an actual fabrication process as closely as possible. From each thermal run several wafers were tested for slip lines by proper dislocation etching (11). They were also probed by scanning a focused ultrasonic beam across the region in question (12). Slip lines cause an additional acoustic attenuation and can be detected in position and strength (dislocation density) from the plotted level of the transmitted acoustic signal.

During the heating and cooling process, the temperature on a single wafer was measured at several points as a function of time. These data form the basis for a calculation of the stress field in the Theoretical Analysis section. The calculated stresses are compared with the actual (*i.e.*, temperature-dependent) yield stress, and a decision is made whether thermoplastic deformation and resulting warping are to be expected or not. In the two final sections, the results are discussed and summarized, also with respect to applications in device processing.

Experimental

We have measured the radial temperature distribution on 4 in. diameter single side polished silicon wafers when they are inserted or withdrawn from a processing furnace. The temperature distribution was measured on a monitor wafer placed in the middle of a stack of 20 wafers. The monitor wafer was provided with 12 Pt-Pt 10% Rh thermocouples of 100 μm diameter, placed at various locations on the surface as shown in Fig. 1. The thermocouples were embedded with Fibrefrax QF150 Cement (Carborundum) into 500 μm diameter holes in the wafer. These holes were produced with a miniature sandblasting unit whereby the diameter of the holes was confined with a nickel mask. Since silicon forms binary alloy reactions with platinum which results in the fracture of the thin thermocouple wires, it is essential that all silicon surfaces that could be in contact with the platinum-rhodium thermocouples are covered with a few hundred nm SiO_2. We have chosen a four-rod wafer carrier and used a wafer spacing of 2.5 mm which is typical for today's device processing. The silicon wafer to be evaluated for warpage and slip was placed next to the temperature monitor wafer as shown in Fig. 1. The 10 wafers towards the furnace entrance contained the same matrix of holes through which the thermocouple wires were guided to a distributor block. This distributor block is used for convenience in order to preassemble the wafer stack in a separate operation. Between the wafer stack and the distributor block we have provided the thermocouple wires with a woven quartz sleeving (Refrasil, Darlington, England) for electrical insulation.

The distributor block consists of two rectangular pieces cut out from a silicon wafer with an array of holes through which 0.5 mm diameter platinum or platinum-rhodium wires are inserted as shown in Fig. 1. These rather stiff wires are used as terminal points onto which

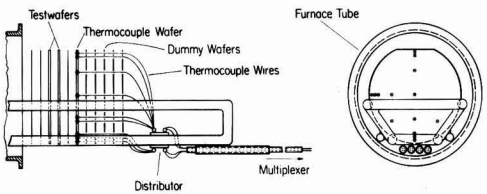

Fig. 1. Location of the thermocouples in the wafer stack

the 100 μm thermocouple wires from the monitor wafer are fused by means of a fine butane-oxygen torch.

The push and pull rod for the wafer carrier consists of four Al_2O_3 4-hole tubing through which the thermocouple wires are extended outside the furnace into an array of miniature thermocouple connectors. The data from the 12 thermocouples were multiplexed (repetition rate 6s) and stored in a Commodore 8032 computer for numerical and graphical evaluation. No furnace ramping technique was used for this investigation.

Figure 2 shows a graphical representation of a typical radial temperature distribution along the vertical axis from the center of the wafer towards the periphery. The small dots indicate the temperature at the center, whereas the larger marks give the temperature difference between the points indicated and the center.

The wafers were inserted starting from room temperature, and we used a nitrogen gas flow of 2 l/min as an ambient in the furnace tube. To investigate the influence of interstitial oxygen on the plastic deformation, we have included in some runs Czochralski-pulled silicon wafers with low (14 ppm) and high (20 ppm) levels of oxygen. This material was p-type, boron doped, and had a resistivity of 10-15 Ω cm, and no prior oxygen precipitation treatment was done. These wafers were placed in slots close to the temperature monitor wafer as shown in Fig. 1 so that they experienced identical temperature fields.

The temperature distribution across the wafer is nonuniform for two reasons. The outer regions of the wafer see the environment (furnace walls or open space) under a wider solid angle than the central parts and experience a more rapid heat exchange by radiation. These relationships, leading to a circularly symmetric temperature field, have been modeled by Hu (6). The thermal mass of the wafer carrier and its shadowing action cause deviations from circular symmetry and render the temperature angle-dependent. For the used four-rod boat, the highest temperature gradients were measured along the positive vertical axis for insertion and along the negative vertical axis for withdrawal. The radial temperature variation is represented in Fig. 3a and 3b for various furnace temperatures between 800° and 1150°C and for insertion and withdrawal speeds of 100 and 500 mm/min. Plotted is the maximum difference in temperature between a point at a given radius along the vertical axis and the center. Figure 4a and 4b show the maximum temperature difference for the thermocouple closest to the periphery and the actual temperature at this point as a function of insertion or withdrawal speed for different furnace temperatures. These values approximate the conditions at the periphery where the highest stresses are expected to occur.

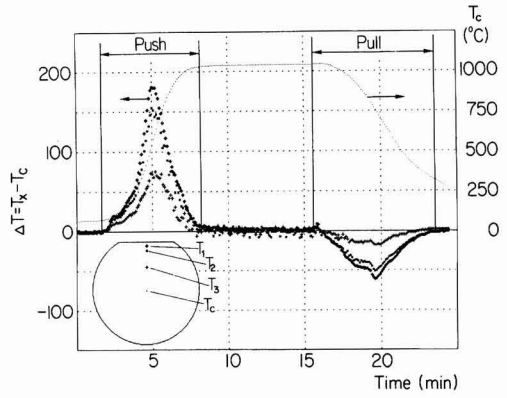

Fig. 2. Time dependence of the radial temperature distribution for a furnace temperature of 1050°C and an insertion/withdrawal speed of 100 mm/in. The temperature in the center is indicated by small dots (right-hand scale). Squares and crosses mark the temperature difference between the indicated thermocouple location and the center (left-hand scale).

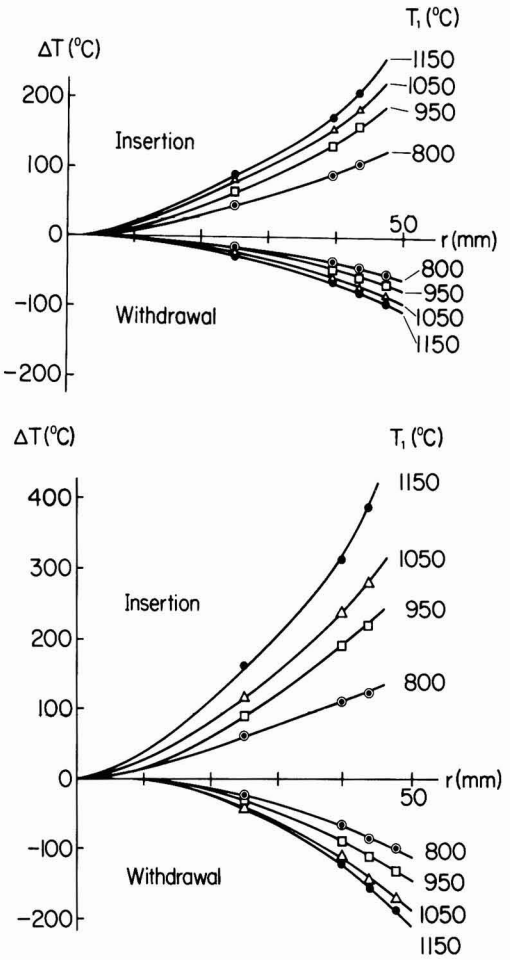

Fig. 3. (a, top) Temperature difference between a point at radius r and the center for various furnace temperatures T_1; vertical direction upward. Insertion/withdrawal speed = 100 mm/min. (b, bottom) Temperature difference between a point at radius r and the center for various furnace temperatures T_1; vertical direction upward. Insertion/withdrawal speed = 500 mm/min.

After thermal treatment these sample wafers were characterized for slip-line patterns after dislocation etching, following the recipe of Wright (11), and by ultrasonic probing (12).

The temperature data obtained in this way are used in the subsequent stress calculation.

Theoretical Analysis

General calculation of stresses from the temperature field.—In the following analysis, several simplifying assumptions are made. All surface and volume forces acting upon the wafer are neglected. The wafer is considered to be thin compared to its lateral dimension, and all displacements in axial direction (Z-axis, thickness direction) are neglected. This allows us to treat the stress field as two-dimensional and to limit it to the components $\sigma_r = \sigma_{rr}$, $\sigma_\phi = \sigma_{\phi\phi}$, and $\sigma_{r\phi}$ of the whole stress tensor, written in cylindrical coordinates. During the calculation of the stress field, silicon is taken as an elastically isotropic material, characterized by two of the three elastic parameters E (Young's modulus), G (shear modulus), and ν (Poisson ratio). When thermoplastic deformation and slip are discussed, the anisotropic elastic properties of silicon have to be taken into account.

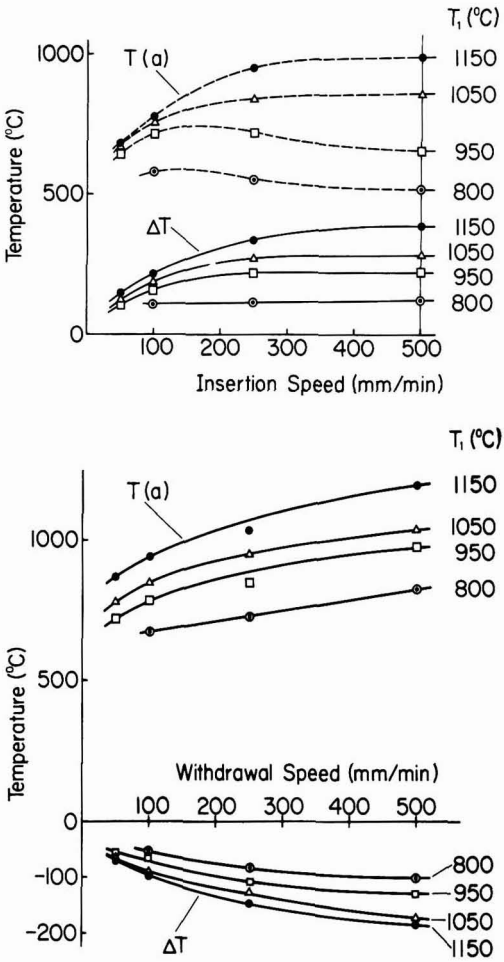

Fig. 4. (a, top) Actual temperature $T(a)$ at the periphery and temperature difference ΔT to the center as a function of insertion and withdrawal speed and for various furnace temperatures T_1-insertion. (b, bottom) Actual temperature $T(a)$ at the periphery and temperature difference ΔT to the center as a function of insertion and withdrawal speed and for various furnace temperatures T_1-withdrawal.

The components of a two-dimensional stress field can be obtained from a stress potential F, also called Airy's stress function, by double differentiation (13). In cylindrical coordinates, *e.g.*

$$\sigma_r = \frac{1}{r}\frac{\partial F}{\partial r} + \frac{1}{r^2}\frac{\partial^2 F}{\partial \phi^2} \quad [1]$$

$$\sigma_\phi = \frac{\partial^2 F}{\partial r^2} \quad [2]$$

$$\sigma_{r\phi} = -\frac{\partial}{\partial r}\left(\frac{1}{r}\frac{\partial F}{\partial \phi}\right) \quad [3]$$

When the temperature is constant in space, the stress potential is determined by a fourth-order differential equation, that is the analogue to Laplace's equation in electrostatics

$$\nabla^2\nabla^2 F = \left(\frac{\partial^2}{\partial r^2} + \frac{1}{r}\frac{\partial}{\partial r} + \frac{1}{r^2}\frac{\partial^2}{\partial \phi^2}\right)\left(\frac{\partial^2 F}{\partial r^2} + \frac{1}{r}\frac{\partial F}{\partial r} + \frac{1}{r^2}\frac{\partial^2 F}{\partial \phi^2}\right) = 0 \quad [4]$$

When the temperature is nonuniform, the differential equation becomes inhomogeneous

$$\nabla^2\nabla^2 F = -\alpha E \nabla^2 T \quad [5]$$

with α denoting the thermal expansion coefficient. The general solution of this is a linear combination of the general solution F_0 of the homogeneous equation and a particular F_1 of the nonhomogeneous one

$$F = F_0 + F_1$$

with

$$\nabla^2\nabla^2 F_0 = 0 \quad [6]$$

and

$$\nabla^2 F_1 = -\alpha E T$$

The total potential F has to satisfy the boundary condition of zero force at the surfaces of the body. In the case of a circular disk of diameter $2a$, this amounts to

$$\sigma_{r4}(a) = \sigma_{r\phi}(a) = 0 \quad [7]$$

In general, the temperature field is not circularly symmetric. The reason for this is that the wafers always rest in a boat that disturbs the radial heat flux by its thermal mass and its shadowing effect. In order to take this into account, we expand our general solution, as well as the temperature field, into a Fourier series of the azimuthal angle ϕ. If we count ϕ from the bottom (or top) position, these series contain only terms with $\cos n\phi$. This results in the following equations

$$T(r, \phi) = -\frac{1}{\alpha E}\sum_{n=0}^{\infty} b_n(r)\cos n\phi \quad [8]$$

$$F_0(r, \phi) = a_{20}r^2 + a_{11}r^3\cos\phi + \sum_{n=2}^{\infty}(a_{1n}r^{n+2} + a_{2n}r^n)\cos n\phi \quad [9]$$

$$F_1(r, \phi) = \sum_{n=0}^{\infty}\left[\frac{r^n}{2n}\int_0^r \frac{b_n(x)dx}{x^{n-1}} - \frac{1}{2nr^n}\int_0^r x^{n+1}b_n(x)dx\right]\cos n\phi \quad [10]$$

The Fourier components b_n of the temperature distribution enter the final result in the form of radial momenta $M_n(r)$ and $N_n(r)$

$$M_n(r) = \int_0^{r/a} x^{n+1}b_n(x)dx \quad [11]$$

for $n \geq 0$, and

$$N_n(r) = \int_0^{r/a}\frac{b_n(x)dx}{x^{n-1}} \quad [12]$$

for $n > 0$.

Here, the normalized coordinates r/a have been introduced. Application of the boundary conditions determines the coefficients in F_0

$$a_{1n} = M_n(1)/(2a^n) \quad [13]$$

for all n, and

$$a_{2n} = N_n(1)/(2na^{n-2}) - (n+1)M_n(1)/(2na^{n-2}) \quad [14]$$

for $n \geq 2$.

Finally, we obtain the stress components in terms of the Fourier coefficients of the temperature field, with $x = r/a \leq 1$

$$\sigma_r(r, \phi) = M_0(1) - \frac{M_0(x)}{x^2} - \frac{1}{2}\sum_{n=1}^{\infty}\left\{(n+1)M_n(1)\cdot[(n-2)x^n - (n-1)x^{n-2}] + \frac{n+1}{x^{n+2}}M_n(x) + (n-1)[N_n(1) - N_n(x)]x^{n-2}\right\}\cos n\phi \quad [15]$$

$$\sigma_\phi(r,\phi) = M_0(1) + \frac{M_0(x)}{x^2} - b_0(x) + \frac{1}{2}\sum_{n=1}^{\infty}\left\{(n+1)M_n(1)\cdot[(n+2)x^n - (n-1)x^{n-2}] + \frac{n+1}{x^{n+2}}M_n(x) + (n-1)x^{n-2}\cdot[N_n(1) - N_n(x)] - 2b_n(x)\right\}\cos n\phi \quad [16]$$

$$\sigma_{r\phi}(r,\phi) = \frac{1}{2}\sum_{n=1}^{\infty}\left\{(n+1)M_n(1)[nx^n - (n-1)x^{n-2}] - \frac{n+1}{x^{n+2}}M_n(x) + (n-1)x^{n-2}[N_n(1) - N_n(x)]\right\}\sin n\phi \quad [17]$$

The case of circularly symmetric temperature distribution has been treated in Ref. (6, 13)

$$\sigma_r(r) = M_0(1) - M_0(x)/x^2 \quad [15a]$$

$$\phi_\phi(r) = M_0(1) + M_0(x)/x^2 - b_0(x) \quad [16a]$$

$$\sigma_{r\phi}(r) = o \quad [17a]$$

Calculation of the stress field from measured temperature distributions.—The temperatures have been measured at the center and at four points along the radius in each of the directions $\phi = 0, 90°$. The flat of the wafer is in the upper position ($\phi = 180°$); in this direction, only three measurements along the radius are possible (Fig. 1). This gives a total of twelve sampling points for the temperature field. For the radial dependence, we use a polynomial interpolation of third degree. Mirror symmetry and the knowledge of the temperature in three directions allows us to calculate the Fourier components b_0, b_1, and b_2, and by integration the momenta M_n and N_n up to second order. From this, the three stress components σ_r, σ_ϕ, and $\sigma_{r\phi}$ can be determined at any point on the wafer up to second order in the angular dependence.

Figure 5 shows σ_r and σ_ϕ as a function of the radius in three different directions during the cooling process at a time close to the maximum temperature difference center/periphery. These diagrams resemble those given by Hu (6) in his model calculation for a circularly symmetric temperature profile. The differences between the various directions are small compared with the overall radial variation. Close to the center, not enough details of the temperature field are known; therefore, the uncertainty of the calculated stresses is larger here. The same holds for $\phi = 180°$, where the temperature at $r/a = 0.95$ had to be determined by extrapolation. The stresses for the heating process are of opposite sign and generally higher. The third stress component $\sigma_{r\phi}$ is about one order of magnitude smaller and vanishes both at $r = o$ and $r = a$.

The highest stresses appear at the periphery $r = a$ and are of tangential type: tension during cooling and compression during heating. Therefore, our main interest in the further discussion will be concentrated on $\sigma_\phi(a)$ and its variation with time. Figure 6 shows the time dependence of the tangential stress at the periphery for heating and cooling and also for the two insertion/withdrawal speeds 500 and 100 mm/min. These curves resemble those for the temperature difference as a function of time (Fig. 2). Curves for heating and cooling are not symmetrical. For the chosen experimental conditions with small wafer separations and large wafer stacks, our measurements agree with those of Kasper and Clauss (5), revealing larger temperature differences for insertion than for withdrawal. The stresses during the insertion process also decay faster in time after they have passed the maximum. When the wafer stack is moved slowly, the temporal variation of temperature and stress is also determined by the temperature profile at the entrance of the furnace. This results in a double-peak structure in $\sigma_\phi(t)$ and $\Delta T(t)$.

Conditions for plastic deformation.—When plastic deformation by slip occurs, it will start first at the periphery. It is carried by generation, multiplication, and motion of dislocations, which are in general thermally activated processes and, therefore, strongly temperature dependent. Hence, for the discussion, it is more suitable

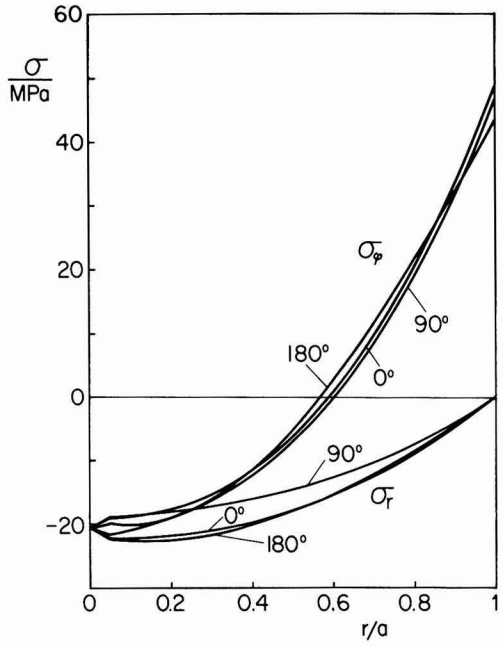

Fig. 5. Radial dependence of the stresses σ_ϕ and σ_r under three different azimuthal angles, calculated from a withdrawal process with 500 mm/min speed and a furnace temperature of 1050°C.

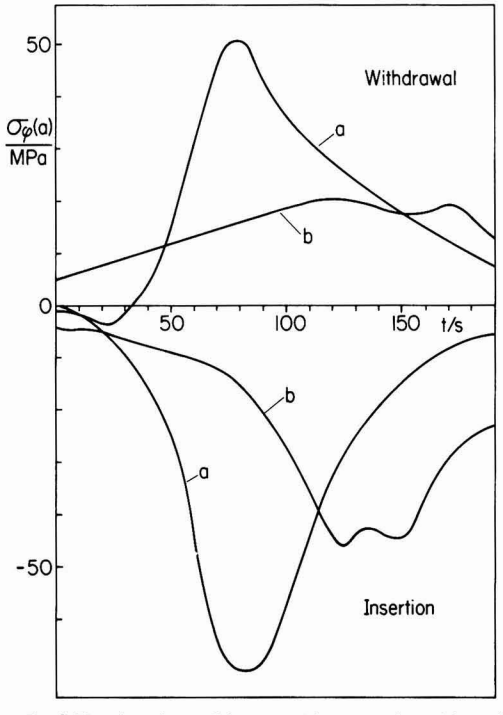

Fig. 6. Time dependence of the tangential stress on the periphery of a 100 mm (= 4 in.) wafer at $\phi = 0$ (bottom) for two different insertion (withdrawal) speeds; (a) 500 mm/min, (b) 100 mm/min.

to plot the stress as a function of local temperature with time as an implicit parameter running along the curve. If the temperature dependent yield stress is plotted in the same diagram, it can easily be decided whether slip occurs or not.

This is the point where the anisotropic properties of silicon come into play. Slip occurs in silicon, as in most of the face-centered cubic crystals. by a glide motion along a [$\bar{1}$10]-direction in a (111)-plane or any other glide system related to it by cubic symmetry. The relevant quantity is the "resolved shear stress," σ_g, *i.e.*, the projection of σ_ϕ upon the glide system (111) [$\bar{1}$10]

$$\sigma_g = \frac{1}{\sqrt{6}}\sigma_\phi \cdot \sin 2\beta \qquad [18]$$

where β denotes the angle measured from the [110] direction. σ_g has extrema for $\phi = 45°, 135°$, etc. Under these angles, the first glide lines are expected to appear running from the rim along [$\bar{1}$10] and [1$\bar{1}$0] towards the center.

The yield stress for a certain loading depends on (*i*) the angles to the corresponding glide system, (*ii*) the temperature, (*iii*) the rate of deformation, (*iv*) the initial density of dislocations, and (*v*) the type and number of other bulk and surface defects, such as interstitial or precipitated oxygen in Czochralski-grown silicon or mechanical surface damage. In the literature, stress-strain curves on silicon are published that have been obtained in tension experiments under constant temperature and shear rate [Patel and Chaudhuri (14), Yonenaga and Sumino (15)]. Siethoff and Haasen studied the yield behavior of nominally pure silicon under constant compression rates at various temperatures (16). Kondo (17) has determined the upper yield stress σ_F in a static experiment under constant stress but with variable temperature. The results of all four references can be written in the form

$$\sigma_F = A\left(\frac{\dot{e}}{\dot{e}_0}\right)^{1/n} \exp\,(T_0/T) \qquad [19]$$

with the reference strain rate $\dot{e}_0 = 10^{-3}\ s^{-1}$ and the activation energy $\Delta E = kT_0$. The parameters, A, n, and T_0 are given in Table I, converted to normal stresses along [100], where necessary.

In our heating and cooling experiments, the largest strain rates occur around half the maximum stress (see, *e.g.*, Fig. 6). As will be shown later, (*e.g.*, Fig. 7) at these stress levels, plastic deformation becomes most probable. So the point of maximum strain rate approximately coincides with the onset of plastic flow. From Fig. 6 a strain rate of $\dot{e} = 1.2 \cdot 10^{-5}\ s^{-1}$ can be estimated for push/pull operation with a speed of 500 mm/min, whereas for the lower speed of 100 mm/min the values are $5.1 \cdot 10^{-6}\ s^{-1}$ for insertion and $1.1 \cdot 10^{-6}\ s^{-1}$ for withdrawal.

Figure 7 shows the maximum tangential stress $\sigma_\phi(a)$ as a function of local temperature for three different directions on the wafer, $\phi = 0$, 90°, and 180°. These data have been calculated from temperatures measured during a heating and cooling run with a furnace temperature of 1050°C and a push/pull speed of 500 mm/min.

In Fig. 8, results from a similar experiment are plotted, but with a push/pull speed of 100 mm/min. We can see that the direction of ϕ plays only a minor role and that assuming a circularly symmetric temperature distribution would be a sufficiently accurate approximation. As in

Table I. Yield stress parameters from various authors

Author	Ref.	T_0/K	ΔE/eV	n	A/Pa
Patel and Chaudhuri	(14)	12,450	1.073	2.45	3,630
Kondo (CZ-Si)	(17)	7,750	0.67	(∞)	55,100
Yonenaga and Sumino	(15)	14,190	1.22	2.4	254
Siethoff and Haasen	(16)	11,950	1.03	2.1	3,190

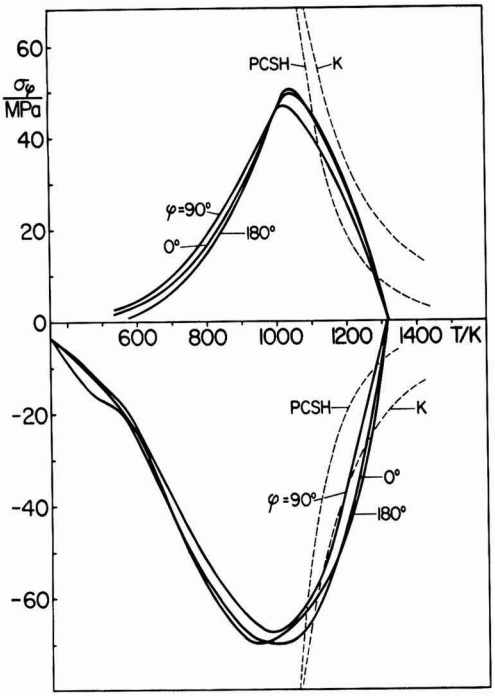

Fig. 7. Maximum tangential stress under three different angles as a function of local absolute temperature; the insertion/withdrawal speed is 500 mm/min and the furnace temperature 1050°C (= 1323 K). Dashed lines indicate the expected yield stress, calculated as mentioned in the text.

Fig. 6, insertion produces larger stresses than withdrawal. The smaller the insertion/withdrawal speed, the lower the temperature differences and the resulting stresses. Table II gives the maximum stress values ob-

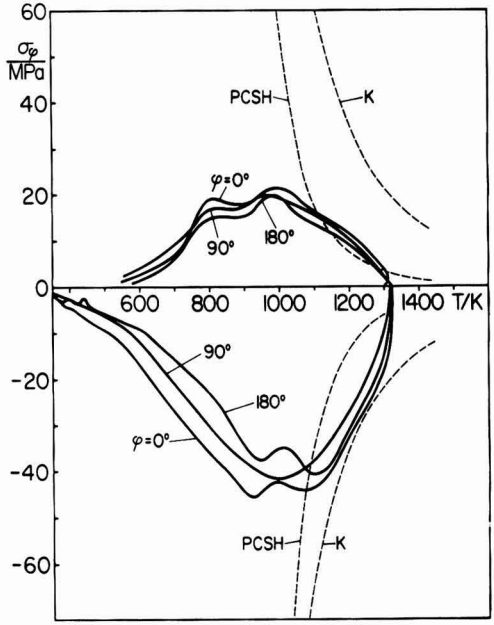

Fig. 8. The same data as in Fig. 7, but with an insertion/withdrawal speed of 100 mm/min.

Table II. Maximum tangential stress at the periphery, calculated from measured temperatures

Furnace temperature T_1/°C	Insertion Speed mm/min	Insertion max. $\sigma_\phi(a)$/MPa	Withdrawal Speed mm/min	Withdrawal max. $\sigma_\phi(a)$/MPa
1150	500	−95	500	56
	250	−83	250	43
	100	−50	100	22
	50	−30	50	13
1050	500	−70	500	50
	100	−44	100	21
950	500	−53	500	48
	250	−48	250	31
	100	−34	100	16
	50	−22	50	9
800	500	−24	500	29
	250	−21	250	25
	100	−12	100	22

tained in experiments with varying furnace temperature and insertion/withdrawal speed. The general trends are also seen in these values. The ratio between the stresses during insertion and withdrawal decreases continuously with decreasing furnace temperature and goes below one for T_1 = 800°C. This is most probably due to the fact that at the higher temperatures heat is predominantly transported by radiation, whereas at lower furnace temperatures conduction and convection also begin to contribute. In the case of fast insertion and withdrawal (250 and 500 mm/min), heat exchange with the furnace walls or the environment starts nearly instantaneously. For lower speeds, the temperature profile at the entrance of the furnace becomes relevant, and the resulting stresses decrease strongly with decreasing speed.

In Fig. 7 and 8 we plotted two additional curves for the yield stress $\sigma_F(T)$. One curve is based on data by Kondo (17); the other, marked PCSH, refers to Patel and Chaudhuri (14), as well as to Siethoff and Haasen (16). Data for the latter two references are nearly identical and depend upon the strain rate. Therefore, in each diagram, the strain rate was estimated from the $T(t)$ curves and taken into account. In all three references, Czochralski-grown silicon had been used. Kondo gives the amount of interstitial oxygen in his samples: $x(O_i)$ = 19 ppm. On the other hand, the yield stress data from Yonenaga and Sumino (15) had been obtained from float-zone grown silicon; the corresponding values are smaller by a factor of four than those from the curve marked PCSH and are not plotted in our diagrams.

Figure 9, finally, demonstrates the case where no plastic deformation should occur. For furnace temperatures of 800° and 950°C, the stress at $r = a$ and $\phi = o$ is plotted in the same way as in Fig. 7 and 8. (The $\phi = o$ direction generally has the highest stress). The stress curves are safely separated from the yield stress $\sigma_F(T)$.

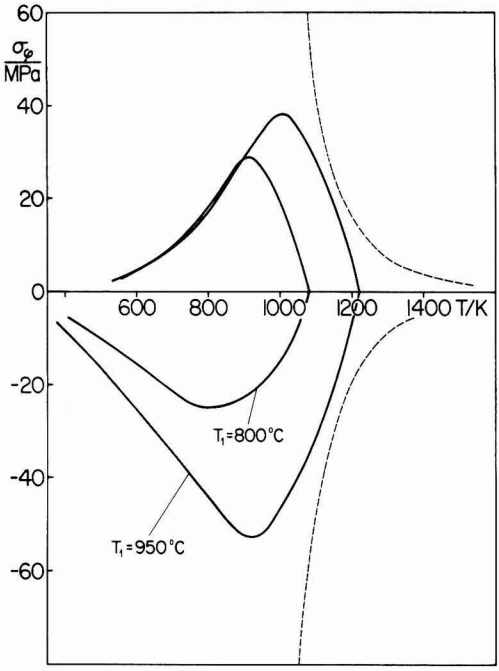

Fig. 9. Maximum tangential stress under ϕ = 0 (bottom) as a function of local absolute temperature from two runs with 500 mm/min insertion/withdrawal speed and furnace temperatures of 800° and 950°C, respectively. Dashed lines indicate the expected yield stress, calculated from PCSH data.

Results and Discussion

Plots like Fig. 7 and 8 allow us to discuss the occurrence of plastic deformation (slip) under given processing parameters. If the curves of the actual stress $\sigma_\phi(T)$ and the yield stress $\sigma_F(T)$ intersect, then slip is likely to occur. Similar plots were drawn for all the other conditions investigated and listed in Table II.

For a furnace temperature of 1150°C, the stresses always rise beyond yield stress, with the exception of the slowest insertion/withdrawal speed of 50 mm/min, where the yield stress curve just touches $\sigma_\phi(T)$ in one point. For 1050°C furnace temperature, the case shown in Fig. 7 and 8, the situation is similar. It is only for temperatures below 1050°C that the curves do not cross and the thermal stresses remain below the yield stress (5). Two facts are worth noting: (*i*) When the insertion/withdrawal speed is lowered, also the strain rate decreases, and, if Eq. [19] is assumed to be valid, the yield stress at a fixed temperature becomes smaller. This partially compensates the lower stresses obtained with smaller speeds. (*ii*) It does not help to consider only the maximum stresses occurring. Since the yield stress varies strongly with temperature, the critical phase is reached somewhere between maximum stress and zero stress at thermal equilibrium at the furnace temperature.

In order to verify these statements experimentally, several sample wafers were taken from some selected runs and tested for slip. Strong plastic deformations can be seen, even before etching, by a fine line pattern at the polished surface and by the resulting strong warping. More sensitive is visual inspection under the microscope after chemical etching for dislocations. Wafers subjected to furnace temperatures of 1150°C show strong slip patterns for 500 mm/min withdrawal speed and slightly weaker and shorter ones for 100 mm/min. Samples heated up to 1050°C showed weaker slip marks for 500 mm/min, and none for 100 mm/min. No slip occurred for lower furnace temperatures.

Comparing these observations with the theoretical predictions, we can locate the critical yield stress between the two curves marked K and PCSH in Fig. 7 and 8. We have not observed any significant difference between wafers with different initial oxygen content ($x(O_i)$ = 14 and 20 ppm). Of course, more data points in $x(O_i)$ would be needed for a detailed study of the influence of interstitial oxygen.

We also compared the calculated maximum stresses with the measured maximum temperature differences ΔT periphery/center and found a linear relationship to hold approximately

$$(\sigma_\phi/\Delta T)_{max} \approx 0.265 \text{ MPa/K}$$

for withdrawal, and

$$(\sigma_\phi/\Delta T)_{max} \approx 0.394 \text{ MPa/K}$$

for insertion. Evaluation of Hu's model (6) gives a similar relationship with a ratio of 0.465 MPa/K. This allows an estimate of the maximum stress from a simple tempera-

ture measurement at two points on the wafer. In order to decide whether slip is likely to occur, the curves from Fig. 7 and 8 have to be properly scaled between maximum stress and zero stress at furnace temperature.

Summary and Conclusions

We have measured the temperature distribution across 4 in. diameter silicon wafers for process temperatures between 800° and 1150°C and for insertion and withdrawal speeds between 50 and 500 mm/min. The temperatures were measured with 12 fine thermocouples on a wafer which was located in the middle of a stack of 20 wafers which were spaced 2.5 mm apart. Wafers placed adjacent to the thermocouple wafer were characterized for slip by etching and ultrasonic probing in order to correlate the results with calculated predictions. These wafers contained interstitial oxygen of 14 and 20 ppm; they were uniformly doped and no additional films such as SiO_2 or Si_3N_4 were present on the surface. All experiments were made with direct furnace insertion without applying a temperature ramping technique.

The results can be summarized as follows.

1. Before thermal equilibrium is reached, there is a nonuniform temperature distribution over the wafer. For the insertion process, the temperature rises nonlinearly from the center to the periphery; for the withdrawal process, the temperature distribution is inverted and the corresponding temperature differences are generally smaller. There exists a pronounced maximum in the absolute value of this temperature difference.

2. From the measured temperature distribution, one can calculate the stress field. The temperature difference between the center and the periphery of the wafer is a rough measure for the maximum tangential stress at the periphery. Simulating process conditions with small wafer separations (2.5 mm) and large wafer stacks (20), we find, in agreement with Kasper and Clauss (5), higher (compressive) stresses for the insertion process than for withdrawal. Similar conclusions can be drawn from work by Morizane and Gleim (4). Both authors studied in detail the heating and the cooling process, whereas Hu (6, 18) investigated the cooling cycle only.

3. The condition for slip to occur is that the thermal stress becomes larger than the yield stress valid for the temperature at the point in question. This means that thermoplastic deformation, if it occurs at all, does not take place at maximum stress but at a smaller stress value, corresponding to a temperature between the furnace temperature and the temperature of maximum stress.

4. A limit exists around 1000°C furnace temperature. For lower furnace temperatures, plastic deformation is safely avoided. For temperatures above 1000°C, slip occurs when insertion/withdrawal speeds of 100 mm/min or higher are used. Since the yield stress most probably decreases with decreasing insertion/withdrawal speed, the positive effect of a low speed is partially annihilated by this rate dependence. The latter statements show that the temperature ramping technique, which has been used in device fabrication for some time, is required when higher process temperatures are needed.

Acknowledgments

The authors would like to thank R. Fehlmann for writing the computer programs for the data collection and A. Oberholzer for experimental assistance. We have also benefited from P. Seitz and E. F. Steigmeier with data processing. We also thank G. Harbeke for critically reading the manuscript.

Manuscript submitted Feb. 3, 1986; revised manuscript received June 5, 1986.

Laboratories RCA Ltd., Zurich, assisted in meeting the publication costs of this article.

REFERENCES

1. B. Leroy and C. Plougenven, *This Journal*, **127,** 961 (1980).
2. D. Thebault and L. Jastrzebski, *RCA Rev.*, **41,** 592 (1980).
3. L. Jastrzebski, R. Soydan, B. Goldsmith, and J. T. McGinn, *This Journal*, **131,** 2944 (1984).
4. K. Morizane and P. S. Gleim, *J. Appl. Phys.*, **40,** 4104 (1969).
5. E. Kasper and H. Clauss, *Wiss. Ber. AEG-Telefunken*, **48,** 183 (1975).
6. S. M. Hu, *J. Appl. Phys.*, **40,** 4413 (1969).
7. Y. Yoriume, *This Journal*, **129,** 2076 (1982).
8. J. R. Patel, in "Semiconductor Silicon 1977," H. R. Huff and E. Sirtl, Editors, p. 521, The Electrochemical Society Softbound Proceedings Series, Princeton, NJ (1970).
9. S. M. Hu, *Appl. Phys. Lett.*, **31,** 53 (1977).
10. H. Shimizu, T. Watanabe, and Y. Kakui, *Jpn. J. Appl. Phys.*, **24,** 815 (1985).
11. M. Wright Jenkins, *This Journal*, **124,** 757 (1977).
12. W. Rehwald and A. Vonlanthen, *Semicond. Sci., Technol.*, 7 Nov. (1986). To be published.
13. S. P. Timoshenko and J. N. Goodier, in "Theory of Elasticity," 3rd ed., p. 31 and 441, McGraw Hill International, New York (1982).
14. J. R. Patel and A. R. Chaudhuri, *J. Appl. Phys.*, **34,** 2788 (1963).
15. I. Yonenaga and K. Sumino, *Phys. Status Solidi A*, **50,** 685 (1978).
16. H. Siethoff and P. Haasen, in "Lattice Defects in Semiconductors," R. R. Hasiguti, Editor, p. 491, University of Tokyo Press, Tokyo (1968).
17. Y. Kondo, in "Semiconductor Silicon 1981," H. R. Huff, R. J. Kriegler, and Y. Takeishi, Editors, p. 220, The Electrochemical Society Softbound Proceedings Series, Pennington, NJ (1981).
18. S. M. Hu, *Appl. Phys. Lett.*, **22,** 261 (1973).

Stability of Molten Carbonate Fuel Cell Nickel Anodes

C. D. Iacovangelo*

General Electric Company, Schenectady, New York 12301

ABSTRACT

The effectiveness of three methods of stabilizing nickel anodes in molten carbonate fuel cell (MCFC) operating environments was examined. Alloying with chromium was effective in retarding sintering at levels as low as 1 weight percent (w/o) chromium. The mechanism of stabilization, however, involved the formation of oxide films which dramatically altered electrode morphology. Dispersion of refractory oxides, *e.g.*, Al_2O_3, was effective in stabilizing anode structures at loadings of 1 volume percent. The most promising method of stabilizing the electrode structure was found to be "electroless" plating of Ni and/or Cu onto refractory oxides of Al_2O_3, $SrTiO_3$, and $LiAlO_2$. This approach stabilized the structure, while providing optimum flexibility in electrode morphology design.

State-of-the-art (SOA) anodes for molten carbonate fuel cells (MCFC) are porous Ni plaques having porosities of 60-70% and 4-6 μm median pore diameters. Typically, chromium is added to these plaques to stabilize the nickel against sintering at the cell operating temperature of ~923 K (~650°C) (1-3). Sintering occurs in a porous body in an attempt to lower surface energy by diffusion of material to regions of small radii of curvature. This process tends to reduce the number of small diameter pores and to lower the overall porosity. Various stages of sintering exist from minor surface diffusion altering pore shape and size to bulk transport of material from the core of particles causing severe densification (4). The purpose of this study was to investigate three methods of slowing down these transport processes in order to retain the original high open porosity and tailored pore size distribution.

The first method employed was the addition of chromium to the nickel plaque. Although the use of this technique has been widespread by the fuel cell community (1-3), there exists a scarcity of information in the open literature on the mechanism of stabilization or on the optimum chromium content. Alternatives to chromium have been explored. For example, Johnson (4) and his coworkers (5) have studied the effect of surface dispersed refractory oxides on retarding the sintering of Ni and Cu sinusoids. Studies conducted at Energy Research Corporation (6) have suggested relatively stable cell performance using porous Ni structures impregnated with $LiAlO_2$.

Each of the above methods involves additions of a second substance to nickel powder. A novel method to stabilize the anode structure: electroless plating of Ni and/or Cu onto refractory oxides, *e.g.*, Al_2O_3, $LiAlO_2$, and $SrTiO_3$ was also evaluated. In this approach, refractory oxides were used as the core and metallic skins were applied. These powders were then sintered into a porous plaque, achieving an initial morphology similar to the previous approaches. In this paper, the viability of each method was explored by examining the effect of additive content [Cr 1-10 weight percent (w/o) Al_2O_3 1-20 volume percent (v/o)], additive particle size, and fabrication temperature on the degree of sintering, *i.e.*, the change in pore size distribution and total open porosity.

Experimental

Out-of-cell sintering studies were conducted at 923 K within a dense alumina tube (Fig. 1). The temperature was maintained to ±1°C with a Love[R] controller using a Chromel-Alumel thermocouple and monitored with a separate Chromel-Alumel thermocouple positioned in the center of the samples. A gas mixture of 34% H_2, 24% CO_2, 42% N_2 was used to simulate a typical fuel cell anode operating environment. The gas flowed past the samples at 10 ml/min. A stainless steel screen was used to separate the samples and to provide a catalyst for the fuel gas shift reactions. At 923 K the shifted gas composition is 0.2204 H_2, 0.1204 CO_2, 0.1196 H_2O, 0.1196 CO, with the balance N_2. The suitability of the screen as a catalyst was checked by gas chromatographic analysis of the exit gas and was found to be adequate for the flow rates used. Sample sizes were standardized at 1 × 2 × 0.075 cm. Sample plaques were examined after sintering 150, 450, 750, 1,000, 2,000, 3,000, 4,000, 5,000, and 6,000h. Porosity and pore size distributions were measured with an Aminco no. 5-7121B porosimeter; pressure ranged from 6.67 × 10^{-5} to 1,034 bar. Measurements taken at 150, 450, 750, 1,000, and 2,000h were on separate samples from the same larger plaque. Data collected at 3000, 4000, 5000, and 6000h were for a single sample which was reintroduced to the furnace to collect additional time.

Out-of-cell sintering tests were conducted with two series of samples. In the first study, 12 different samples were examined. The composition of each sample is shown in Table I. Samples no. 1-7 and no. 10 were fabricated from Inco Type 255[R] carbonyl-nickel powder which has a chain-like morphology with a 2.6-3.4 μm median particle size (7, 8). Samples no. 2-6 had 400 mesh (38 μm) Cr powder. Sample no. 7 had 2 μm average particle size Cr powder. In samples no. 2-7 and no. 10, the Ni and additive powders, either Cr or Al_2O_3, were blended by ball milling for 1h using Al_2O_3 balls. The Nichrome powder, sample no. 9, was purchased from Atlantic Equipment Engineers. Samples no. 11 and 12 were prepared inhouse by electroless plating of Ni and Cu onto the ceramic substrate. The method of preparing these powders has been described previously (9-12). Except for sample no. 8, the 12 plaques were prepared by doctor-blading the pre-blended powders on graphite plates using Grafoil[R] shims to adjust the thickness of the plaque.

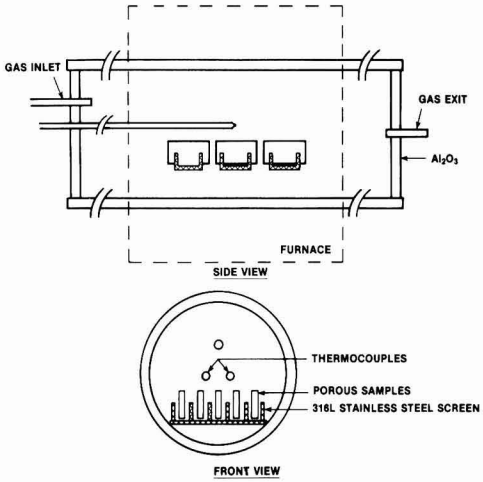

Fig. 1. Apparatus employed in out-of-cell sintering studies

* Electrochemical Society Active Member.

Table I. Sample descriptions

Sample no.	Composition (w/o)	Temp.	Plaque preparation time	Environment
1	100 Ni 255[a]	900°C	15 min	10% H_2/Ar
2	99 Ni 255-1 Cr[b]	900°C	15 min	10% H_2/Ar
3	97 Ni 255-3 Cr[b]	900°C	15 min	10% H_2/Ar
4	95 Ni 255-5 Cr[b]	900°C	15 min	10% H_2/Ar
5	93 Ni 255-7 Cr[b]	900°C	15 min	10% H_2/Ar
6	90 Ni 255-10 Cr[b]	900°C	15 min	10% H_2/Ar
7	90 Ni 255-10 Cr[c]	1000°C	15 min	10% H_2/Ar
8	90 Ni-10 Cr[d]	—	—	—
9	80 Ni-20 Cr[e]	1000°C	1h	10% H_2/Ar
10	90 Ni 255-10 Al_2O_3	1000°C	15 min	10% H_2/Ar
11	75 Cu 25 $SrTiO_3$	1000°C	15 min	10% H_2/Ar
12	75 Ni 12.5 $SrTiO_3$, 12.5 Al_2O_3	1000°C	15 min	10% H_2/Ar

[a] INCO carbonyl nickel Type 255.
[b] Cr powder purchased from R.O.C./R.I.C. 400-mesh.
[c] Cr powder purchased from Alfa Products, 2 μm median particle size.
[d] Purchased from Gould in plaque form.
[e] Nichrome powder from Atlantic Equipment Engrg., 10-30 μm.

The powder was then fired in a 10% H_2 balance Ar atmosphere with a moisture content of ≤5 ppm H_2O to prevent oxidation of Cr during fabrication. The fabrication temperature and time are shown in Table I. Sample no. 8 was a SOA plaque purchased from Gould.

In the second series of tests, four Ni-Cr plaques were prepared having 1, 3, 5, and 7 w/o Cr. All plaques were prepared with 2 μm particle size Cr powder and sintered at 1273 K for 15 min. In addition, two plaques were fabricated with 1 and 5 v/o Al_2O_3 for comparison with the much higher level tested in the first test series. Also, a Ni-Cu plated $SrTiO_3$ plaque was prepared from electroless plated powders. The pivotal differences between this plaque and the two electroless plated-plaques examined in the first series were a longer initial sintering time (1273 K for 1h) and the use of a Ni-Cu alloy instead of Ni or Cu. This alloy was found to provide a stronger and more developed sintered structure than either Ni or Cu alone (11, 12).

For comparison with out-of-cell sintering results, selected SOA Ni-10% Cr Gould anodes and metal plated $SrTiO_3$ plaques were examined from in-cell tests. These plaques were tested at 923 K, 50-75% utilization of H_2 in the 34% H_2, 24% CO_2, 42% N_2 fuel, and in contact with a 62 mole percent (m/o) Li_2CO_3:38 m/o K_2CO_3 electrolyte. Cells were operated at 0.68V and current densities of 120-160 mA/cm². After cell testing, the carbonate eutectic was washed from the porous plaque using a buffered acetic acid solution under a vacuum of 6.67×10^{-5} bar.

In addition to porosity and pore size analysis of all samples, selected samples were periodically examined for compositional and morphological changes. These studies were done with an International Scientific Instruments Super IIIA and 40 scanning electron microscope equipped with an EDS x-ray unit. An x-ray diffractometer was also used to examine compositional changes.

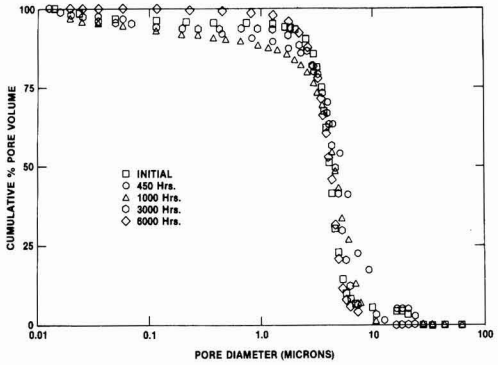

Fig. 2. Pore distribution of a Ni-10 Cr plaque (sample no. 6) as a function of time on test at 650°C in a standard fuel environment: 34% H_2, 24% CO_2, 42% N_2.

Results and Discussion

The total porosity and median pore size are shown in Tables II and III for each sample after the stated times at 923 K. The median pore size was calculated from Hg-intrusion porosimetry using the Washburn (13) relationship

$$Pr = 2\gamma \cos\theta \quad [1]$$

where P is the pressure, r the pore radius, γ the surface tension of mercury, and θ the contact angle of mercury with nickel. In our calculations, we used values for γ and θ of 473 dynes/cm and 130°, respectively, as determined by Winslow and Shapiro (14). This reduces Eq. [2] to the working formula

$$D = \frac{2538}{P} \quad [2]$$

where D is the pore diameter in micrometers and P is the absolute pressure in bars. The porosity of the sample was calculated from the volume of Hg forced into the sample under pressure. This volume was corrected for the compressibility of Hg using a value of 0.39×10^{-11} cm²/dyne. Repeated testing of a single sample revealed a variation of ±0.2% porosity. Testing of different locations of a larger plaque showed variation of ±0.5%.

Table II shows that a pure Ni plaque, sample no. 1, undergoes a considerable loss of porosity, from 80 to 14%, by sintering for 6000h. This change is not tolerable for MCFC's which must last 40,000h. These results empha-

Table II. Porosity of sintered samples (% porosity) time (hours)

	Sample	0	150	450	750	1,000	2,000	3,000	4,000	5,000	6,000
1	Ni-0 Cr	80	75	71	—	59	47	20	27	31	14
2	Ni-1 Cr	76	74	74	74	71	72	69	67	66	66
3	Ni-3 Cr	78	78	77	75	76	76	75	76	75	75
4	Ni-5 Cr	75	73	71	70	70	70	70	71	72	70
5	Ni-7 Cr	72	70	69	70	69	70	74	73	73	73
6	Ni-10 Cr	65	65	63	64	66	64	61	64	62	61
7	Ni-10 Cr (2 μm)	72	—	73	72	73	70	72	72	71	72
8	Gould Ni-10 Cr	67	—	67	55	53	54	54	56	55	54
9	Nichrome (20 Cr)	62	—	56	57	57	55	58	56	56	56
10	Ni-10 Al_2O_3	75	—	76	75	75	73	75	73	72	73
11	Cu-plated $SrTiO_3$	72	—	65	62	63	60	64	62	63	62
12	Ni-plated $SrTiO_3$, Al_2O_3	74	—	70	72	71	73	69	69	71	69
13	Cell 81-36	65	—	—	59	—	—	—	—	—	—
14	Cell 81-3	68	—	63	—	—	—	—	—	—	—
15	Cell 81-7	68	—	—	—	—	66	—	—	—	—

Table III. Median pore size (μm) time (hours)

	Sample	0	150	450	750	1,000	2,000	3,000	4,000	5,000	6,000
1	Ni	4.9	5.4	5.8	5.8	6.1	4.0	5.5	4.8	5.1	4.0
2	Ni-1 Cr	4.8	5.3	5.6	7.2	6.0	5.7	7.4	6.8	6.4	6.1
3	Ni-3 Cr	5.2	5.8	5.5	6.2	7.0	5.3	7.5	6.5	6.3	6.1
4	Ni-5 Cr	4.7	6.1	5.2	6.0	7.0	5.2	6.1	5.7	5.4	5.2
5	Ni-7 Cr	5.7	6.0	5.2	5.2	5.2	4.9	6.6	6.0	5.8	5.6
6	Ni-10 Cr	4.1	4.5	5.4	4.0	4.5	3.8	4.6	4.3	4.0	4.2
7	Ni-10 Cr (2 μm)	5.0	—	5.0	4.0	5.0	4.8	5.7	5.6	5.2	5.2
8	Gould Ni-10 Cr	4.2	5.3	4.3	2.5	2.7	2.7	3.4	3.0	3.0	3.2
9	Nichrome (20 Cr)	12.8	—	8.9	6.7	9.0	8.8	10.0	7.9	8.4	8.3
10	Ni-10 Al_2O_3	6.3	—	6.0	4.8	6.2	4.7	7.7	6.8	6.4	6.5
11	Cu-plated $SrTiO_3$	5.0	—	3.6	2.8	3.6	3.6	3.4	3.3	2.9	2.8
12	Ni-plated $SrTiO_3$, Al_2O_3	3.2	—	2.6	2.5	2.8	3.0	2.9	2.8	2.9	2.9
13	Cell 81-36	4.2	—	—	2.3	—	—	—	—	—	—
14	Cell 81-3	4.2	—	2.1	—	—	—	—	—	—	—
15	Cell 81-7	4.5	—	—	—	—	2.9	—	—	—	—

size the need for a method to stabilize the porous nickel structure.

The first method studied for stabilizing a porous nickel structure, the addition of Cr, is represented in Tables I-III by samples no. 2-8. As can be seen, Cr additions as low as 3 w/o, sample no. 3, were successful in greatly retarding loss of porosity. This sample maintained 75% open porosity through 6000h on-test. Sample no. 2, containing 1 w/o Cr, substantially reduced the loss of porosity, although appreciable sintering did occur. Table II shows the variations of median pore size accompanying the observed decreases in porosity. Although as little as 3 w/o Cr did stabilize the Ni structure against a large drop in porosity, continual altering of the median pore size occurred at all levels of Cr. In an operating fuel cell, where location of gas and electrolyte are controlled by pore size distributions among the various components, substantial change in the pore size distribution is unacceptable. Such a change in pore size distribution with time is shown in Fig. 2 for sample no. 6 (10 w/o Cr), which was the most stable of the 38 μm Cr containing plaques. In contrast, the Gould plaque, sample no. 8, Fig. 3, demonstrated an initial drop in median pore size over the first 750h but was quite stable after that. Each sample revealed a total loss of small pores indicating a significant degree of sintering (diffusion of metal to the smallest radii of curvature) not evidenced by loss in mean porosity.

Although incorporation of 400-mesh Cr (samples no. 2-6) into nickel plaques greatly retarded the loss of porosity, Table II shows that it did so at the expense of a reduction of the initial porosity from 80 to 64% and a reduction of the median pore size from 5 to 4 μm. These disadvantages were overcome by incorporating 2 μm particle size chromium powder and raising the fabrication temperature to 1273 K (sample no. 7). As shown in Fig. 4, this plaque maintained a porosity ≥70% and a median pore size of 5 μm. In order to help understand the mechanism for Cr stabilization, the evolution of the structure was examined in a series of samples with scanning electron microscope. Figure 5 shows the structure of two Ni-10 Cr plaques, samples no. 6 and no. 8, prior to sintering. Both exhibit smooth, well-necked structures. As can be seen, there are areas where the Cr and Ni did not alloy during fabrication. Cr particles were

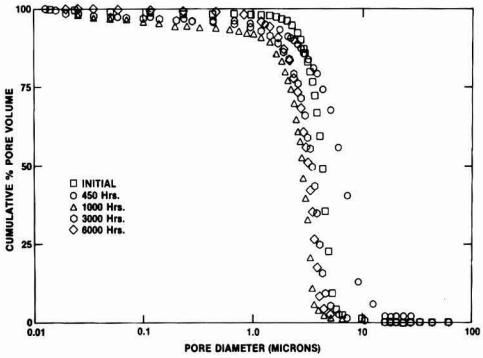

Fig. 3. Pore distribution of a Gould Ni-10 Cr plaque (sample no. 8) as a function of time on test at 650°C in a standard fuel environment: 34% H_2, 24% CO_2, 42% N_2.

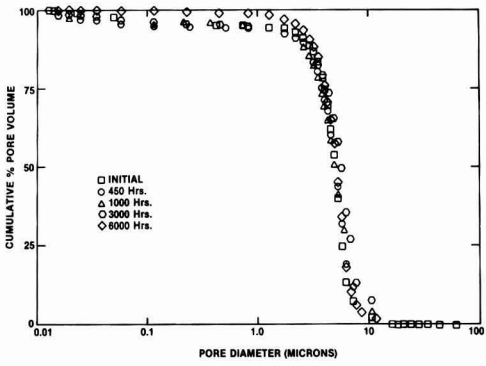

Fig. 4. Pore distribution of a Ni-10 Cr (2μ) plaque (sample no. 7) as a function of time on test at 650°C in a standard fuel environment: 34% H_2, 24% CO_2, 42% N_2.

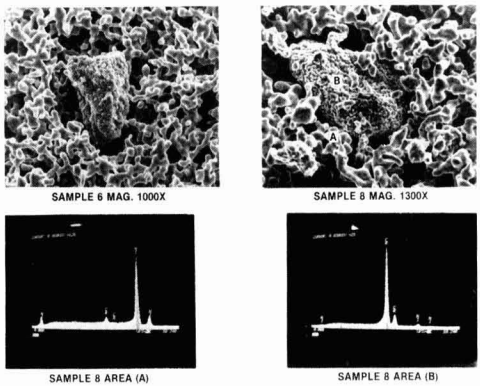

Fig. 5. SEM's and EDS of two Ni-10Cr plaques as fabricated. Top left—sample no. 6, top right—sample no. 8, bottom left—area (A) of sample no. 8, bottom right—area (B) of sample no. 8.

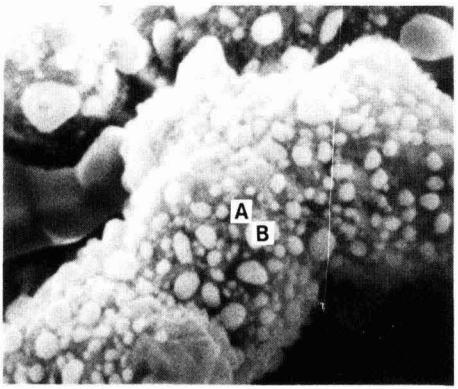

SAMPLE 8, 1000 Hrs., MAG. 9300X

Fig. 6. SEM and EDS of a Gould Ni-10 Cr plaque (sample no. 8) after 1,000h on test. Bottom left—spectra of strand surface, bottom right—spectra of metal rich nodule.

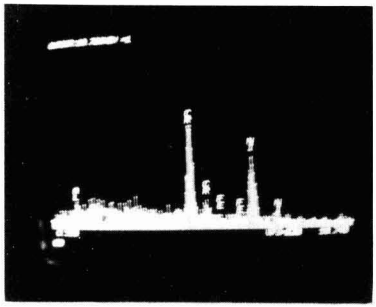

STRAND SURFACE AREA (A)

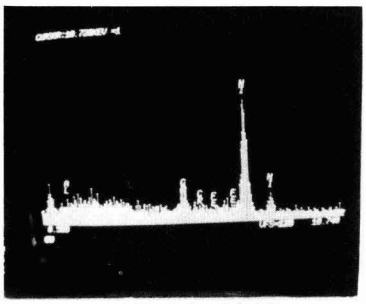

NODULE AREA (B)

visible in all the 400-mesh (38 μm) Cr containing plaques, as well as the two shown here, but not in samples which used 2 μm Cr at 1273 K fabrication temperature. The dissolution of Cr was due in part to the smaller size of the Cr powder and to the increase in diffusivity of Cr into Ni. At 1173 K, the diffusivity of Cr in Ni is 2.15×10^{-12} cm²/s, and at 1000°C it is 1.7×10^{-11} cm²/s (15). Assuming diffusion of Cr into a 2 μm Ni particle as the rate-determining step, 15 min at 1173 K would not be sufficient to completely alloy the Ni and Cr, whereas 15 min at 1273 K would be sufficient.

After exposure at 923 K in fuel gas, the morphology of the Ni-Cr plaques was greatly altered. In this environment, $P_{O_2} \cong 10^{-23}$ bar, chromium is readily oxidized Ni is stable. As the Cr in the Ni-Cr alloy oxidizes, but Ni-rich nodules are extruded out of the surface of the strands, as shown in Fig. 6 (sample no. 8) after 1000h. This morphology is even more evident in sample no. 9 which was fabricated from a Ni-20 Cr Nichrome powder. This sample is shown in Fig. 7 for 450 and 6000h on-test. This structure is in agreement with results reported by Mazandarany *et al.* (16, 17), who proposed a mechanism involving Cr oxidation initiating at nucleation sites. As the Cr diffuses from adjacent areas to support further oxidation, it leaves Ni-rich areas which do not oxidize in low P_{O_2} environments. The chromium oxide on the surface thus retards Ni metal surface diffusion and loss of pore size and porosity. The better alloying of sample no. 7, therefore, resulted in a more uniform dispersion of oxide on the nickel strands and a greater retarding of nickel transport.

Samples no. 13, 14, and 15 were Gould Ni-10% Cr plaques, which were run in operating cells. These samples were examined to determine if sintering of these structures was affected by the presence of the carbonate melt. Table III shows that, like that for the out-of-cell samples, the median pore size dropped from 4 to 2-3 μm. Figure 8 shows, however, that a broadening of the pore size distribution occurred rather than the narrowing typically seen in gas phase sintering. The presence of a large number of small pores accounts for the smaller drop in porosity shown in Table II.

A SEM micrograph of sample no. 15 after 2000h on test is shown in Fig. 9. Although the overall structure is very similar to the out-of-cell samples, the composition and morphology of the oxide skin are different. The composition of the out-of-cell oxide, as determined by x-ray diffraction, was a mixture of CrO and Cr_2O_3, with Cr_2O_3 being the predominant phase. The oxide formed in the cell was $LiCrO_2$. It would appear from Fig. 6, 7, and 9 that the Cr_2O_3 skin formed in the absence of lithium from the electrolyte is very tight; therefore, as it grows it decreases the void volume of the sample. The $LiCrO_2$ formed in-cell, however, was a voluminous structure having many small pores.

The formation of these small pores has a marked effect on fuel cell operation and electrolyte management. For example, the small pores draw electrolyte from the pores in the electrolyte structure, which are typically 0.8 μm (18). In addition, control of other electrode functions, *e.g.*, electrolyte storage and bubble-pressure barriers, becomes exceedingly difficult. Wilemski (19), in his modeling of fuel cell anode performance, projected an electrolyte film thickness of ~1 μm even though the formation of such a thick film on metallic nickel with a wetting angle of ~70° (20) could not be justified. The success of his model indicates that the surface of the anode is not metallic Ni, but is a porous oxide, which has a 0° wetting angle and which fills with electrolyte providing a thick film coverage.

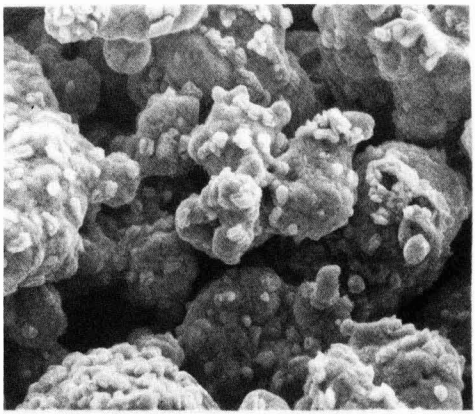

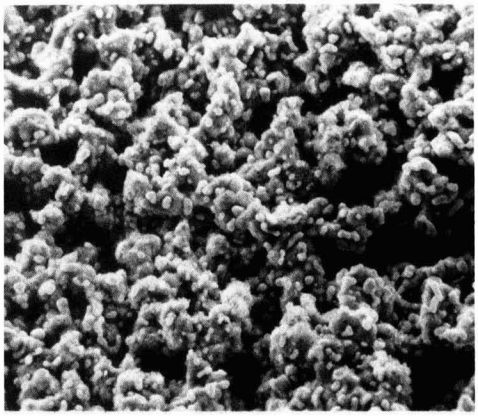

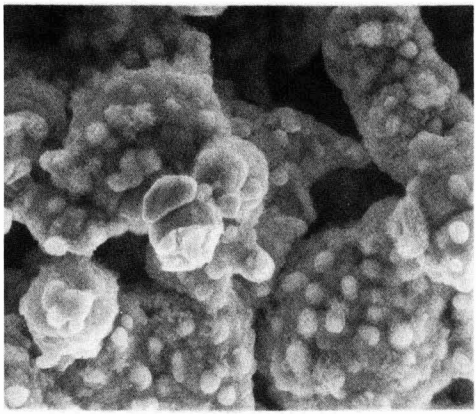

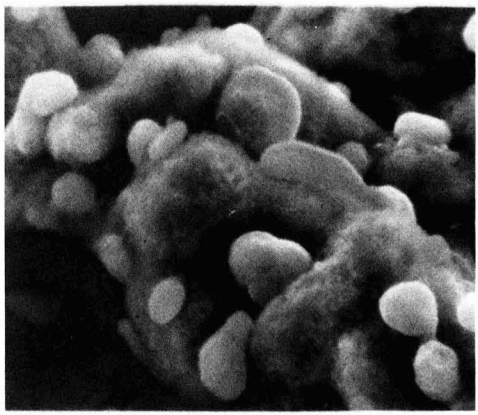

Fig. 7. SEM of a Nichrome Ni-20 Cr plaque (sample no. 9) after 450h (top) and 6,000h (bottom) on test.

Fig. 9.SEM of a Gould Ni-10 Cr plaque (sample no. 15) after 2,000h of in-cell testing.

Sample no. 10 represents the behavior of a dispersed oxide in retarding loss of porosity. Johnson (4) has demonstrated that the presence of surface oxides, *e.g.*, MgO and Al_2O_3, were effective in retarding the sintering of Ni sinusoids by "pinning" the surface to prevent metal surface diffusion. This sample was very stable, showing a trivial drop in porosity from 75 to 73% over 6000h. Although some scatter was observed in the pore size distribution, the morphology was essentially unchanged.

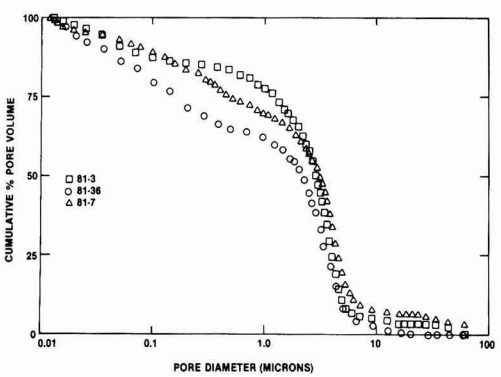

Fig. 8. Pore distributions of three in-cell tested Gould anodes after 450-2,000h on test.

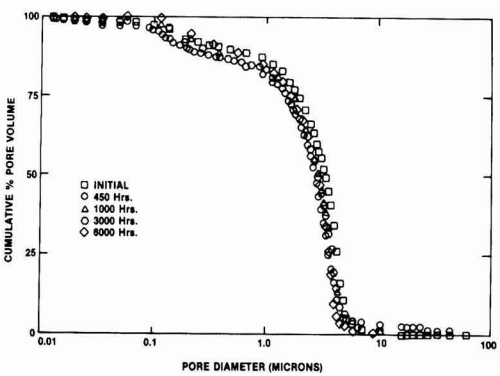

Fig. 10. Pore distribution of a nickel-plated ceramic plaque (sample no. 12) as a function of time on test at 650°C in a standard fuel environment: 34% H_2, 24% CO_2, 42% N_2.

Table IV. Total porosity of sintering samples (% porosity) time (hours)

Sample	Initial	150	500	2,000
Ni-1 Cr (2 μm)	73	68	68	68
Ni-3 Cr (2 μm)	74	74	75	74
Ni-5 Cr (2 μm)	75	77	77	78
Ni-7 Cr (2 μm)	72	74	74	75
Ni-1 Al_2O_3	77	73	74	74
Ni-5 Al_2O_3	74	73	73	71
Ni/Cu-$SrTiO_3$	63	62	62	63

Table V. Median pore size of sintering samples (μm) time (hours)

Sample	Initial	150	500	2,000
Ni-1 Cr (2 μm)	9.0	7.6	7.0	6.6
Ni-3 Cr (2 μm)	9.5	8.7	8.3	8.3
Ni-5 Cr (2 μm)	9.6	8.3	8.2	8.1
Ni-7 Cr (2 μm)	7.2	7.2	7.0	7.0
Ni-1 Al_2O_3	9.0	8.6	8.9	8.6
Ni-5 Al_2O_3	9.6	8.5	8.6	8.6
Ni/Cu-$SrTiO_3$	4.5	3.7	3.3	3.6

Samples no. 11 and 12 are examples of the third method of stabilizing a metal plaque, *i.e.*, plating a ceramic particle with a metal. The Cu-plated-plaque, sample no. 11, showed an initial collapse in porosity and pore size but was stable from ~450 through 6000h. The Ni-plated-plaque, sample no. 12, shown in Fig. 10, also exhibited an initial drop in porosity from 74 to 70% but demonstrated excellent stability over the remainder of the 6000h. Figure 10 demonstrates the excellent retention of pore size distribution. Unlike the Ni-Cr samples, which lost small pores, this sample retained the small pores. In addition, SEM analysis revealed no oxidation or morphological change in the structure.

Based on the improved performance of samples no. 7, 10, 11, and 12, a second series of tests was conducted. The results of this study through the 2000h of testing are shown in Tables IV and V, which list the total porosity and median pore size of each sample. The properties of the Ni-Cr (2 μm) samples were essentially unchanged from the Ni-Cr (38 μm) samples with the exception of the lack of small pores owing to oxidation of the unalloyed Cr particles. The Ni-Cr (2 μm) series demonstrated very high stability against sintering. The 1 w/o Cr sample (Fig. 11) did exhibit an initial drop in porosity and median pore size during the first 150h from 73 to 68% and 9.0 to 7.6 μm, but then remained unchanged. The remaining Ni-Cr samples (3, 5, and 7% Cr), were essentially unchanged in porosity and demonstrated slight decreases in pore size. Figure 12, for example, shows the slight decrease in pore size for the 3 w/o Cr sample.

The two plaques prepared from Ni powder and a lower level of 1 and 5 v/o Al_2O_3 demonstrated excellent resistance to sintering, maintaining 70% porosity with little change in pore size distribution. Figure 13 shows the pore size distribution for the 5 v/o Al_2O_3 plaque. The Ni-Cu plated $SrTiO_3$ plaque, Fig. 14, did undergo an initial collapse in pore size during the first 500h on test, but then remained stable and the small pores were not lost. No observable change in porosity was detected.

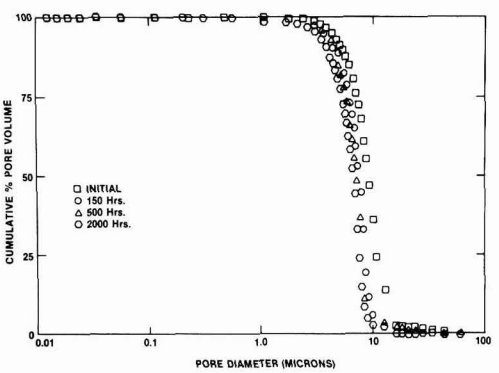

Fig. 11. Pore distribution of a Ni-1 Cr plaque as a function of time at 650°C.

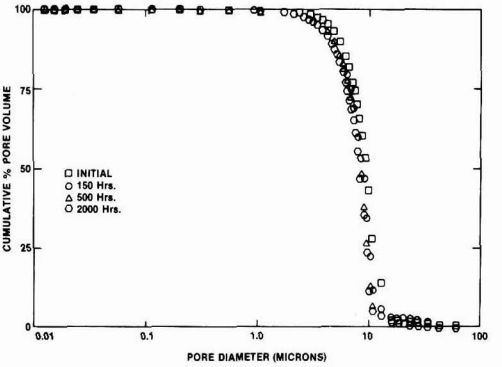

Fig. 12. Pore distribution of a Ni-3 Cr plaque as a function of time at 650°C.

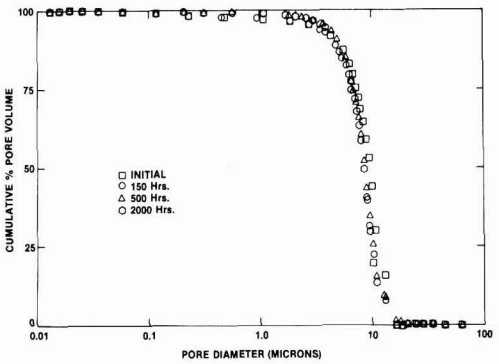

Fig. 13. Pore distribution of a Ni-5 Al_2O_3 plaque as a function of time on test at 650°C.

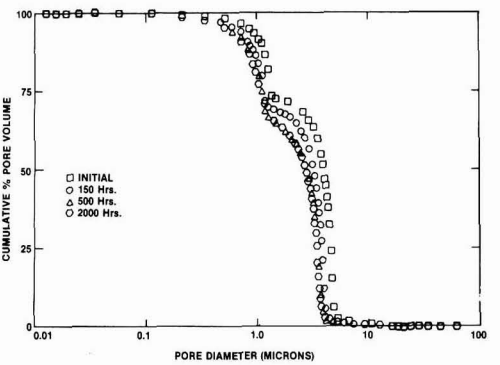

Fig. 14. Pore distribution of a Ni and Cu plated $SrTiO_3$ plaque as a function of time on test at 650°C.

Conclusions

This study has examined three methods of stabilizing a porous nickel structure against sintering at 923 K in reducing environments. Each technique stabilizes the structure by a different mechanism. Addition of Cr

forms a protective oxide skin, whose composition and morphology is a function of the environment in which it is grown. In the presence of a carbonate melt, the skin that forms is $LiCrO_2$. Associated with this reaction is the creation of small pores ≤ 1 μm, which drains electrolyte from the electrolyte matrix. Both the dispersion of Al_2O_3 within the nickel plaque and metal plated ceramic particles stabilize the structure without causing morphological changes. Structures formed from metal plated ceramic particles showed the unique capability of retaining small pores within a bi-modal pore size distribution. The useful application of each of these structures in a MCFC electrode also depends on other factors; electrode kinetics, electrolyte wetting and inventory control, creep, flexibility of pore size distribution, and cost.

Acknowledgments

The author wishes to express his appreciation to The United States Department of Energy for support of this work under Contract DE-AC-02-80ET17019 and to K. P. Zarnoch for his assistance throughout this study. The author also wishes to acknowledge his colleagues at CRD for their valued interactions, especially E. C. Hayes and E. C. Jerabek for their help in conducting cell tests.

Manuscript submitted Oct. 15, 1985; revised manuscript received April 17, 1986.

General Electric Company assisted in meeting the publication costs of this article.

REFERENCES

1. United Technologies Corp., Contract DE-AC-01-79ET15440, FCR-4267 (April 1982).
2. Energy Research Corp., Final Report, DOE/ET/11304-19, (February-December 1980).
3. Institute of Gas Technology, Contract no. EC-78-C-03-1735, SAN-1735-3 (June 1978).
4. D. L. Johnson, EPRI, EM-624 Project 371-1 (March 1978).
5. E. M. Perry, Master Thesis, Northwestern University, IL (August 1982).
6. Energy Research Corp., DOE/ET/11304-29 (Sept. 1983).
7. V. A. Tracy and A. J. Williams, *Electrochem. Technol.*, (Jan.-Feb. 1965).
8. V. A. Tracy, The International Nickel Company, Publication 2M-10-80 (15C 11-79) (1979).
9. C. D. Iacovangelo, U.S. Patent 4,361,631 (1982).
10. C. D. Iacovangelo, U.S. Patent 4,386,960 (1983).
11. C. D. Iacovangelo, U.S. Patent 4,404,267 (1983).
12. C. D. Iacovangelo, U.S. Patent 4,423,122 (1983).
13. E. W. Washburn, *Proc. Nat. Acad. Sci.*, **7**, 115 (1921).
14. N. M. Winslow and J. J. Shapiro, *ASTM Bull.*, **236**, 39 (Feb. 1959).
15. C. J. Smithells, "Metals Reference Book," 5th ed., Butterworth Co., Ltd. (1976).
16. F. N. Mazandarany and P. C. Rittenhouse, General Atomic Project 9126, GA-A13553 (1975).
17. F. N. Mazandarany, USERDA Contract AT(04-3)-167 (1975).
18. C. D. Iacovangelo, *This Journal*, **133**, 280 (1986).
19. G. Wilemski, DOE Contract No. DE-AC-03-79ET11322 (August 1979).
20. P. Lessing and M. Johnston, Contract no. DE-AC03-77ET11320 (April 1981).

Dopant Redistribution During Prebake and Epitaxial Deposition

Hong H. Lee*

Department of Chemical Engineering, University of Florida, Gainesville, Florida 32611

ABSTRACT

The dopant profiles that result at the end of prebake are given in analytical form for both diffused (buried layer) and nondiffused regions. Because of the position dependence of the profile in the nondiffused region, a transport model is developed. The model is shown to describe the experimental results reported in the literature quite well both with respect to position and carrier gas velocity. The dopant profiles at the end of prebake, in turn, are used to obtain analytical solutions for the dopant redistribution in the course of epitaxial deposition following the prebake. The results obtained for both diffused and nondiffused regions in the presence of dopant in gas during the epitaxial deposition lead to relatively simple expressions for the final dopant profiles. A relatively simple expression for the final maximum lateral autodoping level is also given. A rather complete description of the dopant redistribution in the course of prebake and subsequent epitaxial deposition presented here should allow one to determine exactly how a change in any operating condition affects the final profiles, thereby enabling one to manipulate the operating conditions for the desired dopant profiles.

The distribution of dopant in semiconductor devices is the prime factor that determines the performance of the device fabricated for a certain purpose. Because of the importance of the distribution, numerous papers in the literature dealt with the distribution of dopant as affected by various processing steps. Although arcane procedures are followed to obtain sharp junctions, "diffused" distributions at the boundaries usually result due to thermal treatments, that have led to ion implantation methods. When buried layer structures are used as device elements, there is an additional problem of autodoping (1), which causes not only a diffused boundary (as opposed to a sharp boundary) between the epi- and buried layers but, more importantly, a significantly high dopant concentration peak at the epi-substrate (nondiffused) boundary due to lateral autodoping (2-4). Since the dopant distribution, and redistribution for the case of buried layer structures, encompasses almost all elements of the distribution problem, our efforts will be centered on the buried layer structures.

In the process of growing an epitaxial layer onto a substrate with a buried layer, the first step is to prebake the substrate so as to establish stabilized thermal and flow conditions. In this prebake, the dopant profile in the buried layer changes. Because of dopant evaporation taking place at the buried layer surface exposed to flowing gas, the dopant is carried away by the flowing gas and deposits onto the nondiffused substrate. This lateral autodoping was systematically studied by Srinivasan (4-5). The evaporation process at the buried layer surface has been studied as a mass-transfer process (6-8) between the dopant in the bulk fluid and that at the surface in equilibrium with the buried layer dopant concentration (4) at the surface. The lateral autodoping onto the nondiffused substrate is complicated by the fact that the dopant concentration in equilibrium with the surface concentration changes with position and flow conditions. This problem was also studied by Srinivasan (5) with an emphasis on the autodoping peak concentration. During the epitaxial deposition following the prebake, the dopant profiles in both buried and nondiffused regions change again. Because of the thermal diffusion taking place in the solid, the dopant profiles at the epi-substrate boundary become diffused.

It is clear from the above discussion that the final dopant profiles at the end of the epitaxial deposition will depend on many factors pertaining to the prebake and epitaxial deposition conditions. Although many studies

*Electrochemical Society Active Member.

on the subject have been carried out (1-12) and many important facts have been established as a result of these studies, it is still difficult to determine in a precise manner how a change in the operating (deposition) conditions affects the dopant profiles. The purpose of this paper is to provide the relationships for the dopant profiles, both at the end of prebake and at the end of epitaxial deposition in the form of analytical solutions for the profiles, so that the effect of any change can be clearly delineated. For this purpose, the dopant profiles that result at the end of prebake, both in the buried and nondiffused regions, are considered first. These results, in turn, provide the initial conditions for the dopant profiles at the end of epitaxial deposition.

Dopant Distributions during Prebake

Consider the dopant distribution resulting from preepitaxial bake. Consider in particular redistribution of dopant in the diffused buried layer region in the direction perpendicular to the surface, and the deposition of dopant on the nondiffused substrate, and its distribution in the substrate due to lateral autodoping (5). One dimensional conservation equation for the dopant in the buried layer and in the substrate right below the buried layer can be written as

$$\frac{\partial C}{\partial t} = D\frac{\partial^2 C}{\partial x^2} \qquad [1]$$

where C is the dopant concentration, x is the coordinate perpendicular to the solid surface, and D is the dopant diffusivity. The ideal initial dopant distribution in the buried layer is considered such that the initial condition is

$$C(x, o) = \begin{cases} C_o & 0 \le x \le L \\ 0 & x > L \end{cases} \qquad [2]$$

where L is the vertical depth of the buried layer. Because of the initial distribution, Eq. [1] is rewritten as follows

$$\begin{aligned} \frac{\partial C_1}{\partial t} &= D\frac{\partial^2 C_1}{\partial x^2} & 0 \le x \le L \\ \frac{\partial C_2}{\partial t} &= D\frac{\partial^2 C_2}{\partial x^2} & x > L \end{aligned} \qquad [3]$$

where C_1 is the concentration in the buried layer and C_2 is the concentration beyond the buried layer depth L. The coordinate system is chosen in such a way that $x = 0$ at the surface, as shown in Fig. 1. The dopant flux at the surface is equal to the rate of dopant mass transfer

$$D\frac{\partial C_1}{\partial x} = k_m(C_s - C_\infty) \qquad \text{at } x = 0 \qquad [4]$$

where C_s is the gas phase dopant concentration at the surface in equilibrium with the surface dopant concentration in the solid, ([*i.e.*, $C_1(o, t)$]), k_m is the mass-transfer coefficient, and C_∞ is the gas-phase dopant concentration in the bulk fluid, *i.e.*, outside the boundary layer above the substrate, which can be taken as zero for the prebake being considered. In accordance with the finding by Rai-Choudhury and Salkovitz (3), Henry's law is applied for the equilibrium relationship between C_s and $C_1(o, t)$

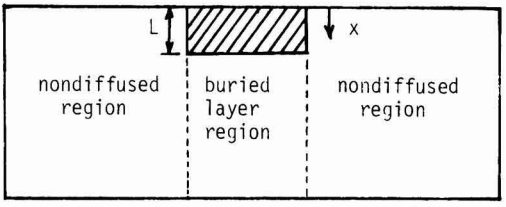

Fig. 1. Coordinate system for prebake period. Shaded area is the buried layer.

$$C_s = C_1(o, t)/K_e \qquad [5]$$

Thus, Eq. [4] becomes for $C_\infty = 0$

$$D\frac{\partial C_1}{\partial x} = \frac{k_m}{K_e}(C_1) \equiv (hC_1) \text{ at } x = 0;\ h = k_m/Hk_BT \qquad [6]$$

where h has been defined as k_m/K_e. One of the boundary conditions for C_2 follows from the fact that the dopant concentration is zero at some point far away from the buried layer

$$C_2 = 0 \qquad \text{for } x \to \infty \qquad [7]$$

The other two boundary conditions for C_1 and C_2 result from the continuity of both the dopant concentration and the flux at $x = L$

$$\begin{aligned} C_1 &= C_2 \\ \frac{\partial C_1}{\partial x} &= \frac{\partial C_2}{\partial x} \end{aligned} \qquad \text{at } x = L \qquad \text{for } t > 0 \qquad [8]$$

The method of Laplace transformation can be used to obtain the solutions of Eq. [2] through Eq. [8], which are

$$\frac{C_1}{C_0} = \frac{1}{2}\left[\operatorname{erfc}\left(\frac{L + x}{2\sqrt{Dt}}\right) - \operatorname{erfc}\left(\frac{L - x}{2\sqrt{Dt}}\right)\right] + \operatorname{erf}\left(\frac{x}{2\sqrt{Dt}}\right) + Y \qquad 0 \le x \le L \qquad [9]$$

$$\frac{C_2}{C_0} = \frac{1}{2}\left[\operatorname{erfc}\left(\frac{L + x}{2\sqrt{Dt}}\right) - \operatorname{erfc}\left(\frac{x - L}{2\sqrt{Dt}}\right)\right] - \operatorname{erf}\left(\frac{x}{2\sqrt{Dt}}\right) + Y \qquad [10]$$

where Y is given by

$$Y = \exp\left(\frac{hx + h^2t}{D}\right)\left[\operatorname{erfc}\left(\frac{x}{2\sqrt{Dt}} + h\sqrt{\frac{t}{D}}\right) - e^{hL/D}\operatorname{erfc}\left(\frac{x + L}{2\sqrt{Dt}} + h\sqrt{\frac{t}{D}}\right)\right] \qquad [11]$$

It is noted that Eq. [9] reduces to the well-known out-diffusion equation (*e.g.*, [9])for a uniform dopant distribution for $L = \infty$.

As will be shown later, one of the quantities of interest for the dopant distribution in the course of epitaxial deposition following the prebake is the surface dopant concentration at the end of prebake. This follows directly from Eq. [9] by setting $x = 0$

$$\frac{C_1}{C_0} = \exp\left(\frac{h^2t}{D}\right)\left[\operatorname{erfc}\left(h\sqrt{\frac{t}{D}}\right) - e^{hL/D}\operatorname{erfc}\left(\frac{L}{2\sqrt{Dt}} + h\sqrt{\frac{t}{D}}\right)\right] \qquad [12]$$

This is exactly the same expression as that obtained by Srinivasan (4) by Green's function approach.

Consider now the dopant deposition during the prebake due to lateral autodoping onto the nondiffused substrate. The dopant distribution in the nondiffused substrate, $C_n(x, t)$, is given by

$$\frac{\partial C_n}{\partial t} = D\frac{\partial^2 C_n}{\partial x^2} \qquad [13]$$

with

$$\begin{aligned} C_n(x, o) &= 0, & C_n(\infty, t) &= 0 \\ C_n(o, t) &= K_e\bar{C}_s(t); & K_e &= Hk_BT \end{aligned} \qquad [14]$$

The last boundary condition states that the dopant concentration at the surface of the nondiffused substrate is in equilibrium with the concentration of the gas phase dopant at the nondiffused solid surface, which is consistent with Henry's law applied for the diffusion in the buried layer region. In order to solve the problem posed, however, one has to know the gas phase surface concentration, $\bar{C}_s$. Only one basic case will be considered for $\bar{C}_s$, since others can be analyzed in the same manner.

Suppose that a substrate with a buried layer is placed in a horizontal reactor with a tilted susceptor, as shown in Fig. 2. Because of the difference in the way the gas phase dopant above the buried layer is transported, depending on whether the transport is in the direction of flow (downstream) or in the opposite direction (upstream), two separate coordinate systems are used, as shown in Fig. 2. It is apparent from the experimental work of Srinivasan (4) that the transport is not only by gas phase diffusion but also by weak convection due to the small velocity component in the boundary layer right above the surface. Thus, one can write the mass balance of dopant in the boundary layer as follows

$$-D_g\frac{d^2\bar{C}_s}{dz^2} + (\alpha U)_d\frac{d\bar{C}_s}{dz} + (k_m)_d\bar{C}_sW = 0 \qquad [15]$$

for downstream

$$-D_g\frac{d^2\bar{C}_s}{dz^2} - (\alpha U)_u\frac{d\bar{C}_s}{dz} + (k_m)_u\bar{C}_sW = 0 \qquad [16]$$

for upstream

where D_g is the gas phase molecular diffusivity of the dopant in a carrier gas, W is the length of the buried layer in the direction perpendicular to the flow, U is the bulk fluid velocity, and k_m is the mass-transfer coefficient. The subscripts d and u denote downstream and upstream, respectively. The second term in the above equations represents the weak convection due to the small velocity component u in z direction in the boundary layer, as shown in Fig. 2. In general, the z-directional velocity component u in the boundary layer can be written (14) as

$$\frac{u}{U} = f'(\eta); \qquad \eta = y\sqrt{\frac{U}{\nu z}} \qquad [17]$$

where ν is the kinematic viscosity, y is the coordinate perpendicular to z, and f' is the first derivative of f, which is the function resulting from the similarity transformation of the boundary layer momentum Ref. (14). Since the velocity that is of interest is that at a certain small distance away from the solid surface, one can rewrite Eq. [17] as

$$u = Uf'(\eta_f)$$

where η_f is the position at a given z. If the distance the dopant travels between buried layers is small, as in the case of monolithic integrated circuits, one may use a value of $f'(\eta_f)$ averaged over the small interval in z and can write

$$u = \alpha U; \qquad \alpha = [f'(\eta_f)]_{avg.} \qquad [18]$$

where α is a constant dependent on a given configuration. This result was used in writing the convection term in Eq. [15] and Eq. [16]. The last term in these equations represents the dopant transport away from the boundary layer to the bulk fluid. Since the dopant concentration is relatively very small in the bulk fluid ($C_\infty \approx 0$), the mass transfer rate, $k_mW(\bar{C}_s - C_\infty)$, reduces to $k_mW\bar{C}_s$. Here again, k_m is an average mass-transfer coefficient.

One important assumption made in writing the conservation Eq. [15] and [16] is the pseudo steady-state assumption of the gas phase concentration with respect to the change in the dopant concentration in the solid. Thus, no accumulation term (time derivative) appears in the equations. The justification for the assumption is that the solid phase diffusion is inherently a much slower process than the gas phase diffusion. One of the boundary conditions for Eq. [15] and [16] is that the gas phase concentration is at C_s at each end of the boundary layer, *i.e.* at $z = 0$ for both downstream and upstream cases

$$\bar{C}_s = C_2 \qquad \text{at } z = 0$$

For the case shown in Fig. 2, the concentration should approach zero far away from the buried layer

$$\bar{C}_s = 0 \qquad z \to \infty$$

Equations [15] and [16] can now be solved with the boundary conditions to give

$$\bar{C}_s(z;\,t) = C_s(t)\exp\left[-\left(\frac{\sqrt{(\alpha_dU)^2 + 4D_g(k_m)_d} - \alpha_dU}{2D_g}\right)z\right]$$

downstream [19]

$$\bar{C}_s(z;\,t) = C_s(t)\exp\left[-\left(\frac{\sqrt{(\alpha_uU)^2 + 4D_g(k_m)_u} - \alpha_uU}{2D_g}\right)z\right]$$

upstream [20]

where $C_s(t)$ is the pseudo steady-state gas phase concentration of the dopant in equilibrium with the dopant concentration (solid phase) at the buried layer surface.

Since the pseudo steady-state assumption for the gas phase concentration is also valid for the last boundary condition in Eq. [14], the solution of Eq. [13] can be written as

$$C_n(x,\,t;\,z) = K_n\bar{C}_s\,\text{erfc}\left(\frac{x}{2\sqrt{Dt}}\right) \qquad [21]$$

where $\bar{C}_s$ given by Eq. [19] has been treated to be constant for the integration on the basis of the pseudo steady-state assumption.

The dopant redistribution resulting from the prebake has been considered. The dopant profile in the buried layer region is given by Eq. [9] and [10]. The dopant profile in the nondiffused region is given by Eq. [21]. Because of the gas phase dopant transport leading to the lateral autodoping, the profile in the nondiffused region is dependent on the position in the direction of flow (downstream) or in the opposite direction (upstream). This dependence is given by Eq. [19] or [20]. All parameters involved are physical parameters that can be determined from independent experiments. The only uncertainty is with α, which is the uncertainty involved with the precise point above the solid surface at which the z-directional local velocity u should be evaluated. The dopant profiles at the end of prebake become the initial conditions for the redistribution of the dopant during epitaxial deposition, which is considered next.

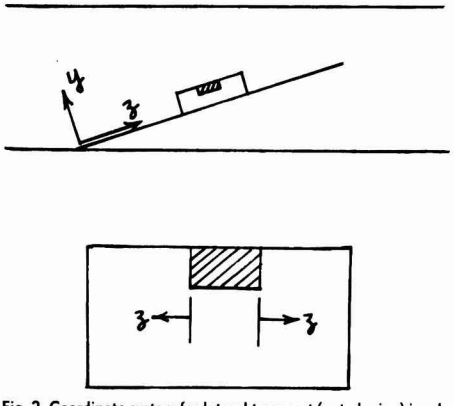

Fig. 2. Coordinate system for lateral transport (autodoping) in a horizontal reactor with susceptor tilting.

Dopant Distribution during Epitaxial Deposition

After the prebake during which thermal and gas flow conditions are stabilized, reactants and dopant are introduced to a reactor for epitaxial deposition. The dopant redistribution during the epitaxial deposition is distinctly different from that during the prebake in that the solid surface moves with time due to the deposition. This diffusion problem with a moving boundary, which is quite similar to the Stefan problem, has very often been formulated in the framework of the diffusion of impurities in molten metal (15), which contains a convection term in the conservation Eq. [1] with the velocity given by the growth rate. Although many papers refer to the work of Hulme (15) for the conservation equation with the convection term, the citations eventually lead to the work of Wilson (16), who considered the temperature of a moving medium that contains a heat source. The problem of Wilson cannot be analogous to the diffusion problem at hand since in the former, the medium moves, and, thus, the convection term is required whereas in the latter, the movement is only at the boundary and the dopant does not flow in the solid. Therefore, the correct problem formulation of Grove *et al.* (9) is used here.

Consider the deposition process in which the reactant and dopant concentrations in the carrier gas are constant. Consider, in particular, redistribution of dopant in the buried and nondiffused regions as the epitaxial growth takes place during the deposition. One-dimensional conservation equation is still that given by Eq. [1] for the buried layer region. In accordance with the coordinate system of Grove *et al.* (9), the x coordinate is negative in the direction of substrate, as shown in Fig. 3, which contrasts the coordinate system in Fig. 1. The boundary condition at the moving boundary is

$$-D\frac{\partial C}{\partial x} = k_m(C_s - C_\infty) + VC \qquad \text{at } x = x_f;\ x_f = Vt \qquad [22]$$

where V is the constant growth rate and x_f is the moving boundary given by Vt. This is the boundary condition of Grove *et al.* (9) in the presence of dopant, which reduces to the original boundary condition of Grove *et al.* in the absence of dopant in the bulk flow, *i.e.* $C_\infty = 0$. Use of Eq. [5] in [22] leads to

$$-D\frac{\partial C}{\partial x} = (h + V)C - K_e k_m C_\infty; \quad h = k_m/K_e \qquad [23]$$

The initial condition is

$$C = C_i(x) \qquad \text{at } t = 0 \qquad [24]$$

where $C_i(x)$ is the concentration profile at the end of prebake. This is given by Eq. [9] and [10] for the buried layer region and by Eq. [21] for the nondiffused region with t set to t_p, where t_p is the duration of prebake.

Of major interest in the dopant profiles are the maximum dopant concentration in the substrate and the dopant profile around the epi-substrate boundary. Therefore, one can approximate the initial distribution in a form suitable for the purpose of obtaining these quantities of interest in an analytical form. The analytical solution of the problem for uniform initial buried layer concentration with the condition of finite, constant concentration for $x \to -\infty$ and intrinsic deposition conditions (9) is a subset of the problem being considered. Hu (17) obtained an analytical solution by approximating an initial erfc distribution by a Gaussian. However, the solution required the assumption of zero surface concentration at the growing surface, which is not applicable to the prebake/epitaxial deposition being considered.

An approximation of the profile at the end of prebake is made here on the basis of the surface concentration and the maximum dopant concentration at the end of prebake for the buried layer region. Typical dopant profiles in the buried layer and the nondiffused substrate at the end of prebake are shown in Fig. 4. Consider the buried layer first. If the maximum concentration is denoted by C_m and the surface concentration by C_l as shown in Fig. 4, a simple approximation of the profile for $|x|$ up to L_m by an exponential function is

$$C_i(x) = C_m + e^{\gamma x}(C_l - C_m) \qquad -L_m \le x \le 0 \qquad [25]$$

where $-L_m$ is the position at which the maximum occurs. This approximation is exact at $x = 0$, *i.e.* $C_i = C_l$, and at the maximum, $C_i = C_m$, provided the last term vanishes for an appropriate value of γ. The exact expression for C_l is already given by Eq. [12], which yields a number upon substituting the value of t_p into the expression for t. The value of C_m can also be evaluated from Eq. [9] by plotting C_l against x. A close examination of Eq. [9] in conjunction with the very slow nature of solid phase diffusion should reveal that the diffusion process is largely governed by the dimensionless group $(L/\sqrt{Dt_p})$. A dimensionless group representing the loss of dopant to gas phase is (h^2t_p/D). Thus, the constant γ that represents the rate of approach to the maximum C_m should be a function of these dimensionless groups. It turns out that a very accurate approximation of Eq. [9] at the end of prebake can be made by expressing γ as follows

$$\gamma = \frac{L}{\sqrt{Dt_p}}\left(1 + \frac{h^2 t_p}{D}\right) \qquad [26]$$

A comparison between Eq. [25] along with Eq. [26] and Eq. [9] is given in Table I, for the dopant profile at the end of prebake for two prebake times. The parameter values used in the comparison are those obtained by Srinivasan (5) for silicon substrate with arsenic buried layer, which

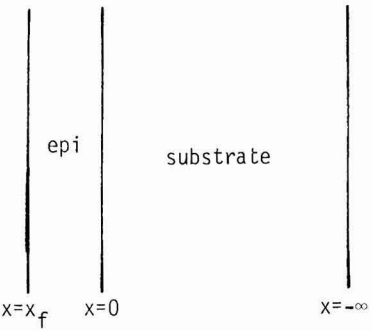

Fig. 3. Coordinate system during epitaxial deposition

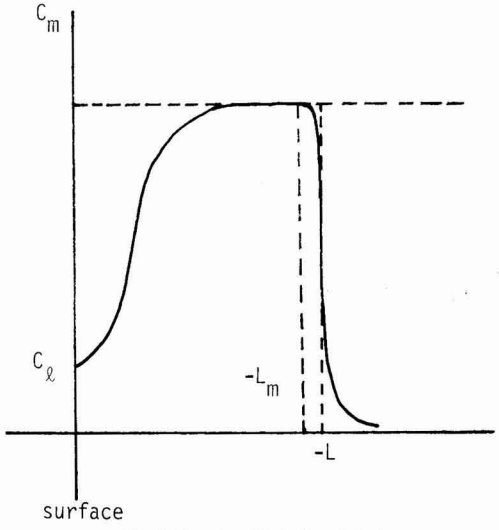

Fig. 4. Dopant profile in the substrate

Table I. Comparison between Eq. [9] and Eq. [25]

$D = 8 \times 10^{-14}$ cm²/s $h = 5.8 \times 10^{-9}$ cm/s $L = 10^{-4}$ cm

	C/C_o for t_p = 2 min (γ = 33.9)		C/C_o for t_p = 10 min (γ = 18.1)	
x/L	Eq. [9]	Eq. [25]	Eq. [9]	Eq. [25]
0	0.79	0.79	0.65	0.65
0.02	0.89	0.90	—	—
0.05	0.96	0.96	0.82	0.85
0.1	0.998	0.993	0.93	0.94
0.2	—	—	0.995	0.991

are: $D = 8 \times 10^{-14}$ cm²/s and $h = 5.8 \times 10^{-9}$ cm/s. The buried layer thickness was taken as 1 μm. The comparison shows that the approximation is very good. Further, the use of Eq. [25] in place of Eq. [9] for the dopant profile at the end of prebake does not involve any adjustable parameter. Therefore, Eq. [25] will be used as the initial condition for Eq. [1]. Another boundary condition is that the dopant concentration in the buried layer should be finite. The solution of Eq. [1] with the conditions of Eq. [23] and [25] along with the finite condition is

$$C(x,t)/C_o = \frac{K_e k_m C_\infty}{(h+V)C_o}\left[\frac{C_m}{C_o} + \left(\frac{C_1 - C_m}{C_o}\right) e^{\gamma x + \gamma^2 Dt}\right] + \left[1 - \frac{K_e k_m C_\infty}{(h+V)C_o}\right]\left[\frac{C_m}{C_o}\, y_1 + \left(\frac{C_1 - C_m}{C_o}\right) y_2 e^{\gamma x + \gamma^2 Dt}\right] \qquad x \geq -L_m \qquad [27]$$

where

$$y_1 = \frac{1}{2}\operatorname{erfc}(\alpha_1) - \frac{h+V}{2h} e^{\beta_1} \operatorname{erfc}(\alpha_2) + \frac{V+2h}{2h} e^{\beta_2} \operatorname{erfc}(\alpha_3) \qquad [28]$$

$$y_2 = \frac{1}{2}\operatorname{erfc}(\alpha_1) - \frac{h+V+D\gamma}{2(h+D\gamma)} e^{\beta_1} \operatorname{erfc}(\alpha_2) + \frac{V+2(h+D\gamma)}{2(h+D\gamma)} e^{\beta_3} \operatorname{erfc}(\alpha_4) \qquad [29]$$

Here α's and β's are

$$\alpha_1 = \frac{x}{2\sqrt{Dt}} \qquad \alpha_2 = \frac{2Vt - x}{2\sqrt{Dt}}$$

$$\alpha_3 = \frac{2(V+h)t - x}{2\sqrt{Dt}} \qquad \alpha_4 = \frac{2(V+h+D\gamma)t - x}{2\sqrt{Dt}} \qquad [30]$$

$$\beta_1 = \frac{V}{D}(Vt - x) \qquad \beta_2 = \left(\frac{V+h}{D}\right)[(V+h)t - x]$$

$$\beta_3 = \left(\frac{V+h+D\gamma}{D}\right)[(V+h+D\gamma)t - x] \qquad [31]$$

It is instructive to compare the solution with that obtained by Grove *et al.* (9). The solution of Eq. [27] reduces to the problem considered by them when $\gamma = 0$, $C_\infty = 0$, and $C_m/C_o = C_1/C_o = 1$, and it is

$$\frac{C(x,t)}{C_o} = y_1 = \frac{1}{2}\operatorname{erfc}\left(\frac{x}{2\sqrt{Dt}}\right) - \frac{h+V}{2h} e^{\frac{V}{D}(Vt-x)} \operatorname{erfc}\left(\frac{2Vt - x}{2\sqrt{Dt}}\right) + \frac{V+2h}{2h} e^{\frac{V+h}{D}[(V+h)t-x]} \operatorname{erfc}\left(\frac{2(V+h)t - x}{2\sqrt{Dt}}\right) \qquad [32]$$

It is seen that this solution is the same as that obtained by Grove *et al.* (9). One can verify the correctness of the solution of Eq. [27] by direct substitution. It should be noted in verifying the solution that at time zero, $x/\sqrt{Dt}$ tends to $-\infty$ and that the moving boundary x_f is given by Vt.

Although the solution given by Eq. [27] is quite complex, a quite simple solution results, if one is interested in only the final dopant profile. Usually, $Vt/\sqrt{Dt} >> 1$ in such a case and $\gamma^2 Dt << \gamma x$ such that Eq. [27] reduces to

$$\frac{C(t_e, x)}{C_o} = \left\{\frac{C_m}{C_o} + e^{\gamma x}\left(\frac{C_1 - C_m}{C_o}\right)\right\}\left\{W + \frac{(1-W)}{2}\operatorname{erfc}\left(\frac{x}{2\sqrt{Dt_e}}\right)\right\} \qquad [27a]$$

where t_e is the duration of epitaxial deposition and W is defined by

$$W = \frac{K_e k_m C_\infty}{(h+V)C_o}$$

If no dopant is present in the bulk gas during the deposition, *i.e.* intrinsic deposition, the dopant profile is simply Eq. [27a] with W set to zero.

Consider now the change of dopant profile in the nondiffused region in the course of epitaxial deposition. The dopant profile at the end of prebake, which is the initial condition for the epitaxial deposition, is that given by Eq. [21] with t set to t_p

$$C_n(x;z) = K_e \bar{C}_s \operatorname{erfc}\left(\frac{x}{2\sqrt{Dt_p}}\right) \qquad [33]$$

The same differential equation and boundary conditions as for the buried layer region also apply, *i.e.* Eq. [1] and [23] along with the condition of C_n being finite, which in this case is

$$C_n(-\infty, t) = 0$$

In order to obtain an analytical solution, the initial profile of Eq. [33] is approximated by an exponential function as follows

$$C_n(x) = K_e \bar{C}_s \exp\left(-\epsilon\omega \frac{x}{L}\right); \qquad \omega \equiv \frac{L}{2\sqrt{Dt_p}} \qquad [34]$$

where ϵ is a constant and L is the length of the buried layer. The value of ϵ may be chosen in such a way that the total initial dopant in the substrate is the same, *i.e.* the value of the exponential integrated over the total substrate length is the same as that of the error function integrated over the same interval. An approximate value of ϵ satisfying the condition is 1.7, as shown in Fig. 5 for the

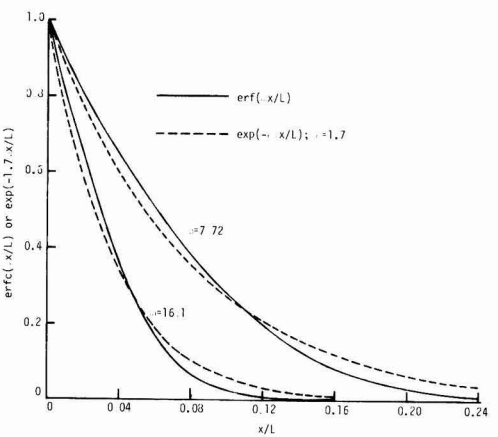

Fig. 5. Comparison between erfc (ωx/L) and the approximation by exp (−1.7 ωx/L).

two prebake times considered earlier in Table I. The solution follows directly from Eq. [27], which is

$$\frac{C_n}{K_e C_s} = \left\{ \frac{K_e k_m C_\infty}{(h+V)C_0} + \left[1 - \frac{K_e k_m C_\infty}{(h+V)C_0} \right] y_3 \right\}$$

$$\exp(\phi x + \phi^2 Dt); \qquad \phi \equiv -1.7\omega = \frac{-1.7L}{2\sqrt{Dt_p}} \qquad [35]$$

where

$$y_3 = \frac{1}{2}\operatorname{erfc}(\alpha_1) - \frac{h+V+D\phi}{2(h+D\phi)} e^{\beta_4} \operatorname{erfc}(\alpha_2) + \frac{V+2(h+D\phi)}{2(h+\phi D)} e^{\beta_4} \operatorname{erfc}(\alpha_5) \qquad [36]$$

Here β_4 and α_5 are

$$\beta_4 = \frac{D+h+D\phi}{D}[(V+h+D\phi)t - x]$$

$$\alpha_5 = \frac{2(V+h+D\phi)t - x}{2\sqrt{Dt}} \qquad [37]$$

Here again, the solution simplifies considerably, if only the final distribution is of interest

$$\frac{C_n}{K_e C_s} = \left\{ W + \frac{1-W}{2} \operatorname{erfc}\left(\frac{x}{2\sqrt{Dt_e}} \right) \right\} \exp(\phi x) \qquad [35a]$$

since usually $Vt_e/\sqrt{Dt_e} >> 1$ and $\gamma^2 Dt << \gamma x$, as discussed earlier in conjunction with Eq. [27a].

Final Dopant Distributions

The dopant profile at the end of epitaxial deposition is given by Eq. [27] for the buried layer region and by Eq. [35] for the nondiffused region, if t_e is substituted into the equations for t, where t_e is the duration of the epitaxial deposition. It should be pointed out that the final dopant profile for the buried layer region is based on the dopant profile at the end of prebake represented by the dotted line in Fig. 4 rather than the true profile given by the solid line. Both profiles lead to the same final dopant profile for $x > -L_m$, provided the maximum value C_m is unchanged during the epitaxial deposition. Since the duration of the epitaxial deposition is of the order of several minutes, the maximum value is not likely to change in most situations of practical interest. If the duration is much longer than several minutes, the dopant profile given by Eq. [27] will give an approximate dopant profile. As pointed out earlier, the final dopant profile for the nondiffused region is based on the approximation of the profile at the end of prebake by Eq. [24], which is shown in Fig. 5.

Of prime interest in the nondiffused region is the maximum autodoping level. Since the maximum occurs at around the epi-substrate boundary, an approximate expression for the maximum can be obtained directly from Eq. [35] by setting $x = 0$

$$\frac{(C_n)_{max}}{K_e C_s} = \left\{ \frac{K_e k_m C_\infty}{(h+V)C_0} + \left[1 - \frac{K_e k_m C_\infty}{(h+V)C_0} \right] y_3(x=0) \right\} \exp(\phi^2 Dt)$$

Since $\phi^2 Dt << 1$, $D\phi/V << 1$, and $Vt/\sqrt{Dt} >> 1$ under typical epitaxial deposition conditions, it follows from Eq. [36] and [37] that the expression further reduces to

$$\frac{(C_n)_{max}}{K_e C_s} \approx \frac{K_e k_m C_\infty}{(h+V)C_0} + \frac{1}{2}\left[1 - \frac{K_e k_m C_\infty}{(h+V)C_0} \right] \qquad [38]$$

It is seen that a very simple relationship results for the maximum lateral autodoping level. It is also seen that the choice of the value of $\phi(\epsilon\omega)$ for the approximation of Eq. [34] does not have any significant effect on the maximum.

Now that the expressions for the final dopant profiles are known, let us consider the dependence of the lateral autodoping maximum on flow rate and position in the light of the experimental results reported by Srinivasan (5). Consider in particular the results reported in Fig. 5 and 6 in Srinivasan's article. Since the experimental values were obtained in the absence of dopant in the bulk flow and for the same duration of epitaxial deposition, $(C_n)_{max}$ dependence on the position is

$$\ln \frac{(C_n)_{max}}{A} = \begin{cases} -\left[\dfrac{\sqrt{(\alpha_d U)^2 + 4D_\kappa (k_m)_d} - \alpha_d U}{2D_\kappa} \right] z \text{ downstream} \\ -\left[\dfrac{\sqrt{(\alpha_u U)^2 + 4D_\kappa (k_m)_u} + \alpha_u U}{2D_\kappa} \right] z \text{ upstream} \end{cases} \qquad [39]$$

where A is a constant. The relationship follows from Eq. [19], [20], and [38]. As discussed earlier, average values of α and k_m can be used, if the distance from the buried layer region (Fig. 2) is not large. In such a case, a plot of $\ln (C_n)_m$ against z should yield a straight line for an interval of z. Further, the intercept should be the same, as is apparent from Eq. [39]. Such a plot is shown in Fig. 6. It is seen that straight lines with a common intercept can be drawn for the position dependence of the maximum lateral autodoping level. As expected, deviations from the straight lines occur at large distances, *i.e.* $z > 0.6$ cm. If a small interval is involved, α_u may be set equal to α_d, and the difference in the slopes can be used to determine the value of α, since then the absolute value of the difference is $\alpha U/D_\kappa$, which is 2.94 cm^{-1} according to the slopes in Fig. 6 [value of U is not given in Ref. (5)]. The theoretical relationship for the mass-transfer coefficient k_m (17) is

$$\frac{k_m}{U} = 0.3387 g^{1/3} Sc^{-2/3} Re^{-1/2}$$

$$Re = \frac{Uz}{(m+1)\nu} \qquad m = \frac{\theta^o/90^o}{2 - \theta^o/90^o} \qquad [40]$$

where g is a factor dependent solely on the incidence angle for a tilted susceptor θ, Sc is the Schmidt number, and Re is the Reynolds number. In this regard, it should

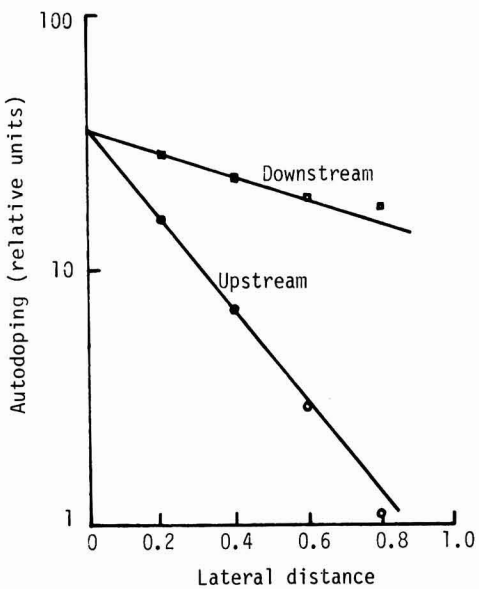

Fig. 6. Autodoping peak maximum points reported by Srinivasan (5) and the lines given by Eq. [39].

be noted that z in Eq. [40] is the distance measured from the leading edge of the susceptor as opposed to the coordinate shown in Fig. 2. The dependence of the maximum lateral autodoping level on carrier gas velocity reported in Fig. 6 of Srinivasan's article (5) is also consistent with the relationship given by Eq. [39]. Equation [39] can be rewritten in this case as

$$\ln (C_n)_{max} \sim \begin{cases} -\sqrt{(\alpha_d U)^2 + 4D_g(k_m)_d} + \alpha_d U \text{ downstream} \\ -\sqrt{(\alpha_u U)^2 + 4D_g(k_m)_u} - \alpha_u U \text{ upstream} \end{cases} \quad [41]$$

It is seen that the dependence is parabolic with the carrier gas velocity U and that the relationship can describe the experimental results quite well.

Summary

Dopant distributions in both the buried layer and nondiffused regions as affected by prebake and subsequent epitaxial deposition have been considered. The dopant profiles resulting at the end of prebake are given by Eq. [9] and [10] for the buried layer region and by Eq. [21] for the nondiffused region. Because the dopant profile in the nondiffused region is dependent on the distance from the buried layer edge due to lateral autodoping, the dopant profile given by Eq. [21] is also dependent on the position. Based on pseudo steady-state assumption, which is quite valid due to very low diffusivity in solid compared to that in gas, a model has been developed for the position dependence of the gas phase concentration in equilibrium with the surface dopant concentration in solid. These relationships are given by Eq. [19] in the direction of flow (downstream) and by Eq. [20] in the opposite direction to the flow (upstream). The relationships can be used in Eq. [21] for the dopant profile in the nondiffused region. It has been shown by comparison with the experimental data by Srinivasan (5) that the relationships can describe quite well the position and flow dependence of the maximum lateral autodoping level.

The dopant profiles at the end of prebake have been used to determine the redistribution of dopant in the course of epitaxial deposition following the prebake. For the purpose of obtaining an analytical solution, the dopant profile at the end of prebake was approximated by Eq. [25], which is accurate to within 4% in terms of relative error and, at the same time, does not require any adjustable parameters. The redistribution in the buried layer region is given by Eq. [27]. If only the final dopant profile is of interest, the simple version of the solution given by Eq. [27a] should be sufficiently accurate in most cases of practical interest. The dopant profile given by Eq. [27] is exact as long as the maximum in the substrate does not change. If it does, it is only an approximate solution for the profile but should be quite accurate at around $x = 0$ and for $x > 0$. The final dopant profile in the nondiffused region is given by Eq. [35]. This result was obtained by approximating the profile at the end of prebake by Eq. [34], which does not contain any adjustable parameters. Here again, Eq. [35a] should be sufficiently accurate for all practical purposes, if only the final profile is of interest. One quantity of prime interest for the nondiffused region is the maximum lateral autodoping level. This is given by Eq. [38]. The approximation of Eq. [34] does not have any significant effect at all on the maximum lateral autodoping level, and thus the expression for the maximum is very accurate.

A rather complete description of dopant profiles and redistribution in the course of prebake and epitaxial deposition presented here should allow one to determine exactly how a change in any operating condition affects the final dopant profiles, thereby enabling one to accordingly manipulate the operating conditions so as to obtain the desired profiles.

Manuscript submitted Feb. 20, 1985; revised manuscript received June 30, 1986.

LIST OF SYMBOLS

C	dopant concentration
C_i	dopant profile in solid at the end of prebake
C_1	C_i at the surface
C_m	maximum value of C_i
C_n	dopant concentration in nondiffused (off-buried layer) solid
C_o	initial constant dopant concentration in buried layer
C_s	gas phase dopant concentration at the buried layer surface
$\bar{C}_s$	gas phase dopant concentration at the nondiffused solid surface
C_1	dopant concentration in buried layer
C_2	dopant concentration below buried layer
C_∞	gas phase dopant concentration in bulk fluid flow
D	dopant diffusivity in solid
D_g	gas phase molecular diffusivity of dopant
f'	quantity given in Eq. [17]
g	factor dependent on incidence angle in Eq. [40]
h	k_m/K_e
H	Henry's constant
k_B	Boltzmann constant
k_m	mass-transfer coefficient
K_e	equilibrium constant defined by Eq. [5]
L	depth of buried layer
L_m	position L at which maximum concentration occurs
m	constant defined in Eq. [40]
Re	Reynolds number in Eq. [40]
Sc	Schmidt number
t	time
t_p	duration of prebake
t_e	duration of epitaxial deposition
u	z component velocity in boundary layer
U	bulk fluid velocity
V	growth rate
W	width of buried layer; quantity defined below Eq. [27a]
x	coordinate for solid perpendicular to solid surface
x_f	forefront of growing surface ($= Vt$)
y	gas phase coordinate, perpendicular to substrate
y_1, y_2, y_3	quantities defined by Eq. [28], [29], and [36], respectively
Y	quantity defined by Eq. [11]
z	gas phase coordinate parallel to substrate

Greek Letters

α	constant given in Eq. [18]
$\alpha_1, \alpha_2, \alpha_3, \alpha_4$	quantities defined in Eq. [30]
$\beta_1, \beta_2, \beta_3$	quantities defined in Eq. [31]
β_4, α_5	quantities defined in Eq. [37]
γ	constant defined by Eq. [26]
ϵ	constant in Eq. [34]
η	similarity transformation variable in Eq. [17]
η_f	η at a fixed z
θ	tilting angle
ν	kinematic viscosity
ω	quantity defined in Eq. [34]
ϕ	quantity defined in Eq. [35]

Subscripts

d	downstream
u	upstream

REFERENCES

1. D. Khang, R. C. Manz, C. O. Thomas, and S. K. Tung, presented at the AIME Semiconductor Metallurgy Conference, Los Angeles, CA, Vol. 15, J. R. Schroeder, Editor, p. 69, Interscience Publishers, Inc., New York (1961).
2. H. B. Pogge, D. W. Boss, and E. Ebert, in "Chemical Vapor Deposition," J. M. Blocher and J. C. Withers, Editors, p. 767, The Electrochemical Society Softbound Proceeding Series, Princeton, NJ (1970).

3. M. Ogirima, H. Saida, M. Suzuki, and M. Maki, *This Journal*, **124**, 903 (1977).
4. G. R. Srinivasan, *ibid.*, **125**, 146 (1978).
5. G. R. Srinivasan, *ibid.*, **127**, 1334 (1980).
6. R. C. Miller and F. M. Smits, *Phys. Rev.*, **107**, 65 (1957).
7. R. N. Ghostagore, *Solid-State Electron.*, **15**, 1113 (1972).
8. E. Arai and Y. Terunuma, *Jpn. J. Appl. Phys.*, **9**, 410 (1970).
9. A. S. Grove, A. Roder, and C. T. Sah, *J. Appl. Phys.*, **36**, 802 (1965).
10. P. H. Langer and J. I. Goldstein, *This Journal*, **124**, 591 (1977).
11. R. Reif, *ibid.*, **129**, 1122 (1982).
12. G. K. Ackermann and E. Ebert, *This Journal*, **130**, 1910 (1983).
13. P. Rai-Choudhury and E. I. Sakovitz, *J. Cryst. Growth*, **7**, 353 (1970).
14. H. Schlichting, in "Boundary Layer Theory," 4th ed., McGraw-Hill, Inc., New York (1965).
15. K. F. Hulme, *Proc. Phys. Soc., B* **68**, 393 (1955).
16. H. A. Wilson, *Proc. Cambridge Philos. Soc.*, **12**, 406 (1904).
17. K. J. Klingman and H. H. Lee, *J. Cryst. Growth*, **72**, 670 (1985).

Applications of Redox Contacts for Metal and Semiconductor Rotating Ring-Disk Electrodes

Lynn F. Schneemeyer,* Joseph M. Rosamilia,* and Barry Miller*

AT&T Bell Laboratories, Murray Hill, New Jersey 07974

ABSTRACT

A design of a rotating ring-disk electrode with an electrolytic back-contact cell for the disk has been implemented and tested. Both the disk, acting as a bipolar electrode between a conventional cell and back compartment, and the back-electrolyte are made readily interchangeable. The most significant application is to semiconductor disks where ohmic contacts may be intricate to fabricate, as for the p-InP example experimentally investigated here. However, control of the back-cell characteristics when there is a front metallic disk allows blocking current flow (anodic or cathodic) in a selected direction over some potential range. Application of this principle to amperometric end-point detection in titrimetry illustrates how selective response to mixed redox couples introduced by this diode-like effect can be put to effective use with conventional metal electrodes.

While making ohmic contacts to clean metal electrodes is normally routine, contacting semiconductors is mostly nontrivial (1). A resistive or rectifying characteristic on the back-contact under current flow adds an unknown factor to the measured potential of the electrode of interest. In the extreme, the experiment itself may become contact limited. We treat here the use of electrolytic back-contacts to the disk of rotating disk (RDE) and ring-disk (RRDE) electrodes, in the voltammetry of semiconductors and in schemes taking advantage of the back-cell impedance characteristic with metals. Ready demountability of the disk and exchange of the contacting solution are incorporated.

Kireev, Trukhan, and Filimonov (2) earlier demonstrated an electrolytic scheme for contacting semiconductor specimens. The material to be investigated is clamped between two solutions. One, with a counterelectrode, serves as "back-contact," the other (front side) faces a conventional cell. On current flow, the semiconductor acts as a bielectrode (cathode on one side, anode on the other) joining the two compartments.

The ease of formation of solid-liquid junctions at ambient temperature is in contrast to that for most solid-solid metal-semiconductor contacts. In the latter, the technical difficulties encountered in producing low resistance ohmic behavior vary, as a function of material and majority carrier type (n or p), from simple attachment to multilayer depositions with thermal diffusion steps. Especially for the latter, processing may perturb the subsequent behavior of the substrate in unpredictable ways.

In the bielectrode electrolytic case, the semiconductor in the dark back-cell compartment will be a blocking contact in one direction (reverse) and an anode (p-type) or cathode (n-type), respectively, in the opposite (forward) direction. If held in the inversion layer region by an appropriate redox couple or with the introduction of sufficient surface-state density by chemical treatment, the semiconductor will conduct both ways (act metallic) in the dark. Blocking contact behavior and the consequent potential shifts introduced by the back cell voltage are clearly evident in the current-potential (i-E) curves for titanate semiconductors and Ag/AgCl counterelectrodes in chloride media (2).

* Electrochemical Society Active Member.

The static configuration of Kireev *et al.* (2) has limitations that tend to offset its convenience for semiconductor and other studies. It has poorly defined transport conditions for any effort to achieve a steady-state condition. On the other hand, cyclic voltammetry is not feasible, when the back-contact is rectifying and blocking the current in the reverse sweep. Thus, means to study product chemistry, a vital issue, are very limited in this configuration. Quantitative study of product distribution, in any case, is better implemented by the real-time analysis available with controlled convective-diffusion and dual electrode designs, best represented by the RRDE. Achieving the virtues of a generator-detector system with the convenience of the electrolytic contacting scheme was a major motivation for this work.

Figure 1a shows a schematic of the electrolytically contacted electrode sections, with the conventional potentiostat measuring connections for current and refer-

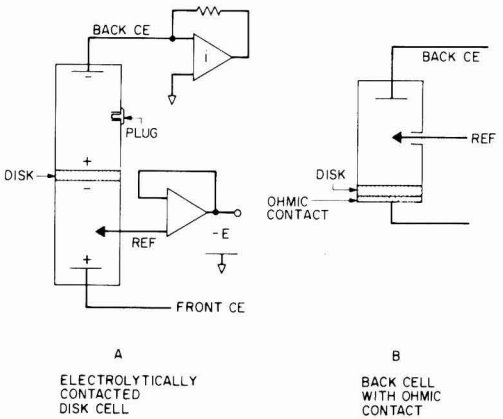

Fig. 1. (a) Schematic of electrolytically contacted disk electrode. (b) Schematic of back-cell compartment with front of disk ohmically contacted and reference electrode inserted through hole.

ence electrode indicated. The measured potential of the front side of the semiconductor *vs.* reference (as reference to ground) includes the entire voltage drop across the back-cell. For later purposes of confirming overall operation of such electrodes, an ohmically contacted semiconductor and a reference inserted in the side plug hole, as in Fig. 1b, were used to characterize the individual electrodes in the back-cell. Experimental work with p-InP disks illustrates the capabilities and limitations of electrolytic back-contacts in the study of semiconductors.

Translation of the schematic Fig. 1 into a working RRDE arrangement with demountable disks and permanent ring electrode is discussed in the Experimental section. Easy exchange of disks and contacting solutions is desired so that, in the semiconductor case, new materials need only be fashioned in disk form for survey studies.

The coupling of separate photodiode and metal disk electrode/electrolyte junctions has been used in our laboratories to study mass transport, kinetics, and light flux interaction in photoelectrochemical cells (3, 4). Certain features of current rectification can be imitated by the double layer (no faradaic current) region of metal electrodes in appropriate solvents. Useful electroanalytical functions can be obtained this way from the back-cell and are illustrated by using an electrolytically contacted glassy carbon disk in amperometric end-point detection for titrimetry.

Experimental

All electrolyte solutions were prepared in 18 MΩ Milli-Q-water and reagent grades of sodium acetate, acetic acid, potassium chloride, nitric acid, and hydrochloric acid. Hexaammine ruthenium (II) chloride (Alfa), hexaammine ruthenium (III) chloride (Alfa), iron (II) chloride (Fisher), iron (III) chloride (Fisher), potassium ferrocyanide (Fisher), potassium ferricyanide (Fisher), silver nitrate (Alfa), cerium (IV) bisulfate (G. Fredrick Smith), and vanadium pentoxide (Fisher) were used as obtained. The V(II)/V(III) redox couple was prepared after dissolving 1.8g of V_2O_5 in 25 ml of 12*M* HCl and diluting to 100 ml. Reduction of V(V) → V(II) was accomplished by passing the solution through a zinc column into a vessel flushed with dry nitrogen. Partial air oxidation of this solution yields the V(III)/V(II) redox solution with 0.2*M* total vanadium. To prepare the 0.1*M* $Ru(NH_3)_6Cl_3$/0.1*M* $Ru(NH_3)_6Cl_2$ solution, appropriate amounts of the Ru(II) and Ru(III) compounds were weighed out under inert atmosphere and placed in a volumetric flask sealed with a serum cap. The mixture was diluted to volume with deoxygenated 1.0*M* NaOAc/HOAc.

The RRDE was fabricated using materials and dimensions indicated in Fig. 2. The nominal theoretical collection, *N*, for this electrode is 0.418 (5). Dimensions were taken from metallurgical microscope measurements, after assembly and polishing, for accurate calculations of *N*. Disks of 0.48 cm diameter of glassy carbon and p-InP, which was kindly supplied by W. P. Bonner, were cut using a Gulton Industries ultrasonic cutter. Ultra F purity pyrolytic graphite (Ultra Carbon Corporation, Bay City, Michigan) was used as the ring material. A connection to the stainless steel tube was made with a gold wire through a predrilled hole and silver epoxy contacts. The upper epoxy insulation was backfilled and shaped.

Conventional ohmic contacts to p-InP are formed in a two-step procedure (6). A Au:Zn alloy is evaporated onto a clean InP surface, followed by alloying at ~400°C under an inert or reducing atmosphere. Easy disk mounting, as in a previous design (7), was achieved by filling the small gap between the disk edge and the epoxy insulator with Loctite super bonder 416 gap filling instant adhesive (Loctite Corporation, Newington, Connecticut). Loctite Tak Pak accelerator was used to achieve fast curing (minutes). The electrode surface was polished with 1 μm Al_2O_3 to remove excess adhesive and to make the ring and disk coplanar. p-InP was etched in 12*M* HCl to remove surface damage prior to use.

To demount, the electrode surface was immersed in ultrasonically agitated acetone for 1h, dissolving the gap filling adhesive and releasing the disk. The chosen redox electrolyte was injected into the back-cell via the side hole using a syringe. An epoxy plug was pressed in the hole and covered with the Loctite 416 adhesive. Gas evolution in a closed compartment can be a problem. Thus, consideration needs be paid that this plug fail should gas evolve in

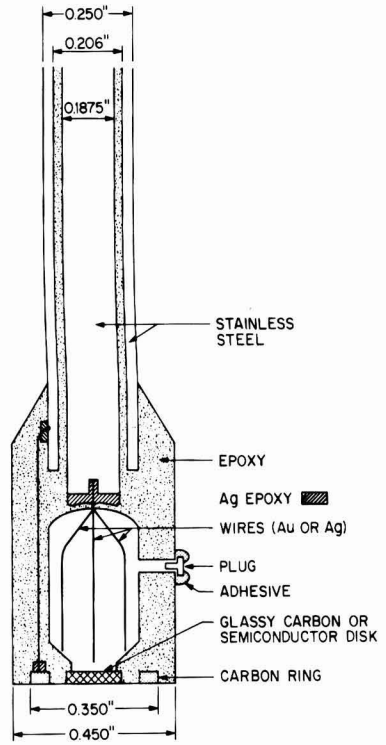

Fig. 2. Structural diagram of electrolytically contacted ring-disk electrode.

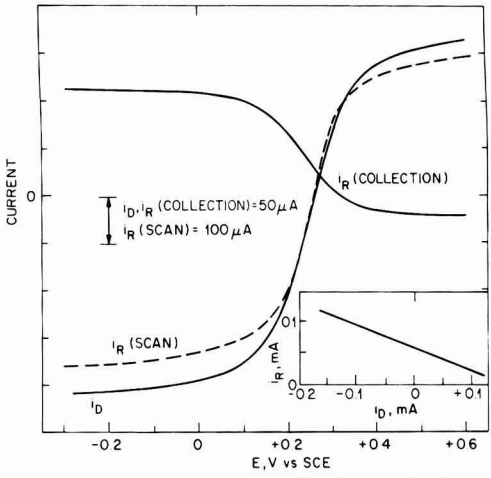

Fig. 3. Pyrolytic graphite ring-glassy carbon disk rotated at 900 rpm with 2M $AgNO_3$-1M HNO_3 back-contact, 2 mM each $Fe(CN)_6^{+4/}$ $Fe(CN)_6^{-3}$-1M KCl front solution. Solid lines: disk scanned at 10 mV s^{-1} and E_R fixed at +0.4V vs. SCE. Inset shows a i_R-i_D curve recorded under disk potential scan for the same conditions. Dashed line: E_R scan (disk open) at 10 mV s^{-1}.

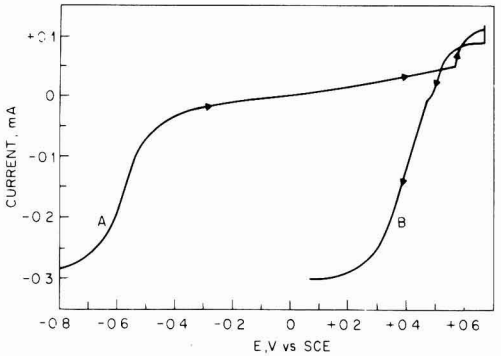

Fig. 4. Glassy carbon disk with 2M $AgNO_3$-1M HNO_3 in back-cell and 5 mM Fe^{+3}/1 mM Fe^{+2}/1M H_2SO_4 in front. Scan rate: 10 mV s^{-1}; ω = 900 rpm. (A) Potential scan of disk from −0.8V vs. SCE with no silver plated on the back of the disk. (B) Scan in negative direction after holding at +0.67V vs. SCE.

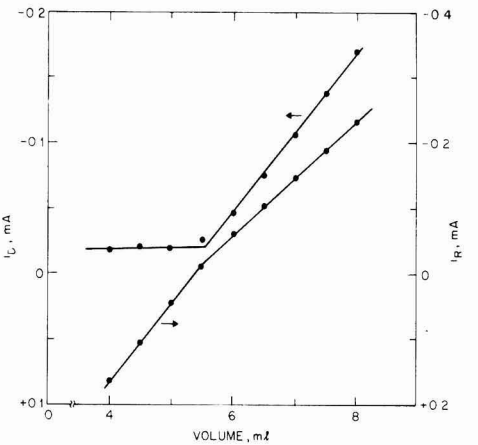

Fig. 6. Amperometric titration curves for indicator electrodes: (left axis) glassy carbon disk with 2M $AgNO_3$-1M HNO_3 back-cell (no silver on disk), E_D = −0.35V vs. SCE, and (right axis) graphite ring, E_R = +0.6V vs. SCE. Solution Fe^{+2}/1M H_2SO_4 with volume of Ce^{+4} titrant on abscissa.

the sealed back compartment. The plug could be removed to change back-cell solution by dissolving the adhesive in acetone.

Electrochemical measurements were made using a Pine Instruments Model RDE3 bipotentiostat. Rotation of the RRDE assembly at fixed or scanned speeds (ω) was provided using electronics described previously (8). Voltammograms were recorded using a HP Model 7046A X, Y, Y' recorder. Experiments with a semiconductor disk utilized a cell equipped with an optical flat bottom, permitting illumination with a 10 mW He-Ne laser beam, which was expanded and projected uniformly over the entire semiconductor disk surface. Light levels were much greater than the flux corresponding to mass transport limitation at the rotating semiconductor disk.

Results

Metallic disks.—With carbon or metal disks, the use of a reversible metal/metal ion couple in the back-cell can provide two functions: (*i*) a minimum resistance ohmic characteristic, or (*ii*) a double layer, "infinite resistance" potential region. The ideal operation of a contact, as in (*i*), is shown for a C/Ag/2*M* $AgNO_3$, 1*M* HNO_3/Ag back-cell, and the application of (*ii*) is demonstrated by amperometric end-point detection with the same cell when Ag is anodically stripped from the back side of the disk and the front side is a cathodic monitor. As will be made clear, case (*ii*) introduces a diode-like behavior, which can be used to block either the anodic or cathodic response (depending on the situation) of the front side electrode to enhance its selectivity of response to redox couples.

In Fig. 3, case (*i*) is illustrated for RRDE voltammetry of $Fe(CN)_6^{-4}$/$Fe(CN)_6^{-3}$ in 1*M* KCl. The i_D-E_D curve of the electrolytically contacted glassy carbon disk is virtually superimposable on that of the pyrolytic carbon ring, scanned independently (subscripts *D* and *R* will refer to disk and ring parameters, respectively). This is proof of satisfying the requirement of a minimum resistance ohmic contact. The collection properties of the dual electrode are seen from either the linear i_R-i_D plot or the i_R-i_D-E_D traces to be well behaved. In similar experiments for an electrode with calculated N = 0.476 and $\beta^{2/3}$ = 1.87, measured values were 0.467 and 1.91, respectively. ($\beta^{2/3}$ is the geometrically determined ratio of ring-to-disk limiting currents for a given reaction, measured independently.)

The measured current-voltage slope of the 2*M* $AgNO_3$-1*M* HNO_3 back-cell is <50Ω [both electrode surfaces silver and the front of the glassy carbon contacted through Hg-In (50 atom percent)]. The minimum resistance of the i_D-E_D or i_R-E_D traces in Fig. 3 is at least 10 times greater, consistent with observing no perceptible difference between ohmic and electrolytic contacts in this case. Ideal operation of the bipolar electrode structure is confirmed by these RRDE results.

In case (*ii*), when there is no silver on the back of the carbon disk, oxidation of the carbon surface or the electrolyte proceeds, with corresponding overpotential, at nearly a volt above the Ag/Ag^+ value. The E_D-i_D curve for a $Fe^{+3/+2}$ mixture in the front cell when there is no silver on the back of the disk is shown in curve A of Fig. 4. The curve is displaced negative on the E_D scale by about a volt from the usual value, and the Fe^{+2} oxidation wave is missing. However, during the scan to positive potentials, the back side of the disk eventually becomes cathodic and, when silver

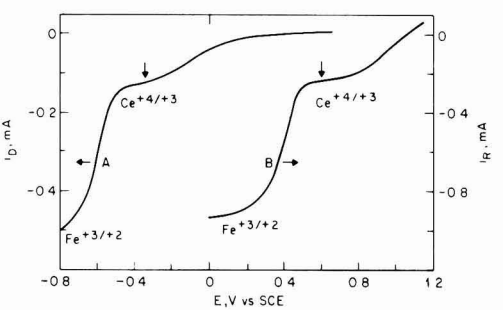

Fig. 5. Separately performed potential-controlled scans of: (A) glassy carbon disk with 2M $AgNO_3$-1M HNO_3 back-contact (no silver on the disk), and (B) graphite ring, both with 6 mM Fe^{+3}/2 mM Ce^{+4}/1M H_2SO_4 front cell. Scan rate: 10 mV s^{-1}; ω = 900 rpm.

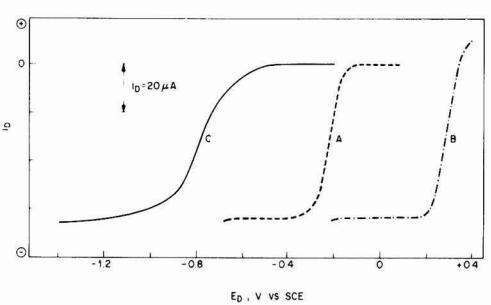

Fig. 7. i_D vs. E_D for 1 mM $Ru^{+3}(NH_3)_6$-1.0M NaOAc/HOAc. ω = 1600 rpm; scan rate: 20 mV s^{-1}; disk electrodes as indicated. (A) Au disk; (B) p-InP disk with metal ohmic back-contact; (C) p-InP semiconductor disk with 0.2M V(II)/V(III)-3M HCl back-contact.

begins to deposit, anodic current abruptly increases in the front cell. Stopping the scan at +0.67V *vs.* SCE until sufficient silver has deposited permits a negative-going potential scan to yield a composite Fe^{+3}/Fe^{+2} wave, curve B, at essentially its expected position. If the silver becomes stripped from the back, the trace will return to curve A behavior.

Scans toward positive potentials are shown in Fig. 5 for a Ce^{+4}/Fe^{+3} solution with the redox-contacted disk at a silver-stripped back carbon surface (curve A), and at the graphite ring electrode (curve B). On the basis of these curves, consider monitoring the titration of Fe^{+2} by Ce^{+4} by amperometric measurement of Ce^{+4} reduction at a fixed potential on the $Ce^{+4} \rightarrow Ce^{+3}$ limiting current plateau. Such a point is indicated by the arrows on each of the curves A and B. With a graphite (or noble metal) electrode ohmically contacted, as in curve B, this potential will also correspond to a limiting current for $Fe^{+2} \rightarrow Fe^{+3}$ oxidation prior to the end point. For the case of the redox-contacted electrode with half the couple missing (as in curve A), the anodic current will not pass (see Fig. 4). We can take advantage of this in amperometrically monitored redox titrimetry to improve the angle of intersection of the lines defining the end point.

Titration curves with the redox-contacted disk and graphite ring electrodes as simultaneous amperometric detectors under the conditions of the Fig. 5 traces are shown in Fig. 6. The graphite electrode shows only a small change in slope at the end point, whereas the redox-contacted disk response shows a well-defined end point between the extrapolated "zero" current of blocked Fe^{+2} oxidation and reductive detection of excess Ce^{+4}. The behavior of the redox-contacted disk is not different in principle from pairing a diode (in the appropriate direction) in series with a noble metal electrode.

Semiconductor disks.—Deposition of metals on semiconductors leads to variable results in terms of contact behavior, and, thus, we initially chose soluble redox couples as back-contact solutions for semiconductor use. For the experiments with p-InP, $V^{+2/+3}/H^+$ and $Ru(NH_3)_6^{+2/+3}$-pH 5 were selected. In practice, they showed distinguishable cyclic behaviors, however.

Figure 7 shows potential scans in a 1.0 m*M* $Ru(NH_3)_6^{+3}$ solution with: (curve A) a gold disk; (curve B) a metallically (ohmically) contacted p-InP disk under illumination; and (curve C) a zinc-reduced $V^{+3/+2}/H^+$ redox-contacted p-InP disk under illumination. The positive shift of the photovoltage of the p-InP/$Ru^{+3/+2}$ junction in curve B *vs.* the gold electrode is offset in the case of curve C by the characteristics of the back-cell compartment, which we shall discuss after the RRDE collection characteristics.

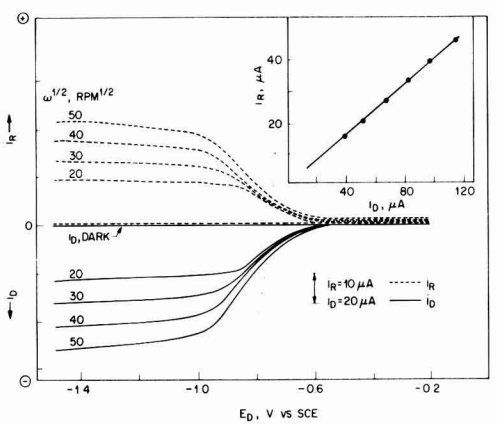

Fig. 8. i_D and i_R *vs.* E_D, p-InP disk −0.2M V(II)/V(III) −3M HCl back-contact in 1 mM Ru^{+3} −1.0M NaOAc/HOAc. Graphite ring curves are shown for indicated values of $\omega^{1/2}$. Scan rate: 20 mV s^{-1} at disk; E_R fixed at −0.2V *vs.* SCE. Insert: i_R *vs.* i_D, data obtained at $E_D = -1.4V$ and $E_R = +0.2V$ by changing $\omega^{1/2}$.

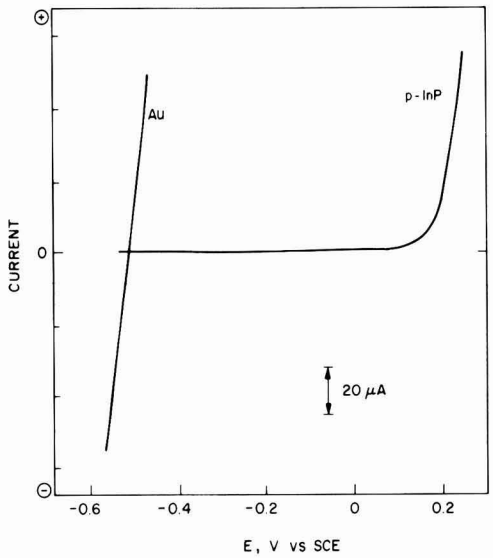

Fig. 9. *i vs. E* for 0.2M V(II)/V(III)-3M HCl at a p-InP disk with a metal ohmic back-contact. Also shown is the response at Au wires. Scan rate = 20 mV s^{-1}.

A set of ring-disk curves for the electrode with the $V^{+3/+2}/H^+$ back-contact solution is shown in Fig. 8. The inset is a i_R-i_D plot obtained by changing rotation speed under fixed $E_D = -1.4V$ and $E_R = 0.2V$ *vs.* SCE. The slope of the linear plot is 0.406 *vs.* a calculated *N* of 0.416, confirming quantitative reduction of $Ru(NH_3)_6^{+3}$ by photogenerated electrons.

The behavior of the back-cell elements was investigated using the configuration of Fig. 1b and a carbon reference electrode at the redox potential of the $V^{+3/+2}/H^+$ solution. In Fig. 9 are shown the *E*-*i* traces for the gold interior electrode and the back-surface of the p-InP disk, as obtained from three-electrode scans of each as working electrode. The sum of the potential drops in the back-compartment at each current are, in principle, the required correction to make an electrolytically contacted semiconductor equiva-

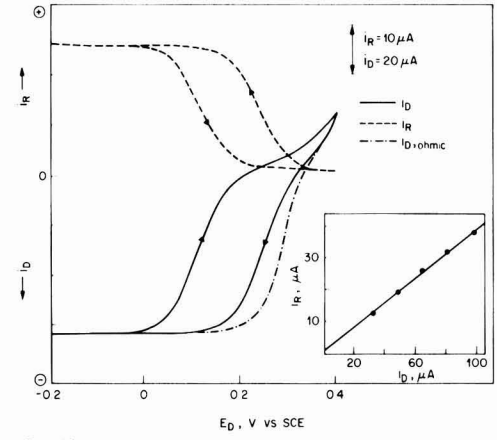

Fig. 10. i_R and i_D *vs.* E_D for p-InP disk with 0.1M $Ru^{+3/+2}$-1.0M NaOAc/HOAc back-contact in 1 mM Ru^{+3}-1M NaOAc/HOAc front solution. ω = 1600 rpm; scan rate: 20 mV s^{-1}; $E_R = +0.2V$. Dash-dot line: p-InP disk with a metal ohmic back-contact for the same conditions. Inset: i_R *vs.* i_D as a function of $\omega^{1/2}$, E_R and E_D controlled at −0.2 and +0.2V, respectively.

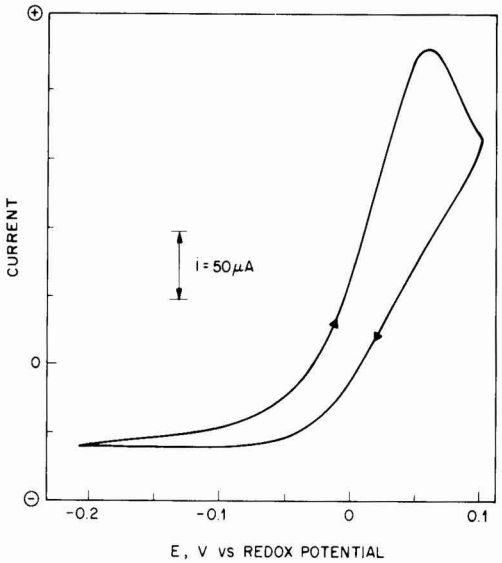

Fig. 11. Current-voltage curve for dark p-InP disk with metal ohmic back-contact in 0.1M $Ru^{+3/+2}$-1M NaOAc/HOAc. Scan rate: 20 mV s^{-1}.

lent to a "zero-loss" conventional electrode. We note that the back side p-InP conformed to the behavior noted in the study of this cell for photoelectrochemical energy conversion (9).

The result in Fig. 7-9 demonstrates the utility and limitations of the bielectrode scheme when the semiconductor-electrolyte junction in the back-cell has classical rectifying behavior. To the extent this may be modified in the direction of more metallic-like behavior, the voltage "losses" in the back-cell or "error" in the measured front side potentials may be reduced. A specific case of this intermediate behavior was observed when the $Ru(NH_3)_6^{+3/+2}$ couple (as 0.10*M* $Ru(NH_3)_6Cl_3$-0.10*M* $Ru(NH_3)_6Cl_2$ in 1*M* pH 5 total acetate buffer) was used as the back-cell solution for p-InP.

A cyclic potential scan for this system with a front side solution of 1 m*M* $Ru(NH_3)_6^{+3}$ at pH 5, after numerous previous cycles, is shown in Fig. 10 (solid line), with the accompanying ring collection response and derived i_R-i_D plot (inset). The disk behavior is close to that observed for the Au-Zn contacted p-InP disk (dash-dot line).

Examination of a three-electrode back-cell scan of the p-InP electrode, in Fig. 11, after multiple Fig. 10-type disk cycles, shows the p-InP electrode to be acting quasi-metallically, with little potential offset from the solution redox level in forward conduction and considerable "leakage" in the normally blocking direction. A comparison to the corresponding Fig. 9 situation would "explain" the resemblance of the Fig. 10 trace to that with the alloy ohmic contact.

The evolution of Fig. 11 behavior can be seen in Fig. 12, which contains several cycles of the back-cell p-InP i-E curves (cycles 1, 7, 13, and 19). The electrode is initially rectifying but becomes more metallic on cycling. The peak reached in the anodic half-cycle and the fact that more positive potential excursions alter the behavior (make it more rectifying, see inset for effect of positive scan at lower concentration) are consistent with film formation on the p-InP surface in this medium. This process appears clearly to be the origin of the more metallic behavior, though further investigation of the surface chemistry was not pursued.

Summary and Conclusions

The use of an electrolytic back-contact for rotating disk electrodes and a convenient demountable disk design for rotating ring-disk electrodes has been demonstrated. With metallic disks, where ohmic contact formation is not a major issue, the form of the series i-E characteristic of the

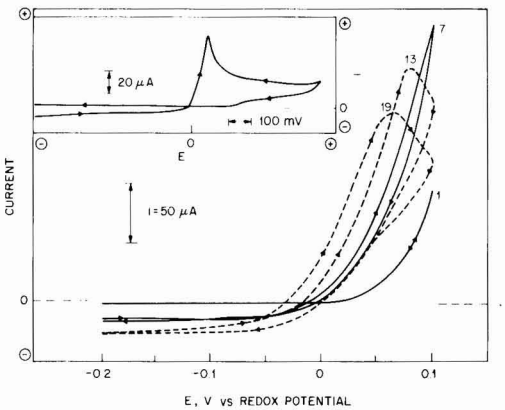

Fig. 12. Cyclic voltammograms at a dark p-InP disk with ohmic metal back-contact in 0.1M $Ru^{+3/+2}$-1M NaOAc/HOAc. Scan rate: 20 mV s^{-1}. Cycle numbers as indicated. Inset, see text.

back-cell can be applied to modifying the corresponding voltammetry at the front side. An example was shown for amperometric end-point detection in redox titrations, applicable generally to the common case of systems with all four half-reactions (waves) possible at the indicator electrode.

General utility for semiconductor disks, which are difficult to contact ohmically or have not been investigated in that regard, was demonstrated with two types of back-cell situation. In one, exemplified by the $V^{+3/+2}/H^+$ case, the rectifying nature of the back-cell conduction is accepted and less knowledge of the potential of the semiconductor under investigation is exchanged for the power to study very conveniently the photogenerated charge transfer processes and photocorrosion by the ring-disk electrode method. The second, as with the 0.1*M* total $Ru(NH_3)_6^{+3/+2}$-pH 5 solution, shows more metallic behavior, and more exact knowledge of the front side behavior is then achievable as well. With more solvent resistant insulating materials, nonaqueous electrolytes could be used in the back-cell. The greater corrosion stability of these systems for semiconductors would, in many cases, allow choice of couples that give perfectly metallic-looking behavior, *e.g.*, as in Ref. (10), in the inversion regions outside the bandgap. Though such applications imply some prior knowledge of band-edge locations, the range of nonaqueous couples that is available at quite negative or positive potentials still offers wide possibilities for finding inversion situations.

The general scope of properties of the semiconductor-electrolyte junction that may be applied in the context of the back-cell contact, coupled with the ease of exchange of the solution and the disk provided for in this design, suggests numerous opportunities in photoelectrochemical studies.

Manuscript submitted Feb. 10, 1986; revised manuscript received June 19, 1986.

AT&T Bell Laboratories assisted in meeting the publication costs of this article.

REFERENCES

1. E. H. Rhoderick, "Metal-Semiconductor Contacts," Clarendon Press, Oxford (1978).
2. V. B. Kireev, E. M. Trukhan, and D. A. Filimonov, *Russ. J. Phys. Chem.*, **52,** 1216 (1978).
3. S. Bruckenstein and B. Miller, *This Journal*, **129,** 2029 (1982).
4. S. Bruckenstein, J. M. Rosamilia, and B. Miller, *J. Phys. Chem.*, **89,** 677 (1985).
5. W. J. Albery and S. Bruckenstein, *Trans. Faraday Soc.*, **62,** 1920 (1966).
6. L. M. Schiavone and A. A. Pritchard, *J. Appl. Phys.*, **46,** 452 (1975).

7. S. Menezes, L. F. Schneemeyer, and B. Miller, *This Journal*, **128**, 2167 (1981).
8. B. Miller and S. Bruckenstein, *Anal. Chem.*, **46**, 2026 (1974).
9. A. Heller, B. Miller, H. J. Lewerenz, and K. J. Bachmann, *J. Am. Chem. Soc.*, **102**, 6555 (1980).
10. R. N. Dominey, N. S. Lewis, and M. S. Wrighton, *ibid.*, **103**, 1261 (1981).

Technical Notes

The Characterization of Via-Filling Technology with Electroless Plating Method

Yusuke Harada, Kimihisa Fushimi, Shoji Madokoro, Hideo Sawai, and Shintaro Ushio

Oki Electric Industry Company, Limited, Hachioji, Tokyo 193, Japan

A multilevel interconnection technology has become indispensable for fabricating VLSI circuits in which complicated circuits are required. Planarization in interlayer insulators has been extensively studied to fabricate a multilevel interconnection structure with higher reliability. A planarized via-hole filling is also indispensable for achieving a reliable multilevel interconnection structure. However, serious process problems occur from poor step coverage of the second metal layer in via-holes with a high cross-sectional aspect ratio. Several technologies for via-hole filling have been developed (1, 2). These technologies, however, have not yet been put into practical uses.

In this paper, we discuss a new via-hole filling technology using electroless nickel plating method (3) by which easy-to-process, damage-free, and mass production are possible (4). As a result, planarized via-filling into 2.0 μm in diameter via-holes having 100 percent yield has been achieved.

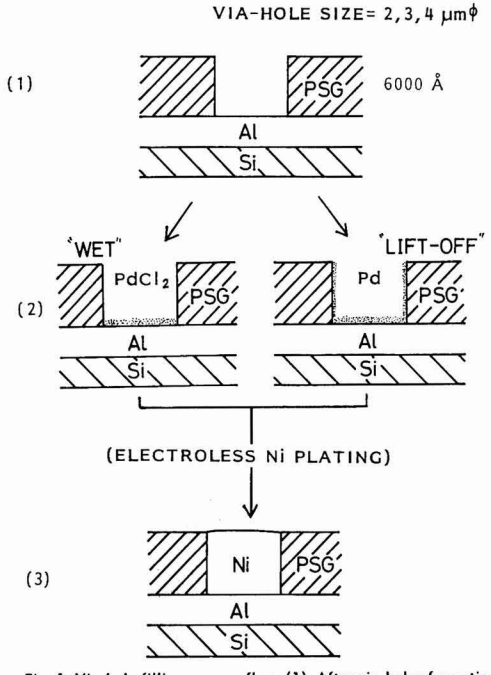

Fig. 1. Via-hole filling process flow. (1), After via-holes formation using a reactive ion etching method. (2), After selective activation into via-holes. (3), After completion of via-filling using electroless Ni plating method.

Experimental

The via-hole filling process flow used in this experiment is shown in Fig. 1. Aluminum films were patterned on 4 in. silicon substrates, and then 600 nm thickness phosphosilicate glass (PSG) films were deposited on the Al patterns for interlayer insulator. Via-holes having 2, 3, and 4 μm in diameter were formed using a reactive ion etching (RIE) method (Fig. 1-1). The bottom surface was activated for electroless plating with "wet method" or "lift-off method." In the wet method, a sample was immersed in palladium chloride ($PdCl_2$) solution, which resulted in substitution reaction between Al and Pd^{2+}. Only the bottom surface of via-holes was selectively activated. On the other hand, in the lift-off method, after via-holes were formed by the RIE method with a resist mask, Pd was vacuum evaporated followed by stripping of the mask resist. As a result, sidewall as well as bottom surfaces in the via-holes were selectively activated (Fig. 1-2). And then electroless Ni plating was performed, using Ni-B solution, only in the via-holes, which lead to planarization of upper layer interconnection (Fig. 1-3).

The shape of the via-hole filling was observed with a scanning electron microscope. Filling yields were evaluated with an optical microscope. Resistivity of the Ni film plated was measured with a 4-point probe method.

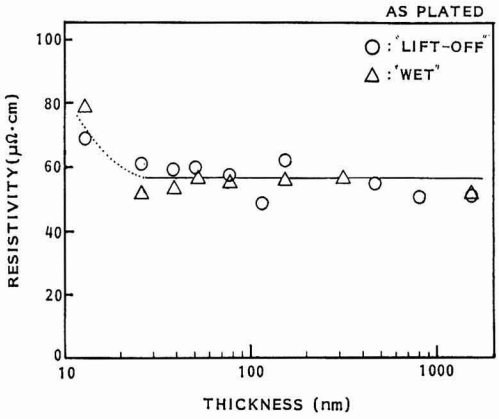

Fig. 2. The relationship between resistivity and thickness of the Ni film as plated in "wet" or "lift-off" method.

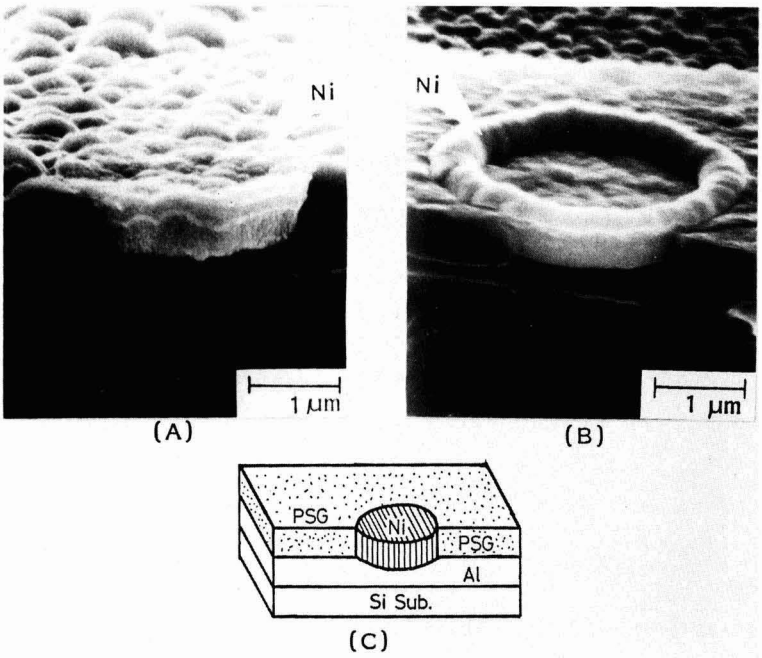

Fig. 3. Cross-sectional SEM micrographs of shape of via-holes having 2 μm in diameter filled with Ni plated films. (A), "Wet" method. (B), "Lift-off" method. (C), Schematic drawing of via-hole filling.

Results and Discussion

The relationship between resistivity and thickness of the Ni film plated in both activation methods is shown in Fig. 2. Resistivity became constant in the both samples where film thickness is more than 30 nm. This shows that "thin film effect" is diminished in a film having 30 nm in thickness. Therefore, both methods will be suitable for electroless Ni plating.

SEM micrographs showing the shape of via-holes having 2 μm in diameter filled with Ni films are given in Fig. 3. It is clearly shown that, in the both methods, the Ni film is selectively plated only in the via-holes of PSG, and via-holes are perfectly filled with the Ni films. The shape of the top of via-hole filled is different between the wet and the lift-off methods. In the wet method, an excellent flat surface was obtained. In the lift-off method, on the other hand, a bank-like surface at the periphery of the holes was obtained. The difference in the shape is due to the difference in the activated region. In the wet method, Ni films are grown only on the bottom surface because only the bottom surface is activated. As a result, a flat surface is obtained. On the other hand, in the lift-off method, both sidewall and bottom surfaces are activated, and Ni films begin to be plated on both surfaces simultaneously. And they grow isotropically. So it is presumed reasonably that bank-like surface at the periphery of the holes are formed.

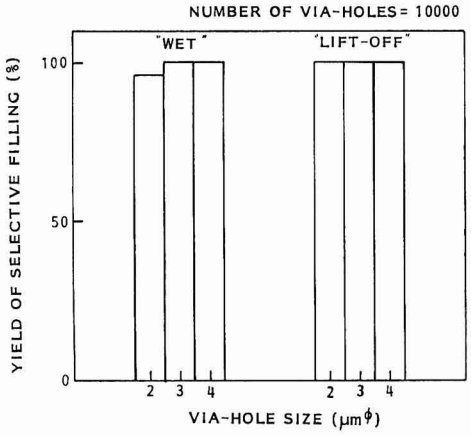

Fig. 4. Yield of the selective filling of Ni films into via-holes with 2, 3, and 4 μm in diameter for "wet" and "lift-off" methods, respectively. These were obtained by observing 10,000 via-holes with an optical microscope.

Yields of selective filling into via-holes with 2, 3, and 4 μm in diameter for both methods, respectively, are shown in Fig. 4. These results were obtained by observing 10,000 via-holes with an optical microscope. Even in the case of 2 μm via-holes, 100 percent yield was obtained by the lift-off method. On the other hand, in the wet method, 100 percent yield was obtained in the cases of 3 and 4 μm via-holes; however, a lower yield than that in the lift-off method was obtained in the case of 2 μm via-holes. The lower yield may be due to nonuniformity of substitution reaction between Al and Pd^{2+} because of imperfection of removing Al oxide films on the Al films in via-holes.

Conclusion

Electroless plating technology was investigated with a view to be applied to filling into via-holes in LSI devices. The result obtained is that selective filling into 2 μm via-holes with Ni-plated films was achieved, and planarized via-hole filling was obtained with a 100 percent process yield.

Therefore, judging from the above results and easy mass production process, it can be concluded that electroless Ni plating technology using Pd activation method is effective for planarized via-hole filling in VLSI devices.

Acknowledgment

The authors gratefully acknowledge the encouragement provided by Dr. K. Nihei.

Manuscript received May 1, 1986.

Oki Electric Industry Company, Limited assisted in meeting the publication costs of this article.

REFERENCES

1. R. E. Oakley, S. J. Rhodes, E. Armstrong, and Marsh, Proceedings of IEEE VLSI Multilevel Interconnec-

tion, p. 23, New Orleans, June 1984.
2. T. Mogami, H. Okabayashi, E. Nagasawa, and M. Morimoto, Proceedings of IEEE VLSI Multilevel Interconnection, p. 17, Santa Clara, June 1985.
3. A. Brenner, *Metal Finishing*, **52** (11), 68, **52** (12), 61 (1954).
4. T. R. Antony, *J. Appl. Phys.*, **52**, 5340 (1981).

Using Photoresist Photosensitivity Values to Maintain Critical Dimensions

Thomas R. Pampalone* and Anne M. Gilfillan

RCA Microelectronics Center, Somerville, New Jersey 08876

Maintaining the critical dimensions (CD's) of photoresist patterns during device fabrication is a major concern to device manufacturers. The successful performance of most devices depends upon the size of critical elements *e.g.*, gate electrodes. This is especially true as the circuit density increases and feature size is reduced. Linewidth control is affected by a variety of variables relating to equipment, processing, and materials (1). All these variables are subject to change and must be carefully monitored to maintain their consistency and the subsequent consistency of pattern replication.

Photoresist manufacturers do their best to provide products with consistent performance, however lot-to-lot variations in photoresist photosensitivity (2) are difficult to control (3) and result in significant CD variations unless offset by adjustments in processing conditions. Adjustments for photoresist photosensitivity are most often made on the production line by plotting the CD's of a feature with exposure dose and selecting the dose required to produce the CD desired. This operation requires additional manpower and disrupts and delays the flow of product. We propose that adjustments in exposure be made on the basis of photoresist photosensitivity values which are already determined by the photoresist manufacturer for each lot of photoresist.

Photoresist is functionally characterized by plotting the normalized film thickness after development with the logarithm of the exposure dose. The slope of the flat portion of the curve is a measure of the contrast of the photoresist and the exposure dose value at the intercept point of the slope line with the exposure dose axis is the photosensitivity value (4). Several computerized interferometry instruments are now commercially available[1] for measuring the dissolution rates of photoresist films and calculating the photoresist photosensitivity and contrast values (5). Such instruments are currently used by photoresist manufacturers to qualify photoresist lots. Other characterization tests performed by the manufacturer include percent water, particle count, percent solvents, viscosity, specific gravity, absorptivity, and percent solids. Although these latter tests are necessary to attain consistent photoresist composition, they do not measure the functional properties of the photoresist of interest to the user, such as film thickness, photosensitivity, and contrast. The functional properties of a resist are influenced by the molecular weight and dissolution rate of the novolac resin (3), and the photoresponse and dissolution rate of the diazoquinone photoactive component. Some photoresist suppliers are now providing film thickness specifications for photoresist lots, however photosensitivity values are not generally available.

Experimental

Characterization of photoresist samples.—Three samples of Acculith® (Allied Corporation) P-6010 positive photoresist (A, B, and C) were supplied by the manufacturer for this study. The photosensitivity and contrast values were determined for each sample using a Perkin-Elmer DRM development rate monitor. The resists were exposed through a multidensity resolution mask using a PLA-501F® (Canon Corporation) exposure unit in the proximity mode, and developed with LMI-600® (Allied Corporation) at 25°C. Two more photoresist samples of intermediate photosensitivity (AB and BC) were made by mixing equal weights of A and B, and B and C, respectively. The photosensitivity and contrast values for the AB and BC samples were not actually measured, but assumed to fall halfway between A and B, and B and C, respectively. Table I lists the photosensitivity and contrast values for the five photoresist samples.

Correlation of linewidth with photoresist photosensitivity.—The five photoresist samples were spun on silicon wafers primed with HMDS and baked at 90°C for 1 min to give thicknesses 1.18-1.22 μm. Two exposure sources were used, a TRE-800 SLR® (TRE Semiconductor Equipment Corporation) stepper set at 500 MS and a Microalign 241® (Perkin-Elmer Corporation) aligner using aperature 1 and 400 carriage speed setting. The 10× stepper reticle produced nominal 1.25 μm isolated photoresist lines, and the aligner mask produced nominal 1.0 μm isolated photoresist lines. For each photoresist, 5 wafers were exposed with the stepper and 5 wafers with the aligner, as described above. All of the wafers were static developed with LMI-600 developer for 90s at room temperature.

The resultant linewidths, nominally 1.25 μm for the stepper and 1.0 μm for the aligner, were measured with a System 80® (ITP, Incorporated) optical brightfield video scan instrument programmed for silicon substrate and calibrated by scanning electron microscopy. Each wafer was measured 10 times in 4 places, and average linewidth values calculated. Figure 1 correlates the measured stepper linewidth value with the photoresist photosensitivity value, and Fig. 2 correlates the measured aligner linewidth value with the photoresist photosensitivity value.

Varying stepper exposure time to maintain linewidth.—The exposure time for each resist was varied on the stepper to maintain linewidths equal to 1.25 μm. Using photoresist sample B (from Fig. 1) as the reference, exposure time for each resist sample was increased or decreased in inverse proportion to its photosensitivity

Table I. Photosensitivity and contrast values for photoresists used in the study

Photoresist sample	Photosensitivity (mJ/cm²)	Contrast
A	38	1.96 ± 0.06
AB	36*	1.94 ± 0.06*
B	34	1.90 ± 0.05
BC	32*	1.92 ± 0.04*
C	30	1.93 ± 0.03

* These values were not measured directly but determined by interpolation.

* Electrochemical Society Active Member.

[1] Commercially available are the DRM® (Perkin-Elmer Corporation) Multichannel Development Rate Monitor and the PTM® (Laserlith Corporation) Photoresist Thickness Monitor.

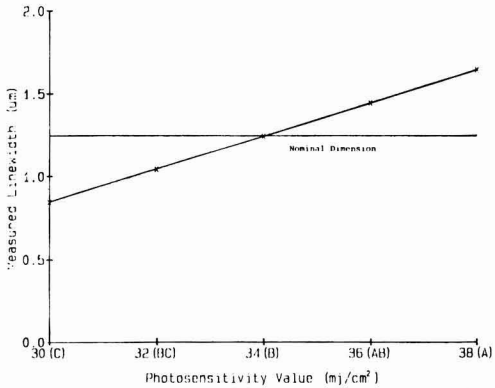

Fig. 1. Correlation of measured linewidth with photosensitivity value (stepper).

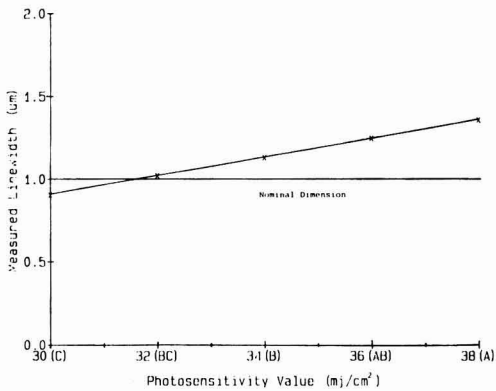

Fig. 2. Correlation of measured linewidth with photosensitivity value (aligner).

value. For instance, sample C was 13% faster than sample B (30 *vs.* mJ/cm²), therefore sample C received 13% less exposure time than sample B (435 *vs.* 500 ms). As above, each of the photoresist samples was coated on 5 wafers and soft-baked before exposure, then developed with LMI-600. The linewidths were measured and averages calculated. Table II presents the exposure times and the resultant linewidths for each photoresist sample.

Varying aligner exposure time to maintain linewidth.—The exposure time for each resist was varied on the aligner to maintain linewidths equal to 1.25 μm. Using photoresist sample AB (from Fig. 2) as the reference, the carriage speed setting for each resist sample was increased or decreased in direct proportion to its photosensitivity value. For instance sample C was 20% faster than sample AB (30 *vs.* 36 mJ/cm²), therefore sample C was exposed with carriage speed setting 20% higher (480 *vs.* 400). The wafers were developed and the linewidths measured. Table III presents the carriage speed settings and the resultant linewidths for each photoresist sample.

Using metal ion developer.—The experiment described in Table III was repeated using metal ion developer instead of metal ion free developer. After exposure with the aligner, the wafers were developed in AZ® 400K (American Hoechst Corporation) diluted 4:1 (water:developer) for 90s. The results are presented in Table IV.

Discussion

The results demonstrate that critical dimensions can be maintained by adjusting the exposure time of steppers or aligners to the photoresist photosensitivity

Table II. Varying stepper exposure time to maintain linewidth

Photoresist sample	Photosensitivity (mJ/cm²)	Exposure time (ms)	Measured linewidths (μm)
A	38	565	1.32
AB	36*	532	1.26
B	34	500	1.27
BC	32*	467	1.27
C	30	435	1.33

* These values were not measured directly but determined by interpolation.

Table III. Varying aligner exposure time to maintain linewidth

Photoresist sample	Photosensitivity (mJ/cm²)	Carriage speed setting	Measured linewidths (μm)
A	38	379	1.19
AB	36*	400	1.19
B	34	423	1.19
BC	32*	450	1.19
C	30	480	1.13

* These values were not measured directly but determined by interpolation.

Table IV. Using metal ion developer instead of metal ion free developer

Photoresist sample	Photosensitivity (mJ/cm²)	Carriage speed setting	Measured linewidths (μm)
A	38	379	1.19
AB	36*	400	1.20
B	34	423	1.20
BC	32*	450	1.20
C	30	480	1.18

* These values were not measured directly but determined by interpolation.

values. The resists studied in this paper varied ±13% in photosensitivity, more than the lot-to-lot variability generally acceptable or actually encountered (2) in production. The adjustment using the photosensitivity value appears to produce the critical dimension even when the developer used for device fabrication is different than the developer used by the manufacturer to characterize and qualify the photoresist. By knowing the photosensitivity values for each lot in advance, device makers can readily make exposure adjustments.

In this work, wafers were developed by placing them in a boat and manually immersing the boat into excess developer. This procedure is not as reproducible as automated wafer processing. For this reason, the average CD's resulting for a boat of developed wafers often differed from what was expected. For instance, in Table III, the measured linewidth for sample AB was 1.19 μm instead of 1.25 as in Fig. 1, even though the processing conditions were presumably the same. Variations may occur because of small differences in development time or agitation. However, the CD's measured in all cases (Table II-IV) corresponded to the reference wafers (photoresist sample B, AB, and AB respectively) and support the validity of the technique.

The measured linewidth variability for each photoresist sample using metal ion free developer in Table III was ± 0.06 (1σ) μm, based on 200 readings (5 wafers, measured 10 times in 4 places). The corresponding measured linewidth variability using metal ion developer in Table IV was ± 0.015 (1σ) μm. This discrepancy is due to the optical brightfield metrology technique which gives less precision for photoresist features with oblique sidewalls. Metal ion developers generally yield features with steeper sidewalls than metal ion free developers. The measured linewidth variability for the photoresist sam-

ples exposed with the stepper and developed with metal ion free developer (Table II) was ± 0.044 (1σ) μm. All of the measured linewidth values reported in Tables II, III, and IV are averages for the 200 readings taken for each photoresist sample. This statistical procedure eliminates the precision errors associated with the measurement.

More work is required to test the general applicability of using photoresist photosensitivity values to make exposure corrections. Other photoresist and developer systems need to be tested. Photoresist manufacturers can help in the evaluation by making their photosensitivity values for resist lots available to their customers.

Acknowledgment

We wish to thank Dr. Robert Owens and Mr. Robert Rinehart, who were previously with Allied Corporation, for their help in characterizing and supplying the photoresist samples used in this study.

Manuscript submitted Dec. 12, 1985; revised manuscript received June 6, 1986.

RCA Microelectronics Center assisted in meeting the publication costs of this article.

REFERENCES

1. L. F. Thompson and M. J. Bowden, in "Introduction to Microlithography," Chap. 4, p. 161, American Chemical Society, Washington, DC (1983).
2. T. R. Pampalone, M. R. Hannifan, S. Jain, and C. D. Krieger, *This Journal*, **131**, 2670 (1984).
3. T. R. Pampalone, *Solid State Technol.*, **27**, 115 (1984).
4. G. C. Willson, in "Introduction to Microlithography," Chap. 3, p. 105, American Chemical Society, Washington, DC (1983).
5. S. P. Grindle and E. K. Pavelchek, in "Proceedings of the 4th Annual Test and Measurement World Expo," Vol. 2, p. 676, Technical Publishing Company, Boston, MA (1985).

JOURNAL OF THE ELECTROCHEMICAL SOCIETY

ACCELERATED

—BRIEF COMMUNICATIONS—

NOVEMBER 1986

The Electron Energy Loss Imaging Microscope

A New Look at Oxide Scales

D. F. Mitchell and M. J. Graham*

Division of Chemistry, National Research Council of Canada, Ottawa, Canada, K1A 0R9

Electron energy loss microscopy which provides high resolution elemental maps of thin films is a developing technique in the field of biology (1). This paper reports, for the first time, the use of the technique in materials science, specifically to examine thin oxide films.

The microscope used was a Zeiss Model EM 902, an 80 kV machine. It employs a double-focussing Castaing/Ottensmeyer prism-mirror-prism as the energy dispersive unit, located before the final projector lens. With this arrangement, images can be formed with energy loss electrons of energy E and range δE (where δE is typically 15 to 40 eV), and recorded by a SIT TV camera. Fig. 1 schematically presents an electron energy loss spectrum. These spectra represent the energy lost by an incident high energy electron beam on excitation of core electrons. The absorption edges are characteristic of the atom with which the interaction occurred. To produce a useful image free of diffraction contrast it is necessary to determine the background, B, at each pixel. This can be accomplished by taking two images below the adsorption edge (2), assuming that the background is of the form AE^{-r}, where E is the energy loss in electron volts and A and r are constants that may vary from pixel to pixel. An image, I, produced by taking the ratio, peak (P)/background (B) for each pixel, effectively removes the contrast due to diffraction effects, as well as the effects of uneven illumination and screen sensitivity. The resulting image contains both concentration variation and thickness information. This can be reduced to concentration information when energy loss images are taken for two elements, and the images are processed pixel by pixel as $I_1/(I_1+I_2)$, where I_1 is the image of element 1 and I_2 is the image of element 2.

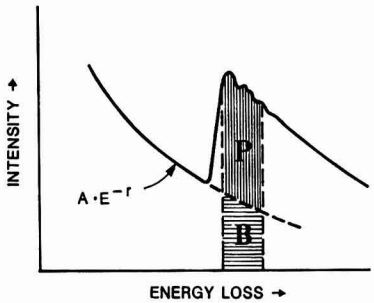

Fig. 1. Schematic of electron energy loss spectrum indicating the peak (P), and background (B) of the form AE^{-r} where E is the energy loss and A and r are constants.

Fig. 2 shows three P/B images for O, Fe and Cr from a ~30nm-thick oxide produced on Fe-25%Cr alloy by a short term oxidation at 800°C. (In all images shown in the paper, the image contrast in each picture quadrant has been expanded to use the entire gray scale range; white is maximum concentration.)

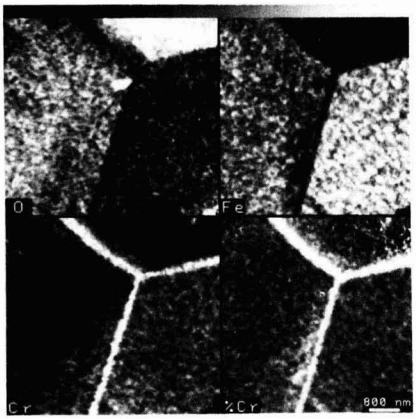

Fig. 2. Electron energy loss images for O, Fe and Cr of a ~30nm-thick oxide, produced by short term oxidation at 800°C and stripped from the Fe-25%Cr substrate. The % Cr, (Cr/Cr+Fe) x 100, image is also shown.

*Electrochemical Society Active Member

Also shown in Fig. 2 is the % Cr concentration derived from the second stage of image processing, $I_{Cr}/I_{Cr}+I_{Fe}$. Strong enrichment of Cr above the metal grain boundaries is apparent. (An electron energy loss spectrum taken of these grain boundary regions indicates pure Cr_2O_3, while a spectrum taken within a grain shows an average Cr:Fe ratio ~1.) A variation in oxide thickness both from grain-to-grain and within a grain is also indicated. There is also a non-uniform distribution of cations within each grain. This can be seen more clearly at higher magnification and expanded contrast in Fig. 3. The variation in Fe and Cr concentration, while readily visible, is quite small, as selected area diffraction shows the oxide to be a single crystal spinel. Figs. 2 and 3 are each the result of nine separate electron energy loss images (three for each element - one above and two below the absorption edge), taken with a 16 eV energy window. The total data collection time for each figure was only ~1 sec. Similar x-ray images from an analytical TEM/STEM would have taken hours to produce.

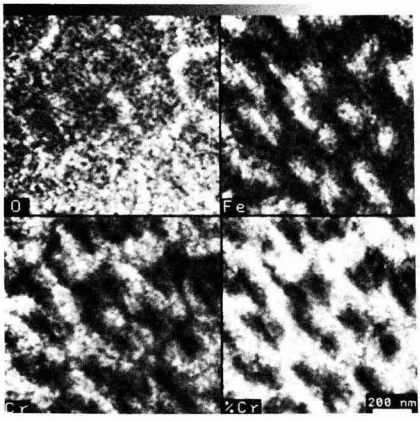

Fig. 3. As in Fig. 2, but taken at higher magnification from within an oxide grain.

An indication of the lateral resolution of the technique, and of the detection limit is shown in Fig. 4. The sample was a 5nm-thick sputtered alumina film onto which was deposited ~$3x10^{16}$ Ag atoms per cm^2. The Ag was in the form of small isolated spheres <20nm in diameter. The smallest spheres which can be readily identified in Fig. 4 in both the energy loss image and the bright field (B.F.) micrograph have a diameter ~1.5nm, and contain about 100 Ag atoms.

Manuscript received Aug. 25, 1986.

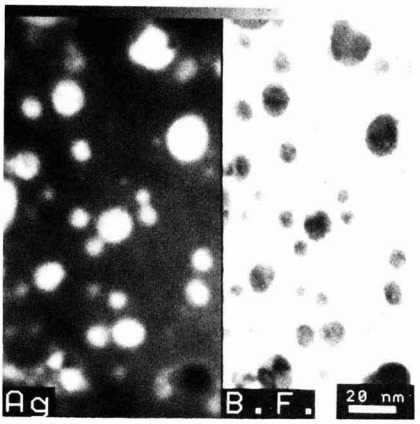

Fig. 4. Electron energy loss image for <20nm dia. Ag spheres deposited onto a 5nm-thick alumina substrate. Resolution observed ~1.5nm diameter spheres, or about 100 Ag atoms. The bright field (B.F.) image is also shown.

In this communication we have demonstrated the power and speed of electron energy loss microscopy for the chemical mapping of thin crystalline films. Resolution ~1.5nm is indicated and a hundred or so atoms can be detected with data collection times the order of one second. This capability has been achieved using an 80 kV tungsten source. The advantages offered by this microscopic technique compared to microprobe-based techniques (EDX, EELS, or Auger imaging) are such that important new information can be expected in studies of the atomistics of mass transport during metal oxidation. We intend to use the microscope to try to determine the role of reactive elements in high temperature corrosion, and to ascertain the distribution of halide ions within electrochemically-formed oxide films. The technique, of course, has readily foreseeable applications in many other areas of materials science, e.g., in microelectronics and catalysis studies.

References

1. F.P. Ottensmeyer and J.W. Andrew, J. Ultrastr. Res. 72, 336 (1980).

2. Thierry Pun and J.R. Ellis, Microbeam Analysis, Ron Gooley Ed. San Francisco Press, p. 156 (1983).

The National Research Council of Canada assisted in meeting the publication costs of this article.

Microelectrodes in Corrosion Studies

Electrodissolution and Corrosion of Copper in H_2O_2/0.1*N* HCl

R. T. Atanasoski,* H. S. White,** and W. H. Smyrl**

Department of Chemical Engineering and Materials Science, Corrosion Research Center, University of Minnesota, Minneapolis, Minnesota 55455

The application of microelectrodes in corrosion studies is a natural extension of their use in other situations (1). Corrosion may occur in low conductivity media, and very often the surface under attack resembles the size of a microelectrode. The anodic dissolution of copper on the other hand is a typical example of a process studied in order to predict the stability of this material under corrosion attack. Therefore, as a test of the applicability of microelectrodes in this classical corrosion process, copper microelectrodes have been used during this study. Other investigations of metal deposition and dissolution have utilized microelectrodes on an inert substrate (2), but the anodic dissolution of bulk metal superimposed on a second (cathodic) process, is reported here for the first time. It is proposed that the study of such bulk metal electrodes simulates real corrosion situations.

Recently, the anodic dissolution of copper in 0.1 N HCl has been used extensively as a model system for rotating disk (RDE) studies in our laboratory (3,4). The dissolution reaction is:

$$Cu + 2Cl^- = CuCl_2^- + e.$$

The reaction is mass transport-kinetic controlled and proceeds with a 60 mV slope over a wide range of the electrode potential. The possible use of copper based materials in radioactive waste disposal has led to a study of corrosion in H_2O_2 solutions (5). Besides RDE measurements, experiments with copper microelectrodes have been performed, with a final goal of performing an on site corrosion test in an irradiated environment.

Experiments and Results.--The cross section area of a sealed copper wire (25μm diameter, 99.99%) was used as an electrode in these initial tests. Some difficulty experienced in obtaining a good metal to glass seal without formation of a copper oxide at the surface was overcome by sealing under inert gas. The total anodic current passed through each microelectrode during each experimental run was integrated and not allowed to exceed an equivalent of 0.5μm of copper. Additional inspection under a microscope after the experiments did not reveal any nonuniformly dissolved parts at the copper surface. The polarization curve for anodic dissolution of copper obtained in deaerated 0.1 N HCl as well as the curves for H_2O_2 reduction are depicted in Fig. 1. The measurements were done in a cyclic voltammetry mode at a potential scan rate of 1 mV/S. There was no hysteresis in the anodic branches of the voltammograms, and a very small one in the cathodic region.

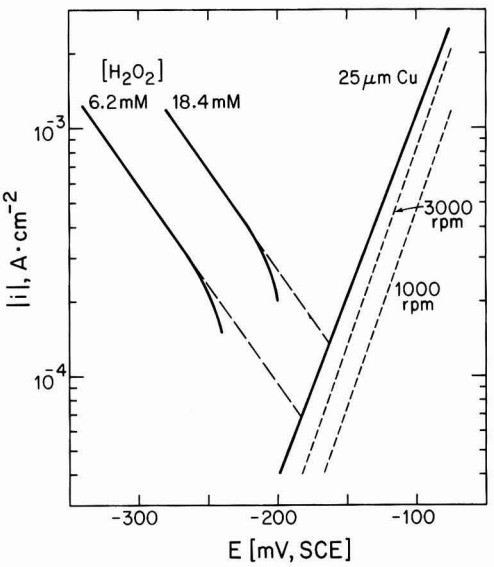

Fig. 1: Polarization curves on copper microelectrode in H_2O_2/0.1 N HCl; Rotating copper disk data at 1000 and 3000 rmp from (3).

*Institute of Electrochemistry ICTM, University of Belgrade, Yugoslavia
**Electrochemical Society Active Member
Keywords: Microelectrode, corrosion, copper dissolution.

Extremely reproducible curves were obtained going from one microelectrode to another in the same solution. Well defined straight lines with the slope of 68mV were obtained for the anodic dissolution of Cu in agreement with the reported values of 64-69 mV (3; and ref. therein) obtained with a RDE. This allows one to make comparison of the rate of the mass transport process, diffusion of $CuCl_2^-$ away from this disk as a limiting step, for the two electrodes. The difference between the anodic curve for the microelectrode and the curves for the RDE, allows one to estimate the mass transfer rate for the 25μm microelectrode to be equivalent to 4000-9000 rpm at a RDE.

The curves for the reduction of H_2O_2 exhibit a well defined slope of 120 mV/decade, with the distance between the lines in agreement with the H_2O_2 concentration. Assuming superposition of cathodic and the anodic processes, the justification for which has been indicated recently in RDE studies (5), one may calculate corrosion current densities of 6.7×10^{-5} Acm^{-2} in 6.42 mM H_2O_2 and 1.32×10^{-4} Acm^{-2} in 18.4 mM H_2O_2. This compares favorably with the RDE results.

Extending the positive potential limit in the cyclic voltammograms revealed another important similarity with the behavior noticed with the RDE. In Fig. 2, the two cyclic voltammograms differ because of the different anodic potential limit. In the anodic direction, identical current traces exhibiting ~60mV slope were recorded for the two scans. In the reverse scan, a substantial reduction current was observed in the voltammogram with the more positive anodic limit. Cathodic current in the cathodic scan direction, ascribed to CuCl film reduction, has been measured during the RDE studies in the same potential range (5).

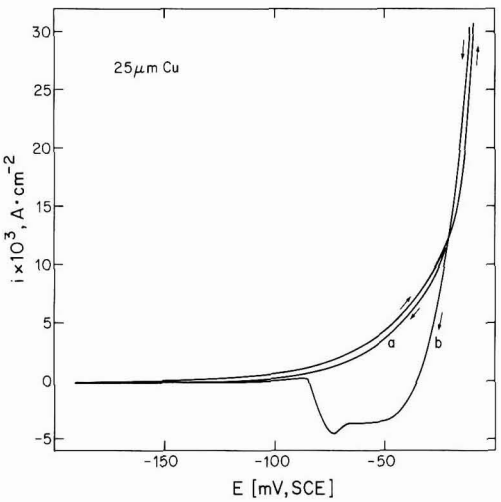

Fig. 2: Cyclic voltammograms on copper microelectrode in the presence of 18.4 mM H_2O_2; (a) anodic limit at - 20 mV, (b) anodic limit at - 5 mV; sweep rate: 5 mV/s.

Concluding remarks.--The electrochemical behavior of copper microelectrodes exhibit the property of enhanced mass transport due to spherical diffusion(1). A qualitative comparison with RDE studies (3) reveals that mass transport equivalent to rotation rates of more than 4000 rpm takes place at the 25μm Cu microelectrode.

The complete qualitative reproduction of the features noticed during the RDE studies of the anodic dissolution of copper in the presence of H_2O_2 suggest that bulk metal microelectrodes are a viable tool for in situ corrosion investigations. Moreover, the quantitative agreement with the RDE could justify the simple, speedy measurements with microelectrodes for some laboratory studies. The disadvantage of the use of a dissolving electrode is easily overcome by repolishing, with an additional benefit of having freshly polished electrode surfaces at any point of the investigation.

Further evaluation of microelectrodes in corrosion studies in low conductivity media, such as moist films, is in progress.

Acknowledgement.--The Cu microelectrodes were made in the glassblowing shop of Lawrence Livermore National Laboratory, and were provided to us by Dr. Robert Glass. Support for this work was provided by Subcontract 705760

References.--

1. R. M. Wightman, Anal. Chem., 53, (1981), 1125A.

2. W. M. Hedges and D. Pletcher, J. Chem. Soc., Farady Trans. 82, (1966), 179.

3. W. H. Smyrl, This Journal, 132, (1985), 1555.

4. W. H. Smyrl, This Journal, 132, (1985), 1563.

5. R. Atanasoki, B. Bell, and W. Smyrl, to be published.

Manuscript received July 9, 1986.

The University of Minnesota assisted in meeting the publication costs of this article.

A Highly Conductive Li^+-Glass System: (1-x) ($0.4SiS_2$-$0.6Li_2S$)-xLiI

John H. Kennedy* and Yuan Yang

Department of Chemistry, University of California, Santa Barbara, California 93106

Intensive study of amorphous fast ionic conductors, especially glasses, is presently underway because of their significance to both fundamental science and practical applications (1-3). Basically, there are two approaches for improving conductive glasses. The first is to extend glass-forming regions of known systems to higher concentrations of network modifiers and dopant salts, thereby increasing carrier concentrations. The second is to identify new glass systems or modify the structure of known systems to increase ion mobility, i.e. decrease activation energy and thereby increase conductivity.

Because of the interest in lithium batteries and the high polarizability of the sulfide ion that leads to lower potential barriers for ion migration than corresponding oxide glasses, many recent investigations have been devoted to lithium-conducting sulfide glasses (4-10). The first network formers reported were P_2S_5 (6) and B_2S_3 (4) but recent work with SiS_2 has shown it, too, can produce glasses with high conductivity (7,9,10). Moreover, SiS_2 glasses can be prepared at ambient pressure allowing more flexibility in synthesis techniques. Also, SiS_2 glasses have quite high glass transition temperatures (~300°C), which may allow higher temperature operation. Pradel and Ribes (10) recently reported that by using a twin-roller quenching technique glasses containing Li_2S up to $0.4SiS_2$-$0.6Li_2S$ could be produced. Doping with LiI gave a glass ($0.28SiS_2$-$0.42Li_2S$-0.30LiI) with a room temperature conductivity of $8.2x10^{-4}$S-cm^{-1}. We now report an extension of this glass system to 40 mol % LiI ($0.24SiS_2$-$0.36Li_2S$-0.40LiI) using a direct liquid nitrogen quench yielding conductivity of $1.8x10^{-3}$S-cm^{-1}, one of the highest values ever reported for Li^+-glasses.

*Electrochemical Society Active Member.

Key words: lithium conductor, sulfide glass, solid electrolyte

EXPERIMENTAL

Because the starting materials and glass products were extremely hygroscopic, all preparation and measurement operations, except heating and quenching, were carried out in a helium-filled glove box (<2 ppm H_2O). Anhydrous SiS_2 and Li_2S were mixed in a 2:3 mole ratio, placed in a vitreous carbon crucible, covered, and then placed in a Vycor tube. The tube was heated in a vertical furnace for 1 hr at 950°C under argon. Then the covered crucible containing the melt was removed from the tube and plunged directly into a liquid nitrogen bath. Our previous quenching method was to immerse the entire Vycor tube into ice water or liquid nitrogen.

The resultant base glass was transparent and amber-colored. This glass was ground, mixed with anhydrous LiI and given the same heating/quenching treatment as above.

X-ray diffraction patterns of the powdered glass samples sealed in plastic bags were obtained using a Norelco-Philips Diffractometer with CuK_α radiation to detect crystallinity.

Samples for conductivity measurements were prepared by pressing 0.74 cm diameter pellets uniaxially followed by an isostatic pressing at ~3 kbar. The pellets consisted of the powdered glass sandwiched between powdered TiS_2 electrodes. Conductivity was measured using the complex plane technique utilizing a Solartron 1174 Frequency Response Analyzer interfaced to a Hewlett-Packard 9845B desktop computer and a General Radio 1435 programmable decade resistance box. The 100 mV (or smaller) ac signal ranged from 1 to 10^5 Hz and measurements were taken from 20-110°C.

RESULTS

X-ray diffraction patterns showed that 40 mol % LiI could be dissolved in the glass without detectable crystallinity. Above this value small peaks due to LiI were observed.

The complex impedance plots for the samples were straight lines intersecting the real axis at ~45° angle, and the intersection was taken as the electrolyte resistance. Over the temperature range investigated, conductivities of all glasses obeyed the simple Arrhenius law form: $\sigma = \sigma_0 \exp(-E_a/kT)$, from which the values of activation energy, E_a, were determined. These values and, for comparison, the values reported by Pradel and Ribes (10) are listed in Table I. The variation of conductivity with LiI content for $(1-x)(0.4SiS_2-0.6Li_2S)-xLiI$ glasses (fast and slow quenching) and for $(1-x)(0.5SiS_2-0.5Li_2S)-xLiI$ glasses is shown in Fig. 1. The latter glasses were reported previously (9) and were prepared by the slower ice water quench technique noted above.

These results show that the direct liquid nitrogen quenching technique yields rapid cooling rates that allows higher LiI saturation values and higher conductivities. The properties are comparable to those obtained with the roller quenching method. It should be noted that Pradel and Ribes (10) reported somewhat lower activation energies and lower conductivity for x = 0, 0.3 glasses (see Table I). The conductivity value of 1.8×10^{-3} S-cm^{-1} at 25°C for $0.24SiS_2-0.36Li_2S-0.40LiI$ is one of the highest values reported for a Li^+-conducting sulfide glass and exceeds Li^+-conducting crystalline materials. These glasses, therefore, are worthy of additional study and consideration for practical applications.

ACKNOWLEDGEMENT

Partial support from Union Carbide Corporation and from the Petroleum Research Fund, administered by the American Chemical Society is gratefully acknowledged.

REFERENCES

1. J.L. Souquet, Ann. Rev. Mater. Sci., 11, 211 (1981).
2. C.A. Angell, Solid State Ionics, 18/19, 72 (1986).
3. J.P. Gabano, in "Glass..Current Issues", (NATO ASI Series), Editors A.F. Wright and J. Dupuy, Martinus Nijhoff Pub., Dordrecht, p. 457 (1985).
4. H. Wada, M. Menetrier, A. Levasseur, and P. Hagenmuller, Mat. Res. Bull., 18, 189 (1983).
5. B. Carette, M. Maurin, M. Ribes, and M. Duclot, Solid State Ionics, 9/10, 655 (1983).
6. R. Mercier, J.P. Malugani, B. Fahys, and G. Robert, Solid State Ionics, 5, 663 (1981).
7. J.R. Akridge, U.S. Patent No. 4,465,745 (1984).
8. S.J. Visco, P.J. Spellane, and J.H. Kennedy, This Journal, 132, 1766 (1985).
9. J.H. Kennedy, S. Sahami, S.W. Shea, and Z. Zhang, Solid State Ionics, 18/19, 368 (1986).
10. A. Pradel and M. Ribes, Solid State Ionics, 18/19, 351 (1986).

Table I. Conductivity and activation energy for the glasses: $(1-x)(0.4SiS_2-0.6Li_2S)-xLiI$

x	σ, S-cm^{-1} (25°C)	E_a, eV
0	5.3×10^{-4}	0.33
0.10	6.5×10^{-4}	0.31
0.20	7.7×10^{-4}	0.30
0.30	11.5×10^{-4}	0.29
0.40	17.8×10^{-4}	0.28
0.45	14.1×10^{-4}	0.29
0 (10)	5.0×10^{-4}	0.25
0.30 (10)	8.2×10^{-4}	0.27

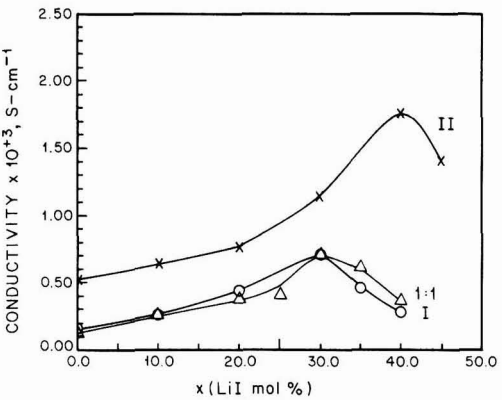

Fig. 1. Comparison of new direct liquid nitrogen quenching (II) with previous quenching technique (I) for $(1-x)(0.4SiS_2-0.6Li_2S)-xLiI$ and $(1-x)(0.5SiS_2-0.5Li_2S)-xLiI(1:1)$.

Manuscript received May 13, 1986.

The Petroleum Research Fund, American Chemical Society, assisted in meeting the publication costs of this article.

Electrochemical and Spectroscopic Studies of Metal Hexacyanoferrate Films

II. Cupric Hexacyanoferrate and Prussian Blue Layered Films

L. M. Siperko,*[,1] and T. Kuwana*[,2]

Department of Chemistry, The Ohio State University, Columbus, Ohio 43210

Considerable current interest in the immobilization of thin films of Prussian Blue (PB) and its analogous compounds on electrode surfaces (1-4) arises from several factors: i) the electrochemistry of these compounds has not been studied in detail, ii) the ability to form thin films facilitates that study, iii) the compounds are known semiconductors, iv) they exhibit a visible spectrum which is characteristic of the oxidation state of the constituent metal ions indicating potential use in electronic devices, v) such films may have use as electron transfer mediators.

This laboratory previously reported a method for immobilizing thin films of cupric hexacyanoferrate (CuHCF) on conducting substrates (4a). More recently, we have effectively produced layered ("sandwich") films of CuHCF and PB enabling the conducting properties of the films to be studied. This brief report concerns our preliminary results of the cyclic voltammetric response of these layered films.

CuHCF and PB are both semiconductors which can be electrochemically cycled in 1M K^+. PB films show two well-defined redox couples at +0.20V, $Fe^{3+/2+}$ and +0.90V, ferrate (FeIII/II). CuHCF yields only one well-defined couple at +0.69V, FeIII/II and an irreversible couple at +0.12V, $Cu^{2+/1+}$. The c-t rate of the $Fe^{3+/2+}$ couple for PB > FeIII/II and the c-t for CuHCF < PB.

The conducting properties of the films should allow transfer of charge across the film/film interface as shown in Figure 1. Thickness is calculated from charge assuming an ideal lattice. The $Fe^{3+/2+}$ couple appears at +0.20V, the CuHCF FeIII/II couple at +0.88V and the $Cu^{2+/1+}$ couple appears at +0.10V.

Reversal of the layers causes alteration of the CV response (Figure 2). Both the oxidative and reductive waves for the PB($Fe^{3+/2+}$) couple are distorted somewhat and the broad $Cu^{2+/1+}$ peaks are not now discernible. The HCF (FeII→ III) wave is displaced to more positive potential (40mV) and the PB (FeII→ III) wave is shifted negatively

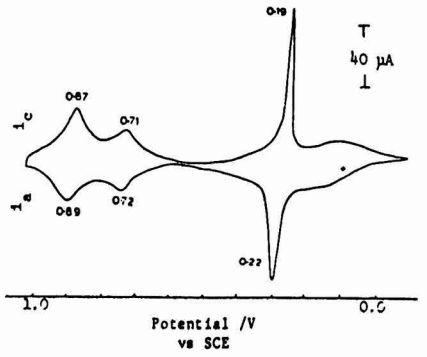

Figure 1: 2mV/s CV in 0.5M K_2SO_4 of "sandwich" electrode made by depositing PB (500A) on a CuHCF (150A) modified glassy carbon electrode.

Present address:
1 IBM systems Technology Division, Endicott, NY 13760
2 University of Kansas, Center for Bioanalytical Research, Lawrence, KS 66046

* Electrochemical Society Active Member

Keywords: Prussian blue, conducting films, semiconductors.

10 mV. Only one reductive wave (containing the charge for both films) appears for both the PB and HCF (FeIII⟶II wave, at +0.85V. Several factors may contribute to the distortion of the i-E wave, indluding: 1) interdiffusion of the two films, 2) nonuniformity of the overlying CuHCF film and/or nonuniformity of the underlying PB film, 3) chemical reduction, 4) complex resistive or kinetic effects and 5) electron trapping (5).

SEM studies showed a roughened surface with superficial cracks for the PB on CuHCF "sandwich". Since the i-E wave is not distorted (Figure 1), cracks in the film apparently have no effect on the CV response. A roughened surface with no cracks is observed for the reversed "sandwich" and all films, both layered and unlayered, completely cover the substrate surface. EDX confirmed the presence of both CuHCF and PB in the layered films as well as trace sulfur considered to be a contaminant from the electrochemical cycling process. Elemental mapping of the reduced films showed a uniform distribution of all elements across the surface with no clustering of potassium, suggesting again that nonuniformity (cracks) of the PB on CuHCF "sandwich" does not appreciably contribute to distortion of the i-E wave.

In summary, these preliminary experimental results indicate that both CuHCF and PB can transfer charge across the film/film interface and the distortion observed in the i-E response of a CuHCF on PB "sandwich" is not due to macroscopic nonuniformity of the film. Determination of the charge transfer mechanism will require additional studies.

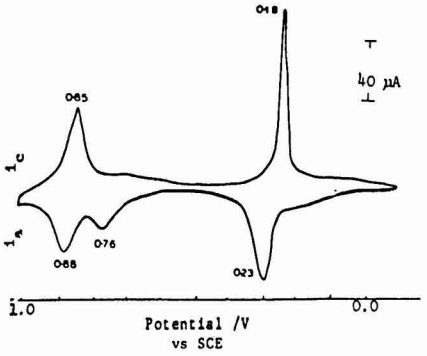

Figure 2: 2mV/s CV in 0.5M K_2SO_4 of "sandwich" electrode made by depositing CuHCF (210A) on a PB (500A) modified glassy carbon electrode.

Manuscript submitted April 11, 1986; revised manuscript received Aug. 20, 1986.

ACKNOWLEDGMENT

This work was supported by a grant from the National Science Foundation. We are grateful to V. Neff and K. Itaya for making preprints of their studies available to us.

REFERENCES

1. a) V.D. Neff, This Journal, 125, 886 (1978).
   b) D. Ellis, M. Eckhoff and V.D. Neff, J. Phys. Chem., 85, 1225 (1981).
   c) V.D. Neff, This Journal, 132, (1985).
   d) T. Ohzuku, K. Sawai and T. Hirai, This Journal, 132, 2829 (1985).

2. a) K. Itaya, H. Akahoshi, S. Toshima, This Journal, 129, 1498 (1982).
   b) K. Itaya, K. Shibayama, H. Akahoshi, S. Toshima, J. Appl. Phys., 53, 1 (1982).
   c) K. Itaya, T. Ataka, S. Toshima, J. Am. Chem. Soc., 104, 4767 (1982).
   d) K. Itaya, T. Ataka, S. Toshima, J. Am. Chem. Soc., 104, 3751 (1982).

3. a) H. Kellawi and D.R. Rosseinsky, J. Electroanal. Chem., 131, 373 (1982).
   b) R.J. Mortimer and D.R. Rosseinsky, J. Chem. Soc. Dalton Trans., 2059 (1984).
   c) A. Viehbeck and D.W. DeBerry, This Journal, 132, (1985).

4. a) L.M. Siperko and T. Kuwana, This Journal, 130, 396 (1983).
   b) L.M. Siperko, Ph.D. Thesis, The Ohio State University (1983).

5. a) P.G. Pickup, C.R. Leidner, P. Denisevich and R.W. Murray, J. Electroanal. Chem., 164, 39 (1984).

The IBM Corporation assisted in meeting the publication costs of this article.

JOURNAL OF THE ELECTROCHEMICAL SOCIETY

REVIEWS AND NEWS — NOVEMBER 1986

Reports on Electrochemical Society Summer Fellowship Awards

During the summer of 1985, the following students received grants of $2000.00 for use in electrochemical research, as part of the three Summer Fellowship Awards of The Electrochemical Society, Inc.

Mr. John N. Harb, University of Illinois, Champaign-Urbana, Illinois, received the Edward G. Weston Fellowship.

Mr. Dean A. Van Galen,[1] Kansas State University, Manhattan, Kansas, was the winner of the Colin Garfield Fink Fellowship.

Mr. Charles M. Lieber,[2] Stanford University, Stanford, California, was awarded the Joseph W. Richards Fellowship.

The Summer Fellowship Awards are made "without regard to sex, citizenship, race, or financial need, to a fellow or teaching assistant pursuing work between the degrees of B.S. and Ph.D. on a subject in a field of interest to The Electrochemical Society," They are intended to cover a period during which the recipient has no financial support for the continuance of his or her work.

The Edward G. Weston Summer Fellowship Report

Critical Hydrodynamic Conditions for Disruption of Single Corrosion Pits on Stainless Steel

John N. Harb

Localized pitting corrosion is particularly detrimental, since perforation of a metal may occur with dissolution of only a small fraction of the metal volume. The present study investigates the role of transport during pit growth. Evidence that mass transfer controls the pitting process has been presented by Rosenfeld and Danilov (1) and Isaacs (2). Indeed, the local pit environment has been shown to be chemically different than that of the bulk solution (3), and, in some systems, there is evidence for the precipitation of salt films on the active pit surfaces (2, 4, 5).

Forced convection influences the pitting process by changing the mass-transfer rate and thus the local solution composition. In a study of artificial pits on iron and multiple pits on stainless steel, Beck and Chan (6) observed that the initiation of flow led to either an increased dissolution rate or repassivation, depending on the system involved. The effect of flow on the pitting of stainless steel has also been studied by Sato *et al.* (7) and Macdonald *et al.* (8).

The Peclet number (Pe), a dimensionless group that characterizes the ratio of convective mass transport to diffusive transport, is an important parameter for describing mass transfer in cavities (9, 10). In a recent theoretical study related to pitting, Alkire, Reiser, and Sani (10) introduced the concept of a critical Peclet number above which precipitation of a salt film on the cavity surface was not possible. If a saturated surface film were necessary for pit stability, pit deactivation would be expected above this critical value of the Peclet number.

A major obstacle to quantitative analysis of the pitting process has been the high density of pits usually found on a metal surface. With multiple pits on the surface, it is necessary to consider pit interactions and the age distribution of pits over the surface (as all pits do not nucleate simultaneously) in addition to the individual pit growth process. These problems were avoided in the present study through the use of single pits, which allow quantitative examination of the pit growth process.

Experimental

The pitting of 304 stainless steel was examined in an electrolyte consisting of 0.1*M* Na_2SO_4 (Reagent grade, Mallinckrodt) and 0.2*M* NaCl (Reagent grade, Fisher Scientific) in distilled-deionized water with a small amount of H_2SO_4 to bring the solution pH to 3.5. The working electrode was the flat cross section of a 304 stainless steel wire (0.004 in. diam, A. D. McKay Incorporated), which had been annealed according to the ASM Metals Handbook (11) and cast into epoxy (Epoxide Resin 20-8130-032 and Epoxide Hardener 20-8132-008, Buehler). The reference electrode was a solid Ag/AgCl electrode. The platinum counterelectrode was large with respect to the working electrode.

The working electrode was mounted flush with the bottom wall of a rectangular flow channel whose cross section was 8 mm wide by 4 mm high. The flow channel was part of a flow system equipped to provide flows over the range of 0.005-11.7 liters/min. Piping, tubing, and fittings were all of polypropylene. The system reservoir was of polyethylene and had a 10 liter capacity. The desired flow was provided by one of two different corrosion-resistant centrifugal pumps, depending on the velocity desired. The maximum channel Reynolds number was 31,000.

Potential was controlled with a potentiostat/galvanostat (PAR Model 173) equipped with a current follower (PAR Model 176). Current *vs.* time data were recorded on a X-Y recorder (Series 2000, Houston Instruments).

The surface preparation of the working electrode was found to be important in determining its pitting behavior. After having been cast into epoxy, the electrode was polished with 600 grit paper on an irrigated polishing wheel. After polishing, the surface was rinsed with distilled water, ethanol (U.S.I. Pure, U.S. Industrial Chemicals), and again with distilled water. The surface was then hand polished with 4/0 emery paper (Buehler) without lubricant. Without this final polishing step, the electrode was not observed to pit at times less than one or two hours. The surface after the polishing had a roughness on the order of 1 μm. The final polishing was done in the direction of flow so that any residual roughness would have little effect, if any, on the flow field near the wall. There was no significant change in height between the epoxy and the embedded electrode.

After the final polishing step, the electrode was rinsed with distilled water and placed immediately into the flow cell. A potential of 0.8V *vs.* Ag/AgCl was then applied between the working and reference electrode and the current was recorded as a function of time. Initiation of pitting was evident by a rise in current. The pit was allowed to grow under stagnant conditions until the current reached a predetermined value at which time flow was initiated. All experiments were done at 25° ± 1°C.

Examination of corrosion samples was performed with an inverted optical microscope (EPIPHOT-TME, Nikon). The fine focus knob was calibrated in microns to make possible accurate and facile measurement of depth. The diameter of the pit opening was obtained from calibrated photomicrographs of the pit.

[1]Currently at the University of California, Berkeley, California.
[2]Currently at the California Institute of Technology, Pasadena, California.

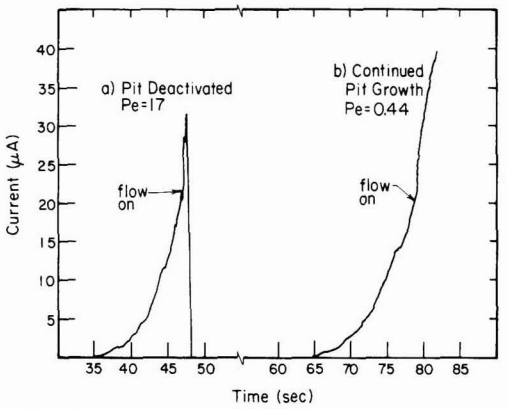

Fig. 1. Current *vs.* time curves for two different experiments in which a single pit growing under potentiostatic control (0.8V *vs.* Ag/AgCl) was subjected to flow. Electrode: 304 stainless steel; electrolyte: 0.1M Na_2SO_4, 0.2M NaCl (pH = 3.5).

Results and Discussion

By the procedure given above, single corrosion sites were obtained, which permitted quantitative characterization of the effect of fluid flow on the pitting process. Corrosion pits were round when viewed from above, indicating the presence of a resistive surface layer, which caused isotropic dissolution of the pit surface as opposed to the crystallographic dissolution observed near the equilibrium potential. The pits were shallow (*i.e.*, the depth was less than the radius of the pit opening) and showed no evidence of a cover (14).

The purpose of the experiments was to determine the effect of convection on a pit growing under potentiostatic control in a stagnant medium. A typical current *vs.* time plot for two experiments is given in Fig. 1. In each case, the pit grew under stagnant conditions until the time indicated at which flow was initiated. In the first case (Fig. 1a), the influence of flow caused a sudden increase in current, followed by a subsequent decrease to zero current as the pit died. The dependence of the current upon time was different for pits that did not die, as shown in Fig. 1b. While the current rose quickly when flow was initiated, no subsequent decrease was observed. In fact, after the rapid rise, the current continued to increase at an accelerated rate.

As mentioned previously, the Peclet number ($u_o r_o/D$) is a dimensionless group that can be used to characterize diffusive and convective transport in cavities (9, 10). For the present application, the characteristic length was chosen to be the radius of the pit opening (r_o). The diffusion coefficient (D) was taken from the literature and corrected for the viscosity of the present solution (12, 13). The characteristic velocity (u_o) was taken as one tenth of the velocity of the undisturbed flow field at a distance of one radius above the channel wall, based on theoretical calculations (14) that showed this velocity to be characteristic of the velocities inside the cavity. The assumption of a linear velocity profile very near the wall yielded

$$u_w = \frac{r_o}{10} \left.\frac{\partial u}{\partial y}\right|_{y=0} \quad [1]$$

where y is the distance normal to the wall. The velocity gradient at the wall was approximated by the theoretical solution for fully developed flow in laminar flow experiments. For turbulent flow in the channel, the velocity gradient at the wall was approximated with a turbulent pipe correlation with use of the hydraulic diameter of the channel. Use of velocity gradients for fully developed flow was justified owing to the short time required for the wall shear stress to approach its steady-state valve.

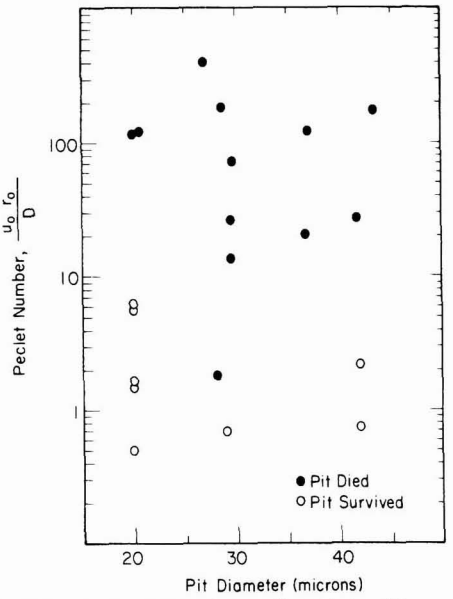

Fig. 2. Deactivation of pitting due to sudden initiation of flow over a pit growing under stagnant conditions as a function of the Peclet number for the system. Electrode: stainless steel 304; electrolyte: 0.1M Na_2SO_4, 0.2M NaCl (pH = 3.5); potential: 0.8V *vs.* Ag/AgCl.

Results shown in Fig. 2 illustrate results obtained for various pit sizes and for various flow rates expressed as Peclet numbers. The solid and open symbols represent, respectively, pits that died and pits that did not die when flow was initiated. At high values of the Peclet number (*i.e.*, Pe > 10), corrosion pits were deactivated by the flow. At low Pe (*i.e.*, Pe < 1), increased convection did not disrupt the pit growth sufficiently to cause deactivation. In fact, the growth rate actually increased with flow in cases where the pit did not die. Thus, we see that flow had a significant effect on the pitting process even at low Pe, and that Pe was a critical parameter for predicting the response of the pit to sudden initiation of flow for the system under study.

Conclusion

The effect of fluid flow on pitting corrosion of 304 stainless steel was investigated experimentally with use of single corrosion pits grown under potentiostatic control. Under certain conditions, the sudden initiation of flow caused the dissolution current of a corrosion pit to increase rapidly to an upper limit and then drop to zero, resulting in deactivation of the pit. A critical condition for the disruption of pit growth by fluid flow was defined in terms of the Peclet number. Pit deactivation was found for Pe > 10; corrosion pits were found to survive the sudden initiation of flow for Pe < 1. The results demonstrate the importance of mass transfer in the pitting process and the utility of hydrodynamic flow as an experimental probe for the study of pitting corrosion and other related phenomena.

Acknowledgments

The author wishes to thank The Electrochemical Society, Incorporated, for generous support through the Edward G. Weston Fellowship for the Summer of 1985. This work was also funded in part by the Department of Energy, Office of Basic Energy Sciences, via the Materials Research Laboratory, University of Illinois, Urbana, Illinois (ER1198).

REFERENCES

1. I. L. Rosenfeld and I. S. Danilov, *Corros. Sci.*, **7**, 129 (1967).
2. H. S. Issacs, *This Journal*, **120**, 1456 (1973).

3. Z. Szklarska-Smialowska, in "Localized Corrosion," R. W. Staehle, B. F. Brown, J. Kruger, and A. Agrawal, Editors, p. 312, NACE-3, Houston, TX (1974).
4. T. R. Beck and R. C. Alkire, *This Journal*, **126**, 1662 (1979).
5. T. R. Beck, *ibid.*, **120**, 1317 (1973).
6. T. R. Beck and S. G. Chan, *Corrosion*, **37**, 665 (1981).
7. N. Sato, T. Nakagawa, K. Kudo, and M. Sakashita, in "Localized Corrosion," R. W. Staehle, B. F. Brown, J. Kruger and A. Agrawal, Editors, p. 447, NACE-3, Houston, TX (1974).
8. D. D. Macdonald *et al.*, in "Proceedings of International Symposium on Environmental Degradation of Materials in Nuclear Power Systems-Water Reactors," sponsored by NACE, Met. Soc. AIME, and ANS, Myrtle Beach, SC, Aug. 22-25, 1983.
9. R. K. Schroeder, M.S. Thesis, University of Illinois, Urbana, IL (1984).
10. R. C. Alkire, D. B. Reiser, and R. L. Sani, *This Journal*, **131**, 2795 (1984).
11. "ASM Metals Handbook," 9th ed., Vol. 4, p. 624, American Society for Metals, Metals Park, OH (1981).
12. A. M. Baticle, F. Perdu, and P. Vennereau, *C. R. Acad. Sci. Paris*, **264**, 12 (1967).
13. A. J. Bard and L. R. Faulkner, "Electrochemical Methods," p. 154, John Wiley and Sons, New York (1980).
14. J. N. Harb, M.S. Thesis, University of Illinois, Urbana, IL (1986).

The Colin Garfield Fink Summer Fellowship Report

The Electrochemical Reduction of Diazodimedone: Formation of the Carbene Anion Radical

Dean A. Van Galen

Recent work in our laboratory has examined the electrochemical reduction of diazoalkanes ($R_2C=N_2$) in hopes that the initially formed diazoalkane anion radical ($R_2C=N_2^{\cdot}$) would react by loss of dinitrogen to yield the carbene anion radical ($R_2C^{\cdot}$). This species represents a potentially useful reactive intermediate. Thus far, evidence consistent with the formation of $R_2C^{\cdot}$ by loss of N_2 from $R_2C=N_2^{\cdot}$ has been reported in only two cases: $(EtO_2C)_2C^{\cdot}$ and $PhC(O)CPh^{\cdot}$ (1, 2).

This report summarizes studies involving the electrochemical reduction of diazodimedone (2-diazo-5,5-dimethyl-1,3-cyclohexanedione or DM = N_2). This compound was examined in an attempt to better understand what types of diazoalkane structures and solution conditions favor the reaction of $R_2C=N_2^{\cdot}$ species by loss of N *vs.* other possible pathways. DM = N_2 was chosen for study because of its unique cyclic structure and because it was felt that it would be a viable $R_2C^{\cdot}$ precursor due to the relatively high acidity of its corresponding methylene carbon acid (pK_a (dimedone) = 11.2) (3).

Results and Discussion

In the absence of an added proton donor, the cyclic voltammogram for the reduction of DM = N_2 in butyronitrile (BN) – 0.1*M* $(n\text{-Bu})_4NClO_4$ at 22°C consists of a single cathodic peak near −1.84V (*vs.* Pt quasi-reference electrode whose potential is 0.35V *vs.* SCE). On the reverse, anodic sweep there is no apparent anodic peak for the oxidation of unreacted DM = $N_2^{\cdot}$, but an anodic process at 0.4V is observed, which is due to the irreversible oxidation of the conjugate base of dimedone (DMH^-). This assignment is based on the facts that: (*i*) addition of a base to a solution of dimedone (DMH_2) results in the appearance of an anodic peak at 0.4V; and (*ii*) DMH^- is the principal product of the controlled-potential electrolytic reduction of DM = N_2 (yield = 64%, n = 1 in aprotic media). DMH^- was also identified as the major product of the coulometric reduction of DM = N_2 in the presence of $(EtO_2C)_2CH_2$ and/or 1,4-cyclohexadiene (yield = 78-100%).

The basic question that is raised by the electrochemical transformation of DM = N_2 into DMH^- is whether the loss of dinitrogen precedes or follows carbon-hydrogen bond formation. Specifically, is the carbene anion radical, $DM^{\cdot}$, formed as an intermediate in the reaction of DM = $N_2^{\cdot}$? In order to determine the sequence of bond making and bond breaking in DM = $N_2^{\cdot}$, a study of its reaction kinetics was performed. Since DM = $N_2^{\cdot}$ is too unstable at room temperature to permit these studies with our instrumentation, subambient temperatures were used in order to increase the lifetime of DM = $N_2^{\cdot}$. Kinetics studies involving DM = $N_2^{\cdot}$ were performed in BN (mp −112°C) (4) at temperatures equal to or less than −64°C.

At −84°C and a scan rate of 10 V/s, the cyclic voltammogram of DM = N_2 at a platinum working electrode consists of a cathodic peak ($E_{p,c}$ = −2.2V) due to the reduction of DM = N_2 and two major anodic peaks at −0.2 and 0.8V. The more positive anodic peak ($E_{p,a}$ = 0.8V when v = 10 V/s and T = −84°C) corresponds to the irreversible oxidation of the principal product, DMH^-. The relative magnitude of the DMH^- peak increases at the expense of the anodic peak at $E_{p,a}$ = −0.2V with either a decrease in the scan rate or an increase in the temperature. At a scan rate of only 0.2 V/s, the anodic peak at −0.2V is no longer observable. Although the cathodic peak for the reduction of DM = N_2 and the anodic peak at −0.2V at −84°C (v = 10 V/s) are separated by 2V, these peaks constitute a chemically reversible couple. The assignment of the anodic peak at −0.2V to the oxidation of unreacted DM = $N_2^{\cdot}$ is based on the results of a triple-potential-step chronoamperometry (TPSCA) study (5). The results of the TPSCA experiment indicate that the reduction of DM = N_2 involves an EC process. The rate constant for the reaction of DM = $N_2^{\cdot}$ in BN was measured under varying conditions of temperature, concentration, and electrode material by double-potential-step chronoamperometry (DPSCA) (Table I). The data give a satisfactory fit for an EC process in which the rate law is $-d[DM=N_2^{\cdot}]/dt = k[DM=N_2^{\cdot}]$ and k = 1.0 ± 0.1 s^{-1}. Since the rate constant was found to be independent of both the concentration of DM = N_2 (3.4 m$M \le [DM=N_2] \le$ 10.4 mM) and cathodic electrolysis time (0.2s $\le \tau \le$ 1s), DM = $N_2^{\cdot}$ must undergo a first-order or pseudo first-order reaction. The reaction of DM = $N_2^{\cdot}$ was found to be somewhat slower when the reduction is effected at a glassy carbon electrode (k = 0.6 ± 0.1 s^{-1}) than at a platinum electrode (k = 1.0 ± 0.1 s^{-1}). This is probably an artifact that arises due to adsorption of DM = $N_2^{\cdot}$ in the case of glassy carbon.

In view of the fact that the electrochemical reduction of DM = N_2 affords DMH^- as the principal product, there are three plausible rate-determining steps for the reaction of DM = $N_2^{\cdot}$: (*i*) abstraction of a hydrogen atom to give DM = NNH^- or $DMHN_2^-$; (*ii*) abstraction of a proton from a component of the solvent-electrolyte system to give either $DMHN_2$· or DM = NNH·; and (*iii*) loss of N_2 to form the carbene anion radical, $DM^{\cdot}$. In order to distinguish among these possibilities, the electrochemical behavior of DM = N_2 was examined in the presence of various hydrogen-atom and proton donors.

The addition of a large excess of 1,4-cyclohexadiene (0.6*M*) caused no discernible change in the lifetime of DM = $N_2^{\cdot}$ at −84°C. Since the methylene carbon-hydrogen bond energy in 1,4-cyclohexadiene (D^o = 70 kcal/mol) (6) should be low relative to that of any of the carbon-hydrogen bonds in BN (for example, $D^o(NCCH_2\text{-}H)$ = 92.9

Table I. Kinetic data for the reaction of the diazodimedone anion radical in $CH_3(CH_2)_2CN$

Entry	Temp (°C)	Electrode	Added species[a]	k, s^{-1} by DPSCA
1	−84	Pt	—	1.0 ± 0.1
2	−84	Glassy C	—	0.60 ± 0.1
3	−84	Pt	Ph_2CH_2	1.0 ± 0.1
4	−84	Pt	$PhNH_2$	1.1 ± 0.1
5	−64	Pt	—	14.5 ± 2
6	−97	Pt	—	0.54 ± 0.1

[a][Added species]/[DM = N_2] ≥ 10.

kcal/mol) (7), it is unlikely that the rate-determining step in the reaction of DM = $N_2^{\cdot-}$ involves hydrogen-atom abstraction. Furthermore, the addition of tenfold or greater excesses of diphenylmethane ($D^0(Ph_2CH\text{-}H)$ = 81.4 kcal/mol) (8) and aniline ($D^0(C_6H_5NH\text{-}H)$ = 80 kcal/mol) (9) had no apparent effect on the rate of DM = $N_2^{\cdot-}$ reaction (entries 3 and 4, Table I).

It is plausible that the rate-determining step in the reaction of DM = $N_2^{\cdot-}$ in the absence of an added proton involves protonation by either trace amounts of adventitious water ($pK_a^{Me_2SO}$ (H_2O) = 31.4) (10) or a component of the solvent-electrolyte system. In order to test this possibility, the cyclic voltammetric and coulometric reductions of DM = N_2 were effected in the presence of a large excess of $(EtO_2C)_2CH_2$, an electroinactive carbon acid ($pK_a^{Me_2SO}$ ($(EtO_2C)_2CH_2$) = 16.4) (3). As determined by rapid-scan cyclic voltammetry, the addition of $(EtO_2C)_2CH_2$ caused no discernible change in the lifetime of DM = $N_2^{\cdot-}$ at −84°C. This means that $(EtO_2C)_2CH_2$ does not protonate DM = $N_2^{\cdot-}$. Furthermore, since $(EtO_2C)_2CH_2$ is a considerably stronger proton donor than either water or BN-0.1*M* (n-Bu)$_4$NClO$_4$, DM = $N_2^{\cdot-}$ cannot be undergoing rate-determining proton abstraction in aprotic media.

The controlled-potential electrolytic reduction of DM = N_2 in the presence of excess $(EtO_2C)_2CH_2$ affords DMH^- in 78% yield. However, in contrast to the n value of 1 that is obtained for the reduction of DM = N_2 in aprotic media, an n value of 2 is obtained when excess $(EtO_2C)_2CH_2$ is present. This change in n value is expected if DM = $N_2^{\cdot-}$ undergoes rate-determining loss of N_2 to give the carbene anion radical, $DM^{\cdot-}$ (Eq. [2]). This species would then either hydrogen-atom abstract from a component of the solvent-electrolyte system in aprotic media (Eq. [3]) or be protonated to give the electroactive radical DMH· in the presence of $(EtO_2C)_2CH_2$ (Eq. [4]). Since DM = $N_2^{\cdot-}$ is quite long-lived under these reaction conditions, it must decompose in bulk solution. The consumption of the second electron occurs, then, when $DM^{\cdot-}$ is protonated by $(EtO_2C)_2CH_2$ to give DMH· and DMH· is subsequently reduced by unreacted DM = $N_2^{\cdot-}$ (Eq. [5]). Because the cathodic peak potential for the reduction of DM = N_2 ($E_{p,c}$ = −1.8V at room temperature) is considerably more negative than the anodic peak potential for the oxidation of DMH^- ($E_{p,a}$ = 0.8V), this homogeneous electron-transfer reaction is thermodynamically favorable and should proceed rapidly.

The following is a proposed scheme for the electroreduction of DM = N_2

$$DM = N_2 + e^- \underset{k_{b,h}}{\overset{k_{f,h}}{\rightleftharpoons}} DM = N_2^{\cdot-} \quad [1]$$

$$DM = N_2^{\cdot-} \xrightarrow{k} DM^{\cdot-} + N_2 \quad [2]$$

$$DM^{\cdot-} + SH \rightarrow DMH^- + S\cdot \quad [3]$$

$$DM^{\cdot-} + HA \rightarrow DMH\cdot + A^- \quad [4]$$

$$DMH\cdot + DM = N_2^{\cdot-} \rightarrow DMH^- + DM = N_2 \quad [5]$$

where SH = hydrogen atom donor and HA = proton donor.

In order to test for possible competition between proton and hydrogen-atom abstraction by $DM^{\cdot-}$, the coulometric reduction of DM = N_2 was carried out in the presence of both $(EtO_2C)_2CH_2$ and 1,4-cyclohexadiene. Since these species have been demonstrated to have no apparent effect on the lifetime of DM = $N_2^{\cdot-}$, any change in the coulometric n value that occurs when either one or both of these species are present must be the result of their reaction with $DM^{\cdot-}$. Accordingly, the coulometric n value is predicted to vary from the lower limit of 1 if reaction of $DM^{\cdot-}$ occurs exclusively by hydrogen-atom abstraction from 1,4-cyclohexadiene (Eq. [1]-[3]) to an upper limit of 2 if $DM^{\cdot-}$ is captured completely by $(EtO_2C)_2CH_2$ (Eq. [1], [2], [4], and [5]). With both 1,4-cyclohexadiene and $(EtO_2C)_2CH_2$ present, an n value of 1.61 is experimentally observed which demonstrates that hydrogen-atom abstraction is competitive with proton transfer under the specified reaction conditions.

In summary, evidence consistent with the formation of the carbene anion radical, $DM^{\cdot-}$, in the electroreduction of DM = N_2 has been obtained. Whether or not carbene anion radical reactions of synthetic importance can compete with hydrogen-atom and proton abstraction pathways will be examined in future studies in this laboratory.

Acknowledgments

The author gratefully acknowledges the support of The Electrochemical Society, Inc. through the Colin Garfield Fink Summer Fellowship. Thanks are also extended to the National Science Foundation for partial support of this work.

REFERENCES

1. D. A. Van Galen, M. P. Young, M. D. Hawley, and R. N. McDonald, *J. Am. Chem. Soc.*, **107,** 1465 (1985).
2. D. Bethell, L. J. McDowall, and V. D. Parker, *J. Chem. Soc., Chem. Commun.*, 308 (1984).
3. W. N. Olmstead and F. G. Bordwell, *J. Org. Chem.*, **45,** 3299 (1980).
4. R. P. Van Duyne and C. N. Reilley, *Anal. Chem.*, **44,** 142 (1972).
5. D. A. Van Galen, M. P. Young, and M. D. Hawley, *J. Electroanal. Chem.*, **53,** 175 (1984).
6. D. G. L. James and R. D. Stuart, *Trans. Faraday Soc.*, **64,** 2752 (1968).
7. A. H. Zimmerman and J. I. Brauman, *J. Am. Chem. Soc.*, **99,** 3565 (1977).
8. M. J. Rossi, D. F. McMillen, and D. M. Golden, *J. Phys. Chem.*, **88,** 5031 (1984).
9. J. A. Kerr, *Chem. Rev.*, **66,** 465 (1966).
10. W. N. Olmstead, Z. Margolin, and F. G. Bordwell, *J. Org. Chem.*, **45,** 3295 (1980).

The Joseph W. Richards Summer Fellowship Report

Probing Polymer-Induced Reactivity Effects in Modified Electrode/Catalyst Systems

Charles M. Lieber

The application of polymer-modified electrodes to electrocatalysis is currently an active area of chemical research (1). A number of reported studies have focused on elucidating the mechanisms of charge propagation through these modified electrodes, and, for outersphere systems, a fairly detailed picture of the factors controlling charge transport is now in hand (2-5). There are, however, few reported studies that address the question of whether or not the polymer environment can be utilized to change the intrinsic reactivity of an electrocatalytic system (6), despite the fact that one of the initial goals in the field of chemically modified electrodes was to determine whether unique reactivity could be observed for these immobilized systems (7).

In the related field of polymer-supported catalysis, it is well documented (8) that the activity of a supported catalyst may be considerably different than that observed for the same catalyst in homogeneous solution. Changes in the experimentally measured activity may be due to factors (9) such as reactant partition coefficients, reaction site homogeneity, and reactant and product diffusion, as well as changes in the intrinsic activation parameters.

The approach we are pursuing to elucidate reactivity effects in modified electrode systems involves using a well-defined (in solution) model catalyst system to probe the polymer environment, *i.e.*, the substitution kinetics of $Ru(NH_3)_5(H_2O)^{2+}$ with substituted pyridines, Eq. [1]

$$Ru(NH_3)_5(H_2O)^{2+} + R\text{-}Py \rightarrow Ru(NH_3)_5(R\text{-}Py)^{2+} + H_2O \quad [1]$$

In our system, the ruthenium(II) complex is electrostatically bound into Nafion films that have been recast on pyrolytic graphite electrodes. The substitution reaction has been well studied in aqueous solution (10-11) providing a point of reference with which to compare the results for the Nafion-phase reaction. Notably, in an earlier communication (12), we reported that the substitution kinetics for the reactions of isonicotinamide, pyridine, and 4-pyridyl-

carbinol at $Ru(NH_3)_5(H_2O)^{2+}$, electrostatically bound into Nafion-modified electrodes, showed substantial differences in reaction rates compared with aqueous solution. In addition, this initial study indicated that these reactivity changes were predominantly controlled by entropic effects. The work described in this report provides additional insight into the unique reactivity effects that can be observed in polymer-modified electrode systems.

Experimental

Materials.—A commercially available (Aldrich) 5.0 weight percent (w/o) solution of 1100 equivalent weight Nafion was diluted with n-propanol to prepare stock Nafion solutions. The pyridine ligands used in this study were obtained from Aldrich and used without further purification. $Ru(NH_3)_5Cl_3$ was synthesized from $Ru(NH_3)_6Cl_3$ using the procedure of Voght *et al.* (13) and recrystallized from 0.1*M* aqueous HCl. All aqueous solutions were prepared from distilled water that was further purified by passage through a Barnstead Nanopure water purification system. Sodium trifluoromethanesulfonate (NaTFMS) electrolyte solutions (0.05*M*) were prepared *in situ* by neutralization of the acid.

Electrode preparation.—Polymer-modified pyrolytic graphite electrodes (14) were prepared by the evaporation of 0.005 g/ml Nafion solutions. The polymer film thickness was estimated from the reported swollen density of the 1100 equivalent weight recast Nafion (15). Most kinetic experiments were conducted using a film thickness of approximately 0.4 μm. Each kinetic experiment was carried out with a freshly prepared electrode surface. Nafion/graphite electrodes containing $Ru(NH_3)_5(H_2O)^{3+}$ were prepared by dipping the Nafion-modified electrode into a 0.05-0.10 m*M* solution of $Ru(NH_3)_5Cl_3$. Prior to a kinetic experiment, the Nafion/Ru(III) electrode was cycled several times between +0.2 and −0.6V (*vs.* SCE) in a 0.05*M* NaTFMS solution to convert the chloride complex to the aquo form. The cyclic voltammograms recorded over this range were linearly dependent on scan rate (to at least 200 mV/s); the concentration of $Ru(NH_3)_5(H_2O)$ in the film was typically 0.01-0.02*M*.

Kinetic measurements.—All kinetic experiments were run under an argon atmosphere in a conventional two-compartment "H-cell." The working compartment, filled with the ligand solution (0.02-0.2*M*, 0.05*M* NaTFMS), was purged with argon and equilibrated with a constant temperature bath, before the modified electrode was placed in the cell. Kinetic experiments were initiated by reducing the Ru(III) to Ru(II) at −0.6V. The reaction progress was monitored at 10-20s intervals by recording the voltammogram that resulted from rapidly sweeping (200 mV/s) the potential of the reduced electrode to +0.2V. The potential of the electrode was then stepped back to −0.6V to "turn on" the substitution reaction again. This procedure was repeated until the substitution reaction was at least 90% complete. Pseudo first-order rate constants were obtained from an analysis of the peak current *vs.* time data (16).

Partition coefficients.—A demountable two-piece thin layer optical cell with quartz windows was used for all partition coefficient measurements (14). Polymer films (0.5-2.0 μm) were deposited on one cell half by evaporation of 0.0125 or 0.025 g/ml Nafion solutions. The quartz window/Nafion film assembly was clamped together with an unmodified one, and the cell was filled by capillary action from an excess of ligand solution placed at the bottom of the cell. Absorbance measurements were made using a Cary-17 spectrometer. The concentration of ligand within the film can be calculated by taking the difference in the absorbance recorded with and without Nafion film in the cell. The ligand concentrations were not corrected for polymer void volume.

Results and Discussion

Kinetics.—We previously reported (12) that the substitution rates (Eq. [1]) for isonicotinamide and 4-pyridylcarbinol are considerably slower than pyridine in Nafion, and that these rate differences could be attributed to less favorable activation entropies for the more polar ligands. These data indicate that a decrease in the ligand polarity should result in an enhanced substitution rate due to a more favorable activation entropy. To test this supposition, the substitution behavior of the more hydrophobic (than pyridine) ligands 3-chloropyridine and N,N-diethylisonicotinamide were investigated.

The partition coefficient corrected substitution rate for N,N-diethylisonicotinamide, the hydrophobic dialkylated analogue of isonicotinamide, 0.20 $M^{-1}s^{-1}$, is five times faster than isonicotinamide, while that for 3-chloropyridine (0.10 $M^{-1}s^{-1}$) is about the same as found for pyridine. The activation parameters for 3-chloropyridine and N,N-diethylisonicotinamide were derived from Eyring plots (5°-45°C). These activation values, as well as the data for isonicotinamide and pyridine, are listed in Table I along with the bimolecular rate constants at 298 K. Examination of the activation terms for N,N-diethylisonicotinamide and isonicotinamide demonstrates that, despite the greater activation enthalpy found for the N-alkylated ligand (17.8 *vs.* 14.8 kcal/mol), this ligand reacts faster due to a much more favorable activation entropy, −2.1 *vs.* −15.2 cal/(K · mol). Although the corrected bimolecular rate constants for 3-chloropyridine and pyridine are approximately equal, the activation parameters are quite different. Notably, 3-chloropyridine has a higher activation enthalpy (17.4 *vs.* 15.1 kcal/mol), which is, however, compensated by the more positive entropy [−4.7 *vs.* −12.3 cal/(K · mol)].

Two reasonable explanations may be invoked to explain the observed entropic control of the substitution reactions in Nafion. The ligand structure may either effect the "solvent" properties of the Nafion environment (*e.g.*, polymer swelling, ion pairing) or influence some step in the substitution mechanism. We have demonstrated that the first possibility is unlikely, because addition of N,N-dimethylbenzamide, a hydrophobic spectator species, does not increase the substitution rate for isonicotinamide, whereas decreasing isonicotinamide's polarity through N,N-dialkylation does cause a factor of five increase in the rate. It is likely, therefore, that the ligand polarity influences one of the elementary steps in the overall reaction.

The rate constants and activation parameters presented in Table I suggest the very interesting possibility that one can also enhance the substitution rates of sterically hindered, 2-substituted pyridines in Nafion relative to aqueous solution (2-methylpyridine is 30 times slower than pyridine in aqueous solution). In fact, we find that the substitution rates for the hydrophobic ligands 2-chloropyridine and 2-propylpyridine are faster than that found for pyridine substitution (Table II), a clear contrast to the aqueous solution results.

Mechanistic implications.—The substitution rates and activation parameters measured for a number of pyridines in Nafion (Table II) vary substantially, whereas in aqueous solution these kinetic parameters have been reported to be nearly constant. The accepted mechanistic interpretation of the aqueous solution results is that substitution involves an initial unimolecular dissociation of water followed by irreversible attack of the entering ligand (10-11). A rate-determining step that involves breaking the ruthenium-water bond is then consistent with the relatively constant rates and activation parameters found in solution.

Our data, which show substantial variations in both the substitution rates and activation parameters, are difficult to rationalize in the framework of the above dissociative mechanism. They are consistent, however, with an associative mechanism involving pre-equilibrium outersphere complex formation between $Ru(NH_3)_5(H_2O)^{2+}$ and the entering ligand, followed by a rate-determining decomposition of this complex to the final products. Within this mechanistic framework, the enhanced substitution rates found for the hydrophobically substituted pyridine ligands results from the formation of more stable intermediate complexes, *i.e.*, the preequilibrium binding constants, K_{eq}, are increased. Larger values of K_{eq} for the more hydrophobic ligands are also consistent with our mea-

Table I. Comparison of rates and activation parameters in Nafion for ligands of varying hydrophobicity at 25°C.

Reactant	k_{bi} ($M^{-1}s^{-1}$)	ΔH^* (kcal/mol)	ΔS^* [cal/(K-mol)]
N,N-diethylisonicotinamide	0.20	17.8 ± 0.4	−2.1 ± 2.2
Isonicotinamide	0.041	14.8 ± 0.1	−15.2 ± 0.5
3-Chloropyridine	0.10	17.4 ± 0.5	−4.7 ± 2.3
Pyridine	0.11	15.1 ± 0.2	−12.3 ± 1.4

sured activation entropies; the ligands that can shield the Ru(II) center from interactions with the ordered Nafion environment, in the intermediate complex, will cause the association constant to be favored on entropic grounds. In conclusion, the unique reactivity trends that we have observed in Nafion suggest that polymer-modified electrodes may be utilized to effect chemical transformations that are considerably different than those found in homogeneous solution.

Acknowledgments

The author acknowledges support through the Joseph W. Richards Summer Fellowship of the Electrochemical Society, Incorporated, and stimulating discussions with Professor Nathan S. Lewis.

REFERENCES

1. For a recent overview of his field, see: L. R. Faulkner, *Chem. Eng. News*, 28 (Feb. 27, 1984).
2. D. A. Buttry and F. C. Anson, *J. Am. Chem. Soc.*, **105,** 685 (1983).
3. H. S. White, J. Leddy, and A. J. Bard, *ibid.*, **104,** 4811 (1982).
4. T. Ikeda, C. R. Leidner, and R. W. Murray, *J. Electroanal. Chem.*, **138,** 343 (1982).

Table II. Summary of rates and activation parameters; 25°C

Ligand	k_{bi} ($M^{-1}s^{-1}$)	ΔH^* (kcal/mol)	ΔS^* [cal/(K-mol)]
2-Chloropyridine	0.27		
N,N-diethylisonicotinamide	0.20	17.8	−2.1
2-Propylpyridine	0.16		
2-Methylpyridine	0.11	15.9	−9.6
Pyridine	0.11	15.1	−12.3
3-Chloropyridine	0.10	17.4	−4.7
4-Pyridylcarbinol	0.070	14.2	−16.4
Isonicotinamide	0.041	14.8	−15.2

5. C. P. Andrieux, J. M. Dumas-Bouchiat, and J. M. Saveant, *ibid.*, **131,** 1 (1982).
6. F. C. Anson, J. M. Saveant, and K. Shigehara, *ibid.*, **145,** 423 (1983).
7. R. W. Murray, *Acc. Chem. Res.*, **13,** 135 (1980).
8. C. U. Pittman, in "Polymer-Supported Reactions in Organic Synthesis," P. Hodge and D. C. Sherrington, Editors, John Wiley and Sons, New York (1980).
9. "Fundamental Research in Homogeneous Catalysis," M. Tsutsui and R. Ugo, Editors, pp. 215-225, Plenum Press, New York (1980).
10. R. E. Shepherd and H. Taube, *Inorg. Chem.*, **12,** 1392 (1973).
11. R. J. Allen and P. C. Ford, *ibid.*, **11,** 679 (1972).
12. C. M. Lieber and N. S. Lewis, *J. Am. Chem. Soc.*, **107,** 7190 (1985).
13. L. H. Vogt, J. L. Katz, and S. E. Wiberly, *Inorg. Chem.*, **4,** 1157 (1965).
14. C. M. Lieber, Ph.D. Thesis, Stanford University, Stanford, CA (1985).
15. C. R. Martin and K. A. Dollard, *J. Electroanal. Chem.*, **159,** 127 (1983).
16. A. J. Bard and L. R. Faulkner, "Electrochemical Methods: Fundamentals and Applications," p. 521, John Wiley and Sons, New York (1980).

Abstracts of Recent News Papers

Presented at the San Diego, California, Meeting of the Society, October 19-24, 1986

819 RNP The Finite Element Method for Microsensors: *S. B. Crary*, General Motors Research Laboratories, Warren, MI 48090-9057

The finite element method is applied to a generic design of a heated silicon-based microsensor. The convergence of a solution of the equations for the temperature field, including temperature-dependent thermal conductivities, is demonstrated. Two prototype designs are compared with discrete models based on one-dimensional and two-dimensional approximations. The finite element approach is shown to reduce modeling inaccuracies from ~ 40 to ≤ 5% for the example demonstrated here. It is expected that the finite element method will play an increasingly important role in microsensor design.

820 RNP Metallurgical Interaction among Aluminum, Polycrystalline Silicon, and $TaSi_2$ or Single-Crystal Silicon in VLSI Contacts: *P. A. Heimann, T. Y. Sheng*, and *S. Abys*, AT&T Bell Laboratories, Murray Hill, NJ 07974

We have found and investigated a metallurgical reaction that occurs between the aluminum and the contact poly in fine-line NMOS devices using the poly-plug contact process. The reaction takes place during the 450°C H_2 annealing step, and it results in the aluminum attacking and penetrating through the polysilicon layer. It occurs mostly with polysilicon on top of tantalum silicide, and to a much lesser degree with polysilicon on top of silicon dioxide or single-crystal silicon. It is more pronounced on contacts with small areas. We have investigated aluminum/polysilicon/silicide thin film structures to clarify the causes and effects of this reaction. The susceptibility to reaction correlates with the smaller polysilicon grain size that is found for polysilicon on top of tantalum silicide, and it correlates with the dopant type of the polysilicon, being more pronounced for phosphorus diffused polysilicon than for arsenic-implanted silicon. The reaction yields a contact with much lower electrical resistance than would be expected for a contact that contains a layer of semiconducting polysilicon. No device reliability problems have been found to result from the reaction.

821 RNP Alloyed AuGeNiAg Ohmic Contacts to n-GaAs: Electrical and Morphological Influence of Ag: *D. E. Houston* and *S. D. Mukherjee*, General Electric Co., Electronics Laboratory, Electronics Park, Syracuse, NY 13221

A study of alloyed NiGeAuAgAu ohmic contacts to n-GaAs, both with and without the n+ contact layer, has been done. The effects of varying the relative thicknesses of the constituents on both surface morphology and transfer resistance, P_t, are presented. An increase in Ag raises the maximum alloy temperature for a smooth surface morphology from 465° to 525°C. Furthermore, increased Ag and reduced Ge result in low P_t ($0.05 < P_t < 0.06\ \Omega$ mm) for alloying temperatures in the range of $420° < T < 460°C$ for samples with an n+ layer. However, P_t is minimized for low Ag and high Ge content for the case of no n+ contact layer. A tentative model for the dependence of transfer resistance on relative metalization compositions is presented.

822 RNP A Comparison of Single-Factor Experimental Design to Fractional Statistical Design for CVD WSi_2 Process Characterization: *T. F. Klemme* and *C. F. Fey*, Xerox Corp., Microelectronics Div., El Segundo, CA 90245

A single-factor experimental method is compared to a fractional factorial technique to characterize the process sensitivity of a CVD WSi_2 deposition process. The statistical approach of the fractional factorial method has been shown to allow the engineer to optimize the process in a short period and provide more robust results than compared to conventional single-factorial methodology. In this study, we review the Taguchi method of fractional factorial design and report the data generated by both single-factor and fractional factorial design methods.

823 RNP Use of AZ Protective Coating as a Sacrificial Planarizing Layer for Multilevel Metalization: *S.-R. Chen*, Xerox Microelectronics Ctr., El Segundo, CA 90245

The planarization properties of several spun-on polymer materials have been considered for application in VLSI double-level metalization systems. It is shown that, among the polymers, AZ protective coating is most effective for achieving high planarity and minimizing the effects of pattern density. This improved sacrificial planarizing layer provides a low cost, simple process. Optimal procedures for producing highly planarized surfaces using AZ protective coating are presented.

824 RNP Oxygen-Related Defects Enhanced by Vacancy Cluster Formation in Ultraheavily B-doped CZ Si Crystals: *M. Kanamori* and *M. Mikami*, NEC Corp., VLSI Development Div., Shimokuzawa, Sagamihara City, Kanagawa 229, Japan

The p/p+ epitaxial wafer for high density megabit DRAM has many advantages such as alpha-particle soft-error suppression. Recently reported intrinsic gettering (IG) difficulty for ultraheavily B-doped crystals ($\rho < 0.003\ \Omega$ cm.), which was interpreted as B-vacancy complex formation, was solved by high temperature preannealing before IG. The inner defect formation was significantly enhanced. This preannealing was estimated to form the vacancy cluster, which acts as oxygen precipitation nucleus.

825 RNP High Temperature Processing of CZ Silicon Substrates: Defects, Denuded Zones, and Minority Carrier Lifetime: *G. A. Rozgoni, D. K. Yong, Y. H. Cao*, and *Z. Radzimski*, Dept. of Materials Engineering, North Carolina State University, Raleigh, NC 27695-7916, and *H. D. Chiou*, Mansanto Electronic Materials Co., St. Peters, MO 63376

We have subjected CZ silicon wafers to furnace and rapid thermal annealing at temperatures of 1250°C (30 min) and 1200°C (2 min), respectively, with the intention of dissolving grown-in native defects and nucleation sites for oxygen precipitation. Subsequent combinations of low (700°C) and moderately high (1100°C) annealing were used to induce precipitation and denuded zone formation. The effectiveness of the above treatments was evaluated using generation and recombination minority carrier lifetimes to probe the near-surface and deeper bulk wafer quality, respectively. The lifetimes were then correlated with the depth of the denuded zone and bulk defect density.

826 RNP ASTM-Oxygen Precipitation Study: *ASTM Task Force Committee: R. Swaroop*, Fairchild Semiconductor, Mountain View, CA 94039, *W. Lin*, AT&T, *N. Kim*, AMI, *M. Bullis*, Siltec, *A. Rice*, Wacker, *E. Castel*, Fairchild Semiconductor, *M. Crist*, Dynamit-Noble, and *L. Shive*, Monsanto

Oxygen in Cz-Silicon has been studied extensively for the last few years due to its role in impurity gettering and its contribution to alloy strengthening. ASTM task force was established to investigate oxygen precipitation test(s) through which material vendors and users could communicate with each other. Test methods were chosen and evaluated to examine (i) the difference in precipitation behavior of silicon wafers from different sources and (ii) the effectiveness of FTIR measurement techniques for oxygen precipitation due to thermal cycle(s).

827 RNP Characterization of Filament Recrystallized SOI Films: *R. P. Anand** and *J. C. C. Tsai**, AT&T Bell Laboratories, Reading, PA 19603-0856, and *L. Pfeiffer*, AT&T Bell Laboratories, Murray Hill, NJ 07974-2070

Thin Si films on SiO_2, produced by melting and recystallization of polysilicon on a traveling-strip-heater furnace have been characterized. N-channel MOS transistors were fabricated. The dc output characteristics of these devices compared favorably with controls fabricated in CVD epitaxial films grown on single-crystal silicon. Low angle grain boundary dislocations were observed in recrystallized SOI films; however, they do not seem to degrade surface mobility. The calculated electron mobility in the inversion layer is 000-700 cm^2/Vs in the SOI and the control samples. These films can be used in fabricating MOS circuits.

828 RNP Absolute Temperature Measurements of Silicon Wafer Surfaces in a High Temperature Epitaxial Reactor: *N. P. Sandler, S. M. Fisher*, and *M. L. Hammond*, Gemini Research, Fremont, CA 94538

Absolute wafer surface temperatures have been measured as a function of optical susceptor and wafer surface temperature in a vertical induction heated reactor. High purity germanium, copper, and manganese samples were used for the absolute melting points. Temperature corrections for the absorption of safety glass and quartz were made, and the effect of the emissivity of silicon as a function of temperature was measured. The latter is compared with previously published data. Temperature correction curves are plotted and discussed.

829 RNP Antimony Diffusion Profile in Silicon: Analysis and Modeling: *F. Gaiseanu* and *C. Postolache*, R&D Ctr. for Semiconductors (CCSIT-CE), R72996, Bucharest, Romania

The antimony diffusion in silicon from Sb-doped SiO_2 glasses acting as an infinite source during the diffusion in an Ar ambient at 1250°C is analyzed. A linear variation of the diffusion coefficient with the diffusion concentration in the high concentration range was found. An adequate solution of the diffusion equation deduced by using the results of the profile analysis allows the easy evaluation of the profile parameters. The very good agreement with the collected experimental data strongly supports the antimony diffusion mechanism in silicon by mono-charged vacancies.

830 RNP New Results Show No Limiting Interface Reactions in the Initial Regime of Silicon Oxidation: *D. R. Wolters* and *A. T. A. Zegers van Duynhoven*, Philips Research Laboratory, 5600 JA Eindhoven, The Netherlands

New results show no limiting interface reaction in the initial regime of silicon oxidation. Published results show that, in the initial regime, the growth of SiO_2 is purely parabolic. This means that here the interface reaction must be nonlimiting in contrast with conventional assumptions. The growth curves are described in a model assuming a water-enhanced oxygen transport. The initial growth is explained by the direct transport of oxygen.

831 RNP Silicon Interstitial Kinetics during the Thermal Nitridation of SiO_2: *S. T. Dunham*, Dept. of Electrical Computer and Systems Engineering, Boston University, Boston, MA 02215

A quantitative model of interstitial kinetics during the thermal nitridation of SiO_2 has been developed. The model explains the large diffusivity enhancement of phosphorus and successfully predicts how the enhancement varies with time. Interstitial injection due to the growth of a thin oxygen-rich layer at the dielectric/silicon interface is magnified by the presence of a nitrogen-rich layer near the interface, which constrains the interstitials in the dielectric to the interface region. An initial transient period exists due to the time required to "fill up" the substrate.

832 RNP The Electrical Properties of Subhundred Angstrom $SiO_2/Si_3N_4/SiO_2$ Dielectric Films Fabricated by Different Reoxidation Processes: *K. W. Teng, B. Y. Nguyen*, and *P. J. Tobin*, Motorola Inc., Advanced Product R&D Laboratory, Austin, TX 78721

Stacked dielectric films of $SiO_2/Si_3N_4/SiO_2$ (ONO) having thicknesses in the range of 83-98Å (SiO_2-equivalent-thickness) were fabricated using steam reoxidation at 830°C for 1, 2, or 3h, or 900°C for 1h. Electrical properties including time-zero breakdown, defect density, dielectric breakdown E-field, I-V, C-V, charge trapping behavior, and ONO/Si interface states, as well as Auger depth profile of those ONO dielectric films, were extensively investigated. Based on the results obtained from both the Auger electron spectroscopy and quasi-static C-V techniques, it appears that the bottom oxide may be converted to oxynitride to an extent that is probably determined by the reoxidation process. It is found that the top oxide thickness plays an important role on the positive i-E characteristics, which can be explained by the hole flow model. Furthermore, thin ONO films fabricated by the 830°C/3h process generally show superior properties to those films reoxidized by other processes.

833 RNP Electrical Characteristics of High Pressure Low Temperature 10 nm Oxides: *A. Kalnitsky, J. P. Ellul*, and *S. P. Tay*, Northern Telecom Electronics Ltd., Ottawa, Ont., Canada K1Y 4H7

This paper presents electrical characteristics of silicon oxides grown at 700°C under 10 atm total pressure of O_2/N_2 or O_2/Ar. They are observed to be independent of the postoxidation anneal ambient (N_2 or Ar) and temperature (900° and 1000°C) employed in this experiment. Breakdown field (10 MV/cm), low field leakage current ($<10^{-10}$ A/cm^2), and Fowler-Nordheim tunneling parameters are comparable to those for oxides grown at 950°C under atmospheric pressure of O_2/Ar and annealed at 950° in Ar. Thickness uniformity (+/− 0.8 nm) and reproducibility (+/− 1.0 nm) was achieved for a 10 nm thick oxide.

834 RNP Convex Corner Rounding Oxidation and Its Effect upon Oxide Leakage Current: *K. Yamabe* and *K. Imai*, Toshiba Corp., VLSI Research Ctr., 1 Komukai-Toshiba-cho, Saiwai-ku, Kawasaki, 210, Japan

Oxide field concentration and curvature radius for a Si/SiO_2 interface at the convex corner are described, based on theoretical calculations. It is indicated in a one-dimensional model and through experiments that, by oxidation in a diluted oxygen ambient or at higher oxidation temperature, stress generated during Si oxidation can easily be reduced and the convex corners are effectively rounded off. The relation between the sacrificial rounding-off oxidation, prior to gate oxidation, and the time-dependent dielectric breakdown for thin gate oxide is also shown.

835 RNP Thin Interpoly Oxides: *J. P. Ellul, S. P. Tay*, and *A. Kalnitsky*, Northern Telecom Electronics Ltd., Ottawa, Ont., Canada K1Y 4H7

In this paper, we present electrical characterization results of 14-30 nm thick interpoly oxides, grown both at 800° and 100°C, with electrical field strength of 6-8 MV/cm. Fabrication techniques for forming the poly electrodes and the poly-oxides are described. Statistical breakdown voltage results and current stress measurements are presented to show that 15 nm thin poly-oxides can be grown reliably with very low defect density.

836 RNP Characteristics of Silicon Thermal Nitride Films Grown in Argon-Diluted Ammonia: *S. W. Sun, P. J. Tobin, J. Weihmeri*, and *E. Reed*, Motorola Inc., Advanced Products R&D Laboratory, Austin, TX 78721

Characteristics of thermally grown silicon nitride films used as local oxidation masks have been studied. The major topics investigated include the origin of oxygen contamination, shift of Si-N infrared absorption band as a function of oxygen content, generation of point defects during thermal nitridation, and masking ability against steam oxidation cycles. Ellipsometry, oxidation resistance, infrared spectroscopy, and Auger electron spectroscopy were used to characterize these films grown in argon-diluted ammonia.

837 RNP Redistribution of Arsenic in Silicon during High Pressure Thermal Oxidation: *S. S. Choi*, Dept. of Physics and Astronomy, University of North Carolina, Chapel Hill, NC 27514, *J. K. Srivastava*, Dept. of Chemistry, University of North Carolina, Chapel Hill, NC 27514, *M. Z. Numan*, Dept. of Physics and Astronomy, University of North Carolina, Chapel Hill, NC 27514, *E. A. Irene*, Dept. of Chemistry, University of North Carolina, Chapel Hill, NC 27514, and *W. K. Chu*, Dept. of Physics and Astronomy, University of North Carolina, Chapel Hill, NC 27514

Redistribution of arsenic impurities in silicon during thermal oxidation has been examined. Pile-up, or depletion of impurity in silicon, is dependent on the relative rate of oxidation and diffusion, $A/D^{1/2}$, as well as on the thermodynamic equilibrium segregation coefficient and the diffusion of impurity within the oxide layer. For the value of $A/D^{1/2}$ larger than the order of 10^2, most of the arsenic impurity has turned out to be trapped in SiO_2. For smaller values of $A/D^{1/2}$, snowplowing of the arsenic impurity results.

838 RNP Study of the Selectivity of Nitride to Silicon Etch Rate and Damage Effect Caused by Dry Etching in a Single-Wafer Etcher: *C. Huynh, G. Beardsley*, and *C. Boye*, IBM General Technology Div., Essex Junction, VT 05454

Silicon surfaces that had been exposed to C_2F_6/40% He reactive ion etching have been studied for the etch rate selectivity of nitride to silicon. Electron spectroscopy for chemical analysis (ESCA), pulsed CV (technique for retention time), dielectric breakdown measurements, and high frequency (1MHz) CV surface state density measurements were made to characterize the effect of etch processing conditions on these surfaces. It was determined through the oxidation of the reactive ion etched silicon substrates and through the extensive analysis of ESCA that the damage was purely a crystalline defect and it extended to a depth of more than 800Å. Low breakdown fields were observed and assumed to be accounted for by the poor morphology of the silicon surface resulting from energetic ion bombardment. In this study, a high pressure, single-wafer etcher was selected to minimize heavy metal contamination from the dry etching chamber and its cathode plate material.

839 RNP Plasma Parameter Control of Etch Rates, Selectivity, and Anisotropy: *C. B. Zarowin*, Perkin-Elmer Research, Danbury, CT 06810

We discuss the experimental verification of earlier derived relations (1) between observable plasma etch rate, selectivity, and anisotropy and reactor parameters for a variety of etch gases. Since the heterogeneous etch reaction is a superposition of neutral and ionic components, it can be shown that such etch chemistry exhibits enhancement and is made anisotropic by the energy transport of ions to the etch surface only when the process is ion dominated. The ion energy transport is controlled by the plasma sheath electric field-electrode area/gas pressure-collision cross section ratio, EsAs/pQ, similarly controlling chemical anisotropy for ion-dominated etch reactions. Under such circumstances, we show that many etch gases can yield identical ion transport, etch rate, and anisotropy for a given RF current, gas pressure, ion-neutral collison cross section, and electrode area, IRF/pQAs.

1. C. B. Zarowin, *J. Vac. Sci. Technol. A*, **2**, 1537 (1985).

840 RNP "Loading" and Selectivity Flow Dependence of Plasma-Assisted Etching/Deposition Processes: *C. B. Zarowin*, Perkin-Elmer Research, Danbury, CT 06810

The "loading" and selectivity flow dependence predicted by a theory (1) of plasma-assisted chemical vapor transport (PACVT) processes are confirmed experimentally. These are applicable to reactive ion or plasma etching and plasma-assisted chemical vapor deposition. The central predictions confirmed by these results are: (*i*) the selectivity flow dependence can approach infinite selectivity at certain "low" flows, and (*ii*) the loading flow dependence is linearly increasing at "low" flow, in agreement with earlier loading behavior, but, in contrast, exhibits a maximum as flow increases and decreases to zero loading at infinite flows. This flow-dependent selectivity and loading is shown to be a very sensitive test of the validity of the above theory (1).

1. C. B. Zarowin, *J. Appl. Phys.*, **57**, 929 (1985).

841 RNP Plasma Etch Considerations for a MB DRAM: *P. D. Cruzan, L. B. Fritzinger, G. K. Herb, G. W. Hills, L. E. Katz*, and *T. Kook*, AT&T Bell Laboratories, Allentown, PA 18103

The MB DRAM developed at AT&T Bell Laboratories has a double-polysilicon, single-metal technology with 1.0 μm minimum feature geometry. Plasma etching processes were developed for polysilicon, tantalum silicide, oxide, silicon nitride, and aluminum levels. Some of the etching problems encountered at these critical structures are discussed as well as the factors involved in developing solutions to the pattern transfer problems.

842 RNP Spectroscopic Diagnostics of Photoresist in Aluminum Etch Plasma: *O. Krogh, H. Slomowitz*, and *Y. Melaku*, Tegal Corp., Novato, CA 94948; and *H.-O. Blom*, Institute of Technology, Uppsala University, 5-75121 Uppsala, Sweden

A spectroscopic investigation of photoresist etching was done during aluminum processing. Etch rate of aluminum is represented by the AlCl emission, and that of photoresist by the CCl emission. Photoresist etch rate is high during removal of the surface aluminum oxide, drops to a low value during etch of the bulk aluminum film, and increases as the film clears. We have also characterized reticulation of the photoresist during etching. Real-time spectroscopically measured selectivity of aluminum to photoresist has been developed and evaluated.

843 RNP Correlation of Postetch Residues to Deposition Temperature in Plasma-Etched Aluminum Alloys: *T. Abraham*, Northern Telecom Electronics Ltd., Ottawa, Ont., Canada K1Y 4H7

A study of the dependence of postetch residue on deposition temperature was carried out on Al 1% Si, Al 2% Cu, Al 4% Cu, and Al 1% Si ½% Ti. The metal was deposited in a Varian 3180 sput-

tering system and the plasma etching was done in an AME 8130 hex etcher using a BC13-based process. The results of the study indicated that the postetch residues were related to the deposition conditions and depended on the distribution of the alloying element through the film.

844 RNP Anisotropic Polysilicon Etching Without Hydrocarbon Polymer Formation: *P. J. Kelleher* and *L. Kammerdiner*, Inmos Inc., Colorado Springs, CO 80935

When not operating in the "RIE" regime, sidewall deposition of polymeric species has been deemed necessary for anisotropic polysilicon plasma etching. Because of extremely high selectivity to gate oxides, a Cl_2-based etch is desirable for current VLSI technology. It will be demonstrated that a Cl_2/He etch can be anisotropic without any carbon containing gases and without a photoresist mask. The determining factors for etch anisotropy will be discussed.

845 RNP Etching of Silicon Through SiO_2 in a CF_4/N_2O Plasma: *X. Wang, M. D. Liu, T. P. Ma*, and *R. C. Barker*, Ctr. for Microelectronic Materials and Structures and Dept. of Electrical Engineering, Yale University, New Haven, CT 06473

In the course of studying the selectivity of various etching gases on Si and SiO_2, it was discovered that for a CF_4/N_2O plasma, when the etching of a thick thermal oxide (up to 1 μm thick) was stopped within 2000-3000Å of the silicon surface, deep trenches ≈ 1 μm deep were found in the underlying silicon, having been etched through pinholes in the thin SiO_2 membrane on top. This phenomenon occurs for a wide range (20-80 mtorr) of the CF_4 pressure. In contrast, no such effect was observed in a CF_4/O_2 plasma under otherwise identical etching conditions. A model for the observations is discussed

846 RNP XPS Characterization of Silicon Etched by SF_6 + N_2O and N_2O + O_2 RF Plasmas: *Y. Tzeng, T. H. Lin, B. J. Tatarchuk*, and *D. M. Littrell*, Plasma Processing Laboratory, Auburn University, Auburn, AL 36849

The addition of N_2O to SF_6 plasma enhances the silicon etch rate much more than the addition of O_2. Although the F atom concentration was measured to be higher in the SF_6 + O_2 plasma, the high concentrations of oxygen species in SF_6 +O_2 plasma retard the silicon etch and lead to lower silicon etch rate than SF_6 + N_2O plasma. Sulfur contamination on silicon wafers etched by SF_6 plasma mixed with either N_2O or O_2 was characterized by means of XPS.

847 RNP The Electrical Properties of MOS Capacitors Fabricated on CF_4/H_2 Reactive Ion Etched Silicon: *J. P. Gambino*, IBM East Fishkill, Hopewell Junction, NY 12533, *G. S. Oehrlein*, IBM T. J. Watson Research Ctr., Yorktown Heights, NY 10598, and *J. F. Shepard, B. Cunningham*, and *C. C. Parks*, IBM East Fishkill, Hopewell Junction, NY 12533

MOS capacitors fabricated on reactive ion etched silicon exhibit low dielectric breakdown fields, high MOS generation currents, and high Si-SiO_2 interface state densities. The low breakdown fields and high interface state densities are probably due to RIE-induced lattice damage or implanted impurities that are incorporated into the growing oxide at the Si-SiO_2 interface. The high MOS generation currents are due to metallic contaminants at oxidation-induced stacking faults.

848 RNP The Temperature Dependence of the Etch Rate of GaAs, InP, and AlGaAs in a Boron Trichloride: Chloride Plasma: *Robert J. Contolini*, Bell Communications Research, Inc., Red Bank, NJ 07701

The pressure, temperature, and power effects are examined independently of each other for GaAs, AlGaAs, and InP in a boron trichloride: chlorine plasma. Conditions are examined for which chemical etching and sputter-assisted etching occur. The variation of etch rate and surface morphology with change in temperature is discussed. For fixed temperatures, the GaAs etch rates actually decrease with increased power in the low pressure regime. For InP, the etch rates increase with increasing power at fixed temperatures.

849 RNP Diamond-Like Amorphous Carbon Film Production by PACVT: *P. J. Clapis, N. Ventkataramanan*, and *C. B. Zarowin*, Perkin Elmer Research, Danbury, CT 06810

Recent work on a theoretical model of plasma-assisted chemical vapor transport has led to production of amorphous carbon films with diamond-like properties (1). These films are deposited at temperatures well below 100°C when a pure hydrogen plasma etches a graphite electrode, generating a volatile transportable hydrocarbon (CH_4). We also report that, while other films contain as much as 50 atom percent hydrogen, the present films made in a hydrogen plasma contain an order of magnitude less.

1. C. B. Zarowin *et al., Appl. Phys. Lett.*, **48**, 759 (1986).

850 RNP Scintillating Glass Fibre Optic Tracking Chambers: *C. G. A. Hill*, Levy Hill Laboratories Ltd., Cheshunt, Herts, England EN8 9TJ

Interest has been growing in the possibility of using solid targets to provide high resolution tracking chambers for particle physics. Known cerium-doped silicate glasses have some of the required properties, but there are serious difficulties in achieving coherent assemblies of clad fibres, 25 μm fibre diameter, 1.5 M attenuation length. Progress can be made by better control of ceric/cerous equilibrium. Encouraging preliminary results have been obtained by Ruchti *et al.* at Notre Dame and Kirkby *et al.* at Cern. We believe many other glass hosts and dopants should be studied.

The Electrochemical Society, Inc.
10 South Main Street, Pennington, New Jersey 08534 • Telephone: 609-737-1902

Instructions to Authors

The **JOURNAL OF THE ELECTROCHEMICAL SOCIETY** is the official monthly journal of the Society. It contains three sections: Electrochemical Science and Technology, Solid-State Science and Technology, and Reviews and News. Technical Papers, Technical Notes, and Accelerated Brief Communications are published in the first two sections and Review Papers in the third. **All manuscripts (in English) submitted are considered for publication, with the understanding that they have not been submitted, accepted for publication, or published elsewhere. Material, e.g., figures and tables, may not be reproduced from another publication unless it absolutely cannot be described in words. If this material must be used, it must be properly referenced and acknowledged, and permission to reproduce it must be obtained from the publisher.** A wide range of subject matter is acceptable. Manuscripts can be handled promptly and efficiently if these instructions are followed.

TYPES OF PAPERS

Technical Papers describe fundamental or applied studies in depth. They contain new data and/or new interpretations of existing data. Abstracts summarizing the results are required.

Technical Notes report briefly on limited research or development that is not being pursued further. No abstracts are required.

Accelerated Brief Communications present, in camera-ready format of limited length, scientific or technological information warranting rapid dissemination. No abstracts are required.

Review Papers furnish critical analyses of topical subjects. Abstracts are required.

SUBMISSION

Submit three complete, clear copies of each manuscript and the originals of all figures and illustrations to:

Editorial Office
The Electrochemical Society, Inc.
10 South Main Street
Pennington, New Jersey 08534

A letter accompanying the manuscript should give (a) the name and mailing address of the author to whom correspondence should be sent, (b) reference to any presentation of the work at a meeting of The Electrochemical Society, (c) the Division or Group of the Society or the Divisional or Group Editor (both are listed in the front of each issue of the Journal) whose interests are most closely related to the work being discussed, (d) the section of the Journal in which the work should appear, and (e) the names and addresses of people able to act as reviewers.

EDITORIAL PRACTICES

Following receipt by the Editorial Office, each manuscript is sent to a Divisional or Group Editor with knowledge of the subject matter. This editor arranges for review of the manuscript and communicates with the author(s) regarding revisions. Final acceptance or rejection of a manuscript is determined by the Editor.

Accelerated Brief Communications are handled as rapidly as possible, ordinarily with a response to the author(s) from the Divisional Editor, the Group Editor, or the Editor within three weeks of their arrival at Pennington. Response to the authors of other manuscripts usually takes place within six weeks. Following acceptance, authors are notified of the Journal issue in which publication is scheduled; about one month before publication, page proofs and an order blank for reprints are provided. Proofs must be promptly corrected and returned. Extensive alterations by the author may delay publication; their cost will be billed to the author(s).

PUBLICATION CHARGE

To help meet publication costs, a payment of $65.00 per printed page is requested for the publication of technical material. If at least one author is a Society member or an employee of a Patron or Sustaining member, a 10% reduction is allowed. Acceptance of manuscripts for publication is, however, based on merit and is in no way dependent on such payment, which may be waived in individual cases upon request.

PRESENTATION

Organization and clarity are essential elements of successful written communication. Identify the subject matter in the title, using words useful in indexing. State the purpose of the work early in the text. Avoid introductory and explanatory material that is overly familiar to those in the field. Present the work and the arguments in an order that leads naturally to clearly specified conclusions. Provide enough information for the work to be reproduced and the logic behind it to be understood. Identify and justify any assumptions that are made; avoid tacit assumptions. Omit details that are generally known or that can be covered by reference to other publications. Give the magnitude and define the significance of experimental errors. Use headings and subheadings as appropriate. Avoid proprietary and trade names, but capitalize them where their use is necessary. Define unusual technical terms and abbreviations. Where symbols are used extensively, list them with their definitions at the end of the paper. Avoid repetition in the text and duplication of material in figures and tables. Be brief but clear.

Edit and proofread the manuscript carefully; these are not the responsibilities of the editors or reviewers.

MANUSCRIPT PREPARATION

Accelerated Brief Communications must be typewritten or printed on standard forms obtained, with detailed instructions for their use, from the Pennington Editorial Office.

All other manuscripts must be typewritten or printed, double-spaced throughout, on one side only of white 21.6 x 27.0 cm paper, with 2.5-3.8 cm margins. Do not use single spacing anywhere, in title, abstract, text, references, tables, or figure captions.

For general matters of style and format, see papers in recent issues of the **Journal** and consult a style manual such as that of the American Chemical Society or that of the American Institute of Physics. These also provide lists of common abbreviations and units. The following specific items should be noted:

(a) Système Internationale (SI) units are to be used; a description may be found in NBS Special Publication 330 or ASTM Metric Practice Guide E-380-72.

(b) The signs of cell and electrode potentials are to follow the IUPAC conventions of 1953.

(c) **Mathematical equations** should be written on a single line, if possible, using parentheses, brackets, the solidus, negative exponents, etc.

(d) **References** are to be listed separately at the end of the paper in the order they are cited in the text, being sure that each listed reference is cited. Authors' initials must be given, and Chemical Abstracts abbreviations must be used. Citations of other than the generally available literature should be avoided if possible.

(e) **Tables** are to be presented on individual sheets, with both captions and body double-spaced.

(f) **Figure captions** and numbers are to be included on a separate sheet and must not appear in the body of any figure or illustration.

(g) **Drawings** and **graphs** will ordinarily be reduced to column width (8.3 cm) and after such reduction should have lettering at least 0.15 cm high. Lettering must be of letter-guide quality. Originals in India ink on tracing cloth or paper are preferred, but India ink on coordinate paper with blue ruling is acceptable. When several curves are shown, each may be lettered and identified in the caption. The Editorial Office will not make corrections or additions to figures.

(h) **Photographs** should be used sparingly. The originals supplied must be glossy prints and should be protected against bending. Micrographs must have a labeled unit length within the body of the picture; reduction for printing makes magnifications meaningless.

Revised August 1, 1984

Printed in the United States of America

Brief Summary of the Workshop on

Electronic Materials and Materials Processing A Key to U.S. Competitiveness

A Workshop on the above topic was held in Washington, DC, on February 26-27, 1986. This Workshop was sponsored by the Federation of Materials Societies, and financially supported by the American Association of Crystal Growth, the American Ceramic Society, the American Chemical Society, the Electric Power Research Institute, The Electrochemical Society, and the Institute of Electrical and Electronic Engineers.

The Workshop Co-Chairmen were G. W. Cullen (RCA), R. Laudise (AT&T Bell Laboratories), and D. Richman (RCA). R. Reynolds (DARPA), D. W. Shaw (Texas Instruments), and A. F. Witt (MIT) served as discussion session leaders. B. Houston (FMS) was the Workshop Coordinator.

The purpose of the Workshop was to discuss the following issues:

- Why are electronic materials a key to U.S. competitiveness?
- What is the present position of U.S. electronic materials technology?
- What can we do in the U.S. to regain our competitive position in electronic materials technology?

Electronic materials were defined as: materials of current and future importance in the development and production of electronic components and devices. These include (but are not limited to) semiconductor, dielectric, magnetic, piezoelectric, and optoelectronic materials, and optical fibers. The various materials may be of importance in the single-crystal, polycrystalline, or amorphous state. Also of interest in this workshop are materials employed in the packaging of electronic devices and components.

The Plenary Session speakers were: H. K. Bowen (MIT), H. Kressel (E. M. Warburg, Pincus, and Company, Incorporated), P. C. Maxwell (Committee on Science and Technology, House of Representatives), H. Nathanson (Westinghouse), E. Pell (Xerox), W. P. Slichter (AT&T Bell Laboratories), and P. A. Tierney (Monsanto). The after-dinner speaker was J. Armstrong (IBM).

In the discussion session, brief presentations were made by: S. Brierley (Raytheon), M. Bullis (Siltec), R. Burmeister (HP), E. Cross (Pennsylvania State University), G. W. Cullen (RCA), R. Flynn (Intel), R. Kelley (Ritter and Bourgaily, Incorporated), G. Moore (SEMI), and J. Vaughan (MA/COM).

Approximately 120 individuals participated in the Workshop. The participants represented a wide cross section of the various disciplines within the category of electronic materials. All of the participants are active in some aspect of the electronic materials arena, and many are in the position to be setting priorities for the research and development of electronic materials. Eighteen participants were associated with academic institutions, 26 with government agencies and Congressional staffs, and 76 with industry. Two attendees were from the press.

A condensation of the Workshop Summary follows.

A Condensation of the Workshop Summary

G. W. Cullen, R. Laudise, and D. Richman, with input from R. Reynolds, D. W. Shaw, and A. F. Witt.

Why are electronic materials and materials processing a key to U.S. competitiveness?—The synthesis and processing of electronic materials are essential "enabling" technologies for the fabrication of a variety of devices and systems that make a major contribution to the success of the U.S. as an industrial nation. Electronic devices are the building blocks of microprocessors and computers. These are the essential control elements of systems that span the range from VCR's and industrial process controls to telecommunications and military command and control systems. Our ability to control electronic materials and materials processing has led to the availability of inexpensive information acquisition, manipulation, and distribution systems. The availability of such systems has started a second industrial revolution. Whoever controls the material and materials processing controls the devices, the systems, and, ultimately, modern electronics. It is important to appreciate the fact that the downstream leverage as an enabling technology is many times greater than the value of the materials.

What is the present position of U.S. materials technology?—Investigators in the U.S. had established a position of world dominance in electronics materials. During the last decade, however, our leadership has been severely eroded, and in a number of areas our leadership has been lost. This is due, to a great extent, to the Japanese capability to transfer advanced electronic materials processing technology rapidly from the laboratory to the factory. In the U.S., there has been little emphasis on materials science and manufacturing technology. Dominance in device and circuit fabrication will lead to dominance in electronically based systems. This has an impact on both civilian and military systems applications. As weaponry becomes more sophisticated, the ability of the U.S. to maintain a strong national defense will hinge on the viability of the domestic electronic materials and materials processing industry.

As more of the manufacturing capability moves offshore, the research and development technology are likely to follow. The first opportunity to design and exploit future new devices and systems will go to the organizations and nations that pursue a vigorous fundamental electronics materials program. For instance, possibilities for new semiconductors based in the quantum levels in strained-layer superlattices and new magnetic and optical materials are inherent in current research. We must appreciate that foreign competitors have made electronic materials science a national priority.

Some conclusions.—Circuit yield, cost, reliability, and performance are closely tied to materials synthesis and materials processing capabilities. Cost, reliability, and performance are key to competitiveness.

Materials are introduced in early stages of high-value-added production, and, therefore, materials costs are highly leveraged. A loss of a competitive electronic materials base inevitably leads to a loss in competitiveness in the manufacture of circuits and systems.

There appears to be a lack of appreciation in management in both government and industry for the impact of materials and materials processing on circuit and system cost, performance, and reliability. Considering the impact of electronic materials and materials processing, there is a disproportionately low amount of government funding in this area. By contrast, foreign nations have targeted electronic materials as a key to the future of their industrial competitiveness. If this trend continues, it can be anticipated that the U.S. will be a minor force in the world market of electronic materials and systems by the early 1990's.

What can we do to regain U.S. competitiveness in electronic materials and materials processing technology?—Academia.—It will be necessary to raise the consciousness of university staff, particularly in the disciplines of chemical engineering and physical chemistry, to fundamental materials science issues in industrial processing and manufacturing of electronic circuits and systems. We must also foster the interaction between industry and university

staff members and encourage proposals for materials processing science and engineering centers through the NSF Initiative for Engineering Research Centers. The long-term needs are for the development of new materials through improved coupling between chemistry, physics, and electrical engineering departments.

Industry.—Close collaboration between materials producers and materials users in the development of synthesis and processing technology should be encouraged, as should interaction between circuit and system designers and materials scientists. The effectiveness of using a single team to follow products from development through processing and manufacturing should be examined, and an appreciation in the corporate board rooms of the leverage available through development in materials synthesis and processing should be developed.

Government.—A constituency for electronic materials should be encouraged to assure appropriate input on materials issues to government advisory boards. In light of the impact of materials and materials processing on the effectiveness of devices and systems, we should examine the balance of government funding in these two areas, give consideration to funding of centers for the development of materials manufacturing and processing, and adopt the perspective that government can become usefully involved in organizing and coordinating interaction among academia, industry, and government laboratories.

Societies, academies, and associations.—Technical and professional societies and trade associations are encouraged to become more involved in collecting quantitative information and implementing activities that promote competitiveness of U.S. materials industries. More coordination among the societies, and between societies and trade associations, would be productive and is encouraged. The National Research Council is strongly urged to sponsor a study on competitiveness while there is still time to reverse the decline in U.S. competitiveness.

Workshop Maxim

"A little neglect may breed mischief:
for the want of a nail the shoe was lost;
for the want of a shoe the horse was lost;
and for the want of a horse the rider was lost."

—Benjamin Franklin
Maxim Affixed to
Poor Richard's
Almanac (1757)

A more detailed summary of the Workshop can be obtained from the Federation of Materials Societies, 1901 L Street, NW, Suite 804, Washington, DC 20076.

Advertisement

New Books, Seminars

1 Progress in Batteries & Solar Cells, Vol. 6 (1987)

Published by JEC Press Inc, 285 pages, $85. Contents: Lithium Batteries, MnO_2 and MnO_2 Batteries, Ni-Cd Batteries, Lead-Acid Batteries, Fuel cells. Available on Oct. 15, 1986. Send your order to JEC Press, 14731 Sprengel Ave., Cleveland, Ohio 44135 USA

2 Articles Solicited for (1) Progress in Batteries & Solar Cells (2) New Materials & New Processes

Please summarize highlights of your research or your new products in a few pages, and send it to: JEC Press Inc., 14731 Sprengel Ave, Cleveland, Ohio 44135 USA. (Page charge is $45). Deadline: March 1, 1987.

The following back issues are available at $85 each. Send your order to JEC Press Inc.: Vol. 3 (1980), Vol. 4 (1982), Vol. 5 (1984), of Progress in Batteries & Solar Cells; Vol. 1 (1981), Vol. 2 (1983), Vol. 3 (1985) of New Materials & New Processes.

3 The 2nd Seminar on Japanese Electrochemical Technologies

Oct. 15-16 (1986) at Case Center Electrochemical Science, Registration $200. Contents: Batteries, New Electrolytic Process, Metal Finishing, Sensors, Fuel Cells. Call 216-368-6525. Organized by R.A. Powers, C.C. Liu, H. Shimotake, A. Kozawa, E.B. Yeager. The seminar text will be published as Vol. 4 of New Materials & New Processes ($85; send your order to JEC Press. See the address in (2)).

4 Battery Material Symposium in Hawaii, Oct. 13-16, (1987)

Oct. 13-16, 1987, Honolulu, Hawaii, Sponsored by IBA Inc. (International Battery Material Assoc.). Organized by Nagayama, Schumm, Kozawa, Friend. Inquire to IBA Inc., 14731 Sprengel Ave, Cleveland, Ohio 44135 USA (Tel. 216-835-7760).

DIVISION NEWS

Corrosion Division

The volume "Electrochemical Methods in Corrosion Research," edited by M. Duprat for the series "Materials Science Forum," is now available.

This volume contains the complete papers of an international symposium held at Toulouse, France, July 9-12, 1985, and cosponsored by the Centre National de la Recherche Scientifique, The Electrochemical Society, the Corrosion Science Division of the Institution of Corrosion Science and Technology, and the National Association of Corrosion Engineers. The primary objective of this symposium was to provide a forum for the discussion of recent developments in electrochemical techniques and their applications in the study of the processes of corrosion and corrosion protection.

The volume consists of approximately 620 pages. It is available from Trans Tech Publications, Ltd., Journal Dept., P.O. Box 10, CH-4711 Aedermannsdorf, Switzerland.

MEETINGS CALENDAR

The Japan Society of Applied Physics and the IEEE Electron Devices Society
1987 VLSI Technology Symposium
May 19-21, 1987
Karuizawa, Nagano, Japan

For further information, contact Pallab Chatterjee, Central Research Laboratory, Texas Instruments, Inc., P.O. Box 225621, Dallas, TX 75264. Telephone 214-995-7914.

The Japan Society of Applied Physics and the IEEE Solid-State Circuits Council
1987 VLSI Circuits Symposium
May 22-23, 1987
Karuizawa, Nagano, Japan

For further information, contact Lewis M. Terman, IBM T. J. Watson Research Center, P.O. Box 218, Yorktown Heights, NY 10598. Telephone 914-945-2029. Telex: 137456.

The American Nuclear Society, The Metallurgy Society of AIME, The National Association of Corrosion Engineers

Third International Symposium on Environmental Degradation of Materials in Nuclear Power Systems—Water Reactors

August 30-September 3, 1987

Traverse City, Michigan

For further information, contact George J. Theus, Technical Program Chairman, Babcock and Wilcox R&D, P.O. Box 835, Alliance, OH 44601. Telephone 216-821-9110.

Driving Lessons Included!

What do the new BAS-100A Electrochemical Analyzer and an Italian sports car have in common? Both are fast, sleek, powerful, fully loaded, and ready for action! The BAS-100A has more ways of reaching the answer to an electroanalytical problem than any other "vehicle" on the road, and it makes the going fun!

New programs and system architecture facilitate the techniques of chronoamperometry, hydrodynamic voltammetry, hydrodynamic modulation voltammetry, hydrodynamic amperometry, AC impedance, and many other pulse and D.C. waveforms. The BAS-100A features improved iR compensation and expanded data handling and storage. New "micro" voltammetric electrodes can now be accommodated! An external computer (the BASpc™) develops methods files for transfer to the BAS-100A and further massages collected data.

Give us a call for a test drive.

P.S. One big difference: you can buy four BAS-100A Analyzers with all the options for the price of one Ferrari, and you won't get a ticket for speeding.

BAS
Bioanalytical Systems, Inc

2701 Kent Ave
West Lafayette
Indiana 47906

Telex: 276141
(317) 463-4527

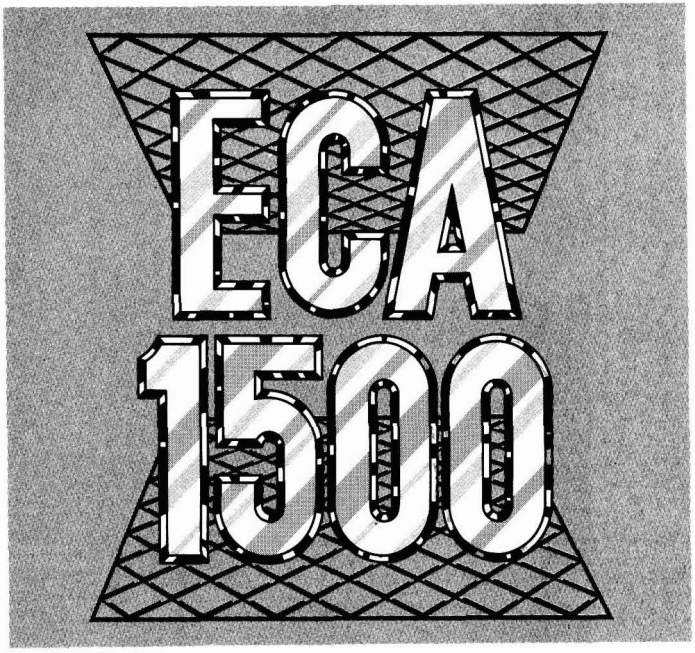

A Super Anode Coating on Titanium for economy and durability.

Engelhard steps ahead again with the versatile new ECA™-1500, designed to be more cost and labor efficient than any other oxygen evolving anode for a wide range of applications.

This unique new electrocatalytic anode was developed specifically to consume less power and deliver superior results over conventional anodes.

Insoluble

Designed for long life and to retain its original dimensions, the ECA-1500 coated anode is non-corrodible even when operated at high current densities.

For more information write Engelhard Corporation, Precious Metals Coated Anodes, Menlo Park, CN 28, Edison, NJ 08818. Or call toll free 1-800-932-0444, in NJ 1-800-624-0818. Telex 13-8552 (domestic), 21-9984 (international).

ENGELHARD

NEW MEMBERS

It is a pleasure to announce the following new members of The Electrochemical Society as recommended by the Admissions Committee and approved by the Board of Directors in August 1986.

Active Members

Beauchamp, C. R., Germantown, MD
Brat, T. E., Grove City, OH
Burbaum, B. W., Cambridge, MA
Chambers, J. Q., Knoxville, TN
Davison, J., Mission Viejo, CA
Elliott, B. T., Tarrytown, NY
Ernes, L. M., Fairport Harbor, OH
Grabowski, K. S., Washington, DC
Hankins, K. T., Palm Bay, FL
Hotaling, T. M., Cambridge, MA
Hussla, I., Hanau, Germany
Jones, C., City of Industry, CA
Kaplan, M. L., Murray Hill, NJ
Lindquist, R. F., Campbell, CA
Morrison, W. G., Roanoke, TX
Porter, M. D., Ames, IA
Ratkje, S. K., Trondheim, Norway
Schirle, M. J., Richardson, TX
Seegopaul, P., Mt. Vernon, NY
Ter Haar, L. W., Murray Hill, NJ
Whetten, T. J., Ithaca, NY

Student Members

Akram, M. F., Stanford, CA
Cody, N., Beaverton, OR
Hwang, S. Y., Pittsburgh, PA
Lishan, D. G., Santa Barbara, CA
Zarnani, H., Fort Collins, CO

Member Representative

Williams, P. C., Diamond Shamrock Chemicals Co.

CHANGES OF ADDRESS SHOULD BE PROMPTLY REPORTED.

ATTACH LABEL HERE

Change of Address

To change your address, place address label here for proper identification. Print your NEW address below.

Mail to the Circulation Department, The Electrochemical Society, Inc., 10 South Main St., Pennington, NJ 08534-2896.

name

address

city state zip code

PEOPLE

Roque J. Calvo, Assistant Executive Secretary of The Electrochemical Society, Inc., has recently earned a Master of Business Administration Degree from Rider College, Lawrenceville, New Jersey. In addition to receiving the Masters Degree, Mr. Calvo was inducted into the Sigma Iota Epsilon National Honorary Fraternity in Management for his outstanding achievement in the postgraduate program.

Mr. Calvo, a native of Bethlehem, Pennsylvania, received his Bachelor of Science Degree from Lebanon Valley College (Annville, Pennsylvania) in 1980. He joined the Society staff that same year as Accounting Supervisor and held that position for two years until he was promoted to Assistant Executive Secretary.

Quit stacking things on your Potentiostat!

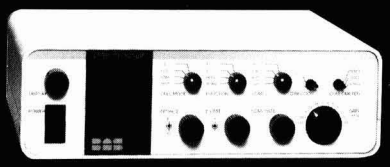

The CV-27 has everything you need in one compact package: signal generator, potentiostat, current-to-voltage converter, amplifier, coulometer, the works! The CV-27 eliminates the clutter, confusion, and redundancy often associated with electrochemical instruments. It's the perfect choice for popular electroanalytical applications and is accompanied by a selection of equally compact cells, voltammetry electrodes, and accessories.

BAS

2701 Kent Ave
West Lafayette
Indiana 47906

Bioanalytical Systems, Inc

Telex: 276141
(317) 463-4527

POSITION WANTED

Electrochemist—Ph.D. in analytical chemistry seeks an entry level position. Two years experience outside academics with one subordinate. Interests and skills include: photoelectrochemistry (solar), electrochemistry, CVT growth of WSe_2, AAS, and water analysis. Available Jan. 1987. Will relocate. Reply 1121 30th Street, #21, Boulder, CO 80303 or phone (303) 447-2573 (h) or (303) 492-3533 (w).

Equipment/Instrumentation

PCSTAT—Turn your IBM-PC into a sophisticated potentiostat. The potentiostat card fits into one slot of a PC. Menu-driven software includes potential sweeps for cyclic voltammograms, potential steps, and coulometry. PCSTAT card and software complete for $2950. Orders accepted now. ETT Inc., P.O. Box 160, Princeton, NJ 08542. 609-921-0070.

REVIEWS & NEWS INDEX

Division News 451C
Meetings Calendar 451C
New Members 452C
People 452C
Position Wanted 453C

ADVERTISERS' INDEX

JEC Press 450C
Bioanalytical Systems .. 451C, 453C
Engelhard 452C
ETT Incorporated 453C
Motorola 454C
MIT 455C, 456C
PAR 459C, 461C

Corrosion Division Award for Summer Study in Corrosion Science

The Corrosion Division of The Electrochemical Society is offering its Award for Summer Study in Corrosion Science to a qualified graduating senior or advanced undergraduate for the summer of 1987. This award provides a minimum grant-in-aid of $1000 and travel expenses toward a summer's (at least two months) research and study in a laboratory of a recognized institute or institution of higher learning.

The objectives of this award are as follows.

1. To stimulate and encourage active and continued participation in the field of corrosion science and corrosion protection by outstanding students of science and engineering.
2. To encourage education in this field for a student likely to attend graduate school for an advanced degree.

To be eligible for the award, the entrant must qualify in at least one of two following categories. He or she must be either (1) a graduating senior of demonstrated ability, regularly enrolled in any recognized college, university, or institute of technology in the United States or Canada, who intends to seek an advanced degree, or (2) an advanced undergraduate similarly enrolled, within six months of graduation who intends to seek an advanced degree. No limitations of sex, race, nationality, or religion are to be imposed by the Award Committee in determining the recipient of the Award.

The award shall be presented on the basis of the following material.

1. A complete transcript of the student's academic record.
2. The original and two copies of a letter, over the signature of the head of the college or department in which the student is enrolled, describing briefly the student's academic work, campus activities, and abilities.
3. The original and two copies of a letter, over the student's signature, containing a brief biographical sketch, a detailed description of the nature and extent of the student's academic work, particularly as it may relate to the field of the Award, and an outline of future plans. The student shall suggest the topic and site for the intended research and his or her basis for this choice. The student's letter should also contain a statement signifying willingness to fulfill the requirements of the Award as described in the Award Rules.

Application forms are available from the Executive Secretary, V. H. Branneky, The Electrochemical Society, 10 South Main St., Pennington, NJ 08534-2896. Deadline for receipt of completed applications is December 1, 1986, and the award winner will be announced by April 1, 1987.

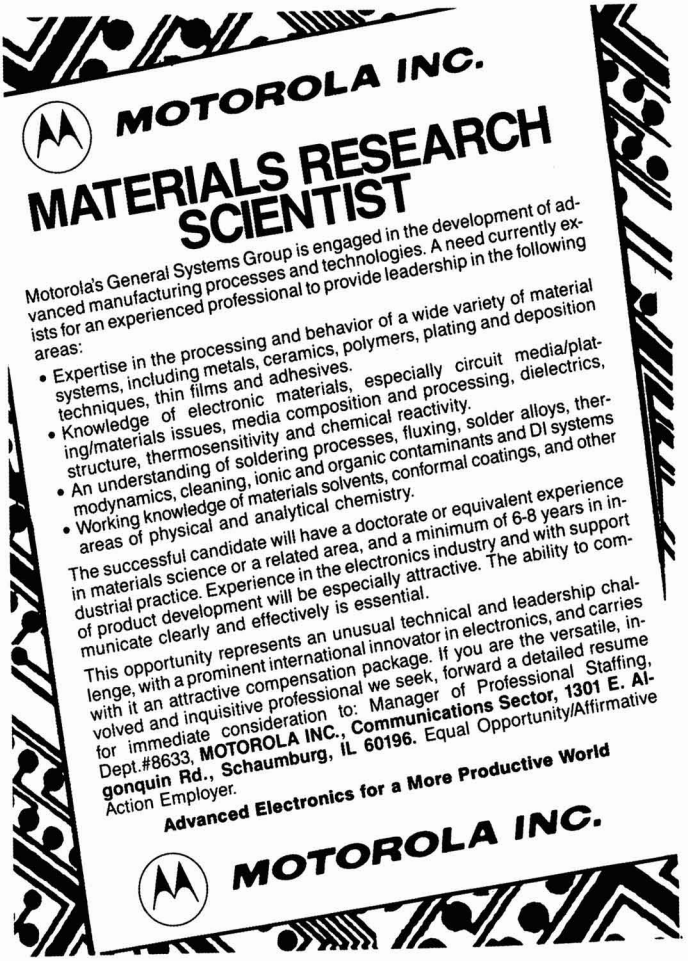

Call for Nominations for the Henry B. Linford Award for Distinguished Teaching

Nominations are solicited for the Henry B. Linford Award for Distinguished Teaching of The Electrochemical Society, Inc. The fourth presentation of this biennial award will be made at the 1988 Spring Meeting of the Society in Atlanta, Georgia.

The nominee shall be distinguished for excellence in teaching in subject areas of interest to the Society. The nominee need not be a member of the Society, nor shall there be any restrictions or reservations regarding age, sex, race, citizenship, or place of origin or residence.

The award shall consist of a silver medal and bronze replica thereof both bearing the recipient's name and the sum of $1000. The recipient shall receive the award in person at the 1988 Spring Meeting of the Society. The award will be presented by the President of the Society at the Awards and Recognition Session. Expenses involved in the acceptance of the award shall be assumed by the recipient.

To be considered for the Henry B. Linford Award, nominations must be accompanied by supporting documents, such as a biography, list of recent courses taught, list of publications, including any textbooks, professional activities, list of former students and their current affiliations, and other appropriate supporting material. Letters of support by distinguished colleagues and former students are also encouraged.

Nomination documents in 8 copies should be submitted to the Chairman of the Selection Committee: Dr. H. W. Pickering, Department of Materials Science, Pennsylvania State University, 326 Steidle Building, University Park, PA 16802. Deadline for receipt of nominations by the Selection Committee Chairman is **May 1, 1987.**

ELECTRONIC MATERIALS FACULTY

A tenure-track assistant professor is sought to teach and conduct research in the Department of Materials Science and Engineering at M.I.T. Candidates are sought who will devote their initial research activities in electronic materials such as:

(1) Processing and properties of multilayer structures and interfaces

(2) Electro-optic, magneto-optic, or piezoelectric materials

(3) Processing and properties of semiconductors and semiconductor devices

Doctorate required and experience desirable. Salaries and benefits competitive. Positions will be filled only if exceptional candidates are found.

Send resume (include citizenship and/or visa status), publications list and references to Professor Merton C. Flemings, Head, Department of Materials Science and Engineering, Massachusetts Institute of Technology, Cambridge, MA 02139.

M.I.T. is an equal opportunity/ affirmative action employer.

MIT

Notice to Subscribers

Your subscription to the JOURNAL OF THE ELECTROCHEMICAL SOCIETY will expire on December 31, 1986. Avoid missing any issue. A subscription renewal card invoice and return envelope have been mailed to all subscribers. To insure proper handling, mail your check for $195 with the completed card invoice in the envelope provided. [Subscribers located outside the United States of America and Canada must add $20.00 to the subscription price for postage ($215.00), and payment must be made by money order or check in U.S. Funds.]

THE ELECTROCHEMICAL SOCIETY BOOKS IN PRINT

Monograph Series

The following hardbound volumes are sponsored by The Electrochemical Society, Inc. and published by John Wiley & Sons, Inc. Members who wish to receive a discount must send their orders to the Society Headquarters, 10 South Main St., Pennington, N. J. 08534. The books will be shipped by John Wiley & Sons, Inc. Invoices for the cost of the volume plus postage and handling will be sent by Society Headquarters. Terms: Payment upon receipt of invoice. All others should send their orders directly to John Wiley, 1 Wiley Dr., Somerset, N. J. 08873. All prices are subject to change without notice.

Corrosion Handbook, edited by Herbert H. Uhlig (1948). 1188 pages, **$74.50.**

Alkaline Storage Batteries, by S. Uno Falk and Alvin J. Salkind (1969). 656 pages, **$91.95.**

Handbook on Corrosion Testing and Evaluation, edited by W. H. Ailor (1971). 873 pages, **$94.95.**

Modern Electroplating, edited by Frederick A. Lowenheim. Third Edition (1974). 801 pages, **$59.95.**

Marine Corrosion, by Francis L. LaQue (1975). 332 pages, **$48.95.**

The Primary Battery, Volume II, edited by George W. Heise and N. Corey Cahoon (1975). 528 pages, **$82.50.**

Thin Films—Interdiffusion and Reactions, edited by J. M. Poate, K. N. Tu, and J. W. Mayer (1978). 576 pages, **$69.95.**

Corrosion of Stainless Steels, by J. A. Sedriks (1979). 282 pages, **$48.95.**

Corrosion of Nickel and Nickel-Base Alloys, by Wayne Z. Friend (1980). 460 pages, **$72.95.**

Atmospheric Corrosion, edited by W. H. Ailor (1982). 1028 pages, **$172.50.**

Lithium Battery Technology, edited by H. Venkatasetty (1984). 247 pages, **$42.50.**

The following volume, sponsored by The Electrochemical Society, Inc., should be ordered directly from the publisher, Plenum Publishing Corporation, 233 Spring St., New York, N. Y. 10013.

Adhesion Aspects of Polymeric Coatings, edited by K. L. Mittal (1983). 658 pages, **$85.00.**

The following hardbound volumes are sponsored by and published by The Electrochemical Society, Inc. They should be ordered from: The Electrochemical Society, Inc., 10 South Main St., Pennington, N. J. 08534. Remittance must accompany order for these volumes.

Society Published Monograph Series

Passivity of Metals (proceedings of The Fourth International Symposium on Passivity). R. P. Frankenthal and J. Kruger, Editors. A 1977 symposium. 1078 pages, **$65.00**

Other Society Books

Bibliography of Electro-Organic Syntheses, by Sherlock Swann, Jr. and Richard C. Alkire, 755 pages, **$35.00**

Faculty Position in MATERIALS SCIENCE AND ENGINEERING

Outstanding candidates are sought for a tenure-track faculty position (preferably at the assistant professor level) in the Department of Materials Science and Engineering, who have demonstrated notable creativity, leadership and teaching ability in any aspect of the fields of materials science or materials engineering. In the exceptional case, the position may be opened to a senior faculty appointment. The area of specific research accomplishment or interest may be in any of the materials classes: electronic materials, ceramics, metals or polymers, or may be broadly in the fields of materials science or engineering, but preference may be given to candidates whose interests either bridge several subdisciplines within these fields or will expand an existing subdiscipline to new frontiers.

Candidates must have a doctorate in a science or engineering discipline. While additional experience is desirable, this position demands, above all, exceptional promise as a research leader and outstanding potential as a faculty member. A resume (including citizenship and/or visa status), publication list and names of potential references should be sent to: Professor Merton C. Flemings, Head, Department of Materials Science and Engineering, Massachusetts Institute of Technology, Cambridge, MA 02139.

M.I.T. is an equal opportunity/ affirmative action employer.

MIT

Notice to Authors for Philadelphia, PA, Meeting

The 75-word and extended abstracts for the Philadelphia, Pennsylvania, Meeting of the Society, May 10-15, 1987, must be received by Society-Headquarters on or before December 1, 1986. These deadlines must be adhered to in order for a paper to be considered for inclusion in the meeting program. Further details appear in the Call for Papers, pages 399C-404C of This Journal.

Positions Wanted

Society members of any class may, at no cost and for the purposes of professional employment, place not more than three identical insertions per calendar year, not to exceed 8 lines each. Count 43 characters per line, including a 4 character box number, which the Society will assign.

F. M. Becket Memorial Award

The Electrochemical Society will offer the F. M. Becket Memorial Award to a qualified graduate student for the summer of 1987. This award commemorates F. M. Becket, a man of great research and administrative ability, and a former President of the Society, whose accomplishments in science and industry were outstanding. The stipend, valued at $2000, provides a grant-in-aid toward a summer's (at least two months) research and study overseas in the laboratory of a recognized research institute or institution of higher learning, selected from the approved list maintained by the F. M. Becket Memorial Award Committee.

The objectives of this award are to stimulate and encourage education and participation in the fields of electrochemical science and industry concerned with specialty materials and processes as follows:

a) **Materials** such as refractory metals and compounds, intermetallics, graphite, fused salts, and rare earth metals;

b) **Equipment** for the utilization of electrical energy in materials synthesis;

c) **Processes** using arcs, vacua, plasmas, and electron and ion beams; and

d) **High temperature kinetics and thermodynamic and related phenomena** such as melting, vaporization, reactions, sintering, diffusion or oxidation occurring at high temperatures, high pressures, or vacua involving high temperature materials.

To be eligible for the award, the entrant must qualify in one of the two following categories. He or she must be either (1) a graduating senior of demonstrated ability, regularly enrolled in any recognized college, university, or institute of technology in continental United States or Canada, who intends to seek an advanced degree, or (2) a graduate student, similarly enrolled, who is seeking an advanced degree. No limitations of sex, race, nationality, or religion are to be imposed by the Award Committee in determining the recipient of the award.

The award shall be presented on the basis of the following material:

1. A complete transcript of the student's academic record.

2. Two copies of a letter, over the signature of the head of the College or Department in which the student is enrolled, describing briefly his or her academic work, his or her campus activities, and presenting an estimate of his or her abilities.

3. Two copies of a letter, over the student's signature, containing a brief biographical sketch, a detailed description of the nature and extent of his or her academic work, particularly as it may relate to the field of the award, and an outline of future plans. The student's letter should also contain a statement signifying willingness to fulfill the further requirements of the award as described in the Award Rules. The student shall indicate, from the list provided by the Award Committee, a choice of a place of residence under the award.

Application forms are available from the Executive Secretary, V. H. Branneky, The Electrochemical Society, Inc., 10 S. Main St., Pennington, NJ 08534-2896. Deadline for receipt of completed applications will be January 1, 1987 and the award winner will be announced on March 30, 1987.

Nominations Solicited for the 1988 Vittorio de Nora-Diamond Shamrock Award of The Electrochemical Society, Inc. in Electrochemical Engineering and Technology

Nominations are solicited by the Honors and Awards Committee for the Vittorio de Nora-Diamond Shamrock Award in Electrochemical Engineering and Technology. The next Award will be presented at the Spring 1988 Meeting of the Society in Atlanta, Georgia.

The recipient shall be distinguished for outstanding contributions to electrochemical engineering and technology. Nominees need not be members of the Society to be considered, and there are no distinctions, restrictions, or reservations regarding age, sex, race, citizenship, or place of origin or residence.

The Award consists of a gold medal and a bronze replica, both bearing the recipient's name, and the sum of $1500. The recipient is required to deliver an address to the Society on a subject related to the contributions for which the Award is presented.

Previous recipients of the Vittorio de Nora-Diamond Shamrock Award are:

1974—Abner Brenner
1976—Robert B. MacMullin
1978—Francis T. Bacon
1980—Henri B. Beer
1982—Joseph C. Schumacher
1984—Donald E. Danly
1986—Karl Kordesch

This is one of The Electrochemical Society's most prestigious awards, and all members are urged to give serious consideration to nominating possible candidates. Nomination forms are available from the Subcommittee Chairman: Brooke Schumm, Jr., Union Carbide Corp., Battery Products Division, Technical Laboratory, 25225 Detroit Rd., Westlake, OH 44145, U.S.A. (telephone 216-835-7735) or from the headquarters office of The Electrochemical Society, Inc., 10 S. Main St., Pennington, NJ 08534-2896 (telephone 609-737-1902). If possible, please submit nominations by April 1, 1987, to facilitate consideration by the Award Committee. Nominations will be closed at the beginning of the Spring 1987 Meeting.

Summer Fellowship Award Program of The Electrochemical Society

The Board of Directors of The Electrochemical Society has voted to allocate $6000 for summer fellowships in 1987. The Award subcommittee shall have the discretion of deciding the number of recipients and the amount granted to each, within the limits of the appropriation.

The purpose of the award is to assist a student in continuing his/her graduate work during the summer months in a field of interest to The Electrochemical Society. According to the rules for the Society Summer Fellowship Program, if one award is given it shall be called the Edward G. Weston Fellowship Award; if two awards are given, the second one shall be designated the Colin Garfield Fink Fellowship Award; if more than two are given, the third award shall be called the Joseph W. Richards Fellowship Award.

Candidate's qualifications: "The award shall be made without regard to sex, citizenship, race, or financial need. It shall be made to a graduate student pursuing work between the degree of B.S. and Ph.D., in a college or university in the United States or Canada, and who will continue their studies after the summer period. A previous holder of an award is eligible for reappointment."

Qualified graduate students are invited to apply for these fellowship awards. Applicants must complete an application form and supply the following information:

1. A brief statement of educational objectives.
2. A brief statement of the thesis research problem including objectives, work already accomplished, and work planned for the summer of 1987.
3. A transcript of undergraduate and graduate academic work.
4. Two letters of recommendation, one of which should be from the applicant's research adviser.
5. Successful recipients of fellowships shall agree not to hold other appointments or other fellowships during the summer of 1987.

Application forms are available from the Chairman of the Fellowship Awards Subcommittee, to whom completed applications and letters of recommendation should be sent: Dr. B. E. Conway, Department of Chemistry, University of Ottawa, Ottawa, Ontario, Canada K1N 9B4.

Deadline for receipt of completed applications will be January 15, 1987 and award winners will be announced on May 1, 1987.

Announcement of Energy Research Summer Fellowships

The Board of Directors of The Electrochemical Society has announced that there will be additional summer fellowships in 1987 subject to approval of the U.S. Department of Energy. Each fellowship grant will be $2000. The Summer Fellowship Award Subcommittee, with the approval of the U.S. Department of Energy, shall have the discretion of deciding the number of recipients and the amount granted to each, within the limits of the appropriation.

The purpose of the award is to assist a student in continuing his/her graduate work during the summer months in a field relating to energy research or technology of interest to The Electrochemical Society. Such field shall address energy-related aspects of electrochemical science and engineering as well as solid-state science and engineering and shall involve the areas of batteries, fuel cells, photoelectrochemistry, photovoltaics, and electrochemical processes of materials aimed at reducing energy consumption.

Candidate's qualifications: "The award shall be made without regard to sex, citizenship, race, or financial need. It shall be made to a graduate student pursuing work between the degree of B.S. and Ph.D., in a college or university in the United States or Canada, and who will continue their studies after the summer period. A previous holder of an award is eligible for reappointment."

Qualified graduate students are invited to apply for these fellowship awards. Applicants must complete an application form and supply the following information:

1. A brief statement of educational objectives.
2. A brief statement of the thesis research problem including objectives, work already accomplished, and work planned for the summer of 1987.
3. A transcript of undergraduate and graduate academic work.
4. Two letters of recommendation, one of which should be from the applicant's research adviser.
5. Successful recipients of fellowships shall agree not to hold other appointments or other fellowships during the summer of 1987.

Application forms are available from the Chairman of the Fellowship Awards Subcommittee, to whom completed applications and letters of recommendation should be sent: Dr. B. E. Conway, Department of Chemistry, University of Ottawa, Ottawa, Ontario, Canada K1N 9B4.

The deadline for receipt of completed applications for these Summer Fellowships will be January 15, 1987 and award winners will be announced on May 1, 1987.

THE ELECTROCHEMICAL SOCIETY SHORT COURSE CHEMICAL SENSORS

Sunday, May 17, 1987, ADAM'S MARK HOTEL Philadelphia
Limited Attendance—Advanced registration required

The Electrochemical Society will sponsor a short course in conjunction with the 171st Meeting of the Society in Philadelphia at the Adam's Mark Hotel on Sunday, May 17, 1987. The course will consist of five lectures, an introduction, and a discussion session. The morning section will run from 9:00 to 12:15 and the afternoon section from 1:30 to 5:00. Lunch and coffee breaks will be provided. Copies of the visual aids, along with a course outline and bibliography, will be distributed to each registrant at the time of the course. The registration fee is $225 for members and $275 for nonmembers. The fee covers the course, luncheon, coffee breaks, and text material; it is not applicable to any other activities of the Society's 171st Meeting. The attached registration form and a check for the correct registration fee must be received not later than April 17, 1987, at The Electrochemical Society, Inc., 10 South Main Street, Pennington, NJ 08534-2896.

CHEMICAL SENSORS

Prof. Richard P. Buck

Department of Chemistry
The University of North Carolina, Chapel Hill, North Carolina

Prof. Jay N. Zemel

Center for Sensor Technologies
School of Engineering and Applied Science, University of Pennsylvania, Philadelphia, Pennsylvania

Dr. Dennis R. Turner

Consultant—Retired from AT&T Bell Laboratories
59 Susan Drive, Chatham, New Jersey

This course will cover the science, technology, and applications of chemical sensors. It will discuss the fundamental principles upon which most chemical sensors are based and develop a pattern on how the phenomena are utilized for sensor applications. The course will provide a broad overview of state-of-the-art chemical sensors, and project what we can expect in the way of new sensors. The course should be of interest to researchers, engineers, and managers active or planning to be active in the research, development, and application of chemical sensors.

The first half of the course will consist of three lectures titled Electrochemical Sensors, Solid-State Sensors, and Optical Sensors. All aspects of these topics will be discussed starting with fundamental principles and progressing through the development of specific sensor types that have useful applications. The second half of the course will deal with applications of chemical sensors in important areas such as biomedical and chemical process monitoring and control. Emphasis will be placed not only on the science and technology of existing chemical sensors but also on what our needs are for new sensors and what are the promising areas for research and development.

SHORT COURSE REGISTRATION FORM

CHEMICAL SENSORS

Payment Enclosed:

☐ ECS Members—$225.00 ☐ Nonmember—$275.00

Name _____

Address _____

City, State, Zip _____

Business Affiliation _____

Please return this form by April 17, 1987, with your payment to:
The Electrochemical Society, Inc., 10 South Main St., Pennington, N.J. 08534-2896.

UNVEILING THE WORLD'S MOST SENSITIVE ELECTROCHEMICAL DETECTOR

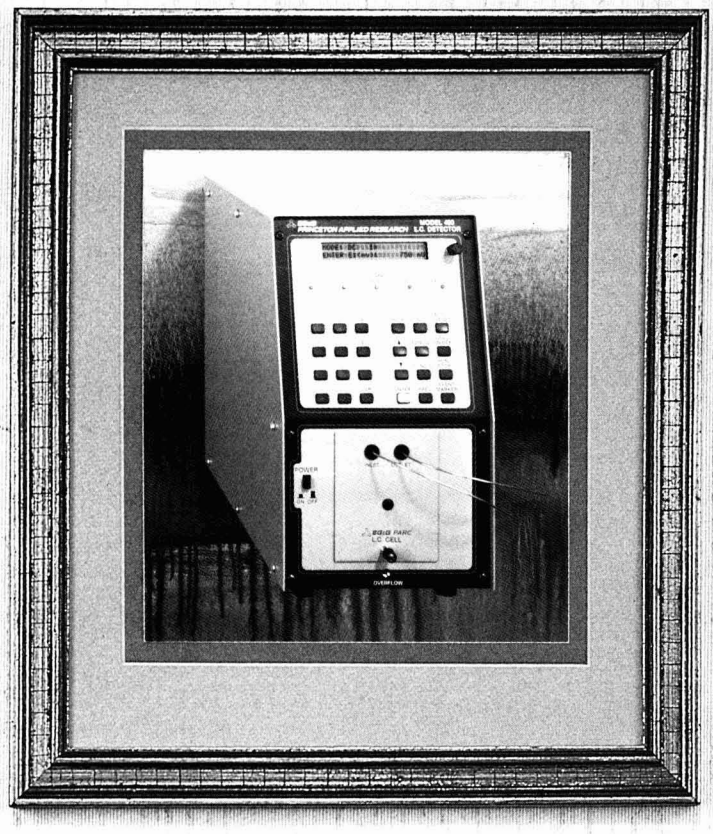

Model 400
Electrochemical Detector

Advancing The Art Of Chromatography

Twenty-five years experience in the development and manufacture of electrochemical instrumentation gives *EG&G Princeton Applied Research* the know-how to develop an Electrochemical Detector for a broad range of measurements down to the low picogram range of detection. The new Model 400 is able to detect and measure extraordinarily low signals permitting truly usable operation at currents down to 10 picoamps.

A Masterpiece Of Convenience...

The Model 400 proves that electrochemical detectors do not have to be finicky. Its unique cell design plus remote autoffset, computer control, menu-driven display operation and pre-electrolysis control are some of the features that make the Model 400 convenient and easy to use.

...And Of Versatility

The *EG&G Princeton Applied Research* Model 400 provides a unique combination of: ▪ DC Mode ▪ Dual Potential Mode ▪ Pulse Mode ▪ Oxidative and Reductive Detection ▪ Cyclic Voltammetry ▪ A Complete Selection of Cell Components (including a metal-free cell system) ▪ Computer Interface (IEEE and RS232) and Pre-electrolysis Control, to name a few.

With these features you can use the Model 400 for more applications than any other Electrochemical Detector.

An Exhibition Of Quality And Of Service

When you select the Model 400, you get the world's most sensitive electrochemical detector.

You also receive the *EG&G Princeton Applied Research* commitment to total customer support. Experienced chromatographers are on hand to answer your questions and to help you get the most out of your Model 400. And our 48-hour repair/replacement service program insures minimum down time.

Contact our LC Applications Group for a demonstration or for more information on how the Model 400 Electrochemical Detector advances the art of chromatography.

***Call (609) 895-0100* today!**

EG&G PRINCETON APPLIED RESEARCH

Quality Electrochemical Instruments

Electrochemical Instruments Division

CN 5206 ▪ Princeton NJ 08543-5206 ▪ (609) 895-0100 ▪ TELEX: 843409

Germany: 92692-0 ▪ England: 990-23491 ▪ France: 077/93/66 ▪ China: 890721 ▪ Netherlands & Belgium: 30-887520 ▪ Taiwan: 731-2911 ▪ Italy: 7386294 ▪ Sweden: 468 768 3250 ▪ Korea: 546-7771 ▪ Japan: 354-1411 ▪ India: 827577

JO6018E

CALL FOR PAPERS

FIRST INTERNATIONAL BI/CMOS SYMPOSIUM

MAY 10-15, 1987—PHILADELPHIA, PENNSYLVANIA

The First International BI/CMOS Symposium, cosponsored by the Electronics Division and the Luminescence and Display Materials Group, will be held as a part of the 171st Meeting of The Electrochemical Society in Philadelphia, Pennsylvania, May 10-15, 1987.

BI/CMOS technology is the dream of the IC design engineers. It combines the virtues of low power, high noise immunity, simple logic implementation, and high input impedance of CMOS, with the high current drive capability, excellent device-to-device matching, and low noise performance of bipolar transistors.

This International BI/CMOS Symposium consists of two parts:

1. BI/CMOS Design
2. BI/CMOS Process Technology

The objective of the BI/CMOS Design Session in this symposium is to bring together design engineers to discuss the design advantages, limitations, and applications of BI/CMOS. Specifically, issues relating to BI/CMOS in both analog and digital VLSI designs will be highlighted.

The objective of the BI/CMOS Process Technology Session in this symposium is to bring together the process engineers to discuss the various technology options for BI/CMOS, key advances in BI/CMOS fabrication techniques, device optimization, and emerging trends. In order to realize the advantages of both bipolar and CMOS functions, the process and device technologies must be carefully optimized.

This symposium will include both invited and contributed papers covering the topics listed above. Both experimental and theoretical contributed papers are solicited covering the design and process technology issues. Please submit a 75-word abstract and an extended abstract of the paper(s) using the standard formats given in the **Journal of The Electrochemical Society.** The deadline for submitting both the abstracts is **December 1, 1986.** The original of each must be sent to the Headquarters Office of The Electrochemical Society, and a copy of each should be sent to one of the Symposium Co-Chairmen listed below:

Arjun N. Saxena
Gould AMI Semiconductors
3800 Homestead Road
Santa Clara, CA 94306
Telephone: 408-554-2184
FAX: 408-554-2112

Takahiro Nagano
Hitachi Laboratory
4026 Kuji Cho, Hitachi City
Ibaragi Prefecture, Japan 319-12
Telephone: 0294-53-1111 X2709
FAX: 294-53-5857

ELECTROCHEMISTRY SOFTWARE AND THE IBM PC

The latest innovative software from ***EG&G*** *Princeton Applied Research* gives the IBM Personal Computer the power to perform computer-controlled electrochemical measurements. Our three new software packages marry the power and the IBM PC's ease-of-use with the extraordinary capabilities of our *Model 273 Potentiostat/Galvanostat.*

Software packages available include:

- ***Softcorr Corrosion Software*** *(Model 342)* offers automatic measurement, data analysis and documentation for the nine most widely used electrochemical techniques.
- ***Electrochemical Impedance Software*** *(Model 378)* provides the most versatile and effective approach to electrochemical impedance measurements. This program completely automates an experiment... From automatic control of the potentiostat and lock-in amplifier to automatic data modeling aids for easier data interpretation.
- ***Head Start™ Software*** *(Model 273)* enables you to run the most common electrochemical research techniques right out of the box. This working tutorial also lets you write custom electrochemistry software with a minimum of programming effort using our highly flexible *Electrochemical Command Set.*

These first members of our IBM PC software family are available as individual software packages or as part of a complete system of instrumentation. Find out how our software and the IBM PC work together to enhance your power to perform effective electrochemical measurements.

Call *today*: **(609) 895-0100.**

EG&G PRINCETON APPLIED RESEARCH

Electrochemical Instruments Division

CN 5206 • PRINCETON, NJ 08543 U.S.A. • (609) 895-0100 • TELEX: 843409

IBM PC is a registered trademark of International Business Machines Corporation.

JO1004EC

CALL FOR PAPERS

TENTH INTERNATIONAL CONFERENCE CHEMICAL VAPOR DEPOSITION (CVD-X)

OCTOBER 18-23, 1987

The Tenth International Conference on Chemical Vapor Deposition will be held October 18-23, 1987, at the Hilton Hawaiian Village, Honolulu, Hawaii, as part of the 172nd Meeting of The Electrochemical Society, Inc., which will be cosponsored by The Electrochemical Society of Japan and The Japan Society of Applied Physics.

CVD-X will provide a forum for those interested in CVD to exchange recent results. The broad scope of the Conference will include, but is not limited to, papers on the following CVD topics:

Fundamentals—kinetics, thermodynamics, gas-flow dynamics, reaction mechanisms, interface chemistry, gas-phase chemistry, structure-property-process relationships.
Materials Types—high-purity materials, optical materials, elemental and compound semiconductors, nuclear materials, insulators, hard coatings, refractories.
Approaches—homoepitaxial growth, silicon-on-insulators, heteroepitaxial deposition on insulating and semiconducting substrates, selective epitaxial growth, chemical vapor infiltration (CVI), modified CVD (MCVD) for optical fibers.
Measurement and Control—advanced *in situ* characterization for diagnostics, *in situ* measurements for reactor control, computer and microprocessor control.
Methods—reduced-pressure, low-temperature, plasma, laser, photo, ion beam, organometallic sources, new reactor types.

As in the preceding conferences of this series, a Proceedings volume will be published and made available at the Conference. This requires that the following early deadlines be carefully observed.

January 15, 1987:	Send 75-word abstract (containing sufficient detail for refereeing) to J. M. Blocher, Jr.
February 15, 1987:	Authors to receive notice from reviewers.
April 15, 1987:	Send full manuscript to G. W. Cullen.
May 1, 1987:	75-word abstract and extended abstract due at Electrochemical Society Headquarters Office.

Suggestions for invited speakers and Conference topic emphases should be sent to any of the Conference Co-Chairmen:

- J. M. Blocher, Jr., 915 Silvoor Lane, Oxford, OH 45056, USA
- G. W. Cullen, RCA Laboratories, Princeton, NJ 08543-0432, USA
- Werner Kern, RCA Laboratories, Princeton, NJ 08543-0432, USA
- P. Rai-Choudhury, Westinghouse R&D Center, Pittsburgh, PA 15235, USA
- K. Sugawara, Hitachi, Ltd., Semicon. and IC Div., Kodaira, Tokyo 187, JAPAN

APPLICATION FOR ADMISSION

TO

The Electrochemical Society, Inc.

Return completed application to:

Secretary
The Electrochemical Society, Inc.
10 South Main Street, Pennington, New Jersey 08534-2896
609-737-1902

For office use only

Date Rec'd. _____ $ _____

Notice of Ackn. _____

Checked: _____

Approved: _____

To the Board of Directors of The Electrochemical Society, Inc:

Please print complete name and address as it should appear on mailings.

Name: _____

Address: _____

_____

_____

_____

_____

Business Telephone: (include area code) _____

I hereby make application for admission to The Electrochemical Society, Inc., as an _____ member, and enclose the amount of $_____ covering the first year's dues. (Please see reverse side for proper class of membership and dues applying thereto, noting the options with regard to the date of election and active life membership and the credit available for nonmember meeting registration.)

1. Date of Birth: _____ (month) _____ (day) _____ (year)

2. Please check LOCAL SECTION with which you wish to affiliate:

—— Boston (05)	—— Detroit (25)	—— Midland (Mich.) (40)	—— Philadelphia (70)	—— So. Calif.-Nevada (90)
—— Canadian (60)	—— European (27)	—— Natl. Capital Area (45)	—— Pittsburgh (75)	—— Southern Wisconsin (92)
—— Chicago (10)	—— Indianapolis (30)	—— North Texas (55)	—— Rocky Mountain (80)	—— Twin Cities (96)
—— Cleveland (15)	—— Japan (33)	—— Oregon (62)	—— San Francisco (85)	—— None (99)
—— Columbus (20)	—— Metropolitan N.Y. (35)	—— Pacific Northwest (65)	—— South Texas (88)	

3. Please indicate your DIVISIONAL and GROUP interests, noting your primary interest(s) with the number 1 and secondary interest(s) with the number 2.

—— Battery (AO)	—— Electronics (EO)	—— Industrial Electrolytic (IO)
—— Corrosion (BO)	☐ New Electronic Technologies (E1)	—— Luminescence and Display Materials (KO)
—— Dielectrics and Insulation (CO)	☐ Semiconductors (E3)	—— Organic and Biological Electrochemistry (FO)
—— Electrodeposition (DO)	—— Energy Technology (GO)	—— Physical Electrochemistry (JO)
	—— High Temperature Materials (HO)	

4. Education:

Institution	Dates Attended	Major Subject	Degree Earned

5. Work Experience:

Name of Employer (current, followed by previous)	Dates	Position

6. The Society's Constitution provides that two Active Members of the Society (who can substantiate the above record) must recommend you for admission to membership. It will facilitate the handling of your application if you are able to have your references sign this application form; if this is not convenient, please list their names and addresses. On a student application, only a single faculty member recommendation with signature (including title and and institution) is required.

Name (please print)	Signature	Address
Name (please print)	Signature	Address

The undersigned certifies that the above statements are correct and agrees, if elected to the Society, to be governed by its Constitution and Bylaws and to promote the objects of the Society as stated in its Constitution.

Date _____ 19 __ _____ (Signature)

Rev. 7/85

EXTRACTS FROM THE CONSTITUTION AND BYLAWS

CONSTITUTION—Article II

Membership

Section 1. The individual membership shall consist of Active, Honorary and Emeritus Members. The Board of Directors may from time to time authorize other classifications of membership as defined in the Bylaws of the Society.

(Active Member—Annual Dues $60.00)

Active Member

Section 2. An Active Member shall be interested in electrochemistry or allied subjects and possess a Bachelor's degree, or its equivalent, in engineering or natural science. In lieu of a Bachelor's degree, or its equivalent, any combination of years of undergraduate study and years of relevant work experience in electrochemistry or allied subjects adding to at least seven years shall be required. Election to Active Membership shall require the recommendation of two Active Members in good standing.

BYLAWS—Article II

Non-Voting Membership
(Student Member—Annual Dues $10.00)

Student Member

Section 1. Student Member. A Student Member shall be a full-time undergraduate or graduate student registered for a degree in natural science or engineering. The applicant for Student Membership shall be recommended by a member of the faculty of the school. Upon graduation with a Bachelor's degree or equivalent in natural science or engineering, the Student Member may apply for Active Membership. The application shall be approved by two Active Members of the Society in good standing. If the Student Member enters graduate school as a full-time student, the person may choose to apply for Active Membership or remain a Student Member.

BYLAWS—Article XXI

Dues and Fees

Dues

Section 1. The annual dues for Active Members shall be sixty dollars. The annual dues for Student Members shall be ten dollars. Each member shall receive the JOURNAL OF THE ELECTROCHEMICAL SOCIETY.

Date of Election

Section 2. When individuals are elected to membership, they must elect to initiate their membership as of January 1 or July 1 of the year of election; or, if elected during the last quarter, January 1 of the year following election. In the case of a July 1 election for starting membership, dues will be prorated.

Active Life Membership

Section 3. Any Active Member who shall pay in one lump sum the amount equivalent to two-thirds of the remaining dues to age sixty-five at the time of payment, but not less than an amount of 5 years of full dues, shall be exempt from payment of any further dues and shall be considered an Active Member during the remainder of his or her life.

Nonmember Meeting Registration Credit

BOARD OF DIRECTORS ACTION OF OCTOBER 9, 1960

If application for new membership is received within four months of the payment of nonmember registration at a Society Meeting by the applicant, the difference between the nonmember and member registration fees shall be credited toward the first year's dues.

CONSTITUTION—Article III

Admission and Dismissal of Members

Section 1. Application for individual membership shall be in writing on a form adopted by the Board of Directors.

Section 2. The Admissions Committee shall be a rotating committee consisting of three members. One member shall be appointed each year by the President with the approval of the Board of Directors for a term of three years to replace the outgoing member. This Committee shall receive from the Secretary all properly executed and properly recommended applications for admission which he has received from persons desirous of becoming members of the Society. It shall be the duty of this Committee, after examining the credentials of applicants, to make appropriate recommendation to the Board as to approval or rejection of the applications. Unanimous approval of an applicant by this Committee shall be required before the candidate's name may be submitted to the Board of Directors for election. The election to membership shall be by a mail vote of the Board of Directors. The candidate shall be considered elected two weeks after the date the proposed membership list is mailed to the Board if no negative votes have been received by the Secretary. If a candidate receives one negative vote, his application shall then be considered and voted upon at the next meeting of the Board of Directors. Two negative votes cast at this meeting shall exclude a candidate. The Board of Directors may refuse to elect a candidate who, in its opinion, is not qualified for membership. The names of those elected shall be announced to the Society. Duly elected candidates shall have all the rights and privileges of membership as soon as their entrance fee, if any, and dues for the current year have been paid.

Section 3. A member desiring to resign shall send a written resignation to the Office of the Society.

Section 4. Upon the written request of ten or more Active Members that, for cause stated therein, a member be dismissed, the Board of Directors shall consider the matter and, if there appears to be sufficient reason, shall advise the accused of the charges against him. He shall then have the right to present a written defense, and to appear in person before a meeting of the Board of Directors, of which meeting he shall receive notice at least twenty days in advance. Not less than two months after such meeting the Board of Directors shall finally consider the case and, if in the opinion of the majority of the Board of Directors a satisfactory defense has not been made and the accused member has not in the meantime tendered his resignation he shall be dismissed from the Society.

Section 7. The entrance fee, if any, annual dues and any other payments to be made by the members of the Society shall be paid in accordance with regulations set forth in the Bylaws.

Section 8. Any member delinquent in dues after April 1 shall not receive the Society's publications and will not be allowed to vote in any Society election until such dues are paid. All members in arrears for one year after April 1 shall lose their membership status and can be reinstated only by action of the Board of Directors.

APPLICATION FOR AWARDED STUDENT MEMBERSHIP
TO
THE ELECTROCHEMICAL SOCIETY, INC.
AND
THE ELECTRONICS DIVISION OF THE ELECTROCHEMICAL SOCIETY, INC.

Includes subscriptions to the JOURNAL OF THE ELECTROCHEMICAL SOCIETY and Electronics Division Newsletter.

Limited to: undergraduate students in final two years; graduate students in science or engineering; or education majors in science or engineering

1. Name: _____

2. Home address: _____

_____

_____

3. School, Division, and Department: _____

4. School address: _____

_____

5. Undergraduate year beginning in September 1986 (check one):

Next to final year: _____ Final year: _____

Graduate year beginning in September 1986 (circle one): 1 2 3 4 5

6. Current or future major subject: _____

7. Undergraduate grade point average: _____ out of possible _____

Graduate school grade point average: _____ out of possible _____

8. Have you won this award before? (check one) Yes _____ No _____

If yes, how many times? _____

9. Are you a member of a Local Section of The Electrochemical Society? Yes _____ No _____

Signature of student: _____

Faculty member signature attesting to full-time enrollment of student:

Signature: _____

Department: _____ Date: _____

APPLICATIONS MUST BE POSTMARKED BY OCTOBER 31, 1986

Send application to: A. Reisman, Professor
Microelectronics Center of North Carolina
and North Carolina State University
P.O. Box 12889
Research Triangle Park, NC 27709

AWARD RULES

This award is available to qualified full-time students worldwide, who will be starting, or are already in, their final two years as undergraduates or who are graduate students in science, engineering, or education (with a science or engineering degree). It is renewable for up to a total of four years. Qualifiers will be determined by a committee of the Electronics Division of The Electrochemical Society, Inc. Qualifiers and nonqualifiers will be notified by January 1, 1987. Membership will begin on January 1, 1987.

THE ELECTROCHEMICAL SOCIETY BOOKS IN PRINT

Society Proceedings Series
1972-1981

The following softbound proceedings volumes are sponsored and published by The Electrochemical Society, Inc., 10 South Main Street, Pennington, NJ 08534-2896. Orders filled at the list price given, subject to availability. Enclose payment with order.

Electron and Ion Beam Science and Technology, Fifth International Conference. R. Bakish, Editor. A 1972 symposium. 420 pages, **$5.50.**

Electrochemical Bioscience and Bioengineering. H. T. Silverman, I. F. Miller, and A. J. Salkind, Editors. A 1973 symposium. 268 pages, **$8.00.**

Chlorine Bicentennial Symposium. T. C. Jeffery, P. A. Danna, and H. S. Holden, Editors. A 1974 symposium. 404 pages, **$11.00.**

Fine Particles. W. E. Kuhn and J. Ehretsmann, Editors. A 1974 symposium. 352 pages, **$15.00.**

Metal-Slag-Gas Reactions and Processes. Z. A. Foroulis and W. W. Smeltzer, Editors. A 1975 symposium. 1032 pages, **$20.00.**

Chemistry and Physics of Aqueous Gas Solutions. W. A. Adams, G. Greer, J. E. Desnoyers, G. Atkinson, G. S. Kell, K. B. Oldham, and J. Walkley, Editors. A 1975 symposium. 522 pages, **$11.00.**

Thermal and Photostimulated Currents in Insulators. D. M. Smyth, Editor. A 1975 symposium. 215 pages, **$7.00.**

International Symposium on Molten Salts. J. P. Pemsler, J. Braunstein, K. Nobe, D. R. Morris, and N. E. Richards, Editors. A 1976 symposium. 632 pages, **$16.00.**

Properties of High Temperature Alloys. Z. A. Foroulis and F. S. Pettit, Editors. A 1976 symposium. 851 pages, **$12.00.**

Semiconductor Silicon 1977. H. R. Huff and E. Sirtl, Editors. A 1977 symposium. 1100 pages, **$15.00.**

A History of The Electrochemical Society. The first 75 years. R. M. Burns with E. G. Enck, 160 pages. **$5.00.**

Semiconductor-Liquid Junction Solar Cells. A. Heller, Editor. A 1977 symposium. 340 pages, **$10.00.**

Load Leveling. N. P. Yao and J. R. Selman, Editors. A 1977 symposium. 412 pages, **$13.00.**

High Temperature Metal Halide Chemistry. D. L. Hildenbrand and D. D. Cubicciotti, Editors. A 1977 symposium, 678 pages, **$17.00.**

Selected Topics in the History of Electrochemistry. George Dubpernell and J. H. Westbrook, Editors. A 1977 symposium. 523 pages, **$11.00.**

Second International Symposium on Molten Salts. J. Braunstein and J. R. Selman, Editors. A 1978 symposium. 420 pages, **$16.00.**

Laser and Electron Beam Processing of Electrode Materials. C. L. Anderson, G. K. Celler, and G. A. Rozgonyi, Editors. A 1979 symposium. 560 pages, **$13.00.**

Electrode Processes, S. Bruckenstein, J. D. E. McIntyre, B. Miller, and E. Yeager, Editors, A 1979 symposium. 500 pages, **$21.00.**

Power Sources for Biomedical Implantable Applications and Ambient Temperature Lithium Batteries. B. B. Owens and N. Margalit, Editors. A 1979 symposium. 652 pages, **$18.00.**

Electronic and Optical Properties of Polycrystalline or Impure Semiconductors and Novel Silicon Growth Methods. K. V. Ravi and B. O'Mara, Editors. A 1980 symposium. 280 pages, **$15.00.**

Electron and Ion Beam Science and Technology, Ninth International Conference. R. Bakish, Editor. A 1980 symposium. 672 pages, **$28.00.**

Lithium Nonaqueous Battery Electrochemistry. E. B. Yeager, B. Schumm, Jr., G. Blomgren, D. R. Blankenship, V. Leger, and J. Akridge, Editors. A 1980 workshop. 328 pages, **$18.00.**

Ion Exchange: Transport and Interfacial Properties. R. S. Yeo and R. P. Buck, Editors. A 1980 symposium. 396 pages, **$15.00.**

Materials and New Processing Technologies for Photovoltaics. J. A. Amick, E. Sirtl, P. Rai-Choudhury, and J. P. Dismukes, Editors. A 1980 symposium. 368 pages, **$14.00.**

Lithium Batteries, H. V. Venkatasetty, Editor. A 1980 symposium, 516 pages, **$26.00.**

Semiconductor Silicon 1981. H. R. Huff, R. J. Kriegler, and Y. Takeishi, Editors. A 1981 symposium. 1064 pages, **$25.00.**

Electrocrystallization. R. Weil and R. G. Barradas, Editors. A 1981 symposium. 352 pages, **$13.00.**

Corrosion and Corrosion Protection. R. P. Frankenthal and F. Mansfeld, Editors. A 1981 symposium. 304 pages, **$10.00.**

Third International Symposium on Molten Salts. G. Mamantov, M. Blander, and G. P. Smith, Editors. A 1981 symposium. 600 pages, **$23.00.**

High Temperature Materials Chemistry. D. D. Cubicciotti and D. L. Hildenbrand, Editors. A 1981 symposium. 498 pages, **$21.00.**

Electrocatalysis. W. E. O'Grady, P. N. Ross, Jr., and F. G. Will, Editors. A 1981 symposium. 428 pages, **$18.00.**

Photoelectrochemistry: Fundamental Processes and Measurement Techniques. W. L. Wallace, A. J. Nozik, S. K. Deb, and R. H. Wilson, Editors. A 1981 symposium. 736 pages, **$35.00.**

The Nickel Electrode. R. G. Gunther and S. Gross, Editors. A 1981 symposium. 324 pages, **$15.00.**

Plasma Processing. J. Dieleman, R. G. Frieser, and G. S. Mathad, Editors. A 1981 symposium. 528 pages, **$25.00.**

Corrosion in Batteries and Fuel Cells and Corrosion in Solar Energy Systems. C. J. Johnson and S. L. Pohlman, Editors. A 1981 symposium. 554 pages, **$22.00.**

7/86

Call for Papers
171st Meeting
Philadelphia, Pennsylvania, May 10-15, 1987

Selected symposium topics and planned General Sessions are described in the following pages.

Procedure for Submitting Papers

1. Submit one original 75-Word Abstract on the attached form or a facsimile together with one original Extended Abstract to The Electrochemical Society, Inc., 10 South Main St., Pennington, NJ 08534-2896. The deadline for receipt of **both** the 75-Word and Extended Abstract at The Electrochemical Society Headquarters Office is **December 1, 1986.**

2. Send a copy of **both** the 75-Word and Extended Abstract to the appropriate organizing symposium or General Session chairman listed. **No paper will be considered unless both the 75-Word and Extended Abstract are received at Society Headquarters by December 1, 1986. Both abstracts and the oral presentation are required in English.**

Instructions for Preparation of Extended Abstract

1. New Deadline—Extended Abstract must be submitted with the 75-Word Abstract by **December 1, 1986.**

2. All scheduled papers will be published in the EXTENDED ABSTRACTS volume for this meeting. The volume is published photo-offset directly from typewritten copy submitted by the author. The volume will be 7 × 10 in.; therefore, it is essential that the typing be clear and all lettering should be the size of ordinary type or at least 1/16 in. high so that it will be legible after reduction. The EXTENDED ABSTRACTS volume is in a double-column format. Camera-ready typing mats may be obtained from The Electrochemical Society, Inc., 10 South Main St., Pennington, NJ 08534-2896, or you may use any white bond paper 11 × 17 in. The diagram below gives the dimensions of the Extended Abstract form.

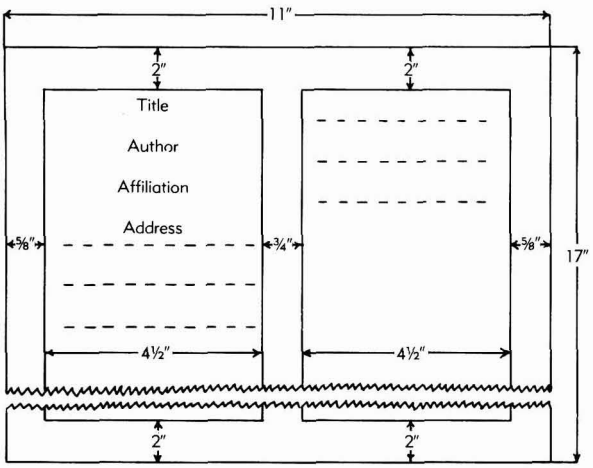

A. Use black typewriter ribbon only; type single-spaced.

B. Opaque lacquer may be used for corrections.

C. Type title, author(s), affiliation(s), and address(es) at top of first column (see diagram).

D. Tables and figures must be securely mounted within the margins with rubber cement.

E. Place references and figures after text.

3. The text of the abstract, including references, must not exceed one page (two columns) in length. An additional two columns are permitted for figures, if necessary. Papers exceeding this limit will be returned or rejected.

Mailing Instructions

Mail the original Extended Abstract together with the original 75-Word Abstract to The Electrochemical Society, Inc., 10 South Main St., Pennington, NJ 08534-2896 and a copy to the organizing chairman **for receipt before December 1, 1986.**

Notification of Paper Acceptance

Programming for this meeting will occur in early January. Organizing chairmen will notify those authors whose papers have not been accepted. In early March, a complete packet of program materials, including an Advance Program, will be sent to the presenting authors. Coauthors will receive a meeting packet without an Advance Program.

Manuscript Publication in the JOURNAL OF THE ELECTROCHEMICAL SOCIETY

Upon presentation, all meeting papers become the property of The Electrochemical Society, Inc. However, presentation incurs no obligation to publish. If publication in the JOURNAL OF THE ELECTROCHEMICAL SOCIETY is desired, papers should be submitted as promptly as possible in full manuscript form in order to be considered. "Instructions to Authors" for JOURNAL publication are available from the Society Headquarters office and are published monthly in the JOURNAL. If publication elsewhere is desired after presentation, written permission from Society Headquarters is required.

Philadelphia, Pennsylvania, Meeting Symposia Plans—Spring 1987 May 10-15, 1987

Extended Abstract must be submitted with the 75-Word Abstract by December 1, 1986.

BATTERY

Battery History

This symposium will be devoted to the history of battery developments on a worldwide basis, with special emphasis on contributions by members of The Electrochemical Society.

Historical papers of early inventors, including Thomas Edison and others, will be reviewed. Contributions on any aspect of research, development, operations, or commercialization of batteries are welcome.

Publication of a proceedings volume is being considered. Papers published in a proceedings volume may also be submitted to the JOURNAL, but must be received no later than 6 months after the date of the symposium at which the paper was presented.

Suggestions and inquiries should be sent to the Symposium Chairman: A. J. Salkind, UMDNJ, Rutgers Medical School, P.O. Box 101, Piscataway, NJ 08854.

General Session

Papers concerning any aspects of batteries, fuel cells, battery and fuel cell analysis, testing, etc. not included in the topic areas of the symposia are welcome.

Suggestions and inquiries should be sent to the Session Chairman: J. Broadhead, AT&T Bell Laboratories, Rm. 1E-244, Murray Hill, NJ 07974.

CORROSION

General Session

Papers on all aspects of low and high temperature corrosion and associated phenomena will be considered. Experimental techniques for the study of corrosion processes and corrosion products are also of interest.

Suggestions and inquiries should be sent to the Session Chairman: R. A. Rapp, Dept. of Metallurgical Engineering, The Ohio State University, 116 W. 19th Ave., Columbus, OH 43210.

DIELECTRICS AND INSULATION/ PHYSICAL ELECTROCHEMISTRY

Critical Issues in the Structure and Chemistry of Organic Monolayers at Electrode Surfaces

This is the first in a series of symposia that will examine critical issues concerning the structure and chemistry of organic monolayers at electrode surfaces. The objective is to provide a forum that will address these issues from the perspective of electrochemistry as well as from the fundamental chemistry and physics of organic monolayers. The symposium format will consist of sessions for invited papers and those currently being solicited. The invited papers will review the status of this area and examine the fundamental properties of organic monolayers.

Papers are solicited that examine all aspects of electrochemistry and/or organic monolayer chemistry at surfaces. Examples include: 1. approaches to the fabrication and control of the structure of monolayers; 2. approaches to the stabilization of monolayers; 3. charge transfer, the electrochemical double layer, and ion transport at these interfaces; 4. The importance of orientation on charge transfer; 5. characterization methods (*ex situ/in situ*/HV/UHV, macroscopic/microscopic, atomic/molecular/topographic); 6. fundamental chemical and physical properties of organic monolayers; 7. the chemistry and physics of monolayer/surface interactions; 8. defect structure; 9. theoretical models for charge transfer at modified interfaces; 10. theoretical models of the fundamental chemistry and physics of organic monolayers; and 11. the application of these interfaces to problems such as energy conversion and analysis. Reviews on these topics are also welcomed.

Suggestions and inquiries should be sent to the Symposium Chairman: M. D. Porter, Dept. of Chemistry, Iowa State University, Ames, IA 50011.

ELECTRONICS

Entrepreneurship in the Semiconductor Industry

This symposium is the third in a series on the business aspects of the electronics industry and will focus on the role of the entrepreneur in the development of the electronics business. It will be comprised entirely of invited papers.

Silicon Valley and Route 128 have become home to a multitude of new dynamic, high technology, electronically oriented, start-up companies. Some have grown to industry giants; others have gone belly up and passed into obscurity. The speakers at this symposium will describe factors that contribute to both outcomes.

Suggestions and inquiries should be sent to the Symposium Chairman: F. J. Strieter, 7814 Fallmeadow Ln., Dallas, TX 75248.

Large Diameter Crystal Growth

This symposium will cover the fundamental and practical aspects of growing, characterizing, and utilizing large diameter crystal for semiconductor device and circuit fabrication. Emphasis will be on silicon crystals 150 mm in diameter or larger. Invited papers are planned to provide a solid basis for considering the various issues associated with large diameter crystal. In addition, papers are solicited to describe original, previously unpublished, work on production and applications of large diameter crystal, including growing technology, continuous feed growth, growth models, impurity incorporation, uniformity considerations, and wafer shaping, handling, and utilization.

Inquiries should be sent to either of the Symposium Co-Chairmen: W. M. Bullis, Siltec Silicon, 423 National Ave., Mountain View, CA 94043; or H. R. Huff, Monsanto Electronic Materials Co., P.O. Box 10123, Palo Alto, CA 94303. **Papers will not be considered for inclusion in the symposium unless copies of both the 75-word and extended abstracts are sent to one of the Co-Chairmen before December 1, 1986.** Papers not selected for inclusion in the symposium will be transferred to the Joint General Session unless the author specifically requests that this not be done.

ELECTRONICS/DIELECTRICS AND INSULATION

High Voltage and Smart Power Devices

This symposium will focus on processing, structures, and modeling of high voltage and smart power devices. Papers are solicited on special technologies (*e.g.*, RESURF or dielectric isolation), special processing techniques (*e.g.*, thin film coverage over severe topography, working with high resistivity silicon, special annealing and gettering schemes), stimulation of devices and structures, special devices for the smart power/high voltage environment (*e.g.*, integrated DMOS, IGT's, GDX's), material characterization (*e.g.*, low impurity concentrations, effects of trace impurities, dislocations, and polarization effects), and reliability factors.

The publication of a proceedings volume is being considered. Papers published in a proceedings volume may also be submitted to the JOURNAL, but must be received no later than 6 months after the date of the symposium at which the paper was presented.

Suggestions and inquiries should be sent to the Symposium Chairman: P. W. Shackle, Siliconix, 2201 Laurelwood Rd., Santa Clara, CA 95054.

Beam Testing of Integrated Circuits

As the thrust into VLSI and ULSI intensifies, the requirements for integrated circuit testing will become increasingly difficult to meet. Despite significant progress in design-for-testability techniques, this situation will persist so long as the test engineer remains dependent on the I/O pins for the observation and control of internal gates. In recent years, the use of electron and laser beams to probe internal gates has been the focus of considerable research activity in the U.S., Europe, and Japan. Several versions of both E-beam and laser beam testers are already on the market. Open forum discussions about the comparisons among the various beam testing technologies have heretofore been somewhat disparate. The objective in bringing together this symposium is to enable the IC testing community to perform much needed evaluation of the relative merits of these technologies.

Original papers and reviews are solicited in the following general areas: 1. physical phenomenology associated with laser-IC interactions; 2. schemes for collecting test data using lasers; 3. schemes for achieving exhaustive testing using lasers; 4. laser-induced latch-up in IC's; 5. physics of E-beam-IC interactions; 6. methods of collecting data with voltage contrast SEM and EBIC; 7. dynamic fault imaging; and 8. accuracy and reliability of photon and E-beam probes.

Suggestions and inquiries should be sent to the Symposium Co-Chairmen: G. R. Woolhouse, Lockheed R&D Div., 0/91-50, B/201, 3251 Hanover St., Palo Alto, CA 94304; J. Orloff, Oregon Graduate Center, 19600 Von Neumann Dr., Beaverton, OR 97006; or F. Hohn, IBM T. J. Watson Research Center, Yorktown Heights, NY 10598.

Contacts to Compound Semiconductors

The science and technology of Schottky barriers and ohmic contacts to compound semiconductors are of crucial importance to the rapidly expanding field of III-V and II-VI devices, integrated circuits, and integrated optoelectronics.

This symposium is intended to bring together researchers interested in all aspects of metal-compound semiconductor interfaces and related properties. Several key invited papers are planned, and contributed papers are solicited. Areas of interest include: 1. theoretical models of metal semiconductor interfaces; 2. electrical characterization, including IV, CV, and transient spectroscopy (*e.g.*, DLTS) techniques; 3. accurate determination of specific contact resistance; 4. epitaxial or "grown" contacts; 5. interface studies such as AES, ESCA, Raman, SIMS, RBS, and TEM, especially when related to electrical characteristics; 6. approaches to eliminate "alloyed" ohmic contacts; and 7. design and realization of low leakage Schottky barriers on narrow bandgap semiconductors. Semiconductors of interest include the III-V's and II-VI's and their ternary and quaternary alloys.

Publication of all proceedings volume is planned. Papers published in a proceedings volume may also be submitted to the JOURNAL, but must be received no later than 6 months after the date of the symposium at which the paper was presented.

Prospective authors must submit five copies each of: 1. A 75-word short abstract, and 2. an extended abstract, using the accepted Electrochemical Society format, by December 1, 1986. The extended abstracts will be used as the basis for selecting papers for presentation. Acceptance of a paper for presentation at this symposium obligates the author(s) to submit a typed camera-ready copy of their work by no later than the first day of the Spring Meeting in May of 1987. A list of key words must be submitted with a paper to aid in indexing. Abstracts standing alone will not be published. Deadlines are firm.

Suggestions and inquiries should be sent to the Symposium Co-Chairmen: V. G. Keramidas, Bell Communications Research, 331 Newman Springs Rd., Navesink, NJ 07701-7020; or P. A. Barnes, 206 Allison Laboratory, Dept. of Physics, Auburn University, Auburn, AL 36849-3501.

First International Symposium on ULSI Science and Technology

This symposium will focus on processing, structure, and properties of integrated circuits with submicron features. It will cover a wide variety of topics including: 1. ULSI device structures and technologies; 2. submicron device and process modeling and evaluation; 3. submicron feature patterning; 4. scaled vertical geometries; 5. ULSI interconnect schemes; and 6. ULSI manufacturing systems.

The publication of a proceedings volume is planned. Papers published in a proceedings volume may also be submitted to the JOURNAL, but must be received no later than 6 months after the date of the symposium at which the paper was presented. Instructions concerning participation in this symposium appear in the special Call for Papers published in the March-August 1986 issues of **This Journal.** A letter containing the title of the paper, the names of the authors, and the address and telephone number of the senior author must be sent to one of the Symposium Co-Chairmen **no later than September 1, 1986.** Both the 75-word and extended abstracts must be sent to one of the Co-Chairmen **(not to Society Headquarters)** no later than November 15, 1986. Full manuscripts will be due by April 1, 1987.

Suggestions and inquiries should be sent to the Symposium Co-Chairmen: S. Broydo, ZyMOS Corp., P.O. Box 62379, Sunnyvale, CA 94088; or C. M. Osburn, MCNC, P.O. Box 12889, Research Triangle Park, NC 27709.

High Current Ion Implantation in Silicon

Topics to be discussed are effects associated with high current, high dose rate, and high dose implantation of Si including: 1. materials and device aspects of formation of amorphous layers by implantation for fabrication of shallow junction structures, suppression of channeling effects, and other process applications, with special attention to the effects of target temperature and dose rate on as-implanted damage, electrical activation,

and the character of residual defects; 2. very high dose applications such as direct formation of buried dielectric layers, surface modification, and ion beam mixing for silicide formation; 3. materials effects of very high dose rate implantation with focused ion beam systems; and 4. device yield effects associated with high current implantation such as breakdown and wearout damage in dielectric layers resulting from local charge buildup, sputtered film contamination, dose measurements, and wafer temperature control.

Publication of a proceedings volume is being considered. Papers published in a proceedings volume may also be submitted to the JOURNAL, but must be received no later than 6 months after the date of the symposium at which the paper was presented.

Suggestions and inquiries should be sent to the Symposium Co-Chairmen: M. I. Current, Applied Materials, Implant Div., Santa Clara, CA 95051; or W. O. Holland, Motorola Inc., APRDL, Austin, TX 78721.

State-of-the-Art Program on Compound Semiconductors VI

This is the sixth of a new series of special symposia intended to provide a forum for the presentation and discussion of the latest developments in areas involving compound semiconductor processing. Original papers and reviews dealing with all aspects of compound semiconductors are solicited for this program. In recognition of the interdependence between materials, properties fabrication processes, and device characteristics, papers that correlate these topics for high speed, microwave, millimeter wave, photonic, optoelectronics sensing devices (discrete and integrated circuits) are welcome

Of particular interest are papers in the following general areas: material growth technologies; gate and interconnect technologies; fine feature patterning; lithography, etching, and plasma process; ion implantation/capping/annealing; dielectrics/passivation; surface/interface effects; metal-semiconductor interactions; Schottky barriers and ohmic contacts; radiation effects; via formation/packaging techniques; field limiting effects; and manufacturing trends/status.

The symposia are also aimed at providing a forum for synergistic interactions between those working in compound semiconductors and those involved in silicon technologies.

To ensure the timely nature of the SOTAPOCS VI effort, a special deadline has been set. Abstracts will be accepted until **February 1, 1987.** The standard 75-word Electrochemical Society abstract (refer to form in this Call for Papers) is sufficient for paper presentation at SOTAPOCS VI. **There is no need to submit an Extended Abstract.**

Abstracts, suggestions, and inquiries should be sent to the Symposium Co-Chairmen: A. D. M. Chen, Anadigics, Inc., 35 Technology Dr., Warren, NJ 07060; C. E. Weitzel, Motorola, Inc., Semiconductor R&D Laboratory, Phoenix, AZ 85008; or R. E. Enstrom, RCA Laboratories, Princeton, NJ 08540.

Joint General Session

Papers are solicited on all aspects of electronic materials and processing technologies except those covered by more specialized symposia at this meeting. Topics of interest include: electronic materials preparation, characterization, interactions, and device applications; basic chemistry and physics of materials and device processing; process and device modeling; sensor technology; and computer-aided manufacturing of electron devices and integrated circuits. Of particular interest are new or novel materials and processes.

Inquiries may be sent to any of the Session Co-Chairmen: W. M. Bullis, Siltec Silicon, 423 National Ave., Mountain View, CA 94043; G. C. Schwartz, IBM Corp., Dept. 206, Bldg. 300-48A, Hopewell Junction, NY 12533; or H. R. Huff, Monsanto Electronic Materials Co., P.O. Box 10123, Palo Alto, CA 94303. **Papers will not be considered for inclusion in these sessions unless copies of both the 75-word and extended abstracts are sent to W. M. Bullis at the above address.**

Joint Recent News Papers Session

Recent News Papers and Extended Recent News Papers consisting of topics covered by the symposia and sessions being sponsored or cosponsored by the Electronics and Dielectrics and Insulation Divisions are invited for presentation.

A special call for Recent News Papers will appear in the January, February, and March 1987 issues of the JOURNAL.

Suggestions and inquiries should be sent to the Session Chairman: W. A. Pliskin, IBM Corp., Dept. 025, Zip 48A, Hopewell Junction, NY 12533.

ELECTRONICS/LUMINESCENCE AND DISPLAY MATERIALS

First International BI/CMOS Symposium

BI/CMOS technology is the dream of the IC design engineer. It combines the virtues of low power, high noise immunity, simple logic implementation, and high input impedance of CMOS with the high current drive capability, excellent device-to-device matching, and low noise performance of bipolar transistors.

This International BI/CMOS Symposium consists of two parts: 1. BI/CMOS design; and 2. BI/CMOS process technology.

The objective of the BI/CMOS Design Session in this symposium is to bring together design engineers to discuss the design advantages, limitations, and applications of BI/CMOS. Specifically, issues relating to BI/CMOS in both analog and digital VLSI designs will be discussed.

The objective of the BI/CMOS Process Technology Session in this symposium is to bring together the process engineers to discuss the various technology options for BI/CMOS, key advances in BI/CMOS fabrication techniques, device optimization, and emerging trends. In order to realize the advantages of both bipolar and CMOS functions, the process and device technologies must be carefully optimized.

This symposium will include both invited and contributed papers covering topics listed above. Both experimental and theoretical contributed papers are solicited covering the design and process technology issues.

Suggestions and inquiries should be sent to the Symposium Co-Chairmen: A. N. Saxena, Gould AMI Semiconductors, 3800 Homestead Rd., Santa Clara, CA 94306; or T. Nagano, Hitachi Laboratory, 4026 Kuji Cho, Hitachi City, Ibaragi Prefecture, Japan.

ENERGY TECHNOLOGY GROUP

10th Anniversary Review and General Session

The session will be devoted to the celebration of the tenth anniversary of the Energy Technology Group. Invited speakers will review the status of key energy technology areas and provide perspectives for future developments. In addition, papers are solicited on the fundamental and applied aspects of energy conversion, storage, and transmission not covered by current symposia.

Suggestions and inquiries should be sent to the Session Co-Chairmen: V. Jalan, Electrochem, 400 W. Cummings Park, Woburn, MA 01801; or H. Maru, Energy Research Corp., 3 Great Pasture Road, Danbury, CT 06813.

ENERGY TECHNOLOGY/CORROSION/ INDUSTRIAL ELECTROLYTIC

Electrochemistry of Coal Slurries

Papers are invited for inclusion in a symposium dealing with the electrochemistry of coal slurries and/or other carbonaceous materials. Suitable topics include: electrochemistry of coal or carbon slurries as an anodic depolarizer for electrolytic production of hydrogen, cleaning of coal by electrochemical processes, electrolytic generation of humic acids in both alkaline and acidic media, mechanistic studies of coal slurry oxidation, and erosion as well as corrosion processes by coal slurries. Papers dealing with electrolytic hydrogenation, electrochemical liquefaction, and electrochemical characterization of coal in nonaqueous media are also appropriate.

Publication of a proceedings volume is being considered. Papers published in a proceedings volume may also be submitted to the JOURNAL, but must be received no later than 6 months after the date of the symposium at which the paper was presented.

Suggestions and inquiries should be sent to the Symposium Co-Chairmen: S.-M. Park, Dept. of Chemistry, University of New Mexico, Albuquerque, NM 87131; J. Postlethwaite, Dept. of Chemical Engineering, University of Saskatchewan, Saskatoon, Sask., Canada S7N 0W0; or G. Kreysa, DECHEMA Institute, Theodore Heuss—Allee 25, 6000 Frankfurt am Main 97, Germany.

ENERGY TECHNOLOGY/ ELECTRODEPOSITION/ CORROSION/ PHYSICAL ELECTROCHEMISTRY

Electrochemistry of Tribology

Papers addressing the particular and general role of electrochemical phenomena in tribology will be presented. The following subjects are of special interest to this symposium: 1. effect of composition and structure of rubbing surfaces on tribological properties, the role of potential in friction coefficient, "Rehbinder effect," etc; 2. synergism between corrosion and wear with electrochemical interplay; 3. control of wear through surface modifications through deposition of tribomaterials-electrochemical (*e.g.,* metal-alloy, metal-ceramic, ceramic, metal-polymer, anodic conversions, etc.), CVD, ion implantation, thermal and mechanical treatments; 4. analysis of wear-related debris, morphology of rubbing surfaces, and solid-state aspects; 5. industrial applications of tribology (*e.g.,* electronic connectors, oil well drilling operations, high velocity fluid-jet machining); and 6. frontiers of future research.

The publication of a proceedings volume is being considered. Papers published in a proceedings volume may also be submitted to the JOURNAL, but must be received no later than 6 months after the date of the symposium at which the paper was presented.

Suggestions and inquiries are solicited and should be sent to the Symposium Co-Chairmen: R. Varma, Chemical Technology Div., Argonne National Laboratory, 9700 South Cass Ave., Argonne, IL 60439-4837; W. Freitag, 1613 Kenmare Dr., Dresher, PA 19025; M. W. Kendig, Rockwell International Science Center, P.O. Box 1805, Thousand Oaks, CA 91360; or V. S. Agarwala, Naval Air Development Center, Warminster, PA 18974-5000.

ENERGY TECHNOLOGY/INDUSTRIAL ELECTROLYTIC/HIGH TEMPERATURE MATERIALS

Application of Fuel Cell Electrodes in Electrolytic Industries

Porous gas diffusion electrodes are an integral part of fuel cell systems. Such electrodes provide reasonable performance and life for oxygen reduction and hydrogen oxidation in phosphoric acid and alkaline fuel cells. Considerable resources have been focused on the reduction of oxygen in porous electrodes, mainly in reducing electrode polarization and increasing electrode life. Recent improvements in fuel cell electrodes have generated interest in the use of these electrodes in other electrochemical technologies.

The symposium will explore the use of fuel cell electrodes in industrial processes. The process utility of fuel cell electrodes from acid, alkaline, molten salt, and solid oxide systems will be considered. Contributions relating to metal/air batteries, alkali-halide electrolysis, metal electrowinning, oxygen generation, hydrogen scrubbing, water electrolysis, electro-organic synthesis, gas sensors, and other technologies utilizing gas depolarized electrodes are sought. Additional contributions describing variations in electrode load profiles and the effects those variations have on electrode life and performance are also solicited. Recognizing that commercialization of new technologies ultimately rests on the economic feasibility of that commercialization, contributions are also sought dealing with process economics and conversion costs in utilizing fuel cell electrodes.

Publication of a proceedings volume is being considered. Papers published in a proceedings volume may also be submitted to the JOURNAL, but must be received no later than 6 months after the symposium at which the paper was presented.

Suggestions and inquiries should be sent to the Symposium Co-Chairmen: L. J. Gestaut, ELTECH Systems Corp., 625 East St., Fairport Harbor, OH 44077; K. Kinoshita, Applied Science Div., 90-3026, Lawrence Berkeley Laboratory, Berkeley, CA 94720; or D. A. Shores, Corrosion Research Center, University of Minnesota, 151 Amundson Hall, Minneapolis, MN 55455.

ENERGY TECHNOLOGY/PHYSICAL ELECTROCHEMISTRY/ORGANIC AND BIOLOGICAL ELECTROCHEMISTRY

Applications of Macromolecules in Energy Conversion

This symposium will be devoted to papers dealing with macromolecules and macromolecular assemblies in energy conversion applications. Topics for discussion will include, but are not limited to: macromolecules as active catalytic elements, as charge transfer intermediates, and as primary photoreceptors. Dye sensitization using macromolecules will be covered, as well as the use of multilayer dye assemblies for sensitization and as semiconductor electrodes. Papers in the areas of photoeffects in polymer-modified electrodes, photoeffects in organic metals employed as semiconductor electrodes, and photoeffects in Langmuir-Blodgett films and organized micellular systems will also be included. The symposium will include several invited lectures plus contributed papers.

Publication of a proceedings volume is being considered. Papers published in a proceedings volume may also be submited to the JOURNAL, but must be received no later than 6 months after the date of the symposium at which the paper was presented.

Suggestions and inquiries should be sent to the Symposium Co-Chairmen: N. R. Armstrong, Dept. of Chemistry University of Arizona, Tucson, AZ 85721; E. B. Yeager, Case Center for Electrochemical Sciences, Case Western Reserve University, Cleveland, OH 44106; or D. S. Ginley, Sandia National Laboratories, P.O. Box 5800, Albuquerque, NM 87185.

HIGH TEMPERATURE MATERIALS/ DIELECTRICS AND INSULATION

Ceramics and Ceramic Composites: Electrochemical and Other Applications

The purpose of this symposium is to provide an opportunity for interdisciplinary exchange for researchers in material science and electrochemistry. Topics will include preparation, characterization, and applications of ceramic materials, especially ceramic composites. Papers are being sought that include: 1. fundamental studies of the microscopic and macroscopic properties of ceramics, ceramic composites, ceramic fibers, and felts; 2. the preparation of such materials including surface modifications by laser treatment; 3. the surface properties of these materials; and 4. their applications and future prospects.

Suggestions for papers and inquiries should be sent to the Symposium Co-Chairmen: I. Joyce, Glass and Ceramics Centre, Ontario Research Foundation, 2395 Speakman Dr., Sheradon Park, Mississauga, Ont., Canada L5K 1B3; or S. Reddy, IBM Corp., Bldg. 300-40E, East Fishkill Facility, Hopewell Junction, NY 12533.

HIGH TEMPERATURE MATERIALS/ PHYSICAL ELECTROCHEMISTRY/ CORROSION/BATTERY/ENERGY TECHNOLOGY/DIELECTRICS AND INSULATION

In Situ Nonelectrochemical Techniques for Study of Electrode Reactions

Papers are solicited that are concerned with nonelectrical methods of studying surface processes. These techniques include, but are not limited to, ellipsometry, vibrational spectroscopy (IR, FTIR, Raman, SERS, etc.), and various related spectroscopy techniques. Sessions will be organized around the following topics: 1. electrolyte studies, including complex formation, kinetics, and equilibria in aqueous, nonaqueous, and molten salt solvents; 2. the detection and characterization of transient species, especially by means of pulsed laser to observe time-resolved Raman scattering; 3. studies of the composition and structure of surface films on metals by infrared (FTIR) and Raman spectroscopy as related to corrosion problems and electrocatalysis; and 4. advanced techniques applied to electrochemical problems such as surface-enhanced laser Raman scattering, coherent anti-Strokes Raman scattering (CARS), resonance Raman scattering, Raman microprobe, and computer-controlled data acquisition and manipulation.

Suggestions and inquiries should be sent to the Symposium Co-Chairmen: A. S. Nagelberg, Lanxide Corp., 1 Tralee Industrial Park, Newark, DE 19711; or R. H. Heidersbach, California Polytechnic, State University, San Luis Obispo, CA 93407.

INDUSTRIAL ELECTROLYTIC

Science and Engineering of Multiphase Electrolytic Systems

This symposium focuses on the industrial applications of multiphase systems in electrolysis and related electrochemical processes. Papers are solicited on fundamental and applied aspects of multiphase interactions (liquid-liquid, liquid-gas, liquid-solid, liquid-gas-solid, etc.). A broad range of interests is being sought, with special emphasis on multiphase electrolytic processes within batteries, fuel cells, chlor-alkali cells, electrosynthesis, water electrolysis, and organic, inorganic, and biological electrochemistry.

This symposium will bring together recent advances in multiphase systems. Special focus will be on: 1. fundamental chemical reactions, kinetics, current and potential distribution, and mass-transfer processes; 2. overall cell and component modeling and design for multiphase systems; and 3. general process synthesis, development, and optimization of the multiphase process. Discussions of existing or unique potential applications are invited.

Publication of a proceedings volume is planned. Papers published in a proceedings volume may also be submitted to the JOURNAL, but must be received no later than 6 months after the date of the symposium at which the paper was presented.

Suggestions and inquiries should be sent to the Symposium Co-Chairmen: J. M. Fenton, Dept. of Chemical Engineering, University of Connecticut, U-139, Storrs, CT 06268; or J. D. Lisius, Dept. of Chemical Engineering, University of Maine, Orono, ME 04469.

General Session

Original papers concerning any aspect of industrial electrochemistry not included in other scheduled symposia are invited for this session. Both experimental and theoretical papers are welcome.

Suggestions and inquiries should be sent to the Session Chairman: D. E. Hall, American Cyanamid Co., 1937 W. Main St., Stamford, CT 06904-0060.

ORGANIC AND BIOLOGICAL ELECTROCHEMISTRY

General Session

Papers concerning any aspects of organic and biological electrochemistry not included in the topic areas of the symposia are welcome.

Suggestion and inquiries should be sent to the Session Chairman: P. Zuman, Dept. of Chemistry, Clarkson University, Potsdam, NY 13676.

ORGANIC AND BIOLOGICAL ELECTROCHEMISTRY/PHYSICAL ELECTROCHEMISTRY

Kinetics of Interfacial Charge Transfer Processes

The theme of this symposium is the characterization of the kinetics and mechanisms of heterogeneous charge transfer processes involving both electrons and ions in organic and biological systems. Interfacial charge transfer occurring at electrode/solution interfaces and at membrane/solution interfaces will be discussed from both theoretical and experimental perspectives. New methods and novel applications of existing methods will also be described.

Suggestions and inquiries should be sent to the Symposium Co-Chairmen: H. N. Blount III, Chemical Analysis, National Science Foundation, Washington, DC 20550; F. M. Hawkridge, Dept. of Chemistry, Virginia Commonwealth University, Box 2006, Richmond, VA 23284; or B. S. Pons, Dept. of Chemistry, University of Utah, Salt Lake City, UT 84112.

PHYSICAL ELECTROCHEMISTRY

Double Layer Symposium

The papers presented will emphasize the nontraditional aspects of the polarizable interface. The symposium will bring together those involved with both theoretical and experimental aspects of the field. Experimentally, the papers will emphasize double layers at single-crystal and polycrystalline solid metals at semiconductors, in nonaqueous media including molten salts, and at liquid-liquid interfaces. Theoretically, the papers will deal with any new aspect of the theory of polarizable interfaces, especially with the effects of the nature of the metal or polarizable phase, and with the structure of the solution phase, for instance, with respect to the solvent.

Suggestions and inquiries should be sent to the Symposium Co-Chairmen: W. R. Fawcett, Dept. of Chemistry, University of California, Davis, CA 95616; or D. Henderson, IBM Research Laboratories, 650 Harry Road, San Jose, CA 95120.

Quantum Electrochemistry

The objective of this symposium is to provide an opportunity for discussion between individuals with differing backgrounds and points of view who share a common interest in attempting to understand the physics and chemistry of processes that take place at the surface of an electrode. We wish to encourage debate on all aspects of the theory of electron transfer at the electrode. To this end, we solicit contributions from a variety of people. Example areas of expertise, to mention a few subjects, may include surface quantum physics and chemistry, solution and surface statistical mechanics, quantum chemistry of electron transfer in solution and at the surface, and double layer structure theory only as it applies directly to the electron transfer process.

We wish especially to encourage contributions from experimentalists who have definite opinions concerning the strengths and weaknesses of the present state of theory and who may wish to suggest avenues for the further development of the theory.

We discourage, at the outset, any contributions that merely recite lists of past accomplishments, add minor embellishments to the theory as it now stands, or that seek, once again, to point out the well-known inadequacies of the dielectric continuum approximation. We welcome any contributions that may help to resolve the lingering issue of how properly to include an adequate account of the role of solvent in the theory of the electron transfer.

Suggestions and inquiries should be sent to the Symposium Co-Chairmen: P. P. Schmidt, Dept. of Chemistry, Oakland University, Rochester, MI 48063; or L. Blum, Dept. of Physics, University of Puerto Rico, Rio Piedras, PR 00931.

General Session

Papers concerning any aspect of physical electrochemistry not included in the topic areas of symposia at this meeting are welcome.

Suggestions and inquiries should be sent to the Session Chairman: B. Miller, AT&T Bell Laboratories, Rm. ID-350, Murray Hill, NJ 07974.

PHYSICAL ELECTROCHEMISTRY/ BATTERY

Nonaqueous Electrochemistry

This symposium will focus on electrochemical and transport phenomena in inorganic and organic nonaqueous electrolytes, including ambient temperature molten salts. Papers on the following topics are of particular interest: 1. electrolyte preparation, purification, and characterization; 2. ion solvation, conductivity, and transport phenomena; 3. thermodynamics and kinetics of electrode processes; 4. reference electrodes in nonaqueous media; 5. solvent effects on mechanisms of electrochemical reactions; 6. corrosion processes in chemical reactions; 7. corrosion processes in nonaqueous and mixed solvents; 8. nonaqueous photoelectrochemistry; and 9. electrocatalysis.

Suggestions and inquiries should be sent to the Symposium Co-Chairmen: J. Auborn, AT&T Bell Laboratories, Rm. 652 111, Murray Hill, NJ 07974; or R. D. Rauh, EIC Laboratories, Inc., 111 Downey St., Norwood, MA 02062.

PHYSICAL ELECTROCHEMISTRY/ BATTERY/ENERGY TECHNOLOGY

Electrode Materials and Processes for Energy Conversion and Storage

This symposium will include theoretical and experimental papers. Emphasis should lie on fundamental aspects and understanding of reaction mechanisms and of material properties, rather than on development and testing of devices and systems. Specific areas of interest include: 1. effects of bulk and surface properties on electrode behavior, including such properties as chemical bonding, crystal structure, alloying, electron band structure, dopants, bulk defects and surface states, and ionic and electronic conduction; 2. electrocatalysis on crystalline and amorphous materials, including single and mixed oxides, and modified surfaces; 3. alkaline metal insertion cathodes and lithium anodes interfacing solid, aqueous, and nonaqueous electrolytes; 4. conducting polymer electrodes and electrolytes; 5. electrochemical and photoassisted electrolysis of water; 6. novel methods for hydrogen storage; and 7. advances in the understanding of electrode processes in fuel cells. Papers on these and related topics are solicited.

The publication of a proceedings volume is being planned. Papers published in a proceedings volume may also be submitted to the JOURNAL, but must be received no later than 6 months after the date of the symposium at which the paper was presented.

Inquiries and suggestions should be sent to the Symposium Co-Chairmen: S. Srinivasan, Los Alamos National Laboratory, M.S. D429, Los Alamos, NM 87545; S. Wagner, Dept. of Electrical Engineering, Princeton University, Princeton, NJ 08544; or H. Wroblowa, Ford Motor Co., S.R.L. S-2079, P. O. Box 2053, Dearborn, MI 48121-2053.

NEW TECHNOLOGY SUBCOMMITTEE

New Horizons in Electrochemical Science and Technology

This symposium provides a forum for the dissemination of the conclusions and recommendations contained in the report to the Department of Energy by the National Academy of Sciences, National Research Council, Committee on Electrochemical Aspects of Energy Conservation and Production. The report reviews the status of electrochemical knowledge with respect to current applications and identifies technological opportunities in several areas of electrochemistry. It also identifies opportunities for cross-cutting research in some specific areas of the field including electrochemical corrosion and *in situ* characterization of electrochemical processes. The symposium will consist of three overview presentations by members of the committee followed by panel discussions of the conclusions and recommendations. No contributed papers are solicited.

Suggestions and inquiries should be sent to the Session Co-Chairmen: A. R. Landgrebe, U.S. Department of Energy, Washington, DC 20585; or S. Wolf, National Research Council, Joseph Henry Bldg., 21st and Pennsylvania Ave. NW, Washington, DC 20418.

75-Word Abstract Form

Extended Abstract must be submitted with the 75-Word Abstract by December 1, 1986

Philadelphia, Pennsylvania—May 10-15, 1987

Submit to: The Electrochemical Society, Inc.
10 South Main Street, Pennington, NJ 08534-2896
With a copy to the Organizing Chairman

Abstract No. .....
(to be assigned by the Society)

Schedule for .....
(Title of Symposium)

Sponsored by .....
(Division/Group)

Title of paper .....

.....

Authors (Underline name of author presenting paper.) .....

.....

Business affiliation and address .....

.....

..... (State or Country) (ZIP Code) (Telephone No.)

(Type abstract in this area—double-spaced.)

Do you require any audiovisual equipment?

- ☐ **35 mm (2 x 2 in.) slide projector**
- ☐ **Overhead projector**
- ☐ **Specify other (subject to availability and cost)**

Has the information in this abstract been presented verbally, submitted for publication, or published?
☐ **Yes** ☐ **No**
If the answer is yes, please provide the reference (except in the case of invited review presentations). _____

Is a full length paper on this work to be submitted for Society Journal publication? ☐ **Yes** ☐ **No**

Papers presented before a Society technical meeting become the property of the Society and may not be published elsewhere without written permission of the Society. Papers presented at Society technical meetings must be authored by a member or sponsored by an active member.

..... Insert name of Society member author or sponsor

This form should accompany your Extended Abstract.

SUSTAINING MEMBERS (CONTINUED)

Fairchild Semiconductor Corp.
Research Center
Palo Alto, CA

Focus Semiconductor Systems, Inc.
Sunnyvale, CA

Ford Motor Co.
Dearborn, MI

The Gates Corporation
Denver, CO

General Motors Corp.
Delco-Remy Div., Anderson, IN
Research Laboratories Div.
Warren, MI

Giner, Inc.
Waltham, MA

Gould Inc.
Gould Research Center
Rolling Meadows, IL

GTE Laboratories
Waltham, MA

GTE Sylvania Inc.
Chemical & Metallurgical Div.
Towanda, PA

Hewlett Packard Co.
Loveland, CO

Hewlett Packard Laboratories
Palo Alto, CA

Hill Cross Co., Inc.
West New York, NJ

Hoechst-Uhde Corp.
Englewood Cliffs, NJ

Honeywell, Inc.
Power Sources Center
Horsham, PA

Hughes Research Laboratories
Div. of Hughes Aircraft Co.
Malibu, CA

IMI Marston Limited
Wolverhampton, England

International Lead Zinc Research Organization, Inc.
New York, NY

Johnson Controls, Inc.
Milwaukee, WI

Kaiser Aluminum & Chemical Corp.
Pleasanton, CA

KBI
a division of Cabot Corp.
Boyertown, PA

Kerr-McGee Chemical Corp.
Chemical Corporation, Oklahoma City, OK
Technical Center, Oklahoma City, OK

Leclanche S. A.
Yverdon, Switzerland

Lockheed Missiles & Space Co., Inc.
Research Laboratory
Palo Alto, CA

LSI Logic Corp.
Santa Clara, CA

Marathon Battery Co.
Waco, TX

Max-Planck-Institut f. Festkorperforschung
Stuttgart, Germany

Medtronic Energy Technology
Minneapolis, MN

Mepco/Electra, Inc.
Columbia, SC

Microbeam, Inc.
Newbury Park, CA

Microwave Associates, Inc.
Burlington, MA

Molycorp, Inc.
a Unocal company
White Plains, NY

Monsanto Co.
St. Louis, MO

Motorola Inc.
Phoenix, AZ

M&T Chemicals Inc.
Detroit, MI

NEC Corporation Central Research Laboratories
Kawasaki, Japan

NTT Electrical Communication Laboratories
Atsugi, Japan

Noranda Research Centre
Pointe Claire, Que., Canada

North American Philips Lighting Corp.
Advanced Engineering Group
Hightstown, NJ

Northern Telecom
Ottawa, Ont., Canada

Occidental Chemical Corporation
Research & Development
(2 memberships)
Grand Island, NY

Olin Corp.
Metals Research Laboratories
New Haven, CT

OMI International Corp.
Udylite/Sel-Rex
Warren, MI

Philips Laboratories, Inc.
Briarcliff Manor, NY

Prototech Co.
Newton Highlands, MA

Public Service Electric and Gas Co.
PSE&G Research Corp.
Newark, NJ

Rayovac Corp.
Madison, WI

RCA Corp.
Color Picture Tube Div.
Lancaster, PA

Reynolds Metals Co.
Reduction Laboratory Library
Sheffield, AL

Rockwell International
El Segundo, CA

SAB NIFE AB
Oskarshamn, Sweden

SAFT America, Inc.
Power Sources Division,
Valdosta, GA
Advanced Battery Systems Division,
Cockeysville, MD

Sandia National Laboratories
Albuquerque, NM

Sanyo Electric Co., Ltd.
Osaka, Japan

Schlumberger-Doll Research
Ridgefield, CT

Searchlight Industries, Inc.
Las Vegas, NV

Shipley Company, Inc.
Newton, MA

Siemens Aktiengesellschaft
Munich, Germany

Siltec Corp.
Menlo Park, CA

Sonnenschein GmbH
Budingen, Germany

Sprague Electric Co.
North Adams, MA

St. Joe Minerals Corp.
Monaca, PA

Texas Instruments Inc.
Attleboro, MA

Toshiba Corp.
Toshiba Research and Development Center
Kawasaki, Japan

Toyota Central Research and Development Labs, Inc.
Nagoya, Japan

Tracor Applied Science, Inc.
Alexandria, VA

Varian Associates
Palo Alto, CA

VARTA Batterie AG
Kelkheim, Germany

Wacker Chemitronic
Burghausen, Germany

Wilson Greatbatch Ltd.
Clarence, NY

Xerox Corp.
Webster Research Center
Rochester, NY

Yardney Corp.
Pawcatuck, CT

Yuasa Battery Co., Ltd.
Osaka, Japan

THE ELECTROCHEMICAL SOCIETY PATRON MEMBERS

AT&T Bell Laboratories
Murray Hill, NJ

Dow Chemical Co.
Inorganic Chemicals Dept.
Midland, MI

ELTECH Systems Corp.
Chardon, OH

Exxon Research and Engineering Co.
Corporate Research
Advanced Energy Systems Laboratory,
Materials and Catalysis Sciences Laboratory
Linden, NJ
Technology Dept.
Chemical Engineering Technology Div.
Materials Technology Div.
Florham Park, NJ

Fujitsu Limited
Tokyo, Japan

General Electric Co.
Chemical Laboratory, Knolls Atomic Power Laboratory,
Schenectady, NY
Chemical Products, Engineering
& Technical Support, Cleveland, OH
Research and Development Center,
Inorganic Materials Laboratory
Schenectady, NY

General Electric Co. (continued)
Signal Processing & Communication Laboratory,
Schenectady, NY
Semiconductor Products Dept.,
Syracuse, NY

Hitachi, Ltd.
Central Research Laboratory
Tokyo, Japan

International Business Machines Corp.
New York, NY

Olin Corp.
Chemicals Div.
Charleston Technology Center
Charleston, TN

Philips Research Laboratories
Eindhoven, The Netherlands

Texas Instruments Inc.
Dallas, TX

Union Carbide Corp.
Battery Products Div.
Corporate Research Dept.
Danbury, CT

Westinghouse Electric Corp.
Electronic Tube Div., Elmira, NY
Nuclear Center, Monroeville, PA
Semiconductor Div., Youngwood, PA
Research Laboratories, Pittsburgh, PA

THE ELECTROCHEMICAL SOCIETY SUSTAINING MEMBERS

The Aerospace Corp.
Los Angeles, CA

Airco Industrial Gases
Murray Hill, NJ

Air Products and Chemicals, Inc.
Allentown, PA

Allied Corporation
C&D Power Systems
Plymouth Meeting, PA

Aluminum Co. of America
New Kensington, PA

AMAX Inc.
Greenwich, CT

AMP Inc.
Harrisburg, PA

Analog Devices, Inc.
Norwood, MA

Applied Materials, Inc.
Santa Clara, CA

ASARCO, Inc.
South Plainfield, NJ

AT&T Technologies
Princeton, NJ

AT&T Teletype Corp.
Skokie, IL

Ballard Research, Inc.
North Vancouver, B.C., Canada

Battelle Memorial Institute
Columbus, OH

Bioanalytical Systems Inc.
West Lafayette, IN

Boeing Co.
Seattle, WA

BP Research Centre
Middlesex, England

Brown, Boveri & Co., Ltd.
Research Center
Baden, Switzerland

C-I-L Inc.
Chemicals Research Laboratory
Mississauga, Ont., Canada

Comdial Semiconductor, Inc.
Sunnyvale, CA

Cominco Ltd.
Trail, B.C., Canada

COMSAT Laboratories
Clarksburg, MD

Corning Glass Works
Corning, NY

Crawford & Russell Inc.
Stamford, CT

CSIRO Division of Mineral Chemistry
Port Melbourne, Victoria, Australia

Diamond Cubic Corp.
Oceanside, CA

Diamond Shamrock Chemicals Co.
Painesville, OH

Duracell Inc.
A Division of Duracell International
Tarrytown, NY (2 memberships)

Duro-Test Corp.
North Bergen, NJ

Eagle-Picher Industries, Inc.
Electronics Div.
Joplin, MO

Eastman Kodak Co.
Rochester, NY

ECO Energy Conversion
Newton, MA

EG&G Princeton Applied Research Corp.
Princeton, NJ

Elcap Electronics Ltd.
Tai Po, Hong Kong

Electric Power Research Institute
Palo Alto, CA

Electrochemical Technology Corp.
Seattle, WA

Energy Conversion Devices, Inc.
Troy, MI

Energy Development Associates
A Gulf and Western Co.
Greensboro, NC

Engelhard Corp.
Engelhard Industries Div.
Iselin, NJ

Ever Ready Co. (Holdings) Ltd.
Whetstone, London, England

Exide Corp.
Yardley, PA

Exmet Corp.
Bridgeport, CT